华南晚中生代伸展构造

Wenbin Ji

ÉCOLE DOCTORALE SCIENCES DE LA TERRE ET DE L'UNIVERS

Institut des Sciences de la Terre d'Orleans (ISTO)
Institut des Géologie et Géophysique (IGGCAS)

THÈSE EN COTUTELLE INTERNATIONALE présentée par **:**

Wenbin Ji

soutenue le : 17 Octobre 2014

pour obtenir le grade de :
Docteur de l'université d'Orléans
et de l'Institut des Géologie et Géophysique

Discipline : Sciences de la Terre et de l'Univers

Late Mesozoic extensional tectonics in South China

THÈSE dirigée par :

Michel FAURE	Professeur, Université d'Orléans
Wei LIN	Professeur, Institute of Geology and Geophysics, CAS

RAPPORTEURS :

Yunpeng Dong	Professeur, Northwest University (Xi'an)
Guang ZHU	Professeur, Hefei University of Technology

JURY :

Michel FAURE	Professeur, Université d'Orléans
Wei LIN	Professeur, Institute of Geology and Geophysics, CAS
Yan CHEN	Professeur, Université d'Orléans
Bruno SCAILLET	Professeur, Université d'Orléans
Bei XU	Professeur, Peking University
Junlai LIU	Professeur, China University of Geosciences (Beijing)
Shihong ZHANG	Professeur, China University of Geosciences (Beijing)
Tao WANG	Professeur, Chinese Academy of Geological Sciences

华南晚中生代伸展构造

摘 要

欧亚大陆东缘晚中生代伸展构造发育十分显著, 表现为大量的伸展穹隆(变质核杂岩, 岩浆穹隆或同构造岩浆岩, 以及相应的拆离断层或韧性正断层)和断陷盆地. 本论文选取华南板块三个不同构造部位发育的晚中生代伸展构造: (1)华南板块北缘高压/超高压造山带中的桐柏山和大别山, 以及红安地块西南部的双峰尖和大磊山; (2)江南造山带中段的大云山-幕阜山复式岩体; (3)扬子克拉通之上的黄陵背斜, 进行了详细的构造地质学、磁化率各向异性(AMS)和年代学(锆石和榍石U-Pb, 独居石U-Th-Pb, 角闪石、云母和钾长石$^{40}Ar/^{39}Ar$)研究.

研究表明不同构造部位的伸展构造表现并不完全一致. 桐柏山核部的桐柏杂岩和大别山中部的中大别杂岩构成了两个叠加在三叠纪高压/超高压造山带之上的白垩纪伸展构造, 在构造样式上分别表现为巨型的A型伸展背形和造山带规模的变质核杂岩. 拆离断层围绕于杂岩的周缘, 杂岩与拆离断层的主期变形以NW-SE向的矿物拉伸线理和上部向NW的运动学为特点. 伴随同时期的混合岩化作用和同构造的侵入体, 这一伸展作用可能开始于约145 Ma, 至130 Ma以造山带山根的垮塌为标志达到峰期. 此外, 桐柏山、双峰尖、大磊山和大别山还共同记录了稍晚一期(110-90 Ma)伸展构造. 大云山-幕阜山岩基由晚侏罗世(150 Ma左右)和早白垩世(132 Ma左右)两期侵入体组成, 其中晚期侵入体是在NW-SE向伸展作用下同构造侵位的, 以岩体西部边缘发育单向拆离断层为特点, 对应于早白垩世的地壳减薄过程; 而早期侵入体则记录了NE-SW向应力场, 推测其可能代表了晚侏罗世挤压作用下地壳的加厚过程. 黄陵背斜表现为发育于盖层中近N-S向的不对称穹状构造, 两翼西陡东缓, 相应的岩石变形以相背的重力滑脱和层滑特点, 构造叠加关系和冷却史均一致指示其形成于晚侏罗-早白垩纪之间. 这一系列由深至浅的白垩纪伸展构造(具极强伸展强度的中下地壳折返, 具有限伸展幅度的同构造花岗岩侵位, 沉积盖层记录的极弱伸展变形)表明华南地区同样经历了与华北克拉通破坏过程中相对应的区域伸展作用.

通过区域上的对比研究, 认为欧亚大陆东缘晚中生代伸展构造呈大范围“面状”发育(从俄罗斯泛贝加尔一直至我国华南内陆地区均有分布), 构成了全球最大的地壳伸展区, 其记录了大区域上的 NW-SE 向伸展作用, 并且这一伸展作用似乎具有向华南内陆减弱的趋势. 这些伸展构造使地壳不同层次的岩石沿拆离断层折返至地表, 从而使中下地壳结构发生了强烈的改造. 各个研究区所涉及的伸展穹隆及其相关的拆离断层所表现的伸展峰期时间均在早白垩世, 集中于 130-126 Ma 之间. 绝大多数的伸展穹隆发育在岩石圈薄弱带位置(或叠加在先存造山带之上), 岩石圈根部不同规模的拆沉是这个巨型伸展区形成的主导机制. 本论文为探讨欧亚大陆东缘晚中生代伸展构造发育的时空格架及其动力学背景提供了直接的构造证据.

关键词: 华南板块, 晚中生代伸展构造, 变质核杂岩, 同构造花岗岩, 华北克拉通破坏

Late Mesozoic extensional tectonics in South China

Abstract

Late Mesozoic extensional tectonics is widespread in the eastern Eurasia, as manifested by extensional domes (metamorphic core complexes (MCC), syn-tectonic plutons and related ductile normal faults or detachments) and rift basins. This thesis selected Late Mesozoic extensional structures developed in three different tectonic locations of the South China block: (1) the Tongbai-Dabie HP/UHP orogenic belt along the northern edge of the South China block; (2) the Dayunshan-Mufushan batholith in the middle segment of the Jiangnan orogen; (3) the Huangling anticline within the Yangtze craton. Detailed studies by structural geology, anisotropy of magnetic susceptibility (AMS) and geochronology (zircon and titanite U-Pb dating, monazite U-Th-Pb dating, amphibole、mica and K-feldspar $^{40}Ar/^{39}Ar$ dating) were conducted.

The expression of these extensional structures is not same. The Tongbaishan complex and the Central Dabieshan complexes constitute two extensional structures superimposed on the Triassic Tongbai-Dabie orogen. They behaved respectively as a huge A-type extensional antiform and an orogen-scale metamorphic core complex. Detachment faults developed at periphery of these two complexes. The deformation is characterized by a NW-SE trending mineral and stretching lineation and top-to-the-NW kinematics. Coeval with migmatization and syn-tectonic magmatism, the extensional regime started at ca. 145 Ma, and approached its climax at ca. 130 Ma that was signaled by removal of the pre-eixsting orogen root. Additionally, the Tongbaishan and Dabieshan, together with the Shuangfengjian and Daleishan in the Hong'an area also recorded a late (110-90 Ma) extensional event. The Dayunshan-Mufushan batholith is composed of two phases of granitic intrusions with Late Jurassic (ca. 150) and Early Cretaceous (ca. 132 Ma) ages, respectively. The late pluton emplaced under a NW-SE extensional setting corresponding to the Early Cretaceous crustal thinning process, with a single detachment fault developed along its western margin; while the early pluton recorded a NE-SW stress, which might represent a crustal thickening process by Late Jurassic compression. The Huangling anticline is a nearly N-S striking asymmetric dome, with a steep western flank and a gentle eastern flank. The sedimentary cover on

the two flanks was involved in a series of oppositely directed gravitational décollement and layer-parallel slipping that accommodated to its uplifting. According to the structural superposition relationships, the Huangling anticline formed between the Late Jurassic and Early Cretaceous, which is consistent with the obvious cooling process revealed by thermochronology. Above series of Cretaceous extensional structures in different tectonic levels (exhumation of middle-lower crust by strong stretching, syn-tectonic emplacement of granitic pluton with limited stretching amount, deformation of sedimentary cover under a weak extension) indicates that the South China was involved in the regional extensional regime responsible for the destruction of the North China craton.

Late Mesozoic extensional tectonics in eastern Eurasia (from the Transbaikalia region in Russia to inland of the South China) constitutes the largest crustal extensional province in the world. A general Cretaceous NW-SE stretching has been documented, which seems to become weak toward the South China inland. Deep crustal rocks were exhumed from different levels by detachment faults in these extensional structures that induced intensive reworking of the middle-lower crustal structure. Studies on the extensional domes and related detachment faults reveal that peak of exhumation occurred at 130-126 Ma. Most the extensional domes developed in the lithospheric weak zones (or overprinted on pre-existing orogens), delamination of thickened lithospheric keel in different sizes could be considered as the leading mechanism of the extensional province. This work provides fist-hand structural evidence for further discussing the temporal-spatial framework and geodynamic setting of the Cretaceous extensional tectonic in the eastern Eurasia.

Key word: South China block, Late Mesozoic extensional tectonics, Metamorphic core complex, Syn-tectonic pluton, Destruction of the North China craton

致 谢 Acknowledgements

六年硕博研究生的结束无疑是对学生时代划上了一个句号.

感谢导师林伟研究员在这六年时间内为我付出的一切. 从论文的选题、野外和室内工作、学术报告的讲演、学术论文的发表、最终毕业论文的写作, 每一步都少不了林老师的悉心指导和心血. 林老师高度的责任感、严谨的学术态度和广博的专业知识, 这一切都在教导着我如何做人、做事和做学问.

感谢法方导师奥尔良大学地球科学研究所(ISTO)的陈岩教授和 Michel Faure 教授对我的指导. 陈岩教授一切为学生的崇高人格魅力让我很受感动, 不仅在专业上让我受教, 在生活上的帮助也让我顺利地度过了在法国的时光. Michel Faure 教授深厚的学术造诣以及真诚的性格让我受益匪浅.

感谢学科组王清晨研究员和李忠研究员在研究生期间对我的关怀. 感谢合肥工业大学石永红教授对我的帮助, 犹记得石老师带我第一次挺进大别山. 感谢西北大学董云鹏教授自我从本科到研究生期间一直对我的鼓励.

感谢司机师傅李金雁在多次野外工作中不辞辛苦的帮助, 他的豁达开朗给每次野外都增添了无限的欢乐.

和师兄弟陈科、褚杨、王军、陈泽超、王镇远、刘飞、薛振华、万加亮、阳孝法、陶辉飞、邱振、姜琳、卫巍等在一起快乐生活和努力学习的时光将成为我美好的记忆, 感谢他们兄弟般的情谊. 感谢室友饶松六年的陪伴. 感谢同班同学对我的关心和帮助.

感谢所教育处和图书馆的老师为我们提供了良好的生活条件和学习环境.

在法留学期间, 有幸参加了 ISTO 的阿尔卑斯和爱琴海地区野外教学实习, 感谢 Laurent Jolivet 教授的组织和讲解以及在野外对我的帮助, 同时还有在 ISTO 与我交流较多的法国老师及研究生. 感谢许多同在奥尔良留学的国内同学对我生活上的帮助.

最后, 特别感谢我的父母及家人. 二十余年求学生涯, 父母的辛苦和负担我无法描述. 你们无私的爱以及对我默默的支持, 给了我一路向前的勇气和力量.

谨以此论文献给我所有的亲人、师长、朋友和同学!

作者: 冀文斌

2014 年 10 月

目 录

Content

第一章 前 言Chapter 1 Introduction

1 研究背景及科学问题 Study background and scientific questions

华北克拉通是目前世界上唯一得到确证的原有巨厚太古宙岩石圈地幔遭受强烈破坏的地区. 华北克拉通破坏研究已经成为当今国际地球科学领域的前沿和热点问题之一(Carlson et al., 2005; 周新华, 2009). 自上世纪90年代早期, 中外学者提出华北岩石圈减薄或克拉通破坏这一命题以来, 大量的研究工作集中于对这一问题的研究. 尤其是以“华北克拉通破坏”重大研究计划的开展为契机, 掀起了新一轮研究热潮.

尽管目前学术界多数认同华北克拉通破坏这一基本事实, 但关于华北克拉通破坏的一些重大问题存在激烈的争论(Menzies et al., 2007; 吴福元等, 2008; 朱日祥等, 2011). (1)时间: 绝大部分学者认为中国东部岩石圈减薄发生在晚中生代, 但对减薄发生的起始时间和高峰期存在三叠纪、侏罗纪、早白垩世或新生代等不同认识(徐义刚等, 2009; R.X. Zhu et al., 2012). (2)空间范围: 主要集中在太行山以东区域, 中部和西部只是局部减薄, 即以南北重力梯度带为界, 相应的岩石圈厚度由西部鄂尔多斯盆地约200 km, 至东部华北裂谷盆地只有约80 km (陈凌等, 2010; Chen, 2010); 但仅限于华北克拉通本身, 还是包括东北和华南地区在内的整个中国东部也经历过同样的过程? 破坏出现在华北克拉通内部还是边缘或者是在碰撞造山带的根部? 在深度上, 华北克拉通破坏发生在岩石圈地幔的内部还是涉及到地壳? (3)机制: 目前提出的模型主要是热-化学侵蚀(Xu, 2001)和拆沉作用(Gao et al., 2002)两类, 分别对应岩石圈减薄的化学过程(自下而上)和物理过程(自上而下); 此外还有橄榄岩-熔体反应(Zhang, 2005)、俯冲脱水模型和岩石圈拉张等. (4)动力学背景: 多倾向于与古太平洋板块俯冲密切相关(Ren et al., 2002; Wu et al., 2005; G. Zhu et al., 2012), 也提出了西伯利亚-蒙古板块与华北板块的拼合(即与蒙古-鄂霍次克洋的闭合相关)(Zorin, 1999; Meng, 2003)、华北与华南板块的拼合(杨进辉和吴福元, 2009)、印度-欧亚大陆的碰撞和地幔柱等模式, 抑或多板块相互作用(董树文等, 2007, 2008; Zhai et al., 2007; S.Z. Li et al., 2012a).

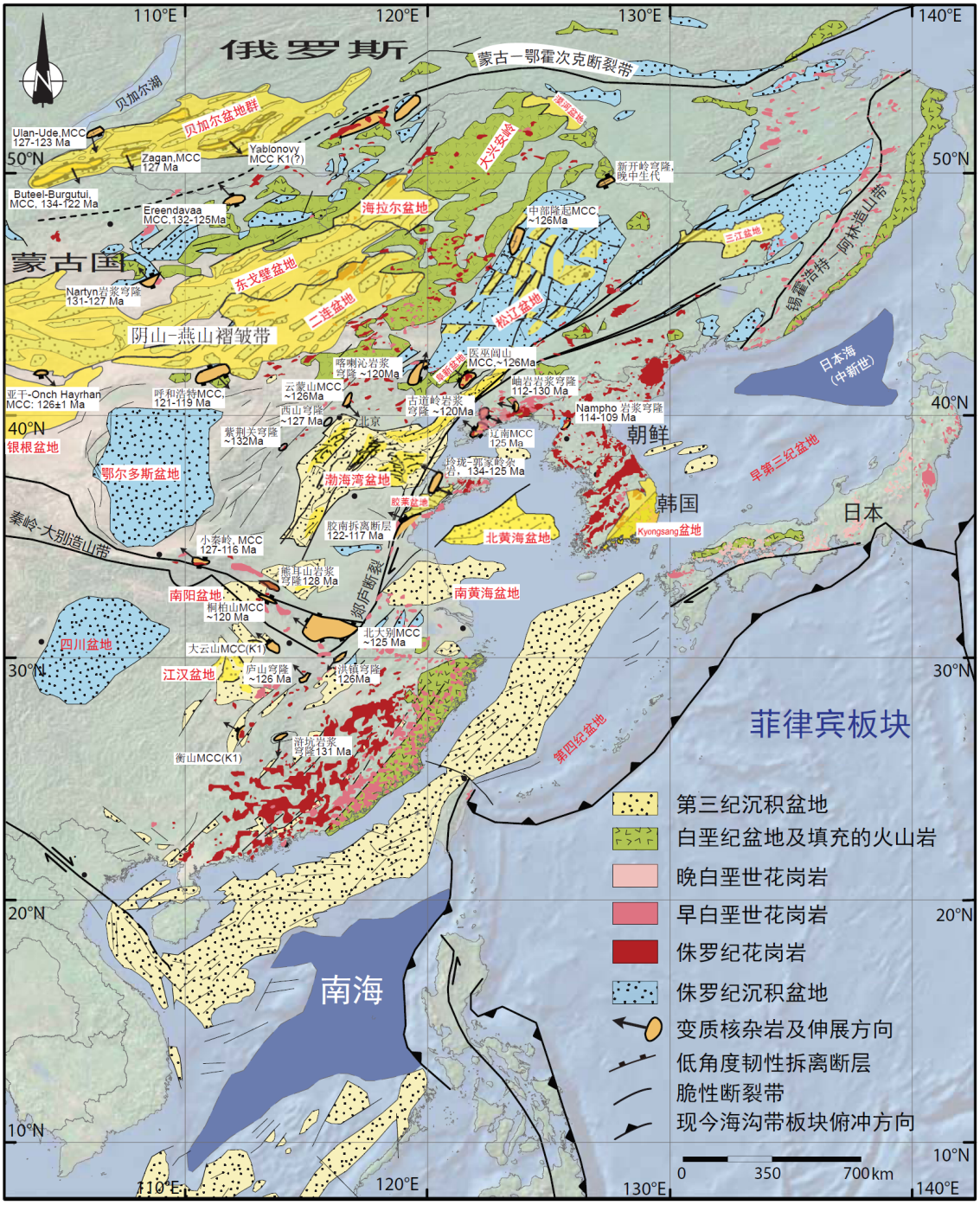

图 1-1 欧亚大陆东缘晚中生代伸展构造图(引自林伟等, 2013a)

Figure 1-1 Tectonic map of Late Mesozoic extensional tectonics in the eastern margin of Eurasin (modified after Lin et al., 2013a)

事实上，在欧亚大陆东缘发育有一系列晚中生代的伸展构造如伸展穹隆 (Lin and Wang, 2006; T. Wang et al., 2011; Lin et al., 2013a; 林伟等, 2013a)和断陷盆地 (Ren et al., 2002; Meng et al., 2003; S.Z. Li et al., 2012a)，以及与之相伴的巨量岩浆活动(Wu et al., 2005; Yang et al., 2008). 近二十年来，大量的地质、地球化学和地球

物理成果加深了对华北克拉通破坏的科学认识, 多学科的综合研究形成了从浅层次地壳构造-岩浆-沉积作用到深部岩石圈-软流圈结构及壳幔相互作用等完整的研究体系. 其中深入的构造地质学工作为限定克拉通破坏的峰期时间和空间范围做出了重要的贡献(林伟等, 2013a及其参考文献). 晚中生代的变质核杂岩及岩浆穹隆作为伸展构造的典型表现形式广泛分布于华北克拉通及其邻区, 构成了全球最大的地壳伸展区(图1-1), 例如俄罗斯泛贝加尔和蒙古国北部地区的Buteel-Burgutoy变质核杂岩(Mazukabzov et al., 2006; Donskaya et al., 2008)、Zagan变质核杂岩(Sklyarov et al., 1994; Donskaya et al., 2008)、Ereendavaa变质核杂岩(Daoudene et al., 2009, 2011)等; 华北西部和东部地区的亚干(郑亚东和张青, 1993; Webb et al., 1999a)、呼和浩特变质核杂岩(Darby et al., 2001; Davis et al., 2002; Davis, and Darby, 2010; Guo et al., 2012)、喀喇沁岩浆穹隆(邵济安等, 2001; Han et al., 2001; 王新社和郑亚东, 2005)、医巫间山变质核杂岩(马寅生等, 1999; Darby et al., 2004; Zhang et al., 2012; Lin et al., 2013a, 2013b)、西山岩浆穹隆(宋鸿林, 1996; He et al., 2009; Yan et al., 2006, 2010; Y. Wang et al., 2011)、云蒙山变质核杂岩(Davis et al., 1996, 2001)、辽东半岛伸展区包括辽南变质核杂岩及一些同构造花岗岩和拆离断层(Liu et al., 2005; Lin et al., 2007a, 2008a, 2011; 林伟等, 2011a; 刘俊来等, 2011; Charles et al., 2012; Liu et al., 2013)、胶东半岛伸展区包括玲珑-郭家岭杂岩体(Charles et al., 2011)和胶南拆离断层带(Hacker et al., 2009); 华北南缘的小秦岭变质核杂岩(Zhang and Zheng, 1999).

华南板块和华北板块自三叠纪拼合以来, 共同作为欧亚大陆的一部分转入古太平洋俯冲构造体系之中. 晚中生代华南板块同样发育大规模的岩浆岩以及众多的白垩-第三纪地堑-半地堑盆地, 这一地质面貌被誉为“华南盆岭省”(Glider et al., 1996; Li, 2000; 舒良树等, 2004; 舒良树和王德滋, 2006; Shu et al., 2009). 另外, 华南西部四川盆地的岩石圈厚度与东部华夏地区也存在着明显的东西差异(Zhang et al., 2011). 这些都表明华南板块在晚中生代可能也经历了类似于华北克拉通破坏的岩石圈减薄或地壳伸展过程. 与华北克拉通相比较而言, 有关华南晚中生代构造演化的研究则主要以大规模分布的岩浆岩为重心, 开展了大量的岩石学、地球化学和年代学工作, 并由此探讨了古太平洋俯冲作用与岩浆活动之间可能的动力学联系, 涉及活动大陆边缘、弧后扩张、俯冲后撤、平板俯冲、洋脊俯冲或板片撕裂

等(Zhou and Li, 2000; Zhou et al., 2006; Li and Li, 2007; Ling et al., 2009; Jiang et al., 2009, 2011; Wu et al., 2012; X.H. Li et al., 2013). 但是这些研究并没有形成华南晚中生代构造演化的完整动力学模式, 究其原因是缺少了浅表构造研究的约束(舒良树和周新民, 2002; 沈晓明等, 2008; 张岳桥等, 2012). 此外, 南北重力梯度带作为中国大陆地壳和岩石圈厚度变化的东西界线, 它在华南是否也代表着岩石圈减薄的西部边界值得深入探究. 因此, 开展详细的构造地质学工作对于研究华南板块晚中生代构造演化将会起到十分重要的推动作用.

华南板块北部无论是板块边缘与大陆深俯冲相关的桐柏-大别造山带, 还是近内陆地区的大云山-幕阜山岩基和黄陵背斜, 在晚中生代均发育了明显的伸展构造. 最新的年代学结果指示桐柏山核部的桐柏杂岩可能是一个早白垩世的花岗杂岩体, 而非前寒武纪地质体(刘晓春等, 2011). 初步研究表明大别山具有典型变质核杂岩特点, 其受白垩纪构造-热事件影响最为明显——大规模的岩浆活动, 造山带中部强烈的混合岩化作用及穹隆周缘发育明显的拆离断层(冀文斌等, 2011). 位于江南造山带中段的大云山-幕阜山岩基西部大云山地区岩体与盖层之间发育半环状韧性剪切带, 被认为具变质核杂岩的特点(喻爱南等, 1998). 野外调查显示黄陵背斜两翼沉积盖层以相背的滑脱和层滑变形为特点, 白垩纪磨拉石盆地叠覆于卷入变形的地层之上(王军等, 2010; Ji et al., 2014).

本论文以华南板块北部晚中生代伸展构造发育的典型地区：桐柏-大别造山带、大云山-幕阜山和黄陵背斜为研究靶区, 将科学问题立足于“**华南典型地区晚中生代伸展构造的发育特征及其对华北克拉通破坏时空上的响应**”, 通过针对性的研究, 约束华南地区晚中生代伸展构造发育的精确时限和空间展布范围, 并与华北进一步对比探讨其成因, 为我国东部晚中生代岩石圈减薄的相关问题提供新的思路.

2 研究内容和方法Scope and methods

本论文以“华南板块晚中生代伸展构造”为研究主题, 选取桐柏-大别造山带、黄陵背斜、大云山-幕阜山为研究区, 涉及的研究方法主要包括构造解析、磁组构(AMS), 锆石和榍石U-Pb定年、独居石电子探针定年和$^{40}Ar/^{39}Ar$定年.

2.1 研究内容Research scope

(1)桐柏-大别造山带白垩纪伸展构造的厘定

桐柏山核部的伸展背形和大别山中部的穹隆、红安地体西南部的双峰尖和大磊山地区均显示出白垩纪伸展构造的叠加作用. 对这些伸展构造进行详细的构造解析, 勾画其几何学和运动学特征; 选取构造岩进行$^{40}Ar/^{39}Ar$变形年代学研究, 确定伸展构造发生的精确时限; 探讨这一造山后伸展垮塌过程对我国东部高压/超高压造山带的改造作用及其动力学背景.

(2)大云山-幕阜山岩基的构造侵位过程研究

从花岗岩和围岩及其接触带的构造几何学和运动学入手, 对与岩体侵位相关的构造变形进行分析; 为了全面的了解岩体的内部构造特征, 本次研究对岩体进行了系统的磁化率各向异性(AMS)研究, 以获得岩石的磁组构; 利用锆石U-Pb及独居石电子探针定年确定岩体的侵位时代及相关的变质变形时代; 综合探讨岩体的构造侵位过程及其构造含义.

(3)黄陵背斜构造解析及其热演化历史研究

黄陵背斜的构造几何学形态, 核部变质基底和外围沉积盖层的变形特征; 选取黄陵背斜核部不同类型岩石(花岗岩、片麻岩和混合岩)中的钾长石进行多重扩散域(MDD)热模拟研究, 结合已有U-Pb, $^{40}Ar/^{39}Ar$, Rb-Sr和FT与(U-Th)/He多系统年代学数据构建黄陵背斜自新元古代以来的热演化历史; 并结合区域构造和黄陵地区沉积发展史, 探讨黄陵背斜的隆升过程及其成因机制.

(4)华南晚中生代伸展构造的演化特点

综合已有研究, 分析华南晚中生代伸展构造的时空特点, 并与华北克拉通破坏研究相对比, 以期为整个中国东部晚中生代岩石圈减薄的时间、范围、方式及其动力学机制问题提供制约.

2.2 研究方法Research methods

(1)资料调研: 全面收集和评估与论文相关的地质、地球化学、地球物理资料; 在及时了解和掌握研究领域的国内外前沿动态和研究区研究进展的基础上, 归纳

已有的研究成果和存在问题, 为后续的野外和室内研究提供指导和依据.

(2)野外地质调查和构造地质学研究: 以 1: 20 万区域地质资料为基础同时结合局部地区 1: 5 万区域地质资料, 以关键剖面为重点并结合面上的观测点, 开展详细的野外地质调查, 对研究区进行岩石构造单元的划分, 并系统采集岩石学和构造研究所需样品. 将野外露头-手标本-薄片不同尺度的构造变形特征有机地结合在一起, 精细刻画不同岩石构造单元的几何学和运动学; 恢复不同类型变形发育的空间展布范围及其构造配置和叠加关系, 进而进行变形期次的划分; 探讨不同期次构造事件发生的区域构造背景, 结合已有的地球化学和地球物理资料对构造解释进行佐证.

(3)磁化率各向异性(AMS)研究: 对大云山-幕阜山岩基及大磊山花岗片麻岩地体进行了磁组构研究. 首先对研究区交通情况和野外露头进行调研, 为AMS的采样工作做准备, 然后使用钻机在野外系统采集定向样品. 通过磁组构的测量获得岩石的磁面理和磁线理, 进而结合构造从整体上分析地质体的构造几何学及其受到的区域应力场特征.

(4)年代学研究: 利用岩锆石和榍石U-Pb定年以及独居石电子探针定年示踪变质岩的原岩和变质时代, 岩浆岩的侵位时代. 在构造解析和矿物变形特征观察的基础上, 选择研究区内的韧性剪切带或强应变带中构造岩的同变形矿物(角闪石、白云母、黑云母、钾长石等)开展$^{40}Ar/^{39}Ar$年代学分析, 限定变形发生的时代

3 论文工作量、主要研究成果和创新点 Workload, main results and innovative points

3.1论文工作量Workload

本论文所涉及的工作量如下表所示

表 1.1 论文工作量

序号	工作内容	数量	单位
1	野外地质调查时间	6	月

2	野外观测点	963	个
3	野外照片	> 1000	张
4	实测剖面	20	条
5	样品采集	275	块
6	绘制图件	60	幅
7	岩石薄片观察	350	片
8	AMS 采样点	128	个
9	AMS 样品测试	901	个
10	岩石磁学实验	18	件
11	锆石和榍石 U-Pb 定年	9	件
12	独居石电子探针定年	3	件
13	$^{40}Ar/^{39}Ar$ 年代学	12	件

3.2 主要研究成果Main results

1)多数研究者认为桐柏山核部的桐柏杂岩是在走滑作用下发生向南东的侧向挤出而隆升的, 本论文的研究结果并不支持这一认识. 构造解析表明桐柏杂岩总体上是在NW-SE近水平伸展作用下形成的具有A型褶皱特点的伸展背形或变质核杂岩. 虽然桐柏杂岩南北坡的面理倾向相反, 且靠近边界剪切带面理时常较陡, 但矿物拉伸线理稳定在NW-SE向, 运动学一致显示为上部向NW的剪切变形. 也就是说, 从杂岩内部到边界剪切带, 其几何学和运动学具有协调一致的特点. 这表明桐柏杂岩南北边界并不是典型的走滑剪切带, 现今表面上观察到的走滑现象实际上是早期的拆离面发生弯曲的表现.

大别山中部的中大别穹隆作为一个大规模的伸展构造已被人们广泛接受, 然而涉及中大别杂岩及其边界剪切带或断裂带的构造解析和穹隆的形成机制仍存在较大的争议. 结合前人的工作及我们详细的构造解析, 认为中大别穹隆为形成于NW-SE向伸展体制下的具造山带规模的变质核杂岩. 现今大别山的几何形态几乎完全由中大别穹隆所控制. 中大别杂岩(混合片麻岩以及残存的超高压变质岩)代表了变质核杂岩的下盘. 北部边界晓天-磨子潭断裂与西部边界商麻断裂构

成了穹隆西北翼的一个统一的弧形拆离断层. 而南部边界水吼-五河剪切和浠水剪切带(表现为马尾状, 包括早期的XSF-N和晚期的XSF-S两条剪切带)则构成了穹隆东南翼的多重拆离断层组合. 中大别杂岩与拆离断层发育一致的NW-SE向矿物拉伸线理和上部指向NW运动学.

一般认为夹持于桐柏山和大别山之间的红安地体受白垩纪构造-热事件影响较小, 本次研究在红安地体西南部的双峰尖和大磊山地区识别出了白垩纪的伸展构造. 双峰尖的几何形态与桐柏杂岩类似表现为A型伸展背形, 大磊山(或大悟穹隆)则显示为半环状单斜构造. 双峰尖伸展背形的变形特征以NW-SE向矿物拉伸线理和上部指向NW运动学为特点. 大磊山穹隆核部花岗质片麻岩线性构造发育不明显,磁化率各向异性(AMS)研究表明磁线理以NW-SE向为主导. 在构造层次上, 这两个伸展构造明显位于桐柏杂岩和中大别杂岩之上, 代表了地壳浅层次的拆离.

在构造解析的基础上, 年代学研究揭示桐柏山和大别山伸展作用开始时间可能在145 Ma, 并在130 Ma左右达到了峰期, 以造山带根部的大规模垮塌或拆沉为标志. 此外, 桐柏山、大别山、双峰尖和大磊山还共同记录了稍晚一期大致约110-90 Ma的伸展构造. 双峰尖和大磊山主要显示此晚期伸展的记录, 晚期伸展构造在桐柏山完全以早期原有的拆离断层为基础持续发育; 在大别山则共用了部分早期拆离断层, 并有新生拆离断层的形成. 从几何学和运动学的匹配关系来看, 推测桐柏-大别山造山带中发育的白垩纪拆离断层在早期其原始发育状态为处于中地壳的近水平拆离面, 可能对应于中下地壳物质在早白垩世发生部分熔融而塑性流动的顶面与上覆高压/超高压变质岩片之间的解耦面. 早期(145-130 Ma)以高温条件下的近水平拆离为主, 代表了研究区的主期变形. 之后由于折返过程中的褶皱作用, 拆离面发生了弧形褶曲, 并可能在递进变形过程中发生了晚期(110-90 Ma)的二次拆离.

综合分析, 认为桐柏杂岩和中大别杂岩是由相对原地的扬子基底片麻岩和位于中下地壳的高压/超高压变质岩在早白垩世发生深熔作用的产物. 白垩纪伸展构造的叠加强烈地改造了桐柏-大别造山带早中生代的构造格局. 桐柏杂岩上覆的高压岩片被分割成了南北两部分, 而大别山南部三叠纪的变质序列(包括高压/超

高压岩片、宿松群和张八岭群)则表现为被拆离断层肢解的构造岩片. 桐柏-大别造山带伸展构造的形成体现了岩石圈不同层次地质过程的综合效应, 具体表现为核部杂岩体上覆岩片的拆离和剥蚀去顶, 中下地壳可能存在向SE的通道流, 造山带根部的垮塌或拆沉作用. 对比于中国东部广泛发育的白垩纪伸展构造, 认为其与华北克拉通破坏具有相同的动力学背景, 是中国东部晚中生代岩石圈减薄的响应, 只不过叠加在高压/超高压造山带之上.

2)华南分布有大面积晚中生代的花岗岩类, 但关于花岗岩的构造研究十分薄弱. 大云山-幕阜山复式岩体是华南内陆江南造山带中段较大的晚中生代花岗岩基之一. 本论文应用构造、磁化率各向异性和年代学相结合的方法对该岩体的构造侵位过程进行了详细的研究, 厘定出了早晚两期同构造的侵入体及其相应的两期构造变形. D_1 事件在早期侵入体(黑云母二长花岗岩和黑云母花岗闪长岩)南部边缘的片麻状花岗岩及其围岩接触变质带中表现较为明显, 可见 NE-SW 向矿物拉伸线理及上部向 SW 的剪切变形. D_2 事件以晚期侵入体(二云母二长花岗岩)西部舌状边缘大云山拆离断层的发育为鲜明特色, 卷入韧性变形的花岗岩及其围岩接触变质岩中发育 NW-SE 向的矿物拉伸线理及上部向 NW 的剪切变形. AMS 结果揭示早晚两期侵入体的内部组构均以岩浆流动组构为主, 同样分辨出了两组线理, 与野外观察到的两期构造十分吻合. 重力资料的初步分析也表明早晚两期侵入体的根部或重心分别位于岩体的北部和中部偏东位置, 这从侧面印证了构造和 AMS 的研究结果.

SIMS 锆石 U-Pb 定年和独居石电子探针定年结果表明早期侵入体的侵位年龄在 150 Ma 左右, 也即 D_1 事件发生在晚侏罗世, 而晚期侵入体的侵位年龄及其相关的变质变形时代在 132 Ma 左右, 也即 D_2 事件发生在早白垩世. 综合分析, 倾向于认为 D_1 事件可能代表了近 N-S 向的地壳挤压加厚过程, 而 D_2 事件与桐柏-大别造山带中发育的白垩纪伸展构造完全可以对比, 体现了中国东部早白垩世区域 NW-SE 向的伸展作用无疑.

3)扬子克拉通之上的黄陵背斜是研究华南构造演化的一个重要窗口, 但其成因问题一直悬而未决. 详细的构造解析表明, 黄陵背斜的几何形态表现为一个西翼陡东翼缓的不对称穹状背斜构造. 响应于穹隆作用, 黄陵背斜两翼沉积盖层以

相背的滑脱和层滑变形为特点. 随后的脆性正断作用还控制了背斜两侧地堑-半地堑盆地的发育. 背斜西翼晚侏罗世地层的卷入和两翼之上早白垩世砾岩的不整合覆盖, 将黄陵背斜的形成时间约束在晚侏罗-早白垩世之间. 从背斜核部不同类型岩石中分别选取钾长石进行 MDD 模拟研究, 并结合已有的热年代学数据, 可以给出一条约束较好的冷却曲线. 热演化历史揭示黄陵背斜自震旦纪以来可能为扬子克拉通上的继承性古隆起, 华南早古生代和早中生代的构造事件对其影响微弱. 直至晚侏罗世-早白垩世(160 Ma-110 Ma)期间经历了明显但实际上十分缓慢(2-3 °C/Ma)的冷却隆升过程, 对应于背斜的形成. 从整个中国东部考虑, 认为黄陵背斜所记录的微弱伸展作用体现了中国东部晚中生代岩石圈减薄在稳定克拉通上的表现.

4)结合洪镇、庐山、武功山和衡山等地区发育的晚中生代伸展构造,华南晚中生代伸展构造大致沿板块北缘的高压/超高压造山带和中部的江南造山带两个构造线方向展布. 北缘的高压/超高压造山带体现了明显的巨量伸展-A 型伸展背形或变质核杂岩构造, 而在靠近内陆地区的伸展构造多表现为岩浆穹隆或同构造花岗岩及局部发育的拆离断层 (洪镇、庐山、武功山、大云山和衡山). 此外, 位于刚性华南(扬子克拉通)基底之上的黄陵背斜仅仅表现为缓慢的冷却及抬升去顶过程而已, 虽然其也表现出了一定的岩石变形. 与华北相比, 华南晚中生代的伸展构造表现出明显的不均一性, 但总体上伸展方向和发育峰期时间与华北一致. 晚中生代伸展构造从俄罗斯泛贝加尔地区至我国华南内陆均十分发育, 其记录了大区域上 NW-SE 向的伸展作用, 并且不同地区伸展穹隆及其相关的拆离断层所表现的折返峰期时间集中在 130-126 Ma 之间. 明显不同于美国西部的盆岭省的弧后伸展扩张机制, 欧亚大陆东缘的伸展构造在成因机制很大程度上受深部岩石圈拆沉作用的控制. 它揭示了在稳定大陆岩石圈性质和厚度发生变化的过程中, 中下地壳的结构受到强烈的改造, 伸展构造的研究为其提供了独立的构造地质学证据.

3.3 创新点Innovative points

1)将桐柏-大别造山带中叠加的白垩纪伸展构造从早期的高压/超高压造山带中有效地分离出来, 并将这一造山后伸展垮塌过程与中国东部的岩石圈减薄相关联.

2)从方法学上将构造地质学、磁化率各向异性(AMS)和年代学有效结合对花岗岩的构造侵位过程进行多学科研究, 识别出大云山-幕阜山复式岩体所记录的两期构造事件, 这对了解华南晚中生代的构造演化具有突出的意义.

3)提出了伸展隆升模式来解释黄陵背斜的成因机制, 认为黄陵背斜可能代表了中国东部晚中生代岩石圈减薄的西部边界.

4)从华南的视角审视华北克拉通破坏, 华南板块一系列晚中生代伸展构造的发育表明华北克拉通破坏并不是“孤独”的, 其从属于欧亚大陆东缘巨大的地壳伸展区.

第二章 华南板块中生代构造演化的基本特征

Chapter 2 Principal features of the Mesozic tectonic envolution in South China

华南板块主要由扬子克拉通和华夏陆块组成，周缘被一系列造山带所围限，其北缘为秦岭-大别造山带、西北缘为龙门山褶皱冲断带，西南缘通过红河断裂与印支地块相连，而东南缘和东缘则为欧亚大陆的大陆架-边缘海区域(图 2-1).

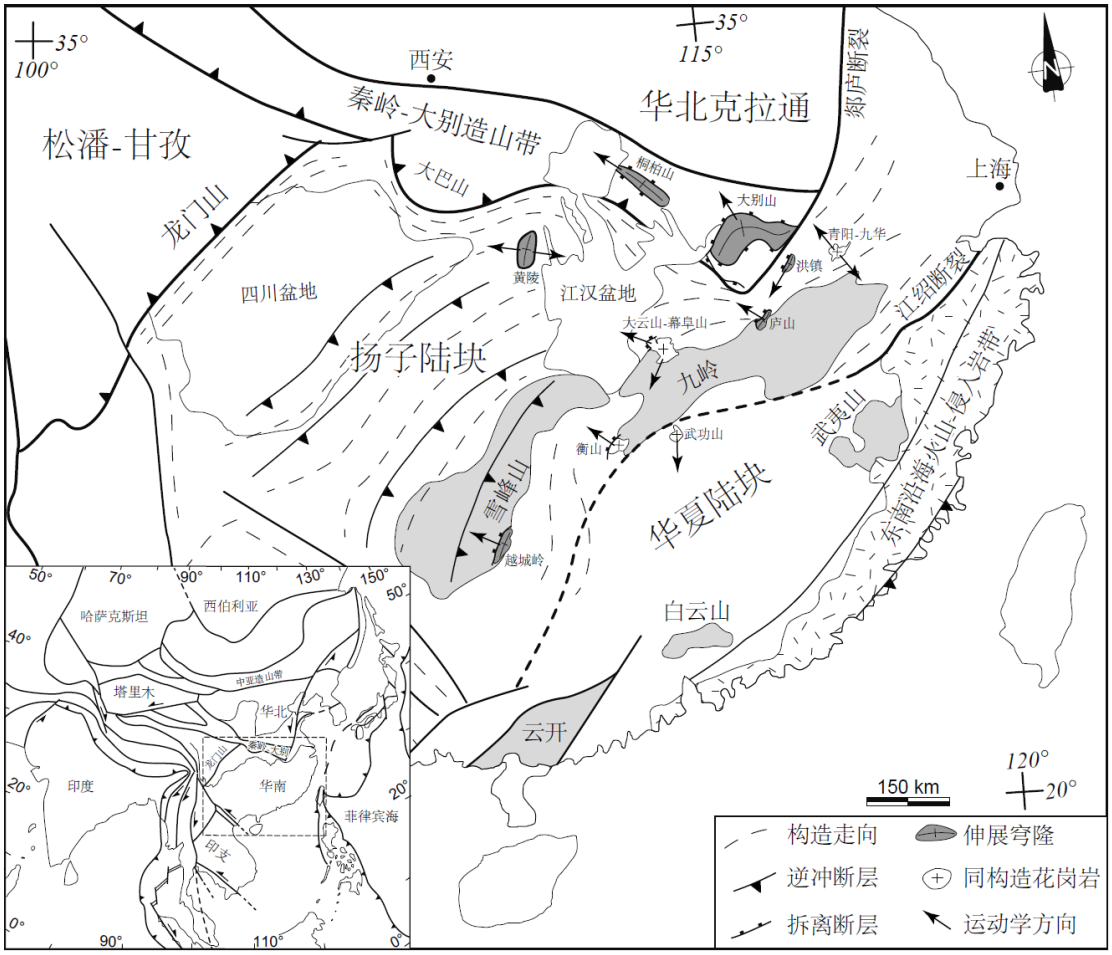

图 2-1 华南板块大地构造简图

Figure 2-1 Sketch tectonic map of South China

研究表明，扬子地块和华夏地块于中-晚元古代沿江绍缝合带拼合，导致了江南造山带的形成，而后经历了新元古代南华裂谷的发育和早古生代的陆内造山作

用(Guo et al., 1989; Charvet et al., 1996, 2013; 王清晨和蔡立国, 2007; Faure et al., 2008; Lin et al., 2008b; X.H. Li et al., 2009a; Z.X. Li et al., 2010). 华南在中生代经历了从特提斯构造域向滨太平洋构造域的转换, 早中生代多向造山作用和晚中生代构造-岩浆事件的叠加极大地改造了早期的构造形迹.

1 早中生代多向造山作用 Early Mesozoic multi-directional orogeny

早中生代华南的构造演化可谓多灾多难, 华南板块周缘的造山带基本均是在这个时期形成的. 东亚地区的东古特提斯洋发生了闭合, 华南板块受到周围板块的多向挤压造山作用. 华南北缘的秦岭-大别-苏鲁造山带以出露大规模三叠纪高压/超高压变质岩而闻名, 代表了华南板块向北发生大陆深俯冲的产物(Hacker et al., 2004; Faure et al., 2008; 郑永飞, 2008). 在秦岭-大别造山带的南缘前陆形成了一个统一的前陆盆地体系, 自东向西包括现今的鄂东南盆地、当阳盆地、秭归盆地、四川盆地北部和松潘-甘孜盆地(S.F. Liu et al., 2005; 王清晨和蔡立国, 2007). 华南板块西北缘的龙门山褶皱冲断带记录了其西侧松潘-甘孜地块在晚三叠世向四川盆地的逆冲作用, 同时在松潘-甘孜地块内发育了大量的同期岩浆岩(Burchfiel et al., 1995; Chen and Wilson, 1996; Roger et al., 2008, 2010; Yan et al., 2011). 在华南板块的西南缘, 存在一条从云南一直延伸到越南境内的被红河断裂肢解的早中生代缝合线(包括金沙江缝合线、Song Ma 缝合线-Song Chay 缝合线), 代表了印支板块与华南板块的边界, 对应于著名的印支运动(Carter et al., 2001; Lepvrier et al., 2008, 2011; Carter and Clift, 2008). 近年的研究表明受印支板块的挤压作用, 广西的云开地体和越南东北部的 Song Chay 地体均记录了印支造山带前陆地区上部向 NE 的逆冲推覆作用(Lin et al., 2008b; 林伟等, 2011b; 陈泽超等, 2013; Faure et al., 2014). 然而, Y.J. Wang et al. (2007)则认为云开大山的三叠纪变形以走滑为主, 是华南板块受到印支和华北板块的联合挤压而产生的走滑山系. 此外, Xu et al. (2011)对武夷山地区多条韧性剪切带的研究表明其在 239-230 Ma 期间经历了右旋走滑剪切作用, 认为其动力学机制和印支与华南的碰撞有关.

华南板块内部发育了宽约 1300 km 的 NE-NNE 向褶皱造山带, 这一陆内构造现象引起了众多学者的关注. 为了解释华南复杂的构造变形样式, Hsü et al. (1988, 1990)曾提出扬子与华夏在中生代发生碰撞造山的模型. 但现今华南不存在中生代

碰撞造山带, 而以陆内变形为主已经成为共识. 综合构造、岩浆和沉积等多方面证据, Li and Li (2007) 提出了古太平洋的平板俯冲模式来统一解释华南 250-190 Ma 期间的陆内造山及中生代岩浆岩的演化过程, 认为古太平洋向华南板块之下的俯冲作用可能自晚二叠世就已经开始. 不同于 Wang et al.（2005a）关于华南中部的雪峰山为形成于 217-195 Ma 期间的类似走滑断层控制的逆花状构造的认识, Chu et al. (2012a, 2012b)认为雪峰山是以发育韧性基底滑脱带和多期变形(包括早期上部向NW的主逆冲剪切, 中期上部向SE的反冲和晚期近水平的共轴挤压)为特点的典型陆内造山带, 其形成时间在 245-225 Ma 期间, 动力学机制可能与古太平洋俯冲的远程效应有关. 然而, 人们对于古太平洋开始俯冲的时间也有不同认识, 不少研究者认为这一俯冲作用始于侏罗纪(Zhou and Li, 2000; Zhou et al., 2006; 张岳桥等, 2009). 例如, 张岳桥等(2009)通过构造编图和叠加褶皱分析, 认为华南早中生代存在两个世代褶皱的横跨叠加, 早期近东西向褶皱是对三叠纪华南板块南北边缘造山事件的远程响应, 而晚期 NE-NNE 向褶皱则起源于中侏罗世古太平洋向华南大陆之下的低角度俯冲作用.

2 晚中生代构造-岩浆事件 Late Mesozoic tectonic-magamatic events

早侏罗世是华南构造-岩浆活动的相对平静期, 标志着早中生代造山作用的结束. 随着古特提斯洋的关闭, 古太平洋板块的俯冲开始起主导作用. 晚中生代, 华南板块的构造总体以伸展体制下盆-岭构造的发育为特点(Glider et al., 1996; Li, 2000; 舒良树和王德滋, 2006). 最引人注目的地质面貌是众多中-小型断陷盆地和大量岩浆岩的产出, 相邻的盆地与同期或稍早的花岗岩之间经常以正断层的关系耦合在一起. 这些盆地多由 NE-SW 走向的正断层所控制, 少数可能为走滑边界(舒良树等, 2004; Shu et al., 2009).

华南晚中生代的花岗岩在时代上可明显地划分为两个阶段, 早期(180-150 Ma)的花岗岩主要分布在南岭地区及内陆, 而晚期(140-85 Ma)的花岗岩主要分布在东南沿海地区, 长江中下游地区也有分布, 但沿长江向内陆延伸较远. 并显示出从内陆向沿海逐渐年轻的趋势(Zhou and Li, 2000; Zhou et al., 2006). 研究表明 150-140 Ma 是华南岩浆活动的一个相对平静期, 此期间的花岗岩只在长江中下游地区较为发育(X.H. Li et al., 2010, 2013; Wu et al., 2012). 另外, 在早白垩世晚期 120-110 Ma,

岩浆活动也大幅度锐减. 目前, 大多数学者倾向认为华南晚中生代大规模的岩浆活动与古太平洋板块的俯冲过程相关, 但对于古太平洋板块(太平洋 Pacific 板块或伊泽奈崎 Izanagi 板块)俯冲的开始时间和方式及其如何影响华南大陆却存在较大的争论(Zhou and Li, 2000; Zhou et al., 2006; Li and Li, 2007; Ling et al., 2009; X.H. Li et al., 2010, 2013; Wu et al., 2012).

与华北相比, 晚中生代的变质核杂岩在华南内陆发育不显著, 仅有少数几个沿江南造山带展布的伸展穹隆被报道, 如洪镇(朱光等, 2007; Zhu et al., 2010)、庐山(Lin et al., 2000)、大云山(俞爱南等, 1998)、武功山(Faure et al., 1996)和衡山(J.H. Li et al., 2013a)等. 值得注意的是, 位于四川盆地北缘的大巴山和东缘的川东-湘鄂西褶皱带在晚侏罗至早白垩世期间分别经历了向SW和NW的逆冲扩展作用, 这说明华南板块西部在晚中生代仍存在着挤压应力场(Yan et al., 2003, 2009; Hu et al., 2012; Shi et al., 2012; S.Z. Li et al., 2012b; J.H. Li et al., 2013b).

3 华南晚中生代构造演化的不同模式 Diverse models of the Late Mesozoic tectonic evolution in South China

关于华南晚中生代构造-岩浆事件的动力学背景认识仍有很大的分歧. 已提出的模式包括: 走滑或裂解、俯冲角度变陡及后撤、平板俯冲、拆沉或高原垮塌、洋脊俯冲和地幔柱等.

走滑或裂解模式 Strike-sliping or rifting

Xu et al. (1987)曾提出中国东部晚中生代的构造背景处于以郯庐断裂为代表的左行走滑体系控制之下, 认为晚白垩世之前古太平洋板块的俯冲方向与大陆边缘斜交(图 2-2). 一些研究者将湘东-赣西地区的 NNE 向断裂体系看作是郯庐断裂的南延部分(图 2-2; Li et al., 2001). 此外, 东南沿海的长乐-南澳断裂也通常被认为是古太平洋板块斜向俯冲引起的典型左行走滑剪切带(Tong and Tobisch, 1996; Wang and Lu, 1997). 然而, 仅依靠这些走滑断裂的活动很难诱发华南大面积晚中生代花岗岩的出露, 况且大部分花岗岩既没有变形也与断裂无关.

Gilder et al. (1996)则强调古太平洋板块俯冲所引起的走滑加之同时的裂解作

用对华南大陆中生代构造演化的影响(图 2-2). 这一模式可以解释华南 NE 向展布的断裂与伸展盆地以及岩浆岩的形成, 但很难解释岩浆活动的时空迁移规律. Li (2000)指出华南白垩纪岩浆岩带的宽度(超过 1000 km)远大于一般板块俯冲作用形成的岩浆弧宽度(300-400 km), 并认为白垩纪幕式的岩浆活动与岩石圈的伸展作用有关, 而与古太平洋板块的俯冲作用可能无关.

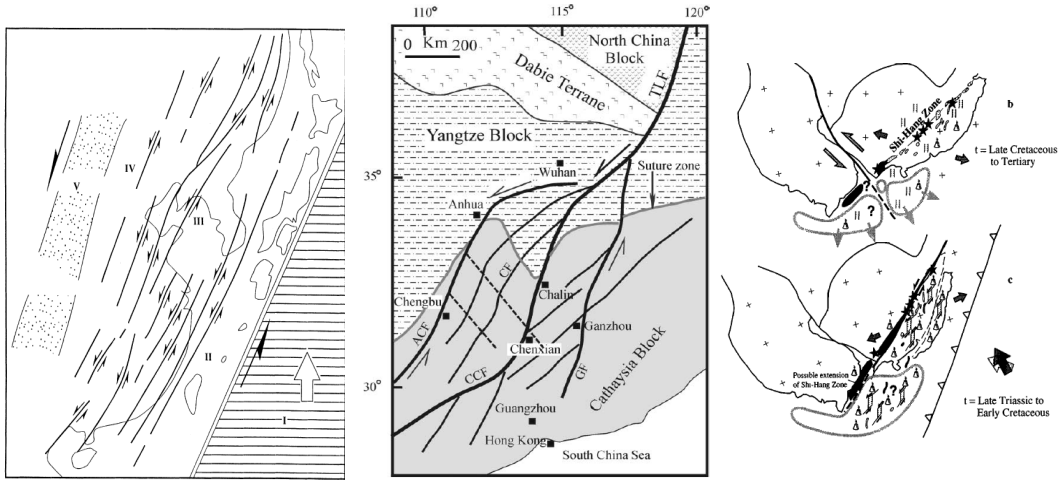

图2-2 中国东部侏罗纪-早白垩世走滑断裂体系(左引自Xu et al., 1987); 郯庐断裂的南延(中引自Li et al., 2001); 走滑加裂解模式(右引自Gilder et al., 1996)

Figure 2-3 Strike-slip fault system of eastern China in Jurssic-Early Cretaceous (left, modified after Xu et al., 1987); Southward extension of the Tan-Lu fault in South China (middle, modified after Li et al., 2001); strike-slip plus rifting model (right, modified after Gilder et al., 1996)

俯冲角度变化及后撤模式 Change of subduction angle and slab roll-back

Zhou and Li (2000)注意到华南晚中生代岩浆岩从内陆向沿海方向存在显著极性变化规律, 即岩浆岩逐渐变年轻, 且岩石中地幔组分逐渐增多, 提出古太平洋板块的俯冲角度从侏罗纪至白垩纪(180-80 Ma)逐渐变陡的模式, 并用岩石圈消减和玄武岩底侵相结合的观点来解释晚中生代岩浆岩在时空上的带状迁移以及巨量长英质岩浆产生和演变的原因(图 2-3). 这一模式得到了许多后续研究者的支持或改进(Zhou et al., 2006; Jang et al., 2009, 2011).

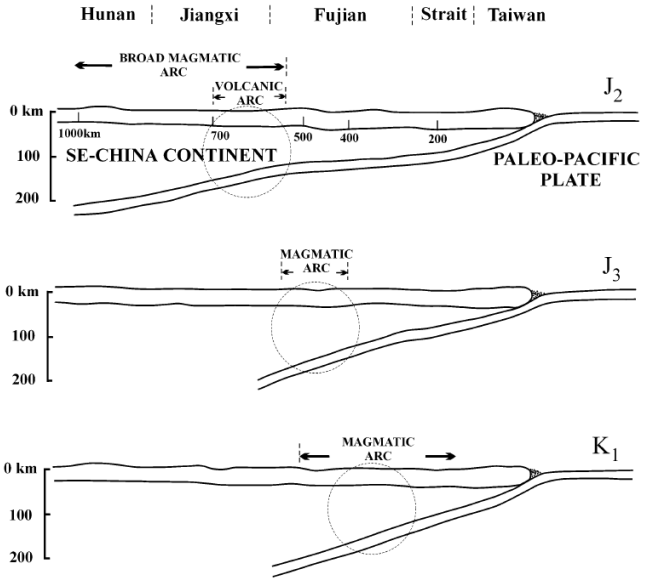

图2-3古太平洋俯冲角度变陡及后撤模式(引自Zhou and Li, 2000)

Figure 2-3 Change of subduction angle of the paleo-Pacific plate from flat to steep, and slab roll-back of the paleo-Pacific plate (modified after Zhou and Li, 2000)

然而, Sun et al. (2007)的总结研究显示太平洋板块的俯冲方向在中生代发生过多次改变, 并不是单一地西向俯冲. 依据太平洋板块在 125 Ma 之前可能为向 SW 俯冲, 且华南 180-125 Ma 期间的岩浆岩也大体上向 NE 方向年轻化, F.Y. Wang et al. (2011)提出了太平洋板块向 SW 俯冲而相应向 NE 后撤的模式.

平板俯冲模式 Slab subduction

在 Li and Li (2007)提出的平板俯冲模式中, 认为古太平洋板块向华南大陆长距离的平板俯冲起始于晚二叠世末, 导致了华南 250-190 Ma 期间约 1300 km 宽的褶皱造山带的形成, 并主导了中生代岩浆岩的演化. 而后在 190-150 Ma 期间, 平俯冲板片发生了断离, 中部下沉, 引发大规模早期板内岩浆活动; 150 Ma 以后, 俯冲板片发生后撤, 岩浆作用向沿海方向迁移. 最近 X.H. Li et al. (2013)进一步完善了这一模式, 认为其也可以用于解释长江中下游地区埃达克质岩的成因(图 2-4).

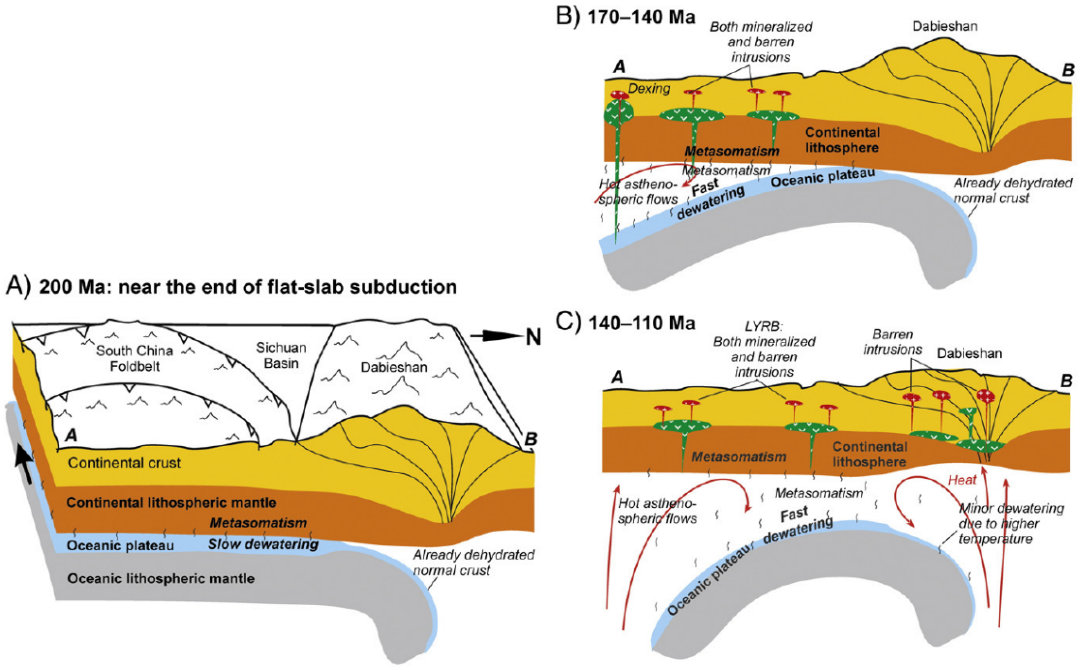

图2-4 平板俯冲模式(引自X.H. Li et al., 2013)

Figure 2-4 Slab subduction model (modified after X.H. Li et al., 2013)

拆沉或高原垮塌模式 Delamination or plateau collapse

大量的研究表明大别山早白垩世的岩浆活动可分为两期，早期(143-130 Ma)的花岗岩多为埃达克质岩石，指示了加厚下地壳的部分熔融，而晚期(130-120 Ma)的花岗岩不具埃达克质地球化学特征，为正常地壳部分熔融产物. 因此，大别山造山带根部在130 Ma左右发生了垮塌，以加厚下地壳拆沉为特点(Q. Wang et al., 2007a; Xu et al., 2007, 2012; He et al., 2011, 2013; 李曙光等, 2013). 长江中下游地区是我国重要的岩浆-成矿带，其岩浆-成矿时代介于150-120 Ma之间. 与Cu-Au成矿相关的岩浆岩多具有埃达克质岩的地球化学属性，一些研究者认为长江中下游地区可能同样经历过加厚下地壳的拆沉(Xu et al., 2002; Wang et al., 2004, 2006, 2007b). 张旗等(2001)对中国东部中生代的埃达克质岩进行了系统总结，推测源区深度至少大于50 km，提出中国东部(范围包括华北东部以及大别山和长江中下游地区)曾经可能存在一个可与现今青藏高原类比的高原. 这一高原形成和存在的主要时期在中侏罗世-早白垩世早期(170-130 Ma)，至125 Ma左右高原发生了垮塌(张旗等, 2008).

洋脊俯冲模式 Rige subduction

考虑到约在 140-125 Ma 之间, 太平洋板块向 SW 俯冲, 而伊泽奈崎板块则向 NNW 俯冲, 两者之间的洋脊可能正对长江中下游地区(Sun et al., 2007). 由于两个板块都有向西的运动分量, 因此可以导致洋脊俯冲(Ling et al., 2009; 孙卫东等, 2010). 洋脊俯冲模式可以很好地解释长江中下游地区埃达克岩、钙碱性岩、富铌岛弧岩石、A 型花岗岩以及相关矿床的时空分布(图 2-5).

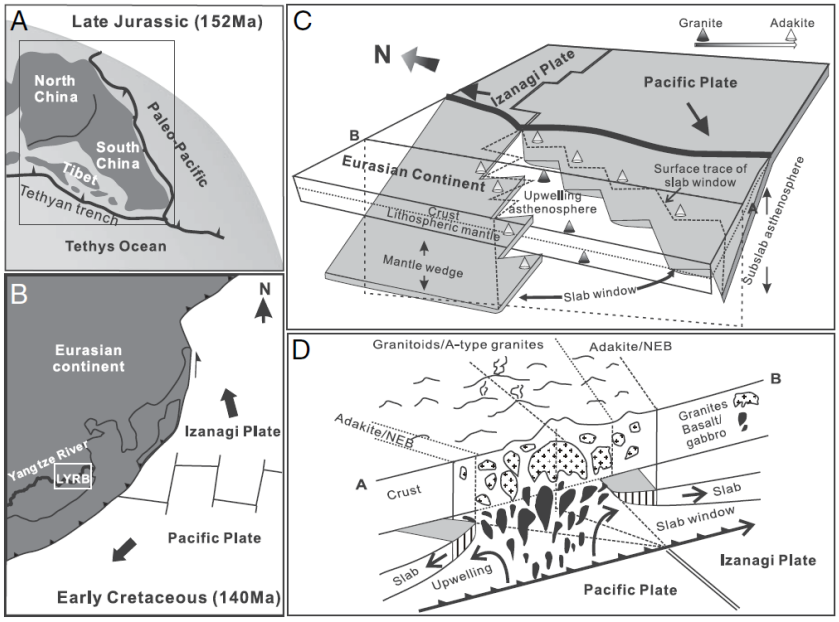

图2-5 洋脊俯冲模式(引自Ling et al., 2009)

Figure 2-5 Rige subduction model (modified after Ling et al., 2009)

值得注意的是, 长江中下游岩浆岩带的走向垂直于大陆边缘, 并且向内陆延伸较远, 鄂东地区距现今大陆边缘超过 1200 km. 假设鄂东地区的埃达克岩形成于 25-90 km 的深度, 需要俯冲角度小于 5°的平俯冲, 这显得洋脊俯冲似乎难以实现(X.H. Li et al., 2010). 另外, 洋脊俯冲一般会导致岩浆岩的时代向内陆变年轻, 而长江中下游却显示出相反的极性. 同样都可以形成板片窗, Wu et al. (2012)认为以板片撕裂来替代洋脊俯冲可能更为合理.

地幔柱模式 Mantle plume

研究表明大别-苏鲁造山带广泛出露的早白垩世岩浆岩是造山带根部发生构造垮塌的产物, 在物质来源上具有“就地取材”的特点, 源区是俯冲加厚的华南陆块北

缘岩石圈(Zhao et al., 2004; 赵子福和郑永飞, 2009). 实际上, 同时期的岩浆岩在中国东部大陆内部地区广泛分布, 尽管太平洋板块俯冲构成了中国东部岩浆活动的宏观地球动力学背景, 但这些岩浆岩均缺乏新生洋壳贡献的记录. Zhao et al. (2004)设想这类大面积岩浆活动可能反映了西南太平洋地幔超级上涌事件的远程响应. 郑永飞(2008)进一步指出中国东部大陆内部早白垩世时期造山带跨塌的构造机制涉及以下 4 个循序渐进的地球动力学过程(图 2-6): (a)西南太平洋超级地幔上涌及其与太平洋板块西南端之间的相互作用, (b)中国大陆东部太平洋板块俯冲方向发生变化, (c)中国东部陆下地幔对流体制发生改变, (d)造山带根部岩石圈受到扰动发生跨塌乃至部分熔融.

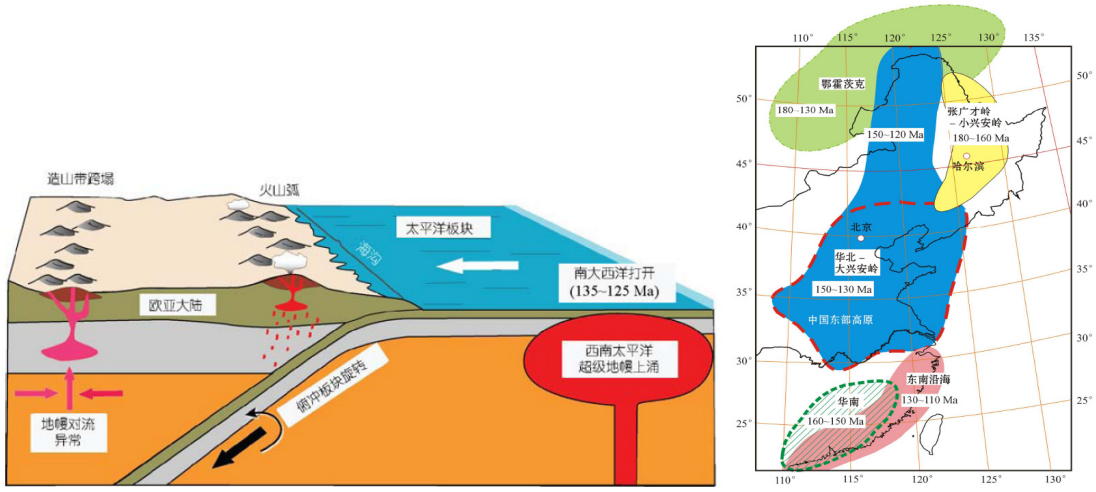

图2-6 中国东部早白垩世岩浆活动的构造启动机制(左引自郑永飞, 2008); 中国东部长英质大火成岩省分布图(右引自张旗和李承东, 2012)

Figure 2-6 Tectonic initiation of Early Cretaceous magmatism in eastern China (left, modified after 郑永飞, 2008); Distribution of felsic large igneous province in eastern China (right, modified after 张旗和李承东, 2012)

事实上, 一些学者很早就曾试图从地幔柱角度来解释中国东南部中生代大规模的岩浆和成矿作用(谢窦克等, 1996; 谢桂青等, 2001). 但由于一般多认为华南晚中生代的岩浆作用与古太平洋板块俯冲有关, 这一观点并不为大多数学者所接受. 最近, 张旗和李承东(2012)提出中国东部中生代大规模岩浆活动可能相当于几个不同时期发育的长英质大火成岩省, 与太平洋板块向西俯冲无关, 而与地幔柱的活动有关(图 2-6).

第三章 华南板块北缘高压/超高压造山带造山后伸展垮塌过程——以桐柏-大别造山带为例

Chapter 3 Extensional collapse of the HP/UHP orogenic belt in northern margin of the South China block: The case of the Tongbai-Dabie orogen

Most researchers believe that the Tongbaishan complex in the core of the Tongbai orogen was exhumed by lateral extrusion under strike-slip faulting. However, this study does not support such a model. Structural analysis shows that the Tongbaishan complex with characteristics of large A-type fold was formed by a NW-SE subhorizontal stretching. Although the foliation at north and south limbs of the Tongbaishan complex dips oppositely, sometime becomes steep near the boundary shear zone, but the mineral stretching lineation keeps NW-SE direction and the kinematics consistently shows a top-to-the-NW sense of shear. That is to say, from inside to boundary faults, the geometry and kinematics of the Tongbaishan complex are harmonious. This indicates that the north and south boundaries of the complex are not typical strike-slip shear zones. Actually, the apparent phenomenon strike-slip observed presently is a result of progressive bending of the early detachment surface.

The central Dabieshan dome has been widely accepted as a large-scale extensional structure. However, structural analysis of the central Dabieshan complex and its boundary shear zones or faults, and the formation mechanism of this domal structure are still controversial. Combined previous work with our detailed structural analysis, we defined the central Dabieshan dome as an orogen-scale metamorphic core complex (MCC) formed under NW-SE extensional regime. Nowadays, the geometry of the whole Dabieshan was almost controlled by the central Dabieshan dome. The central Dabieshan complex (migmatite-gneiss and remnants of UHP metamorphic rocks) represents the footwall of the MCC. The northern boundary Xiaotian-Mozitan fault and the western boundary Shang-Ma fault constitute an integrated and arched detachment fault in the northwest dome margin. Besides, the Shuihou-Wuhe fault and the Xishui shear zone (as a horsetail shear zone, including early XSF-N and late XSF-S) along the

southeastern dome margin constitute a multi-level detachment system. The central Dabieshan complex and the detachment faults recorded a consistent NW-SE trending mineral stretching lineation and top-to-the-NW kinematics.

The Hong'an massif located between the Tongbaishan and Dabieshan was previously considered to be less affected by the Cretaceous tectono-thermal event. This study identified Cretaceous extensional structures in southwest part of the Hong'an massif, named the Shufengjian dome and Daleishan dome (or Dawu dome). The geometry of the Shufengjian dome as an A-type extensional antiform is similar to the Tongbaishan complex, while the Daleishan dome displays as a curved monocline. The deformation of the Shufengjian dome is characterized by NW-SE trending mineral stretching lineation and top-to-the-NW kinematics. In the granitic gneiss from the core of Daleishan dome, no obvious linear structure developed. The AMS (anisotropy of magnetic susceptibility) study revealed that the magnetic lineation is dominated by NW-SE trending. These two extensional structures relatively overlaying the Tongbaishan complex and central Dabieshan complex represent crustal detachment in a shallow tectonic level.

Geochronology studies show that the Tongbai-Dabie orogen started extensional regime at ca. 145 Ma, and approached its climax at ca. 130 Ma that was signaled by removal of the pre-eixsting orogen root. Additionally, the Tongbaishan and Dabieshan, together with the Shuangfengjian and Daleishan in the Hong'an massif also recorded a late (110-90 Ma) extensional event. The Shuangfengjian and Daleishan were mainly controlled by the late extension. In the Tongbaishan, the late extension completely reused the early detachment faults, while in the Dabieshan it formed secondary detachment fault, except for partly share of the early detachment fault. Considering the compatibility between geometry and kinematics, it is inferred that the Cretaceous detachment faults in the Tongbai-Dabie orogen initiated as a coherent, flat-lying detachment surface at the middle crustal level, possibly corresponding to the decoupled surface between the partial melted crust and already exhumed HP-UHP slab. The early (145-130 Ma) deformation is characterized by subhorizontal detachment under high-temperature condition, representing the main tectonic event in the Tongbai-Dabie orogen. Subsequently, the detachment surface was folded during the doming, and secondary detachment might occur due to late (110-90 Ma) adjustment.

It is proposed that the Tongbaishan complex and the central Dabieshan complex are product of Early Cretaceous anatexis that expended the Yangtze basement gneiss and HP/UHP metamorphic rocks in middle-lower crust. The Cretaceous extensional tectonics intensively reworked the Early Mesozoic tectonic framework of the Tongbai-Dabie orogen. The HP unit originally overlying the Tongbaishan complex was divided into the two slices, while the Triassic metamorphic sequence (including the HP/UHP units, Susong and Zhangbaling groups) in the southern Dabieshan is dismembered into tectonic slices as the hanging wall of the detachment fault. The extensional collapse of the Tongbai-Dabie orogen is manifested by a combined effect of geological process in different lithospheric level: detachment and unroofing of the core complex, possibly SE-directed channel flow of the middle-lower crust, and removal or delamination of the orogen root. Compared with the Cretaceous extensional structures widely developed eastern China, we suggest that extensional tectonics developed in the Tongbai-Dabie orogen shares the same geodynamic setting as the destruction of the North China craton, and is also response of the Late Mesozoic lithospheric thinning, but just overprinted on the HP/UHP orogenic belt.

1 引言 Intruduction

我国东部的桐柏-大别-苏鲁高压/超高压造山带代表了华北和华南两大板块之间的拼合带, 以含有世界上最大的高压/超高压变质带而闻名(Hacker et al., 1995; Wang et al., 2008; Liou et al., 2009). 该造山带自西向东分为五个主要的块体, 即桐柏山、红安地体、大别山、肥东-张八岭地体和苏鲁地体(图 3-1). 研究表明桐柏-大别-苏鲁造山带是一条典型的复合造山带, 其形成和演化经历了从晚古生代到中生代复杂的构造过程(Ratschbacher et al., 2003, 2006; Liu et al., 2013; Wu and Zheng, 2013).

研究表明从胶东半岛到桐柏山, 沿高压/超高压变质带发育大量晚中生代的伸展构造(图 3-1): 胶北的玲珑-郭家岭变质核杂岩及同构造花岗岩、鹊山同构造花岗岩，胶南楔形伸展构造(五莲拆离断层), 大别山前陆的洪镇穹隆，大别山中部的罗田穹隆, 桐柏山核部的背形构造. 正是由于这些造山后的伸展构造使同造山期折返之后仍然滞留在中地壳的高岩/超高压变质岩折返至地表. 同时, 特别是中大别混合岩及花岗岩中赋存的榴辉岩和麻粒岩残余体(侯振辉等, 2005; 刘贻灿和李曙

光, 2008; Lin et al., 2007b)，大规模碰撞后的岩浆活动包括源于较浅地幔源的镁铁-超镁铁岩等(赵子福和郑永飞, 2009)均指示大陆深俯冲造山带加厚的岩石圈在白垩纪发生了巨量的岩石圈减薄. 以上的现象表明我国东部的高压/超高压造山带存在一个规模巨大的造山后垮塌过程(林伟等, 2013b).

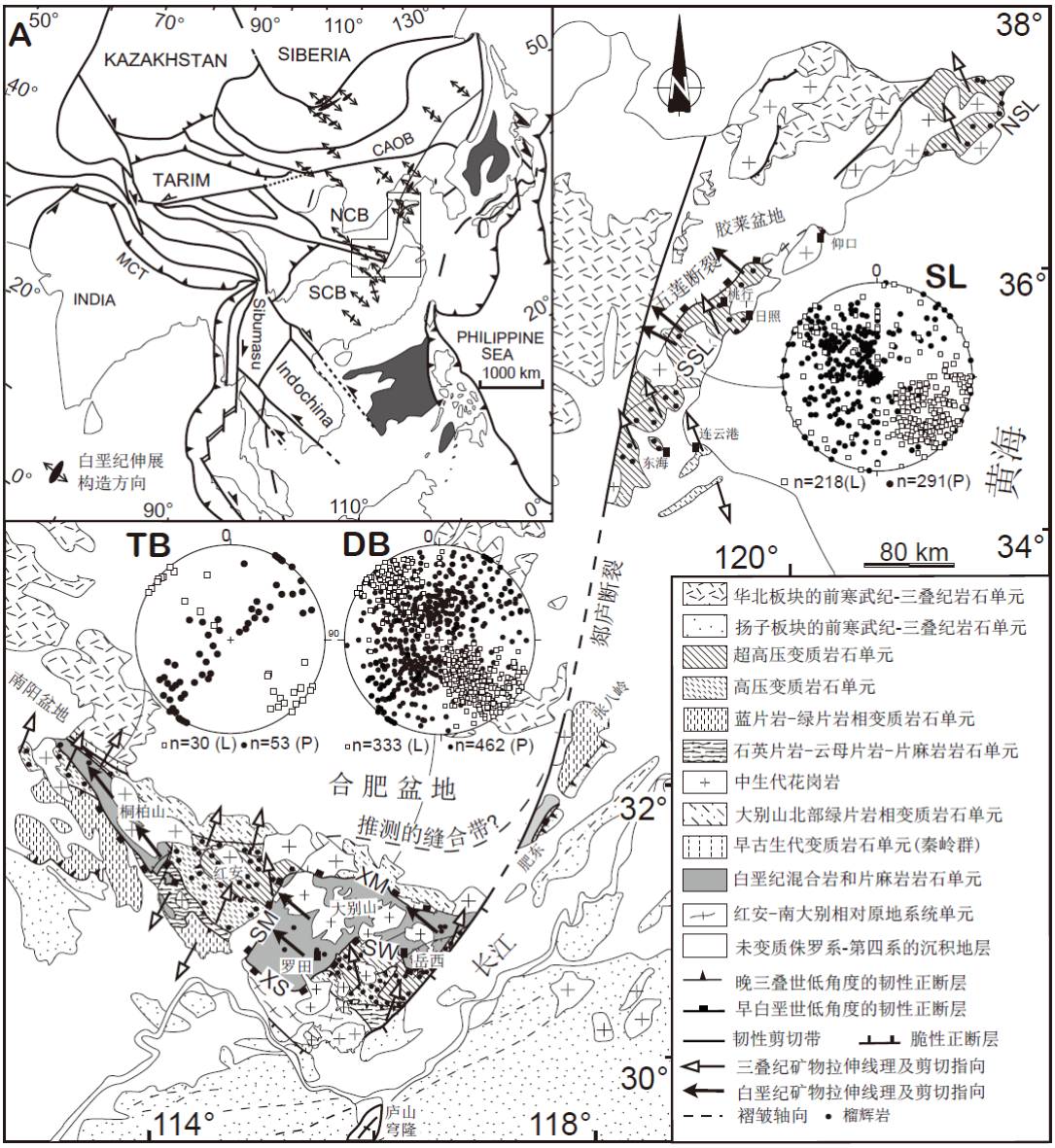

图 3-1 中国东部高压/超高压造山带构造图

Figure 3-1 Tectonic map of the HP/UHP orogenic belt in eastern China

在论文研究期间, 选取桐柏山中部、红安地体西南部和大别山中部发育的白垩纪伸展构造进行了详细的构造几何学、运动学和年代学研究. 将大陆深俯冲的碰撞造山带同我国东部的岩石圈减薄相结合, 深入探讨造山后过程对高压/超高压造山带早期构造格架的改造作用及其可能的动力学机制.

2 区域地质概况 Overview of the regional geology

桐柏-大别造山带(桐柏山和大别山及其所夹红安地体)在区域上呈现NW-SE走向, 向西越过南阳盆地与东秦岭早古生代造山带相接, 东端被郯庐断裂所截 (图3-2). 与三叠纪碰撞造山相关的变质岩是桐柏-大别造山带的主体部分, 自南向北依次包括蓝片岩-绿片岩相单元(随县-张八岭群)、绿帘-角闪岩相单元(红安-宿松群)、高压-超高压榴辉岩相单元和北淮阳构造带的浅变质岩(信阳群和佛子岭群的复理石单元, 定远杂岩和卢镇关杂岩的变质火山岩和侵入岩). 除北淮阳构造带, 变质级别总体上呈现出向北升高的趋势, 表明三叠纪大陆深俯冲具有向北的俯冲极性(Okay, 1993; Carswell et aI., 1997; Eide and Liou, 2000; X.C. Liu et al., 2004; J.B. Liu et al., 2006; 石永红等, 2013). 近年的研究工作还在红安地体北部的浒湾高压变质带中发现了具有洋壳地球化学属性的石炭纪榴辉岩, 其原岩被认为代表了古特提斯洋壳的残片(吴元保, 2009; Sun et al., 2002; Cheng et al., 2009, 2010, 2013; Wu et al., 2009; Liu et al., 2011a). 另外, 古生代的造山体系可以在桐柏山的北缘被追索到, 自北向南包括宽坪群、二郎坪群和秦岭群. 这些岩石构造单元可与东秦岭地区相似的岩石组合相对应(Ratschbacher et al., 2006; Liu et al., 2011b, 2013). 在构造位置上, 桐柏山核部的桐柏杂岩和大别山中部(传统上称之为北大别)的中大别杂岩位于高压/超高压变质地体之下, 代表了桐柏-大别造山带中出露的中下地壳岩石. 两者具有相似的岩石组成(主体为正片麻岩及混合岩), 在构造样式上分布表现为背形或穹隆构造(图 3-2).

目前, 由于多数研究者将桐柏杂岩的边界断裂看作大型的走滑剪切带, 从而认为桐柏山连同西部的红安地体和大别山在中生代期间(主要是白垩纪)发生过向东的侧向挤出过程(Webb et al., 1999b, 2001; Wang et al., 2003; 崔建军等, 2009; 许光和王二七, 2009; 刘鑫等, 2010; X. Liu et al., 2011; Cheng et al., 2012; Cui et al., 2012). 但是对于桐柏杂岩的具体隆升过程也存在着不同的认识, 例如许光和王二七(2009)认为桐柏杂岩原本是秦岭的中下地壳物质, 它是在晚白垩世早期(102-85 Ma)被从秦岭向东挤出至现今的位置; Cui et al. (2012)则认为桐柏杂岩主体是一个早白垩世(141-139 Ma)的花岗杂岩体, 其走滑剪切的主变形期在 135-120 Ma.

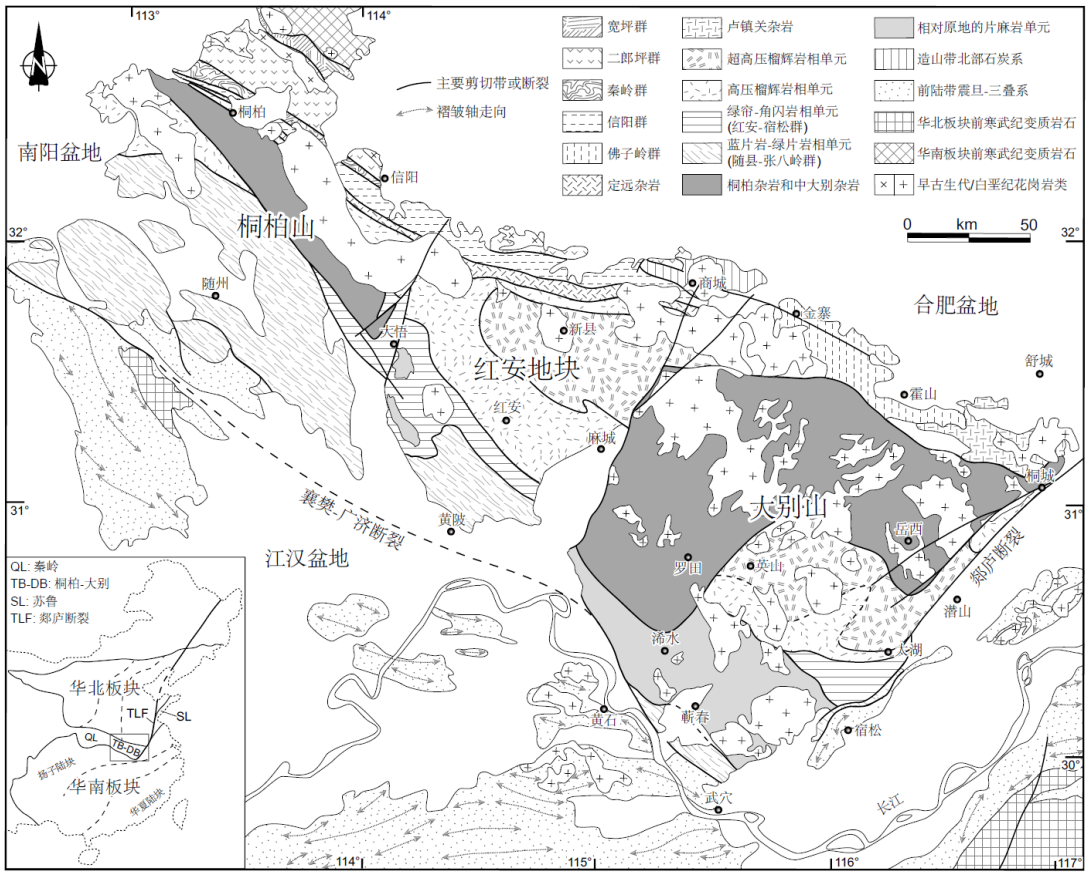

图 3-2 桐柏-大别造山带构造简图

Figure 3-2 Tectonic map of the Tongbai-Dabie orogen

关于中大别杂岩的折返时代曾经存在三叠纪和白垩纪的不同观点. 着眼于高压/超高压变质岩的折返过程, Faure et al. (1999, 2003)和林伟等(2003)最初认为中大别杂岩记录了与高压/超高压变质岩折返相关的主期变形, 在构造上代表了晚三叠世伸展作用形成的同折返穹隆. 现今中大别穹隆已经被人们广泛接受为白垩纪的伸展构造(王国灿和杨巍然, 1996, 1998; Hacker et al., 1998, 2000; Wang et al., 1998; Ratschbacher et al., 2000; 许长海等, 2001; 侯泉林等, 2007; Y.S. Wang et al., 2011). 然而, 涉及中大别杂岩及其边界剪切带或断裂的构造解析和穹隆的形成机制仍存在较大的争议. 例如, 王国灿和杨巍然(1996, 1998)将中大别穹隆的形成时间限定在 150-96 Ma 之间, 认为其表现为顶托式穹隆和剥离滑脱构造, 成因与加厚岩石圈拆沉引起的伸展作用相关; Wang et al. (1998)强调中大别杂岩与其上覆的高压/超高压岩片在早白垩世的构造并置是由上部指向 SEE 的低角度韧性正断层(相当于水吼-五河剪切带)控制, 并指出侧向挤出是这一平行造山带伸展作用的机制; Ratschbacher et al. (2000)支持中大别杂岩为一个早白垩世岩浆杂岩的假说(Hacker

et al., 1998), 引入枢纽旋转-均衡回弹(rolling hinge-isostatic rebound)模式来解释中大别杂岩在140-120 Ma沿其北部边界晓天-磨子潭断裂的不对称侵位; Y.S. Wang et al. (2011)则认为中大别穹隆是在其南北边界断裂(即水吼-五河断裂和晓天-磨子潭断裂)共同作用下形成的, 两条断裂在早期应为处于中地壳水平的同一韧性剪切带, 韧性变形发生时间在 143-132 Ma.

实际上, 索书田等(2000, 2001)和钟增球等(2001)最早提出现今桐柏-大别山造山带的整体构造格架类似于变质核杂岩, 即由桐柏杂岩和中大别杂岩及其上覆变质岩片和沉积盖层组成, 并发育多层拆离滑脱带, 为碰撞后(200-170 Ma, 可能延续至 130 Ma)伸展体制下的产物(Suo et al., 2005). 但这一模式并没有有效地将白垩纪的构造叠加从三叠纪高压/超高压造山带中分离出来. 由此可见, 对桐柏杂岩和中大别杂岩的深入研究无疑是解析桐柏-大别高压/超高压造山带造山后垮塌构造的关键. 值得指出的是, 桐柏-大别造山带现今的地壳厚度约为 35 km, 没有山根. 自三叠纪华北和华南碰撞以来, 直至白垩纪之前桐柏-大别造山带未见明显的岩浆活动. 早白垩世发育的大面积花岗岩类和少量镁铁质侵入岩成为造山带最显著的特点之一(图 3-2). 系统的年代学和地球化学研究表明桐柏-大别造山带白垩纪的花岗岩类可以分为两类(Zhao et al., 2004, 2007, 2011; Q. Wang et al., 2007b; Xu et al., 2007, 2012; Huang et a., 2008; He et al., 2011, 2013; Zhang et al., 2013): 早期花岗岩类的侵位年龄集中在 143-130 Ma, 普遍受到了变形的影响(发育片麻理), 具有埃达克质岩的特点, 指示了加厚下地壳的部分熔融; 晚期花岗岩类的侵位年龄集中在 130-117 Ma, 基本没有变形, 为正常地壳部分熔融的产物. 而对应于地幔上涌活动的镁铁质岩浆岩的侵位时代(130-123 Ma)则与晚期花岗岩类一致(Jahn et al., 1999; Zhao et al., 2005; Huang et al., 2007; Dai et al., 2011). 因此, 桐柏-大别造山带很可能在 130 Ma 左右发生了山根的垮塌(李曙光等, 2013).

3 桐柏山白垩纪伸展构造 Cretaceous extensional structures in the Tongbaishan

3.1 桐柏山主要岩石构造单元及其特征 Main litho-tectonic uints and their characteristics

前人对桐柏地区构造单元划分已有不少工作，例如从构造方面 Webb et al. (1999b, 2001)、索书田等(2001)和黄少英等(2006) 在桐柏地区划分了若干岩石-构造单元，确定了与折返过程有关的构造格局. 魏春景等(1999)、索书田等(2001)和刘晓春等(2005a)在桐柏地区发现了多处榴辉岩，确立了桐柏山南北两条高压变质带. 特别是刘晓春等(刘晓春等, 2011; X.C. Liu et al., 2008, 2010, 2011b, 2013)近几年的工作从岩石学和年代学方面很大程度地推动了桐柏山大尺度构造单元的划分.

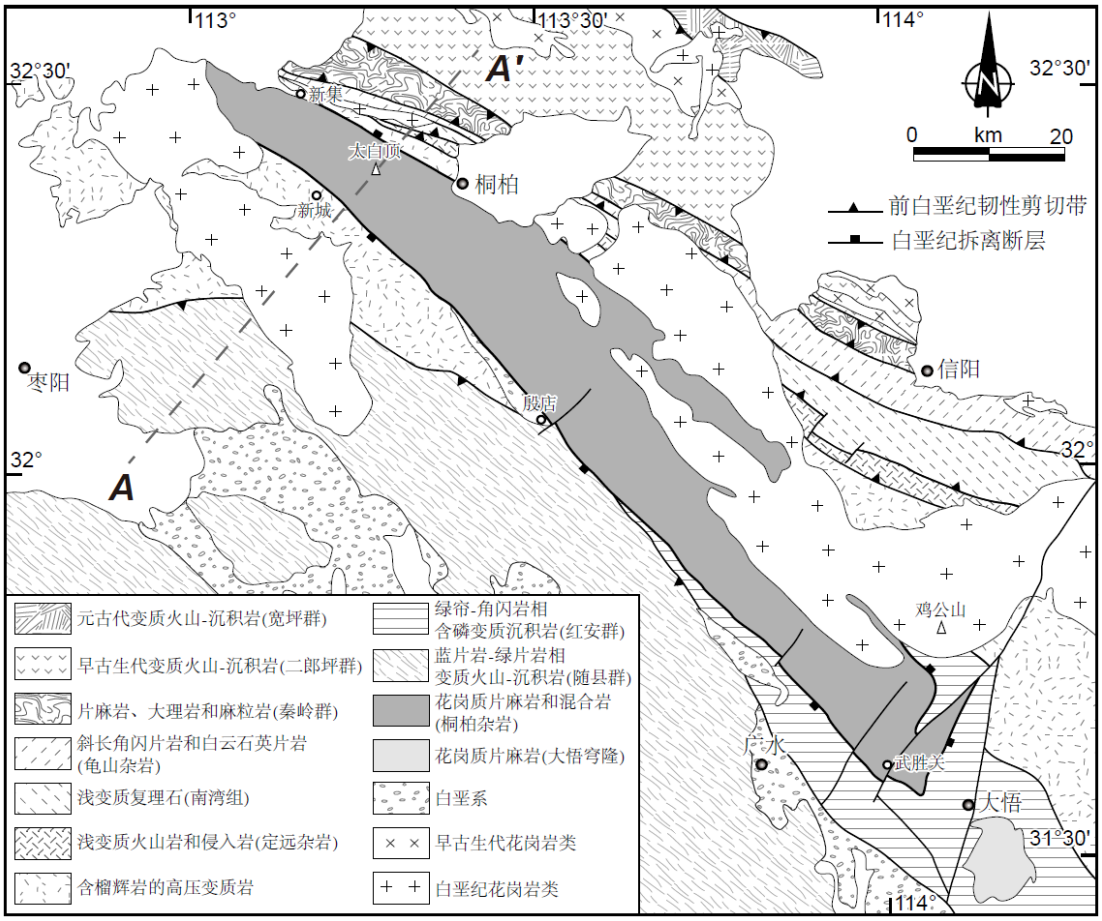

图 3-3 桐柏山地质构造简图

Figure 3-3 Geological and structural map of the Tongbaishan

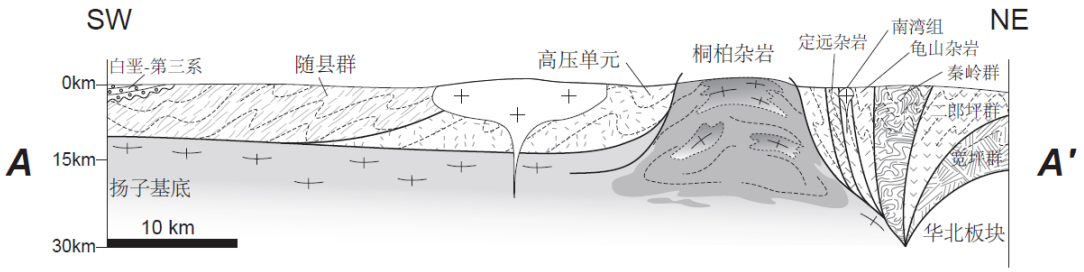

图 3-4 桐柏山构造剖面示意图

Figure 3-4 Schematic cross-section of the Tongbaishan

根据前人的研究结果以及我们的实际调查, 桐柏山的主要岩石构造单元以桐柏杂岩为核心, 向北依次为北部含榴辉岩高压单元、定远杂岩、南湾组、龟山杂岩、秦岭群、二郎坪群和宽坪群, 向南依次为南部含榴辉岩高压岩片、红安群(仅指与宿松群的对应部分)和随县群(图 3-3). 这些岩石构造单元在平面上总体以 NW-SE 向的带状展布, 在剖面上呈为一系列构造岩片相互叠置(图 3-4). 现今各单元之间多以剪切带或断裂带相分割.

宽坪群、二郎坪群和秦岭群代表了早古生代的造山体系, 为北秦岭造山带的东延. 宽坪群主要由云母片岩、石英岩、大理岩和斜长角闪岩组成. 原岩为一套变质火山-沉积岩, 形成于新元古代. 二郎坪群为一套早古生代的变质火山-沉积岩, 北部被早古生代的花岗岩所侵入. 秦岭群由正/副片麻岩、大理岩和麻粒岩组成. 相关的岩石学和年代学研究表明桐柏山地区的宽坪群和二郎坪群普遍经历了角闪岩相变质作用, 而秦岭群则广泛发育麻粒岩相变质作用, 其变质作用发生时代均在 440-400 Ma 期间(Kröner et al., 1993; Ratschbacher et al., 2006; X.C. Liu et al., 2011b, 2013; H. Wang et al., 2011; Xiang et al., 2012). 关于三者的构造属性尚存争议, 通常认为宽坪群代表华北陆块南缘被动陆缘沉积, 二郎坪群具有岛弧或者弧后盆地属性, 秦岭群则为微陆块及大陆弧.

南湾组主要为一套绿片岩相的变质复理石, 包括变质砂岩和粉砂岩或者千枚岩和板岩, 一般认为其可以与大别山地区的佛子岭群和秦岭地区的刘岭群对比. 最近刘晓春等(2013)报道了南湾组变质砂岩中白云母 $^{40}Ar/^{39}Ar$ 年龄为 261 Ma, 这与大别山佛子岭群所记录的早期变形时代相一致(Faure et al., 2003; 林伟等, 2005). 龟山杂岩主要由角闪岩相变质的斜长角闪片岩和云母石英片岩组成. 杂岩中已获得的角闪石 $^{40}Ar/^{39}Ar$ 年龄在 401 Ma 和 316-304 Ma, 白云母 $^{40}Ar/^{39}Ar$ 年龄为 268 Ma, 表明其可能经历了多期的变质变形作用(牛宝贵等, 1994; Zhai et al., 1995; 黄少英等, 2006). X.C. Liu et al. (2011b, 2013)认为南湾组可能代表了华南陆块在晚古生代北向俯冲过称中形成的加积楔, 而龟山杂岩则是由秦岭群和南湾组的岩石混杂而成.

桐柏杂岩主要由正片麻岩及混合岩组成, 并有少量的副片麻岩、斜长角闪岩和大理岩. 核部英云闪长质片麻岩部分熔融生成的大量浅色脉体顺片麻理发育, 少

量呈不规则状切割片麻理. 关于花岗质片麻岩的原岩时代有新元古代(776-746 Ma)和早白垩世(141-139 Ma)之争(Kröner et al., 1993; 刘晓春等, 2011). 已获得的桐柏杂岩不同岩石的黑云母、白云母和角闪石 $^{40}Ar/^{39}Ar$ 年龄集中分布在 135-119 Ma 和 100-90 Ma 两个区间, 暗示其在白垩纪可能经历了两期冷却过程(Webb et al., 1999b, 2001; 许光和王二七, 2009; Cui et al., 2012).

北部和南部含榴辉岩高压单元呈带状分布于桐柏杂岩两侧. 主要组成岩石为白云钠长片麻岩、白云石英片岩、石英岩和大理岩, 夹有榴辉岩及退变榴辉岩的团块或透镜体. 榴辉岩的锆石 U-Pb 年龄和石榴石-全岩 Lu-Hf 等时线年龄集中在 255 Ma 左右, 被解释为榴辉岩相峰期变质作用时代(X.C. Liu et al., 2008; Cheng et al., 2011). 围岩片麻岩的白云母 $^{40}Ar/^{39}Ar$ 年龄则介于 238-217 Ma 之间, 可能代表了与深俯冲陆壳在三叠纪折返相关的变形及冷却时间(X.C. Liu et al., 2008).

定远杂岩属于原苏家河群的一部分, 主要由绿片岩相变质的火山岩和侵入岩(辉长岩和花岗岩)组成, 刘晓春等(2011)称之为构造混杂岩带. 由于在红安地体北部相同构造单元中获得的锆石 U-Pb 年代学数据主要集中在新元古代, 因此一般认为该带代表华南陆块深俯冲初始阶段被拆离折返的岩片(刘贻灿等, 2013). 定远杂岩普遍经历了强烈的韧性变形, 从而形成各种糜棱岩. 黄少英等(2006)在韧性剪切带中获得了 256 Ma 的白云母 $^{40}Ar/^{39}Ar$ 年龄, 可能代表了构造变形的时间.

原红安群包括了红安地体南部从蓝片岩-绿片岩相到绿帘-角闪岩相再到高压榴辉岩相的不同岩石构造单元. 本文这里所说的红安群仅指其中的绿帘-角闪岩相单元, 对应于大别山地区宿松群的含磷变质沉积岩(徐树桐等, 2002; Xu et al., 2012). 随县群主要为一套变质的双峰式火山岩和变质沉积岩, 经历了蓝片岩-绿片岩相变质作用. 其中变质火山岩的原岩年龄在 741-763 Ma, 为扬子陆块北缘新元古代裂谷作用产物(薛怀民等, 2011). 随县群向西与红安地体南部木兰山地区的蓝片岩-绿片岩带相连.

3.2 桐柏杂岩的构造解析 Structural analysis of the Tongbaishan complex

桐柏山核部的桐柏杂岩呈 NWW-SEE 向，延伸达 120 km 以上，南北宽 10-20 km (图 3-4). 向西被掩盖于南阳盆地之下，向东延伸至湖北广水县境内. 桐柏杂岩主体的花岗质片麻岩普遍发育不同程度的糜棱岩化现象，它与南北两侧的构造单元均以大型韧性剪切带相分隔. 南界韧性剪切带沿新城-殷店-武胜关一线展布. 北界韧性剪切带西段沿新集-桐柏出露较好，向东被鸡公山岩体所破坏. 边界剪切带的韧性变形向桐柏杂岩内部及两侧构造单元中深入较远. 前人多认为桐柏杂岩的南北边界分别表现为右行和左行走滑剪切带，代表桐柏杂岩向 SE 侧向挤出的结果 (Webb et al., 1999b, 2001; Wang et al., 2003; 许光和王二七, 2009; 刘鑫等, 2010; X. Liu et al., 2011; Cheng et al., 2012; Cui et al., 2012)

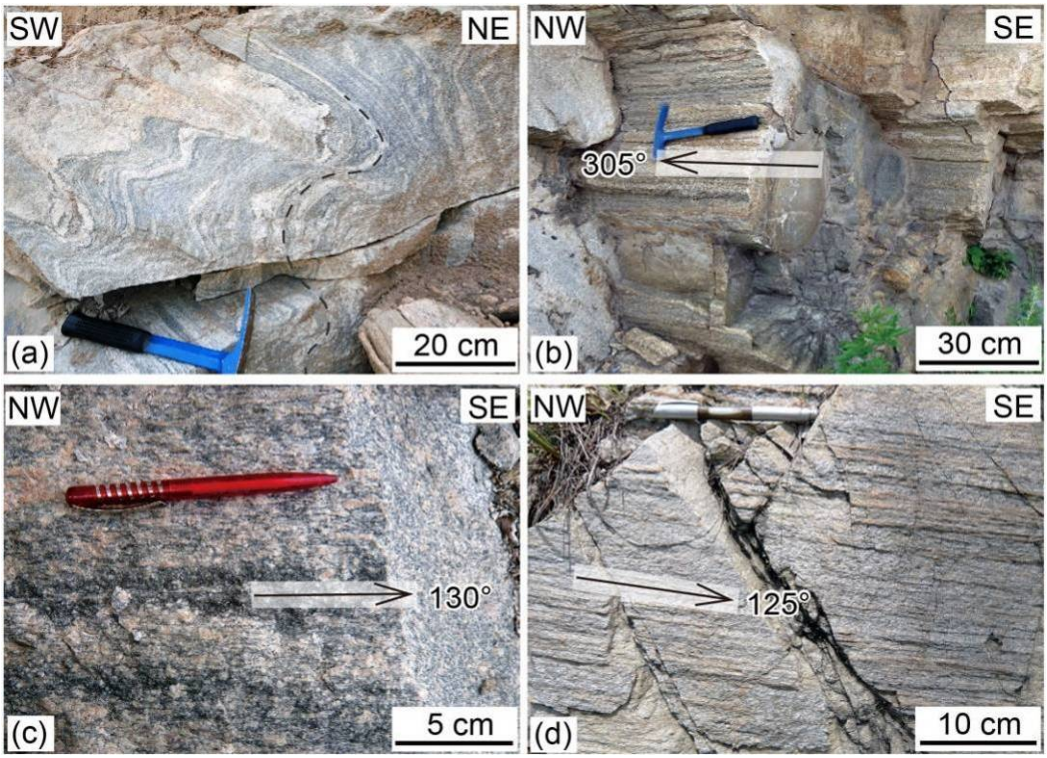

图3-5 桐柏杂岩野外构造特征

(a)桐柏杂岩核部混合岩中的同斜褶皱; (b)桐柏杂岩中的大型线理构造; (c)桐柏杂岩中发育的 L 型构造岩; (d)桐柏杂岩南侧靠近边界剪切带的红安群变质岩中发育的 NW-SE 向近水平线理

Figure 3-5 Structural characteristics of the Tongbaishan complex

(a) isoclinal fold in migmatite from the Tongbaishan complex; (b) large lineation in the Tongbaishan complex; (c) L-type tectonite of the Tongbaishan complex; (d) NW-SE trending subhorizontal lineation developed in the metamorphic rocks of the Hong'an Group near the southern boundary shear zone

桐柏杂岩的整体几何形态呈现为一个狭长的背形构造. 片麻理产状总体北部向 NE 倾, 南部向 SW 倾(图 3-1). 靠近北界面理向 NE 陡倾, 向杂岩核部迅速变缓; 南界则正好相反, 面理向 SW 陡倾, 向杂岩核部逐渐变缓. 由于不同尺度同斜褶皱的广泛发育, 局部产状变化较大(图 3-5a). 实际上, 桐柏杂岩自身可以被看做是一个巨型的 A 型褶皱. 桐柏杂岩及其边界剪切带中从小型到大型的线性构造十分发育, 并具透入性特征. 大型线理在露头上常呈现为柱状体, 在纵截面上可见长英质矿物强烈拉伸形成的杆状或拔丝构造(图 3-5b). 小型线理多为面理上发育的由长石、石英和黑云母构成的矿物拉伸线理, 局部可见角闪石的定向. 杂岩核部面理往往不甚发育, 反而线理非常明显. 面状构造甚至完全被线性构造取代, 从而形成典型的 L 型构造岩, 尤其在太白顶地区 L 型构造岩十分常见(图 3-5c). 这些线性构造的走向均与桐柏杂岩的长轴方向平行, 线理倾伏向的统计方位集中在 130°或 310°, 倾伏角一般小于 20° (图 3-1).

在野外露头和薄片尺度, 沿线理方向可见桐柏杂岩混合岩浅色体的布丁构造(图 3-6a), 花岗质糜棱岩中发育的 S-C 组构和长石旋转残斑等剪切标志(图 3-6c 和 c′, d), 指示了一致的上部向 NW 的剪切变形. 桐柏杂岩边界剪切带的韧性变形同样影响到了其南北两侧上覆的构造单元. 在广水地区, 靠近剪切带的红安群白云钠长片麻岩中可以清晰地观察到由白云母强烈定向构成的近水平线理(图 3-5d), 镜下的 S-C 组构和云母鱼构造同样指示了与桐柏杂岩相同的运动学(图 3-6e).

此外, 桐柏杂岩的边界剪切带还明显受到晚期脆性变形的叠加改造, 在断裂带内可见花岗质糜棱岩的碎裂岩及假玄武玻璃. 沿南界断裂, 还发育有白垩纪的山间磨拉石盆地.

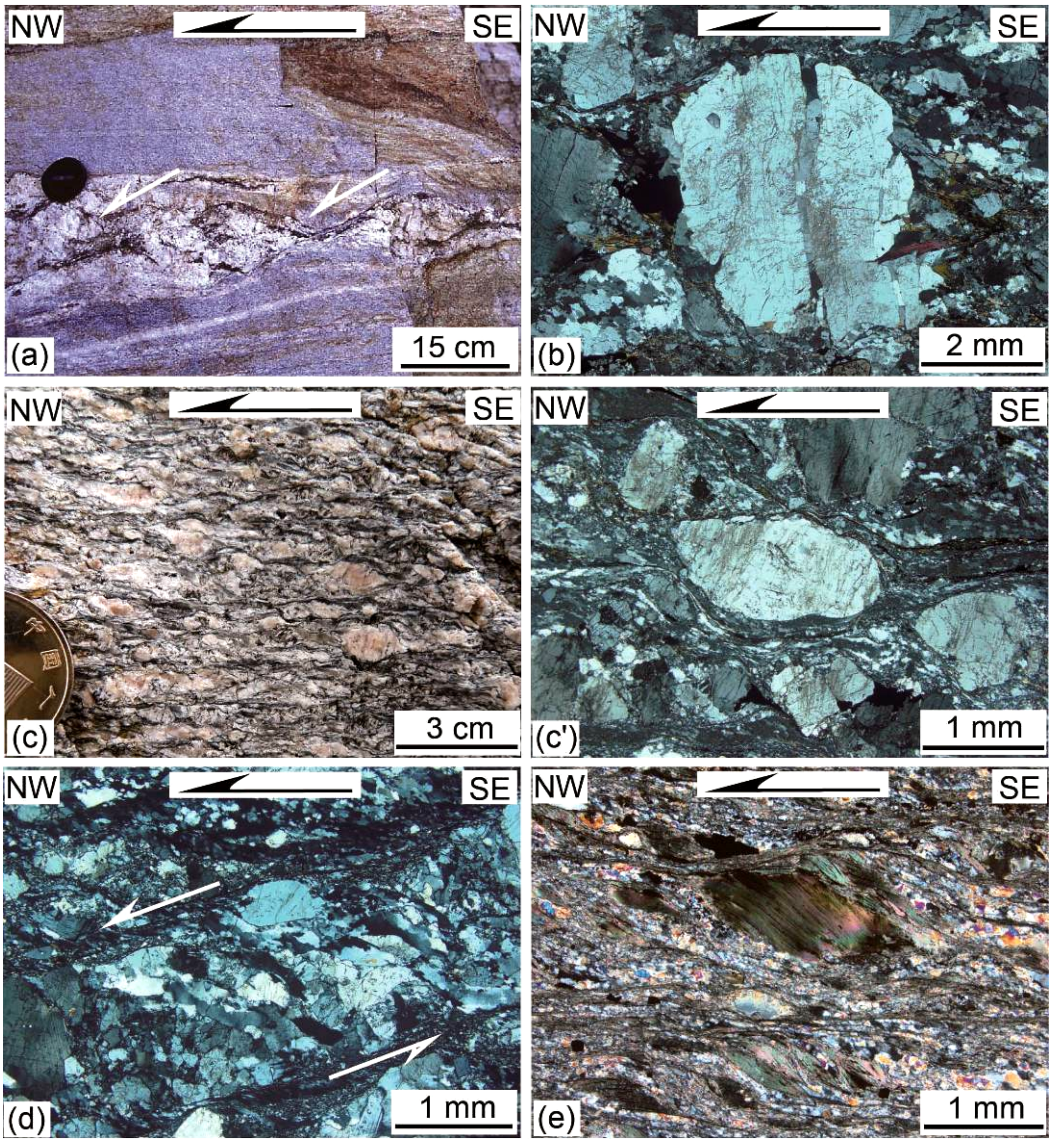

图 3-6 桐柏杂岩及其边界剪切带的运动学

(a)桐柏杂岩混合片麻岩中浅色脉体剪切形成的布丁构造; (b)桐柏杂岩花岗质片麻岩中发育的长石旋转残斑; (c)和(c′)北界剪切带花岗质糜棱岩中发育的S-C组构和长石旋转残斑; (d)南界剪切带花岗质糜棱岩中的S-C组构; (e)靠近南界剪切带上盘的变质岩中发育的S-C组构和云母鱼构造. 以上剪切标志均指示了上部向NW运动学

Figure 3-6 kinematics of theTongbaishan complex and its bondury faults

(a) boudins of sheared light-colored veins in the migmatite of the Tongbaishan cpmplex; (b) σ-type feldspar porpyroclasts in the granitc gneiss of the Tongbaishan complex; (c) and (c′) S-C fibric and σ-type feldspar porpyroclasts in the granitc mylonite from the northern bondury shear zone; (d) S-C fabric in the granitc mylonite from the southern boundary shear zone; (e) S-C fabric and mica fish in the metamorphic rocks of the Hong'an Group near the southern boundary shear zone. All above indicators indicate a top-to-the-NW sense of shear

一般认为桐柏杂岩是在走滑作用下发生向南东的侧向挤出而隆升的, 然而我们的构造解析并不支持这一认识. 虽然桐柏杂岩南北坡的面理倾向相反, 且靠近边界剪切带面理时常较陡, 但矿物拉伸线理稳定在 NW-SE 向, 运动学一致显示为上部指向NW的剪切变形. 这表明从杂岩内部到边界剪切带, 其几何学和运动学具有协调一致的特点. 因此, 推测桐柏杂岩的边界剪切带在早期应为处于中地壳水平的同一拆离面, 两侧的高压变质带也应为位于拆离面之上的同一构造岩片. 总体上, 桐柏杂岩是在NW-SE近水平伸展作用下形成的具有A型褶皱特点的变质核杂岩. 因此, 桐柏杂岩南北边界并不是典型的走滑剪切带, 现今表面上观察到的走滑现象实际上是早期的拆离面发生弯曲的表现.

3.3 桐柏杂岩的年代学研究 Geochronological studies

3.3.1 前人的年代学工作 Previous geochronological data

由于桐柏杂岩具有高级片麻岩的外貌特征而传统上被认为具有太古宙古老基底的属性(河南省区域地质志, 1989; 湖北省区域地质志, 1990). Kröner et al. (1993)最早使用单颗粒锆石 Pb-Pb 蒸发法从桐柏杂岩正片麻岩中获得了 746-776 Ma 的新元古代年龄, 认为其代表了原岩的侵位时代. 依此桐柏杂岩一直被认为是一个前寒武纪的地质体(索书田等, 2001; 许光和王二七, 2009; 刘鑫等, 2010). 而后, X.C. Liu et al. (2010)对桐柏杂岩中不同类型岩石进行了 SIMS 锆石 U-Pb 定年: 其中花岗质片麻岩的年龄为 141-139 Ma, 并含有新元古代 780-750 Ma 的继承锆石核; 而具有高级变质特征的英云闪长质片麻岩和石榴角闪岩则记录了 232-220 Ma 的变质作用, 原岩年龄在 933 Ma 和 863-742 Ma. 从而他们认为桐柏杂岩实际上是一个早白垩世的花岗岩杂岩体, 并含有一定数量的三叠纪变质岩包体(刘晓春等, 2011). 苏文等(2013)最近应用 LA-ICP-MS 锆石 U-Pb 定年获得桐柏杂岩中强变形眼球状花岗质片麻岩的侵位时代为 137-138 Ma, 弱变形花岗岩的侵位时代为 134 Ma . 这些年代学数据表明桐柏杂岩主体的花岗质岩石有相当一部分是由早白垩世的花岗岩经过强烈的剪切变形而成的, 而其它的变质岩的原岩时代为新元古代, 可能对应于扬子陆块北缘与罗迪尼亚(Rodinia)超大陆聚合-裂解过程相关的岩浆岩.

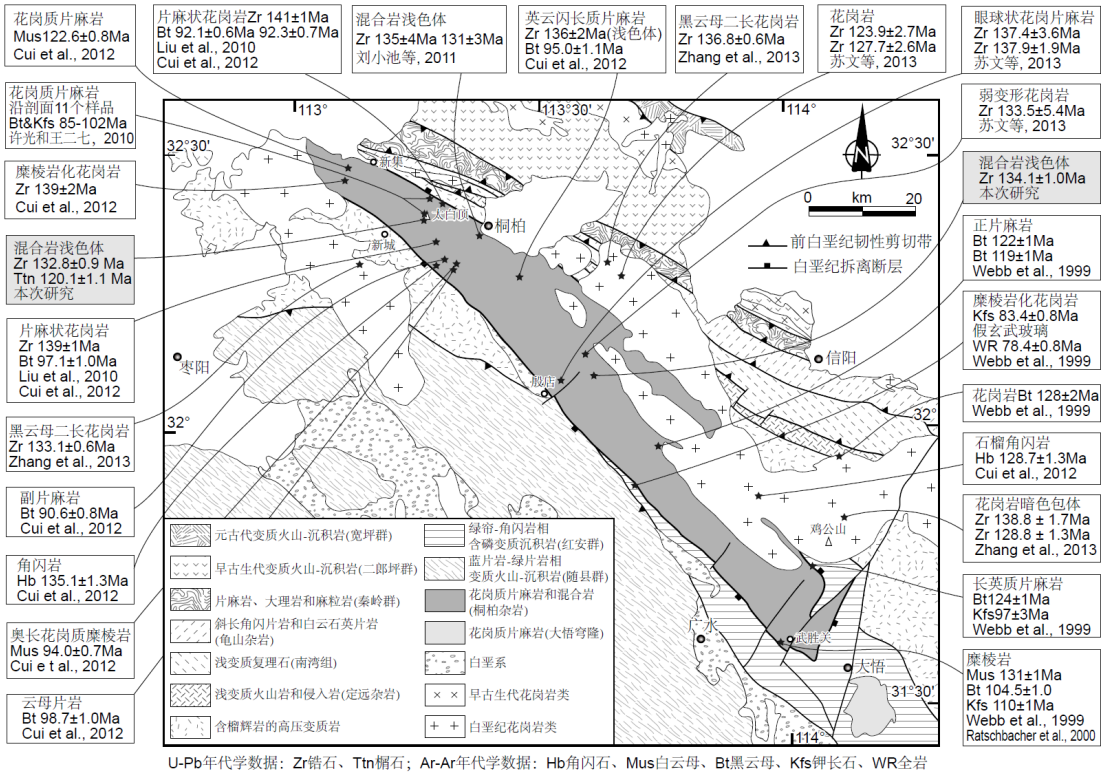

图 3-7 桐柏山白垩纪构造-岩浆年代学

Figure 3-7 Cretaceous tectono-magmatic geochronology of the Tongbaishan

桐柏杂岩中混合岩化现象较常见，指示其曾发生过深熔作用. 刘小池等(2011)对桐柏杂岩中的混合岩进行了 LA-ICP-MS 锆石 U-Pb 定年，其中两个浅色体的年龄为 135 ± 4 Ma 和 131 ± 3 Ma，一个中色体的上交点年龄约为 828 Ma. 而本次研究对混合岩浅色体的 SIMS 锆石 U-Pb 定年获得了 132.8 ± 0.9 Ma 和 134.1 ± 1.0 Ma 两个较为一致的谐和年龄及一个上交点年龄 757 Ma (见下文). 因此，桐柏杂岩混合岩的原岩时代同变质岩一致为新元古代，而混合岩化作用发生的时间在 135-131 Ma. 由此可见，桐柏杂岩主要是造山带的核部物质在早白垩世发生深熔作用的产物，其中强烈变形的花岗岩具有同构造的深熔型花岗岩的特点，而变质岩则可能代表了部分熔融源区岩石的残留体或者围岩的捕掳体.

3.3.2 锆石和榍石 U-Pb 定年 Zircon and titanite U-Pb dating

野外观察表明桐柏杂岩内部的混合岩多与围岩花岗质片麻岩或片麻状花岗岩呈渐变过渡关系，并经历了共同的变形. 因而桐柏杂岩混合岩化作用发生的时间即代表了其构造几何形态形成的时代. 为了确定桐柏杂岩背形构造的形成时代，

本次研究对桐柏杂岩中同变形的混合岩进行了 SIMS 锆石 U-Pb 定年. 两个样品 HO37 和 HO41 均为混合岩中的浅色体, 分别采自桐柏杂岩西部的太白顶地区和中部的殷店地区(图 3-7). 浅色体的主要矿物组成为钾长石、斜长石、石英和黑云母, 含有少量的角闪石以及副矿物.

锆石通过重液和磁选法分离, 然后在双目镜下手工挑纯. 分选出来的锆石颗粒与标样一起粘贴在环氧树脂靶上并抛光. 然后对锆石进行透、反射和阴极发光图像分析, 检查锆石表面和内部结构以方便选点. 锆石 U-Pb 测年在中国科学院地质与地球物理研究所离子探针实验室利用 Cameca IMS-1280 二次离子质谱仪进行, 详细的分析方法和流程见 Li et al. (2009b). 同位素年龄采用 Isoplot 程序进行计算 (Ludwig, 2003). 单个分析数据点和年龄计算结果见表 3-1, 误差均为 1σ. 样品的谐和年龄和上下交点年龄误差为 2σ.

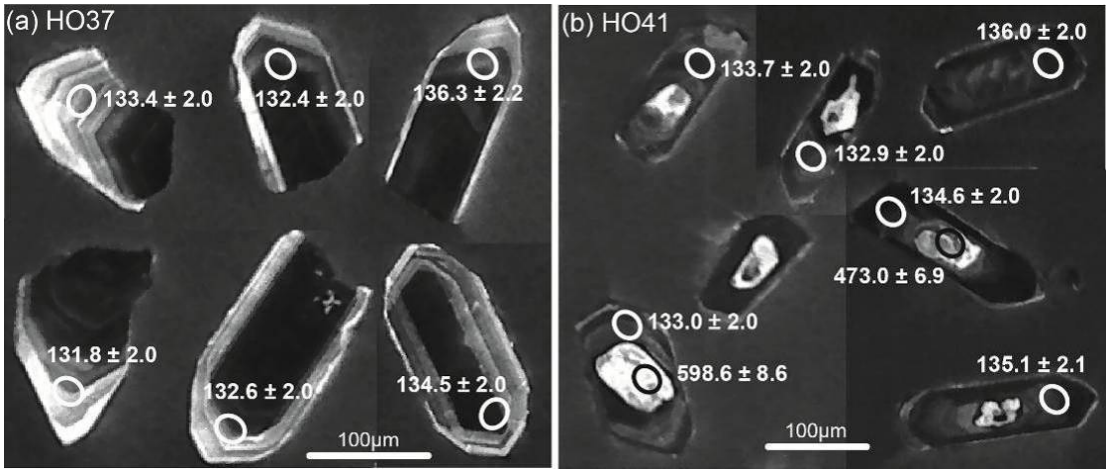

图 3-8 桐柏杂岩混合岩浅色体中代表性锆石的 CL 图像

Figure 3-8 Typical CL images of zircon from migmatite of the Tongbaishan complex

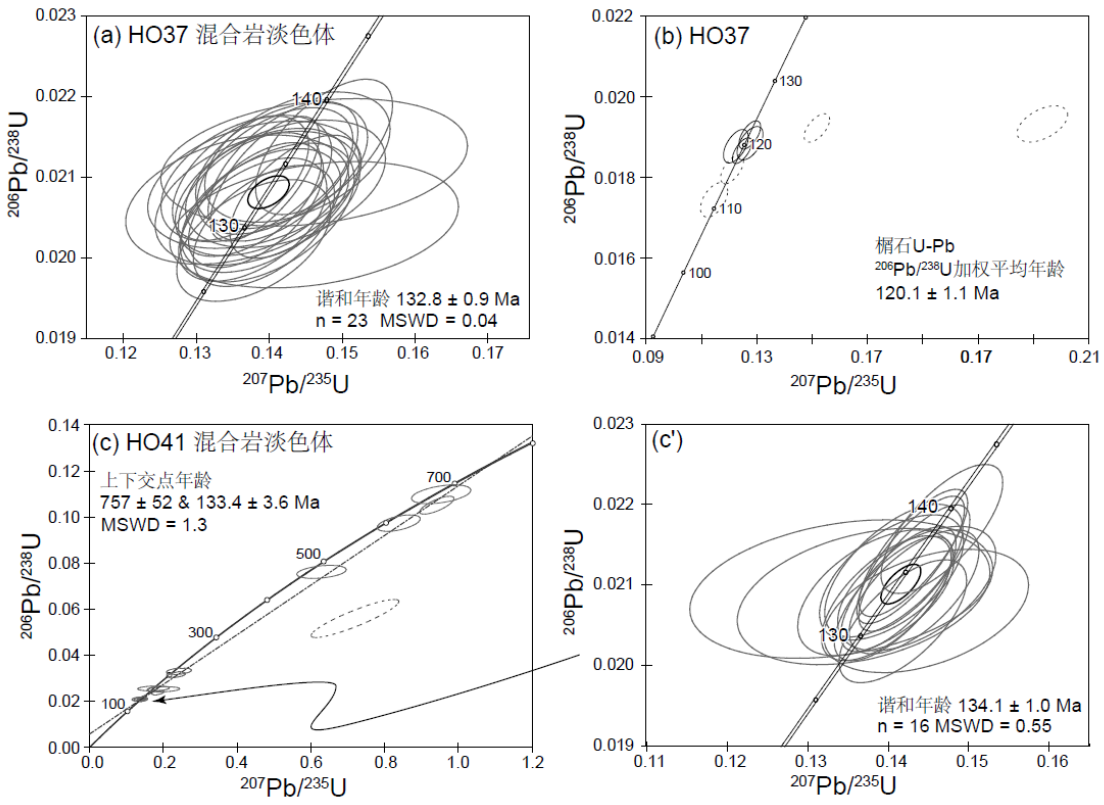

图 3-9 桐柏杂岩混合岩浅色体锆石和榍石 U-Pb 年龄谐和图

Figure 3-9 Concordia diagrams of U-Pb dating for zircon and titanite from migmatite in the Tongbaishan complex

样品 HO37 中锆石呈无色透明的半自形-自形短柱状和长柱状. 锆石边部具强的 CL 发光强度和清晰的面状分带特征, 表明其为典型深熔成因的锆石(图 3-8a). 23 个锆石颗粒的 23 个分析点的 Th/U 比值变化范围在 0.08-0.16, $^{206}Pb/^{238}U$ 表面年龄范围在 129-136 Ma (表 3-1). 所有分析点均位于一致曲线上, 获得谐和年龄为 132.8 ± 0.9 Ma (MSWD = 0.04), 该年龄应代表了混合岩浅色体的结晶时间(图 3-9a).

样品 HO41 中锆石呈无色透明的柱状, 大多数具有明显的核-边结构(图 3-8b). 核部具有弱的振荡环带或无分带, 并有明显的溶蚀现象. 边部没有明显的分带, 为混合岩化过程中变质重结晶形成增生边. 对该样品的 17 颗锆石进行了 28 个分析点的 U-Pb 年龄测定, 其中 12 个点位于锆石的残留核部, 16 个点位于锆石的新生边部. 锆石核部的 Th/U 比值多大于 0.1, $^{206}Pb/^{238}U$ 表面年龄主要分散在 160-672 Ma 区间; 边部 Th/U 比值集中在 0.03-0.07, $^{206}Pb/^{238}U$ 表面年龄从 131 Ma 至 138 Ma (表 3-1). 除去 2 个明显偏离一致线的分析点, 其它分析点获得的不一致线上下交点年龄分别为 757 ± 52 Ma 和 133.4 ± 3.6 Ma (MSWD = 1.3) (图 3-9c). 下交点附近的 16 个谐

和分析点计算得到的谐和年龄为 134.1 ± 1.0 Ma (MSWD = 0.55), 与下交点年龄在误差范围内一致(图 3-9c'). 因此, 757 Ma 可能代表了该样品原岩岩浆岩的侵位年龄, 而其发生深熔作用的时间约在 134 Ma.

此外, 本次研究还对样品 HO37 进行了 TIMS 榍石 U-Pb 定年, 样品的分选和测试在巴黎地球物理所同位素年代学实验室完成, 详细的分析方法和流程见 Schärer and Labrousse (2003). 共计 8 份样品获得了 8 组数据(表 3-2), 其中 2 个分析点偏离一致线, 其余 6 个落在一致线上(图 3-9b). 由 4 个较为集中的分析点计算得到的 $^{206}Pb/^{238}U$ 加权平均年龄为 120 ± 1.1 Ma (2σ). 这一年龄明显小于锆石 U-Pb 年龄, 可能代表了混合岩冷却至榍石 U-Pb 封闭温度(650-700 °C)的时间.

3.4 桐柏杂岩的隆升过程 Uplift process of the Tongbaishan complex

如前所述, 桐柏杂岩中变形花岗岩的侵位时代约在 137-141 Ma (Liu et al., 2010; 苏文等, 2013), 混合岩化作用发生的时间约在 131-135 Ma (刘小池等, 2011; 本次研究). 另外, 一个同构造伟晶岩脉的结晶年龄为 131 ± 1 Ma (Cui et al., 2012), 而侵入桐柏杂岩东部的局部弱面理化的鸡公山岩体的年龄范围在 123-139 Ma (苏文等, 2013; Zhang et al., 2013). 这些年龄数据将桐柏山杂岩韧性变形发生的时间大致限定在 141-130 Ma 之间. 然而, 桐柏杂岩中不同岩石的黑云母、白云母和角闪石 ^{40}Ar-^{39}Ar 定年则获得了 135-119 Ma 和 100-90 Ma 两组年龄(Webb et al., 1999b, 2001; 许光和王二七, 2009; Cui et al., 2012), 表明桐柏杂岩似乎在晚期还经历了第二次的抬升作用. 实际上, 我们从混合岩浅色体中获得的榍石 U-Pb 年龄明显小于其锆石 U-Pb 年龄, 也表明桐柏杂岩在早期的折返过程中部分岩石并未折返至地壳浅部.

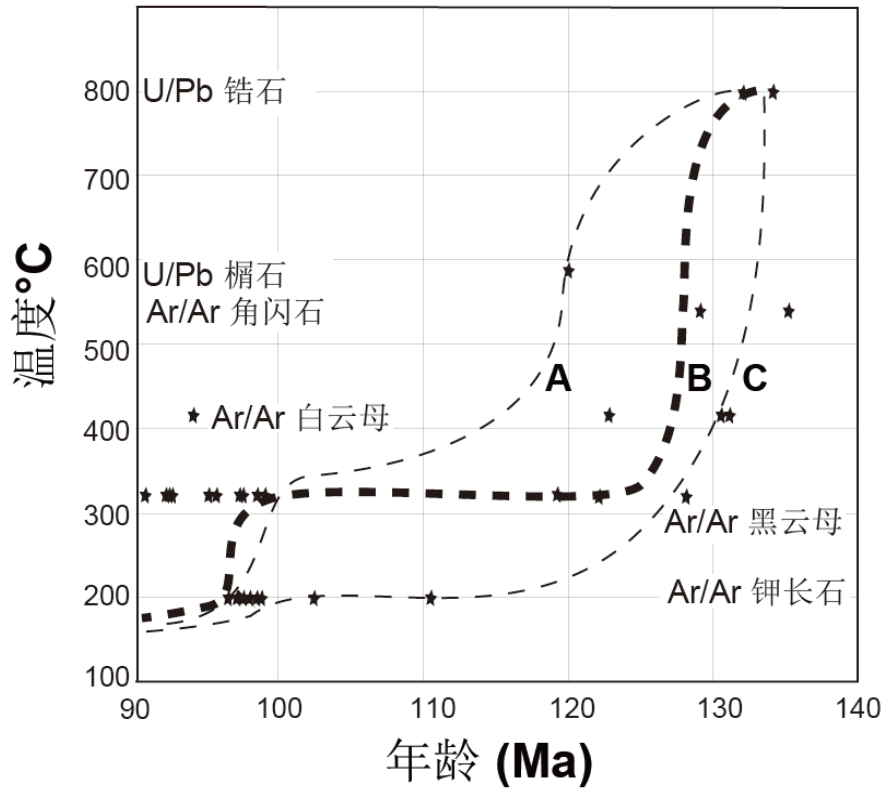

图 3-10 桐柏山变质核杂岩的冷却史

Figure 3-10 Cooling history of the Tongbaishan complex

虽然从构造上很难区分出两阶段拆离折返过程，但是核部杂岩不同的冷却阶段使我们推断桐柏杂岩在白垩纪可能经历了两阶段的构造隆升过程：(1) 141-130 Ma：在区域 NW-SE 向的伸展作用下，桐柏山核部中地壳物质发生了深熔作用，形成了一个巨大的花岗岩-混合岩-变质岩杂岩体，即桐柏杂岩．杂岩在其顶部近水平拆离带的作用下发生了强烈的韧性变形；(2) 100-90 Ma：桐柏杂岩顶部的拆离带被再次活化，并在递进变形和抬升过程中发生褶皱从而形成围限杂岩的韧性剪切带．这也是桐柏杂岩的边界剪切带现今在表面上看似具有走滑特征的原因．抬升至地壳浅层时，边界剪切带还受到了晚期脆性变形的叠加改造．从冷却历史上判断两期冷却过程更类似于图 3-10 中的冷却路径 A．当然，冷却路径 C 也可能通过晚期不明显的冷却过程表现出来；如果是这样，则 100-90 Ma 的云母年龄必须解释为混合年龄．如果忽略各项误差的话，路径 B 则是 A 和 C 的平均结果的表现．无论如何，桐柏杂岩记录了明显的 134-120 Ma 之间的较快速冷却过程，代表了其最为重要的折返时间．

4 红安地体中记录的白垩纪伸展构造 Cretaceous extension recorded in the Hong'an massif

人们一般认为红安地体受白垩纪构造热事件的影响较小, 主要保留了高压/超高压造山带三叠纪的构造格架(王国灿和杨巍然 1998; Webb et al., 1999b, 2001; S.Z. Li et al., 2010, 2011). 通过详细的构造分析及年代学工作, 我们在红安地体西南部的双峰尖和大磊山地区识别出了白垩纪的伸展构造.

4.1 双峰尖伸展构造 Shuangfengjian dome

在红安地体西南缘的双峰尖地区发育一个小型的狭长穹状构造, 即双峰尖穹隆. 穹隆的长轴呈 NW-SE 向延伸约 25 km, 宽度约为 7 km (图 3-2 和图 3-11). 穹隆的核部主要被双峰尖变质花岗岩体所占据, 其它岩石还包括眼球状花岗片麻岩、长英质糜棱岩以及含花岗质砾石的片岩. 双峰尖变质花岗岩体呈斑状结构, 受韧脆性变形改造明显(图 3-12a). 刘晓春等(2005b)对该变质花岗岩的锆石 U-Pb 定年获得了新元古代年龄 813 ± 6 Ma, 应代表原岩花岗岩的侵位年龄. 双峰尖穹隆的外围岩石为红安群的大理岩、白云纳长片麻岩和白云石英片岩以及变质磷块岩, 与穹隆核部岩石以韧性剪切带相接触. 前人关于红安地体的构造研究中, 对双峰尖地区的研究较为薄弱(Webb et al., 1999b, 2001; S.Z. Li et al., 2010, 2011).

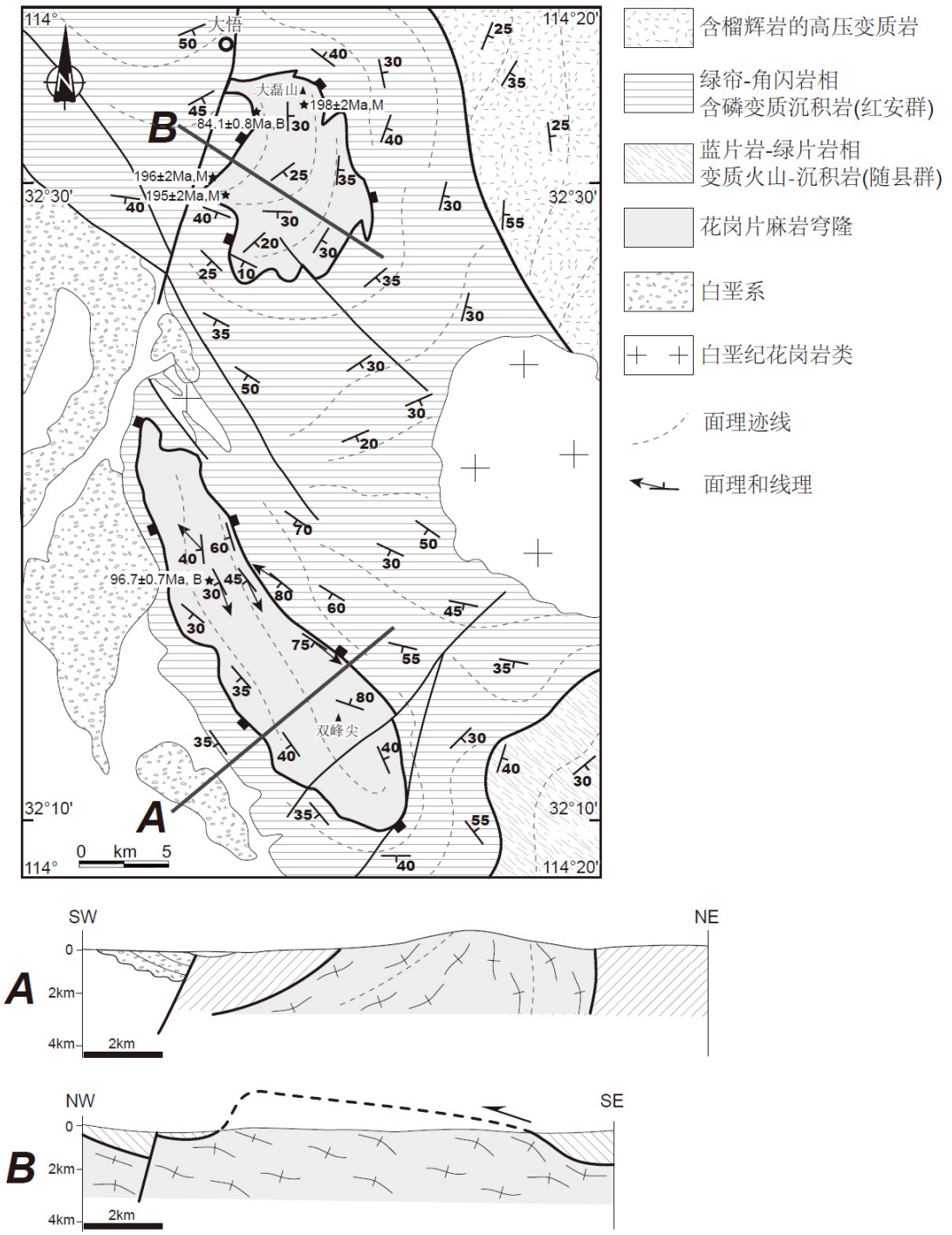

图 3-11 双峰尖和大磊山地质构造简图及构造剖面图

Figure 3-11 Geological and structural map of the Shuangfengjuian and Daleishan area

我们的野外观察显示双峰尖穹隆的南西翼较宽缓, 岩石面理向 SW 中等角度倾斜; 而靠近北界面理向 NE 陡倾, 甚至直立(图 3-11). 这样的构造几何形态整体上构成了一个紧闭的具有 NE 极性的背形构造(图 3-11). 实际上, 类似于桐柏山, 双峰尖背形构造同样可以被看作是一个大型的 A 型褶皱. 穹隆核部出露的花岗质

岩石基本均发生了糜棱岩化，线理构造十分发育(图 3-12b). 这些线理的走向与穹隆长轴平行为NW-SE向，倾伏角较缓，一般小于30°. 靠近边界剪切带围绕在穹隆外围的红安群大理岩同样卷入了糜棱岩化，可见面理上的白云母构成清晰的NW-SE 向矿物拉伸线理(图 3-12c). 沿此线理方向，野外可见眼球状花岗片麻岩中的长石残斑指示上部向 NW 的剪切变形，镜下长英质糜棱岩中发育的 S-C 组构和长石旋转残斑指示了相同的运动学(图3-12d). 双峰尖穹隆中发育的NW-SE向线理和上部向NW的运动学与其外围红安群中普遍所记录的三叠纪NE-SW向线理及其运动学方向可以很容易地相区分开来(图 3-13).

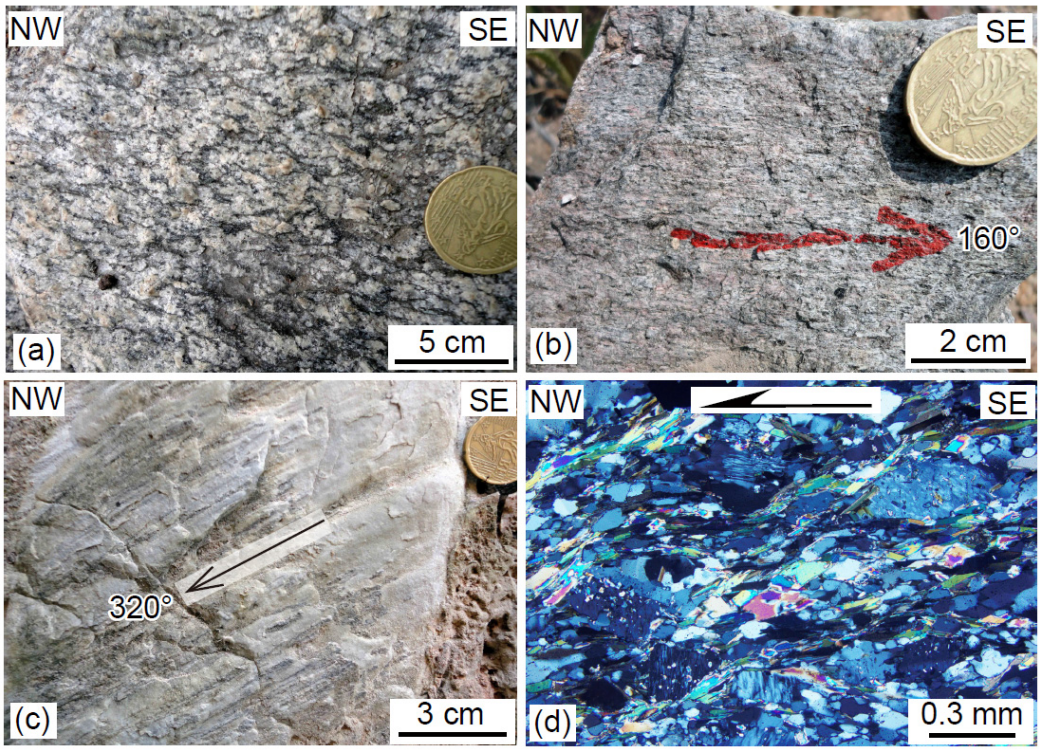

图 3-12 双峰尖穹隆的构造变形特征

(a)双峰尖变质花岗岩体; (b)长英质糜棱岩中发育的 NW-SE 向矿物拉伸线理; (c)糜棱岩化大理岩中白云母定向构成了 NW-SE 向矿物拉伸线理; (d)长英质糜棱岩中 S-C 组构和长石旋转残斑指示了上部向 NW 的剪切变形

Figure 3-12 Structural characteristics of the Shuangfengjian dome

(a) metamorphosed granite in the core of the Shuangfengjian dome; (b) NW-SE trending mineral stretching lineation developed in the felsic mylonite; (c) muscovite in the mylonitic marble formed a NW-SE trending mineral stretching lineation; (d) felsic mylonite with S-C fabric and σ-type feldspar porpyroclasts, indicating a top-to-the-NW shearing

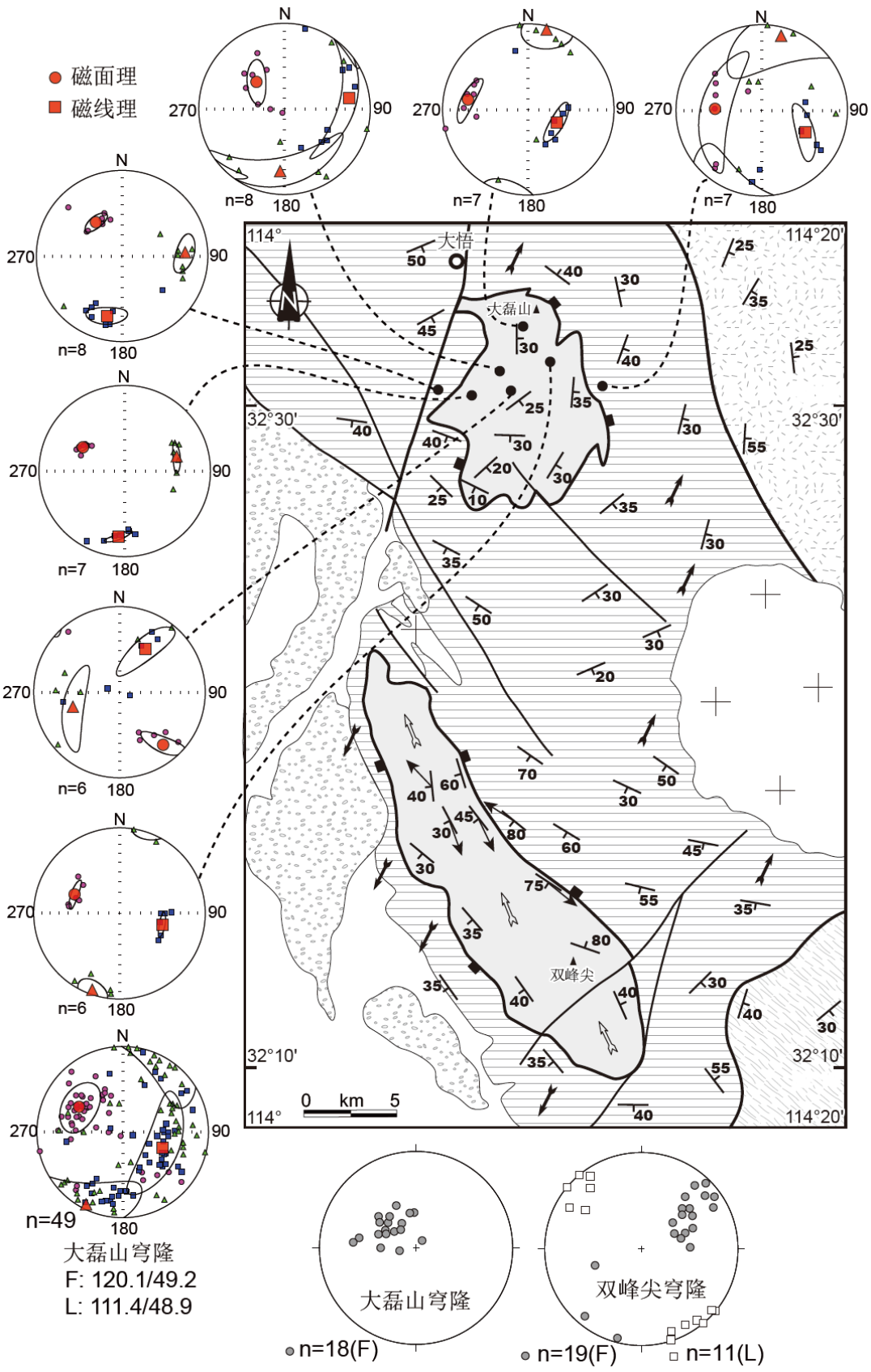

图3-13 双峰尖和大磊山构造要素和运动学图解

Figure 3-13 Structural elements and kinematics map of the Suangfengjian and Daleishan domes

由于双峰尖地区的工作程度较低，其背形构造的形成时代缺乏研究. 为此我们对采自核部的糜棱岩样品 QD88 进行了 $^{40}Ar/^{39}Ar$ 定年，采样位置见图 3-11. 样品中的黑云母给出了 96.7 ± 0.7 Ma 的坪年龄和 96.5 ± 2.1 Ma 反等时线年龄，两者在误差范围内一致(图 3-14). 考虑到研究区岩石的变形条件多为绿片岩相，故黑云母年龄约 97 Ma 应比较接近剪切带的变形时间，这个结果同桐柏山第二期伸展构造在时间上相一致.

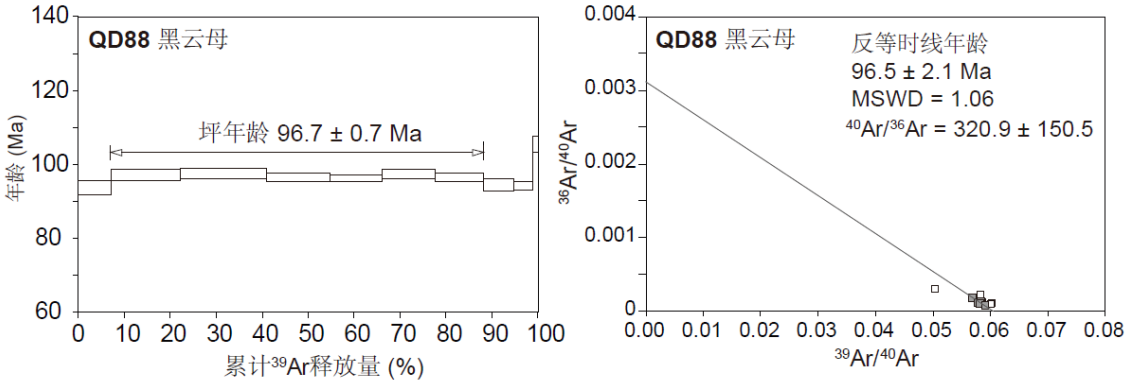

图 3-14 双峰尖构造岩黑云母 $^{40}Ar/^{39}Ar$ 年龄

Figure 3-14 Ar-Ar age of tectonite from the Shuangfengjian dome

虽然双峰尖穹隆南北翼的面理倾向相反，但矿物拉伸线理稳定在 NW-SE 向，且运动学显示为一致的上部向 NW 的剪切变形. 可见从穹隆内部到边界剪切带，其几何学和运动学具有协调一致的特点. 因此，我们推测双峰尖穹隆的边界剪切带在早期应为处于中地壳水平的同一拆离带. 无论从时间上，还是从构造几何学和运动学特点上，双峰尖穹隆同桐柏山变质核杂岩均有很好的对应性. 结合对桐柏-大别造山带区域上的理解，我们认为双峰尖穹隆是在白垩纪 NW-SE 近水平伸展作用下形成 A 型伸展背形构造.

4.2 大磊山伸展构造 Daleishan dome

在红安地体的西部，大悟县城的南东大磊山地区发育一个花岗片麻岩穹隆，通常被人们称为大悟穹隆或者大磊山穹隆(张业明等, 1996; 王国灿和杨巍然, 1998; Webb et al., 1999b, 2001). 大磊山穹隆在空间上具有不甚规则的弯状外貌，略呈南北延长的椭圆形，面积约 300 km^2 (图 3-11). 穹隆核部的大磊山杂岩主体为二长花岗质片麻岩，局部可见眼球状构造，原岩为变质变形的新元古代侵入体(刘晓春等,

2005b). 而环绕穹隆的红安群主要为白云钠长片麻岩、云母石英片岩、大理岩和变质磷块岩等. 大磊山杂岩与红安群以中-低角度的韧性或脆-韧性剪切带相接触. 前人关于大磊山穹隆的成因存在不同的认识, 例如, 张业明等(1996)提出大磊山穹隆为一个新元古代的古老变质核杂岩; 王国灿和杨巍然(1998)认为大磊山杂岩具有整体向北斜向上的楔冲运动特征, 受制于早中生代近 N-S 向的收缩应力背景; 而 Webb et al. (1999b, 2001)认为大磊山穹隆记录了约 195-198 Ma 左右 NE-SW 向近水平伸展作用, 其代表红安地区超高压变质岩折返过程中的晚期局部构造.

大磊山杂岩的片麻理总体以向 ESE 缓倾为主, 在北部和南部与红安群接触带附近, 片麻理发生转折趋于平行穹隆边界. 由于穹隆内部的花岗质杂岩普遍经历了强烈的重结晶作用, 使得我们在野外很难观察到线性构造, 同时岩石所记录的剪切变形也缺乏明显的运动学指向(图 3-13). 相反, 作为穹隆外围的红安群却一如既往地发育了强烈的剪切变形, NE-SW 向的矿物拉伸线理同前人的描述十分吻合(Webb et al., 1999b, 2001). 事实上, 大磊山杂岩构成的仅仅是一个“半”穹隆(图 3-11). 在 NW-SE 的构造剖面上, 大磊山的整体几何形态为一个简单的单斜构造, 而不是完整的穹隆构造, 反而显示出与其西部桐柏山变质核杂岩和谐的几何学配置关系(图 3-11A). 以上的观察促使我们重新思考大磊山穹隆的构造成因，推测大磊山单斜构造可能属于桐柏山变质核杂岩南东转折端构造影响的延续部分.

由于在野外很难观察到线性构造, 因此我们通过岩石磁组构(AMS)对面理化的岩石进行了分析, 结果证实了我们的推断. 从外围红安群到核部花岗片麻岩, 7 个采样点给出了非常复杂的结果: 总体上记录了 NW-SE 向和 NE-SW 向两期线性构造, 并以前者为主体, 具有 111°的极值统计结果(图 3-13). 红安群的线性构造表现出 NE-SW 向, 但是东部“拆离断层”上盘的 1 个采样点的 7 个测点中有 4 个同样给出了 NW-SE 向的磁线理. 核部花岗质片麻岩的 5 个采样点, 虽然也有一些测点记录了 NE-SW 向的磁线理, 但是总体上明显以 NW-SE 向磁线理占主导(图 3-13). 大磊山单斜构造NW-SE向的线性构造及其与桐柏山变质核杂岩和谐的几何学配置关系使我们倾向于将其解释为白垩纪的伸展构造而不是早中生代与超高压变质岩折返相关的收缩或伸展构造. Ratschbacher et al. (2000)报道的大磊山杂岩 84.1 ± 0.8 Ma 的黑云母年龄(图 3-11), 也从侧面印证了我们关于大磊山穹隆成因于白垩纪的观点. 然而, Webb et al. (1999b, 2001)从大磊山杂岩中获得的白云母 ^{40}Ar-^{39}Ar 年龄

集中在 198-195 Ma, 实际上同期的年龄在大别山东南部也广泛存在(Hacker et al., 2000). 我们推测导致这一现象的原因可能是由于大磊山杂岩在白垩纪的折返幅度较小, 且变形主要发生在低温的韧-脆性条件下, 所以致使早期与变质岩石折返相关的冷却年龄并未被白垩纪的事件所完全重置. 这与大磊山穹隆在构造层次上位于桐柏山变质核杂岩之上的构造关系相一致.

5 大别山白垩纪伸展构造 Cretaceous extensional structures in the Dabieshan

5.1 大别山主要岩石构造单元及其特征 Main litho-tectonic uints and their characteristics

不同学者对大别山岩石构造单元的划分存在一定的分歧(Okay et al., 1993; Cong, 1996; Hacker et al., 2000; 索书田等, 2001; 徐树桐等, 2002; Faure et al., 2003; Zheng et al., 2005). 结合已有的研究结果及博士论文期间的实际工作, 我们将大别山分为三个构造带: 北部的北淮阳构造带, 中部的中大别穹隆(传统上称为北大别)和南部的南大别构造堆叠体系(图 3-15 和图 3-16). 大别山最显著的特征之一是分布有大面积花岗岩类以及少量的基性-超基性岩(辉石岩-辉长岩类), 其侵位时代集中在早白垩世(Jahn et al., 1999; Zhao et al., 2004, 2005, 2007, 2011; Huang et al., 2007, 2008; Q. Wang et al., 2007b; Xu et al., 2007, 2012; Dai et al., 2011; He et al., 2011, 2013). 此外，沿北淮阳构造带还发育有同时期的火山岩带(图 3-15).

北淮阳构造带由佛子岭群和卢镇关杂岩组成, 变质程度主体为绿片岩相, 局部达到绿帘-角闪岩相. 佛子岭群为一套浅变质复理(岩性包括变砂岩、石英岩和云母石英片岩), 沉积时代为泥盆纪. 它曾被认为代表被动大陆边缘沉积、弧前或者弧后沉积(Okay et al., 1993; 王清晨和从柏林, 1998; 徐树桐等, 2002). 卢镇关杂岩主要由花岗质片麻岩和石英片岩组成, 其原岩为新元古代(780-750 Ma)的侵入岩和火山岩(Chen et al., 2003; 刘景波等, 2013). 周建波等(2001)将北淮阳构造带视为扬子陆块在俯冲过程中被刮削下来的构造加积楔. 另外, 未变质或轻微变质的石炭纪含煤沉积岩局部零星出露于北淮阳构造带的中段(商城地区). 侏罗-白垩纪的沉积岩不整合覆盖于北淮阳构造带的变质岩之上.

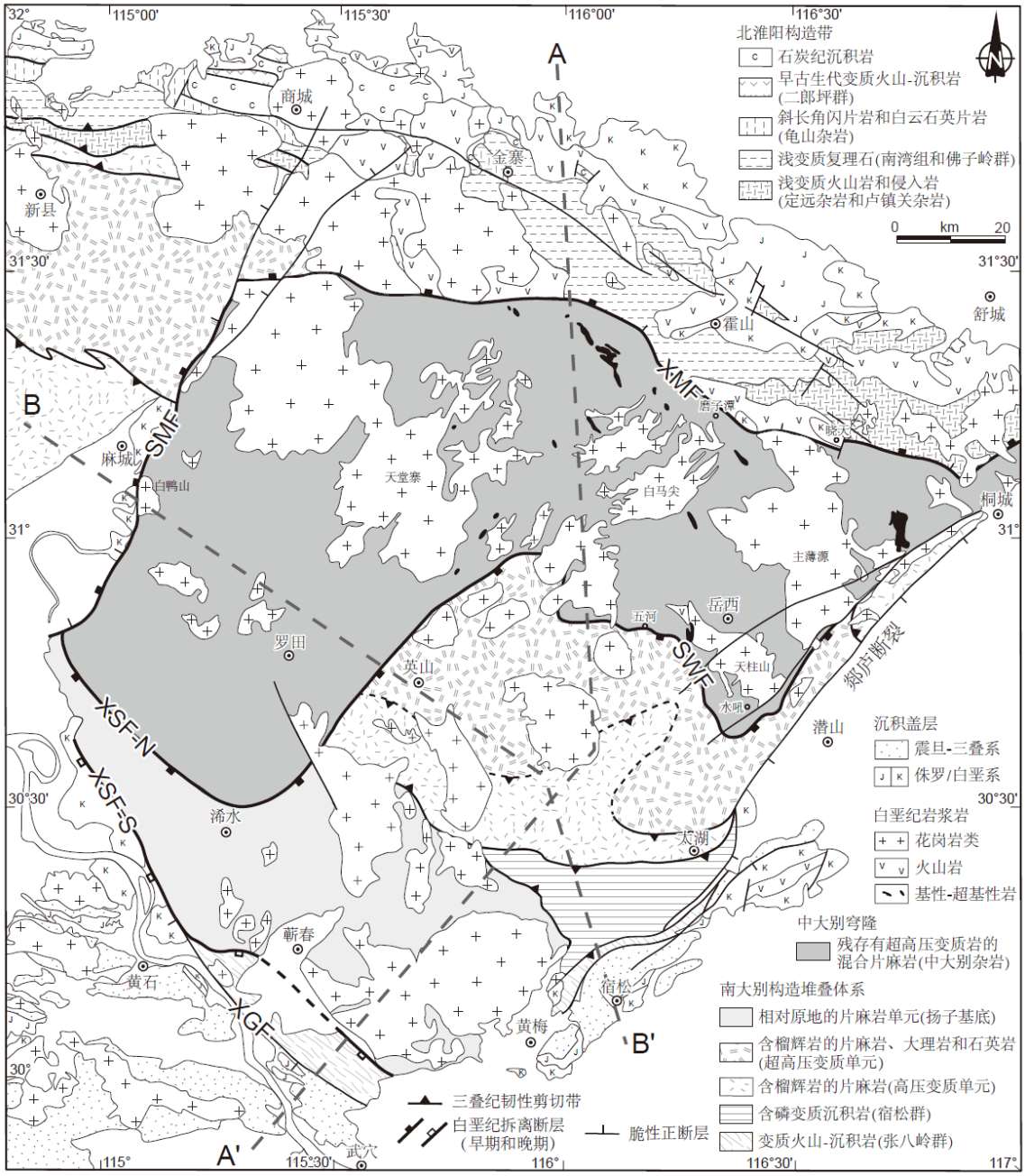

图3-15 大别山地质构造图

Figure 3-15 Geoloical and structural map of the Dabieshan

XMF: 晓天-磨子潭断裂Xiaotian-Mozitan fault; SMF: 商麻断裂Shang-Ma fault; SWF: 水吼-五河剪切带Shuihou-Wuhe shear zone; XSF-N and XSF-S: 北浠水剪切带和南浠水剪切带North Xishui shear zone and South Xishui shear zone; XGF: 襄樊-广济断裂Xiangfan-Guangji fault

中大别穹隆的组成岩石，即中大别杂岩，主要是正片麻岩(英云闪长质片麻岩，花岗闪长质片麻岩和二长花岗岩质片麻岩)、斜长角闪岩和少量的大理岩、麻粒岩、榴辉岩以及变质的橄榄岩类等. 变质程度以角闪岩相为主，穹隆核部出现麻粒岩相变质. 另外，少部分岩石还残留有榴辉岩相矿物组合. 中大别杂岩普遍发生了不

同程度的部分熔融从而形成各种混合片麻岩. 人们对中大别杂岩构造属性的认识众说纷纭, 主要有以下几种观点: (1)变质蛇绿混杂岩, 相当于三叠纪华北和华南的碰撞缝合带(徐树桐等, 2002); (2)古生代安第斯型岛弧杂岩(Zhai et al., 1994, 1995); (3)三叠纪高温变质地体, 属于俯冲带上盘华北板块的一部分(Zhang et al., 1996); (4)白垩纪大规模侵位的岩浆杂岩体, 被称为"northern orthogneiss unit(NOU)"(Hacker et al., 1995, 1998; Ratschbacher et al. 2000); (5)主要由高压/超高压变质岩及其下部未卷入大陆深俯冲的角闪岩相片麻岩两部分经混合岩化作用发展而成(Faure et al., 1999, 2003; 林伟等, 2003); (6)扬子陆块的延伸, 未受到超高压变质作用影响(Bryant et al., 2004); (7)三叠纪的高温-超高压变质地体, 属于扬子深俯冲陆壳的一部分(徐树桐等, 1999, 2003; 刘贻灿等, 2000, 2001, 2005; Tsai and Liou, 2000; Xiao et al., 2001; Y.C. Liu et al., 2005, 2007a, 2007b, 2011a, 2011b; Zheng et al., 2005; Malaspina et al., 2006; 刘贻灿和李曙光, 2005, 2008; 郑永飞, 2008). 直至目前, 关于中大别杂岩是否整体经历过超高压变质作用仍未有定论(R.Y. Zhang et al., 2009; Tong et al., 2011).

南大别构造堆叠体系由一套倾向 SW-SE 的假单斜状岩片叠置而成, 自下而上依次为: 相对原地的片麻岩单元、含榴辉岩的超高压单元、含榴辉岩的高压单元、宿松群和张八岭群(图 3-16). 相对原地的片麻岩单元主要由花岗质片麻岩、黑云(角闪)斜长片麻岩和少量斜长角闪岩组成. 该单元从未经历大陆深俯冲作用, 以角闪岩相变质程度为主, 我们认为其可能代表了扬子陆块的基底. 含榴辉岩的高压/超高压单元主要由正、副片麻岩和少量的云母片岩、大理岩和硬玉石英岩组成, 夹有榴辉岩及退变榴辉岩的团块或透镜体. 虽然经过二十余年的研究, 但关于高压/超高压岩片的结构划分仍存在着不同的意见(Okay, 1993; Carswell et al., 1997; Li et al., 2004; Shi and Wang, 2006; Lin et al., 2009; 石永红等, 2013; Shi et al., 2014). 宿松群为一套含磷变质沉积岩, 岩性包括白云斜长片麻岩、白云石英片岩、石英岩、大理岩、石墨片岩和变质磷块岩等, 变质程度为绿帘-角闪岩相. 张八岭群主要为一套变质的双峰式火山岩, 可与桐柏山地区的随县群对比, 变质程度为蓝片岩-绿片岩相. 关于南大别的年代学研究主要集中于高压/超高压岩片, 大量的年龄数据(Li et al., 1993, 2000; Ames et al., 1993, 1996; Chavagnac and Jahn, 1996; Rowley et al., 1997; Hacker et al., 1998; Chavagnac et al., 2001; Ayers et al., 2002; Wan et al., 2005; Liu et al., 2006; Wawrzenitz et al., 2006; 郑永飞, 2008 及其参考文献)表明高压/超高压变

质作用发生的时代在 240-225 Ma 期间, 其原岩主要为扬子陆块北缘与新元古代(820-740 Ma)裂谷活动相关的岩浆产物. 虽然一般认为宿松群和张八岭群的原岩形成时代也为新元古代, 并经历了三叠纪的变质, 但目前仍缺少精确的年代学约束(徐树桐等, 2002; Xu et al., 2012).

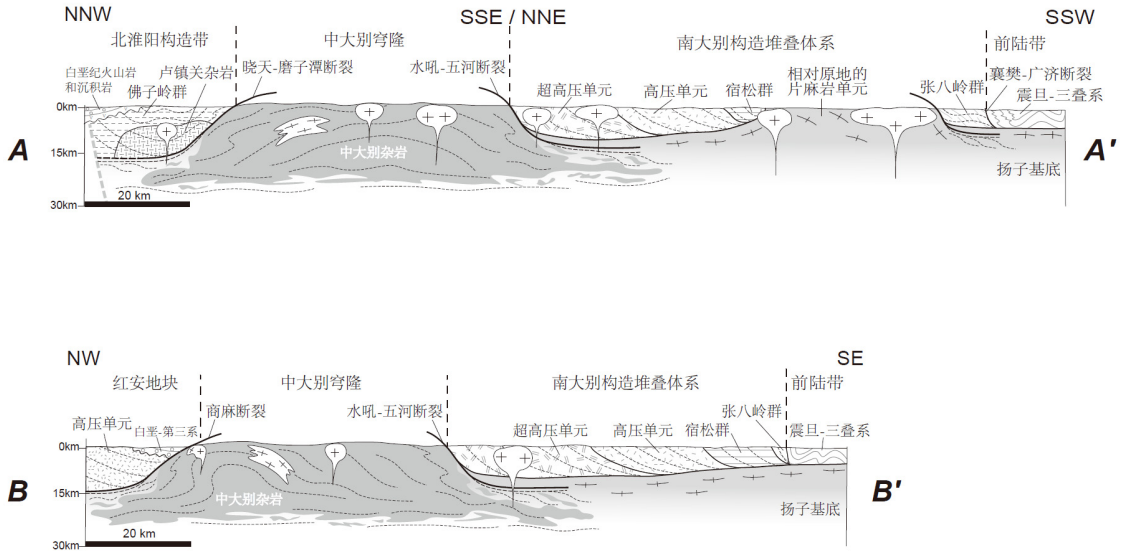

图3-16 大别山剖面示意图(位置见图3-15)

Figure 3-16 Schematic cross sections of the Dabieshan (locations see Figure 3-15)

5.2 大别山白垩纪变质核杂岩的厘定 Recognition of the Cretaceous Dabieshan MCC

中大别穹隆作为一个大规模的伸展构造已被人们广泛接受(王国灿和杨巍然, 1996, 1998; Hacker et al., 1998; X.D. Wang et al., 1998; Ratschbacher et al., 2000; 许长海等, 2001; 侯泉林等, 2007; Y.S. Wang et al., 2011). 然而涉及到详细的构造几何学、运动学剖析及其同高压/超高压变质杂岩之间的关系等细节性工作却缺乏研究, 从而制约了我们对高压/超高压造山带的形成及其演化的理解. 结合前人的工作及我们对中大别杂岩及其边界剪切带或断裂带详细的构造解析, 认为中大别穹隆为形成于NW-SE向伸展体制下的具造山带规模的变质核杂岩(图3-16和图3-17). 现今大别山的几何形态几乎完全由中大别穹隆所控制. 中大别穹隆的北部边界晓天-磨子潭断裂与西部边界商麻断裂构成了中大别穹隆西北翼的一个统一的弧形拆离断层, 北淮阳构造带和红安地体及其上覆的白垩-第三纪半地堑盆地代表了这一

拆离断层的上盘. 中大别杂岩(混合片麻岩以及残存的超高压变质岩)构成了拆离断层下盘的核部杂岩. 而中大别穹隆东南部边界水吼-五河剪切和大别山南缘(浠水地区)发育的马尾状剪切带(简称为浠水剪切带, 包括 XSF-N 和 XSF-S 两条剪切带)则构成了中大别穹隆东南翼的多重拆离断层组合, 南大别三叠纪变质序列(包括高压/超高压岩片、宿松群和张八岭群)代表了被这一拆离断层组合肢解的上盘构造岩片.

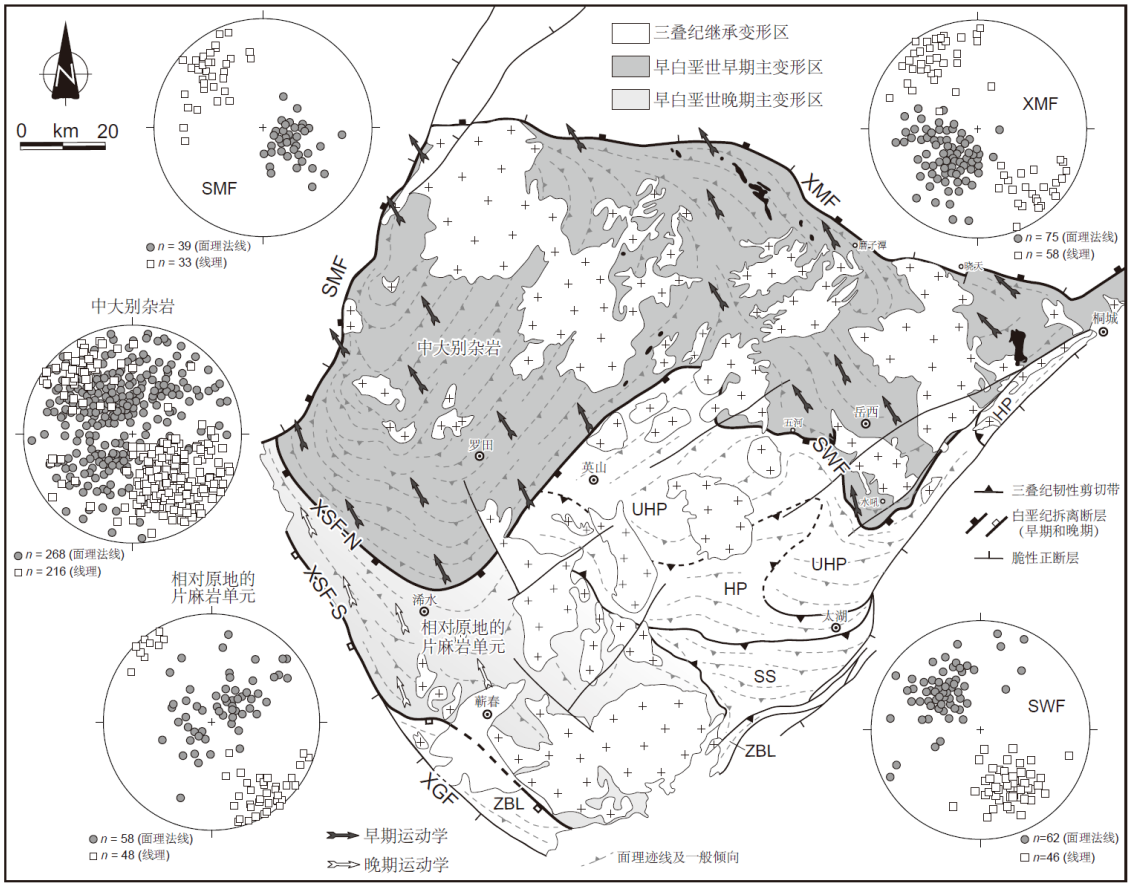

图3-17 大别山变质核杂岩的构造要素和运动学图解

Figure 3-17 Structural elements and kinematics map of the Dabieshan MCC

XMF: 晓天-磨子潭断裂Xiaotian-Mozitan fault; SMF: 商麻断裂Shang-Ma fault; SWF: 水吼-五河剪切带Shuihou-Wuhe shear zone; XSF-N and XSF-S: 北浠水剪切带和南浠水剪切带North Xishui shear zone and South Xishui shear zone; XGF: 襄樊-广济断裂Xiangfan-Guangji fault; UHP: 超高压单元UHP unit; HP: 高压单元HP unit; SS: 宿松群Susong Group; ZBL: 张八岭群Zhangbaling Group

研究表明中大别杂岩及其拆离断层具有统一的NW-SE向矿物拉伸线理和上部指向NW的运动学, 变形时间主体在早白垩世. 与美国西部盆岭省发育的典型变质核杂岩类似, 我们推测大别山变质核杂岩的拆离断层在早白垩世初期其原始发育

状态为处于中地壳近水平的同一韧性剪切带, 可能对应于早白垩世大别山中下地壳物质发生部分熔融而塑性流动的顶面与高压/超高压岩片之间的拆离面. 随后在变质核杂岩形成的穹隆作用下, 拆离面发生了褶曲并被剥蚀出露成为现今观察到的“弧形”构造.

5.2.1 中大别穹隆的构造特征 Structural features of the central Dabieshan dome

构成中大别穹隆的中大别杂岩主体为普遍经历了不同程度混合岩化作用的片麻岩(混合片麻岩), 含有少量大理岩、斜长角闪岩、麻粒岩和榴辉岩. 相关的岩石学和地球化学研究表明中大别杂岩相当于扬子陆块的中下地壳岩石, 其中部分岩石(包括榴辉岩及其围岩混合片麻岩)还经历过超高压变质作用(刘贻灿和李曙光, 2008 及其参考文献). 这些残余的超高压变质岩由于在地壳深部滞留时间相对较长而在峰期变质后可能部分叠加了麻粒岩相退变质, 经历了缓慢冷却而明显不同于南大别超高压变质岩的快速冷却过程. 中大别杂岩的混合岩化程度并不均匀, 总体上从穹隆边部向核部增强, 并可大致划分为核部全熔合岩(diatexite)和幔部半熔合岩(metatexite)两个分区(Faure et al., 1999, 2003; J.H. Wang et al., 2002; S.J. Wang et al., 2013). 穹隆核部具有较高的重熔程度, 出现深熔型花岗岩. 相反, 岩石的变形程度则由穹隆核部向边缘递增, 核部未变形或变形较弱, 而边缘部分则发生片麻岩化及糜棱岩化. 这些混合片麻岩的宏观构造特征呈现不均一性, 面理通常由浅色体的条带或褶皱, 暗色体的条带或透镜体或析离体构成(图 3-18a, b).

依据面理迹线的走向趋势, 大别山中部可划分出两个次级穹隆构造: 西部规模较大的罗田穹隆和东部规模较小的岳西穹隆(图 3-17). 罗田穹隆在几何形态上显示为不对称的贝壳状, 穹隆的中心靠近商麻断裂. 穹隆西北翼狭窄, 面理主要倾向 NW, 倾角较缓. 穹隆东南翼较为宽阔, 面理倾向沿顺时针方向变化: 北部倾向 NE, 倾角较缓至中等; 至中部和南部逐渐转为 SE 和 SW, 倾角中等至较陡.岳西穹隆则被花岗岩体所占据, 更多地表现出岩浆穹隆的特点. 统计学结果显示中大别混合片麻岩中发育的矿物生长和矿物拉伸线理优选方位为 NW-SE 向(图 3-17). 在穹隆边部的混合片麻岩中, 沿线理方向在野外露头、手标本和薄片中可见各种剪切运动学标志, 如长英质脉体的不对称褶皱、难熔暗色斜长角闪岩的布丁构造、剪切条带或 S-C 组构、长石旋转碎斑、云母鱼、压力影以及石英 C 轴组构等, 均一致的指

示了上部向 NW 的剪切变形(图 3-18c; Faure et al., 1999, 2003; Hacker et al., 1995, 2000; Ratschbacher et al., 2000; 林伟等, 2003, 2005; 冀文斌等, 2011; Y.S. Wang et al., 2011). 穹隆核部由于混合岩化程度较高, 变形样式复杂并呈现出不均一性, 主要反映了岩石在部分熔融状态下的塑性流变过程.

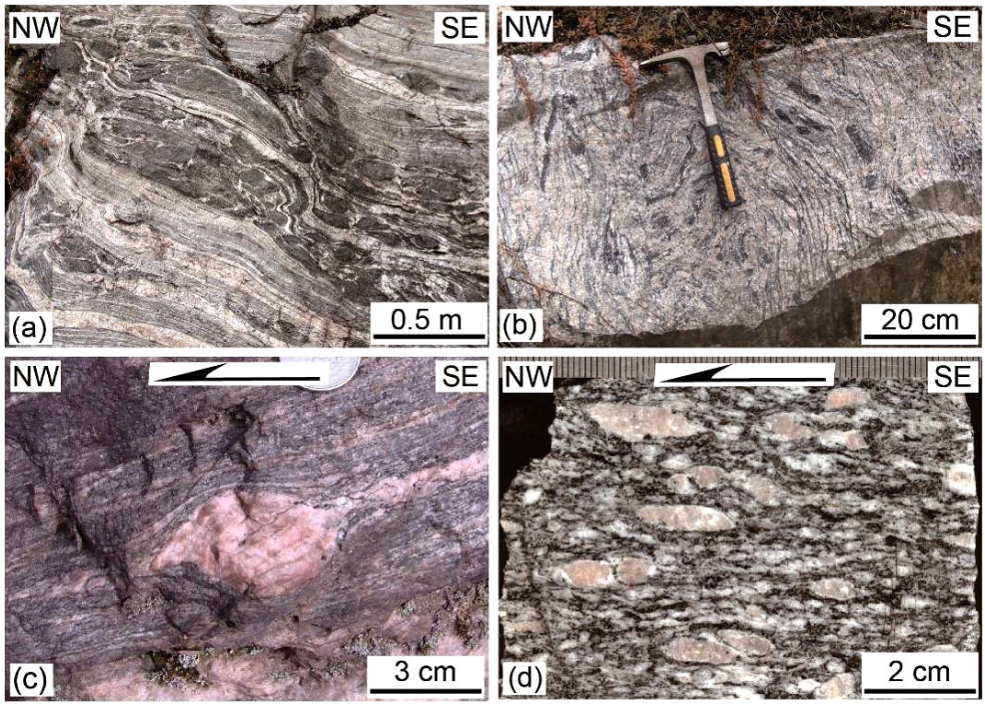

图3-18 中大别杂岩的构造特征

(a)层状混合岩: 浅色体可分为两类, 一类为灰白色的几乎相互平行的微细脉状, orther 另一类为浅粉色的粗晶脉体, 暗色体则呈条带状或透镜状; (b)析离状混合岩:浅色体强烈褶皱, 暗色体以析离体的形式存在构成面理; (c)混合片麻岩中的眼球状钾长石指示了上部向NW的剪切变形; (d)同构造花岗岩中的钾长石旋转残斑指示了上部向NW的剪切变形

Figure 3-18 Structral features of the central Dabieshan complex

(a) stromatic migmatite: there are two categories of leucosome veins, one is light gray color and fine-grain, another is light pink color and coarse-grain, and the melanosome occurs as straps or lens; (b) schlieric migmatite: the leucosome was strongly folded and the melanosome usually occurs as wispy layers of schlieren; (c) megacryst of augen K-feldspar in the migmatite gneiss indicates a top-to-the-NW sense of shear; (d) syn-tectonic granite with σ-type feldspar porpyroclasts, indicating a top-to-the-NW sense of shear

在中大别穹隆内部，分布有大面积的花岗岩类, 较大的岩体有天堂寨、白马尖、主簿源和天柱山等(图 3-15). 其中天堂寨复式岩体的早期侵入相包括九资河和鹅公包等, 普遍发育片麻状构造, 并含有大量混合片麻岩的捕掳体或残留体, 显示出深

熔型花岗岩的特点(Q. Wang et al., 2007b; Xu et al., 2007, 2012). 实际上, 中大别杂岩中一些被认为原岩为早白垩世的片麻岩(Xue et al., 1997; Hacker et al., 1998; Bryant et al., 2004; Xie et al, 2006)极有可能是强烈变形的早白垩世花岗岩. 但由于它们与围岩片麻岩具有相似的矿物组合和协调一致的变形特征, 有时在野外很难将其分离出来. 我们野外调查过程中, 在罗田北部面理化的花岗岩中同样观察到了上部向 NW 的剪切变形(图 3-18d). 由此可见, 中大别穹隆内强变形或弱变形的花岗岩代表了与变质核杂岩形成相关的同构造早期或晚期侵入体.

5.2.2 拆离断层的几何学和运动学 Geometry and kinematics of the detachment faults

如上所述, 中大别杂岩的变形特征具有明显的递变性, 由穹隆中心向边缘变形程度递增, 边缘部分则发育糜棱岩化. 作为穹隆边界的晓天-磨子潭断裂、商麻断裂、水吼-五河剪切带和浠水剪切带构成了大别山变质核杂岩的拆离断层.

中大别伸展构造北部边界——晓天-磨子潭断裂(XMF)

晓天-磨子潭断裂分隔了大别山中部穹隆的混合片麻岩和北淮阳构造带的浅变质岩. 作为大别山一条重要的边界断裂, 其在造山带演化过程中的作用一直以来都存在争议. 索书田等(2000)认为晓天-磨子潭断裂是被强烈改造了的华北和华南在三叠纪时的碰撞缝合带. 在 Faure et al. (1999, 2003)和林伟等(2003)提出的“同折返穹隆”模式中, 将晓天-磨子潭断裂和商麻断裂作为与高压/超高压变质岩早期折返相关的统一的弧形拆离断层, 而后在白垩纪的伸展作用下又再次活化. Ratschbacher et al. (2000)也推测晓天-磨子潭断裂具有多期活动历史: 三叠纪时可能与红安地块北部的浒湾剪切带相连, 共同构成了高压/超高压变质岩折返的顶部拆离断层; 早白垩世为正-左行韧性剪性带, 控制了中大别穹隆的几何学; 100-90 Ma 则表现为与郯庐断裂共轭的右行走滑断层. Y.S. Wang et al. (2011)认为晓天-磨子潭断裂和五河-水吼断裂在早白垩世早期可能为处于中地壳水平的同一剪切带, 构成了所谓的“东大别拆离带”. 现有的地球物理资料显示晓天-磨子潭断裂并未切割整个地壳, 而是处于中上地壳倾向北东的铲状断层, 然而断裂下方的莫霍面却

存在明显的错断(Yuan et al., 2003). 这一现象表明晓天-磨子潭断裂早期的历史已经被完全抹除, 现今主要表现为与中大别穹隆形成相关的拆离断层.

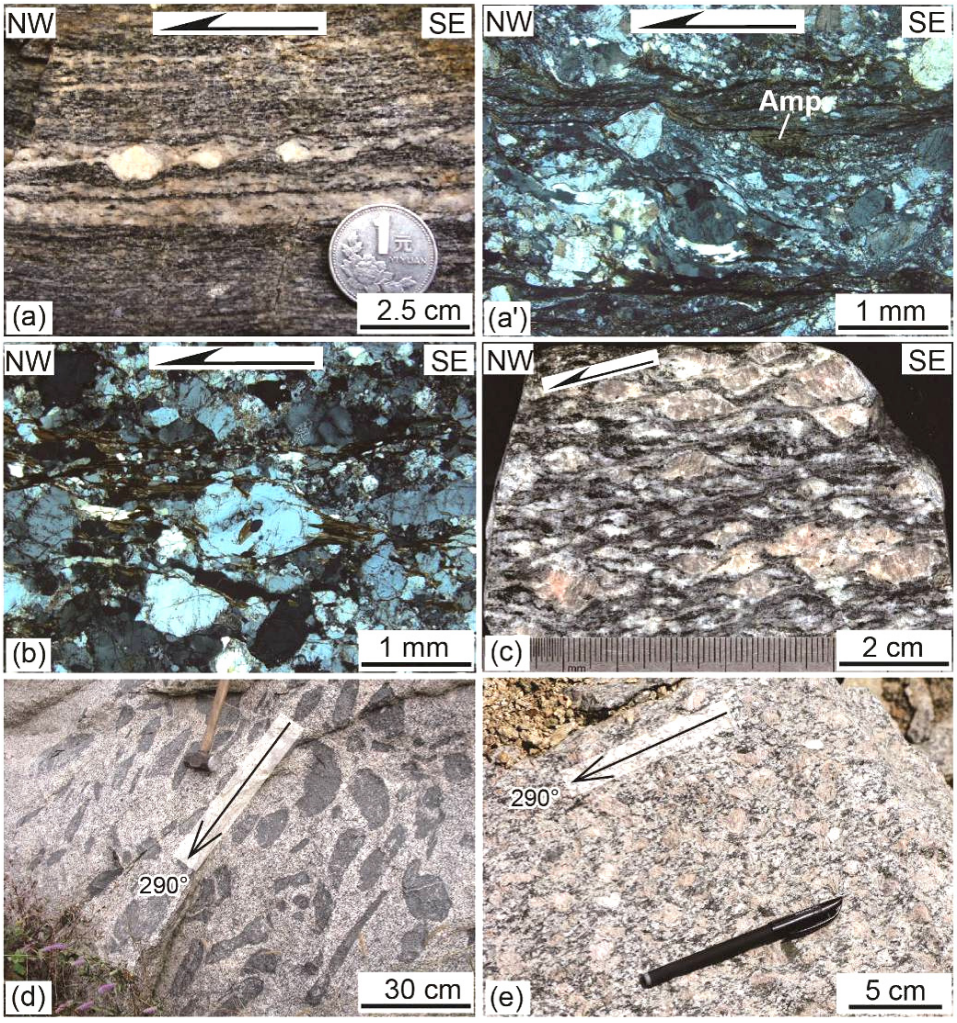

图3-19 晓天-磨子潭断裂的构造变形特征

(a)和(a')糜棱岩化的条带状片麻岩中的长石旋转残斑和角闪石鱼构造指示了上部向NW的剪切变形; (b)花岗质糜棱岩中的长石旋转残斑指示了上部向NW的剪切变形; (c)强烈变形的眼球状花岗岩中发育的S-C组构和长石旋转残斑指示了上部向NW的剪切变形; (d)姚河附近花岗岩中局部富集的暗色包体被强烈拉长定向; (e)姚河附近花岗岩中由黑云母集合体构成的NW-SE向线理

Figure 3-19 Deformation characteristics of the Xiaotian-Mozitan fault

(a) and (a') mylonitic banded gneiss with σ-type feldspar porpyroclasts and amphibole fish, indicating a top-to-the-NW sense of shear; (b) σ-type feldspar porpyroclasts in the granitic mylonite indicate a top-to-the-NW sense of shear; (c) augen granite with S-C fibric and σ-type feldspar porpyroclasts, indicating a top-to-the-NW sense of shear; (d) in the Yaohe granite, mafic enclaves are loclly concentrated and strongly elongated; (e) biotite aggregate in foliated granite near Yaohe constitutes a NW-SE trending lineation

晓天-磨子潭断裂总体走向 NWW-SEE, 具多期变形特点. 断裂深部表现为韧性剪切带, 浅部则以脆性断层与上盘北淮阳构造带的浅变质岩和早白垩世花岗岩及火山岩接触, 并叠加在下盘的韧性变形之上. 晓天火山-沉积盆地的填充作用明显受控于晓天-磨子潭断裂的活动. 韧性剪切带的西段由于早白垩世花岗岩类的侵入而断续出露, 中段和东段经青山、磨子潭、晓天至庐镇关连续出露, 沿南侧的混合片麻岩中广泛发育糜棱岩. 糜棱岩面理主要倾向 NE, 局部向 N, 倾角一般在 20-45° (图 3-17). 在明显发育的面理上, 长英质矿物、黑云母和少量的角闪石及绿帘石构成了清晰的 NW-SE 向矿物拉伸线理(图 3-17). 在剪切带的不同部位, 糜棱岩的矿物组合和变形特征指示剪切带经历了从角闪岩相到绿片岩相不同阶段的演化过程. 野外和显微镜下糜棱岩中发育的剪切标志, 如长石旋转残斑和新生角闪石变形而成的矿物鱼构造, 均指示了上部向 NW 的剪切变形(图 3-19a 和 a', b).

沿断裂带分布的部分早白垩世花岗岩也发生了同构造的变形, 如靠近剪切带中段未被填图的由花岗岩强烈变形而成的眼球状糜棱岩, 其发育的 S-C 组构和长石眼球拖尾同样指示了与围岩片麻岩一致的上部向 NW 的运动学(图 3-19d); 主薄源岩体的姚河单元普遍发育片麻状构造(林伟等, 2005), 野外露头可见岩体中局部富集的暗色包体被强烈拉长定向, 其长轴方向平行于寄主花岗岩中由黑云母集合体构成的 NW-SE 向线理(图 3-19e).

中大别伸展构造西部边界——商麻断裂(SMF)

商麻断裂走向NEE, 同晓天-磨子潭断裂一样具有多期变形特点(Faure et al., 1999, 2003; 林伟等, 2003). 它是划分东、西大别的界限, 也是中大别杂岩的西部边界. 然而, 商麻断裂在中大别穹隆形成过程中所起的作用时常被人们所忽略(X.D. Wang et al., 1998; Ratschbacher et al. 2000; Y.S. Wang et al., 2011). 王义天等(2000)认为商麻断裂带起源于三叠纪华北和华南的碰撞, 是一条垂直造山带走向的横向平移断层. 王朴等(2008)对商麻断裂进行了较为详细的构造解析, 鉴别出3种伸展性断裂构造活动, 从早到晚分别为: 低角度向NWW方向滑脱的韧性剪切、西倾的低角度脆-韧性滑脱正断层、西倾的高角度脆性正断层.

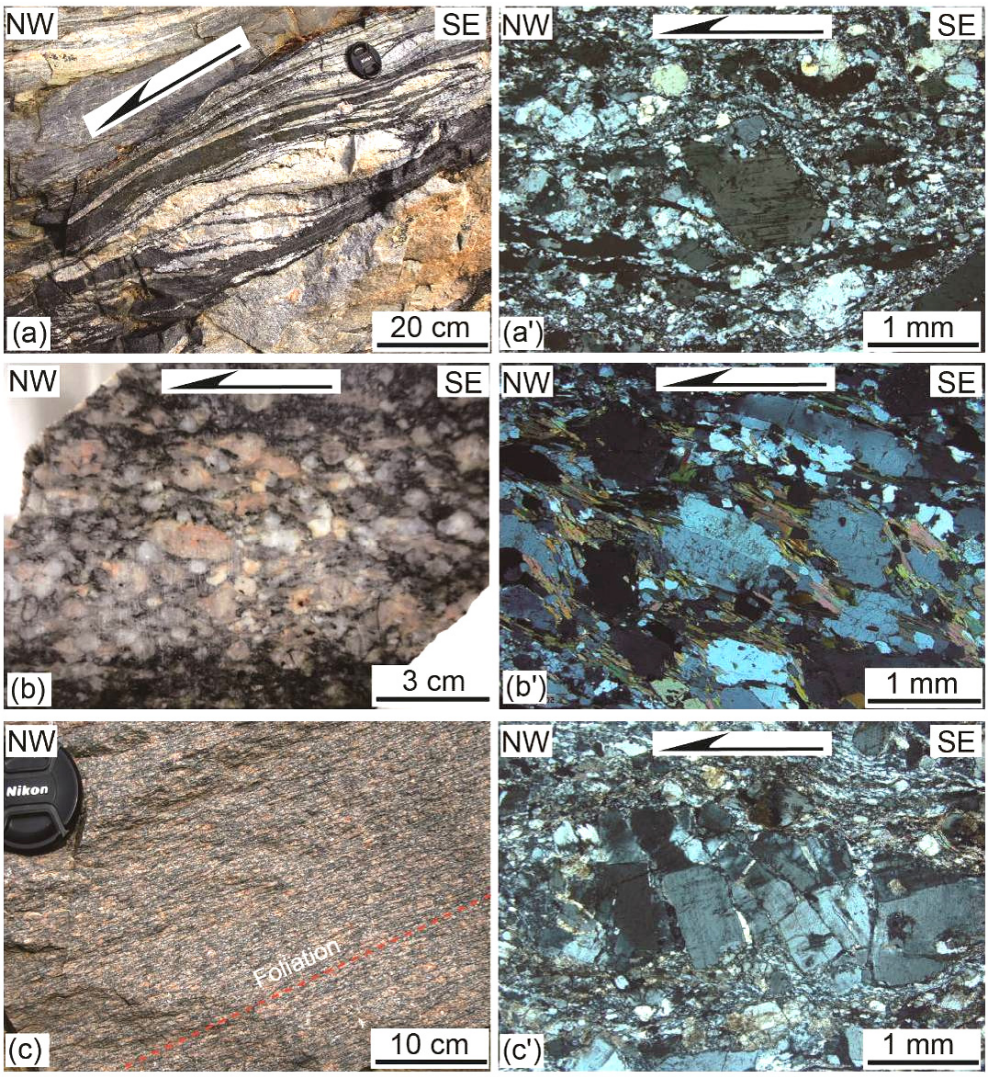

图3-20 商麻断裂构造变形特征

(a)和(a')糜棱岩化的混合片麻岩中浅色脉体受到强烈剪切变形而呈σ状，野外和镜下均可见长石残斑指示了上部向NW剪切变形；(b)和(b')花岗质糜棱岩手标本和薄片中的长石旋转残斑指示了上部向NW的剪切变形；(c)和(c')白鸭山花岗岩的西部卷入了糜棱岩化，显微镜下长石显微破裂形成的多米诺骨构造指示了上部向NW的剪切变形

Figure 3-20 Deformation characteristics of the Shang-Ma fault

(a) and (a') leucosome within the mylonitic migmatite gneiss was stronly sheared into sigmoid shape, and σ-type feldspar porpyroclasts in hand specimen and thin section also indicate a top-to-the-NW sense of shear; (b) and (b') granitic mylonite with σ-type feldspar porpyroclasts, indicating a top-to-the-NW sense of shear; (c) and (c') the western margin of the Baiyashan granite was invloved in mylonitization, and the fragmented feldspar porphyroclasts indicate a top-to-the-NW sense of shear

商麻断裂中的构造岩自东到西由糜棱岩至碎裂岩系列组成，表现出从韧性到脆性的递进变形过程．正是由于晚期脆性断层破坏了早期的韧性剪切带，使我们

在野外观察时将具同等拆离断层性质的商麻断裂和晓天-磨子潭断裂截然分开. 商麻断裂的脆性变形以发育高角度的正断层为特点, 这一正断作用控制了断裂西侧白垩-第三纪半地堑盆地的形成. 商麻断裂韧性剪切带中糜棱岩的面理倾向 NW, 倾角多在 20°-40°, 矿物拉伸线理向 NW 倾伏(图 3-17). 沿此线理方向, 糜棱岩化混合片麻岩中受剪切变形而成的 σ 状浅色脉体和花岗质糜棱岩中眼球状长石旋转残斑均指示了上部向 NW 的剪切变形(图 3-20a 和 a', b 和 b').

值得特别指出的是, 紧邻商麻断裂的白垩纪白鸭山花岗岩体西部边缘靠近断裂部分发生了糜棱岩化(图 3-20c). 而岩体东部则未变形并侵入到已经糜棱岩化的混合岩之中. 显微镜下白鸭山糜棱岩的长石变形以塑性拉长和显微破裂为主, 可见旋转残斑和多米诺骨构造指示了与围岩一致的运动学(图 3-20c'). 但是这一中-低温条件下的变形组构明显不同于围岩中普遍发育的角闪岩相条件下的高温变形. 由此可见, 商麻断裂可能至少经历了发育层次由深到浅的两期韧性剪切活动.

中大别伸展构造南部边界——水吼-五河剪切带(SWF)和浠水剪切带(XSF)

中大别穹隆的南部边界东起安徽天柱山附近, 向NW经水吼镇和五河镇, 至湖北英山地区转向 SW, 后经浠水附近又转为 NW 走向, 止于商麻断裂(徐树桐等, 2002). 前人关于中大别杂岩南部边界的研究多集中在其东段(英山-岳西地区), 由于其沿水吼-五河一线出露较好, 人们通常习惯将其称为水吼-五河断裂或剪切带. 水吼-五河剪切带也是中大别杂岩与南大别高压/超高变压质岩的界限, 但不是高压/超高变压岩片的顶部边界(Wang et al., 1995). 通过构造分析, Wang et al. (1998)认为水吼-五河剪切带为早白垩世的正滑型(即具有上部指向SE的运动学)韧性剪切带, 但这一认识并没有得到之后研究的证实(冀文斌等, 2011; Y.S Wang et al., 2011). 此外, 还有少数研究者曾认为水吼-五河断裂代表了华北-华南三叠纪的缝合线(Zhang et al., 1996; Wang et al., 2005b). 中大别穹隆南部边界的西段(浠水地区)一直缺少详细的构造地质学研究, 通常被人们解释为一条大型的右行走滑剪切带(称为新城-浠水剪切带或者新城-黄陂断裂), 认为它向西甚至可以延伸至桐柏山地区(X.D. Wang et al., 1998; E. Wang et al., 2003; Cheng et al., 2012). 我们的野外调查表明浠水地区发育一条具有多重拆离断层特点的马尾状剪切带. 为了区别起见, 本文将其简称为浠水剪切带. 实际上, 它由南北两条剪切带(XSF-S 和 XSF-N)组合而成, 西端均

起始于商麻断裂，向东两条剪切带逐渐分离，XSF-N 与水吼-五河剪切带合并，XSF-S 则部分与襄樊-广济断裂即传统认为的大别山与其前陆带的边界断裂重合，推测在大别山东南拐角其可能沿张八岭群的北界延伸(图 3-15).

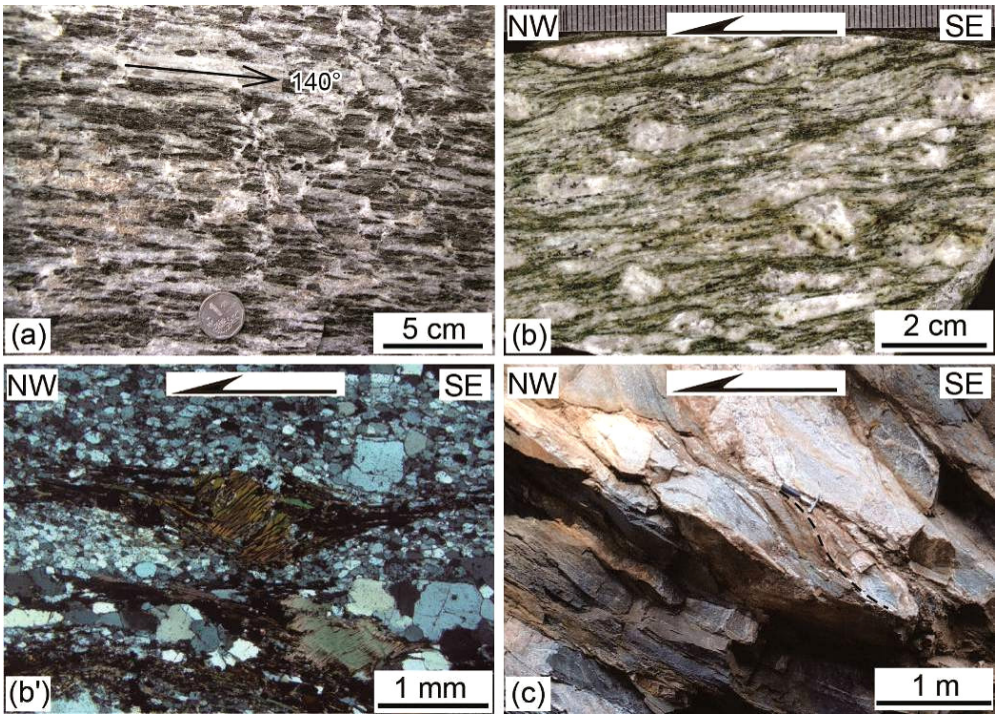

图3-21 水吼-五河剪切带构造变形特征

(a)花岗质糜棱岩中黑云母集合体构成的NW-SE向矿物拉伸线理; (b)和(b')眼球状花岗质糜棱岩中发育的S-C组构、长石旋转残斑和云母鱼构造指示了上部向NW的剪切变形; (c)片麻岩中的剪切条带和σ状的同构造花岗质岩脉指示了上部向NW的剪切变形

Figure 3-21 Deformation characteristics of the Shuihou-Wuhe shear zone

(a) biotite aggregate in granitic mylonite constitutes a NW-SE trending mineral stretching lineation; (b) and (b') augen granitic mylonite with S-C fabric, σ-type feldspar porpyroclasts and mica fish, indicating a top-to-the-NW sense of shear; (c) shear bands and syn-tectonic granitic dike with asymmetric structure in the gneiss indicate a top-to-the-NW sense of shear

水吼-五河剪切带的野外特征主要表现为由一系列与边界走向基本平行的强变形糜棱岩带及其相间的弱变形域构成. 糜棱岩面理在水吼地区以倾向 SE 为主，倾角一般为 30°-60°; 五河地区倾向 S 或 SW, 倾角较陡; 英山地区又转为以倾向 SE 为主，倾角多在 40°-70° (图 3-17). 虽然剪切带的走向发生了弯转，但矿物拉伸线理以向 SE (130°-160°)倾伏为主(图 3-17). 特别是在水吼附近，花岗质糜棱岩面理上发育的由黑云母的集合体定向构成的矿物拉伸线理十分清晰(图 3-21a). 我们对水吼附近的糜棱岩进行了详细的运动学观察，野外、定向标本和薄片中发育的 S-C 组

构, 长石旋转残斑和云母鱼构造等剪切标志均一致地指示了上部向 NW 的剪切变形(图 3-21b 和 b'). 英山西北靠近边界剪切带的片麻岩中发育的剪切条带和 σ 状的同构造岩脉同样指示了相同的运动学(图 3-21c).

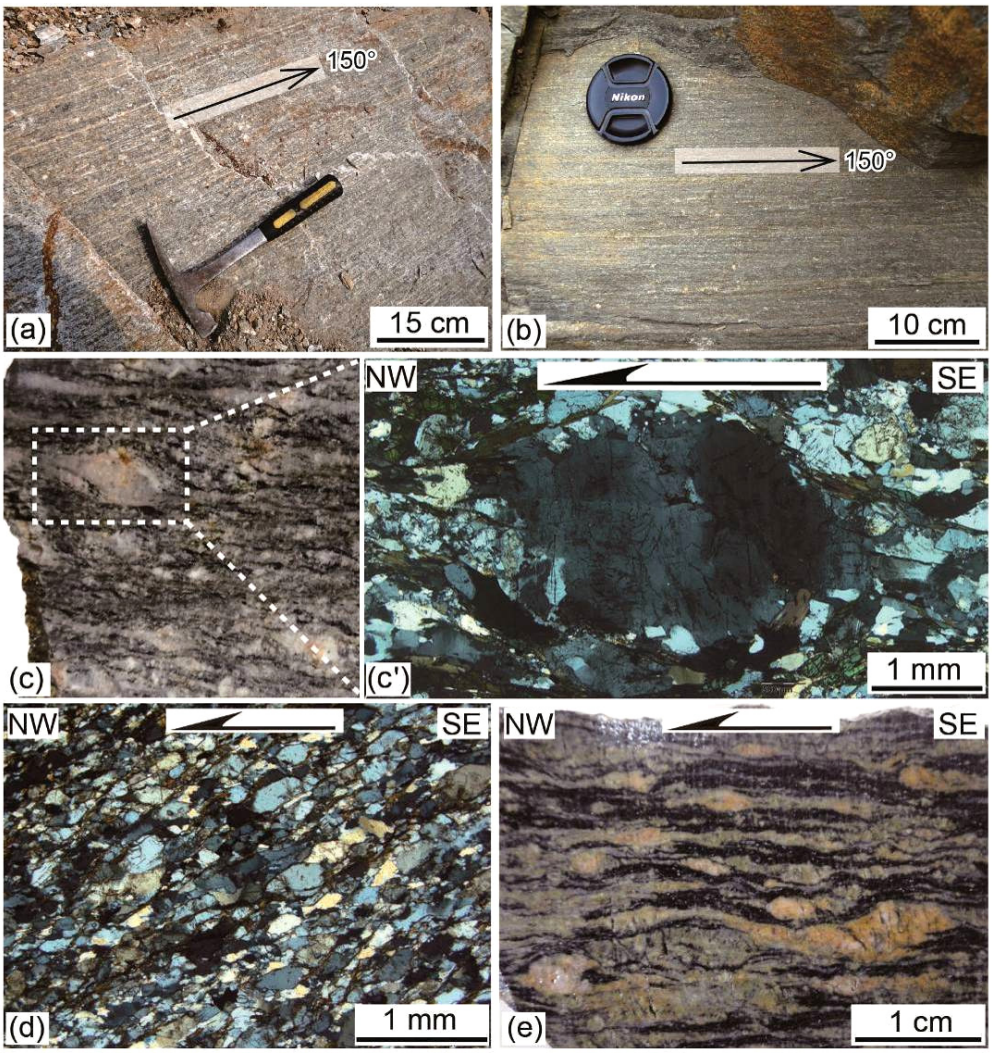

图3-22 浠水剪切带构造变形特征

(a)花岗质糜棱岩中长英质矿物拉长定向构成的NW-SE向矿物拉伸线理; (b)黑云斜长质糜棱岩中由黑云母和绿帘石构成的NW-SE向矿物拉伸线理; (c)和(c')花岗质糜棱岩中长石旋转残斑指示了上部向NW的剪切变形; (d)糜棱岩化的黑云斜长片麻岩中σ状的长石和石英指示了上部向NW的剪切变形; (e)花岗质糜棱岩中眼球状钾长石拖尾指示了上部向NW的剪切变形

Figure 3-22 Deformation characteristics of the Xishui shear zone

(a) quartz and feldspar in granitic mylonite was stretched to form a NW-SE trending lineation; (b) biotite and epidote in biotite-plagioclase mylonite constitute a NW-SE trending lineation; (c) and (c') σ-type feldspar porpyroclast in granitic mylonite indicate a top-to-the-NW sense of shear; (e) σ-type feldspar and quartz grains in mylonitic biotite-plagioclase gneiss indicate a top-to-the-NW sense of shear

在大别山南缘分布有一套相对原地的片麻岩单元, Faure et al. (1999, 2003)和林伟等(2003)将其划归为未经历超高压变质作用的相对原地系统, 实际上它也对应于徐树桐等(2002)重新定义的“大别杂岩”. 中大别的混合岩化作用在这里逐渐消失, 表明相对原地的片麻岩单元是中大别混合岩原岩的一部分. 这套片麻岩普遍发生了糜棱岩化, 浠水剪切带的南北两支即主要叠加在相对原地的片麻岩单元之中. 在浠水以西地区糜棱岩面理大部分倾向 SW, 少部分倾向 NE, 倾角一般平缓至中等, 局部较陡(图 3-17). 在浠水以东地区由于剪切带的分叉, 糜棱岩面理产状相应发生了同步协调的改变. 长英质矿物集合体、黑云母、绿帘石以及少量角闪石构成的矿物拉伸线理方向稳定在 NW-SE 向, 并主要向 SE 缓倾伏(图 3-17, 3-22a、b). 野外可见褶皱轴平行于线理方向的同斜褶皱广泛发育, 推测区域上糜棱岩面理倾向的倒转与此有关. 剪切带中的糜棱岩以花岗质和黑云斜长质为主, 眼球状长石的旋转残斑或拖尾构造以及 σ 状的长英质矿物颗粒皆指示了上部向 NW 的剪切变形(图 3-22c 和 c'、d、e). 虽然浠水剪切带的两个分支 XSF-N 和 XSF-S 在几何学和运动学上很难在野外区分开来，但总体上 XSF-N 显示出比 XSF-S 较深的发育层次。因而，我们推测这两条剪切带在活动时间上可能存在着先后次序，这一点也得到了年代学研究的支持(见后文)。

5.3 年代学研究 Geochronological studies

5.3.1 中大别杂岩的原岩、变质作用和混合岩化作用时代 Protolith ages and timing of metamorphism and migmatization for the central Dabieshan complex

中大别杂岩的组成岩石复杂多样, 主体为正片麻岩和混合岩, 并含有少量的高级变质岩如麻粒岩和榴辉岩等. 前人对中大别杂岩的正片麻岩进行了大量的锆石 U-Pb 年代学研究, 结果多给出新元古代(740-820 Ma)、三叠纪(245-205 Ma)或者早白垩世(145-120 Ma)的年龄及其组合(Xue et al., 1997; Hacker et al., 1998; 刘贻灿等, 2000; 谢智等, 2001, 2004; 江来利等, 2002; 薛怀民等, 2003; 葛宁洁等, 2003; Bryant et al., 2004; Zheng et al., 2004; Liu et al., 2007b; Zhao et al., 2008; Xie et al., 2006, 2010). 绝大部分学者认为新元古代年龄代表了片麻岩的原岩时代, 三叠纪年龄代表片麻岩经历了与印支期大陆深俯冲相关的变质作用, 早白垩世年龄代表片

麻岩受到混合岩化作用或岩浆活动的影响. 当然，由于中大别杂岩的强烈部分熔融以及变形, 前已述及不能排除部分片麻岩的原岩为早白垩世花岗岩的可能.

仅有少数研究者针对混合岩化作用发生的时代进行了年代学研究. 其中 Wang et al. (2002)获得混合岩浅色体 TIMS 锆石 U-Pb 年龄为 131.7 ± 1.1 Ma; Wu et al. (2007)应用 LA-ICP-MS 和 SHRIMP 法对不同地区的混合岩进行了锆石 U-Pb 定年, 认为大部分混合岩的原岩时代为新元古代 768-867 Ma, 混合岩化作用发生的时间在 145-120 Ma 期间, 并具两幕式部分熔融, 峰期时代分别为 139 ± 1 Ma 和 123 ± 2 Ma; 最近 Wang et al. (2013)对混合岩进行了 SIMS 锆石 U-Pb 定年, 获得 135 Ma、130-132 Ma 和 128 Ma 三组年龄, 分别将其解释为混合岩化过程中熔体的早期、峰期和晚期结晶年龄.

中大别存在麻粒岩已广为人知, 但年代学研究比较薄弱(Zhang et al., 1996; Zheng et al., 2001). 被研究最多的是黄土岭麻粒岩, 它代表了大别山已知的最古老岩石, 其原岩时代约为 2.7 Ga, 麻粒岩相变质时代约为 2.0 Ga (Wu et al., 2008; Sun et al., 2008; Jian et al., 2012). 最近, S.J. Wang et al. (2012)对来自中大别穹隆的一个麻粒岩进行了详细的锆石 U-Pb 年代学研究, 获得了多期变质年龄分别为 224 ± 2 Ma, 213 ± 2 Ma 和 200 ± 3 Ma, 认为其分别对应榴辉岩相峰期变质、麻粒岩相退变质和角闪岩相退变质时代. 中大别穹隆中已报道的榴辉岩十分稀少, 主要来自岳西穹隆的北部(如饶拔寨、黄尾河、百丈岩、华庄等)和罗田穹隆的东部(如三里畈、金家铺等), 并发现有微粒金刚石、矿物出溶结构等有关超高压变质的矿物学证据(魏春景等, 1997; 徐树桐等, 1999, 2003; 刘贻灿等, 2001, 2005; Y.C. Liu et al., 2007a, 2011a, 2011b). 另外, 在早白垩世的花岗岩中也发现有高压榴辉岩的捕虏体(Lin et al., 2007). 相关的锆石 U-Pb 年代学研究表明这些榴辉岩的原岩时代为 780-800 Ma, 峰期变质时代在 226 Ma 左右(Y.C. Liu et al., 2007a, 2011b).

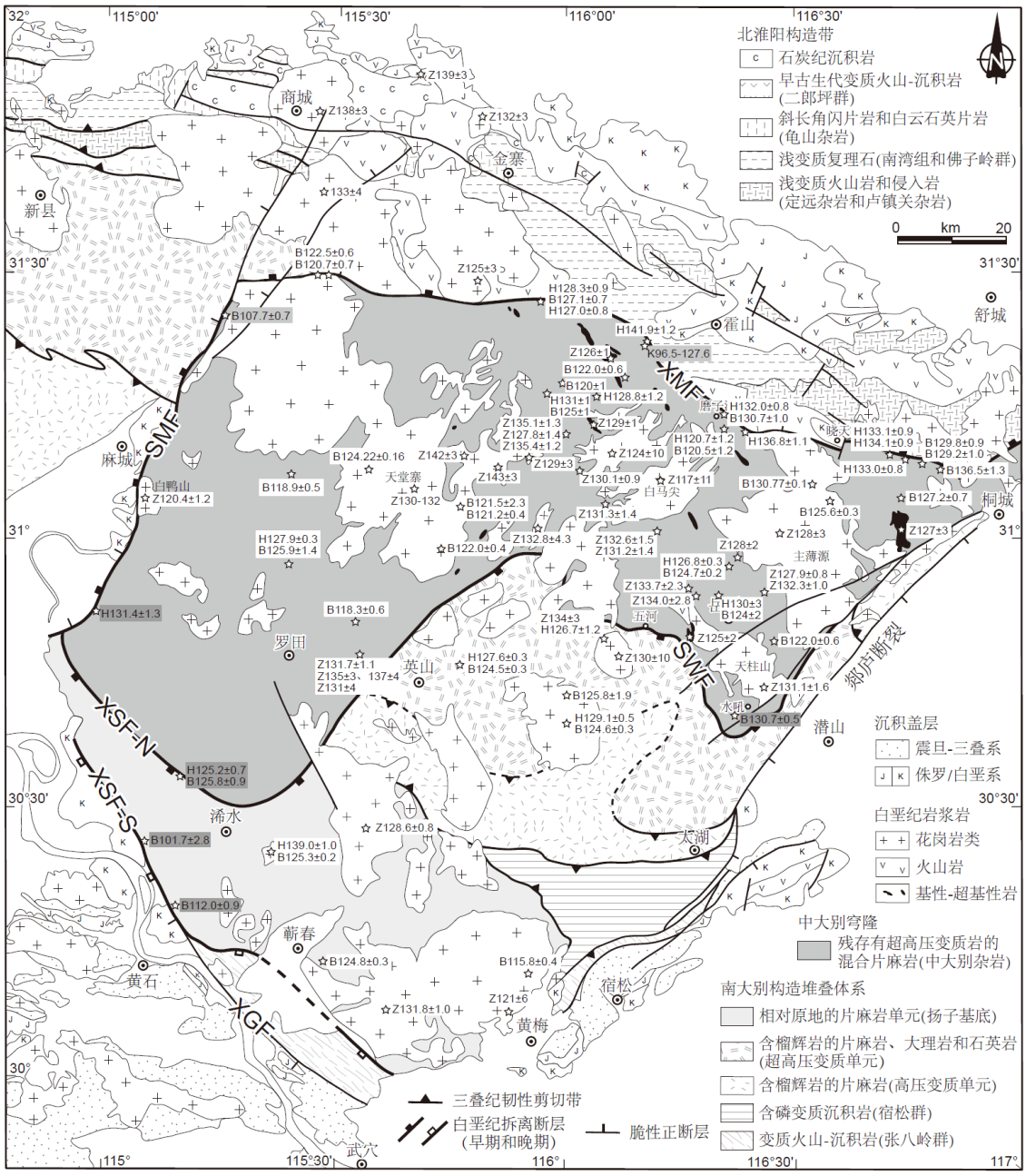

图 3-23 大别山白垩纪构造-岩浆年代学

Figure 3-23 Cretaceous tectono-magmatic geochronology of the Dabieshan

年代学数据来源 references：陈廷愚等,1991; 陈江峰等, 1995; 马昌前等, 2003; 侯泉林等, 2007; 杨坤光等, 2012; Mattauer et al., 1991; Eide et al., 1994; Hacker and Wang, 1995; Xue et al., 1997; Hacker et al., 1998, 2000; Ratschbacher et al., 2000; J.H. Wang et al., 2002; Zhao et al., 2004, 2005, 2007, 2011; Wu et al., 2007; Chen et al., 2009; He et al., 2011; Y.S. Wang et al., 2011; S.J. Wang et al., 2013; 本次研究(灰色底框)this study (grey box)

值得特别指出的是，李秋立等(2013)最近对出露于湖北罗田和安徽百丈崖、麻岩岭、上官庄的中大别榴辉岩，湖北英山月明的石榴辉石岩进行了金红石 U-Pb 年

代学研究和部分样品的锆石定年研究. 分别获得榴辉岩中金红石 U-Pb 年龄如下: 湖北罗田 LT-3 为 129.6 ± 2.8 Ma, LT-4 为 129.4 ± 3.3 Ma, 百丈崖 BZY-1 为 128.1 ± 1.8 Ma, 麻岩岭 MYL-1 为 127.2 ± 3.2 Ma, 上官庄 SGZ-1 为 127.8 ± 2.6 Ma, 月明石榴辉石岩中金红石年龄为 126.9 ± 1.1 Ma. 这些年龄在误差范围内一致, 平均为 128 ± 1 Ma. 不同样品中金红石颗粒大小不一, 差别可达几个数量级(几十微米到厘米级), 然而大小颗粒均记录了一致的年龄, 说明这些岩石经历了快速的冷却过程, 从而使得金红石 U-Pb 体系近同时封闭. 这一点更证明了这些位于中下地壳的榴辉岩是由于早白垩世变质核杂岩的伸展作用而抬升至地表的.

5.3.2 伸展构造的年代学研究 Timing of the extensional tectonics

已有的年代学制约 Previous geochronological data

中大别杂岩混合片麻岩的角闪石、云母和钾长石 $^{40}Ar/^{39}Ar$ 年代学几乎均给出了早白垩世年龄(图 3-23), 表明中大别杂岩的变形及冷却时代发生早白垩世(陈廷愚等, 1991; 陈江峰等, 1995; Mattauer et al., 1991; Eide et al., 1994; Hacker and Wang, 1995; Ratschbacher et al., 2000).

前人关于大别山变质核杂岩拆离断层的变形年代学研究主要集中在北部边界晓天-磨子潭断裂(图 3-23). 例如, 侯泉林等(2007)从金寨县青山镇和张冲乡的剪切带构造岩中获得 124.17 ± 0.25 Ma 和 126.91 ± 0.30 Ma 的黑云母 $^{40}Ar/^{39}Ar$ 年龄; Y.S. Wang et al. (2011)在沿剪切带的糜棱岩中获得了大量的角闪石和黑云母 $^{40}Ar/^{39}Ar$ 年龄, 年龄值介于 142-121 Ma 的一个较宽范围内. 另外, 磨子潭附近弱变形辉长岩角闪石和黑云母 $^{40}Ar/^{39}Ar$ 年龄分别为 120.7 ± 1.2 Ma 和 120.5 ± 1.2 Ma (Ratschbacher et al., 2000).

关于商麻断裂的起源有三叠纪和白垩纪之争. 王义天等(2000)测得商麻断裂内黑云斜长质糜棱岩的黑云母 $^{40}Ar/^{39}Ar$ 年龄为 226.5 ± 0.6 Ma, 认为其代表了商麻断裂的活动时间. 王朴等(2008)应用 LA-ICP-MS 锆石 U-Pb 定年获得商麻断裂中同构造花岗质伟晶岩脉和后期花岗岩侵入体的年龄分别为 125.9 ± 4.2 Ma 和 118.8 ± 4.1 Ma, 从而认为商麻断裂带在白垩纪从韧性剪切向脆性断层转换的时间在 126-119 Ma 之间. 然而如前所述, 白鸭山花岗岩的西部边缘卷入了剪切带, 该岩体的

LA-ICP-MS 锆石 U-Pb 年龄为 120.4 ± 1.8 Ma (Chen et al., 2009). 这表明商麻断裂在 120 Ma 以后仍存在韧性剪切活动.

对于水吼-五河剪切带和浠水剪切带的糜棱岩目前还缺少可靠的定年工作. 侯泉林等(2007)报道了潜山水吼构造岩中黑云母 $^{40}Ar/^{39}Ar$ 年龄为 190.59 ± 0.42 Ma, 认为其代表了与超高压变质岩折返相关的冷却时间, 但并没有给出具体的采样位置和测试分析数据. 而 Ratschbacher et al. (2000)报道了靠近水吼-五河剪切带的团岭弱变形英云闪长岩的角闪石 $^{40}Ar/^{39}Ar$ 年龄为 126.7 ± 1.2 Ma, 指示剪切带在早白垩世存在韧性活动.

本次研究的 $^{40}Ar/^{39}Ar$ 年代学 Ar-Ar dating in this study

为了精确约束白垩纪伸展构造的时间, 在详细构造解析的基础上, 本次研究重点对中大别穹隆的西部边界和南部边界进行了 $^{40}Ar/^{39}Ar$ 年代学研究(采样位置见图 3-23). $^{40}Ar/^{39}Ar$ 测试在中国科学院地质与地球物理研究所 $^{40}Ar/^{39}Ar$ 年代学实验室的 MM-5400 质谱仪上完成, 采用电阻炉阶段加热法. 样品的前处理和详细的分析方法及流程见王非等(2005). 采用 ArArCALC 软件(Koppers, 2002)计算坪年龄和反等时线年龄以及加权平均年龄. 具体分析数据见表 3-5, 年龄谱和反等时线见图 3-24, 年龄误差均为 2σ.

样品 JS109 为晓天-磨子潭断裂中段的花岗质糜棱岩, 野外可见长石旋转残斑指示上部向 NW 的剪切变形. 该样品钾长石的表面年龄范围在 127.6-96.5 Ma, 全熔年龄为 123.9 ± 0.7 Ma.

样品 DS49 为商麻断裂南段糜棱岩化的混合片麻岩, 野外和薄片中均可见上部向 NW 的剪切标志(图 3-20a 和 a'). 该样品中角闪石的年龄谱呈现为下降的阶梯状, 其中低温加热阶段的加权平均年龄分别为 131.4±1.3 Ma. 样品 QD124 为商麻断裂北段的花岗质糜棱岩, 野外可见长石旋转残斑指示上部向NW的剪切变形. 该样品中黑云母获得了较好的年龄谱, 坪年龄 107.7 ± 0.7 Ma 与反等时线年龄 107.5 ± 1.0 Ma 在误差范围内一致. 反等时线的 $^{40}Ar/^{36}Ar$ 初始比值为 321.0, 略高于大气氩标准值.

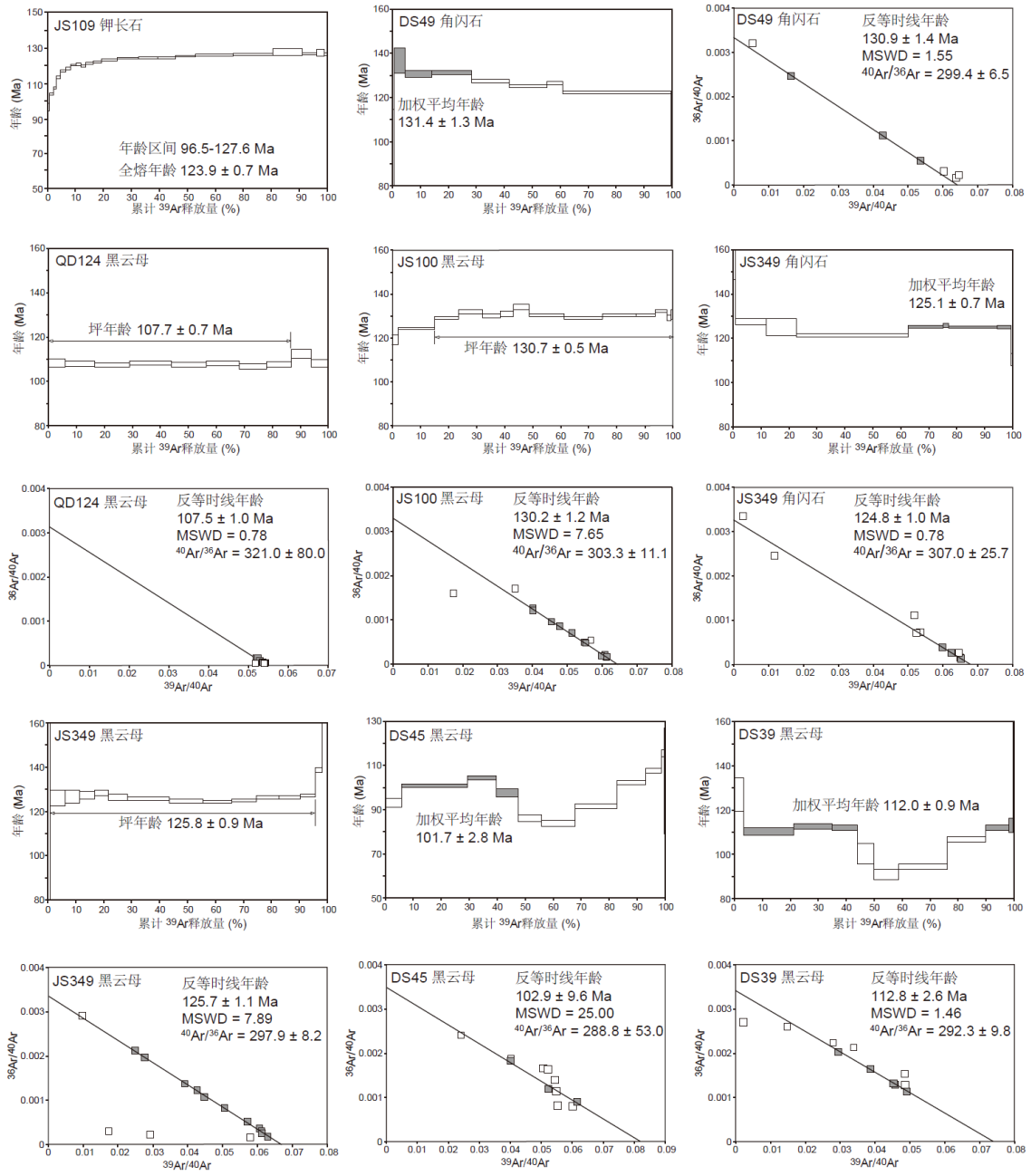

图 3-24 大别山拆离断层构造岩的 $^{40}Ar/^{39}Ar$ 年龄谱和反等时线

Figure 3-24 Ar-Ar age spectra and inverse sochron plots of tectonites from the detachment faults

样品 JS100 为水吼-五河剪切带的东端水吼附近的眼球状二长花岗质糜棱岩，具有上部向 NW 的运动学(图 3-21b 和 b')．该样品中黑云母获得了较好的年龄坪，坪年龄为 130.7 ± 0.5 Ma 与反等时线年龄 130.2 ± 1.2 Ma 在误差范围内一致．反等时线的 $^{40}Ar/^{36}Ar$ 初始比值为 303.3，与大气氩标准值在误差范围内一致．

样品 JS349 为浠水剪切带 XSF-N 的糜棱岩化角闪黑云斜长片麻岩，分离出了角闪石和黑云母．角闪石高温加热阶段的加权平均年龄为 125.1 ± 0.7 Ma，对应的

反等时线年龄为 124.8±1.0 Ma, $^{40}Ar/^{36}Ar$ 初始比值 307.0, 略高于大气氩标准值. 黑云母获得了较理想的年龄坪, 其坪年龄为 125.8 ± 0.9 Ma, 相应的反等时线年龄为 125.7 ± 1.1 Ma. 反等时线的 $^{40}Ar/^{36}Ar$ 初始比值为 297.9, 与大气氩标准值一致.

样品 DS45 和 DS39 为浠水剪切带 XSF-S 的花岗质糜棱岩, 两者黑云母的年龄谱呈马鞍状, 显示可能受杂质或蚀变影响. 其中 DS45 低温加热阶段表面年龄的加权平均年龄为 101.7 ± 2.8 Ma, 而反等时线年龄 102.9 ± 9.6 Ma 具有较大的误差, 但 $^{40}Ar/^{36}Ar$ 初始比值为 288.8, 与大气氩标准值接近. 选取 DS39 中表面年龄相近的 5 个温阶计算得到加权平均年龄为 112.0 ± 0.9 Ma, 与反等时线年龄 112.8 ± 2.6 Ma 在误差范围内一致. 反等时线的 $^{40}Ar/^{36}Ar$ 初始比值为 292.3, 与大气氩标准值一致.

拆离断层的活动时间 Ages of the detachment faults

前人获得的晓天-磨子潭断裂的 $^{40}Ar/^{39}Ar$ 年龄介于 142-120 Ma, 其中角闪石的年龄多大于 130 Ma, 而黑云母的年龄主要在 130-120 Ma (图 3-23). 考虑到晓天-磨子潭断裂的糜棱岩中有新生角闪石的形成, 故角闪石的年龄更接近剪切带的变形时间. 因此, 最大的角闪石年龄 142 Ma 可能代表了韧性变形的开始时间. 而本文获得的 JS109 钾长石 $^{40}Ar/^{39}Ar$ 的表面年龄范围在 128-97 Ma 之间, 指示了剪切带冷却至钾长石封闭温度 350-150°C 期间的时间. 前已述及, 商麻断裂可能经历了两期韧性变形, 样品 DS49 黑云母年龄阶梯中的最大年龄 131 Ma 和样品 QD124 的黑云母年龄 108 Ma 可能分别代表了早期和晚期韧性变形的冷却年龄. 从白鸭山花岗岩的变形特点来看, 两期变形的时限也应分别发生在 120 Ma 之前和之后, 这与野外的观察相佐证.

水吼附近的糜棱岩样品 JS100 中黑云母的坪年龄 130.7 Ma 应代表了水吼-五河剪切带韧性变形的冷却年龄. 采自浠水剪切带 XSF-N 的样品 JS349 的角闪石和黑云母获得了较一致的年龄 126-125 Ma, 表明岩石在此时经历了快速的冷却过程. 而浠水以东侵入剪切带的未变形花岗岩岩体的年龄为 128.6 ± 0.8 Ma (图 3-23), 因而我们推测浠水剪切带 XSF-N 的韧性变形时间应与水吼-五河剪切带一致, 均发生在 130 Ma 以前. 浠水剪切带 XSF-S 两个样品 DS45 和 DS39 虽然未能给出理想的坪年龄, 但表面年龄均小于 120 Ma, 局部温阶计算得到的加权平均年龄分别为 102

Ma 和 112 Ma. 结我们的构造解析, 浠水剪切带 XSF-S 在形成时间上应稍晚于 XSF-N, 所以这两个较年轻的年龄可能代表了浠水剪切带 XSF-S 韧性变形的冷却时间.

5.4 中大别杂岩的构造属性 Nature of the central Dabieshan complex

人们对中大别杂岩的构造属性认识一直存在争议(Tong et al., 2011及其参考文献). 徐树桐等(2002)主要依据中大别杂岩含有大量镁铁-超镁铁岩以及其混杂特征, 认为中大别杂岩为变质的蛇绿混杂岩. 实际上, 中大别穹隆岩石组成的复杂性主要是由白垩纪的深熔作用造成的, 而并非三叠纪华北与华南碰撞的结果. 已有的年代学数据表明中大别绝大多数的基性-超基性岩为早白垩世的侵入体(Jahn et al., 1999; Zhao et al., 2005; Dai et al., 2011). 中大别杂岩还曾被认为是一个古生代的岛弧杂岩, 主要证据是其正片麻岩的地球化学特征具有岛弧属性(Zhai et al., 1994, 1995), 但最大的问题在于目前缺乏任何古生代年代学数据的支持. 最初由于人们在中大别杂岩中未发现榴辉岩, 部分片麻岩锆石U-Pb年龄和几乎所有$^{40}Ar/^{39}Ar$年龄均为早白垩世, 从而部分研究者认为中大别杂岩整体上为白垩纪侵位的岩浆杂岩体(Xue et al., 1997; Hacker et al., 1998; Ratschbacher et al., 2000).

然而, 近年来在中大别穹隆发现了榴辉岩及榴辉岩相岩石, 相关的岩石学和年代学研究证明这些岩石可能经历了三叠纪的超高压变质作用(魏春景等, 1997; 徐树桐等, 1999, 2003; Tsai and Liou, 2000; 刘贻灿等, 2001; Xiao et al., 2001; Xie et al., 2004; Y.C. Liu et al., 2005, 2007a, 2011a, 2011b; Malaspina et al., 2006). 另一方面, 随着中大别杂岩年代学数据的不断的积累, 部分片麻岩也记录了三叠纪的变质作用(刘贻灿等, 2000; 谢智等, 2001, 2004; 江来利等, 2002; 薛怀民等, 2003; 葛宁洁等, 2003; Xie et al., 2010; Zheng et al., 2004; Liu et al., 2007b; Zhao et al., 2008). 这些研究进展使人们不得不重新审视中大别杂岩的构造属性. 由于中大别残存的榴辉岩在峰期超高压变质后大多叠加了麻粒岩相的退变质作用而不同于南大别超高压单元, 以中国科学技术大学为代表的研究群体(刘贻灿和李曙光, 2008; 郑永飞, 2008)将整个中大别杂岩划归为独立的的高温超高压变质地体. 然而, Bryant et al. (2004)注意到中大别的超高压变质岩石仅零星出露并多与围岩呈构造接触, 大部分的片麻岩并没有记录三叠纪的变质年龄, 因而推测中大别杂岩主体代表未卷入三

叠纪的大陆深俯冲的扬子陆块. 已报道的关于中大别杂岩经历过超高压变质作用的岩石矿物学证据(如微粒金刚石包体, 矿物出溶结构等)也受到了质疑(R.Y. Zhang et al., 2009).

依据前述的构造解析, 我们认为中大别杂岩不是纯粹的白垩纪岩浆杂岩或者三叠纪超高压变质地体, 抑或完全未卷入大陆深俯冲的扬子陆块, 也不是变质蛇绿混杂岩或者岛弧杂岩, 而是由相对原地的扬子基底片麻岩和位于中下地壳的超高压变质岩在白垩纪发生深熔作用的产物(冀文斌等, 2011). 三叠纪期间, 扬子陆块向北于华北陆块之下发生大陆深俯冲作用, 在此过程中扬子陆壳在不同深度发生拆离并依次折返, 形成了叠置在扬子基底之上的构造堆叠体系(Faure et al., 1999, 2003; 林伟等, 2003). 然而, 部分超高压变质岩在早期折返阶段并未到达地壳浅部, 而是处于中下地壳水平. 直至早白垩世, 这些滞留在地壳深部的超高压变质岩和未经历三叠纪深俯冲的扬子基底岩石又卷入了深熔作用, 同时叠加了白垩纪的构造变形, 从而形成了中大别杂岩. 这也是中大别杂岩中残存的超高压变质岩普遍经历了麻粒岩相退变质而不同于南大别超高压变质岩只有角闪岩相退变质的原因. 也就是说, 中大别杂岩中残存的超高压变质岩是在白垩纪大规模伸展时期才折返至地表的, 这与三叠纪榴辉岩的金红石 U-Pb 定年得到早白垩世年龄的结果相吻合(李秋立等, 2013).

5.5 大别山变质核杂岩的两阶段折返过程 Two-phase exhumation of the Dabieshan MCC

我们的构造解析表明现今大别山的整体几何形态表现为一个巨型的穹隆构造, 并具有典型变质核杂岩的特点. 其中晓天-磨子潭断裂与商麻断裂构成了穹隆西北翼统一的拆离断层, 而水吼-五河剪切带与浠水剪切带构成了东南翼的拆离断层组合. 变形年代学研究表明, 晓天-磨子潭断裂和水吼-五河剪切带的韧性剪切活动主要发生在 130 Ma 之前, 而商麻断裂则可能经历了两期韧性变形(130 Ma 之前和 107 Ma 左右), 浠水剪切带 XSF-N 的韧性活动时间在 130 Ma 之前, XSF-S 则可能在约 112-102 Ma 期间. 中大别杂岩与其拆离断层具有一致的上部指向 NW 运动学, 因而我们推测大别山变质核杂岩的拆离断层(包括晓天-磨子潭断裂、商麻断裂、水吼-五河剪切带和浠水剪切带 XSF-N)在早白垩世初期其原始发育状态为处于中地壳的

近水平的拆离面. 之后由于穹隆过程中的褶皱作用, 拆离面发生了弧形褶曲, 并可能在递进变形过程中发生了二次拆离, 造成了商麻断裂的第二期韧性变形和浠水剪切带 XSF-S 的发育和形成. 冷却史的研究也显示变质核杂岩的快速冷却和折返发生在 130-120 Ma 期间, 在约 105 Ma 可能还存在晚期的小幅度隆升过程(图 3-25).

大别山白垩纪变质核杂岩的形成还伴随着大量的岩浆活动. Wang et al. (2007) 对天堂寨地区的鹅公包岩体和云峰顶岩体进行了锆石 SHRIMP 定年, 分别获得了 142-143 Ma 的年龄, 代表了大别山最早期的岩浆活动. 而后 134-125 Ma 是大别山岩浆活动的高峰期. 依据地球化学和年代学, 这些岩浆岩大致以 130 Ma 为界可以分为两期(Zhao et al., 2004, 2007, 2011; Q. Wang et al., 2007b; Xu et al., 2007, 2012; He et al., 2011, 2012; 李曙光等, 2013): 早期的花岗岩多具埃达克质岩石的特征, 并存在不同程度的变形, 被解释为加厚下地壳的部分熔融; 而晚期为未变形的块状花岗岩和少量的基性-超基性侵入体, 代表山根垮塌后软流圈上涌的响应. 巧合的是, 大别山的混合岩化作用似乎也显示出 139 Ma 和 123 Ma 两幕式的部分熔融事件, 分别对应于上述两期岩浆活动(Wu et al., 2007).

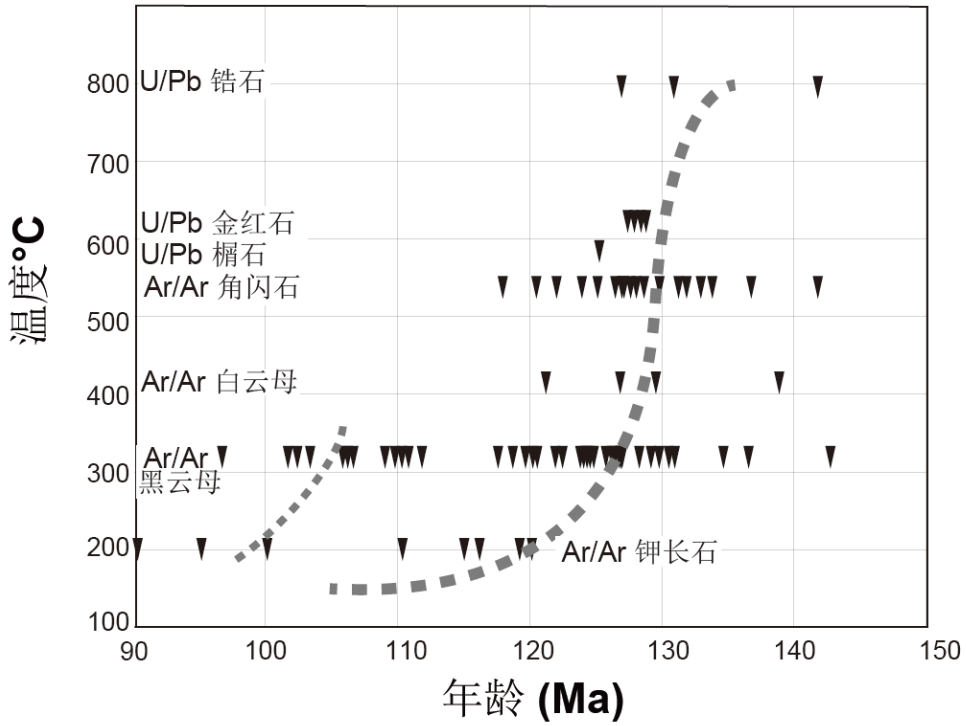

图3-25 中大别变质核杂岩的冷却史

Figure 3-25 Cooling history of the Dabieshan MCC

综上所述，130 Ma 可能是大别山造山后伸展垮塌的转折点，在构造变形和岩浆作用上均具有明显的响应. 据此我们将大别山变质核杂岩的形成与演化过程分为两个阶段(图 3-26): (1)混合岩化作用和壳内拆离阶段(145-130 Ma): 约 145 Ma 可能是大别山地区构造体制转换为伸展作用的开始，随后在区域 NW-SE 向伸展作用下造山带加厚的岩石圈发生了部分熔融，并形成了 143-130 Ma 的埃达克质岩浆岩. 同时地壳的弱化导致了壳内拆离作用的发生，在中地壳形成了近水平的拆离面，以发育高温条件下的韧性变形为特点. 这一拆离面可能对应于中下地壳物质在早白垩世发生部分熔融而塑性流动的顶面与上覆高压/超高压变质岩片之间的解耦面. (2)拆沉和穹隆作用(130-100 Ma): 在 130 Ma 左右伸展作用到达峰期，大别山的山根发生了大规模的垮塌或拆沉，导致软流圈的上涌. 同时第二幕部分熔融发生，并形成了大量非埃达克质岩浆岩. 中大别杂岩在浮力作用下发生了强烈的热穹隆作用，经历了快速的折返. 这致使早期的拆离面发生弯曲而形成弧形的拆离断层，由于晚期的均衡调整作用还导致了 112-102 Ma 期间部分拆离断层的二次活动及次级拆离断层的新生.

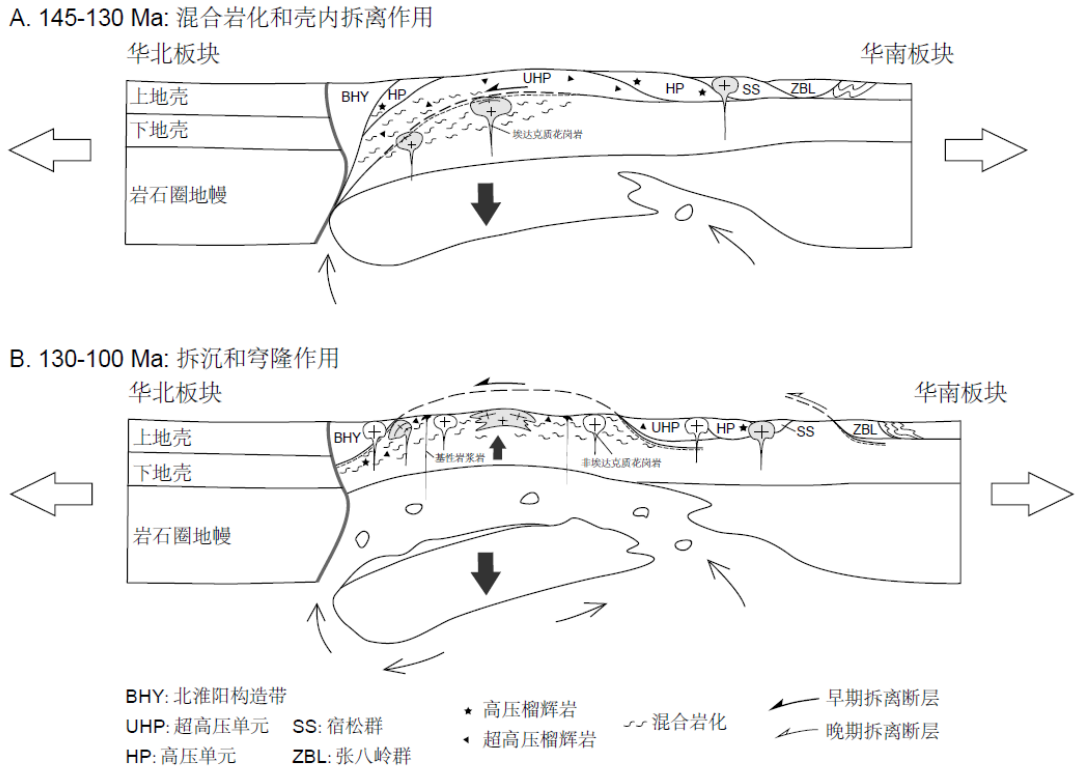

图3-26 大别山变质核杂岩的两阶段折返

Figure 3-26 Two-phase exhumation of the Dabieshan MCC

6 造山后伸展垮塌对早期高压/超高压造山带的改造 Reworking of the pre-existing HP/UHP oroginc belt by extensional collapse

桐柏山和大别山受白垩纪的构造-热事件影响强烈, 以大量的岩浆作用和强烈的混合岩化作用为特点. 桐柏杂岩和中大别杂岩即为早白垩世深熔作用的产物, 构成了造山带核部出露最深的岩石. 两者在构造样式上表现为伸展背形或穹隆, 构成了两个叠加在三叠纪高压/超高压造山带之上的白垩纪伸展构造.详细的构造解析表明桐柏杂岩为一个巨型的 A 型褶皱, 而中大别穹隆则具典型变质核杂岩的特点. 正是由于这期白垩纪伸展构造使得原三叠纪高压/超高压造山带受到了不同程度上的改造. 桐柏杂岩上覆的高压岩片被分割成了南北两部分, 桐柏山除桐柏杂岩的其它构造单元基本保留了白垩纪前的构造特征. 而大别山的高压/超高压变质岩现今则主要以构造岩片的形式保存在穹隆的东南翼. 白垩纪的深熔作用还造成了造山带深部的高压/超高压变质岩和扬子基底岩石的构造混杂, 从而致使人们对桐柏杂岩和中大别杂岩构造属性的各种不同认识. 相比之下, 由于大悟断裂和商麻断裂的错断, 红安地体受白垩纪构造-热事件影响较小, 基本保留了三叠纪的构造格架(Webb et al., 1999b, 2001; S.Z. Li et al., 2010, 2011). 最明显的区别在于红安地区没有类似于桐柏杂岩和中大别杂岩的混合片麻岩单元出露, 仅在西南部的大磊山和双峰尖地区以构造窗的形式出露有基底岩石.

因此, 我们推测在白垩纪之前, 桐柏杂岩和中大别杂岩并未形成和出露. 在白垩纪区域伸展作用下, 桐柏-大别造山带的中下地壳岩石伴随着深熔作用沿拆离断层折返至地表, 从而形成桐柏杂岩和中大别杂岩. 这一推论与前人根据角闪石 Al 压力计算得到中大别杂岩的平均折返深度约为 18 km 的结论相吻合(Ratschbacher et al., 2000). 如果去除白垩纪的伸展构造, 我们会发现桐柏-大别造山带为一个向 NW 倾伏的巨型背斜, 高压/超高压岩片的构造配置似乎指示扬子陆块在三叠纪的俯冲深度具有向西逐渐变浅的特点. 在一定程度上, 早期的构造格局对白垩纪伸展构造的几何学形态和发育程度起到了限定作用. 值得注意的是, 在大别山北部的北淮阳构造带和南大别的高压/超高压单元、宿松群和张八岭群中均发育有一期 NW-SE 向的矿物拉伸线理及上部向 NW 的剪切变形, 但变形年代学均给出了三叠

纪的年龄(Faure et al., 1999, 2003; Hacker et al., 1995, 2000; 林伟等, 2003, 2005). 显然, 这期三叠纪的构造变形与白垩纪变质核杂岩的形成无关, 代表了高压/超高压造山带早期的折返过程, 虽然两者的运动学近乎一致.

7 造山后伸展垮塌的动力学背景和机制探讨 Geodynamic and setting and mechanism of the post-orogenic extension

关于桐柏-大别造山带白垩纪伸展垮塌的可能机制及动力学背景可以归结为: 1)造山带碰撞后岩石圈根部的垮塌或拆沉(李曙光等, 2001, 2013; Q. Wang et al., 2007b; Xu et al., 2007, 2012; He et al., 2011, 2013; 郑永飞, 2008; 赵子福和郑永飞, 2009); 2)华北和华南板块中生代持续汇聚作用导致的侧向挤出(X.D. Wang et al., 1998; E. Wang et al., 2003); 3)燕山运动东亚多向汇聚挤压和陆内造山的后效(董树文等, 2005, 2007, 2008); 4)古太平洋板块向欧亚大陆之下俯冲所引起的弧后拉张(Wu et al., 2005; Ren et al.,2002); 5)西伯利亚与中朝-蒙古大陆碰撞和拉萨与羌唐地体碰撞的远程效应所引起的中国东部陆块向东的构造逃逸, 加之古太平洋俯冲弧后拉张的综合作用(Ratschbacher et al., 2000); 6)西南太平洋超级地幔柱上涌引起古太平洋板块俯冲方向和速率的改变, 进而造成中国东部软流圈地幔对流体制的扰动(Zhao et al., 2004; 郑永飞, 2008; 赵子福和郑永飞, 2009); 7)整个中国东部区域动力学背景上的岩石圈减薄(Lin and Wang, 2006; Lin et al., 2013a; 林伟等, 2013b).

晚中生代是整个东亚地区构造构造演化的关键转换时期, 最突出的构造事件莫过于中国东部岩石圈的减薄及华北克拉通破坏(吴福元等, 2008). 这一事件在中国东部岩石圈地壳浅部响应为诸多伸展构造如变质核杂岩、同构造花岗岩、断陷盆地等的广泛发育,以及相伴的大规模岩浆活动. 变质核杂岩作为伸展构造的典型型式之一, 遍布于华北克拉通内部及其周缘, 其发育的拆离断层几乎均具有 NW-SE 向的矿物拉伸线理和上部指向 NW 或 SE 的运动学, 变形时代均发生在早白垩世, 指示了中国东部早白垩世区域 NW-SE 向的伸展作用(Lin and Wang, 2006; Lin et al., 2013a). 综合桐柏-大别山所发育的早白垩世伸展构造, 不难发现其表现出与区域上相似的构造样式, 在形成时间也具有较好的一致性. 因而我们认为桐柏山伸展背形和大别山变质核杂岩的形成与华北克拉通破坏具有相同的动力学背

景, 而与三叠纪的大陆碰撞或造山过程没有直接成因关系. 它们同样是中国东部晚中生代岩石圈减薄的响应, 只不过叠加在高压-超高压变质带之上.

8 小结 Summary

多数研究者认为桐柏山核部的桐柏杂岩是在走滑作用下发生向南东的侧向挤出而隆升的, 本论文的研究结果并不支持这一认识. 构造解析表明桐柏杂岩总体上是在NW-SE近水平伸展作用下形成的具有A型褶皱特点伸展背形或变质核杂岩. 虽然桐柏杂岩南北坡的面理倾向相反, 且靠近边界剪切带面理时常较陡, 但矿物拉伸线理稳定在NW-SE向, 运动学一致显示为上部向NW的剪切变形. 也就是说, 从杂岩内部到边界剪切带, 其几何学和运动学具有协调一致的特点. 这表明桐柏杂岩南北边界并不是典型的走滑剪切带, 现今表面上观察到的走滑现象实际上是早期的拆离面发生弯曲的表现.

大别山中部的中大别穹隆作为一个大规模的伸展构造已被人们广泛接受, 然而涉及中大别杂岩及其边界剪切带或断裂带的构造解析和穹隆的形成机制仍存在较大的争议. 结合前人的工作及我们详细的构造解析, 认为中大别穹隆为形成于NW-SE 向伸展体制下的具造山带规模的变质核杂岩. 现今大别山的几何形态几乎完全由中大别穹隆所控制. 中大别杂岩(混合片麻岩以及残存的超高压变质岩)代表了变质核杂岩的下盘. 北部边界晓天-磨子潭断裂与西部边界商麻断裂构成了穹隆西北翼的一个统一的弧形拆离断层. 而南部边界水吼-五河剪切和浠水剪切带(表现为马尾状, 包括早期的 XSF-N 和晚期的 XSF-S 两条剪切带)则构成了穹隆东南翼的多重拆离断层组合. 中大别杂岩与拆离断层发育一致的 NW-SE 向矿物拉伸线理和上部指向 NW 运动学.

夹持于桐柏山和大别山之间的红安地体受白垩纪构造-热事件影响较小, 本次研究在红安地体西南部的双峰尖和大磊山地区识别出了白垩纪的伸展构造. 双峰尖的几何形态与桐柏杂岩类似表现为 A 型伸展背形, 大磊山(或大悟穹隆)则显示为半环状单斜构造. 双峰尖伸展背形的变形特征以 NW-SE 向矿物拉伸线理和上部指向 NW 运动学为特点. 大磊山穹隆核部花岗质片麻岩线性构造发育不明显,磁化率

各向异性(AMS)研究表明磁线理以 NW-SE 向为主导. 在构造层次上, 这两个伸展构造明显位于桐柏杂岩和中大别杂岩之上, 代表了地壳浅层次的拆离.

在构造解析的基础上, 年代学研究揭示桐柏山和大别山伸展作用开始时间可能在145 Ma, 并在130 Ma左右达到了峰期, 以造山带根部的大规模垮塌或拆沉为标志. 此外, 桐柏山和大别山以及红安地区的双峰尖和大磊山还共同记录了稍晚一期大致约110-90 Ma的伸展构造. 双峰尖和大磊山主要显示此晚期伸展的记录, 这期伸展构造在桐柏山完全以原有的拆离断层为基础持续发育; 在大别山则共用了部分早期拆离断层, 并有新生拆离断层的形成. 从几何学和运动学的匹配关系来看, 推测桐柏-大别山造山带中发育的白垩纪拆离断层在早期其原始发育状态为处于中地壳的近水平拆离面, 可能对应于中下地壳物质在早白垩世发生部分熔融而塑性流动的顶面与上覆高压/超高压变质岩片之间的解耦面. 早期 (145-130 Ma) 以高温条件下的近水平拆离为主, 代表了研究区的主期变形. 之后由于折返过程中的褶皱作用, 拆离面发生了弧形褶曲, 并可能在递进变形过程中发生了晚期(110-90 Ma)的二次拆离.

综合分析, 认为桐柏杂岩和中大别杂岩是由相对原地的扬子基底片麻岩和位于中下地壳的高压/超高压变质岩在早白垩世发生深熔作用的产物. 白垩纪伸展构造的叠加强烈地改造了桐柏-大别造山带早中生代的构造格局. 桐柏杂岩上覆的高压岩片被分割成了南北两部分, 而大别山南部三叠纪的变质序列(包括高压/超高压岩片、宿松群和张八岭群)则表现为被拆离断层肢解的构造岩片. 桐柏-大别造山带伸展构造的形成体现了岩石圈不同层次地质过程的综合效应, 具体表现为核部杂岩体上覆岩片的拆离和剥蚀去顶, 中下地壳可能存在向 SE 的通道流, 造山带根部的垮塌或拆沉作用. 对比于中国东部广泛发育的白垩纪伸展构造, 认为其与华北克拉通破坏具有相同的动力学背景, 是中国东部晚中生代岩石圈减薄的响应, 只不过叠加在高压/超高压造山带之上.

第四章 江南造山带中段晚中生代大云山-幕阜山岩基的侵位过程

Chapter 4 Emplacement process of the Late Mesozic Dayunshan-Mufushan batholith in middle segment of the Jiangnan orogen

Late Mesozoic granitoids are widespread in South China, but structural study of these plutons is very rare. The Dayunshan-Mufushan composite plutons in the middle segment of the Jiangnan orogen one of the larger Late Mesozoic granitic batholiths in South China inland. This study applied multidisciplinary methods by structural analysis, AMS (anisotropy of magnetic susceptibility) and geochronology in order to reveal the emplacement process the Dayunshan-Mufushan batholith. Two-phase tectonic events respectively related to the early and late plutons of the batholith were distinguished. The D_1 event in early pluton (biotite monzogranite and biotite granodiorite) is obvious in the gneissic granite and contact metamorphic rock on the southern edge of the performance is more in zone, visible NE-SW trending mineral stretching lineation and top-to-the-SW sense of shear. The D_2 event is characterized by to development of the Dayunshan detachment fault along the western tongue-shaped margin of the late pluton (two-mica monzogranite). NW-SE trending mineral stretching lineation and top-to-the-NW shearing can be observed in the deformed granite and contact metamorphic rock.

AMS study reveals that the magnetic fabrics in internal parts of the early and late plutons were dominated by magmatic flow, and two groups of AMS lineations are distinguished. The preferred orientation of AMS lineation in the early pluton is nearly N-S trending (maximum at 190°), while the preferred orientation of AMS lineation in the late pluton is NW-SE trending (maximum at 117°). This result is quite coincident to our field observation. A preliminary analysis of gravity data also shows that the roots of the early and late plutons respectively located in the northern and central-eastern part of the batholith, which is in agreement with the structural and AMS data. SIMS zircon U-Pb and EPMA monazite U-Th-Pb dating results show that the early pluton emplaced at ca. 150 Ma, while emplacement age and related metamorphism of the late pluton were dated at ca. 132 Ma. Namely, the D_1 and D_2 event occurred in the Late Jurassic

and Early Cretaceous, respectively.

In conclusion, we suggest that the D_1 event might represent crustal thickening by nearly N-S compression during the Late Jurassic, while the D_2 event could be comparable to the Cretaceous extension recorded in the Tongbai-Dabie orogen, and indubitably manifested the Early Cretaceous regional NW-SE extension in east China.

1 引言 Intruduction

华南板块晚中生代(燕山期)的地质面貌以发育众多的地堑-半地堑盆地和大量的岩浆岩为特色, 构成了所谓的“华南盆岭省”(Gilder et al., 1991, 1996; Li, 2000; Shu et al., 2009). 实际上, 华南盆岭构造的形成与华北克拉通破坏在时间上几乎同步, 这似乎表明中国东部在晚中生代经历了统一的地壳伸展过程. 不同的是, 在华北板块及其周缘广泛发育伸展穹隆特别是变质核杂岩, 而在华南目前仅有少数几个伸展穹隆被报道, 如长江中下游地区的洪镇穹隆(Zhu et al., 2010), 沿江南造山带分布的庐山穹隆(Lin et al., 2000)、武功山穹隆(Faure et al., 1996; Wang et al., 2001)和衡山穹隆(J.H. Li et al., 2013a). 花岗岩的侵位过程与局部围岩构造和区域构造有着密切的时空关系和成因联系, 蕴含着丰富的构造信息. 变质核杂岩的不发育使得对花岗岩的构造研究成为解译华南晚中生代构造演化的一个重要突破口.

前人针对华南晚中生代的花岗岩开展了大量的岩石学、地球化学和年代学工作, 取得了一系列的研究成果(Li, 2000; Zhou and Li, 2000; Zhou et al., 2006; Li and Li, 2007; X.H. Li et al., 2010, 2013; Wu et al., 2012). 虽然多数研究者认为华南晚中生代的岩浆活动与古太平洋板块的俯冲过程有关, 但对俯冲开始的时间、方式及其影响范围仍存在不同的认识. 花岗岩具有非常复杂的成因, 应用地球化学参数判别其形成的构造环境虽然有一定的参考价值, 但在很多情况下并不确定(吴福元等, 2007). 这无疑显得对花岗岩的构造研究尤为重要, 但在华南关于这方面的研究还较为缺乏(Feng et al., 2012; Wei et al., 2014a). 华南内陆江南造山带中段晚中生代岩浆活动强烈, 大云山-幕阜山复式岩体是其中较大的花岗岩基之一. 本论文应用构造、磁化率各向异性和年代学相结合的方法对该岩体的侵位过程进行了详细的研究, 并探讨了岩体侵位的构造背景, 以期为华南晚中生代的构造演化提供新的构造信息和认识.

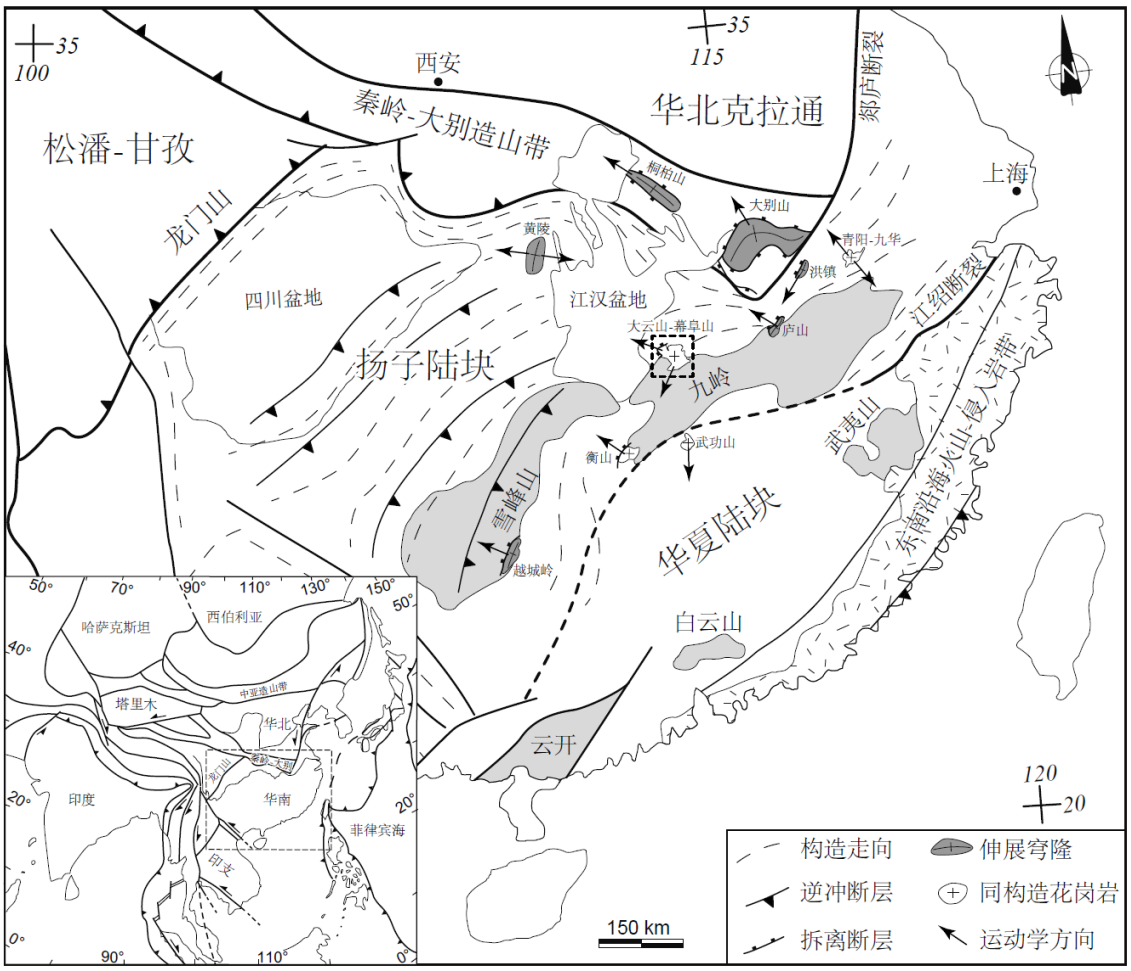

图4-1 华南大地构造简图

Figure 4-1 Tectonic sketch map of South China

2 地质背景 Geological setting

江南造山带代表了扬子陆块和华夏陆块在元古代的拼合带，而后早古生代和早中生代两期陆内造山作用不同程度地再造了江南造山带，因而它又被称作九岭-雪峰山(Charvet et al., 1996, 2010; Shu et al., 2008; Faure et al., 2009; Li et al., 2009a; Chu et al., 2012a, 2012b; Charvet, 2013; Chu and Lin, 2014). 早古生代的造山作用的影响区域主要在武夷至云开大山一线(武夷-云开造山带)，九岭地区也有表现. 早中生代华南进入了多向造山阶段，包括板块北缘的秦岭-大别造山带，南缘的印支造山带，西缘的龙门山冲断带和内陆的九岭-雪峰山，这些造山带挤压作用发生的时期均集中在三叠纪. 古太平洋板块自二叠纪末或侏罗纪开始向欧亚大陆之下的俯冲作用对华南中生代构造演化影响深远，造成华南构造体制由特提斯构造域向濒太平洋构造域的转换，并最终导致了晚中生代“华南盆岭省”的形成. 江南造山带

中段在晚中生代发展成为华南内陆重要的北东向构造-岩浆带. 区内断裂构造发育, 总体以 NE 向为主, 被认为是郯庐断裂南延的重要地段(傅昭仁等, 1999; 李先福等, 2001; Li et al., 2001). 沿断裂带发育有许多断陷盆地和大量晚中生代花岗岩体, 呈现出盆-岭构造的地貌特征. 尤其在湘东北地区, 晚中生代岩浆活动强烈且期次多, 主要的花岗岩体除大云山-幕阜山外, 还包括桃花山-小墨山、长乐街、金井、望湘、连云山等. 由于该区的构造-岩浆活动伴随有一系列的多金属矿床, 因此这些花岗岩的成因引起了众多学者的关注(贾大成等, 2003; 李鹏春等, 2005; 汪洋和邓晋福, 2004; 王连训等, 2008; 许德如等, 2009; 邹慧娟等, 2011).

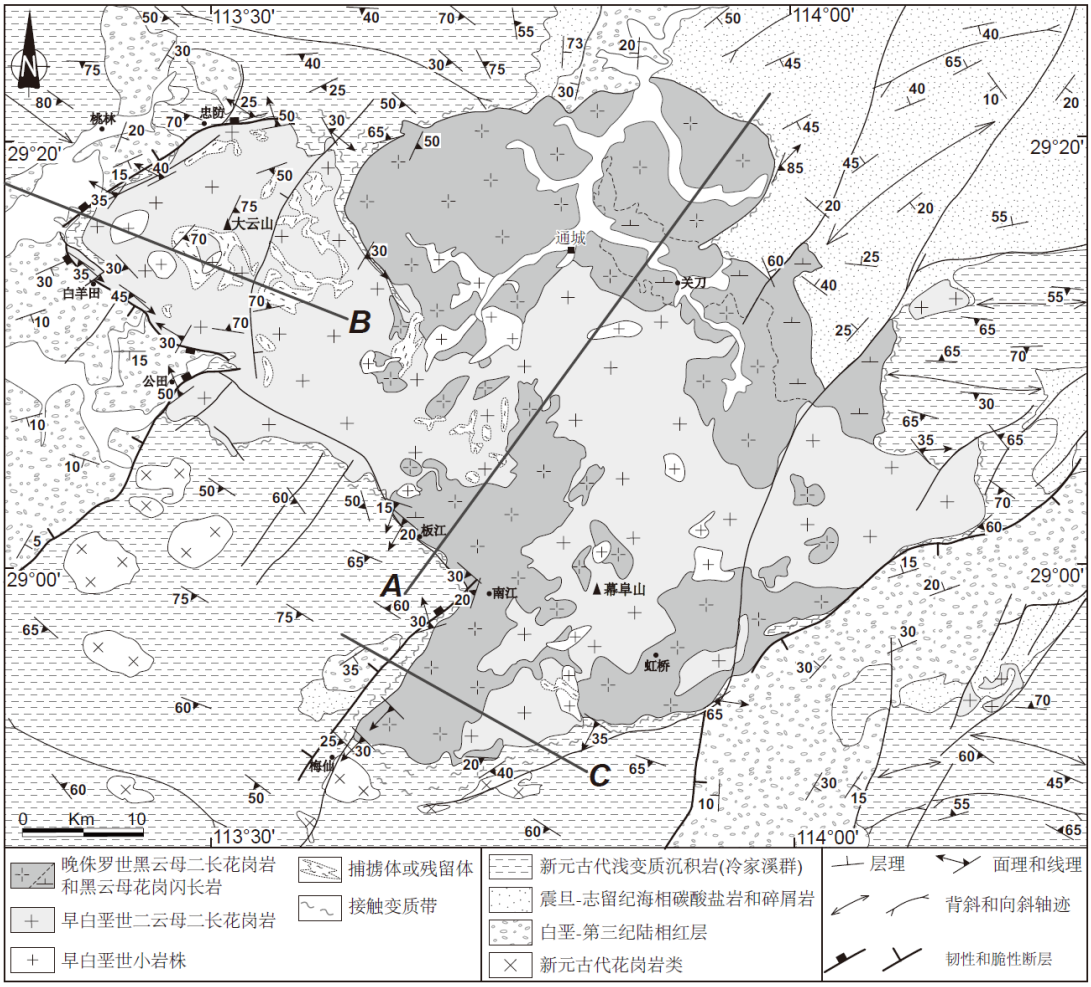

图4-2 大云山-幕阜山地区地质构造图

Figure 4-2 Geological and structural map of the Dayunshan-Mufushan area

大云山-幕阜山岩基位于湘鄂赣三省交界地区, 在构造位置上属江南造山带的中段或九岭地体的西缘. 岩体总面积约 2440 km^2, 西部呈舌状凸出的部分通常被称作大云山(湖南岳阳县和临湘市交界处), 而东部幕阜山的主峰位于湖南平江县境

内, 北连湖北通城县, 东接江西修水县(图 4-2). 大云山-幕阜山岩基被认为是晚中生代多次岩浆侵入活动的产物, 但一直缺乏准确的年代学资料. 邹慧娟等(2011)认为岩体按侵入先后顺序依次为二云母二长花岗岩、黑云母二长花岗岩和黑云母花岗闪长岩. 然而, 我们的野外调查和年代学研究表明大云山-幕阜山岩基主体由晚侏罗世(150 Ma 左右)和早白垩世(130 Ma 左右)两个时代的侵入体组成, 早期为黑云母二长花岗岩和黑云母花岗闪长岩, 晚期为二云母二长花岗岩及一些花岗质小岩株(详见后文). 前人认为大云山具有典型变质核杂岩的特点: 核部是由古老地壳岩石重熔形成的花岗岩, 盖层为发育一系列多米诺式正断层的白垩-第三纪红色砾岩和零星的冷家溪群浅变质岩, 在核部和盖层之间存在着半环状的拆离断层(喻爱南, 1998). 与拆离断层活动相关的热液作用还形成了著名的桃林铅锌矿, 矿体的分布严格受拆离断层的控制.

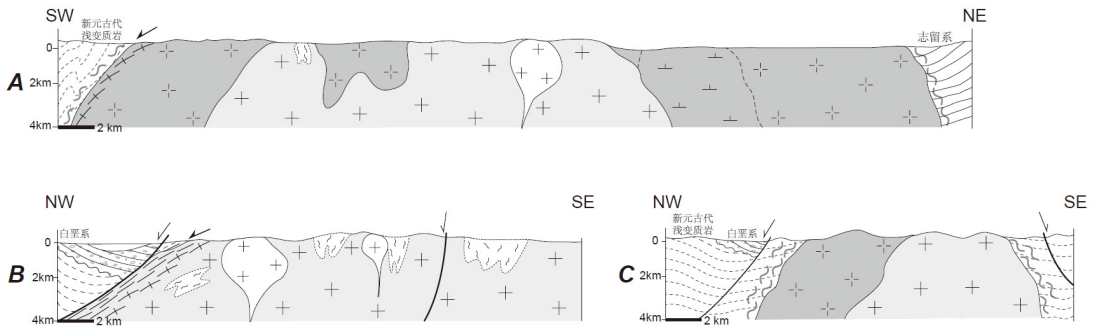

图4-3 大云山-幕阜山构造剖面图

Figure 4-3 Cross-sections of the Dayunshan-Mufushan area

岩体的围岩以元古界冷家溪群和震旦-志留纪地层为主. 冷家溪群为一套由浅变质的碎屑岩构成的类复理石沉积建造, 局部夹有少量的火山岩. 传统认为它可与桂北四堡群、黔东梵净山群、赣北双桥山群和皖南溪口群类比, 代表了华南中元古代的褶皱基底. 近年来, 大量的锆石 U-Pb 年代学研究表明冷家溪群及其相当地层的沉积时代大致在 860-820 Ma, 实属新元古代 (X.L. Wang et al., 2007; 高林志等, 2011). 震旦-志留纪地层主要出露与研究区的东北部, 以寒武-志留纪的海相碳酸盐岩和碎屑岩为主, 震旦系仅零星以狭窄的条带状分布. 在岩体西侧和东南侧均有白垩-第三纪断陷盆地发育, 盆地内以陆相红层沉积为特征. 西侧红盆在构造单元上属于洞庭盆地最东面的一个次级凹陷, 洞庭盆地与江汉盆地共同构成了我国中南地区最大的白垩-第三纪陆内伸展断陷盆地. 岩体的东南侧同样发育小型的

断陷盆地, 属于长(沙)-平(江)盆地的北段. 此外, 研究区西南部尚有许多小的新元古代花岗岩体.

3 大云山-幕阜山岩基的构造几何学特征 Structural geometry of the Dayunshan-Mufushan batholith

3.1 岩体的组成 Bulk architecture of the batholith

大云山-幕阜山岩基在平面上呈菱形, 并具两向伸长的特点. 依据本次研究结果, 我们将该岩体划分为 4 个主要的岩石系列(图 4-2). 其主要特征分述如下:

(1)晚侏罗世黑云母二长花岗岩: 大云山-幕阜山岩基的主体组成部分之一, 长轴为 NNE 向, 并被早白垩世二云母二长花岗岩分割成南北两大部分(图 4-2 和图 4-3). 岩石呈灰白色, 具细中粒-中粒斑状结构(斑晶含量 15-20%), 块状构造或局部发育片麻状构造. 主要矿物组成为钾长石(25%)、斜长石(35%)、石英(30%)和黑云母(10%), 不含或含极少量的白云母(小于 1%), 且常与黑云母伴生或包裹于长石之中(图 4-4a). 副矿物以锆石、独居石和磷灰石为主, 可见磁铁矿.

该期侵入体北部(通城地区)多以块状构造为主, 无明显变形, 局部可见钾长石斑晶的定性. 片麻状构造主要见于侵入体的南部边缘, 沿岩体边界呈带状发育. 片麻理产状以倾向南西为主, 倾角较缓(20°-35°). 局部发育较为明显的 NE-SW 向矿物拉伸线理, 由钾长石斑晶和黑云母的定向构成. 向侵入体内部片麻状构造逐渐过渡为块状构造, 局部流面以及流线构造发育(图 4-5). 在侵入体西南部近直角的拐角一带, 受断裂影响片麻状黑云母二长花岗岩多具碎裂结构, 绿泥石化现象普遍.

(2)晚侏罗世黑云母花岗闪长岩: 主要分布于岩体东北部关刀一带, 呈北西向条带状展布, 出露面积约 100 km^2. 该侵入体大部分与黑云母二长花岗岩接触, 接触关系多为突变, 局部呈渐变关系(图 4-3). 岩石呈浅灰色、灰白色, 具中细粒花岗结构, 块状构造, 无明显的变形. 主要矿物组成为钾长石(15%) 、斜长石(45%) 、石英(25%)、黑云母(10%)和角闪石(5%). 副矿物以磁铁矿和绿帘石含量较高, 其次

为锆石和磷灰石. 另外, 在岩体西南边缘板江一带尚有小面积(15 km^2)片麻状黑云母花岗闪长岩出露(图 4-2 和 4-4b), 其内侧与黑云母二长花岗岩为渐变过渡关系, 故推测非一个独立岩体. 此处片麻理的产状向南西缓倾 210°∠25°, 并可见由黑云母定向构成的向 SW 倾伏的矿物拉伸线理(图 4-6b).

(3)早白垩世二云母二长花岗岩: 大云山-幕阜山岩基的主体组成部分之一, 长轴为 NW 向, 明显侵入黑云母二长花岗岩(图 4-2 和图 4-3). 岩石呈灰白色, 一般具中细粒至细中粒花岗结构, 并常见(少)斑状结构(斑晶含量一般在 5%左右), 块状构造或局部发育片麻状构造. 主要矿物组成为钾长石(20-30%)、斜长石(30-40%)、石英(30%)、黑云母(5%)和白云母(3%). 副矿物以锆石和磷灰石常见.

该期侵入体东部多以块状构造为主, 局部可见流面. 但西部大云山地区沿着岩体舌状边缘发育有一条半环状的韧性剪切带, 并被脆性断裂所叠加, 表现出拆离断层的特点(图 4-7a, 简称为**大云山拆离断层**). 大云山拆离断层由北西侧 NE 向的忠防断裂和南西侧 NW 向的白羊田断裂组成. 韧性剪切带围绕舌状岩基边缘较连续分布, 总长度约为 35 km (图 4-2). 在公田断裂的 NE 端仍可见韧性剪切带发育, 但向南延伸转变为脆性正断层. 构造岩显示出由花岗质糜棱岩至碎裂岩的序列性变化, 反映了拆离断层由韧性到脆性的递进变形过程. 由于拆离断层活动过程中流体的参与, 花岗质构造岩的绿泥石化和钠长石化现象常见. 糜棱岩面理的产状在北西侧以倾向 NW 为主, 南西侧以倾向 SW 为主, 倾角中等(25°-50°). 在花岗质糜棱面理上, 长石、石英、黑云母和白云母构成了 NW-SE 向的矿物拉伸线理(图 4-7b, c).

另外一个引人注目的事实是大云山地区二云母二长花岗岩中捕掳体或残留体(含石榴石的矽线石云母片岩)十分发育, 其分布面积约为大云山舌状岩体的十分之一(图 4-2). 野外调查发现这些捕掳体或残留体与围岩花岗岩多呈渐变过渡关系, 接触边界处的花岗岩中暗色析离体(黑云母富集层)通常较发育, 构成了花岗岩的流面. 捕掳体或残留体中见存诸多褶皱, 其紧闭程度显著地比区域基底褶皱要强烈很多. 系统测量这些褶皱的枢纽以及面理产状, 发现它们大致具有平行岩体边界而呈现环状展布的特点.

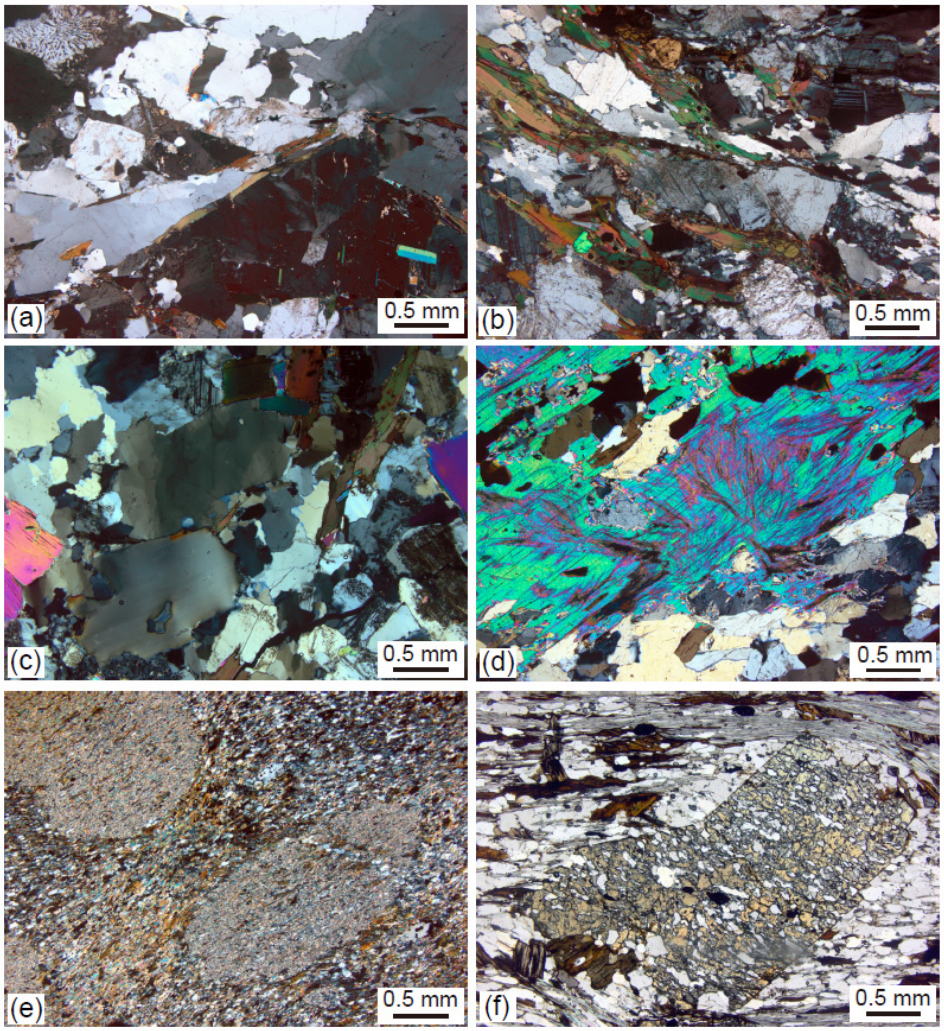

图4-4 大云山-幕阜山岩基及围岩接触变质岩显微照片

(a)片麻状黑云母二长花岗岩，显示了中等的固态条件下的显微组构(蠕虫结构常见，石英可见动态重结晶)；(b)板江地区片麻状黑云母花岗闪长岩，显示了较强的固态条件下的显微组构(石英动态重结晶，黑云母及少量角闪石强烈定向)；(c)大云山中部的二云母二长花岗岩，显示了微弱的固态条件下的显微组构(石英波状消光，云母和长石未明显变形) (d)大云山地区二云母二长花岗岩中的残留体，矽线石云母片岩；(e)岩体东侧黑云母花岗闪长岩的围岩接触变质岩，红柱石板岩；(f)大云山北侧二云母二长花岗岩的围岩接触变质岩，含十字石的云母片岩

Figure 4-4 Microphotographs of the Dayunshan-Mufushan batholith and contact metamorphic rocks (a) Gneissic biotite monzongranite with moderate solid-state fabric (myrmekites, slightly recrystallized quartz grains); (b) Gneissic biotite granodiorite with strong solid-state fabric (recrystallized quartz grains, orientated biotite and minor amphibole) in the Banjiang area; (c) two-mica monzogranite with weak solid-state fabric (quartz grains with undulose extinction, mica and feldspar without obvious orientation) in the middle part of the Dayunshan; (d) restite (sillimanite-bearing mica schist) within the Dayunshan two-mica monzogranite; (e) andalusite slate at the eastern side of the biotite granodiorite; (f) staurolite-bearing mica schist at the northern side of the Dayunshan two-mica monzogranite

(4)早白垩世小岩株: 侵入上述三个系列之中, 岩性以细粒二云母花岗岩和细粒二云母二长花岗岩为主, 最大者出露面积约 12 km^2. 岩石具块状构造, 未见变形.

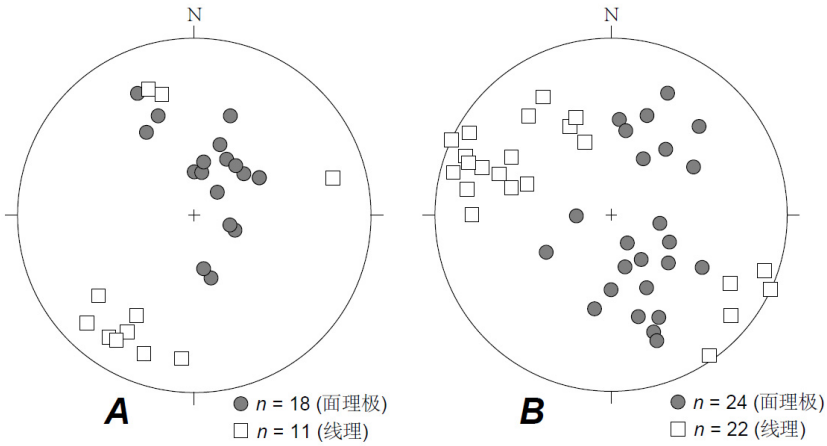

图4-5 大云山-幕阜山岩基构造要素赤平投影图

(A)晚侏罗世黑云母二长花岗岩和黑云母花岗闪长岩及其接触变质带(主要是岩基南部); (B)早白垩世二云母二长花岗岩及其接触变质带(主要是岩基西部)

Figure 4-5 stereographic projection of structural elements from the Dayunshan-Mufushan area

(A) Late Jurassic pluton (biotite monzogranite, granodiorite) and its contact metamorphic belt (mainly the southern part of the batholith); (A) Early Cretaceous pluton (two-mica monzogranite) and its contact metamorphic belt (mainly the weatern part of the batholith)

3.2 围岩及接触变质带 Country rocks and contact metamorphic aureole

从地质构造图上看, 研究区内明显由两个角度不整合面分隔而成的三个构造层组成, 即冷家溪群浅变质褶皱基底、震旦-志留系海相沉积盖层和白垩-第三系陆相红盆, 并发育多组构造线方向(图 4-2). 冷家溪群以粉砂岩和砂岩变质而成的板岩为主, 保留有明显的韵律和波痕构造. 冷家溪群中区域性褶皱的轴线基本呈 NW 或近 EW 向展布, 大云山-幕阜山岩基占据了其中一个大型背斜的核部. 大型褶皱两翼次级褶皱较发育, 其构造形态多以倒转背向斜为主. 在研究区的西北部和东部, 可见褶皱的延伸明显被岩体吞噬. 寒武-志留系地层中褶皱的轴向则以NE向为主, 明显不同于基底褶皱的走向, 暗示研究区在花岗岩侵位之前可能经历了多期的构造事件.

岩体西侧的湘阴凹陷呈 NE 走向，凹陷北段南东边界为忠防断裂，南段南东边界为公田断裂，两边界断裂之间为白羊田断裂相连. 盆地内红层产状总体上倾向 SE 或 SSE，自南东往北西倾角变陡，显示该红盆的沉积明显受南东侧 NE 向断裂正断作用的控制(图 4-2 和图 4-3). 岩体东南侧长平盆地的走向同样为 NE 向，但控盆的边界主断裂倾向 SE，致使盆地内红层的产状相应以倾向 NW 为主(图 4-2). 这两个红盆中粗碎屑沉积岩的砾石成分以冷家溪群浅变质岩和大云山-幕阜山的二长花岗岩为主，并且远离岩体花岗岩砾石逐渐减少.

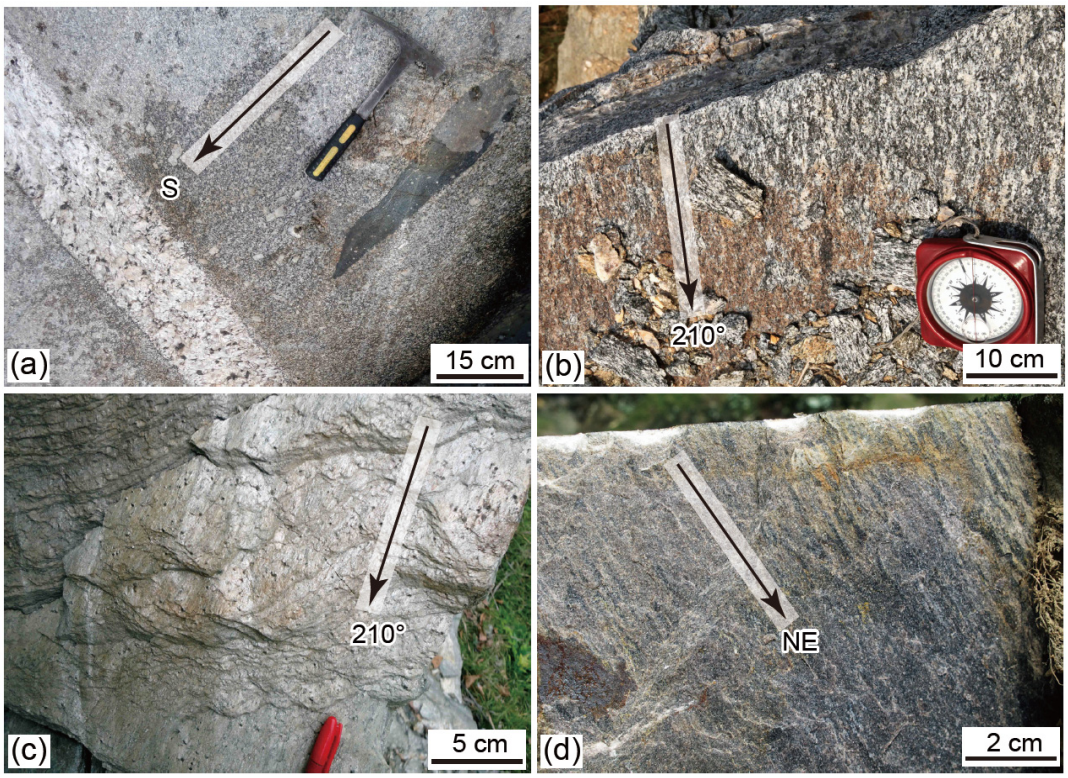

图 4-6 与早期侵入岩侵位相关的线性构造

(a) 岩体东南缘黑云母二长花岗岩中偶见的暗色包体被拉长定向平行于长石斑晶的优选方位; (b) 岩体南部边缘片麻状黑云母花岗闪长岩中黑云母定向构成了 NE-SW 向矿物拉伸线理; (c) 岩体东南侧接触变质带内石榴石云母片岩中发育的 NE-SW 向矿物拉伸线理; (d)岩体东北侧接触变质带内板岩中红柱石定向构成了 NE-SW 向矿物拉伸线理

Figure 4-6 Linear structures related to emplacement of the early pluton

(a) enclaves occasionally in the biotite monzogranite was stretched parallel to the preferred orientation of feldspar phenocrysts (b) NE-SW trending lineation in the gneissic biotite granodiorite on the southern margin of the pluton; (c) NE-SW trending lineation in the garnet-mica schist from the contact metamorphic aureole at southeast side of the pluton; (d) NE-SW trending lineation formed by andalusite in slate from the contact metamorphic aureole at northeast side of the pluton

大云山-幕阜山岩基与冷家溪群的接触带均可见到较明显的热接触变质作用, 产生片岩化或角岩化. 变质岩石以云母(石英)片岩为主, 特征性的变质矿物包括以下一种或几种: 绿泥石、十字石、堇青石、矽线石、红柱石和石榴石等(图 4-4e, f 和图 4-6c). 变质带宽度各地不一, 一般宽 200-2000 m. 岩体北缘向内凹入部分和南缘向外凸出部分, 接触面产状倾角小, 接触界线与围岩地层走向垂直或斜交. 这些地方接触变质带宽度较陡, 并且变质岩中石榴石含量明显较高. 岩体西南边缘接触面产状倾角较大, 接触界线与围岩地层走向一致, 变质带宽度也相应较窄. 在岩体南东侧黑云母二长花岗岩接触变质带的石榴石云母片岩中局部发育清晰的 NE-SW 向矿物拉伸线理(图 4-6c), 这与片麻状黑云母二长花岗岩和片麻状黑云母花岗闪长岩中发育的线理方向一致. 而大云山舌状岩体西缘拆离断层上盘由冷家溪群变质而成的片岩中却见到 NW-SE 向矿物拉伸线理(图 4-7d), 这与韧性剪切带中的线理保持一致. 岩体东北部黑云母二长花岗岩和黑云母花岗闪长岩与寒武-志留系的接触界线较弯曲, 接触面倾角较陡. 这里的接触变质岩石以砂泥质沉积岩变质而成角岩和板岩为主, 局部与碳酸盐岩的接触部位可见轻微的大理岩化. 我们野外在志留纪粉砂岩变质而成板岩中同样观察到由红柱石定向构成的NE-SW向矿物拉伸线理(图 4-6d).

从区域上看, 接触变质带中发育的 NE-SW 向线理与晚侏罗世黑云母二长花岗岩和黑云母花岗闪长岩的侵位有关, 而 NW-SE 向线理与早白垩世二云母二长花岗岩的侵位有关((图 4-2 和图 4-5). 这似乎指示大云山-幕阜山岩基在侵位过程中受到了两期构造事件的影响. 此外, 在黑云母二长花岗岩南部凸出部分的西侧接触变质带中可以观察到两期线理的不明显叠加, 并且 NW-SE 向线理表现较为明显.

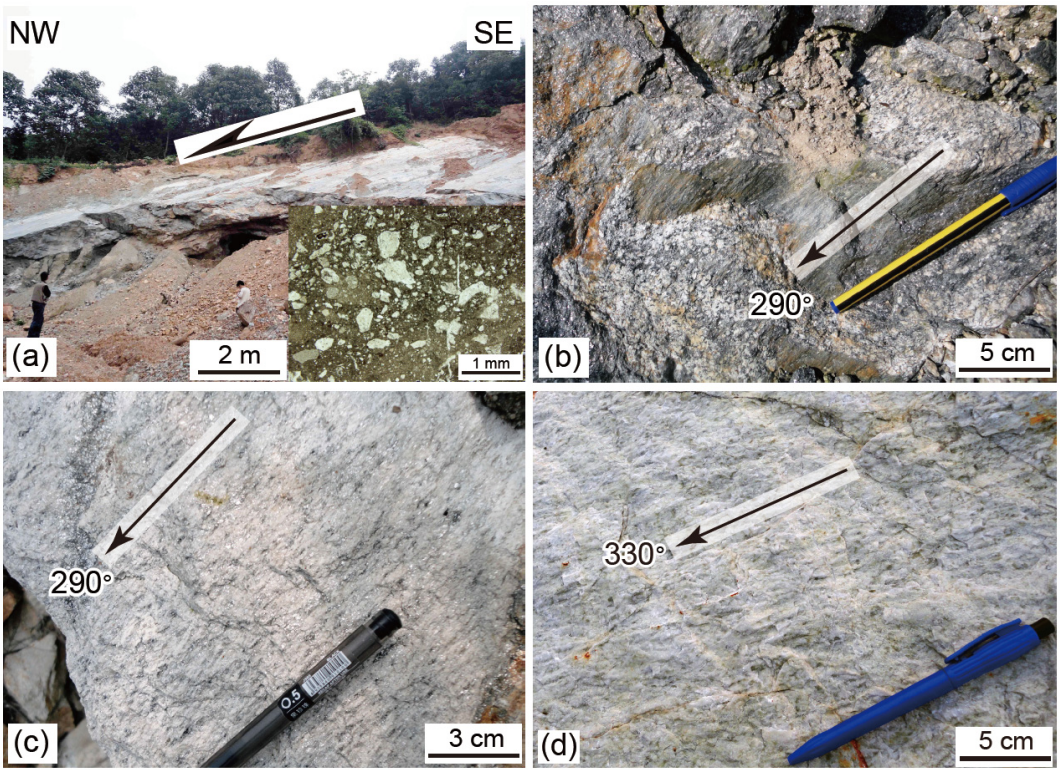

图 4-7 大云山拆离断层的几何学

(a)拆离断层的野外面貌，断层带中发育巨厚的角砾岩层；(b)二云母二长花岗岩中局部黑云母富集的暗色层，半透入性的擦痕平行于长英质矿物的强烈拉伸方向；(c)钠长石化的二云母二长花岗岩，二云母定向构成 NW-SE 向矿物拉伸线理；(d)大云山拆离断层中绢云石英片岩中发育的 NW-SE 向矿物拉伸线理

Figure 4-7 Geometry of the Dayunshan detachment fault

(a) outcrop of the detachment fault, with thick breccia layer; (b) biotite-rich layer locally in the two-mica monzogranite, with semi-penetrative striations parallel to the lineation formed by felsic minerals; (c) two-mica monzogranite was suffered albitization, and oriented mica formed a NW-SE trending lineation; (d) NW-SE trending lineation in sericite quartz-schist from the Dayunshan detachment fault

4 磁化率各向异性(AMS)研究对岩体构造几何学的贡献 Contribution of AMS in understanding geometry of the batholith

4.1 岩石磁组构简介 Brief introduction of AMS

岩石的磁化率具有非均一性，在不同方向上有所差别，即表现为磁化率各向异性(anisotropy of magnetic susceptibility，缩写 AMS)．从结晶学和矿物学角度来看，

磁化率各向异性来源于岩石中所有的磁性矿物(包括石英和方解石等反磁性矿物, 云母、角闪石、辉石、石榴石和橄榄石等顺磁性矿物, 磁铁矿、赤铁矿和钛磁铁矿等铁磁性矿物), 其实质是磁性矿物的颗粒或晶格的定向. 磁化率各向异性可以用磁化率椭球体来表示, 通过矩阵计算可以得到磁化率的三个相互垂直的主轴($K_1 > K_2 > K_3$), 它们在空间上构成的椭球体即代表磁组构(图 4-8).

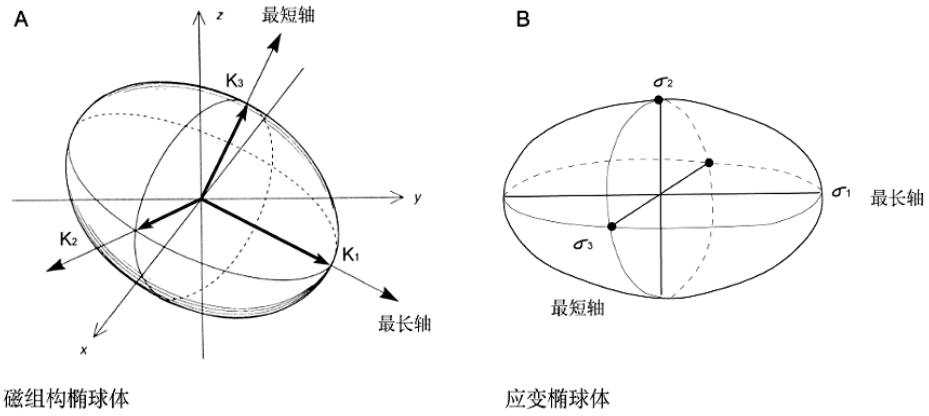

图 4-8 磁组构椭球体与应变椭球体

Figure 4-8 AMS ellipsoid and strain ellipsoid

磁组构之所以能够应用于地质研究中, 是因为岩石磁化率椭球体与应变椭球体具有共轴关系, 两者三个主轴相互平行(Tarling and Hrouda, 1993; Borradaile and Henry, 1997). 因而可以用磁化率椭球来表征应变椭球, 与应变椭球体类似, 磁化率椭球的长轴 K_1 代表最大张应力方向, 短轴 K_3 代表着最大压应力方向. 磁组构的形态可以划分为三种类型(图 4-9): (1)压扁型(烙饼型): 磁面理发育, 磁线理不发育; (2)拉长型(雪茄型): 磁线理发育, 磁面理不发育; (3)偏长型: 介于压扁型和拉长型之间, 代表磁面理和磁线理均较发育.

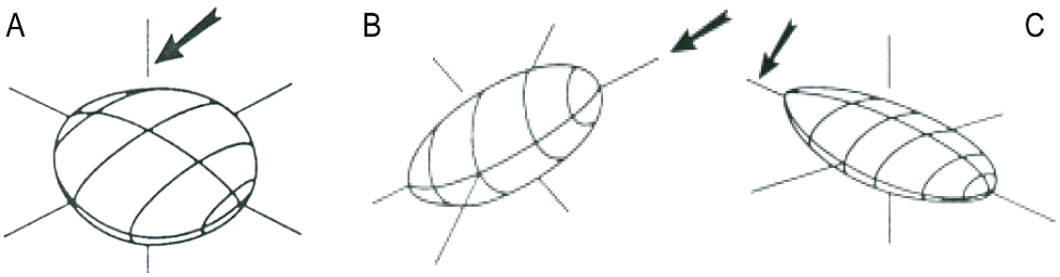

图 4-9 磁组构椭球体的形态类型: (A)压扁型; (B)拉长型; (C)扁长型

Figure 4-9 Patterns of AMS ellipsoid: (A) oblate; (B) prolate; (C) triaxial

磁化率各向异性有着广泛的应用范围, 它几乎遍及地学的各个领域. 产生磁化率各向异性的因素可以是沉积古水流作用、岩浆流动作用或者变质重结晶作用, 也可以是构造应力作用造成的磁性矿物的定向. 利用传统的构造方法分析岩石的构造变形时, 例如在野外露头、手标本和显微尺度上, 需要岩石变形强度达到肉眼分辨能力才能比较好的确定.如果岩石中变形发育不明显时, 磁组构方法在此时就显现出了技术上的优势. 花岗岩在侵位过程中受到力的作用而使花岗质岩浆中的磁性矿物显示出一定的优选方位, 表现为磁化率各向异性. 对于“顽固”的花岗岩来说, 岩体在侵位之后磁组构很难被后期低温的脆性变形所改造, 只有在强烈的构造-热作用条件下磁组构才会被重置. 因此, 磁组构方法作为研究花岗岩的侵位过程的一种重要手段已被人们广泛应用(Talbot et al., 2004; Turrillot et al., 2011; Lin et al., 2013b; Wei et al., 2014a).

4.2 样品采集和测试 Sampling and measurement

如前所述, 大云山-幕阜山岩基变形较为明显的地方主要是其西部和南部凸出的两部分, 岩体内部构造变形不发育. 所以野外构造工作能够获取的信息主要来源于岩体的这两个局部地区以及围岩, 而无法从整体上把握岩体的构造几何学. 为了解决这一局限性, 我们对岩体进行了全面的磁组构研究. 在野外使用汽油钻机对大云山-幕阜山岩基的新鲜露头进行了系统的采样, 尽可能均匀布置采样点以覆盖整个岩体(图 4-10). 相邻两个采样点之间的平均间距约为 3 km, 同一采点相邻两个钻孔之间的间距约为 1-2 m. 每个采样点钻取至少 5 个长度大于 3 cm 的岩心, 并使用磁性罗盘或太阳罗盘对所采岩心进行定向. 这些岩心最终在实验室被切制成标准的磁组构样品, 即长度为 2.2 cm 和直径为 2.5 cm 的圆柱体. 这个形状最接近球体, 以最大限度降级样品形状对磁化率各向异性的影响. 本次研究共部布置采点 121 个, 最终共计获得有效的 AMS 样品 852 个. 通城以北地区由于岩体风化严重, 导致可采样点稀少(图 4-10).

岩石的磁组构测量在法国奥尔良大学地球科学研究所(Université d'Orléans, Institut des Sciences de la Terre d'Orléans)岩石磁学实验室使用 KLY-3 卡帕桥(Kapabridge)完成. 采用 ANISOFT 软件对测量结果进行计算和统计, 以获得每个采点的平均磁化率(K_m)和磁化率椭球体三个主轴的平均方向和大小(长轴 K_1 代表磁

线理，短轴 K_3 代表磁面理极，中间轴为 K_2). 依据 Jelinek (1981)，实验还获得了两个重要的参数，分别是磁化率椭球体的形状因子(T)和磁化率各向异性度(P_J)：$T = (2\eta_2-\eta_1-\eta_3) / (\eta_1-\eta_3)$，范围在$-1<T<1$；$P_J = \{2[(\eta_1-\eta_m)^2 + (\eta_2-\eta_m)^2 + (\eta_3-\eta_m)^2]\}1/2$ (其中 $\eta_1 = \ln K_1$, $\eta_2 = \ln K_2$, $\eta_3 = \ln K_3$, $\eta_m = 3\sqrt{\eta_1.\eta_2.\eta_3}$).

为了鉴别样品中载磁矿物的特征，我们还对不同岩性代表样品进行了磁性矿物学研究. 等温剩磁(isothermal remanent magnetization，缩写 IRM)实验使用奥尔良大学实验室的 JR-5 旋转磁力仪完成. 热磁实验(磁化率随温度的变化曲线)利用 KLY-3 卡帕桥进行，但外加温度控制系统 CS-3. 另外，我们还在巴黎地球物理研究所(Institut de Physique du Globe de Paris)古地磁实验室测试了不同岩性代表样品的磁滞回线.

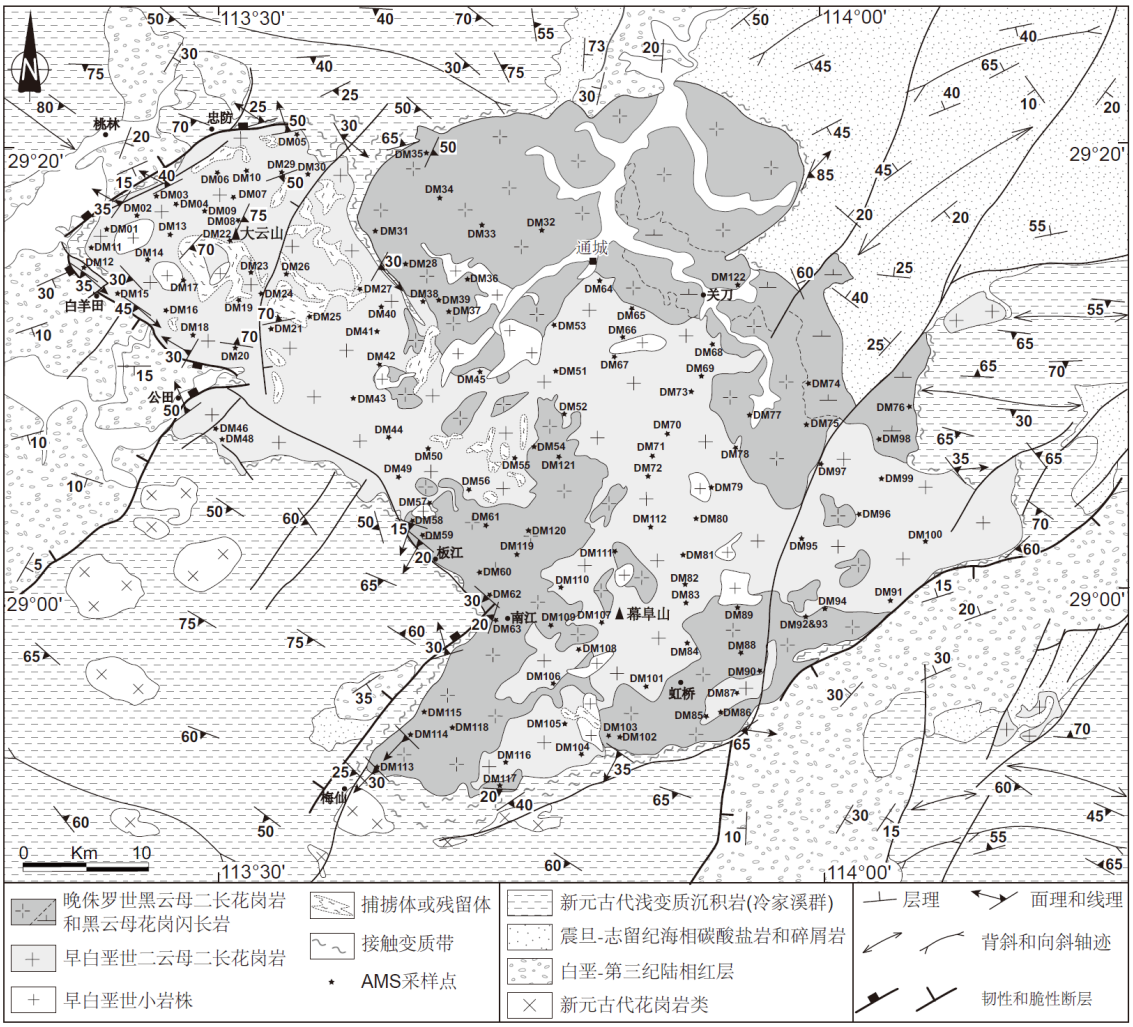

图4-10 大云山-幕阜山岩基磁组构采样位置分布图

Figure 4-10 AMS sites in the Dayunshan-Mufushan batholith

4.3 载磁矿物 Magnetic mineralogy

岩石样品的平均磁化率 K_m 值反映了样品中矿物磁化率的综合特征. 大云山-幕阜山岩基不同岩石类型平均磁化率的直方分布图显示(图 4-11), 绝大多数样品(85%)的 K_m 值小于 500×10^{-6} SI, 其中黑云母二长花岗岩的 K_m 值主要分布 300×10^{-6} SI 以内, 二云母二长花岗岩的体磁化率以小于 100×10^{-6} SI 占主导. 少数样品(主要是黑云母花岗闪长岩)的 K_m 值大于 500×10^{-6} SI, 最大值超过 20000×10^{-6} SI. 总体上, 黑云母二长花岗岩的磁化率略高于二云母二长花岗岩, 而黑云母花岗闪长岩的磁化率又远远大于前两者. 一般来讲, 对于磁化率较低的样品, 顺磁性矿物如黑云母等对磁化率值的贡献较大, 对于磁化率较高的样品($K_m>500\times10^{-6}$ SI), 铁磁性矿物如磁铁矿等的贡献较大.

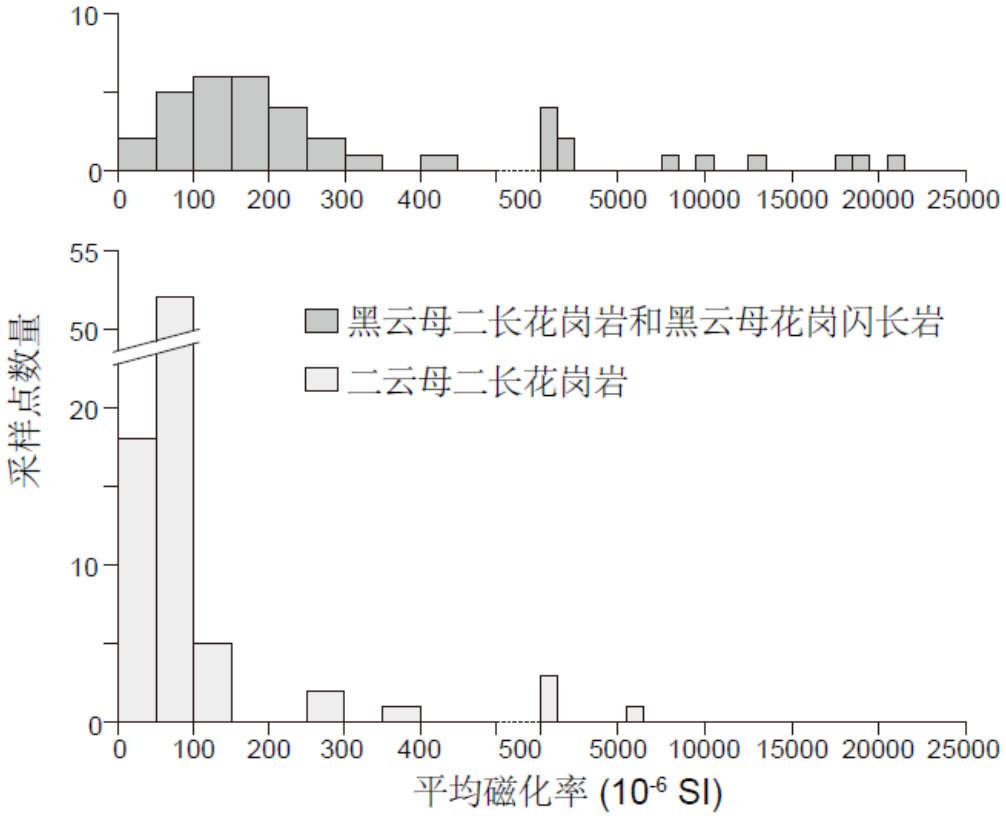

图 4-11 大云山-幕阜山岩基不同期次侵入体磁化率直方分布图

Figure 4-11 Histogram of bulk magnetic susceptibility of the Dayunshan-Mufushan batholith

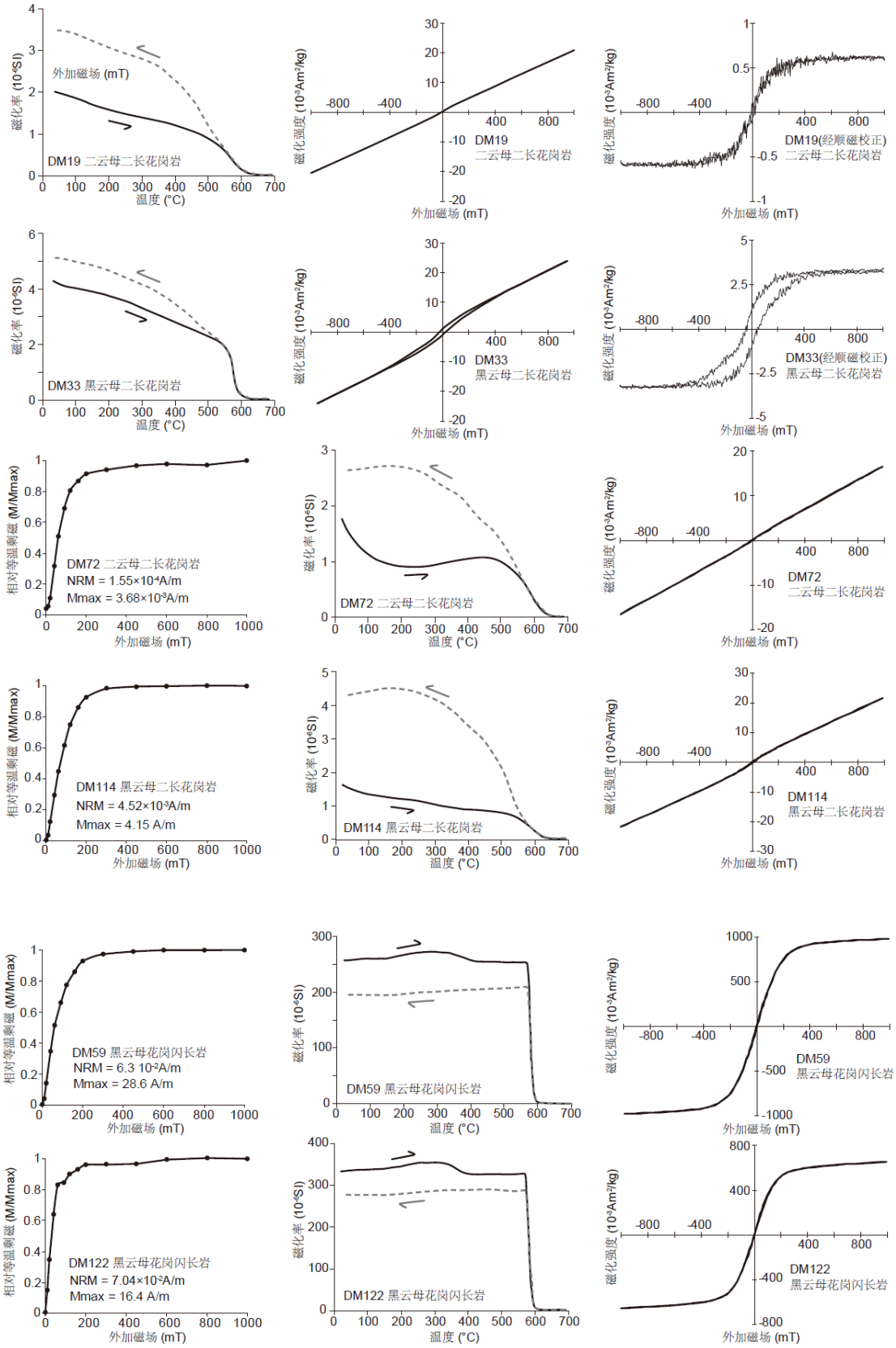

图 4-12 大云山-幕阜山岩基不同岩性的等温剩磁获得曲线、热磁曲线和磁滞回线

Figure 4-12 Isothermic remanent magnetization, thermomagnetic measurements and hysteresis loops for granitic rocks of the Dayunshan-Mufushan batholith

等温剩磁获得曲线是识别磁性矿物种类的重要磁学参数. 本次研究所有样品(DM72、DM114、DM59、DM122)的 IRM 曲线显示, 在低于 200 mT 的外加磁场下, 感应剩磁强度随外加磁场强度的增加而快速递增, 而在约 200 mT 时, 样品已获得饱和等温剩磁的 90% (图 4-11). 这一现象证明虽然样品岩性不同, 但载磁矿物均为一些低矫顽力矿物, 如磁铁矿.

不同的磁性矿物加热和冷却的过程中磁化率随温度的变化表现出不同的特征, 因此可用这些特征来确定磁性矿物的种类. 黑云母二长花岗岩样品(DM33 和 DM114)和二云母二长花岗岩样品(DM19 和 DM72)具有低的磁化率值, 加热曲线初始部分磁化率呈现随温度增加而减小的趋势, 表现出顺磁性矿物的曲线特征, 但温度上升至约 580 °C 左右磁化率明显降低. 由于磁铁矿的居里温度为 580 °C, 说明样品中有磁铁矿的存在(图 4-12). 部分样品的磁化强度在 580 °C 之后才缓慢趋于零点, 而赤铁矿的居里温度为 675 °C, 这意味着样品中可能含有赤铁矿. 冷却曲线与加热曲线是不可逆的, 且冷却曲线具有比加热曲线略高的磁化率值, 暗示在加热过程中存在矿物的转变. 黑云母花岗闪长岩样品(DM59 和 DM122)具有高的磁化率值, 其磁化率在 580 °C 左右时迅速降至零点, 表明磁铁矿为样品的主要载磁矿物(图 4-12). 另外, 加热曲线在 300-400 °C 区间有小幅度下降, 使我们怀疑可能有磁赤铁矿存在.

磁滞回线的形状可以反映磁性矿物的成分和粒度大小, 如磁铁矿的磁滞回线高而窄, 而赤铁矿的磁滞回线矮而宽, 多畴晶粒(MD)的磁滞回线比单畴晶粒(SD)要窄. 本次研究中, 二云母二长花岗岩样品(DM19 和 DM72)和黑云母二长花岗岩样品(DM33 和 DM114)的磁滞回线显示以线性特征为主, 说明这些样品的载磁矿物主要为顺磁性矿物(图 4-12). 部分样品(DM19 和 DM33)经顺磁校正后, 其叠加的曲线形态被明显表现出来, 表明样品中除顺磁性矿物外, 还含有少量磁铁矿(图 4-12). 而黑云母花岗闪长岩样品(DM59 和 DM122)磁滞回线的形状符合典型磁铁矿的特征, 其“细腰状”的曲线形态暗示磁铁矿的颗粒较大, 可能以假单畴(PSD)和多畴(MD)的形式存在(图 4-12).

综合以上的磁性矿物学分析并结合岩石学观察, 本次研究认为大云山-幕阜山岩基的黑云母二长花岗岩和二云母二长花岗岩的载磁矿物主要以黑云母为主, 而

少量磁铁矿也可能作为部分磁性载体，而黑云母花岗闪长岩的载磁矿物以磁铁矿占优势. 研究表明黑云母和磁铁矿的磁组构非常相似，因而我们有理由认为大云山-幕阜山岩基的磁组构可以反映岩石的应变特征.

4.4 磁组构分析 Magnetic fabrics

磁化率椭球体形态及各向异性度 Shape parameter (T) and anisotropy degree (Pj)

磁组构椭球体的形状因子 T 可以判断磁面理和磁线理的相对发育程度. 当 T < 0 时，磁化率椭球体处于拉长区(prolate)；当 T ＞ 0 时，磁化率椭球体形状处于压扁区(oblate). 区分岩浆流动组构和构造变形组构是利用磁组构研究岩体侵位过程的关键. 岩浆流动组构形成于岩浆的成岩过程中，而构造变形组构则受与岩浆岩形成同时或之后的构造变形控制. 一般而言，磁化率各向异性度(P_J 值)越大意味着区域构造应力对该岩石磁组构形态的影响就越大. 依据经验关系，岩浆流动组构的 P_J 值通常小于 1.2，而构造变形组构的 P_J 值多大于 1.2.

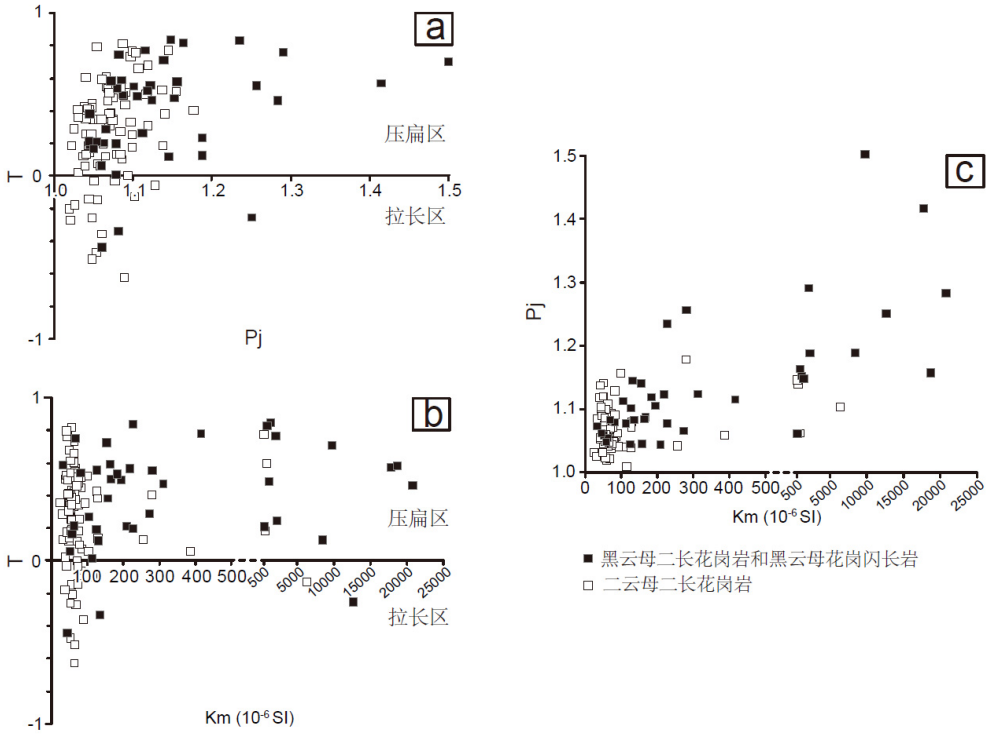

图 4-13 大云山-幕阜山岩基 K_m-T-P_J 关系图

Figure 4-13 AMS scalar parameters (correlation diagrams of K_m-T-P_J) for each AMS site

就大云山-幕阜山岩基来看, 绝大多数样品(85%)的 T 值大于 0, 意味着磁面理较磁线理更为发育(图 4-12). 仅有 7 个采点(DM58 和 DM59 为片麻状黑云母花岗闪长岩, DM62、DM113、DM117 为片麻状黑云母二长花岗岩, DM98 和 DM122 为块状黑云母花岗闪长岩)的 P_J 值大于 1.2, 其中最大的接近 1.5, 剩余 114 个采点的 P_J 值均小于 1.2 (平均值为 1.09) (表 4-1 和图 4-13). 因此, 大云山-幕阜山岩基的磁组构主要反映了岩体侵位时的岩浆流动组构. 虽然 P_J 值以小于 1.2 占据绝对优势, 但分布并不均匀. 一些靠近岩体-围岩侵入边界以及不同期次侵入体接触边界附近的采点, 其样品的 P_J 值整体上相对各个侵入体内部的采点略大, 这说明边界位置往往受到的应力作用相对较强. 这与我们的野外和显微观察相一致, 在岩体边缘尤其是西部和南部凸出部位发育明显构造变形, 而岩体内部基本保持岩浆结构, 仅局部可见流面构造. 另外, $P_J > 1.2$ 的样品其 T 值主要处于压扁区, 而少数磁线理较发育(即 $T > 0$)的样品, 其 P_J 值基本小于 1.2, 说明 T 与 P_J 没有明显的线性关系(图 4-13). T-K_m 图解同样也表明 T 与 K_m 也无明显的相关性, 而 P_J-K_m 图解显示 P_J 与 K_m 似乎存弱的正相关.

磁面理和磁线理 Magnetic foliation and lineation

大云山-幕阜山岩基 121 个采样点的磁组构赤平投影结果如图 4-14A 和 B 所示, 其中磁线理 K_1 为黑色方块, 磁面理极 K_3 为黑色圆点. 多数采样点 K_1 和 K_3 平均方位的 α_{95max} 不超过 25° (121 个数据中, $\alpha_{95} > 25°$的磁面理有 25 个, 磁线理有 38 个), 说明磁组构的结果较理想(即单个采点所有样品磁面理或磁线理的分布较集中, 平均方向误差较小, 可信度高). 因此, 本研究所获得的 AMS 数据可以用于地质解释. 整个岩体磁面理和磁线理的产状及分布见图 4-15A 和 B. 由于大云山-幕阜山岩基由两个时代的侵入体组成, 因此这里我们将晚侏罗世和早白垩世的侵入体区分对待.

(1)晚侏罗世黑云母二长花岗岩和黑云母花岗闪长岩:

北部黑云母二长花岗岩中的采点较少, 主要集中在通城以西地区. 磁组构结果显示磁面理走形基本平行边界, 多倾向于侵入体中心且倾角较陡; 磁线理总体不甚发育, 可信度较高的两个采点(DM35 和 DM36) 磁线理呈 NE-SW 向. 位于东北部的黑云母花岗闪长岩中仅有 4 个采点, 其中 1 个采点(DM122)处于该侵入体中

心区域, 其产状平缓, 磁线理呈近 N-S 走向; 而其它 3 个采点磁面理和磁线理均平行于侵入体边界, 并且磁面理近乎直立. 南部黑云母二长花岗岩的磁面理以倾向 S 至 SWW 为主, 倾角平缓至中等(20°-50°), 在边界拐角部位磁面理往往平行于岩体边界(如 DM63); 磁线理一致性不是很好, 以向 S 和 SW 倾伏为主.

(2)早白垩世二云母二长花岗岩:

西部大云山地区磁面理倾角整体上较陡(多大于 40°), 以倾向 E 或 SE 为主, 靠近边界处磁面理走形多与大云山拆离断层平行; 磁线理在边缘区域以近 E-W 向为主, 中心区域由于含有大量残留体以及晚期小岩株的侵入而比较分散. 东部靠侵入体中心区域磁面理的倾角平缓至中等, 倾向发散, 总体上略显示出由中心向外倾的趋势, 而大多数采点(如 DM53, DM65, DM66, DM67, DM68, DM70, DM71, DM78, DM80)的磁线理显示出一致的 NW-SE 走向. 在东部靠南区域(幕阜山主峰地区), 二云母二长花岗岩中含有大小不等的黑云母二长花岗岩的捕掳体以及由于晚期小岩株的破坏, 磁面理和磁线理均比较散乱. 东部和西部连接部位磁面理和磁线理的走向以 NW-SE 为主, 平行于二云母二长花岗岩的长轴.

从两个时代侵入体各自总的统计结果来看, 可以分辨出两个方向的线理(图 4-15B). 晚侏罗世黑云母二长花岗岩和黑云母花岗闪长岩磁线理的优选方位为近 N-S 向(极值在 190°), 而早白垩世二云母二长花岗岩磁线理的优选方位为 NW-SE 向(极值在 117°). 这与我们野外在岩体边部变形的花岗岩以及其围岩接触变质带中观察到的两期线理十分吻合(图 4-5).

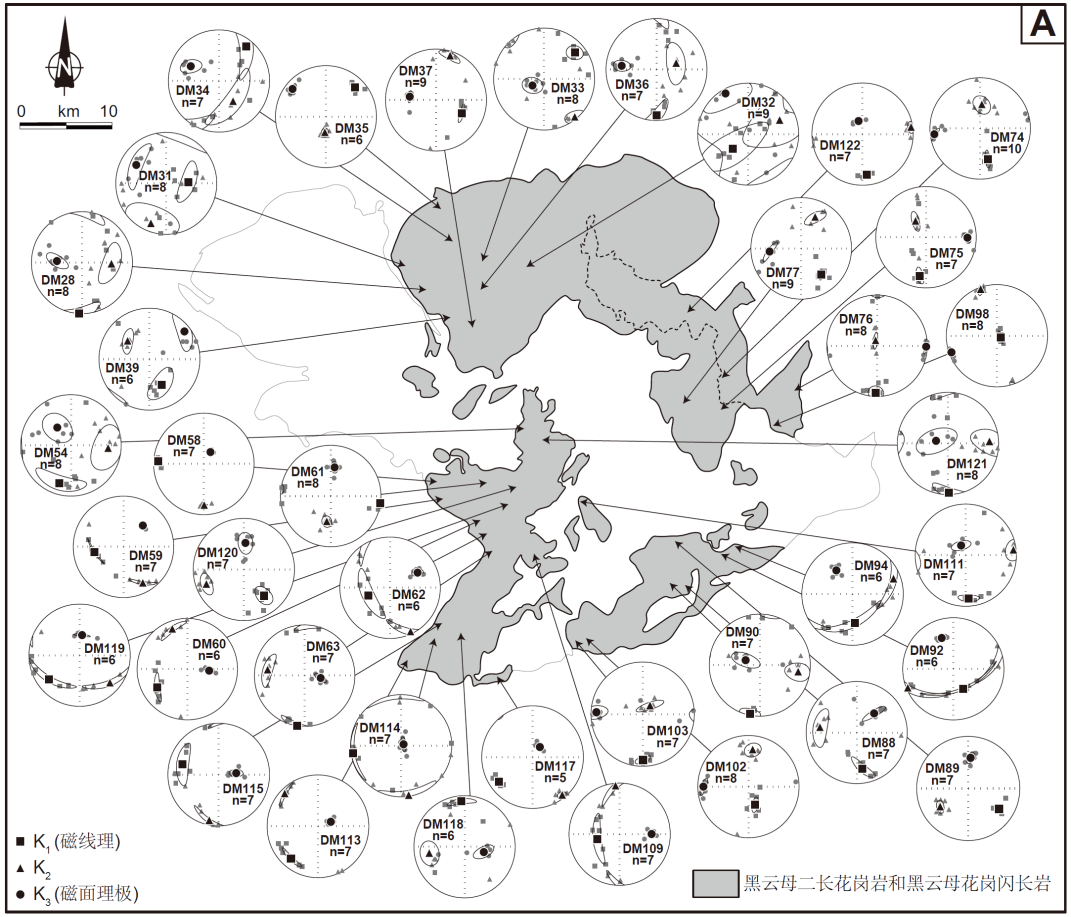

图 4-14A 大云山-幕阜山岩基磁组构赤平投影结果(早期侵入体黑云母二长花岗岩和黑云母花岗闪长岩)

Figure 4-14A Stereographic projection of magnetic fabric from the Dayunshan-Mufushan batholith (biotite monzogranite and biotite granodiorite)

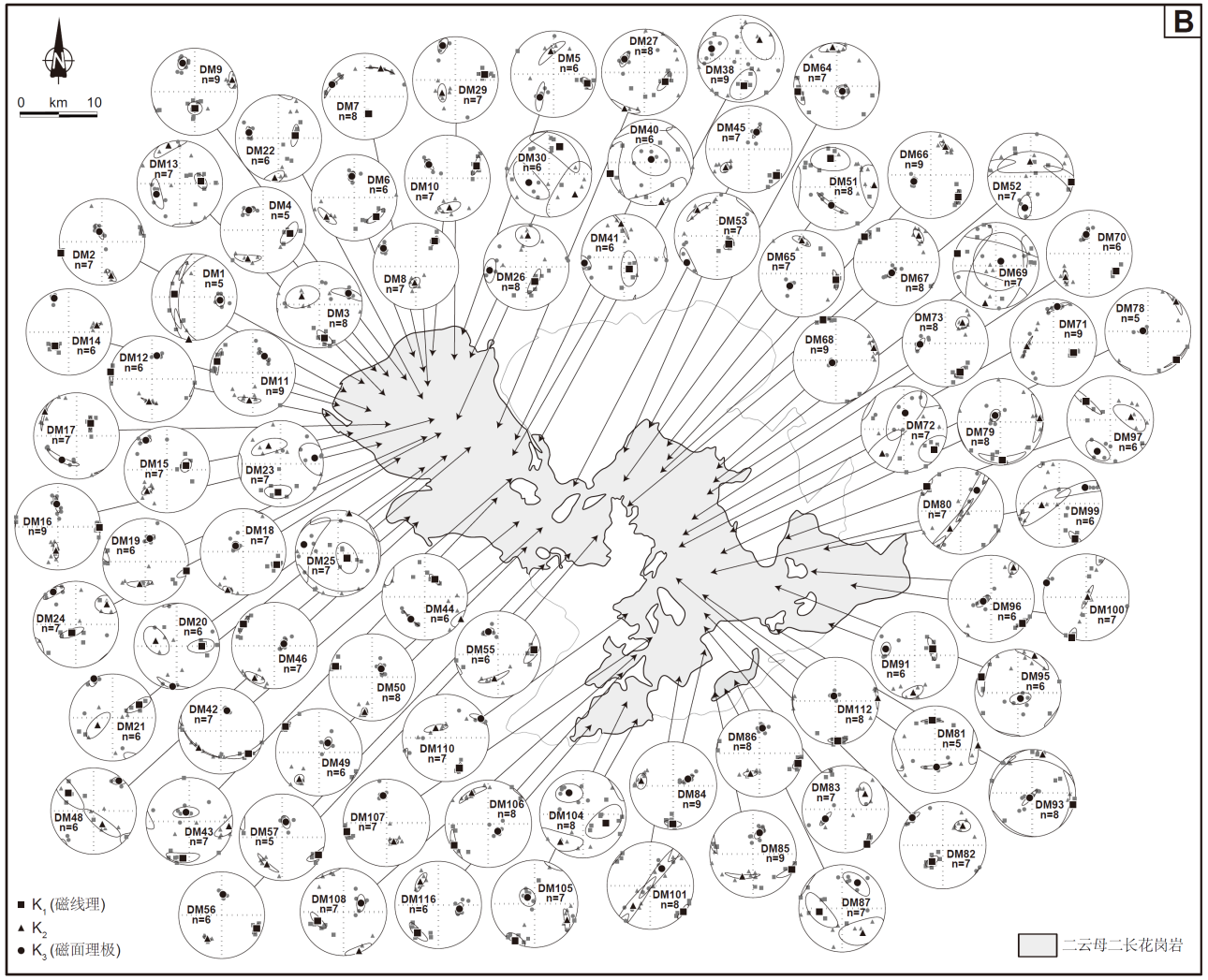

图4-14B 大云山-幕阜山岩基磁组构赤平投影结果(晚期侵入体二云母二长花岗岩)

Figure 4-14B Stereographic projection of magnetic fabric from the Dayunshan-Mufushan batholith (two-mica monzogranite)

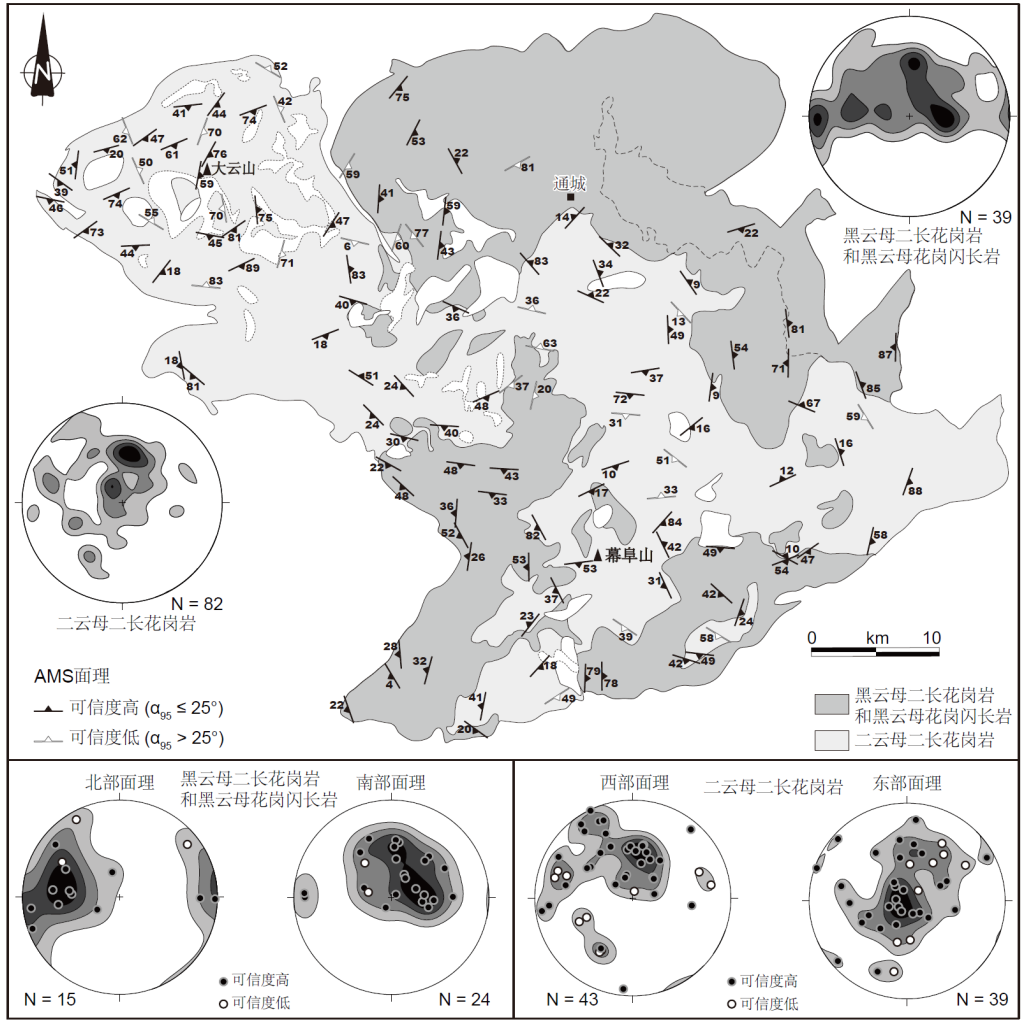

图4-15A 大云山-幕阜山岩基磁面理分布和统计图

Figure 4-15A Magnetic foliation map of the Dayunshan-Mufushan batholith

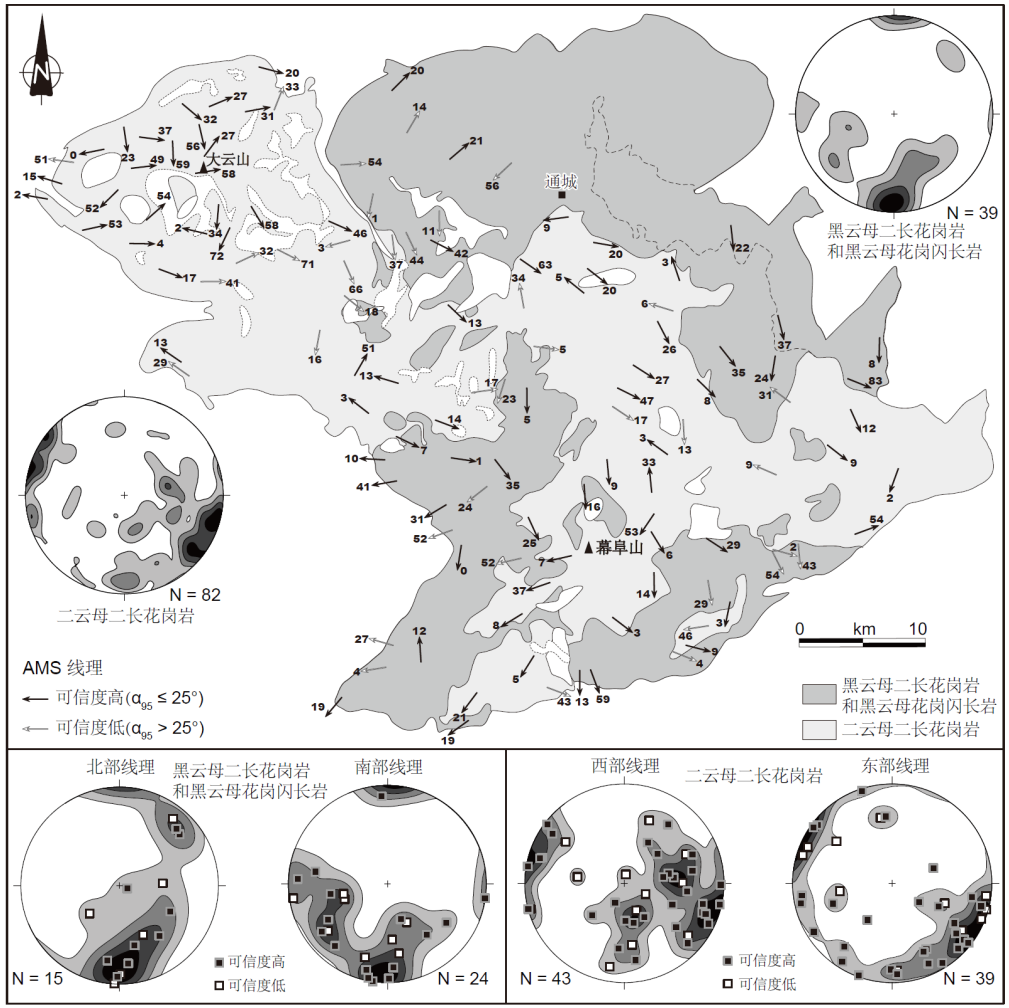

图4-15B 大云山-幕阜山岩基磁线理分布和统计图

Figure 4-15A Magnetic lineation map of the Dayunshan-Mufushan batholith

5 大云山-幕阜山岩基两期变形的运动学特点 Kinematics of two-phase deformation in the Dayunshan-Mufushan batholith

结合区域构造分析和磁组构研究, 我们厘定出了大云山-幕阜山岩基所记录的两期晚中生代构造事件: (1)早期构造事件(D_1): 与晚侏罗世黑云母二长花岗岩和黑云母花岗闪长岩的侵位过程有关, 在侵入体和围岩接触变质带中表现为 NE-SW 向的矿物拉伸线理和磁线理, 具有上部向 SW 的运动学; (2)晚期构造事件(D_2): 与早白垩世二云母二长花岗岩的侵位过程有关, 在侵入体和围岩接触变质带及大云山拆离断层中表现为NW-SE向的矿物拉伸线理和磁线理, 具有上部向NW的运动学.

5.1 早期 D_1 事件的构造表现与运动学 Early (D_1) event

从野外构造观察来看, D_1事件在早期侵入体(黑云母二长花岗岩和黑云母花岗闪长岩)南部边缘及其围岩接触变质带中发育较明显. 沿岩体南部边缘(板江-南江-梅仙-虹桥一带)发育片麻状构造, 局部变形较强显示糜棱岩化. 前已述及, 在片麻状花岗岩中可见由长石斑晶和黑云母定向构成的NE-SW向矿物拉伸线理. 沿着此线理方向, 在野外、手标本和显微镜下不同尺度均可观察到黑云母二长花岗岩中的长石眼球状构造或旋转残斑指示了上部向SW的剪切变形(图4-16a, b, c). 在岩体东南侧黑云母二长花岗岩的接触变质带石榴石云母片中同样发育清晰的NE-SW向矿物拉伸线理, 野外可见该片岩中长英质脉体的剪切透镜体指示上部向SW的剪切变形, 这与定向薄片中石榴石的雪球构造所指示的运动学相一致(图4-16e, f).

总体上, 早期侵入体的片麻状构造由边缘向内部变弱, 逐渐消失并过渡为块状构造. 显微构造也显示出同样的变化规律, 片麻状花岗岩以微弱至中等固态条件下变形组构为主, 局部可见强变形组构(图 4-4a, b 和图 4-16b). 而在侵入体内部长石、石英和云母等多不具明显定向性, 这与 AMS 结果显示黑云母二长花岗岩的内部组构主要为岩浆的流动组构相吻合. 而且, 早期侵入体的磁线理优选方向为 NE-SW 向, 与野外观察到的线理一致. 因此，黑云母二长花岗岩具有同构造花岗岩的特点, 也就是说其侵位年龄即代表了 D_1 构造事件发生的时间.

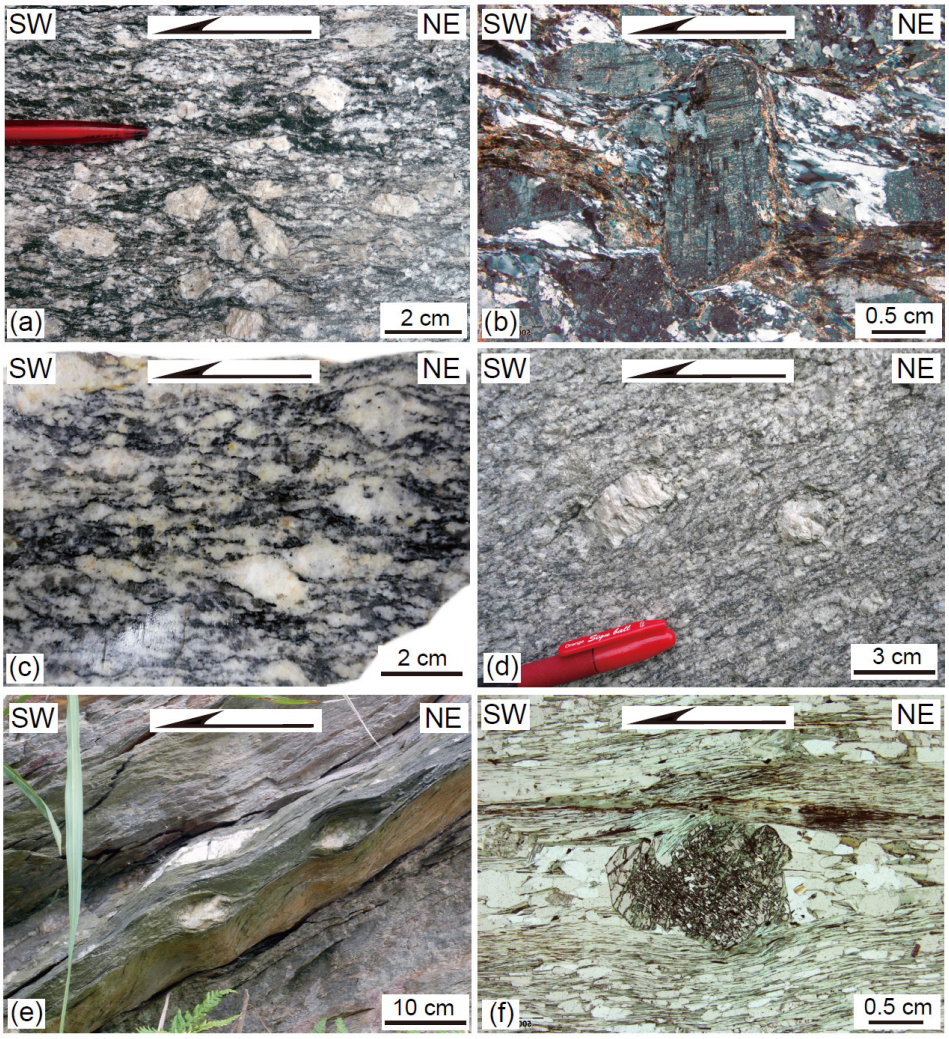

图4-16 D_1事件在黑云母二长花岗岩及其围岩接触带中的表现

(a)-(c)岩体南部边缘不同地区片麻状黑云母二长花岗岩中长石眼球状构造或旋转残斑指示了上部向SW的剪切变形; (e)和(f)岩体东南侧黑云母二长花岗岩的接触变质带内含石榴石云母片中长英质脉体的剪切透镜体和镜下石榴石的雪球构造一致地指示了上部向SW的剪切变形

Figure 4-16 D_1 event in the biotite monzogranite and its contact metamorphic aureole

(a)-(c) augen or σ-type feldspar porphyroclasts in gneissic biotite monzogranite from the southerm margin of the pluton, indicating a top-to-the-NW sense of shear; (e) and (f) sheared lens of quartzo-felsic vein in the contact metamorphic rocks at the southeastern side of the pluton, and snowball structure of garnet in thin section of garnet-bearing mica schist, indicating a top-to-the-NW sense of shear

5.2 晚期 D_2 事件的构造表现与运动学 Late (D_2) event

D_2事件在岩体西部的大云山地区表现最为明显，以大云山拆离断层的发育为典型. 卷入拆离断层下盘的岩石主要是二云母二长花岗岩. 岩体的舌状边缘普遍

受到变形，其宽度约100-2000 m不等，构成了研究区主要的构造变形事件. 从大云山内部向边缘变形逐渐增强，花岗岩由块状构造到发育片麻理，靠近拆离断层则出现糜棱岩. 前已述及，虽然韧性剪切带糜棱面理产状围绕岩体舌状边界呈规律性变化，但线理稳定在NW-SE方向. 在野外露头，手标本和显微镜下，由二云母二长花岗岩变形而成的糜棱岩中，韧性剪切标志十分发育，如长石的眼球状拖尾或旋转残斑, S-C组构，云母鱼等，均一致地指示了上部向NW的运动学(图4-17a-f).

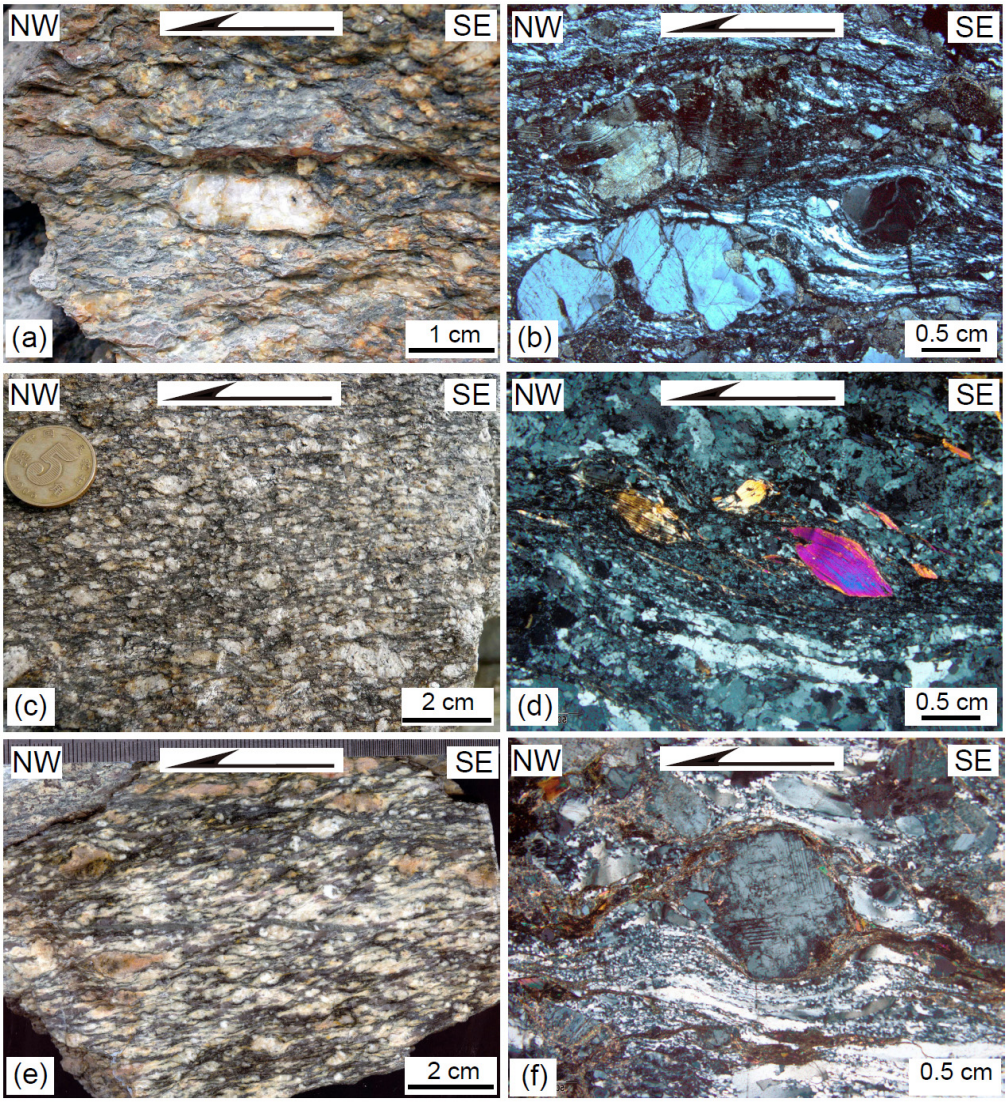

图4-17 D_2事件在二云母二长花岗岩中的表现

(a)-(f)大云山拆离断层韧性剪切带内花岗质糜棱岩中发育的各种剪切标志，均一致的指示了上部向NW的运动学.

Figure 4-17 D_2 event in the two-mica monzogranite

(a)-(f) various indicators in granitic mylonites within shear zone of the Dayunshan detachement fault, consistently indicating a top-to-the-NW sense of shear

在拆离断层上盘零星分布的冷家溪群受到热接触变质而发生片岩化, 靠近拆离带的部分片岩也卷入了韧性剪切带. 在花岗质糜棱岩带外侧呈狭长带状断续分布的构造片岩(主要为绢云石英片岩)中可清晰地观察到NW-SE向线理, 沿线理方向片岩中发育的S-C组构指示了上部向NW的剪切变形(图4-18a). 在岩体内部靠近拆离带的残留体片岩中虽然野外线理发育并不明显, 但在沿NW-SE方向切制的定向薄片中可以见到S-C组构和云母鱼构造, 同样指示了上部向NW的运动学(图4-18b). 另外, D_2事件不仅仅局限于二云母二长花岗岩的接触带, 在岩体南部黑云母二长花岗岩向南突出部分的西侧接触变质岩中也可以局部见到NW-SE向线理的发育. 在此处, 侵入于接触带石榴石云母片中的伟晶岩脉受到了强烈的剪切变形, 其σ状形态指示了上部向NW的运动学, 镜下该片岩中发育的S-C组构也指示了上部向NW的剪切变形(图4-18c, d).

大云山拆离断层剪切带内花岗质糜棱岩的长石多呈残斑, 显微破裂和扭折发育, 石英少数也可呈残斑, 大部分发生了不同程度的动态重结晶, 呈条带状或发育核幔构造, 白云母和黑云母的扭折现象普遍(图 4-17). 这些矿物的变形特征指示韧性剪切带的变形温度约在 400-500 °C, 代表了二云母二长花岗岩在冷凝固结后固态条件下(post-sulidus)受到的构造变形. 从 AMS 的结果来看，二云母二长花岗岩内部组构主要反映了岩浆的流动组构, 即记录了岩浆固结前及亚固态条件下(sub-sulidus)的侵位过程. 但其磁线理总体上以NW-SE向占主导, 说明D_2构造事件所代表的 NW-SE 向应力场在二云母二长花岗岩侵位过程中就已经存在. 因此，D_2构造事件贯穿于二云母二长花岗岩从岩浆形成至岩体侵位、冷凝的整个过程中, 也就是说二云母二长花岗岩同样具有同构造花岗岩的特点.

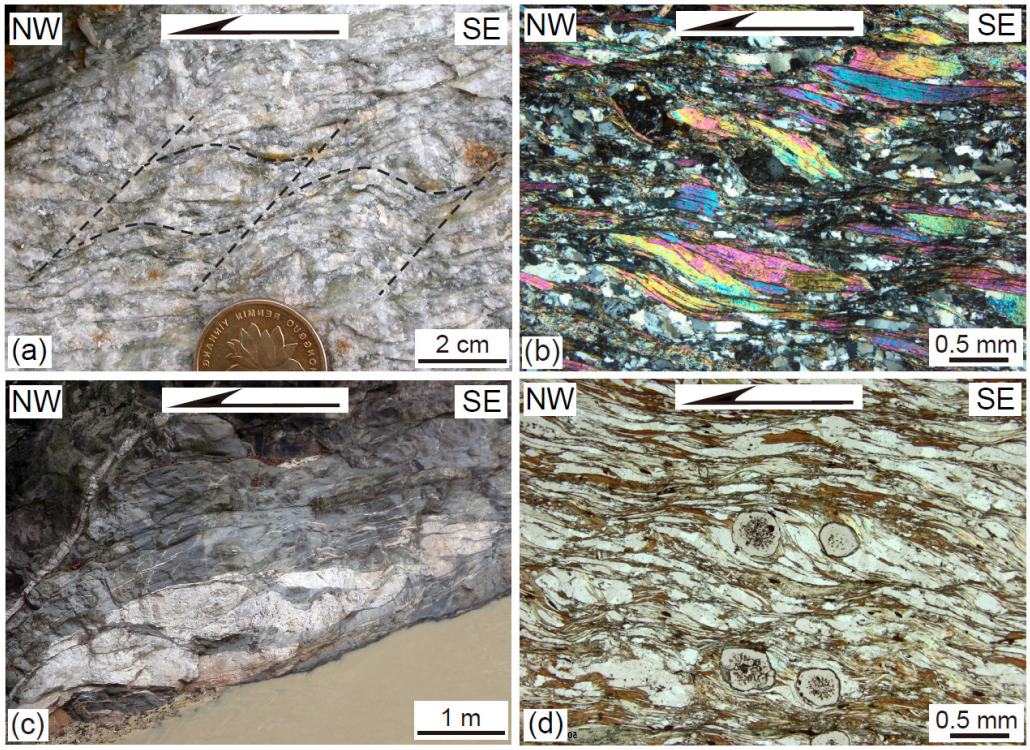

图4-18 D_2事件在围岩接触变质带及残留体中的表现

(a)大云山西缘剪切带内构造片岩中的S-C组构; (b)靠近大云山拆离断层花岗岩内残留体中发育的S-C组构和云母鱼构造; (c)和(d)岩体南部黑云母二长花岗岩向南凸出部分的西侧接触变质带中强烈剪切变形的同构造花岗岩脉以及围岩石榴石云母片岩镜下发育的S-C组构. 以上剪切标志均指示了上部向NW的运动学.

Figure 4-18 D_2 event in contact metamorphic aureole and restite

(a) S-C fabric in tectonic shist from the shear zone on western margin of the Dayunshan pluton; (b) S-C fabric and mica fish in the restite within the granite near the Dayunshan detachement fault; (c) and (d) syn-tectonic dike in contact metamorphic aureole to the west side of the southern protrudent part of biotite monzogranite, S-C fabric in garnet-mica schist of country rock. Above indicators consistently indicate a top-to-the-NW sense of shear

6 布格重力异常的启示 Revelation of the Bouguer gravity data

重力资料可以揭示地质体的深部几何形态, 为此我们收集了研究区1: 50万布格重力异常资料(图4-19). 在大云山-幕阜山岩基的北部存在一个明显的重力负异常中心, 与早期侵入体(黑云母二长花岗岩和黑云母花岗闪长岩)的北部相对应，且重力等值线与侵入岩的边界大致吻合. 虽然整个岩体南部的重力值是由早期和晚期侵入体共同贡献，但南部部分总体上显示出比北部稍弱的重力负异常. 由此可见, 早期侵入体的根部可能位于岩体的北部, 向南厚度逐渐变薄. 实际上, 这与AMS磁

面理所反映的几何形态较一致, 早期侵入体北部的磁面理较陡, 多平行于边界向岩体中心倾斜, 而南部的磁面理多向SW缓倾. 因此, 我们可以推测早期侵入体侵位时受到了上部向南的应力作用, 这也与野外的运动学观察相一致. 前人使用角闪石全铝压力计估算得到早期侵入体的花岗闪长岩侵位深度不小于4.05 kbar (邹慧娟等, 2011).

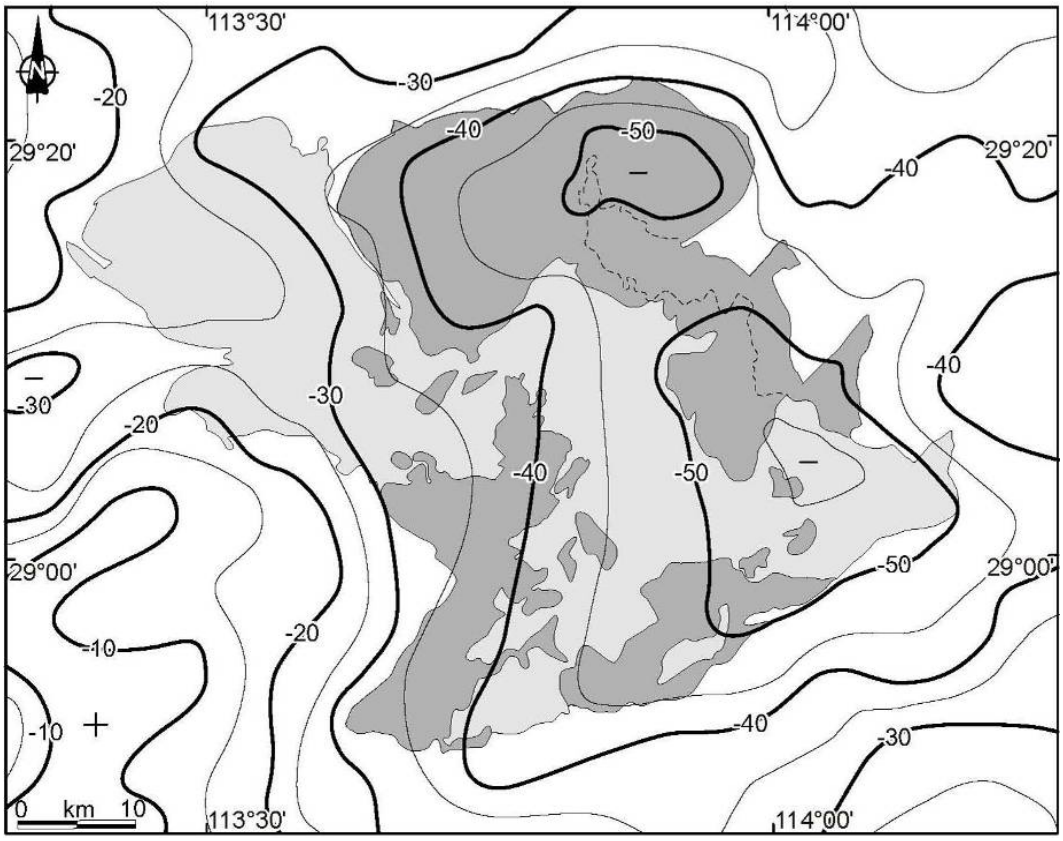

图 4-19 大云山-幕阜山地区布格重力异常等值线(早期侵入体为深灰色, 晚期侵入体为浅灰色)

Figure 4-19 Bouguer gravity anomaly in the Dayunshan-Mufushan area (dark and light gray are early and late plutons, respectively)

另外一个较明显的重力负异常位于岩体的中心偏东部位, 主要被晚期侵入体(二云母二长花岗岩)所占据. 而岩体西部大云山地区则相对表现为正异常, 重力等直线与岩体边界呈镜像关系, 暗示大云山舌状岩体的厚度十分薄, 其下部可能存在高密度的围岩. 大云山地区花岗岩中捕掳体或残留体较发育也从侧面印证了这一点. AMS 结果显示二云母二长花岗岩的东部中心区域磁面理较为发散，倾角平缓至中等, 但磁线理比较一致为 NW-SE 向. 对此可作如下解释: 当岩浆近垂直上涌时由于受到上覆围岩的压力, 在岩体顶部会产生一个较平缓的接触面, 从而致使

岩浆发生侧向流动, 并在区域构造应力作用下显示出比较一致的流动方向. 结合 AMS 研究和重力资料, 可以推测二云母二长花岗岩的重心在东部, 西部大云山部分可能只是在构造作用下从东部岩基伸出的舌状分枝.

7 年代学研究 Geochronological studies

7.1 锆石 U-Pb 定年 Zircon U-Pb dating

大云山-幕阜山岩基的侵位时代一直缺乏高精度的年代学研究, 我们应用 SIMS 方法对岩体不同期次的侵入体进行了精确的锆石 U-Pb 定年. 测年工作在中国科学院地质与地球物理研究所离子探针实验室 Cameca IMS-1280 二次离子质谱仪上完成. 详细的分析方法和流程见 Li et al. (2009b). 同位素年龄计算采用 Isoplot 程序(Ludwig, 2003). 单个分析点测试数据和年龄结果见表 4-2, 误差均为 1σ, 样品谐和年龄和 $^{206}Pb/^{238}U$ 加权平均年龄的误差为 2σ.

DM35 为岩体北部的黑云母二长花岗岩(采样位置同 AMS 采样点 DM35), 样品中锆石多为无色透明的自形短柱状晶体. 锆石 CL 图像显示清晰的岩浆韵律环带, 极少数锆石保留有继承锆石的残留核(图 4-20). 对该样品的 18 颗锆石进行了 18 个分析点的 U-Pb 年龄测定, 其中 2 个点位于锆石核部, 其余 16 个点位于典型的岩浆环带上. 除去 2 个核部给出的不谐和年龄(270 Ma 和 705 Ma), 其它 16 个分析点均集中在谐和线上, 年龄范围在 149-153 Ma, Th/U 比值范围在 0.33-0.65. 由这 16 个分析点计算得到的谐和年龄和加权平均年龄一致为 151.2 ± 1.1 Ma, 代表了黑云母二长花岗岩的结晶年龄(图 4-21).

QD69 为岩体南部的片麻状黑云母二长花岗岩(采样位置同 AMS 采样点 DM114), 样品中锆石多为无色透明的自形-半自形短柱状晶体. 锆石 CL 图像普遍发光较弱, 颜色较深但仍可见岩浆韵律环带, 极少数锆石含有残留核(图 4-20). 对该样品的 19 颗锆石进行了 19 个分析点的测定, 所有分析点均落在谐和线上. 锆石普遍具有较高的 U 含量, 最大可达 7007 ppm, Th/U 比值大部分集中在 0.1-0.2. 位于锆石核部的 1 个分析点给出了新元古代年龄(837 Ma), 它应代表了继承锆石的年龄. 再除去可能由于高 U 效应及核边混合而导致年龄(154-160 Ma)相对偏大的 3 个

分析点，剩余 16 个分析点的年龄集中在 149-153 Ma. 由这 16 个分析点计算得到的谐和年龄为 151.1 ± 1.2 Ma，加权平均年龄为 151.2 ± 1.2 Ma(图 4-21). 因此，该黑云母二长花岗岩的侵位时代在约 151 Ma.

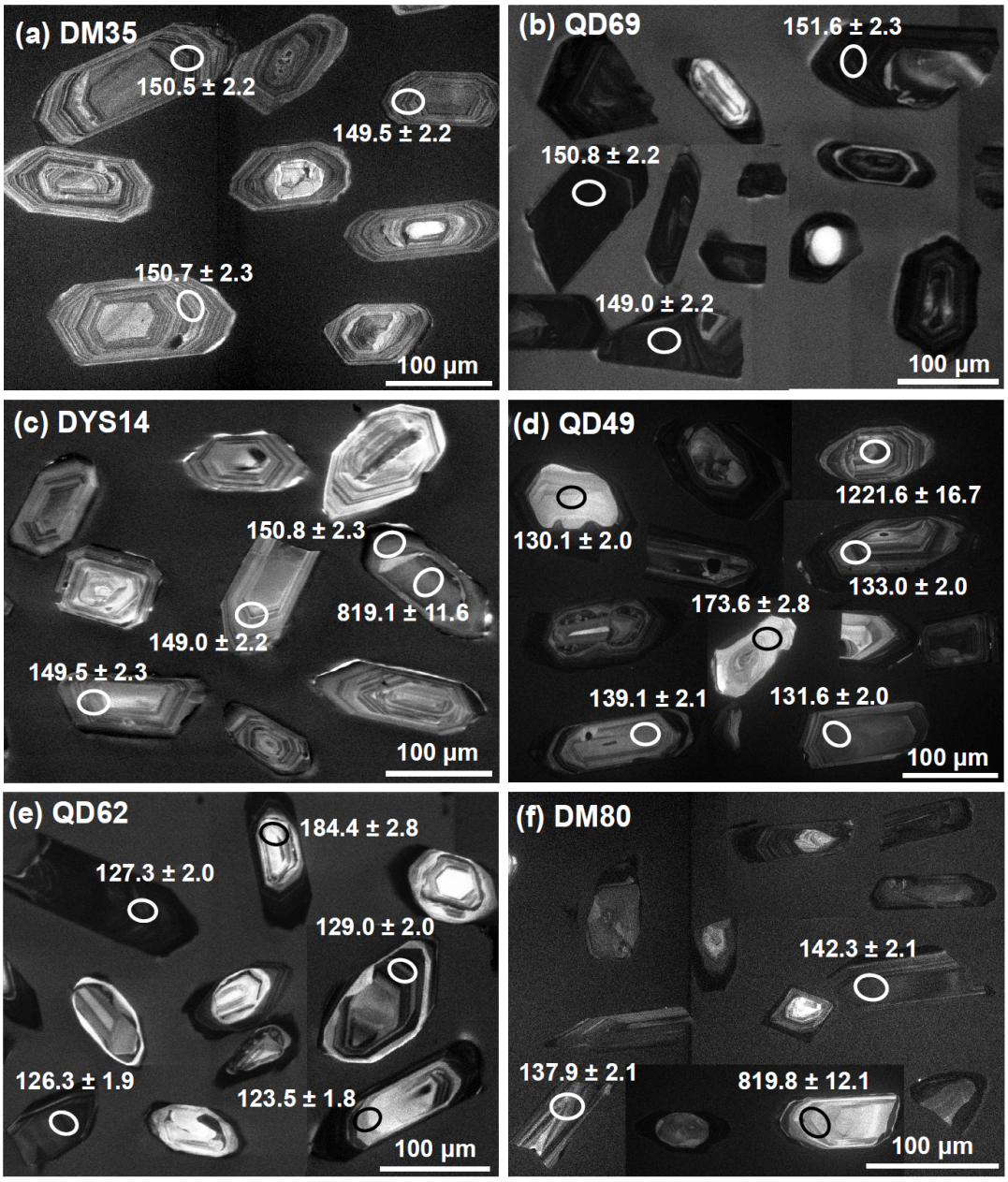

图 4-20 大云山-幕阜山岩基中锆石的典型 CL 图像

Figure 4-20 Typical CL images of zircon in granitic rocks from the Dayunshan-Mufushan batholith

DYS14 为岩体东北部的黑云母花岗闪长岩(采样位置同 AMS 采样点 DM122)，样品中锆石多为无色透明的自形短柱状晶体. CL 图像显示锆石具典型的岩浆韵律环带，极少数锆石含有继承锆石的残留核(图 4-20). 20 颗锆石的 21 个分析点均落在谐和线上，锆石的 U 含量 294-948 ppm. 1 个位于锆石核部的分析点给出了新元古代

年龄(819 Ma), Th/U 比值为 0.08. 其余 20 个分析点除去 1 个年龄略微偏大的分析点(156 Ma)外, 年龄范围在 145-151 Ma, Th/U 比值变化于 0.17-0.89. 由这 19 个分析点计算得到的谐和年龄和加权平均年龄均为 149.0 ± 1.0 Ma, 代表了黑云母花岗闪长岩的侵位年龄(图 4-21).

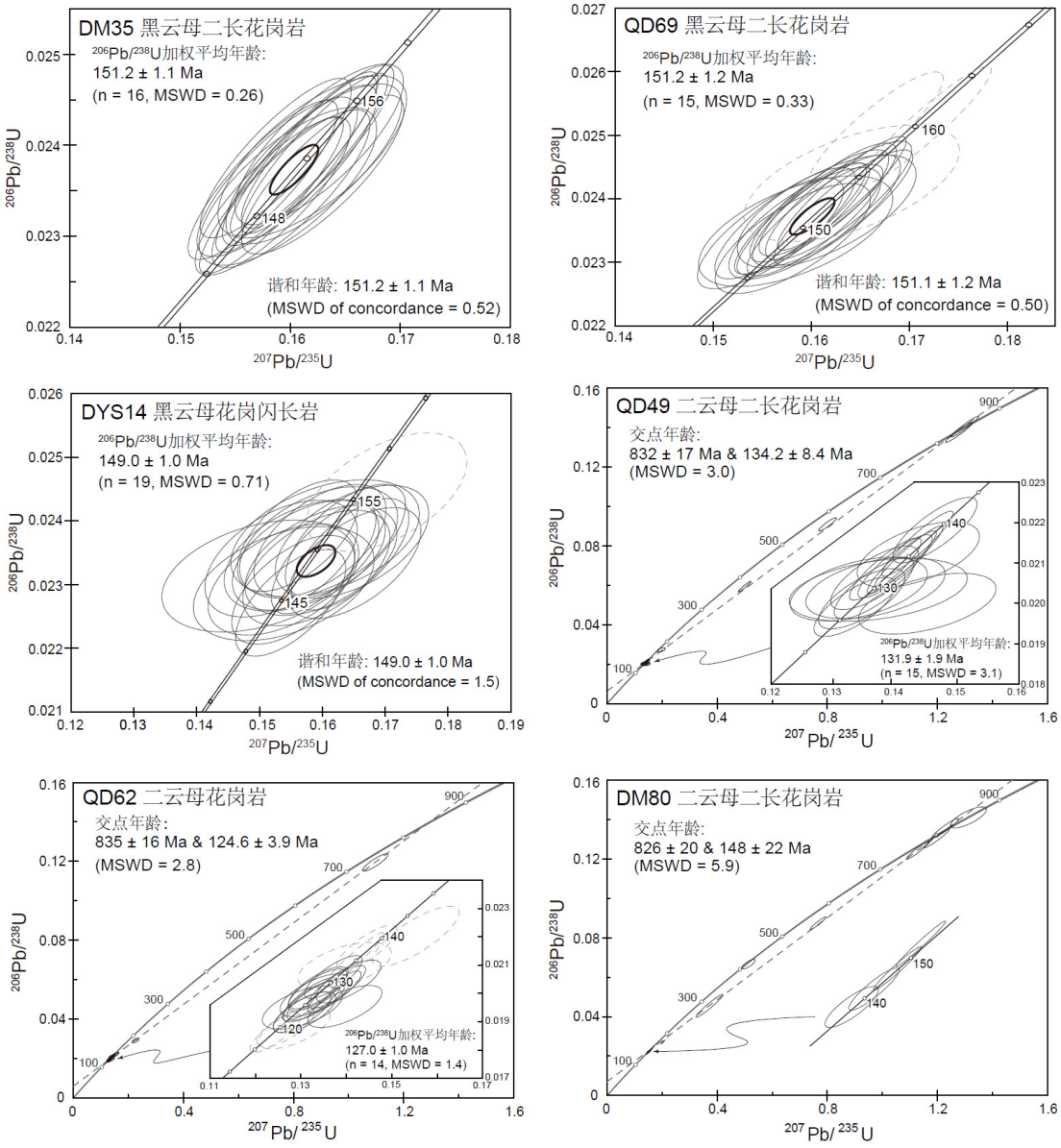

图 4-21 大云山-幕阜山岩基锆石 U-Pb 年龄

Figure 4-21 Zircon U-Pb ages of the Dayunshan-Mufushan batholith

QD49 为岩体西部大云山地区的二云母二长花岗岩(采样位置同 AMS 采样点 DM07), 样品中锆石多为无色透明的半自形短柱状晶体, 大部分具有明显的岩浆震荡环带, 表明为岩浆成因. 少部分锆石还具有明显的核-边结构, 一些核部呈港湾状或斑杂状, 保留有微弱的韵律环带, 另一些核部分 CL 较强, 发育暗色的增生

边, 锆石外形呈颗粒状(图 4-20). 上述特征表明这些继承锆石受到岩浆作用的影响而发生了不同程度的重结晶. 对样品中 21 颗锆石进行了 21 个分析点的测定, U 含量变化范围较大(88-5166 ppm), 除一个分析点的 Th/U 比值低至 0.02, 其余均介于 0.12-1.06 之间. 位于一致线上的分析点最大年龄为 1230 Ma, 这也是本次定年工作中获得的最老年龄, 剩余分析点构成的不一致线上下交点年龄分别为 832 ± 17 Ma 和 134.2 ± 8.4 Ma (MSWD = 3.0). 下交点附近的 15 个分析点的年龄范围在 127-139 Ma, 计算得到的加权平均年龄为 131.9 ± 1.9 Ma (MSWD = 3.1), 代表了二云母二长花岗岩的侵位年龄(图 4-21).

DYS62 为岩体西部大云山地区的晚期小岩株, 岩性为细粒二云母花岗岩(采样位置在 AMS 采样点 DM17 附近). 样品中锆石多为无色透明的自形-半自形的长柱状或短柱状晶体. CL 图像揭示锆石的内部结构复杂多样, 其中一类锆石整体为暗色具不明显的韵律环带; 另一类为具核-边结构的锆石, 并可再分为两种: 一种核部与边部界限截然, 核部呈现为残留核, 并具清晰的韵律环带; 另一种核部韵律环带与暗色环边保持协调一致, 说明在岩浆演化晚期有明显的 U 富集现象, 可能存在高温热液作用(图 4-20). 对样品中 20 颗锆石进行了 23 个分析点的测定, U 含量范围在 537-3402 ppm, Th/U 比值介于 0.08-0.42. 所有分析点构成的不一致线上下交点年龄分别为 835 ± 16 Ma 和 124.6 ± 3.9 Ma (MSWD = 2.8). 除去下交点附近略偏大或偏小的分析点, 选取比较集中的 14 分析点计算得到的加权平均年龄为 127.0 ± 1.0 Ma (MSWD = 1.7), 代表了晚期小岩株的侵位年龄(图 4-21).

DM80 为岩体东部的二云母二长花岗岩(采样位置同 AMS 采样点 DM80). 由于未能挑选出足够多且颗粒较大的锆石, 仅对该样品的 12 颗锆石进行了 12 个分析点的测定. 样品中的锆石多为无色透明的自形-半自形的细长柱状晶体, 并具岩浆韵律环带, 部分锆石可见残留核(图 4-20). 除去一个具古生代年龄(417 Ma)的谐和分析点, 其余 11 个数据构成的不一致线上下交点年龄分别为 826 ± 20 Ma 和 148 ± 22 Ma (MSWD = 5.9) (图 4-21). 而位于下交点附近的 4 个谐和分析点年龄在 138-153 Ma, 但年龄与 U 含量表现出明显的正相关关系, 表明存在高 U 效应. 因此, 岩浆结晶的真实年龄应该比 138 Ma 年轻. 考虑到 DM80 与 QD49 为同期侵入体, 我们认为二云母二长花岗岩的侵位时代应以 QD49 的定年结果为准, 即约为 132 Ma.

7.2 独居石电子探针定年 Monazite EPMA dating

为了进一步限定构造事件发生的时间, 本次研究还选取了研究区三个岩石样品进行了独居石电子探针定年, 包括片麻状黑云母二长花岗岩(QD69)、二云母二长花岗岩中的残留体(DM26, 矽线石云母片岩)和二云母二长花岗岩的围岩接触变质岩(DYS22, 含石榴石的云母片岩). 首先将需要进行定年的岩石磨制成探针片, 在扫描电镜下使用背散射电子成像寻找并观察独居石颗粒. 然后利用法国地质调查局(BRGM)和奥尔良大学地球科学研究所(ISTO)共有的 Cameca SX50 电子探针对选取的独居石沿剖面进行多点成分测定. 设定分析剖面时相邻两个分析点的间距不低于 5 um (电子探针的束斑约为 1 um), 并注意避开裂隙和包裹体. 详细的分析方法和流程见 Cocherie et al. (1998). 所获得的测试数据采用 EPMA dating 程序进行处理以计算单点的 U-Th-Pb 年龄(Pommier et al., 2002), 然后采用 Isoplot 程序进行加权平均年龄的计算(Ludwig, 2003). 对于 Th/U 比值变化范围较大的样品可进行 Th/Pb-U/Pb 图解的投图(Cocherie and Albarède, 2001). 具体的独居石测试数据见表 4-3, 年龄结果见图 4-23.

QD69 采自岩体最南端, 为片麻状黑云母二长花岗岩, 岩石中可见长石斑晶指示上部向 SW 的剪切变形. 样品中独居石主要以包裹体的形式存在于黑云母之中, 大小在 50-200 μm, 偶见环带构造(图 4-22). 在 Th/Pb-U/Pb 图解中, 7 个独居石颗粒上 140 个有效分析点计算得到的年龄为 151 ± 5 Ma, 与加权平均年龄 147.8 ± 4.5 Ma 在误差范围内一致(图 4-23). 这个年龄结果与该样品的锆石 U-Pb 年龄一致.

DM26 采自大云山中部, 为二云母二长花岗岩中包裹的残留体, 样品中的独居石多产出于云母之中, 大小在 20-50 μm (图 4-22). 11 个独居石颗粒上 127 个有效分析点的获得的加权平均年龄为 134.8 ± 6.6 Ma (图 4-23). 如不考虑误差, 这一年龄略大于与二云母二长花岗岩的侵位年龄, 可能代表了岩浆岩源区物质开始发生部分熔融的时间.

DYS22 采自大云山北侧的接触变质带中, 野外可观察到岩石中发育 NW-SE 向的矿物拉伸线理, 薄片中二云母和石英条带定向明显. 样品中的独居石在云母和石英之中均有产出, 大小在 10-30 μm (图 4-22). 17 个独居石颗粒上 84 个有效分析

点获得的加权平均年龄为 130.2 ± 9.7 Ma (图 4-23). 结合构造分析, 我们可以将其解释为与二云母二长花岗岩侵位相关的变质变形作用发生的时间.

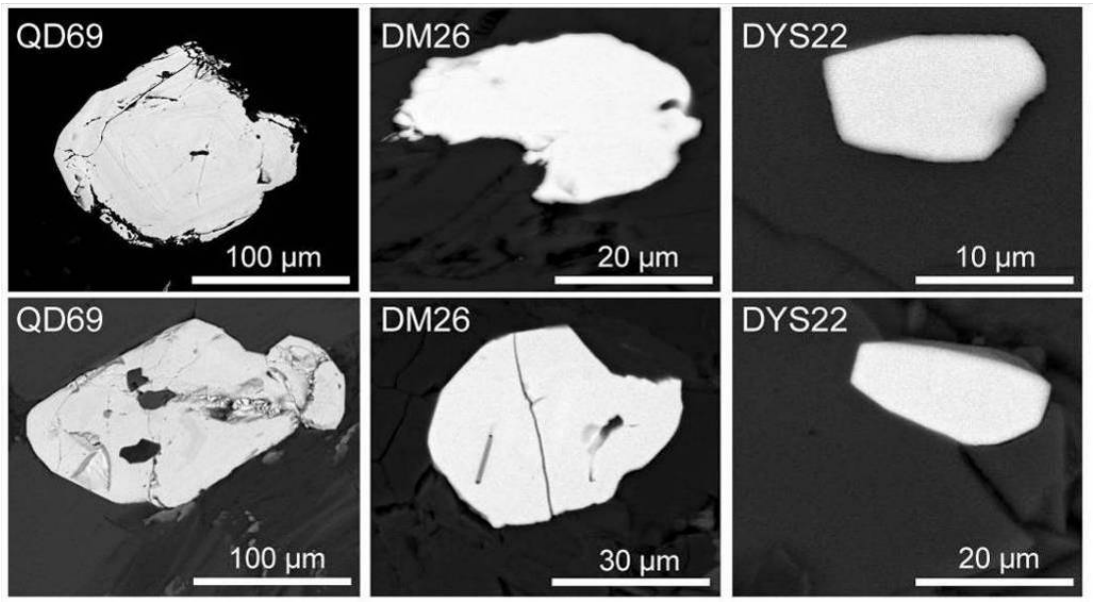

图 4-22 大云山-幕阜山地区岩石样品中典型独居石的背散射图像

Figure 4-22 Typical backscatter images of monazite in samples from the Dayunshan-Mufushan area

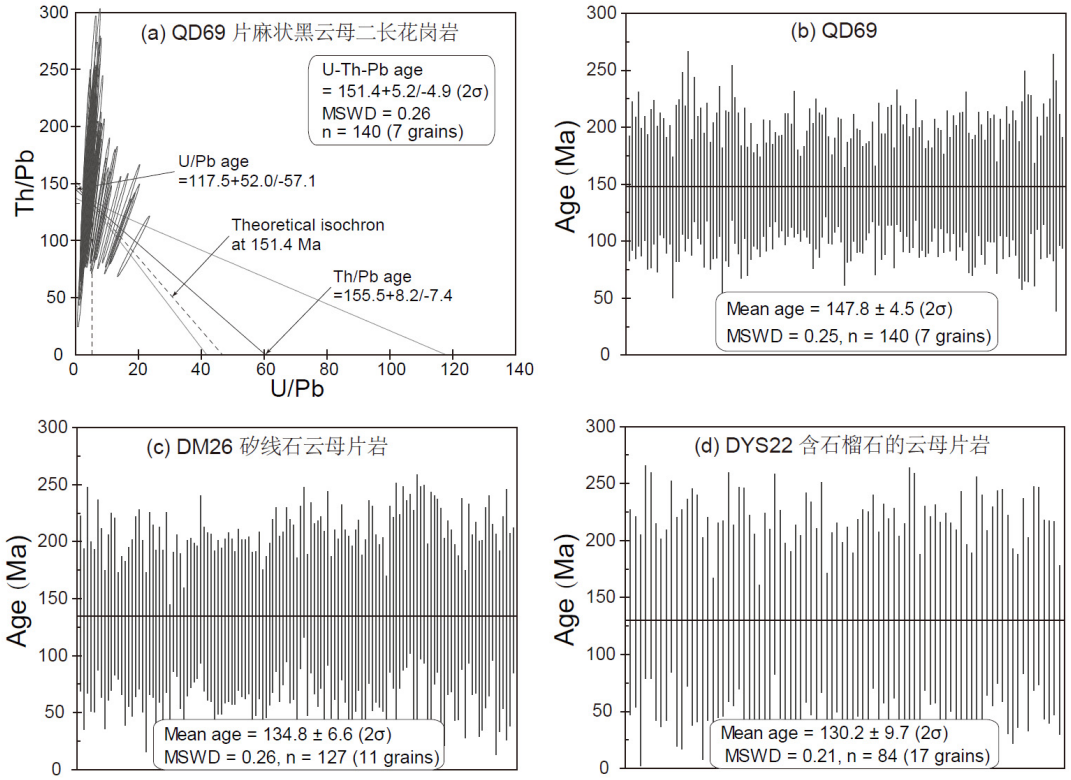

图 4-23 大云山-幕阜山地区岩石样品独居石年龄

Figure 4-23 Monazite U-Th/Pb ages of samples from the Dayunshan-Mufushan area

8 大云山-幕阜山岩基的侵位过程及其构造含义 Emplacement process and tectonic significance of the Dayunshan-Mufushan batholith

结合构造分析、磁组构和年代学研究, 本次研究识别出了大云山-幕阜山岩基侵位过程中所记录的两期岩浆活动和相应的两期构造事件.

D_1 构造事件与早期侵位的黑云母二长花岗岩和黑云母花岗闪长岩相关. 侵入体南部边缘发育片麻状构造, 线理方向为 NE-SW 向, 运动学显示为上部向 SW 的剪切变形,在围岩接触变质带中同样可以观察到这构造变形特征. AMS 结果揭示这期侵入体的内部组构以岩浆流动组构为主, 磁线理的优选方位大致为 NE-SW 向, 与野外在片麻状花岗岩及围岩接触变质带中观察到的线理方向一致, 表明该期侵入体具有同构造花岗岩的特点. SIMS 锆石 U-Pb 和独居石电子探针定年结果表明该期侵入体的侵位年龄在 149-151 Ma, 因而构造变形发生的时间为晚侏罗世. 问题由此提出, D_1 构造事件是挤压还是伸展构造? 目前尚难给出定论, 综合分析本论文倾向于解释为挤压构造, 理由如下: (1)从岩体尺度来看, 早期侵入体呈南窄北宽的几何形态, 磁组构和布格重力异常揭示侵入体的根部位于北部. 侵入体南部变形较强, 但缺少像大云山地区那样的拆离断层及相应半地堑盆地的发育. 这些特征更类似于逆冲推覆的结果, 而不是通常的伸展构造. (2)从区域构造来看, 晚侏罗世向南的逆冲推覆在大巴山前陆可以找到(Hu et al., 2012; Shi et al., 2012; J.H. Li et al., 2013b). 更远至华北北部的阴山-燕山陆内造山带, 向南的逆冲推覆在这里表现较为明显, 如大青山地区、云蒙山地区和医巫闾山地区(Davis et al., 1996, 1998, 2001; Lin et al., 2013a). 相比之下, 晚侏罗世南北向的伸展构造在整个中国东部鲜有报道. (3)从岩浆活动来看, 150-140 Ma 是华南的一个相对岩浆平静期, 可能代表着区域构造体制从挤压向伸展的转换, 而 140 Ma 之后大规模的岩浆活动发生在伸展背景下(X.H. Li et al., 2010; 2013; Wu et al., 2012).

D_2 构造事件与晚期侵位的二云母二长花岗岩相关, 与早期侵入体一样均表现出同构造花岗岩的特点,但以大云山拆离断层的发育为鲜明特色. 侵入体西部边缘卷入拆离断层, 受到了强烈的韧性变形. 变性特征显示为 NW-SE 向的矿物拉伸线理和上部向NW的运动学. 同样, 在围岩接触带中也可观察这些变形特征和岩体内

部均有表现, SIMS 锆石 U-Pb 定年结果表明二云母二长花岗岩的侵位年龄在 132 Ma 左右, 独居石电子探针定年获得侵入体内部残留体和围岩接触变质岩的变质时代分别为 135 Ma 和 130 Ma, 表明韧性剪切变形至少在 130 Ma 左右已经开始. 此外, 在拆离断层的上盘还发育有由晚期脆性正断控制的晚白垩-第三系的红盆, 并可见到以花岗岩为砾石的砾岩沉积, 这进一步将 D_2 构造事件韧性剪切变形时间限定在晚白垩世之前. 结合前文对桐柏-大别山地区白垩纪伸展构造的研究, 我们有理由认为大云山-幕阜山岩基所记录的 D_2 构造事件代表了早白垩世 NW-SE 向的伸展作用, 并可以推断它与大别山变质核杂岩具有相同的构造背景. 最近, Wei et al. (2014a, 2014b)对长江中下游地区的青阳-九华岩体(由 142 Ma 和 130 Ma 两期侵入体组成)的侵位过程进行了详细的构造、AMS 和重力建模研究, 结果表明该岩体是在 NW-SE 向伸展作用下沿着 NE-SW 走向的裂隙注入而上升侵位的. 由此可见, 扬子东部的广大区域在早白垩世均经历了区域上 NW-SE 向的伸展作用.

9 小结 Summary

华南分布有大面积晚中生代的花岗岩类, 但关于花岗岩的构造研究十分薄弱. 大云山-幕阜山复式岩体是华南内陆江南造山带中段较大的晚中生代花岗岩基之一. 本论文应用构造、磁化率各向异性和年代学相结合的方法对该岩体的构造侵位过程进行了详细的研究, 厘定出了早晚两期同构造的侵入体及其相应的两期构造变形. D1 事件在早期侵入体(黑云母二长花岗岩和黑云母花岗闪长岩)南部边缘的片麻状花岗岩及其围岩接触变质带中表现较为明显, 可见 NE-SW 向矿物拉伸线理及上部向 SW 的剪切变形. D_2 事件以晚期侵入体(二云母二长花岗岩)西部舌状边缘大云山拆离断层的发育为鲜明特色, 卷入韧性变形的花岗岩及其围岩接触变质岩中发育 NW-SE 向的矿物拉伸线理及上部向 NW 的剪切变形. AMS 结果揭示早晚两期侵入体的内部组构均以岩浆流动组构为主, 同样分辨出了两组线理: 早期侵入体磁线理的优选方位为近 N-S 向(极值在 190°), 而晚期侵入体磁线理的优选方位为 NW-SE 向(极值在 117°), 这与野外观察到的两期变形十分吻合. 重力资料的初步分析也表明早晚两期侵入体的根部或重心分别位于岩体的北部和中部偏东位置, 这从侧面印证了构造和 AMS 的研究结果. SIMS 锆石 U-Pb 定年和独居石电子探针定年结果表明早期侵入体的侵位年龄在 150 Ma 左右, 也即 D_1 事件发生在晚侏罗世,

而晚期侵入体的侵位年龄及其相关的变质变形时代在 132 Ma 左右, 也即 D_2 事件发生在早白垩世.

综合分析, 倾向于认为 D_1 事件可能代表了近 N-S 向的地壳挤压加厚过程, 而 D_2 事件与桐柏-大别造山带中发育的白垩纪伸展构造完全可以对比, 体现了中国东部早白垩世区域 NW-SE 向的伸展作用无疑.

第五章 扬子克拉通之上黄陵背斜成因解析

Chapter 5 Origin of the Huangling massif within the Yangtze craton

The Huangling massif within the Yangtze craton is an important window to decipher the tectonic evolution of South China, but its formation time and mechanism remain in suspense. Detailed structural analysis shows that the geometry of the Huangling massif is an asymmetric anticline or dome structure, with its western flank relatively steep than the eastern one. The sedimentary cover on the western and eastern flanks of Huangling massif were involved in a series of oppositely-directed collapse folding and layer-parallel slipping accommodated to its uplifting. The subsequently brittle normal faulting controlled the deposition of the graben or half-graben basins on both sides of the massif. The involvement of the Late Jurassic strata and the unconformable superposition of the Early Cretaceous conglomerate indicate that the Huangling anticline formed between the Late Jurassic and Early Cretaceous. K-feldspars from different rock type of the massif were selected to conduct MDD modeling, and combined with the previous thermochronological data, a synthetic cooling curve was constructed. Tectono-thermal history reveals that the Huangling massif might be an inherited paleo-relief within the Yangtze craton at around 750 Ma, and then the Early Paleozoic and Early Mesozoic orogenies of South China had no significant imprint. Until the Late Jurassic to Early Cretaceous (160-110 Ma), the Huangling massif underwent an obvious but actually slow cooling process with an average rate of 2-3 °C/Ma, corresponding to the formation of the anticline. From the view of whole eastern China, the weak extension recorded by the Huangling massif is manifestation of the Late Mesozoic lithospheric thinning in stable craton.

1 引言 Intruduction

扬子陆块和华夏陆块在中-新元古代沿四堡或江南造山带的拼合形成了统一的华南板块(图 5-1) (Li et al., 2009a; Charvet, 2013). 在显生宙期间, 华南板块主要经历了三期构造事件: (1)早古生代的陆内造山作用: 沿武夷山-云开一带发育, 导致

了新元古代南华裂谷的闭合(Lin et al., 2008b; Faure et al., 2009; Charvet et al., 2010; Z.X. Li et al., 2010; Wang et al., 2010); (2)一系列围绕华南板块周缘发育的早中生代造山带, 例如北缘的秦岭-大别-苏鲁高压/超高压造山带(Mattauer et al., 1985; Faure et al., 2003; Hacker et al., 2000)、西北缘的龙门山陆内冲断带(Burchfiel et al., 1995; Chen and Wilson, 1996; Yan et al., 2011)和西南缘的印支碰撞造山带(Carter et al., 2001; Carter and Clift, 2008; Lepvrier et al., 2008), 以及华南内部的九岭-雪峰山陆内造山带(Wang et al., 2005a; Shu et al., 2008; Chu et al., 2012a, 2012b); (3)晚中生代的构造-岩浆事件, 主要表现为伸展作用下东南部盆-岭构造的发育(Gilder et al., 1991, 1996; Li, 2000; Lin et al., 2000; Zhou and Li, 2000; Zhou et al., 2006; Zhu et al., 2010; J.H. Li et al., 2013a), 但西部的川东-鄂湘西弧形褶皱带和大巴山弧形褶皱带的形成, 说明板块内部可能还存在着挤压作用(Yan et al., 2003, 2009; Hu et al., 2012; Shi et al., 2012; J.H. Li et al., 2013b).

晚中生代是在整个欧亚大陆东缘构造体制的一个复杂过渡期, 应力场从以挤压转向伸展为主. 在欧亚大陆东缘发育有一系列的伸展构造, 以变质核杂岩(Lin and Wang, 2006; T. Wang et al., 2011; Lin et al., 2013a)和断陷盆地(Ren et al., 2002; Meng et al., 2003; S.Z. Li et al., 2012a)为代表, 指示了区域大规模的伸展作用. 这一伸展作用同时还伴随着巨量的岩浆活动(Wu et al., 2005; Yang et al., 2008). 华北克拉通破坏正是发生在这一背景之下(Menzies et al., 2007; 吴福元等, 2008; 朱日祥等, 2011). 华南板块和华北板块自三叠纪拼合以来, 共同作为欧亚大陆的一部分转入古太平洋俯冲构造体系之中. 华南板块在晚中生代期间同样发育大量的岩浆岩和众多的小型断陷盆地(Gilder et al., 1996; Li, 2000; Zhou and Li, 2000; Zhou et al., 2006; Shu et al., 2009). 这似乎表明华南板块可能也经历了类似华北克拉通破坏的地壳伸展和岩石圈减薄过程. 然而, 有关华南板块在相应背景下的伸展构造还缺乏研究, 因为目前在华南只有很少的伸展穹隆被报道(图 5-1), 例如洪镇穹隆(Zhu et al., 2010)、庐山穹隆(Lin et al., 2000)、武功山穹隆(Faure et al., 1996)和衡山穹隆(J.H. Li et al., 2013a). 从整个中国东部来看, 这些晚中生代的伸展穹隆多叠加在先存的造山带之上(如中亚造山带或蒙古-鄂霍次克造山带, 阴山-燕山造山带和大别-苏鲁造山带)或着沿地壳尺度的断裂分布(如郯庐断裂), 而很少发育在稳定克拉通内部(Lin and Wang, 2006; T. Wang et al., 2011; Lin et al., 2013a).

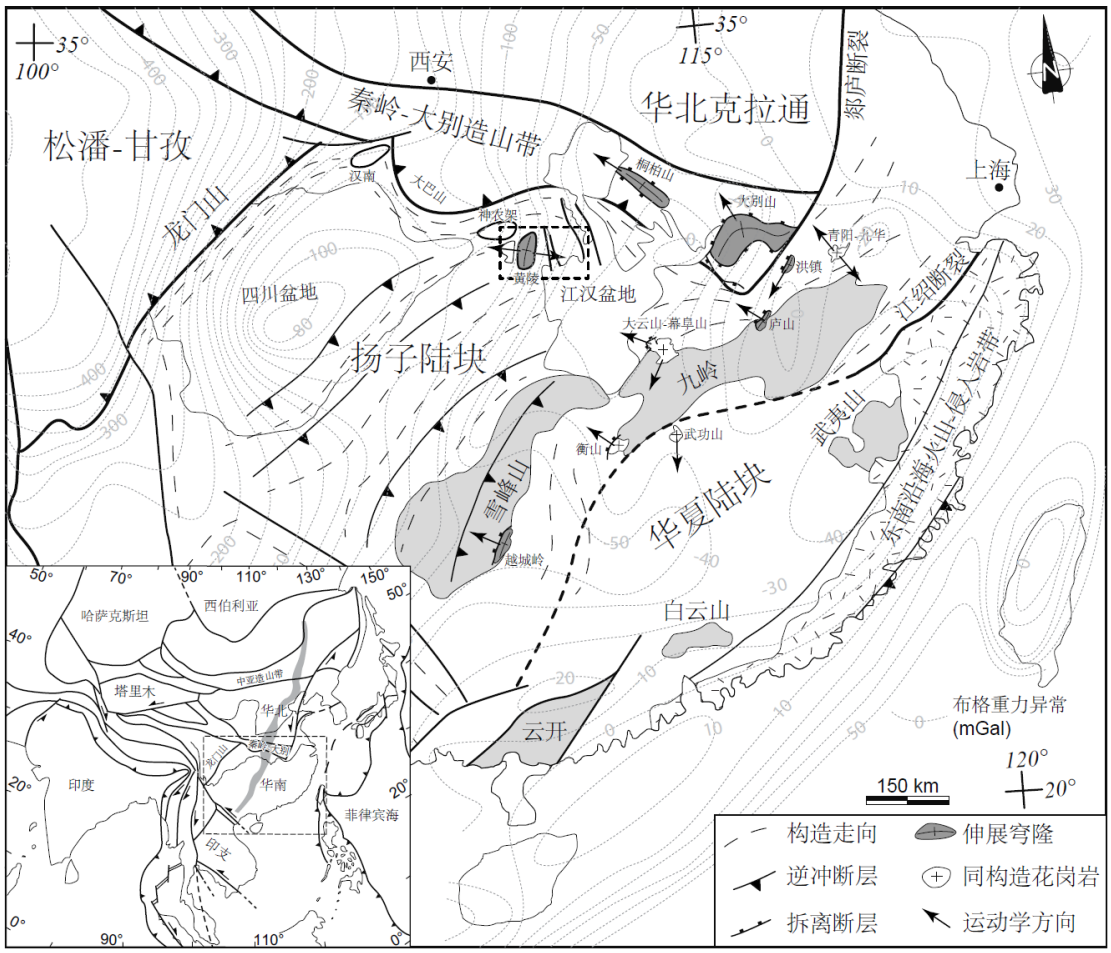

图 5-1 华南大地构造简图

Figure 5-1 Tectonic sketch map of South China

黄陵背斜(或称黄陵穹隆)位于扬子克拉通中北部, 是解译华南构造演化的一个重要窗口(图 5-1). 作为华南最古老基底和显生宙典型盖层的出露地区, 它受到了我国地质学家的广泛重视. 前人的大量工作主要集中在变质基底和花岗岩类以及沉积盖层的岩石学、地球化学、年代学和地层学研究(胡世玲等, 1989; 马国干等, 1984; 冯定犹等, 1991; 马大铨等, 1997, 2002; 凌文黎等, 1998, 2000, 2006; 高山等, 2001; 李志昌等, 2002; 孟繁松和李旭兵, 2003; 李益龙等, 2007; 李旭兵等, 2008; 焦文放等, 2009; 赵小明等, 2010; Gao et al., 1999, 2011; Qiu et al., 2000; Li et al., 2004; S.B. Zhang et al., 2006a, 2006b, 2006c, 2008, 2009; X.M. Liu et al., 2008; Chen et al., 2013), 以及研究区的地壳深部结构的地球物理学探究(Z.J. Zhang et al., 2009), 针对黄陵背斜的构造研究却不多见(张或丹, 1986; 葛肖虹等, 2009; 王军等, 2010). 因而以下问题仍然值得我们关注: 黄陵背斜的形成时间和成因机制? 其隆升过程是由单一的构造事件还是多个构造事件控制? 黄陵背斜对华南板块显生宙多期构

造事件是如何响应的, 尤其是中国东部晚中生代的大规模伸展作用? 本论文通过构造解析和热年代学研究以期回答上述的科学问题.

2 地质概况 Geological outline

黄陵背斜在地理位置上位于宜昌市西北部, 这里不仅以三峡秀丽的风景及举世瞩目的水利工程而闻名于世, 同时也是华南地质研究的热点地区. 不像华北太古宙至古元古代基底岩石分布广泛, 华南前寒武纪基底岩石仅零星出露, 且以新元古代浅变质岩为主. 到目前为止, 华南最古老(ca. 3.2-3.3 Ga)的岩石产于黄陵背斜核部基底变质岩之中(焦文放等, 2009; Gao et al., 2011). 这套基底变质岩石通常被称为崆岭群或崆岭杂岩(图 5-2), 主要由 TTG 片麻岩、变沉积岩(变泥质岩、石英岩和大理石)和少量的基性-超基性岩以及麻粒岩组成(湖北省区域地质志, 1990; 马大铨等, 1997; Gao et al., 1999). 大量的年代学研究表明崆岭杂岩正变质岩的原岩年龄集中在 2.90-2.98 Ga, 而变沉积岩中含有 2.7-3.3 Ga 的碎屑锆石, 二者均记录了两期显著的变质事件, 分布在约 2.7 Ga 和 2.0 Ga (凌文黎等, 1998, 2000; Qiu et al., 2000; Zhang et al., 2006a, 2006b; Gao et al., 2011; Chen et al., 2013). 最近, 在崆岭杂岩西南区域出露的基性-超基性岩(ca.1100-985 Ma)被认为代表了格林威尔期的蛇绿岩(Peng et al., 2012).

巨大的新元古代黄陵花岗岩基侵入于崆岭杂岩之中, 占据了黄陵背斜核部近三分之二的面积(图 5-2). 该岩基可划分为 4 个岩套: 三斗坪石英闪长岩-英云闪长岩、黄陵庙奥长花岗岩-黑云母花岗闪长岩和大老岭石英二长闪长岩-二长花岗岩以及晓峰基性-酸性岩墙(马大铨等, 2002). 锆石 U-Pb 年代学资料显示黄陵花岗岩的侵位年龄主要集中在 794-837 Ma (马国干等, 1984; 冯定犹等, 1991; Li et al., 2004; 凌文利等, 2006; 高维和张传恒, 2009; S.B. Zhang et al., 2008, 2009).

崆岭杂岩和黄陵花岗岩基一同被震旦系莲沱组砂砾岩不整合覆盖, 沉积盖层主要包括震旦-侏罗系(图 5-4). 作为扬子克拉通稳定的沉积区, 一些地层的标准剖面就建立在这里(湖北省区域地质志, 1990). 震旦纪-早三叠世地层以海相碳酸盐和硅质碎屑岩为主, 在中志留世至中泥盆世时期存在一个较明显的沉积间断或缺失. 上三叠统和侏罗系主要为河湖相陆源碎屑沉积, 而中三叠统则具有海-陆过渡相性

质，其顶部局部发育的平行不整合代表了研究区沉积环境和沉积相的转变(孟繁松和李旭兵, 2003; 李旭兵等, 2008; 赵小明等, 2010). 值得指出的是，在晚三叠-中侏罗世期间，位于黄陵背斜东西两侧的当阳盆地和秭归盆地属于秦岭-大别造山带南缘统一的盆地体系(Liu et al., 2005). 研究区的白垩系见于黄陵背斜的西南翼和东南翼以及东侧当阳盆地的两翼，为一套冲积-河流相的红色陆源碎屑岩，与前白垩纪地层以角度不整合或断层接触(图 5-2 和图 5-3).

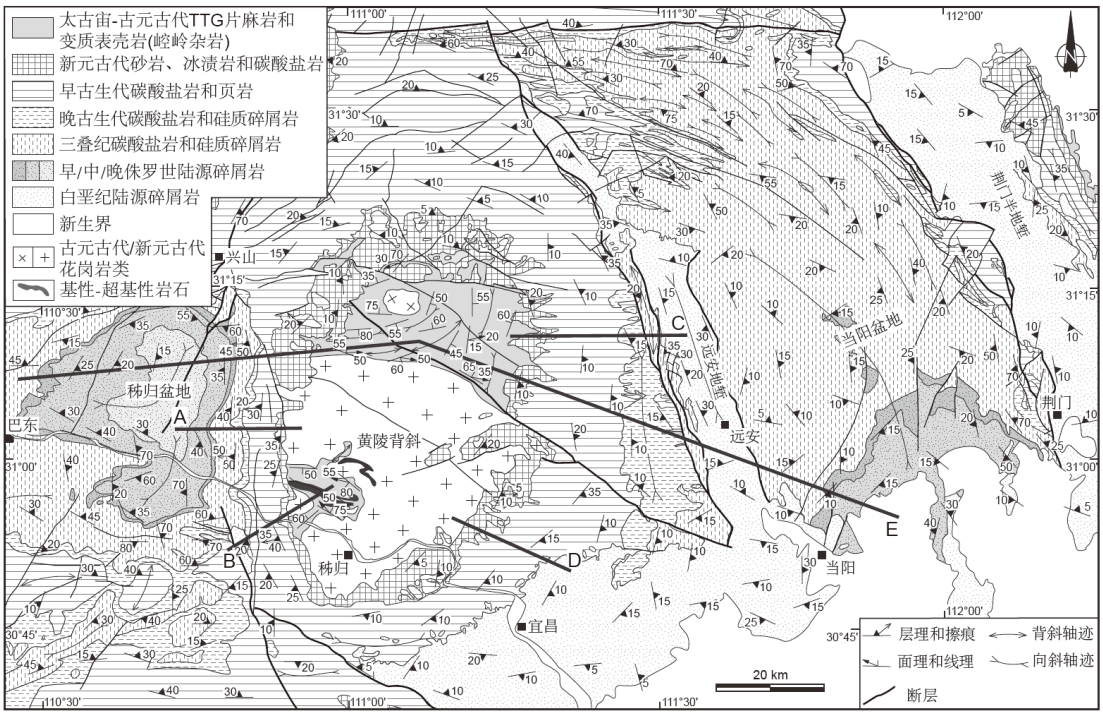

图 5-2 黄陵背斜地质构造图

Figure 5-2 Geological and structural map of the Huangling massif

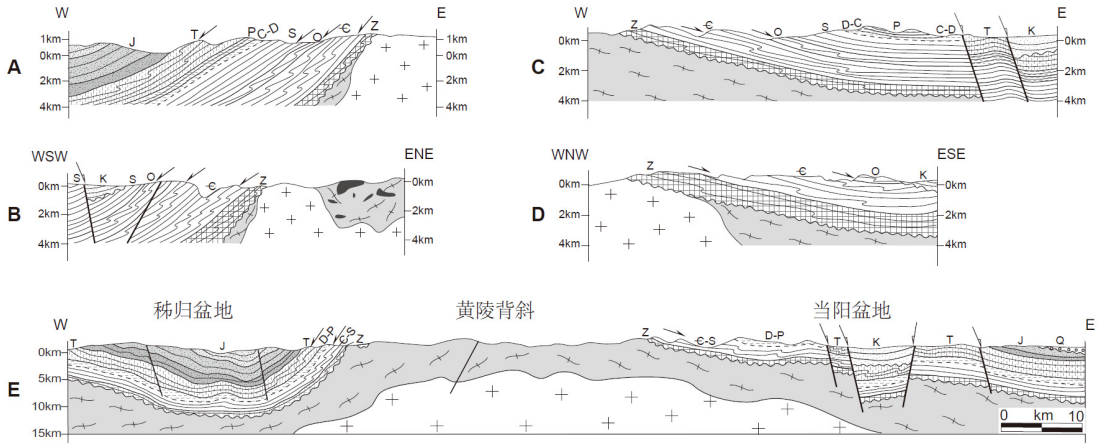

图 5-3 黄陵背斜构造剖面图(位置见图 5.2)

Figure 5-3 Cross-sections across the Huangling massif (locations in Figure 5-2)

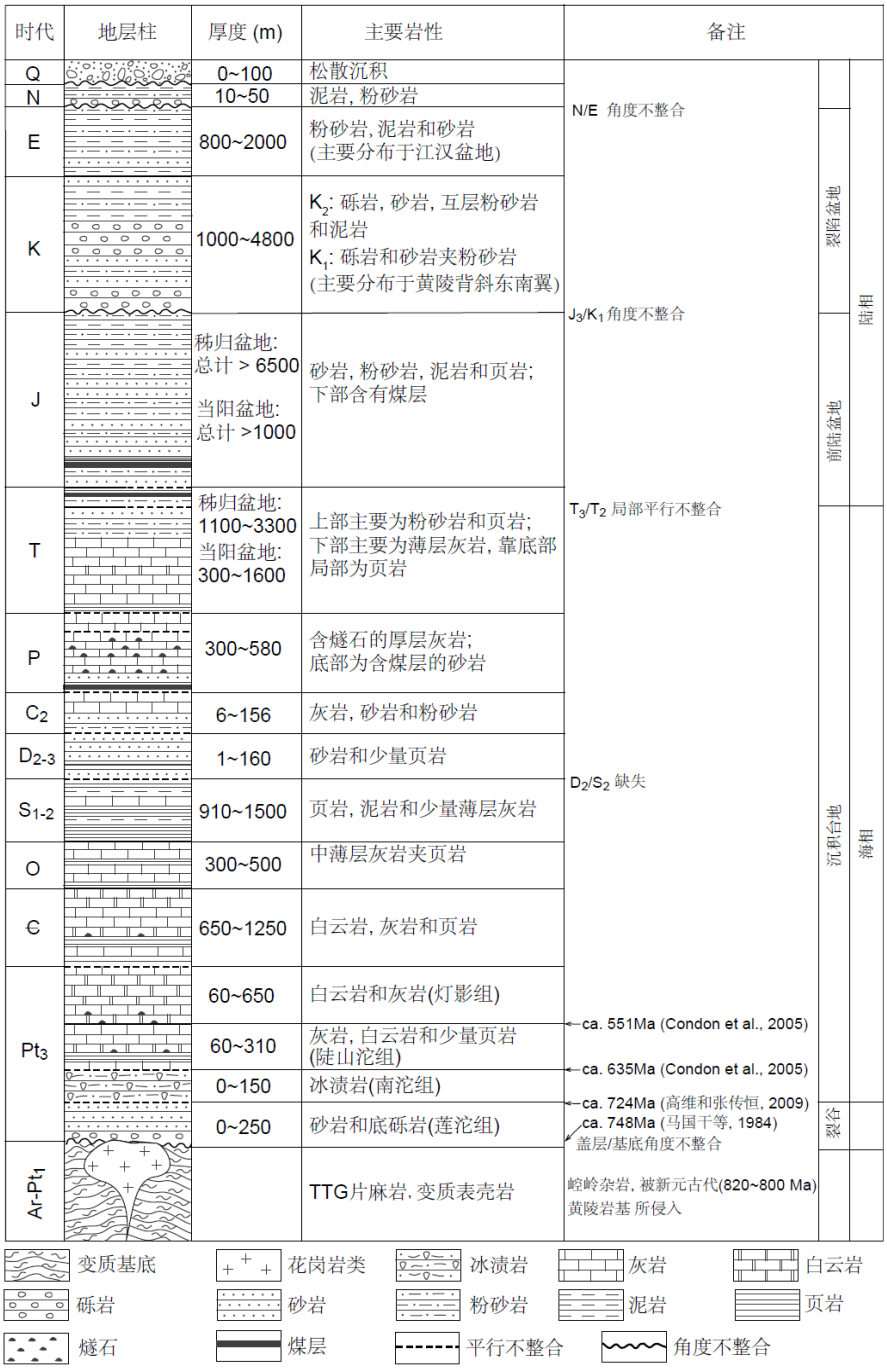

图 5-4 黄陵背斜地区沉积地层柱状图

Figure 5-4 Stratigraphic column of the Huangling area

关于黄陵背斜的形成时间和成因机制历来较有争议. 例如, 张或丹(1986)强调黄陵背斜在震旦-侏罗纪期间为一个继承性的古隆起, 三叠纪和白垩纪的构造事件激化了它的隆升. 江麟生等(2002)注意到区域地层中发育的诸多不连续面, 认为黄陵背斜自新元古代以来经历了频繁的升降运动. 从江汉盆地的构造演化角度, 戴少武(1996)和徐政语等(2004)推测黄陵背斜起源于华北和华南在早中生代以剪刀式

碰撞过程中产生的西向逃逸作用. 葛肖虹等(2009)通过对区域资料的综合分析, 认为黄陵背斜经历了早中生代的挤压, 晚白垩世-古近纪的伸展隆升或变质核杂岩的形成, 而最终的挤压褶皱定形于古近纪末. 王二七等提出华南板块在中生代向北楔入秦岭, 并伴随着四川盆地的顺时针旋转, 导致了桐柏-大别造山带向东的侧向挤出(Wang et al., 2003; 王二七等, 2009). 汉南(HN)和神农架(SNJ)-黄陵(HL)隆起被看作是在这一旋转-挤出-隆升过程中形成的两个构造结(图 5-1). 四川盆地西北部中生代的构造-沉积发展过程似乎也体现了华南板块顺时针旋转的响应(Meng et al., 2005). 同样, 不少研究者也强调汉南和神农架-黄陵隆起在大巴山晚侏罗-早白垩世期间向 SW 的逆冲扩展过程中起到了关键性的阻挡作用(许长海等, 2010; Hu et al., 2012; Shi et al., 2012; J.H. Li et al., 2013b).

3 黄陵背斜的构造几何学形态和岩石变形特征 Structral geometry and deformation styles

3.1 单元划分及其几何学 Bulk architecture and litho-tectonic units

野外观察表明, 黄陵背斜的构造几何形态表现为一个不对称的穹状背形, 南北长约 73 km, 东西宽约 36 km (图 5-2). 黄陵背斜西侧的秭归盆地是由三叠-侏罗系组成的向斜, 它恰居于三组不同方向构造线的交汇部位: 东为近 N-S 向的黄陵背斜, 北为近 E-W 向大巴山弧形褶皱带, 南为 NE-NEE 向的川东-鄂湘西弧形褶皱带. 黄陵背斜东侧的当阳盆地为一个两翼基本对称的复式向斜, 地层同样以三叠-侏罗系为主. 沿盆地两翼依次分布有平行于构造线方向展布的白垩纪远安地堑和荆门半地堑, 它们属于白垩-第三系江汉盆地的次级分支. 虽然黄陵背斜不协调地突兀于区域构造线之上, 但是它同东西两侧的盆地构成了一个整体的隆-凹构造带(图 5-2 和图 5-3E). 根据岩石组成和几何学关系, 黄陵背斜可划分为三个主要岩石-构造单元: 1)TTG 片麻岩和变质表壳岩, 即崆岭杂岩, 其被黄陵花岗岩基所侵入; 2)震旦-侏罗系沉积盖层, 围绕背斜核部呈环状分布; 3)白垩纪红盆, 不整合覆盖或以地堑-半地堑的型式叠加在背斜两翼之上.

在黄陵背斜核部的北部区域, 片麻岩、斜长角闪岩、大理岩、石英岩和少量的麻粒岩构成崆岭杂岩的主要组成部分, 并发育混合岩化现象. 这些岩石普遍发生

了强烈的韧性变形, 局部发育韧性剪切带. 虽然面理产状由于褶皱作用而变化, 但矿物拉伸线理似乎显示为一致的 NEE-SWW 向(图 5-5D). 值得注意的, 北部基底褶皱的轴向以 NEE 至 NE 向为主, 显然与黄陵背斜两翼沉积盖层中所记录的变形无成因上的联系(见后文). 另外, 在背斜核部西南区域尚有小面积基底岩石出露, 其主要由变沉积岩和变质基性-超基性岩(包括蛇纹岩化的橄榄岩类等)组成. 面理的系统测量显示其整体上构成了一个 NWW 向的复向斜构造, 在强烈发育的面理上可见 NWW-SEE 向的矿物拉伸线理(图 5-5B). 上述发育在基底变质岩中的韧性变形被未变形的黄陵花岗岩基所切割, 表明构造变形发生在岩基侵位之前.

背斜翼部的沉积盖层围绕核部向四周倾斜, 构成一个明显的穹隆形态. 西翼震旦-侏罗系地层的产状相对较陡, 倾角一般在 20°-60°(图 5-3A、B 和图 5-5A); 东翼震旦-三叠系地层产状平缓, 倾角一般在 10-20°(图 5-3C、D 和图 5-5E); 而南北两端震旦-志留系地层的产状更为平缓, 倾角多小于 15°(图 5-5C、F). 远安地堑中的白垩系产状平缓, 靠近边界断裂时地层倾角略有变大, 而分布在在背斜东南翼(宜昌附近)的白垩系则构成一个向 SE 缓倾的单斜构造(图 5-5G).

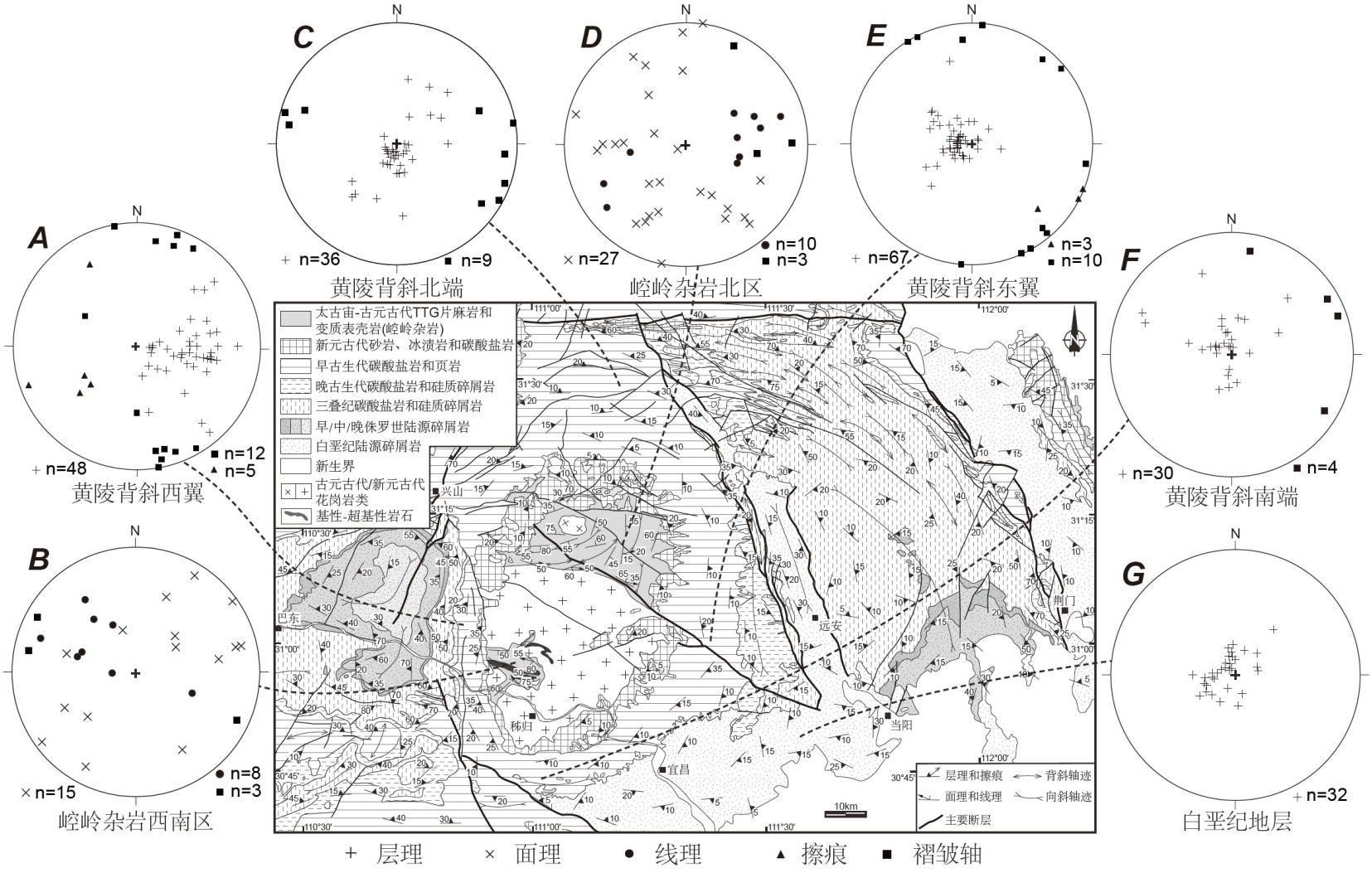

图5-5 黄陵背斜地区构造要素图

Figure 5-5 Structural planar and linear elements of the Huangling massif

3.2 与黄陵背斜隆升相关的变形 Uplift-related deformation of the Huangling massif

据我们的野外调查, 深层次的韧性剪切变形仅局限在崆岭杂岩之中. 在变质基底和沉积盖层以及变质岩和黄陵花岗岩之间, 并没有观察到拆离断层或者基底滑脱层的存在(江麟生等, 2002; 葛肖虹等, 2009). 背斜东西两翼沉积盖层的变形较为简单, 主要以发育在浅表构造层次的褶皱为特点. 此外, 晚期的脆性正断层还控制了白垩纪地堑-半地堑盆地的形成.

穹隆作用 Doming

从秭归向西沿主要道路, 穿越黄陵背斜西翼震旦-三叠纪的地层, 可以观察到一系列的褶皱. 例如在震旦纪、寒武纪、奥陶纪和三叠纪灰岩中, 时常可以见到平卧褶皱的发育, 其近水平甚至外倾的褶皱轴面指示了垂向的缩短作用及上部相对向西的滑脱特点(图 5-6A、B、C). 层理的挠曲和切层缝合线的发育也指示地层在掀斜过程中受到了顺层理方向的应力作用(图 5-6D). 在上述褶皱的灰岩中发育诸多斜切层里的方解石张裂脉, 它们同样显示出向西的层间滑动作用. 结合几何学特点, 我们认为黄陵背斜西翼岩石的变形特征明显地体现了上部向西的重力滑脱作用.

如前所述, 黄陵背斜东翼的地层向东缓倾, 似乎意味着东翼具有比较弱的变形. 事实上, 与西翼相似的变形样式在东翼同样可以被观察到. 例如, 在寒武纪厚层状灰岩和三叠纪薄层状灰岩中滑脱褶皱仍较发育, 只不过运动学相反(图 5-7A、B). 由于卷入褶皱地层的厚度通常十分有限, 推测其具有近水平顺层滑动的特点. 特别的是, 在志留纪页岩中还观察到了泥质结核周缘发育的剪切压力影构造, 其 σ 状形态指示了上部向 E 的剪切变形(图 5-6C). 此外, 在沿东倾的层滑面上所发育的 SEE 向擦痕(图 5-5E), 斜切层理的方解石张裂脉和一些错断标志等均指示了正向的滑动作用.

上述几何学和运动学的分析表明黄陵背斜具有一个明显的穹状背形形态, 除核部杂岩记录了前寒武纪的韧性变形外, 沉积盖层中则发育一系列与穹隆作用相

关的滑脱变形，且背斜东西两翼具有相反的运动学极性. 从整体上考虑，我们认为东西两翼的变形几乎是同时的，并具有相同的力学机制，即在穹隆形成过程中造成了重力势能的积累，并在两翼得以释放进而形成极性相背的滑脱变形. 背斜两翼的这些滑脱褶皱通常具有近南北的轴向，与黄陵背斜的长轴方向平行. 实际上，这种构造广泛见于中国东部地区发育的晚中生代伸展穹隆中，为穹隆形成时重力垂向压缩和侧向扩展作用的产物(Faure et al., 1996, 1998; Lin et al., 2000, 2007a, 2013a). 背斜西翼的侏罗纪地层同样卷入了褶皱的一翼，明显地参与了穹隆几何形态的贡献. 另外，下白垩统的粗碎屑沉积以角度不整合的形式覆盖在背斜两翼震旦-三叠纪褶皱的地层之上. 因此，黄陵背斜穹隆作用发生的时间应在晚侏罗-早白垩世之间.

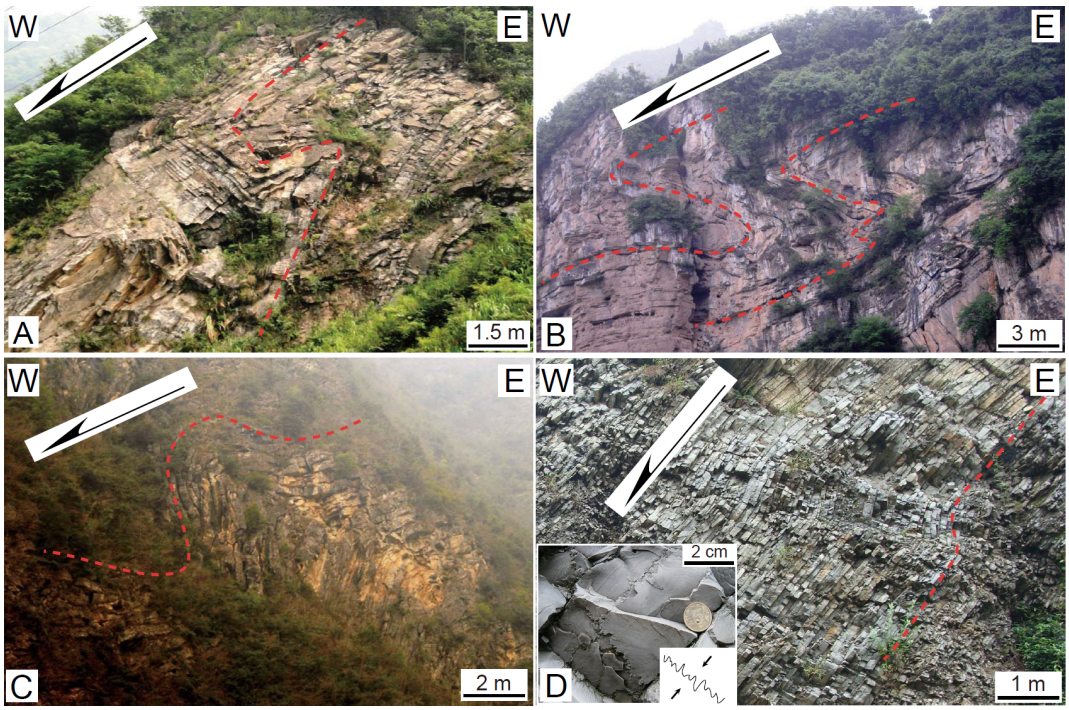

图 5-6 黄陵背斜西翼岩石变形特征

A. 震旦纪灰岩中发育的具有向西滑脱特点的平卧褶皱; B. 寒武纪灰岩中发育的具有向西滑脱特点的平卧褶皱; C. 奥陶纪灰岩中发育的歪斜褶皱，具有向西的极性; D. 三叠纪薄层灰岩中层理的挠曲指示了向西的滑脱变形，而切层缝合线的产出指示了平行层理的缩短作用

Figure 5-6 Field photographs showing deformation on western side of the Huanling massif

(A) Recumbent fold overturned to the west in the Neoproterozoic limestone; (B) Recumbent fold overturned to the west in the Cambrian limestone; (C) Inclined fold overturned to the west in the Ordovician limestone; (D) Décollement-related west-verging fold in the Triassic thin-bedded limestone. It is noted that the transverse bedding stylolites indicate a bedding-parallel shortening.

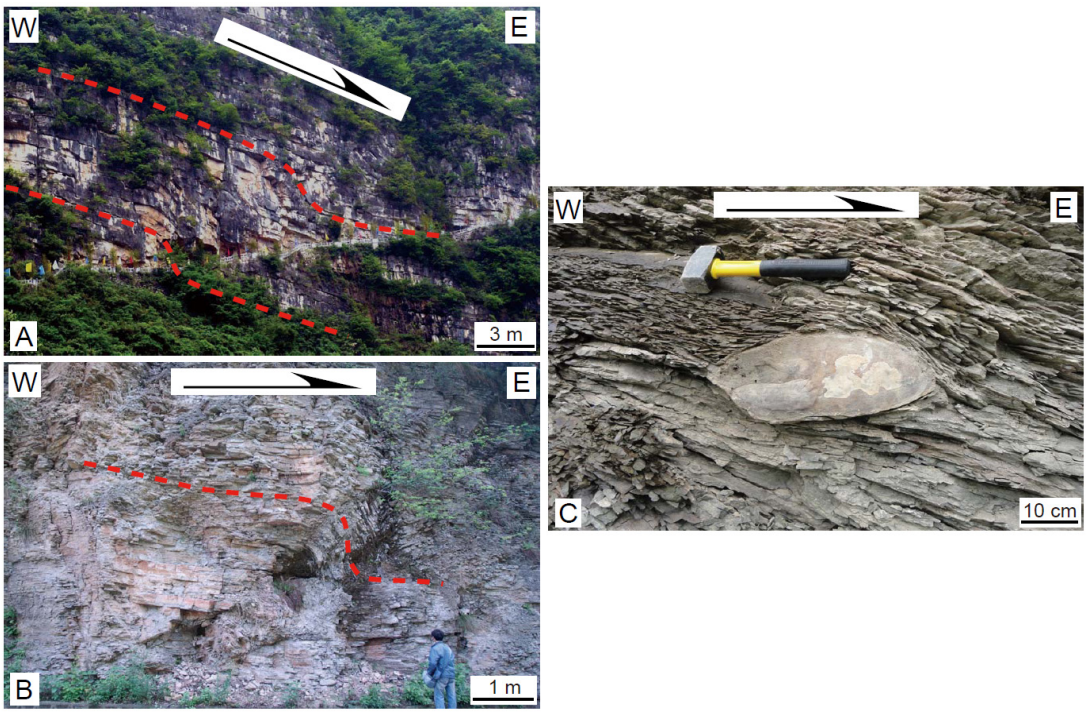

图 5-7 黄陵背斜东翼岩石变形特征

A. 寒武纪灰岩中发育的顺层滑脱褶皱指示了上部向 E 的运动学; B. 三叠纪灰岩中发育的顺层滑脱褶皱指示了上部向 E 的运动学; C. 志留纪页岩中的泥质结核周缘发育的剪切压力影指示了上部向 E 的剪切变形

Figure 5-7 Field photographs showing deformation on eastern side of the Huanling massif (A) Décollement-related east-verging fold in the Cambrian limestone; (B) Recumbent fold overturned to the east in the Triassic limestone; (C) A pelitic nodule with strain fringes in the Silurian shale, showing top-to-the-E shearing

脆性正断作用 Normal faulting

在黄陵背斜东侧当阳盆地的两翼上叠加有 3 条 NNW-SSE 走向的断裂，自西向东包括通城河断裂、远安断裂和荆门断裂(图 5-2). 这些断裂构成了远安地堑和荆门半地堑的边界断裂，它们表现为高角度的正断层(图 5-3C、E). 断层面倾角一般在 60°-80°，断面上发育的擦痕和阶步等均指示了上盘下降的运动学. 断裂主要切割寒武-三叠纪地层，明显地控制了断陷盆地内白垩纪陆源碎屑岩的沉积. 实际上，这些地堑-半地堑属于江汉盆地西北部的断陷带. 研究表明江汉盆地是叠置在中扬子板块上的白垩-第三纪的大型伸展断陷盆地(王必金等，2006；刘景彦等，2009). 盆地内部沉积了较完整的白垩-第三纪地层，厚度近万米. 白垩系与下伏地层之间的角度不整合是盆地内部的一级界面. 此外，在黄陵背斜的西南翼，尚有一个小型

的白垩纪半地堑盆地不整合覆盖在古生代地层之上(图 5-2 和图 5-3B). 由此可见, 在白垩纪黄陵背斜可能作为地垒还经历了断块式的隆升.

4 黄陵背斜的构造-热演化历史 Tectono-thermal evolution

4.1 已有的热年代学数据 Previous geochronological data

前人对黄陵花岗岩进行了大量的年代学研究, 包括锆石 U-Pb, 全岩(-矿物)Rb-Sr, 角闪石和黑云母的 $^{40}Ar/^{39}Ar$ (马国干等, 1984; 胡玲等, 1989; 冯定犹等, 1991; 李志昌等, 2002; 马大铨等 2002; 李益龙等, 2007; Li et al., 2004; 凌文黎等, 2006; 高维和张传恒, 2009; S.B. Zhang et al., 2008, 2009). 这些年龄数据汇编于图 5-8A. 锆石 U-Pb 年龄主要介于 794-837 Ma 之间, 应代表了花岗岩基的侵位时代. 具有较小误差的一个闪长岩的全岩-矿物 Rb-Sr 等时线年龄 805 Ma 可能代表了岩基的冷却年龄. 角闪石和黑云母 $^{40}Ar/^{39}Ar$ 年龄介于 770-900 Ma, 其中来自岩脉的两个较年轻的年龄 770 Ma 和 801 Ma 可能代表了岩基冷却至相应矿物封闭温度时的年龄. 值得注意的是, 黄陵岩基的 Rb-Sr 和 K-Ar 定年体系并没有受到显生宙构造热事件的影响, 说明黄陵背斜的核部岩石自新元古代以来就一直处于较浅的地壳层次(不超过 10 km).

随着低温热年代学的发展, 裂变径迹(FT)和(U- Th)/He 定年已经成为约束地质体隆升剥露历史的一种重要方法. 关于黄陵背斜的裂变径迹和(U-Th)/He 年代学研究已经积累了不少数据, 主要来源于黄陵背斜核部的崆岭杂岩和黄陵花岗岩基(沈传波等, 2009; 许长海等, 2010; S.B. Hu et al., 2006; Richardson et al., 2010; Li and Shan, 2011; J.M. Hu et al., 2012). 这些年龄数据汇编于图 5-8B. 锆石 FT 和(U-Th)/He 年龄比较分散, 年龄范围分布在 158-195 Ma 和 121-309 Ma, 且主要集中在早中生代, 指示黄陵背斜核部岩石在早中生代时仍处于地下 220 °C (锆石 FT 封闭温度)或 180 °C (锆石(U-Th)/He 封闭温度)等温面附近. 磷灰石 FT 的年龄范围在 87-137 Ma, 指示黄陵背斜核部岩石在早白垩世晚期-晚白垩早期已经隆升至地下 100 °C (磷灰石 FT 封闭温度)等温面附近. 磷灰石(U-Th)/He 年龄介于 39-102 Ma 之间, 峰值在 40-45 Ma, 指示黄陵背斜在新生代经历了近地表的隆升剥蚀过程. 另外, 刘海军等(2009)还获得了黄陵背斜东翼寒武纪、志留纪、侏罗纪和白垩纪碎屑岩的

9 个 AFT 年龄 81-148 Ma. 由于这些年龄仅代表岩石样品发生退火的时间, 从数据自身很难获取详细的热演化信息, 因而通常需要进行热历史模拟. 对于前人的模拟结果及其讨论见后文.

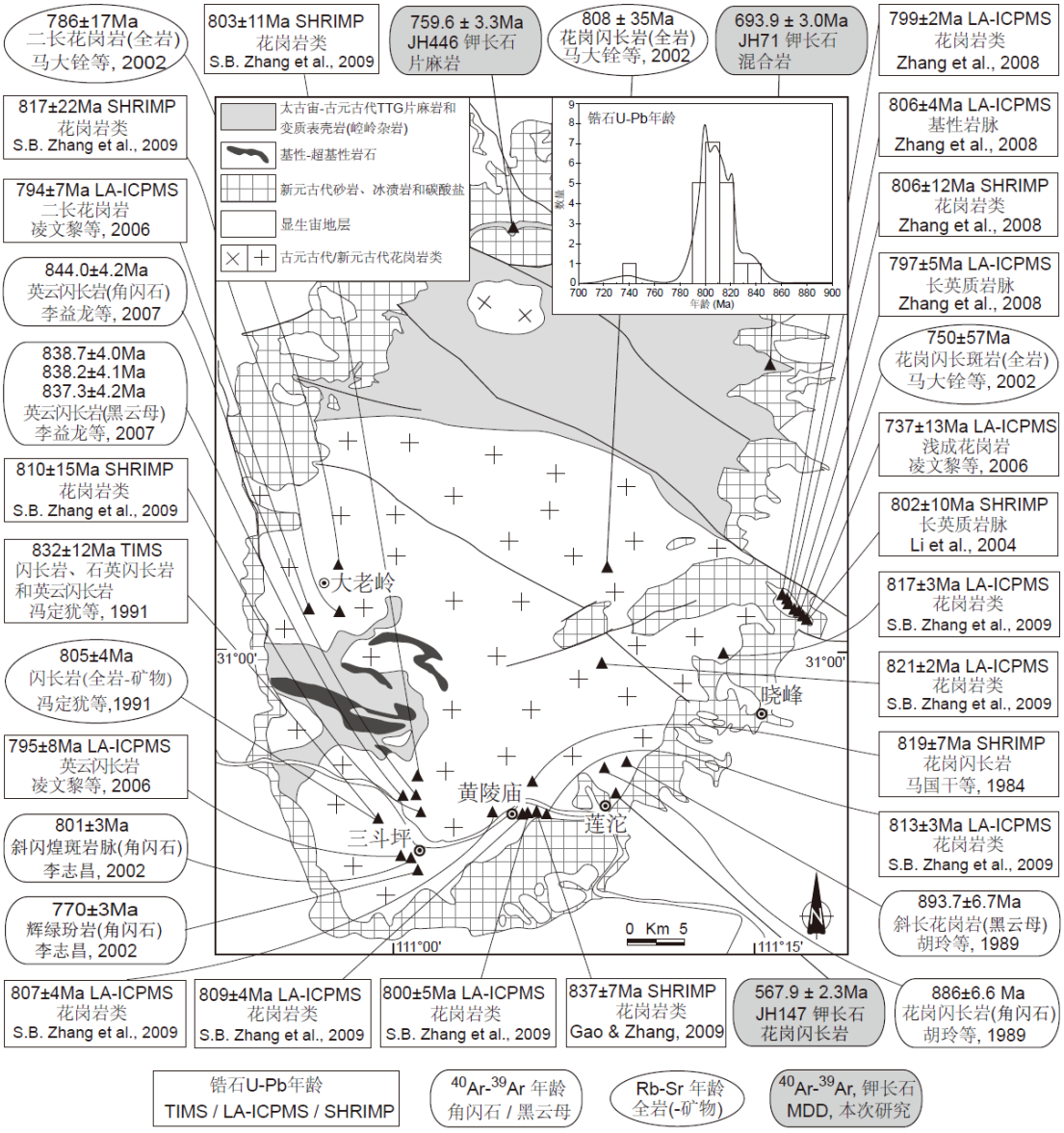

图5-8A. 黄陵背斜的年代学数据(U-Pb、Rb-Sr和Ar-Ar)

Figure 5-8A Compilation of U-Pb, Rb-Sr and Ar-Ar ages from the Huangling granitoids

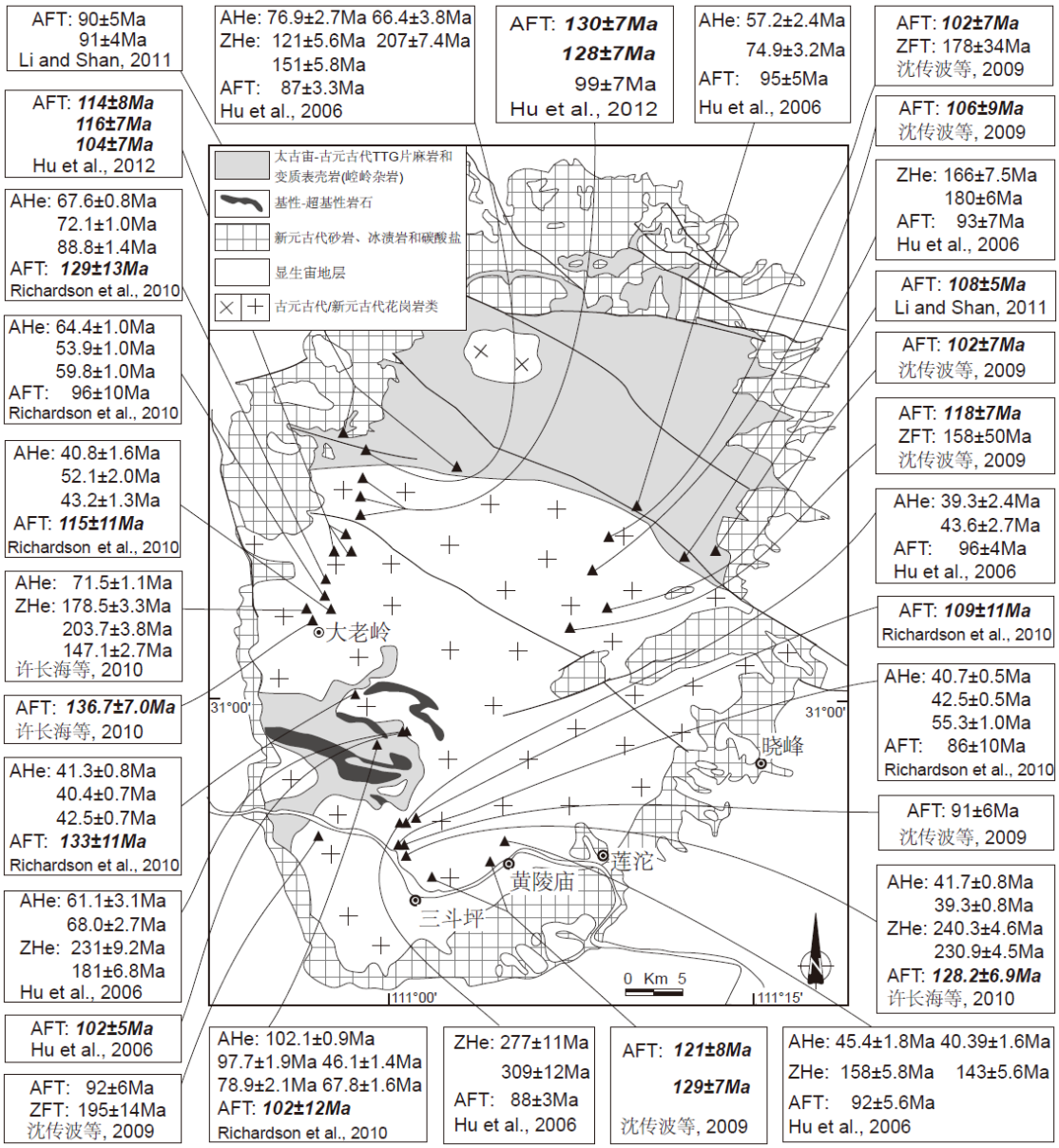

图 5-8B. 黄陵背斜的年代学数据(FT 和(U-Th)/He)

Figure 5-8B Compilation of apatite and zircon FT and (U-Th)/He ages from the Huangling massif AFT: apatite-fission track; ZFT: zircon-fission track; AHe: apatite (U-Th)/He; ZHe: zircon (U-Th)/He

4.2 钾长石 MDD 模拟 K-feldspar MDD modeling

由于缺乏在 800-200 Ma 期间的年代学记录，因此很难准确限定在这漫长的时间内黄陵背斜的详细热演化历史. 为了揭示黄陵背斜自新元古代以来的热演化历史，我们对来自背斜核部不同岩性的岩石的 3 个钾长石样品进行了 $^{40}Ar/^{39}Ar$ 阶段加热分析，并进行了多域扩散域(multi-domain diffusion，缩写 MDD)热史模拟. 采

样位置见图 5-8A, 其中样品 JH446 为崆岭杂岩最北端的条带状片麻岩, 野外可见浅色富石英和长石的成分层和暗色富黑云母的成分层相间构成了清晰的面理. 样品 JH71 为崆岭杂岩北部的混合岩, 野外可见浅色体的强烈褶皱, 表明其在部分熔融过程的发生了同变形作用. 样品 JH147 采自黄陵花岗岩基东南部(莲沱附近), 为块状黑云母花岗闪长岩. 该黑云母花岗闪长岩属于黄陵岩基中的黄陵庙岩套, 其 SHRIMP 锆石 U-Pb 年龄为 819 ± 7 Ma (马国干等, 1984).

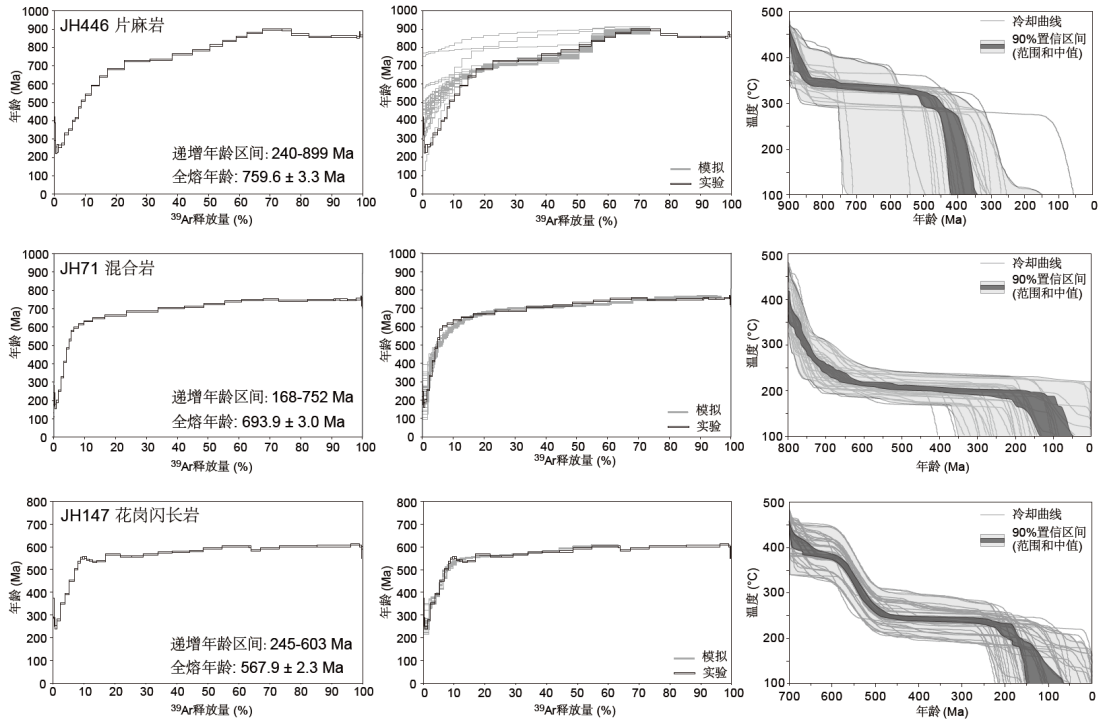

图 5-9 黄陵背斜核部岩石钾长石的 $^{40}Ar/^{39}Ar$ 年龄谱和多重扩散域的冷却史

Figure 5-9 Ar-Ar age spectra and multi-domain diffusion (MDD) modeling results of K-feldspar from different rock types in the core of Huangling massif

钾长石挑选通过矿物分离技术获得, 并在显微镜下除去可见杂质. 样品的照射工作在中国原子能科学研究院 49-2 反应堆中进行. $^{40}Ar/^{39}Ar$ 测年利用中国科学院地质与地球物理研究所古地磁与 $^{40}Ar/^{39}Ar$ 年代学实验室的 MM-5400 质谱仪进行, 采用电阻炉阶段加热法.在加温过程中, 一些温阶重复进行两次, 以保证该温度下 Ar 的完全释出. 一般认为钾长石在真空中加热到 1150 °C 时开始出现熔融现象, 其内部晶体结构开始瓦解. 因此, 实验在 1100 °C 温阶时重复多次, 当样品气体释放量明显下降之后, 再以高温(1200 °C 以上)加热直至其完全释气. 详细的分析方法及流程见王非等(2005, 2007). 数据处理采用 ArArCALC 软件(Koppers, 2002), 具体

测试数据见表 5-1, 所用年龄的误差均为 2σ. 以 MDD 模式为理论依据, 通过适当调整扩散参数如活化能、扩散域大小等, 可能模拟获得钾长石矿物所记录的冷却历史(Lovera et al., 1997, 2002).

三个样品没有获得有意义的坪年龄和等时线年龄, 其表面年龄的范围分别在 239.7-899.0 Ma (JH446, 全熔年龄为 759.6 ± 3.3 Ma)、167.7-762.6 Ma (JH71, 全熔年龄为693.9 ± 3.0 Ma)和244.8-610.7 Ma (JH147, 全熔年龄为567.9 ± 2.3 Ma). 钾长石的 $^{40}Ar/^{39}Ar$ 年龄谱和 MDD 模拟结果见图 5-9 所示, 模拟的年龄谱与实验结果吻合较好, 表明模拟结果的质量比较高. 考虑到钾长石 $^{40}Ar/^{39}Ar$ 的封闭温度, 350-150 °C 区间的冷却历史是比较可信的(McDougall and Harrison, 1999). MDD 模拟结果的解释和讨论见后文.

4.3 冷却历史 Cooling history

黄陵背斜是华南板块复杂构造演化过程的见证者, 从区域地层柱状图可以看到研究区所记录的华南发生在新元古代, 早古生代, 早中生代和晚中生代不同时期的构造事件的缩影(图 3). 热年代学数据和沉积演化的结合能够构建一条黄陵背斜自新元古代以来的热演化曲线(图 5-10A).

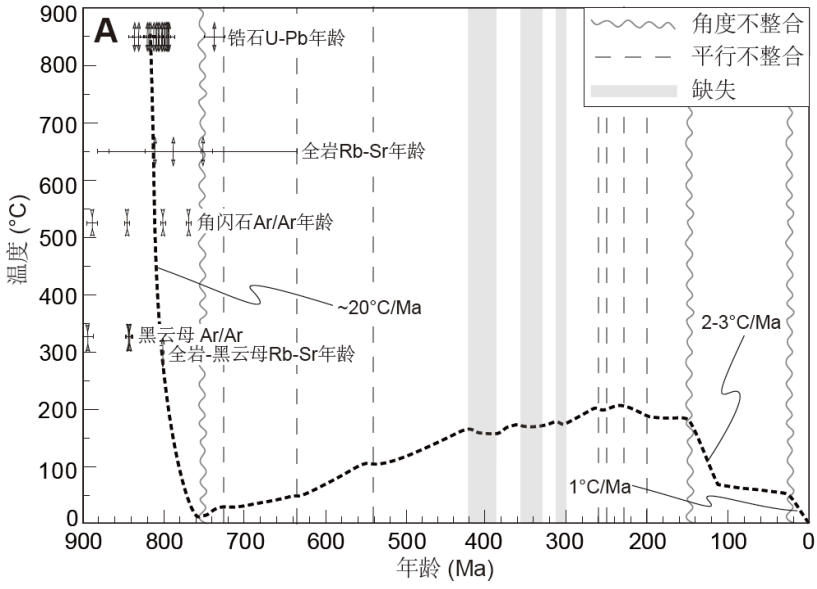

图5-10A 黄陵背斜自新元古代以来的热演化曲线(背斜核部的抬升和沉降过程)

Figure 5-10A A synthetic curve showing tectono-thermal history of the Huangling massif with emphasis on the dome core

黄陵背斜核部的崆岭杂岩被黄陵花岗岩所侵入，而两者又共同被震旦系莲沱组砂砾岩不整合覆盖，说明背斜核部岩石在震旦纪前曾经出露于地表. 已有的年代学数据显示黄陵花岗岩基的侵位年龄约在820 Ma左右，在770 Ma之前经历了从锆石 U-Pb 体系的封闭温度冷却至矿物 Rb-Sr 和 K-Ar 体系的封闭温度(图 5-10A). 而莲沱组最年轻的碎屑锆石指示其沉积时间不晚于 750 Ma (Zhang et al., 2006c; X.M. Liu et al., 2008)，这与莲沱组下部凝灰岩夹层年龄 748 Ma 相一致(马国干等, 1984). 以上的证据表明黄陵地区可能在 820-750 Ma 期间经历了隆升作用，从而发展成为扬子克拉通内的古隆起并遭受到剥蚀. 之后，研究区又转而下降接受盖层沉积，这与黄陵地区震旦纪的沉积岩由砂岩向灰岩转变所反应出的沉降过程相一致. 另外，凌文黎等(2006)发现黄陵地区的岩浆作用在约 740 Ma 由浅成相(晓峰岩套)向喷出相(莲沱组底部火山岩)的演化，并提出区域地壳可能发生了由强烈抬升向快速下降的剧烈构造转变. 实际上，本次研究获得的三个钾长石 MDD 模拟结果同样显示研究区在新元古代期间经历了差异性的冷却抬升过程(图 5-9). 从冷却曲线估算得到的这一新元古代冷却事件的平均冷却速率约为 20 °C/Ma (图 5-10A).

片麻岩样品(JH446)的 MDD 模拟结果显示在 450 Ma 之前为缓慢冷却，约 400 Ma 出现一个明显的冷却过程. 从整个华南板块的来看，这一冷却事件似乎对应于华南早古生代的陆内造山作用. 然而，研究表明早古生代造山作用的影响范围主要集中在武夷-云开地区，扬子克拉通内部基本未受影响(Lin et al., 2008b; Faure et al., 2009; Charvet et al., 2010). 另外，志留-泥盆纪之间的沉积间断或缺失在华南普遍存在，并且从华夏陆块向扬子克拉通由角度不整合过渡为平行不整合. 因此，我们认为早古生代的构造事件在研究区可能主要以海平面的变化为主导，仅仅造成了黄陵地区局部微弱的热扰动.

另外两个样品(混合岩 JH71 和花岗闪长岩 JH147)的 MDD 模拟结果揭示出研究区在整个古生代期间处于长期的热稳定状态，自晚三叠世开始存在一个缓慢的冷却过程，并且冷却速率在晚中生代有递增的趋势. 早中生代的造山作用在华南板块的周缘及内陆广泛发育，如北缘的秦岭-大别造山带(Faure et al., 1999, 2003)和内陆的九岭-雪峰山陆内造山带(Chu et al., 2012a, 2012b; Chu and Lin, 2013). 黄陵地区夹持于这两个造山带前缘的三角形区域内，这里受三叠纪构造影响比较微弱. 作为所谓“印支运动”的响应，中三叠统顶部仅局部可见平行不整合接触(李旭兵等,

2008; 赵小明等, 2010). 而且依据岩性和古生物特征, 黄陵背斜两侧秭归盆地和当阳盆地的上三叠统基本可以对比(孟繁松和李旭兵, 2003). 因此, 伴随着三叠纪的大规模海退, 早中生代的造山作用虽然可能造成了研究区局部地壳的轻微垂直抬升, 但并未使该区发生强烈的褶皱隆升.

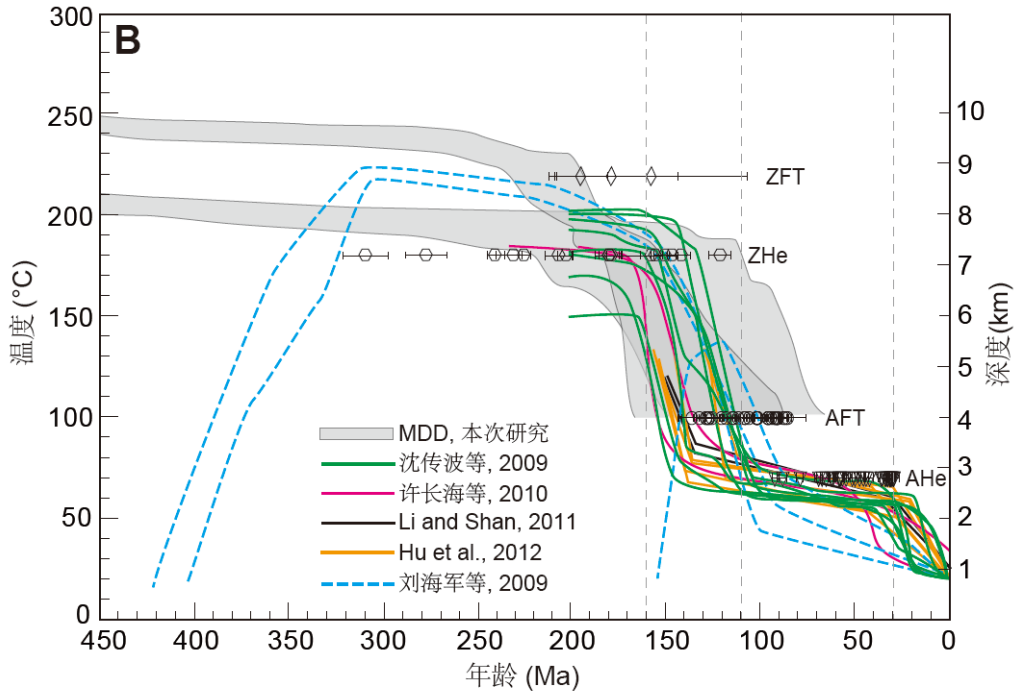

图5-10B 黄陵背斜中-新生代的冷却历史(钾长石MDD和AFT热史模拟结果)

Figure 5-10B Cooling history of the Huangling massif from K-feldspar MDD and AFT modeling

前人的裂变径迹和(U-Th)/He 低温热年代学研究工作很好地揭示了黄陵背斜地区自 200 Ma 以来的详细冷却隆升过程. 不同研究者获得的来自黄陵背斜核部崆岭杂岩和黄陵花岗岩的磷灰石裂变径迹模拟结果基本一致(沈传波等, 2009; 许长海等, 2010; Li and Shan, 2011; Hu et al., 2012). 这些结果共同显示研究区在 200-160 Ma 期间基本处于缓慢冷却阶段, 而最为明显的冷却事件发生在 160-110 Ma 之间, 冷却速率约为2-3 °C/Ma (图 5-10B). 虽然 Richardson et al. (2010)着眼于 40 Ma 以来三峡深切作用的研究, 但其裂变径迹模拟结果显示在晚侏罗-早白垩世期间也存在明显的冷却事件. 例外的是, Hu et al. (2006)的研究结果所揭示出的重要冷却过程发生在 100-40 Ma, 然而从模拟结果的检验值 GOF(goodness of fit)来看, 其模拟质量并不理想(GOF 均小于 0.5). 此外, 刘海军等(2009)对黄陵背斜东翼沉积盖层中的磷灰石进行了裂变径迹热史模拟, 结果同样指示黄陵背斜在 165-100 Ma 期间经历

了明显的隆升作用, 冷却速率为 1.9-2.7 °C/Ma (图 5-10B). 如果假设研究区的地温梯度为一常数(25 °C/km), 则黄陵背斜在 160-110 Ma 期间的剥蚀去顶厚度总计约为 5 km.

黄陵背斜在晚侏罗-早白垩世期间的隆升作用也得到了的沉积学证据的支持. 沉积古地理研究表明秭归盆地和当阳盆地在晚侏罗世之前可以相互连通, 构成了发育在秦岭-大别造山带南缘统一的盆地系统(S.F. Liu et al., 2005). 古流向的分析显示黄陵背斜在晚侏罗世开始成为其西侧秭归盆地充填的主要沉积物源区(渠洪杰等, 2009). 这一隆升作用还形成了研究区晚侏罗和下白垩统间明显的角度不整合, 以及整个下白垩统至上白垩统下部大套的砾岩沉积. 来自黄陵背斜东南翼白垩纪沉积岩的碎屑锆石U-Pb年代学研究结果揭示崆岭杂岩及其上覆沉积盖层是下白垩统地层的主要沉积物源, 而黄陵花岗岩在晚白垩世已经出露地表并开始遭受剥蚀(Shen et al., 2012). 由此可见, 黄陵地区在震旦纪-中侏罗世期间可能一直为处于地壳浅层次的继承性古隆起, 直至晚侏罗-早白垩世才经历了显著的隆升作用.

5 黄陵背斜的形成时间和成因机制 Formation time and mechanism of the anticline

前人关于黄陵背斜的形成时间存在早中生代、晚中生代或新生代, 抑或多期次的观点(戴少武, 1996; 徐政语等, 2004; 葛肖虹等, 2009; Wang et al., 2003)，这些推断主要是依据区域构造对比以及区域不整合. 然而, 低温热年代学研究结果揭示黄陵背斜的明显冷却隆升作用主要发生在 160-110 Ma 期间(刘海军等, 2009; 沈传波等, 2009; 许长海等, 2010; Hu et al., 2012). 从沉积演化来看, 黄陵背斜在晚侏罗世-早白垩世期间的隆升作用导致了其西侧秭归盆地的最终消亡, 而东侧当阳盆地则开始转入裂陷阶段. 实际上, 这些热年代学和沉积学证据与前述的构造观察十分吻合. 在背斜的西翼, 晚侏罗世地层明显地卷入了背斜的一翼, 而在背斜的西南翼和东南翼, 早白垩世的砾岩不整合覆盖于现今观察到的背斜几何形态之上. 这表明黄陵背斜的形成时间应该在晚侏罗世-早白垩世之间，至少造成两翼岩石发生滑脱变形的构造事件发生在这个期间.

关于黄陵背斜的成因机制目前还没有定论, 其中最具代表性的两个模式分别

是:

(1)**西向逆冲**(图 5-11A): 受秦岭-大别造山带和九岭-雪峰山造山带早中生代造山挤压作用的影响, 在中扬子地区构成一个向西开口的对冲构造带, 导致黄陵背斜受到向西的主压应力(戴少武, 1996; 徐政语等, 2004). 这个模式可以很好地解释黄陵背斜西陡东缓的不对称性, 但三叠纪的构造和黄陵背斜晚侏罗-早白垩世的形成时间之间存在着明显的时间差. 值得注意的是, 黄陵背斜近南北向的长轴方向近乎平行于南北两侧造山带的挤压方向, 而且在黄陵背斜以西地区并未见到具向西极性的褶皱或逆冲断层的广泛发育. 相反, 在黄陵背斜南北两端靠近造山带的沉积盖层中可以观察到挤压变形的发育, 其可能对应造山带三叠纪的前陆变形. 尽管如此, 如图 5-11A 所示, 黄陵背斜可以被解释为一个位于向西的隐伏冲断层之上的不对称褶皱. 如果是这样, 这一向西的逆冲作用发生的时间应在晚侏罗-早白垩世期间.

(2)**东向挤出**(图 5-11B): 华南板块在中生代向北挤入秦岭造山带, 四川盆地随之发生顺时针旋转, 进而在大巴山的两端形成汉南和神农架-黄陵两个构造结(Wang et al., 2003; Meng et al., 2005). 这一模式也常被发展用于晚中生代大巴山弧形构造带的成因解释(许长海等, 2010; Hu et al., 2012; Shi et al., 2012; J.H. Li et al., 2013b). 这个模式看似与黄陵背斜的形成时间较吻合, 但向东的挤出势必导致黄陵背斜表现为西缓东陡的几何形态, 这与前述的实际观察不相符(图 5-11B).

实际上, 对应于华北克拉通的破坏, 晚中生代的伸展构造广泛发育于欧亚大陆东缘(Lin and Wang, 2006; T. Wang et al., 2011; Lin et al., 2013a). 从区域伸展构造分布的时空格架来看, 黄陵背斜地区可能也受到了这一动力学过程的影响. 综合前述分析, 这里提出**伸展隆升**模式来解释黄陵背斜的成因(图 5-11C). 在晚中生代区域伸展背景下, 黄陵背斜在穹隆式的隆升过程中东西两翼发生了相背的滑脱变形. 在稍晚阶段黄陵背斜还经历了断块式的隆升过程, 且东侧具有相对较大的断陷幅度. 正是这一伸展隆升过程中的掀斜作用致使黄陵背斜形成现今西翼陡东翼缓的几何形态. 由此可见, 黄陵背斜翼部沉积盖层中发育的滑脱变形和两侧地堑-半地堑盆地的形成应属于同一期伸展构造背景下不同型式的表现. 值得指出的是, 低角度韧性正断层或拆离断层以及同构造花岗岩的缺失, 表明在黄陵背斜的形成过程中地壳的伸展幅度极其有限.

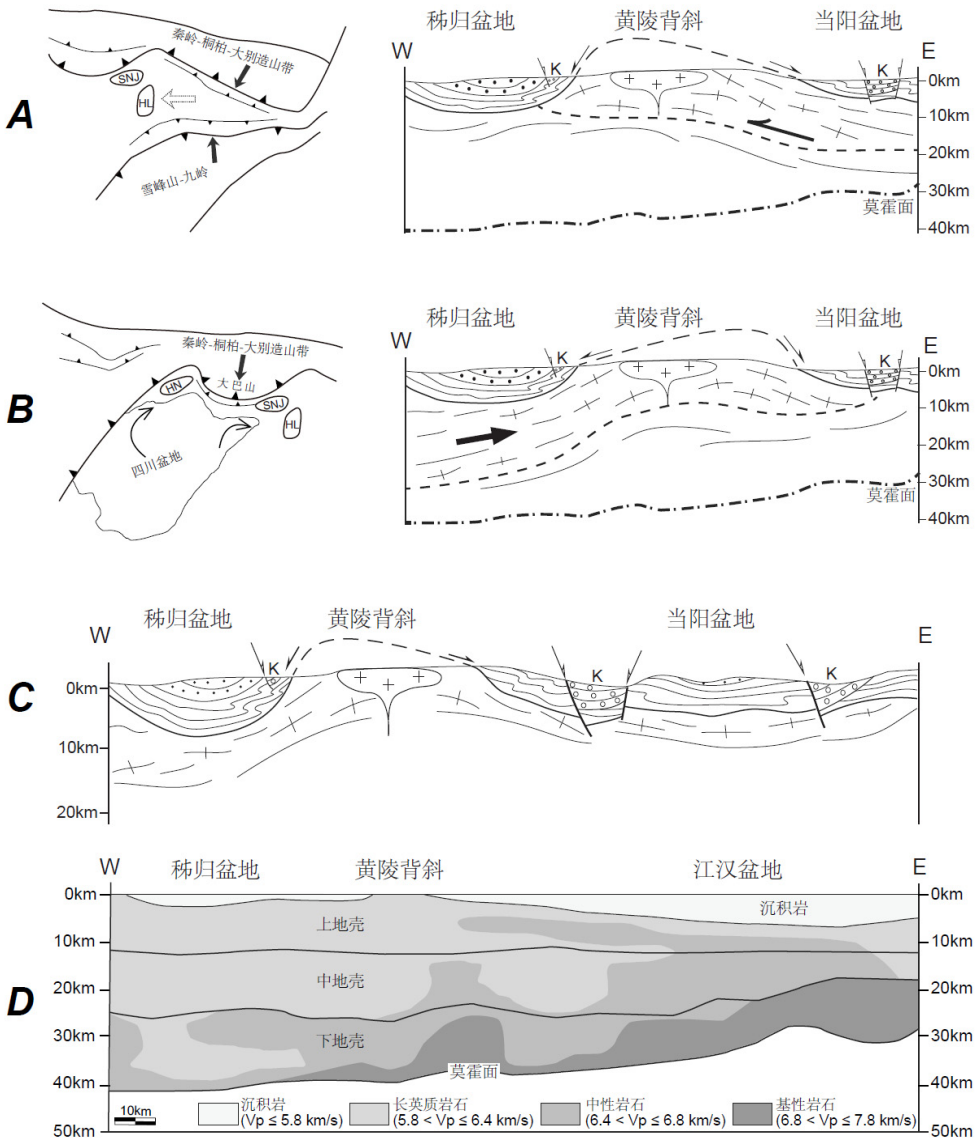

图 5-11 黄陵背斜的三种的成因动力学模式.

(A)西向逆冲模式; (B)东向挤出模式; (C)伸展隆升模式; (D)黄陵背斜地区地壳深部结构(修改自 Z.J. Zhang et al., 2009)

Figure 5-11 Three possible tectonic models for origin of the Huangling massif

(A) westward thrusting; (B) eastward extrusion; (C) extensional uplifting; (D) the profile of P-wave crustal velocity structure across the Huangling massif (modified after Z.J. Zhang et al., 2009)

研究表明华北克拉通破坏的范围大致在南北重力梯度带以东地区，而南北重力梯度带很可能是在白垩纪以来中国东部岩石圈的穿时减薄过程中形成的(朱日祥等, 2011; Xu, 2007). 黄陵背斜恰巧处于南北重力梯度带之上，地震广角反射剖面揭示黄陵背斜地区的地壳厚度从西侧秭归盆地约 42 km 逐渐变薄为东侧江汉盆地约 30 km (图 5-11D, Z.J. Zhang et al., 2009). 这一地壳厚度的不均一性变化可能与

我国东部中-新生代的伸展作用相关. 因此, 黄陵背斜可能代表了中国东部岩石圈减薄的西部边界, 并且由于发育在稳定的克拉通内部, 这里仅记录了弱的地壳伸展.

6 小结 Summary

扬子克拉通上的黄陵背斜是研究华南构造演化的一个重要窗口, 但其形成时间和成因机制问题一直悬而未决. 详细的构造解析表明, 黄陵背斜的几何形态表现为一个西翼陡东翼缓的不对称穹状背斜构造. 响应于穹隆作用, 背斜两翼沉积盖层的变形以相背的滑脱及层滑为特点. 随后的脆性正断作用还控制了背斜两侧地堑-半地堑盆地的发育. 黄陵背斜西翼晚侏罗世地层的卷入和两翼之上早白垩世砾岩的不整合覆盖, 将黄陵背斜的形成时间约束在晚侏罗-早白垩世之间. 从背斜核部不同类型岩石中分别选取钾长石进行 MDD 模拟研究, 并结合已有的热年代学数据, 可以给出一条约束较好的冷却曲线. 热演化历史揭示黄陵背斜自震旦纪以来可能为扬子克拉通上的继承性古隆起, 华南早古生代和早中生代的构造事件对其影响微弱. 直至晚侏罗世-早白垩世(160 Ma-110 Ma)期间经历了明显但实际上十分缓慢(2-3 °C/Ma)的冷却隆升过程, 这与背斜的形成相对应. 从整个中国东部考虑, 认为黄陵背斜所记录的微弱伸展作用体现了中国东部晚中生代岩石圈伸展减薄在稳定克拉通上的表现.

第六章 讨论和结论

Chapter 6 Discussion and conclusions

无论是从空间的分布上还是持续的时间上, 华南板块晚中生代伸展构造十分发育, 被誉为“华南盆岭省”. 对其构造演化和动力学背景的讨论, 不仅能够帮助我们理解华南岩石圈的演化过程, 而且为理解整个欧亚大陆东缘晚中生代伸展构造提供新思路. 在前面各章分述研究的基础上, 本章首先概括性地表述本次研究所获得的新认识, 并结合已有研究重点分析华南晚中生代伸展构造的特点, 然后将这些认识置于欧亚大陆东缘构造格架之下讨论其动力学背景.

1 华南晚中生代伸展构造的特点 Features of the Late Mesozoic extensional tectonics in South China

华南北缘高压/超高压造山带

华南北缘的桐柏-大别造山带强烈地叠加了白垩纪伸展构造(Ratschbacher et al., 2000; 冀文斌等, 2011; Wang et al., 2011; Cui et al., 2012). 沿桐柏-大别造山带自西向东包括桐柏山核部伸展背形、红安地体西南部的双峰尖伸展背形和大磊山半穹隆、大别山中部变质核杂岩. 这些伸展构造核部岩石通常为花岗质片麻岩, 桐柏山和大别山还发育混合岩并残余有榴辉岩. 外围岩石一般为三叠纪的变质序列, 包括浅变质岩至高压/超高压变质岩. 核部岩石与外围岩石之间通常以大型韧性剪切带相接触, 这些剪切带以中低角度的产状围绕于伸展背形或穹隆的周缘, 构成了拆离断层. 核部杂岩和拆离断层最为显著的特征是 NW-SE 向的矿物拉伸线理和上部向 NW 的剪切变形. 同时, 伸展作用还伴随有大量白垩纪花岗岩的侵入, 一些花岗岩的边缘存在明显的面理化, 而岩体核部则为块状, 变形不明显.

结合已有和本论文年代学研究结果, 表明桐柏-大别造山带白垩纪伸展作用可能开始于约 145 Ma, 在区域 NW-SE 向伸展作用, 造山带中下地壳岩石经历了混合岩化作用, 形成了桐柏杂岩和中大别杂岩, 同时壳内拆离作用则形成了早期的

韧性拆离构造，130 Ma 左右造山带根部的大规模垮塌导致了随后的穹隆作用，拆离面发生弯曲并可能在晚期经历了二次活化. 冷却史研究同样揭示在 130-125 Ma 期间桐柏杂岩和中大别杂岩存在一个快速冷却和折返过程，而拆离断层黑云母 $^{40}Ar/^{39}Ar$ 年龄的统计结果也给出了一个 125 Ma 的峰值(图 6-1). 因此，桐柏-大别造山带白垩纪伸展构造发生的时段和构造样式同华北地区完全可以对比.

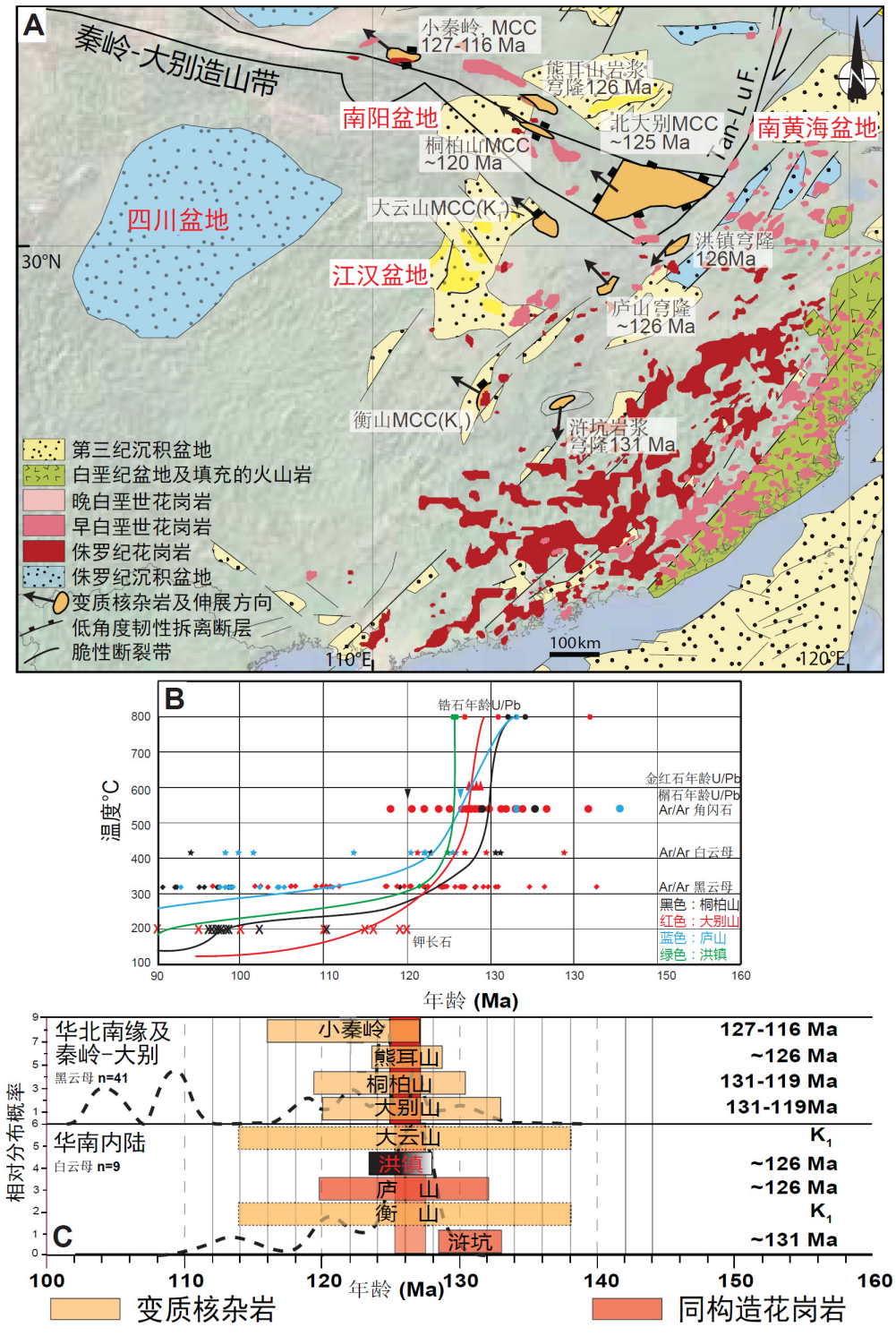

图 6-1 A. 华北南缘及秦岭-大别带和华南内陆晚中生代伸展构造图; B. 华北南缘及秦岭-大别带和华南内陆伸展穹隆冷却史; C. 华北南缘及秦岭-大别带和华南内陆晚中生代伸展构造相关的年代学展布图(相关年代学资料的参考文献见正文).

Figure 6-1 A. Tectonic map of the Late Mesozic extensional tectonics at the southern margin of the North China block, Qingling-Dabie belt and South China inland; B. Cooling paths of the extensional structures; C. Timing of the extensional structures (see text for references on geochronologcal data)

华南内陆地区

对比于华南展现的大规模晚中生代岩浆作用及其所反映的伸展构造背景(Li, 2000; Li et al., 2010; Wu et al., 2012), 华南地区晚中生代伸展构造研究相对有限且局限于伸展盆地和少数的岩浆穹隆(舒良树和周新民, 2002; 舒良树等, 2004; 张岳桥等, 2012). 目前能够确定发育韧性剪切带的伸展穹隆大致沿江南造山带展布, 由 NE 向 SW 依次为洪镇穹隆(朱光等, 2007; Zhu et al., 2010)、庐山穹隆(Lin et al., 2000)、大云山穹隆(俞爱南等, 1998; 本次研究)、武功山核部的浒坑穹隆 (Faure et al., 1996; 舒良树等, 1998)和衡山穹隆(徐汉林等, 1998; J.H. Li et al., 2013a).

华南内陆伸展穹隆整体为近椭圆状, 核部岩石通常为晚侏罗-早白垩世的花岗岩侵入体, 局部有少量变质的新元古代基底(图6-1). 有时伸展穹隆本身即为同构造的岩浆穹隆, 如大云山和浒坑. 除了浒坑岩浆穹隆外, 与伸展相关的韧性剪切带均分布在穹隆西侧, 靠西的大云山和衡山穹隆表现出类似变质核杂岩的特点, 西缘发育具低角度拆离断层特征的糜棱岩带, 而东部的庐山穹隆经历了复杂的多期伸展过程, 浒坑花岗岩则显示出同构造侵位过程中的典型高温变形组构(Lin et al., 2000; 舒良树等, 1998; J.H. Li et al., 2013a). 到目前为止, 华南内陆还未见到像华北地区具有强烈伸展幅度的拆离断层弯曲而形成“弧形”构造的报道. 华南内陆这种单向拆离的特点似乎暗示其非常有限的伸展幅度.

本次研究表明大云山-幕阜山岩基晚期侵入体是在 NW-SE 的伸展作用下构造侵位的, 在西部大云山边缘发育的拆离断层表现为 NW-SE 向矿物拉伸线理和上部向 NW 的运动学. 衡山穹隆西缘低角度拆离断层表现出与大云山一致的构造几何学和运动学特特征(J.H. Li et al., 2013a). 庐山穹隆除早期盖层中发育的上部向 NW 的浅层次顺层滑脱伸展构造外, 基底岩石中还记录了以 NE-SW 向矿物拉伸线理和

沿穹隆长轴分别向 NE 和 SW 的伸展剪切作用(Lin et al., 2000). 而位于洪镇穹隆西侧的韧性剪切带具有 NE-SW 向的矿物拉伸线理和上部向 SW 的剪切变形(朱光等, 2007; Zhu et al., 2010). 浒坑岩体南部边缘的变形带中矿物线理为近 N-S 向, 运动学表现为上部向 S 的剪切变形(Faure et al., 1996, 舒良树等, 1998). 这些似乎暗示除与华北克拉通及桐柏-大别造山带一致的区域 NW-SE 向伸展外, 华南还存在 NE-SW 向伸展构造.

关于上述几个华南内陆的伸展穹隆构造前人已有一些年代学工作. 详细的年代学研究显示庐山穹隆主期 NE-SW 的伸展变形发生在 132-126 Ma, 而晚期切割穹隆东部的韧性正断层的白云母和黑云母 Ar-Ar 年龄在 111-93 Ma (Lin et al., 2000). 朱光等获得洪镇穹隆西缘剪切带的白云母 Ar-Ar 年龄在 129-126 Ma 之间 (Zhu et al., 2010). 本论文研究结果表明与大云山拆断层相关的花岗岩侵位时代在 132 Ma 左右. 浒坑同构造花岗岩边缘的糜棱岩给出了一个黑云母 Ar-Ar 年龄为 132 Ma (Faure et al., 1996, 舒良树等, 1998). 衡山穹隆西缘拆离断层剪切带内同构造的钠长岩脉体的锆石 U-Pb 年龄为 136 Ma, 而剪切带糜棱岩中白云母 $^{40}Ar/^{39}Ar$ 年龄介于 98-108 Ma (J.H. Li et al., 2013a). 这些年代学结果表明华南晚中生代伸展构造发生的时间集中在 136-126 Ma, 这与冷却历所揭示的快速冷却过程相对应(图 6-1). 另外, 庐山和衡山的研究结果似乎指示在 110-90 Ma 期间华南内陆可能还经历了稍晚期伸展作用, 这一点在华南板块北缘的桐柏-大别造山带也有体现.

综上所述, 从华南北缘向内陆伸展强度具有减弱的趋势: 北缘的高压/超高压造山带体现了明显的巨量伸展-表现为巨型的 A 型伸展背形和造山带规模的变质核杂岩(桐柏山和大别山, 事实上, 肥东-张八岭及苏鲁的胶南地区也不同程度叠加了此期伸展构造); 在靠近内陆地区的伸展构造多表现为有限伸展幅度的岩浆穹隆或同构造花岗岩(如洪镇、庐山、武功山、大云山和衡山). 此外, 位于刚性华南(扬子克拉通)基底之上的黄陵背斜仅仅显示出缓慢的冷却及抬升去顶过程而已, 虽然在沉积盖层中也表现出了一定的岩石变形. 与华北相比, 华南晚中生代的伸展构造的发育具有明显的不均一性, 但总体上 NW-SE 的伸展方向和早白垩世(130 Ma 左右)主期变形时间与华北一致.

2 欧亚大陆东缘晚中生代伸展构造综观Overview of the Late Mesozoic extensional tectonics in the eastern margin of Eurasian continent

如前所述, 以变质核杂岩为代表的晚中生代伸展穹隆和断陷盆地在欧亚大陆东缘广泛发育, 构成了全球最大的地壳伸展区(图 1-1). 几乎所有穹隆的构造几何形态均具有近 NE-SW 的长轴方向, 体现了鲜明的大区域上的 NW-SE 方向的伸展(Lin and Wang, 2006). 现有的研究工作表明绝大多数与深部岩石折返相关的拆离断层中矿物拉伸线理为NW-SE向. 而且所表现的运动学特征也存在一定的规律性, 即在一定区域似乎存在对称性拆离的特点. 例如, 在泛贝加尔地区或蒙古-鄂霍次克缝合线北西侧的伸展穹隆其拆离断层表现为上部向 SE 的剪切变形(Zorin, 1999; Mazukabzov et al., 2006, 2011; Donskaya et al., 2008; T. Wang et al., 2011, 2012), 而位于 SE 侧蒙古国北部发育的 Ereendavaa 变质核杂岩和 Nartyn 岩浆穹隆则具有上部指向 NW 的剪切变形(Daoudene et al., 2009, 2011), 这一区带的伸展构造似乎沿蒙古-鄂霍次克断裂带具有轴对称拆离的现象(图 1-1). 相类似的现象在华北地区同样存在, 华北西部带的变质核杂岩如亚干、呼和浩特和云蒙山, 其拆离断层位于穹隆 SE 侧并具有上部向 SE 运动学(Webb et al., 1999a; Davis and Darby, 2010); 而华北东部带的伸展穹隆如医巫闾山变质核杂岩、岫岩岩浆穹隆、辽南变质核杂岩、郭家岭同构造花岗岩及胶南地区发育的拆离断层位于穹隆的 NW 侧, 与西部带刚好对称具有上部向 NW 的运动学(Lin and Wang, 2006; Hacker et al., 2009; Charles et al., 2011), 对称拆离轴线大致沿松辽盆地、阜新盆地、渤海湾盆地中残余的白垩纪盆地展布(图 1-1). 这种对称性还体现在拆离断层构造几何学表现上: 靠近中心的医巫闾山和云蒙山变质核杂岩表现为单向拆离, 而远离中心的呼和浩特、辽南变质核杂岩及岫岩岩浆穹隆则表现为拆离断层弯曲的“弧形”构造(图 6-2). 拆离断层带上部发育的上叠半地堑盆地及核部杂岩沿拆离断层折返至浅表的时间也具有非常强的可对称性和准同时性(Lin and Wang, 2006; 图 6-2). 当然伸展峰期稍早或稍晚的古道岭岩浆穹隆和玲珑杂岩体并没有体现出这个特点而作为一个特例值得深入思考(Charles et al., 2011, 2012). 桐柏-大别带及华南内陆并没有表现出类似于泛贝加尔-鄂霍次克带和华北这种伸展构造“对称性”拆离和展布的特点, 并且代表典型

大规模伸展作用的变质核杂岩在华南发育很少(沈晓明, 2008; 张岳桥等, 2012). 这似乎暗示欧亚大陆东缘晚中生代伸展构造具有向 S 或 SW 减弱的趋势.

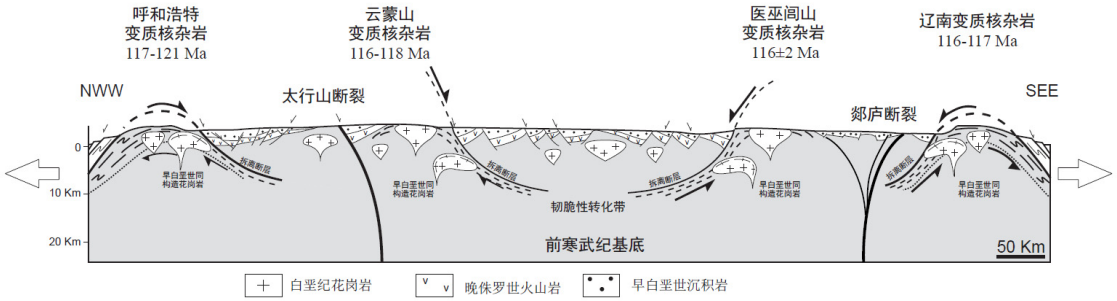

图 6-2 横贯华北北部晚中生代伸展穹隆、岩浆作用及相关拉分盆地的模式剖面图(引自林伟等, 2013a)

Figure 6-2 Schematic crustal scale section showing the Late Mesozoic extensional domes, magmatism and rift basins in the northern part of North China (modified after Lin et al., 2013a)

关于这些大规模区域伸展构造的动力学机制历来是研究和讨论的热点问题(Lin et al., 2013a; 林伟等, 2013a). 中生代-新生代时期, 古太平洋板块对中国东部大陆的影响是一个无法回避的问题. 绝大多数研究者将华北克拉通破坏的驱动力归结为与古太平洋板块向西俯冲相关, 这也是目前最流行的观点(Ren et al., 2002; Wu et al., 2005; G. Zhu et al., 2012; 朱日祥等, 2011). 同样, 对于华南发育的大面积岩浆岩, 古太平洋板块的作用更是被人们所推崇(Zhou and Li, 2000; Zhou et al., 2006; Li and Li, 2007; Ling et al., 2009; X.H. Li et al., 2013). 然而, 关于古太平洋的历史我们知之甚少(Engebretson et al., 1985; Maruyama et al., 1997; Sun et al., 2007). 虽然这种模式可以较好地解释了我国东部沿郯庐断裂展布的伸展构造, 但难以解释沿华北北缘及蒙古-鄂霍次克带和华北南缘及秦岭-大别带展布的几乎垂直于俯冲带的伸展构造, 这与美国西部盆岭省的伸展构造带平行于俯冲边界展布截然不同. 早白垩世岩浆活动峰值在整个中国东部虽然都有记录, 但太平洋的贡献似乎被人们过分地夸大(张旗和李承东, 2012). 也有一些研究者认为俄罗斯泛贝加尔华北北缘及蒙古-鄂霍次克带的伸展构造与蒙古-鄂霍次克洋的演化相关. 例如, 孟庆任提出了非常新颖的蒙古-鄂霍次克洋壳板片的断离及碰撞后的重力扩展模式(Meng, 2003). 这个模式似乎较好地解释了蒙古-鄂霍次克带伸展构造的动力学背景, 但难以解释远离蒙古-鄂霍次克带的华北地区及秦岭-大别带至华南内陆等区域上发育的伸展构造. 王涛等(T. Wang et al., 2011, 2012)最近提出了蒙古-鄂霍次克

洋北向俯冲造山和造山后过程中岩石圈深部收缩而浅部伸展的模式来解释泛贝加尔和蒙古地区发育的伸展构造. 但这一模式要求伸展构造具有向SE变年轻的趋势, 这与该地区的伸展构造具准同时性的特点并不一致(Lin et al., 2013a).

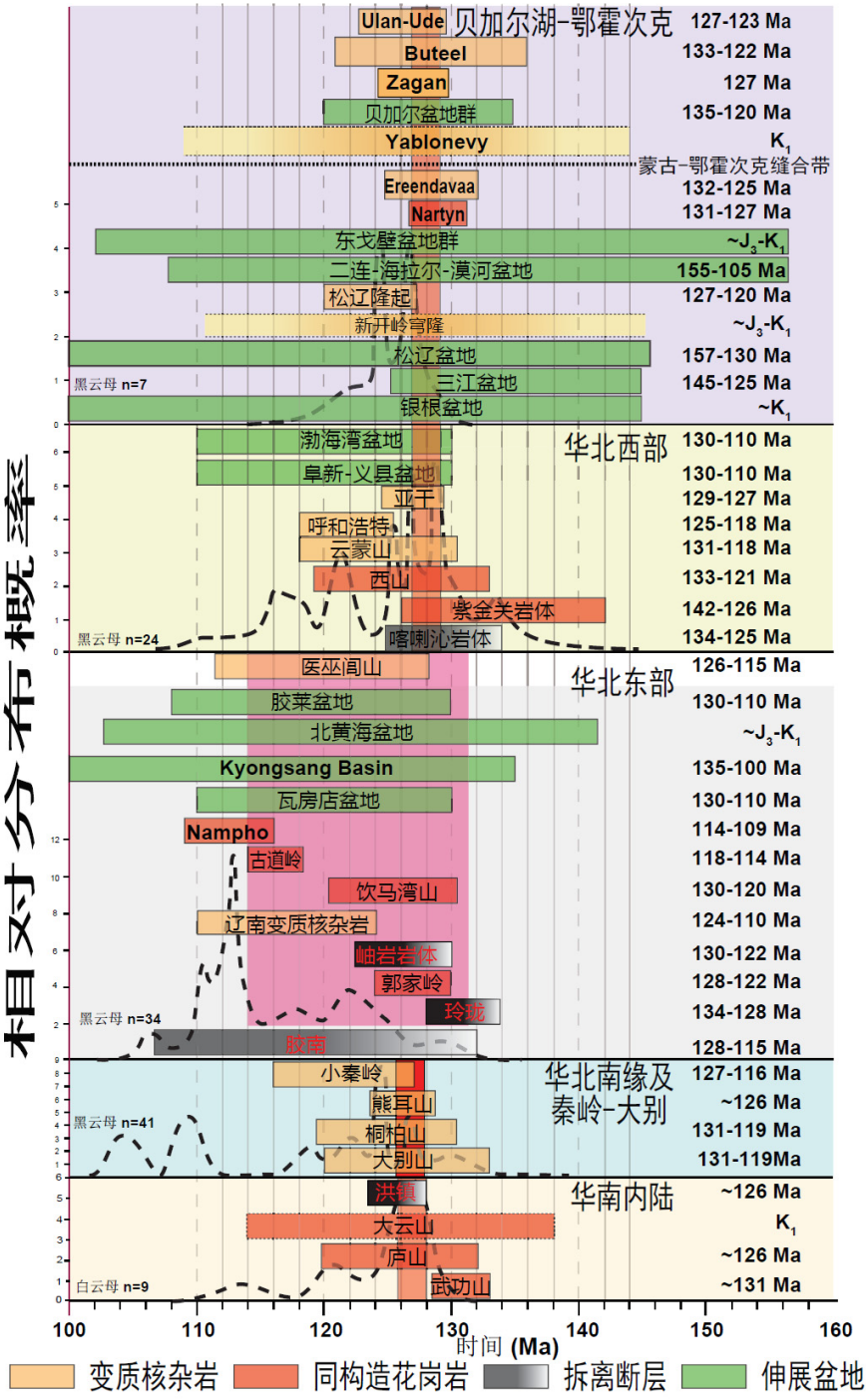

图 6-3 欧亚大陆东缘晚中生代伸展构造及相关的年代学展布图(引自林伟等, 2013a)

Figure 6-3 Extensional structures (extensional domes, syn-tectonic plutons, detachment faults and rift basins) and their geochronological ages in eastern part of the Eurasian continent (modified after Lin et al., 2013a)

此外, 华北-华南三叠纪碰撞或印度-欧亚新生代碰撞同样被解释成这些伸展构造的动力学来源, 但在时间上明显无法与晚中生代的构造匹配, 其局限性更为明显. 从更大区域或全球考虑, 多板块的相互作用过程也被不少研究者所青睐. 例如, Ratschbacher et al. (2000)认为整个欧亚大陆东缘的伸展构造可能源于拉萨与羌塘碰撞和西伯利亚-蒙古与华北碰撞而产生的向东放射状构造逃逸和古太平洋西向俯冲弧后扩张导致的综合作用的结果; 董树文等(2007, 2008)将"燕山运动"定义为起始于 165 Ma 的"东亚多向汇聚"构造体制及其形成的广泛陆内造山和构造变革, 并将中国东部岩石圈巨量减薄视作燕山期陆内造山和陆内变形的后效.

我们将欧亚大陆东缘主要的伸展构造汇集成简图(图 6-3), 蒙古-鄂霍次克板块缝合带也被置于其中. 在空间上, 绝大多数的伸展穹隆发育在岩石圈薄弱带之上, 如中亚造山带(或蒙古-鄂霍次克造山带), 阴山-燕山陆内造山带、秦岭-大别-苏鲁高压/超高压造山带、江南造山带(或九岭-雪峰山陆内造山带)及郯庐断裂带附近, 仅少数发育在克拉通之上, 如西山穹隆、黄陵背斜. 在时间上, 除华北东部带给出一个较为宽泛的伸展时段外, 各个研究区伸展穹隆所涉及的与拆离断层相关的折返和剥露时间均十分相近, 峰期在 130-126 Ma 之间(图 6-3). 中国东部大规模强烈的岩浆作用, 也恰恰位于这个时段, 显示其在地壳伸展中起到了不可忽视的作用(Wu et al., 2005). 如前所述, 这些极其类似且可对比的早白垩世伸展构造如果具有相同构造背景的话, 这个规模远比美国西部的盆岭省宽广得多, 因而其成因需要更加深刻的认识. 上述的任何一种来自板块边缘的作用在某种程度上可能是这个宽广范围内伸展构造发育的诱因, 但不是主导的直接驱动力(Lin et al., 2013a). 那么这是否意味着存在更大规模的深部岩石圈或软流圈的物质流动行为? 岩石圈地幔对流移离或拆沉模式似乎与地表观察到的构造现象相吻合, 这或许是将这些伸展构造与华北克拉通破坏这一地球动力学模型结合起来的有力证据(Lin and Wang, 2006). 克拉通破坏这一概念的提出为我们理解欧亚大陆东缘大范围发育的伸展构造具有十分重要的意义, 通过对这一具有全球意义的大陆岩石圈伸展减薄及破坏的长期深入研究, 可以让我们深入认识大陆动力学更深层次的含义.

3 结论 Conclusions

本论文的研究工作表明, 无论是华南板块北缘的高压/超高压造山带, 还是江

南造山带中段的大云山-幕阜山和扬子克拉通之上的黄陵背斜地区, 均发育了明显的晚中生代伸展构造. 研究表明不同构造部位的伸展构造表现并不完全一致. 桐柏山核部的桐柏杂岩和大别山中部的中大别杂岩构成了两个叠加在三叠纪高压/超高压造山带之上的白垩纪伸展构造, 在构造样式上分别表现为巨型的A型伸展背形和造山带规模的变质核杂岩. 拆离断层围绕于杂岩的周缘, 杂岩与拆离断层的主期变形以NW-SE向的矿物拉伸线理和上部向NW的运动学为特点. 伴随同时期的混合岩化作用和同构造的侵入体, 这一伸展作用可能开始于约145 Ma, 至130 Ma以山根的垮塌为标志达到峰期. 此外, 桐柏山、双峰尖、大磊山和大别山还共同记录了稍晚(110-90 Ma)一期伸展事件. 大云山-幕阜山岩基由晚侏罗世(150 Ma左右)和早白垩世(132 Ma左右)两期侵入体组成, 其中晚期侵入体是在NW-SE向伸展作用下同构造侵位的, 以岩体西部边缘发育单向拆离断层为特点, 对应于早白垩世的地壳减薄过程; 而早期侵入体则记录了近N-S向应力场, 推测其可能代表了晚侏罗世挤压作用下地壳的加厚过程. 黄陵背斜表现为发育于盖层中近N-S向的不对称穹状构造, 两翼西陡东缓, 相应的岩石变形以相背的重力滑脱和顺层滑动为特点, 构造叠加关系和冷却史均一致指示其形成于晚侏罗-早白垩世之间. 这一系列由深至浅的白垩纪伸展构造(具极强伸展强度的中下地壳折返, 具有限伸展幅度的同构造花岗岩侵位, 具极弱伸展特征的沉积盖层变形)表明华南地区同样经历了与华北克拉通破坏过程中相对应的区域伸展作用.

通过区域上的对比研究, 认为欧亚大陆东缘晚中生代伸展构造呈大范围面状发育(从俄罗斯泛贝加尔一直至我国华南内陆地区均有分布), 构成了全球最大的地壳伸展区, 其记录了大区域上的 NW-SE 向伸展作用, 并且这一伸展作用似乎具有向华南内陆减弱的趋势. 这些伸展构造使地壳不同层次的岩石沿拆离断层折返至地表, 从而使中下地壳结构发生了强烈的改造. 各个研究区所涉及的伸展穹隆及其相关的拆离断层所表现的伸展峰期时间均在早白垩世, 集中于 130-126 Ma 之间. 明显不同于美国西部的盆岭省的弧后伸展扩张机制, 欧亚大陆东缘的伸展构造在成因机制很大程度上受先存加厚造山带根部岩石圈拆沉作用的控制. 本论文为探讨欧亚大陆东缘晚中生代伸展构造发育的时空格架及其动力学背景提供了直接的构造证据.它揭示了在稳定大陆岩石圈性质和厚度发生变化的过程中, 中下地壳的结构受到强烈的改造, 伸展构造的研究为其提供了独立的构造地质学证据.

参考文献 References

1. 陈江峰, 谢智, 刘顺生, 李学明, K. A. Foland. 1995. 大别造山带冷却年龄的 Ar-Ar 和裂变径迹年龄测定. 中国科学(B 辑), 25(10): 1086-1092.
2. 陈凌, 危自根, 程骋. 2010. 从华北克拉通中、西部结构的区域差异性探讨克拉通破坏. 地学前缘, 17(1): 212-228.
3. 陈廷愚, 牛宝贵, 刘志刚, 富云莲, 任纪舜. 1991. 大别山腹地燕山期岩浆作用和变质作用的同位素年代学研究及其地质意义. 地质学报, 4: 329-336.
4. 陈泽超, 林伟, Michel Faure, Claude Lepvrier, 褚杨, 王清晨. 2013. 越南东北部早中生代构造事件的年代学约束. 岩石学报, 29(5): 1825-1840.
5. 崔建军, 胡建民, 刘晓春. 2009. 桐柏地区高压变质地体在地壳中的抬升机制. 岩石学报, 25(9): 2165-2176.
6. 戴少武. 1996. 江汉盆地印支期以来区域构造特征探讨. 地质力学学报, 2(4): 80-84
7. 董树文, 胡健民, 李三忠, 施炜, 高锐, 刘晓春, 薛怀民. 2005. 大别山侏罗纪变形及其构造意义. 岩石学报, 21(4): 1189-1194.
8. 董树文, 张岳桥, 龙长兴, 杨振宇, 季强, 王涛, 胡建民, 陈宣华. 2007. 中国侏罗纪构造变革与燕山运动新诠释. 地质学报, 81(11): 1449-1461.
9. 董树文, 张岳桥, 陈宣华, 龙长兴, 王涛, 杨振宇, 胡建民. 2008. 晚侏罗世东亚多向汇聚构造体系的形成与变形特征. 29(3): 306-317.
10. 冯定犹, 李志昌, 张自超. 1991. 黄陵花岗岩类岩基南部岩体侵入时代和同位素特征. 湖北地质, 5(2): 1-12
11. 傅昭仁, 李紫金, 郑大瑜. l999. 湘赣边 NNE 向走滑造山带构造发展样式. 地学前缘, 6(4): 263-272.
12. 高林志, 陈峻, 丁孝忠, 刘耀荣, 张传恒, 张恒, 刘燕学, 庞维华, 张玉海. 2011. 湘东北岳阳地区冷家溪群和板溪群凝灰岩 SHRIMP 锆石 U-Pb 年龄——对武陵运动的制约. 地质通报, 30(7): 1001-1008.
13. 高山, Yumin Qiu, 凌文黎, Neal J. McNanghton, David I. Groves. 2001. 崆岭高级变质地体单颗粒锆石 SHRIMP U-Pb 年代学研究——扬子克拉通 > 3.2 Ga 陆壳物质的发现. 中国科学(D 辑), 31(1): 27-35
14. 高维, 张传恒, 2009. 长江三峡黄陵花岗岩与莲沱组凝灰岩的 SHRIMP U-Pb 锆石年龄及其构造地层意义. 地质通报, 28(1): 45-50.
15. 葛宁洁, 夏群科, 吴元保, 侯振辉, 秦礼萍, 柏林. 2003. 北大别燕子河片麻岩的锆石 U-Pb 年龄: 印支期变质事件的确定. 岩石学报, 19(3): 513-516.
16. 葛肖虹, 王敏沛, 刘俊来. 重新厘定“四川运动”与青藏高原初始隆升的时代、背景: 黄陵背斜构造形成的启示. 地学前缘, 17(4): 206-217.
17. 河南省地质矿产局. 1989. 河南省区域地质志. 地质出版社, 1-772.
18. 侯泉林, 刘庆, 李俊, 张宏远. 2007. 大别山晚中生代剪切带特征及年代学制约. 地质科学, 42(1): 114-123.
19. 侯振辉, 李曙光, 陈能松, 李秋立, 柳小明. 大别造山带惠兰山镁铁质麻粒岩 Sm-Nd 和锆石 SHRIMP U-Pb 年代学及锆石微量元素地球化学. 中国科学(D 辑), 35(12): 1103-1111.
20. 胡世玲, 刘鸿允, 王松山, 胡文虎, 桑海清, 裘冀. 1989. 据 ^{40}Ar-^{39}Ar 快中子年龄新资料讨论震旦系底界年龄. 地质科学, (1): 16-25.
21. 湖北省地质矿产局,1990. 湖北省区域地质志. 地质出版社, 1-705.

22. 黄少英, 徐备, 王长秋, 湛胜, 邓荣敬. 2006. 桐柏造山带几何学、运动学和演化. 中国科学(D 辑), 36(3):242-251.
23. 冀文斌, 林伟, 石永红, 王清晨, 褚杨. 2011. 大别山早白垩世变质核杂岩的结构与演化. 地质科学, 46(1): 161-180.
24. 贾大成, 胡瑞忠, 赵军红, 谢桂青. 2003. 湘东北中生代望湘花岗岩体岩石地球化学特征及其构造特征. 地质学报, 77(1) : 98-103.
25. 江来利, 刘贻灿, 吴维平, 李惠民, 方中. 2002. 大别山北部漫水河灰色片麻岩的锆石U-Pb年龄及其地质意义. 地球化学, 31(1): 66-70.
26. 江麟生, 陈铁龙, 周忠友. 2002. 黄陵地区的几个主要基础地质问题. 湖北地矿, 16(1): 8-13
27. 焦文放, 吴元保, 彭敏, 汪晶, 杨赛红. 2009. 扬子板块最古老岩石的锆石 U-Pb 年龄和 Hf 同位素组成. 中国科学(D 辑), 39(7): 972-978.
28. 李鹏春, 许德如, 陈广浩, 夏斌, 贺转利, 符巩固. 2005. 湘东北金井地区花岗岩成因及地球动力学暗示: 岩石学、地球化学和 Sr-Nd 同位素制约. 岩石学报, 21(3): 921-934.
29. 李秋立, 杨亚楠, 石永红, 林伟. 2013. 榴辉岩中金红石 U-Pb 定年：对大陆碰撞造山带形成和演化的制约. 科学通报, 58(23): 2279-2284.
30. 李曙光, 黄方, 李晖. 2001. 大别-苏鲁造山带碰撞后的岩石圈拆离. 科学通报, 46(17): 1487-1491.
31. 李曙光, 李秋立, 侯振辉, 杨蔚, 王莹. 2005. 大别山超高压变质岩的冷却史及折返机制. 岩石学报, 21(4): 1117-1124.
32. 李曙光, 何永胜, 王水炯. 2013. 大别造山带的去山根过程与机制: 碰撞后岩浆岩的年代学和地球化学制约. 科学通报, 58(23): 2316-2322.
33. 李先福, 傅昭仁, 李建威, 陈小东. 2001. 湘东-赣西 NNE 向走滑构造. 大地构造与成矿, 25(2): 136-140.
34. 李旭兵, 王传尚, 刘安. 2008. 印支运动的沉积学响应——以湖北秭归盆地中、上三叠统为例. 中国地质, 35(5): 984-991
35. 李益龙, 周汉文, 李献华, 罗清华. 2007. 黄陵花岗岩基英云闪长岩的黑云母和角闪石 ^{40}Ar-^{39}Ar 年龄及其冷却曲线. 岩石学报, 23(5): 1067-1074
36. 李志昌, 王桂华, 张自超. 2002. 鄂西黄陵花岗岩基同位素年龄谱. 华南地质与矿产, 3: 19-28
37. 林伟, 王清晨, Michel Faure, 孙岩, 舒良树, Urs Schärer. 2003. 大别山的构造变形期次和超高压岩石折返的动力学. 地质学报, 77(1): 44-54.
38. 林伟, 王清晨, M. Faure, N. Arnaud. 2005. 从北淮阳构造带的多期变形透视大别山构造演化. 中国科学(D 辑), 35(2): 127-139.
39. 林伟, 王清晨, 王军, 王非, 褚 杨, 陈 科. 2011. 辽东半岛晚中生代伸展构造——华北克拉通破坏的地壳响应. 中国科学: 地球科学, 41 (5): 638-653.
40. 林伟, Michel Faure, Claude Lepvrier, 陈泽超, 褚杨, 王清晨, N'guyen Van Vuong, Vu Van Tich. 2011.华南板块南缘早中生代的逆冲推覆构造及其相关的动力学背景. 地质科学, 46(1): 134-145.
41. 林伟, 刘飞, 王军, 冀文斌, 王清晨. 2013a. 华北克拉通及邻区晚中生代伸展构造及其动力学背景的讨论. 岩石学报, 29(5): 1791-1810.
42. 林伟, 冀文斌, 石永红, 褚杨, 李秋立, 陈泽超, 刘飞, 王清晨. 2013b. 高压-超高压变质岩石多期构造折返: 以桐柏-红安-大别造山带为例. 科学通报, 58 (23): 2259-2265.
43. 凌文黎, 高山, 郑海飞, 周炼, 赵祖斌. 1998. 扬子克拉通黄陵地区崆岭杂岩 Sm-Nd 同位素地质年代学研究. 科学通报, 43(1): 86-89.

44. 凌文黎, 高山, 张本仁, 周炼, 徐启东. 2001. 扬子陆核古元古代晚期构造热事件与扬子克拉通演化.科学通报, 45(21): 2343-2348.
45. 凌文黎, 高山, 陈建萍, 江麟生, 袁洪林, 胡兆初. 2006. 扬子陆核与陆缘新元古代岩浆事件对比及其构造意义——来自黄陵和汉南侵入杂岩 ELA-ICPMS 锆石 U-Pb 同位素年代学的约束. 岩石学报, 22(2): 387-396.
46. 刘海军, 许长海, 周祖翼, R.A. Donelick. 2009. 黄陵隆起形成(165-100Ma)的碎屑岩磷灰石裂变径迹热年代学约束. 自然科学进展, 19(12): 1326-1332.
47. 刘景波, 张灵敏, 叶凯, 苏文, 程南飞. 2013. 大别山北部卢镇关群变质火山岩和共生变质的花岗岩全岩和锆石氧同位素、锆石 U-Pb 年代学研究. 岩石学报. 29(5): 1511-1524.
48. 刘景彦, 林畅松, 卢林, 蔡文杰, 王必金, 董伟. 2009. 江汉盆地白垩-新近系主要不整合面剥蚀量分布及其构造意义. 地质科技情报, 28(1): 1-8.
49. 刘俊来, 纪沫, 申亮, 关会梅, G.A. Davis. 2011. 辽东半岛早白垩世伸展构造组合、形成时代及区域构造内涵. 中国科学: 地球科学, 41 (5): 618-637.
50. 刘小池, 吴元保, 彭敏, 汪晶, 王浩, 彭德才. 2011. 桐柏造山带深熔作用: 混合岩 LA-ICP-MS锆石U-Pb年代学证据. 岩石学报, 27(4): 1163-1171.
51. 刘晓春, 娄玉行, 董树文. 2005a. 桐柏山地区低温榴辉岩变质作用的 P-T 轨迹. 岩石学报, 21(4): 1081-1093.
52. 刘晓春, 董树文, 李三忠, 薛怀民, 刘建民, 曲玮. 2005b. 湖北红安群的时代: 变质花岗质侵入体 U-Pb 定年提供的制约. 中国地质, 32(1): 75-81
53. 刘晓春, 江博明, 李三忠, 崔建军, 刘鑫, 娄玉行, 曲玮. 2011. 桐柏高压变质地体: 对桐柏-大别-苏鲁高压/超高压变质带构造框架和俯冲/折返机制的制约. 岩石学报, 27(4): 1151-1162.
54. 刘晓春, 江博明, 李三忠. 2013. 大陆岩板俯冲与折返的穿时性: 桐柏造山带晚二叠-三叠纪高压变质地体提供的制约. 科学通报, 58(23): 2251-2258.
55. 刘鑫, 李三忠, 索艳慧, 刘晓春, 刘恩山, 戴黎明. 2010. 桐柏碰撞造山带及其邻区变形特征与构造格局. 岩石学报, 26(4): 1289-1302.
56. 刘贻灿, 李曙光, 徐树桐, 李惠民, 江来利, 陈冠宝, 吴维平, 苏 文. 2000. 大别山北部榴辉岩和英云闪长质片麻岩锆石 U-Pb 年龄及多期变质增生. 高校地质学报, 6(3): 417-423.
57. 刘贻灿, 徐树桐, 李曙光, 陈冠宝, 江来利, 周存亭, 吴维平. 2001. 大别山北部镁铁-超镁铁质岩带中榴辉岩的分布与变质温压条件. 地质学报, 75(3): 385-395.
58. 刘贻灿, 徐树桐, 李曙光, 陈冠宝, 彭练红. 2005. “罗田穹隆”中的下地壳俯冲成因榴辉岩及其地质意义. 地球科学, 30(1): 71-77.
59. 刘贻灿, 李曙光. 2005. 大别山下地壳岩石及其深俯冲. 岩石学报, 21(4): 1059-1066.
60. 刘贻灿, 李曙光. 2008. 俯冲陆壳内部的拆离和超高压岩石的多板片差异折返: 以大别-苏鲁造山带为例. 科学通报, 53(18): 2153-2165.
61. 刘贻灿, 李远, 刘理湘, 古晓锋, 邓亮鹏, 刘佳. 2013. 大别造山带三叠纪低级变质的新元古代火成岩: 俯冲陆壳表层拆离折返的岩片. 科学通报, 58(23): 2330-2337.
62. 马昌前, 杨坤光, 明厚利, 林广春. 2003.大别山中生代地壳从挤压转向伸展的时间: 花岗岩的证据. 中国科学(D 辑), 33(9): 817-827.
63. 马大铨, 李志昌, 肖志发. 1997. 鄂西崆岭杂岩的组成、时代及地质演化. 地球学报, 18(3): 233-241
64. 马大铨, 杜绍华, 肖志发. 2002. 黄陵花岗岩基的成因. 岩石矿物学杂志, 21(2): 151-161
65. 马国干, 李华芹, 张自超. 1984. 华南地区震旦纪时限范围的研究. 宜昌地质矿产研究所所刊, 8: 1-29.

66. 马寅生, 崔盛芹, 吴淦国, 吴珍汉, 朱大岗, 李晓, 冯向阳. 1999. 医巫闾山变质核杂岩构造特征. 地球学报, 20(4): 385-391.
67. 孟繁松, 李旭兵. 2003. 黄陵穹隆东、西两翼上三叠统的精细对比. 华南地质与矿产, 4: 60-65
68. 牛宝贵, 富云莲, 刘志刚, 任纪舜, 陈文. 1994. 桐柏-大别山主要构造热事件及$^{40}Ar/^{39}Ar$地质定年研究. 地球学报. (1-2): 20-34.
69. 渠洪杰, 胡健民, 崔建军, 武国利, 田蜜, 施炜, 赵陕兰. 2009. 大巴山构造带东段秭归盆地侏罗纪沉积充填过程及其构造演化. 地质学报, 83(9): 1255-1268.
70. 邵济安, 张履桥, 贾文, 王佩瑛. 2001. 内蒙古喀喇沁变质核杂岩及其隆升机制探讨. 岩石学报, 17(2): 283-290.
71. 沈传波, 梅廉夫, 刘昭茜, 徐思煌. 2009. 黄陵隆起中-新生代隆升作用的裂变径迹证据. 矿物岩石, 29(2): 54-60.
72. 石永红, 王娟, 李秋立, 林伟. 2013. 大别造山带变质岩温度压力结构研究. 科学通报, 58(22): 2145-2152.
73. 舒良树, 孙岩, 王德滋, M Faure, J Charvet, P Monie. 1998. 华南武功山中生代伸展构造. 中国科学(D辑), 28: 431-438.
74. 舒良树, 周新民. 2002. 中国东南部晚中生代构造格架. 地质论评, 48(3): 249-260.
75. 舒良树, 周新民, 邓平, 余心起, 王彬, 祖辅平. 2004. 中国东南部中、新生代盆地特征与构造演化. 地质通报, 23(9): 876-884.
76. 舒良树, 王德滋. 2006. 北美西部与中国东南部盆岭构造对比研究. 高校地质学报, 12(1): 1-13
77. 宋鸿林. 1996. 北京房山变质核杂岩的基本特征及其成因探讨. 现代地质, 10(2): 149- 158
78. 苏文, 刘景波, 陈能松, 郭顺, 巴金, 张璐, 刘新, 施雨新. 2013. 东秦岭-大别山及其两侧的岩浆和变质事件年代学及其形成的大地构造背景. 岩石学报, 29(5): 1573-1593.
79. 孙卫东, 凌明星, 杨晓勇, 范蔚茗, 丁兴, 梁华英. 洋脊俯冲与斑岩铜金矿成矿. 中国科学: 地球科学. 40(2): 127-137.
80. 索书田, 钟增球, 游振东. 2000. 大别地块超高压变质期后伸展变形及超高压变质岩石折返过程. 中国科学(D 辑), 30(1): 9-17.
81. 索书田, 钟增球, 张宏飞, 周汉文, 游振东. 2001. 桐柏山高压变质带及其区域构造型式. 地球科学, 26(6): 551-559.
82. 索书田, 钟增球, 游振东. 2000. 大别-苏鲁构造带三叠纪碰撞缝合线的位置. 地球科学, 25(2): 111-116.
83. 汪洋, 邓晋福. 2004. 湘东北地区燕山晚期强过铝质花岗岩的岩石化学特征及构造背景探讨. 大地构造学与成矿, 28(1): 60-68.
84. 王必金, 林畅松, 陈莹, 卢明国, 刘景彦. 2006. 江汉盆地幕式构造运动及其演化特征. 石油地球物理勘探, 41(2): 226-230.
85. 王二七, 苏哲, 许光. 2009. 我国的一些造山带的侧向挤出构造. 地质科学, 44(4): 1266-1288
86. 王非, 贺怀宇, 朱日祥, 桑海清, 王英兰, 杨列坤. 2005. $^{40}Ar/^{39}Ar$ 年代学国际国内标样的对比标定. 中国科学(D 辑), 35(7): 617-626.
87. 王非, 朱日祥, 李齐, 贺怀宇, 罗清华, 卢欣祥, 桑海清, 王英兰. 2007. 秦岭造山带的差异隆升特征——花岗岩 $^{40}Ar/^{39}Ar$ 年代学研究的证据
88. 王国灿, 杨巍然. 1996. 大别山核部罗田穹隆形成的构造及年代学证据. 地球科学, 21(5): 524-528.

89. 王国灿, 杨巍然. 1998. 大别造山带中新生代隆升作用的时空格局——构造年代学证据. 地球科学, 23(5): 461-467.
90. 王军, 褚杨, 林伟, 王清晨. 2010. 黄陵背斜的构造几何形态及其成因探讨. 地质科学, 45: 615-625.
91. 王连训, 马昌前, 张金阳, 陈玲, 张超. 2008. 湘东北早白垩世桃花山-小墨山花岗岩体岩石地球化学特征及成因. 高校地质学报, 14(3): 334-349
92. 王朴, 王国灿, 刘超, 王岸, 叶润青. 2008. 大别山商麻断裂韧-脆性变形转换的时间约束及其构造意义. 地球科学, 33(2): 174-182.
93. 王清晨, 从柏林. 大别山超高压变质带的大地构造框架. 岩石学报, 1998, 14(4): 481-492.
94. 王清晨, 蔡立国. 2007. 中国南方显生宙大地构造演化简史. 地质学报, 81(8): 1025-1040.
95. 王新社, 郑亚东. 2005. 楼子店变质核杂岩韧性变形作用的 $^{40}Ar/^{39}Ar$ 年代学约束. 地质论评, 51: 574-582
96. 王义天, 李继亮, 刘德良, 吴运高, 付永涛, 吴峻. 2000. 大别山商城-麻城断裂带的 ^{40}Ar-^{39}Ar 年龄及其意义. 地质论评, 46(6): 611-615.
97. 魏春景, 单振刚, 张立飞, 王式洸, 常宗广. 1997. 北大别榴辉岩的确定及其地质意义. 科学通报, 42(17): 1832-1836.
98. 魏春景, 吴玉新, 倪云燕, 陈斌, 王式光. 1999. 河南桐柏地区榴辉岩的特征及其地质意义. 科学通报, 44(17): 1882-1885.
99. 吴福元, 李献华, 杨进辉, 郑永飞. 2007. 花岗岩成因研究的若干问题. 岩石学报, 23(6): 1217-1238.
100. 吴福元, 徐义刚, 高山, 郑建平. 2008. 华北岩石圈减薄与克拉通破坏研究的主要学术争论. 岩石学报, 24(6): 1145-1174
101. 吴元保. 2009. 大陆造山过程的多期演化: 以西大别为例. 科学通报, 54(13): 1815-1825.
102. 谢窦克, 马荣升, 张禹慎. 华南大陆壳生长过程与地幔柱构造. 北京: 地质出版社, 1-257
103. 谢桂青, 胡瑞忠, 赵军红, 蒋国豪. 中国东南部地幔柱及其与中生代大规模成矿关系初探. 大地构造与成矿学. 25(2): 179-186.
104. 谢智, 陈江峰, 张巽, 高天山, 戴圣潜, 周泰禧, 李惠民. 2001. 大别造山带北部石竹河片麻岩的锆石 U-Pb 年龄及其地质意义. 岩石学报, 17(1): 139-144.
105. 谢智, 高天山, 陈江峰. 2004. 中大别片麻岩的多阶段演化: 锆石 U-Pb 年代学证据. 科学通报, 49(16): 1653-1659.
106. 徐汉林, 付万德, 徐嘉炜. 1998. 衡山界牌倾滑韧性剪切带的变形特征与应变分析. 湖南地质, 17(2): 85-90.
107. 徐树桐, 刘贻灿, 江来利, 吴维平, 陈冠宝. 2002. 大别山造山带的构造几何学和运动学. 合肥: 中国科学技术大学出版社. 1-133.
108. 徐树桐, 苏 文, 刘贻灿, 王汝成, 江来利, 吴维平. 1999. 大别山北部榴辉岩的发现及其岩相学特征. 科学通报, 44(13): 1452-1456
109. 徐树桐, 刘贻灿, 陈冠宝, R. Compagnoni, F. Rolfo, 何谋春, 刘慧芳. 2003. 大别山、苏鲁地区榴辉岩中新发现的微粒金刚石. 科学通报, 48(10): 1069-1075
110. 徐义刚, 李洪颜, 庞崇进, 何斌. 2009. 论华北克拉通破坏的时限. 科学通报, 54(14): 1974-1989.
111. 徐政语, 林舸, 刘池阳, 王岳军, 郭锋. 2004. 从江汉叠合盆地构造形变特征看华南与华北陆块的拼贴过程. 地质科学, 39(2): 284-295.
112. 许德如, 王力, 李鹏春, 陈广浩, 贺转利, 符巩固, 吴俊. 2009. 湘东北地区连云山花岗岩的成因及地球动力学暗示. 岩石学报, 25(5): 1056-1078.

113. 许光, 王二七. 2010. 桐柏杂岩的中生代隆升机制及其与南阳盆地沉降的耦合关系. 地质科学, 45(3): 626- 652.
114. 许长海, 周祖翼, 马昌前, P. W. Reiners. 2001. 大别造山带 140-85 Ma 热窗伸展作用——年代学约束. 中国科学(D 辑), 31(11): 925-937.
115. 许长海, 周祖翼, 常远, GUILLOT François. 2010. 大巴山弧形构造带形成与两侧隆起的关系: FT 和(U-Th)/He 低温热年代约束. 中国科学: 地球科学, 40(12): 1684-1696.
116. 薛怀民, 董树文, 刘晓春. 2003. 北大别大山坑二长花岗片麻岩的地球化学特征与锆石 U-Pb 年代学. 地球科学进展, 18(2): 192-197.
117. 薛怀民, 马芳, 宋永勤. 2011. 扬子克拉通北缘随(州)-枣(阳)地区新元古代变质岩浆岩的地球化学和 SHRIMP 锆石 U-Pb 年代学研究. 岩石学报, 27(4): 1116-1130.
118. 杨进辉, 吴福元. 2009. 华北东部三叠纪岩浆作用与克拉通破坏. 中国科学: 地球科学, 39(7): 910-921.
119. 杨坤光, 程万强, 朱清波, 李学刚. 2012. 论大别山南缘襄樊-广济断裂的两次向南逆冲推覆. 地质论评, 57(4): 480-494.
120. 喻爱南, 叶柏龙, 彭恩生, 1998. 湖南桃林大云山变质核杂岩构造与成矿关系. 大地构造与成矿, 22(1): 82-88.
121. 张或丹. 1986. 黄陵背斜的形成和构造发展初探. 江汉石油学院学报, 10(1): 29-40.
122. 张旗, 钱青, 王二七, 王焰, 赵太平, 郝杰, 郭光军. 2001. 燕山中晚期的中国东部高原: 埃达克岩的启示. 地质科学, 36(2): 248-255
123. 张旗, 王焰, 熊小林, 李承东. 2008. 埃达克岩和花岗岩: 挑战与机遇. 北京: 中国大地出版社, 1-344.
124. 张旗, 李承东. 2012. 花岗岩: 地球动力学意义. 北京: 海洋出版社, 1-287.
125. 张业明, 熊成云, 韦昌山, 1996, 大磊山变质核杂岩基本特征及成因探讨. 华南地质与矿产, (3): 39-45.
126. 张岳桥, 徐先兵, 贾东, 舒良树. 2009. 华南早中生代从印支期碰撞构造体系向燕山期俯冲构造体系转换的形变记录. 地学前缘, 16(1): 234-247.
127. 张岳桥, 董树文, 李建华, 崔建军, 施炜, 苏金宝, 李勇. 2012. 华南中生代大地构造研究新进展. 地球学报, 33(3): 257-279.
128. 赵小明, 童金南, 姚华舟, 田洋. 2010. 三峡地区印支运动的沉积响应. 古地理学报, 12(2): 177-184.
129. 赵子福, 郑永飞. 2009. 俯冲大陆岩石圈重熔: 大别-苏鲁造山带中生代岩浆岩成因. 中国科学(D 辑), 39(7): 888-909
130. 郑亚东, 张青. 1993. 内蒙古亚干变质核杂岩与伸展拆离断层. 地质学报, 67 (4): 301-312.
131. 郑永飞. 2008. 超高压变质与大陆碰撞研究进展: 以大别-苏鲁造山带为例. 科学通报, 53(18): 2129-2152.
132. 钟增球, 索书田, 张宏飞, 周汉文. 2001. 桐柏-大别碰撞造山带的基本组成与结构. 地球科学, 26(6): 560-567.
133. 周建波, 郑永飞, 李龙, 谢智. 2001. 扬子大陆陆块俯冲的构造加积楔. 地质学报, 75(3): 338-352.
134. 周新华. 2009. 华北中-新生代大陆岩石圈转型的研究现状与方向——兼评“岩石圈减薄”和“克拉通破坏”. 高校地质学报, 15: 1-18
135. 朱光, 谢成龙, 向必伟, 胡召齐, 王勇生, 李鑫. 2007. 洪镇变质核杂岩的形成机制及其大地构造意义. 中国科学(D 辑), 37: 584-592
136. 朱日祥, 陈凌, 吴福元, 刘俊来. 2011. 华北克拉通破坏的时间、范围与机制. 中国科学: 地球科学, 41(5): 583-592.

137. 邹慧娟, 马昌前, 王连训. 2011. 湘东北幕阜山含绿帘石花岗闪长岩岩浆的上升速率: 岩相学与矿物化学证据. 地质学报, 85(3): 366-378.
138. Ames, L., Tilton, G.R., Zhou, G.Z., 1993. Timing of collision of the Sino-Korean and Yangtze cratons: U-Pb zircon dating of coesite-bearing eclogites. Geology 21, 339-342.
139. Ames, L., Zhou, G.Z., Xiong, B.C., 1996. Geochronology and geochemistry of ultrahigh-pressure metamorphism with implications for collision of Sino-Korea and Yangtze cratons, central China. Tectonics 15, 472-489.
140. Ayers, J.C., Dunkle, S., Gao, S., Miller, C.F., 2002. Constraints on timing of peak and retrograde metamorphism in Dabie Shan Ultrahigh-Pressure Metamorphic Belt, east central China, using U-Th-Pb dating of zircon and monazite. Chemical Geology 186, 315-331.
141. Borradaile, G.J., Henry, B., 1997. Tectonic applications of magnetic susceptibility and its anisotropy. Earth-Science Reviews 42, 49-93.
142. Bryant, D.L., Ayers, J.C., Gao, S., Miller, C.F., Zhang, H.F., 2004. Geochemical, age, and isotopic constraints on the location of the Sino-Korean/Yangtze suture and evolution of the northern Dabie complex, east central China. Geological Society of America Bulletin 116, 698-717.
143. Burchfiel, B.C., Chen, Z., Liu, Y., Royden, L.H., 1995. Tectonics of the Longmen Shan and adjacent regions. International Geology Review 37, 661-735.
144. Carlson, R.W., Pearson, D.G., James D.E., 2005. Physical, chemical, and chronological characteristics of continental mantle. Reviews of Geophysics 43, RG1001, doi:10.1029/2004RG000156.
145. Carswell, D.A., O'Brien, P.J., Wilson, R.N., Zhai, M., 1997. Thermobarometry of phengite bearing eclogites in the Dabie Mountains of Central China. Journal of Metamorphic Geology 15, 239-252.
146. Carter, A., Clift, P., 2008. Was the Indosinian orogeny a Triassic mountain building or a thermotectonic reactivation event? Comptes Rendus Géoscience 340, 83-93.
147. Carter, A., Roques, D., Bristow, C., Kinny, P., 2001. Understanding Mesozoic accretion in Southeast Asia: significance of Triassic thermotectonism (Indosinian orogeny) in Vietnam. Geology 29, 211-214.
148. Charles, N., Gumiaux, C, Augier, R., Chen, Y., Faure, M., Lin, W., Zhu, R.X., 2012. Metamorphic Core Complex dynamics and structural development: Field evidences from the Liaodong Peninsula (China, East Asia). Tectonophysics 560-561, 22-50.
149. Charles, N., Gumiaux, C., Augier, R., Chen, Y., Lin, W., Zhu, R., 2011. Metamorphic Core Complex vs. Synkinematic pluton in continental extension setting: insights from key structures (Shandong Province, eastern China). Journal of Asian Earth Sciences 40, 261-278.
150. Charvet, J., 2013. The Neoproterozoic-Early Paleozoic tectonic evolution of the South China Block: An overview. Journal of Asian Earth Science 74, 198-209.
151. Charvet, J., Shu, L.S., Faure, M., Choulet, F., Wang, B., Lu, H.F., Le Breton, N., 2010. Structural development of the Lower Paleozoic belt of South China: Genesis of an intracontinental orogen. Journal of Asian Earth Science 39, 309-330.
152. Charvet, J., Shu, L.S., Shi, Y.S., Guo, L.Z., Faure, M., 1996. The building of south China: Collision of Yangzi and Cathaysia blocks, problems and tentative answers. Journal of Southeastern Asian Earth Science 13, 223-235.
153. Chavagnac, V., Jahn, B.M., 1996. Coesite-bearing eclogites from the Bixiling complex Dabie Mountains, China: Sm-Nd ages, geochemical characteristics and tectonic implications. Chemical Geology 133, 29-51.
154. Chavagnac, V., Jahn, B.M., Villa, I.M., Whitehouse, M.J., Liu, D.Y., 2001. Multichronometric evidence for an in situ origin of the ultrahigh-pressure metamorphic terrane of Dabieshan, China. Journal of Geology 109, 633-646.
155. Chen, F.K., Guo, J.H., Jiang, L.L., Siebel, W., Cong, B.L., Satir, M., 2003. Provenance of the

Beihuaiyang lower-grade metamorphic zone of the Dabie ultrahigh-pressure collisional orogen, China: evidence from zircon ages. Journal of Asian Earth Sciences 22, 343-352.

156. Chen, K., Gao, S., Wu, Y.B., Guo, J.L., Hu, Z.C., Liu, Y.S., Zong, K.Q., Liang, Z.W., Geng, X.L., 2013. 2.6-2.7 Ga crustal growth in Yangtze craton, South China. Precambrian Research 224, 472-490.
157. Chen, L., 2010. Concordant structural variations from the surface to the base of the upper mantle in the North China Craton and its tectonic implications. Lithos 120, 96-115.
158. Chen, L., Ma, C.Q., She, Z.B., Mason, R., Zhang, J.Y., Zhang, C., 2009. Petrogenesis and tectonic implications of A-type granites in the Dabie orogenic belt, China: Geochronological and geochemical constraints. Geological Magazine 146, 638-651.
159. Chen, S.F., Wilson, C.J.L., 1996. Emplacement of the Longmen Shan Thrust-Nappe Belt along the eastern margin of the Tibetan Plateau. Journal of Structural Geology 18, 413-440.
160. Cheng, H., DuFrane, S.A., Vervoort, J.D., Nakamura, E., Zheng, Y.F., Zhou, Z.Y., 2010. Protracted oceanic subduction prior to continental subduction: new Lu-Hf and Sm-Nd geochronology of oceanic-type high-pressure eclogite in the western Dabie orogen. American Mineralogist 95, 1214-1223.
161. Cheng, H., King, R.L., Nakamura, E., Vervoort, J.D., Zheng, Y.F., Ota, T., Wu, Y.B., Kobayashi, K., Zhou, Z.Y., 2009. Transitional time of oceanic to continental subduction in the Dabie orogen: constraints from U-Pb, Lu-Hf, Sm-Nd and Ar-Ar multichronometric dating. Lithos 101, 327-342.
162. Cheng, H., Zhang, C., Vervoort, D.J., Wu, Y.B., Zheng, Y.F., Zheng, S., Zhou, Z.Y., 2011. New Lu-Hf geochronology constrains the onset of continental subduction in the Dabie orogen. Lithos 121, 41-54.
163. Cheng, H., Zhang, C., Vervoort, D.J., Zhou, Z.Y., 2013. New Lu-Hf and Sm-Nd geochronology constrains the subduction of oceanic crust during the Carboniferous-Permian in the Dabie orogen. Journal of Asian Earth Sciences 63, 139-150.
164. Cheng, W.Q., Yang, K.G., Kusky, T.M., Xiao, H., 2012. Kinematic and thermochronological constraints on the Xincheng-Huangpi fault and Mesozoic two-phase extrusion of the Tongbai-Dabie Orogen Belt. Journal of Asian Earth Sciences 60, 160-173.
165. Chu, Y., Faure, M., Lin, W., Wang, Q.C., 2012a. Early Mesozoic Tectonics of the South China block: Insights from the Xuefengshan intracontinental orogen. Journal of Asian Earth Sciences 61,199-220.
166. Chu, Y., Faure, M., Lin, W., Wang, Q.C., Ji, W.B., 2012b. Tectonics of the Middle Triassic intracontinental Xuefengshan Belt, South China: new insights from structural and chronological constraints on the basal décollement zone. International Journal of Earth Sciences 101, 2125-2150.
167. Chu, Y., Lin, W., 2014. Phanerozoic polyorogenic deformation in southern Jiuling Massif, northern South China block: Constraints from structural analysis and geochronogy. Journal of Asian Earth Sciences 86, 117-130.
168. Cocherie, A., Albarère de, F., 2001. An improved U-Th-Pb age calculation for electron micropobe dating of monazite. Geochimica et Cosmochimica Acta 65, 4509-4522.
169. Cocherie, A., Legendre, O., Peucat, J.J., Kouamelan, A.N., 1998. Geochronology of polygenetic monazites constrained by in situ electron micropobe Th-U-total lead determination: Implications for lead behaviour in monazite. Geochimica et Cosmochimica Acta 62, 2475-2497.
170. Condon, D., Zhu, M., Bowring, S., Wang, W., Yang, A., Jin, Y., 2005. U-Pb ages from the Neoproterozoic Doushantuo Formation, China. Science, 308, 95-98.
171. Cong, B.L., 1996. Ultrahigh-pressure metamorphic rocks in the Dabieshan-Sulu region of China. Beijing: Science Press. 1-224.
172. Cui, J.J., Liu, X.C., Dong, S.W., Hu, J.M., 2012. U-Pb and $^{40}Ar/^{39}Ar$ geochronology of the Tongbai complex, central China: Implications for Cretaceous exhumation and lateral extrusion

of the Tongbai-Dabie HP/UHP terrane. Journal of Asian Earth Sciences 47, 155-170.
173. Dai, L.Q., Zhao, Z.F., Zheng, Y.F., Li, Q.L., Yang, Y.H., Dai, M.N., 2011. Zircon Hf-O isotope evidence for crust-mantle interaction during continental deep subduction. Earth and Planetary Science Letters 308, 224-244.
174. Daoudene, Y., Gapais, D., Ledru, P., Cocherie, A., Hocquet, S., Donskaya, T.V., 2009. The Ereendavaa Range (north-eastern Mongolia): an additional argument for Mesozoic extension throughout eastern Asia. International Journal of Earth Science 98, 1381-1393.
175. Daoudene, Y., Ruffet, G., Cocherie, A., Ledru, P., Gapais, D., 2013. Timing of exhumation of the Ereendavaa metamorphic core complex (north-eastern Mongolia)—U-Pb and $^{40}Ar/^{39}Ar$ constraints. Journal of Asian Earth Sciences 62, 98-116.
176. Darby, B.J., Davis, G.A., Zhang, X.H., Wu, F,Y., Wilde, S., Yang, J.H., 2004. The newly discovered Waziyu metamorphic core complex, YiwulüShan, western Liaoning Province, Northwest China. 地学前缘, 11(3): 145-155.
177. Davis, G.A., Qian, X.L., Zheng, Y.D., Tong, H.M., Yu, H., Wang, C., Gehrels, G.E., Shafiquallah, M., Fryxell, J.E., 1996. Mesozoic deformation and plutonism in the Yungmeng Shan: a metamorphic core complex north of Beijing, China. In: Yin, A., Harrison, T.A., eds., The tectonic evolution of Asia. Cambridge University Press, New York, 253-280.
178. Davis, G.A., Wang, C., Zheng, Y., Zhang, J., Zhang, C., Gehrels, G.E., 1998. The enigmatic Yinshan fold-and-thrust belt of northern China: New views on its intraplate contractional styles. Geology 26, 43-46.
179. Davis, G.A., Zheng, Y.D., Wang, C., Darby, B.J., Zhang, C.H., Gehrels, G., 2001. Mesozoic tectonic evolution of the Yanshan fold and thrust belt, with emphasis on Hebei and Liaoning provinces, northern China. In: Hendrix, M,S., Davis, G.A., eds., Paleozoic and Mesozoic tectonic evolution of Central and Asia: From continental assembly to intracontinental deformation. Geological Society of American Memoir 194, 171-194.
180. Davis, G.A., Darby, B.J., Zheng, Y., Spell, T.L. 2002. Geometric and temporal evolution of an extensional detachment fault, Hohhot metamorphic core complex, Inner Mongolia, China. Geology 30, 1003-1006.
181. Davis, G.A., Darby, B.J., 2010. Early Cretaceous overprinting of the Mesozoic Daqing Shan fold-and-thrust belt by the Hohhot metamorphic core complex, Inner Mongolia, China. Earth Science Frontiers 17, 1-20.
182. Deng, J.F., Mo, X.X., Zhao, H.L., Wu, Z.X., Luo, Z.H., Su, S.G., 2004. A new model for the dynamic evolution of Chinese lithosphere: continental roots-plume tectonics. Earth Science Reviews 65, 223-275.
183. Donskaya, T.V., Windley, B.F., Mazukabzov, A.M., Kröner, A., Sklyarov, E.V., Gladkochub, D.P., Ponomarchuk, V.A., Badarch, G., Reichow, M.K., Hegner, E., 2008. Age and evolution of late Mesozoic metamorphic core complexes in southern Siberia and northern Mongolia, Journal of the Geological Society 165, 405-421.
184. Eide, E.A., Liou, J.G., 2000. High-pressure blueschists and eclogites in Hong'an: a framework for addressing the evolution of high- and ultrahigh-pressure rocks in central China. Lithos 52, 1-22.
185. Eide, E.A., McWilliams, M.O., Liou, J.G., 1994. ^{40}Ar-^{39}Ar geochronology and exhumation of high-pressure to ultrahigh-pressure metamorphic rocks in east-central China. Geology 22, 601-604.
186. Engebretson, D.C., Cox, A., Gordon, R.G., 1985. Relative motion between oceanic and continental plates in the Pacific basin. Geological Society of American Special Paper 206, 1-59.
187. Faure, M., Sun, Y., Shu, L., Monié, P., Charvet, J., 1996. Extensional tectonics within a subduction-type orogen. The case study of the Wugongshan dome (Jiangxi Province, SE China). Tectonophysics 263, 77-108.
188. Faure, M., Lin, W., Sun, Y., 1998. Doming in the southern foreland of the Dabieshan (Yangtse

block, China). Terra Nova 10, 307-311.
189. Faure, M., Lin, W., Shu, L., Sun, Y., Schärer, U., 1999. Tectonics of the Dabieshan (eastern China) and possible exhumation mechanism of ultrahigh-pressure rocks. Terra Nova 11, 251-258.
190. Faure, M., Lin, W., Schärer, U., Shu, L, Sun, Y., Arnaud, N., 2003. Continental subduction and exhumation of UHP rocks. Structural and geochronological insights from the Dabieshan (East China). Lithos 70, 213-241.
191. Faure, M., Shu, L.S., Wang, B., Charvet, J., Choulet, F., Monié, P., 2009. Intracontinental subduction: a possible mechanism for the Early Palaeozoic Orogen of SE China. Terra Nova 21, 360-368.
192. Faure, M., Lepvrier, C., Vuong Van Nguyen, Tich Van Vu, Lin, W., Chen, Z.C., 2014. The South China block-Indochina collision: Where, when, and how? Journal of Asian Earth Sciences 79, 260-274.
193. Feng, Z.H., Wang, C.Z., Zhang, M.H., Liang, J.C., 2012. Unusually dumbbell-shaped Guposhan-Huashan twin granite plutons in Nanling Range of south China: Discussion on their incremental emplacement and growth mechanism. Journal of Asian Earth Sciences 48, 9-23.
194. Gao, S., Ling, W.L., Qiu, Y.M., Zhou, L., Hartmann, G., Simon, K., 1999. Contrasting geochemical and Sm-Nd isotopic compositions of Archean metasediments from the Kongling high-grade terrain of the Yangtze craton: Evidence for cratonic evolution and redistribution of REE during crustal anatexis. Geochimica et Cosmochimica Acta 63, 2071-2088
195. Gao, S., Rudnick, R.L., Carlsonet, R.W., McDonough, W.F., Liu, Y.S., 2002. Re-Os evidence for replacement of ancient mantle lithosphere beneath the North China Craton. Earth Planetary Science Letters 198, 307-322.
196. Gao, S., Yang, J., Zhou, L., Li, M., Hu, Z.C., Guo, J.L., Yuan, H.L., Gong, H.J., Xiao, G.Q., Wei, J.Q., 2011. Age and growth of the Archean Kongling terrain, South China, with emphasis on 3.3 Ga granitoid gneisses. American Journal of science 311, 153-182.
197. Gilder, S., Keller, G.R., Luo, M., 1991. Timing and spatial distribution of rifting in China. Tectonophysics 197, 225-243.
198. Gilder, S.A., Gill, J., Coe, R.S., Zhao, X.X., Liu, Z.W., Wang, G.X., Yuan, K.R., Liu, W.L., Kuang, G.D., Wu, H.R., 1996. Isotopic and paleomagnetic constraints on the Mesozoic tectonic evolution of south China, Journal of Geophysical Research 101, 16137-16154.
199. Guo, L., Wang, T., Zhang, J.J., Liu, J., Qi, G.W., Li, J.B., 2012. Evolution and time of formation of the Hohhot metamorphic core complex, North China: new structural and geochronological evidence. International Geology Review 54, 1309-1331.
200. Guo, L.Z., Shi, Y.S., Lu, H.F., Ma, R.S., Dong, H., 1989. The pre-Devonian tectonic patterns and evolution of South China. Journal of Southeast Asian Earth Sciences 3, 87-93.
201. Hacker, B.R., Ratschbacher, L., Liou, J.G., 2004. Subduction, collision, and exhumation in the ultrahigh-pressure Qinling-Dabie orogen. Geological Society, London, Special Publication 226, 157-175.
202. Hacker, B.R., Ratschbacher, L., Webb, L., Dong, S.W., 1995. What brought them up? Exhumation of the Dabie Shan ultrahigh-pressure rocks. Geology 23, 743-746.
203. Hacker, B.R., Ratschbacher, L., Webb, L.E., McWilliams, M., Ireland, T., Dong, S., Calvert, A., Wenk, H.R., 2000. Exhumation of ultrahigh-pressure continental crust in east-central China: Late Triassic-Early Jurassic tectonic unroofing. Journal of Geophysical Research 105, 13339-13364.
204. Hacker, B.R., Ratschbacher, L., Webb. L., Ireland, T., Walker D., Dong, S., 1998. U/Pb zircon ages constrain the architecture of the ultrahigh-pressure Qinling-Dabie orogen, China. Earth and Planetary Science Letters 161, 215-230.

205. Hacker, B.R., Wallis, S.R., McWilliams, M.O., Gans, P.B., 2009. 40Ar/39Ar Constraints on the tectonic history and architecture of the ultrahigh-pressure Sulu orogen. Journal of Metamorphic Geology 27, 1-18.
206. Hacker, B.R., Wang, Q.C., 1995. Ar/Ar geochronology of ultrahigh-pressure metamorphism in central China. Tectonics 14, 994-1006.
207. Han, B.F., Zheng, Y.D., Gan, J.W., Chang, Z.S., 2001. The Louzidian normal fault near Chifeng, Inner Mongolia: master fault of a quasi-metamorphic core complex. International Geology Review 43, 254-264.
208. He, B., Xu, Y.G., Paterson, S., 2009. Magmatic diapirism of the Fangshan pluton, southwest of Beijing, China. Journal of Structural Geology 31, 615-626.
209. He, Y.S., Li, S.G., Hoefs, J., Huang, F., Liu, S.A., Hou, Z.H., 2011. Post-collisional granitoids from the Dabie orogen: New evidence for partial melting of a thickened continental crust. Geochimica et Cosmochimica Acta 75, 3815-3838
210. He, Y.S., Li, S.G., Hoefs, J., Kleinhanns, I.C., 2013. Sr-Nd-Pb isotopic compositions of Early Cretaceous granitoids from the Dabie orogen: Constraints on the recycled lower continental crust. Lithos 156-159, 204-217.
211. Hsü, K.J., Li, J.L, Chen, H.H., Wang, Q.C, Sun, S., Şengör, A.M.C., 1990. Tectonics of South China: key to understanding West pacific geology. Tectonophysics 183, 9-39.
212. Hsü, K.J., Sun, S., Li, J.L., Chen, H.H., Peng, H.P., Şengör, A.M.C., 1988. Mesozoic overthrust tectonics in South China. Geology 16, 418-421.
213. Hu, J.M., Chen, H., Qu, H.J., Wu, G.L., Yang, J.X., Zhang, Z.Y., 2012. Mesozoic deformations of the Dabashan in the southern Qinling orogen, central China. Journal of Asian Earth Sciences 47, 171-184.
214. Hu, S.B., Raza, A., Min, K., Kohn, B.P., Reiners, P.W., Ketcham, R.A., Wang, J.Y., Gleadow, A.J.W., 2006. Late Mesozoic and Cenozoic thermotectonic evolution along a transect from the north China craton through the Qinling orogen into the Yangtze craton, central China. Tectonics 25, TC6009, doi:10.1029/2006TC001985.
215. Huang, F., Li, S.G., Dong, F., He, Y.S., Chen, F.K., 2008. High-Mg adakitic rocks in the Dabie orogen, central China: implications for foundering mechanism of lower continental crust. Chemical Geology 255, 1-13.
216. Huang, F., Li, S.G., Dong, F., Li, Q.L., Chen, F.K.,Wang, Y., Yang,W., 2007. Recycling of deeply subducted continental crust in the Dabie Mountains, central China. Lithos 96, 151-169.
217. Jahn, B.M.,Wu, F.Y., Lo, C.H., Tsai, C.H., 1999. Crust-mantle interaction induced by deep subduction of the continental crust: geochemical and Sr-Nd isotopic evidence from post-collisional mafic-ultramafic intrusions of the northern Dabie complex. Chemical Geology 157, 119-146.
218. Jelinek, V., 1981. Characterization of the magnetic fabric of rocks. Tectonophysics 79, 563-567.
219. Ji, W.B., Lin, W., Faure, M., Chu, Y., Wu, L., Wang, F., Wang, J., Wang, Q.C., 2014. Origin and tectonic significance of the Huangling massif within the Yangtze craton, South China. Journal of Asian Earth Sciences 86, 59-75.
220. Jian, P., Kröner, A., Zhou, G.Z., 2012. SHRIMP zircon U-Pb ages and REE partition for high-grade metamorphic rocks in the North Dabie complex: Insight into crustal evolution with respect to Triassic UHP metamorphism in east-central China. Chemical Geology 328, 49-69.
221. Jiang, Y.H., Jiang, S.Y., Dai, B.Z., Liao, S.Y., Zhao, K.D., Ling, H.F., 2009. Middle to Late Jurassic felsic and mafic magmatism in southern Hunan Province, Southeast China: implications for a continental arc to rifting. Lithos 107, 185-204.
222. Jiang, Y.H., Zhao, P., Zhou, Q., Liao, S.Y., Jin, G.D., 2011. Petrogenesis and tectonic implications of Early Cretaceous S- and A-type granites in the northwest of the Gan-Hang rift, SE China. Lithos 121, 55-73.
223. Koppers, A.A.P., 2002. ArArCALC—software for $^{40}Ar/^{39}Ar$ age calculations. Computers and

Geosciences 28, 605-619.
224. Kröner, A.I., Zhang, G.W., Sun, Y., 1993. Granulites in Tongbai area, Qinling belt, China: geochemistry, petrology, single zircon geochronology, and implications for the tectonic evolution of eastern Asia. Tectonics 12, 245-255.
225. Lepvrier, C., Faure, M., Nguyen, V.V., Tich, V.V., Lin, W., Thang, T.T., Phuong, T.H., 2011. North-directed Triassic nappes in Northeastern Vietnam (East Bac Bo). Journal of Asian Earth Sciences 41, 56-68.
226. Lepvrier, C., Nguyen, V.V., Maluski, H., Phan, T.T., Tich, V.V., 2008. Indosinian tectonics in Vietnam. Comptes Rendus Geoscience 340, 94-111.
227. Li, J.H., Zhang, Y.Q., Dong, S.W., Su, J.B., Li, Y., Cui, J.J., Shi, W., 2013a. The Hengshan low-angle normal fault zone: structural and geochronological constraints on the Late Mesozoic crustal extension in South China. Tectonophysics 606, 97-115.
228. Li, J.H., Zhang, Y.Q., Dong, S.W., Shi, W., 2013b. Structural and geochronological constraints on the Mesozoic tectonic evolution of the North Dabashan zone, South Qinling, central China. Journal of Asian Earth Sciences 64, 99-114.
229. Li, J.W., Zhou, M.F., Li, X.F., Fu, Z.R., Li, Z.J., 2001. The Hunan-Jiangxi strike-slip fault system in southern China: southern termination of the Tan-Lu fault. Journal of Geodynamics 32, 333-354.
230. Li, S.G., Jagoutz, E., Chen, Y.Z., Li, Q.L., 2000. Sm-Nd and Rb-Sr isotopic chronology and cooling history of ultrahigh pressure metamorphic rocks and their country rocks at Shuanghe in the Dabie Mountains, Central China. Geochimica et Cosmochimica Acta 64, 1077-1093.
231. Li, S.G., Xiao, Y.L., Liu, D.L., Chen, Y.Z., Ge, N.J., Zhang, Z.Q., Sun, S.S., Cong, B.L., Zhang, R.Y., Hart, S.R., 1993. Collision of the North China and Yangtse blocks and formation of coesite-bearing eclogites: timing and processes. Chemical Geology 109, 89-111.
232. Li, S.Z, Zhao, G.C., Dai, L.M., Liu, X., Zhou, L.H., Santosh, M., Suo, Y.H., 2012a. Mesozoic basins in eastern China and their bearing on the deconstruction of the North China Craton. Journal of Asian Earth Sciences 47, 64-79.
233. Li, S.Z, Santosh, M., Zhao, G.C., Zhang, G.W., Jin, C., 2012b. Intracontinental deformation in a frontier of super-convergence: A perspective on the tectonic milieu of the South China Block. Journal of Asian Earth Sciences 49, 313-329.
234. Li, S.Z., Kusky, T.M., Zhao, G.C., Liu, X.C., Wang, L., Kopp, H., Hoernle, K., Zhang, G.W., Dai, L.M., 2011. Thermochronological constraints on two-stage extrusion of HP-UHP terranes in the Dabie-Sulu orogen, east-central China. Tectonophysics 504, 25-42.
235. Li, S.Z., Kusky, T.M., Zhao, G.C., Liu, X.C., Zhang, G.W., Kopp, H., Wang, L., 2010. Two stage Triassic exhumation of HP-UHP terranes in the western Dabie orogen of China: constraints from structural geology. Tectonophysics 490, 267-293.
236. Li, X.H., 2000. Cretaceous magmatism and lithospheric extension in Southeast China. Journal of Asian Earth Sciences 18, 293-305.
237. Li, X.H., Li, W.X., Li, Z.X., Lo, C.H., Wang, J., Ye, M.F., Yang, Y.H., 2009. Amalgamation between the Yangtze and Cathaysia Blocks in South China: constraints from SHRIMP U-Pb zircon ages, geochemistry and Nd-Hf isotopes of the Shuangxiwu volcanic rocks. Precambrian Research 174, 117-128.
238. Li, X.H., Liu, Y., Li, Q.L., Guo, C.H., Chamberlain, K.R., 2009. Precise determination of Phanerozoic zircon Pb/Pb age by multi-collector SIMS without external standardization. Geochemistry Geophysics Geosystem 10, Q04010. doi:10.1029/GC002400.
239. Li, X.H., Li, W.X., Wang, X.C., Li, Q.L., Liu, Y., Tang, G.Q., Gao, Y.Y., Wu, F.Y., 2010. SIMS U-Pb zircon geochronology of porphyry Cu-Au-(Mo) deposits in Yangtze River Metallogenic Belt: magmatic response to Jura-Cretaceous tectonic switch in SE China. Lithos 119, 427-438.
240. Li, X.H., Li, Z.X., Li, W.X., Wang, X.C., Gao, Y.Y., 2013. Revisiting the “C-type adakites” of the Lower Yangtze River Belt, central eastern China: In-situ zircon Hf-O isotope and

geochemical constraints. Chemical Geology 345, 1-15.
241. Li, X.M., Shan, Y.H., 2011. Diverse exhumation of the Mesozoic tectonic belt within the Yangtze Plate, China, determined by apatite fission-track thermochronology. Geosciences Journal 15, 349-357.
242. Li, X.P., Zheng, Y.F., Wu, Y.B., Chen, F.K., Gong, B., Li, Y.L., 2004. Low-T eclogite in the Dabie terrane of China: petrological and isotopic constraints on fluid activity and radiometric dating. Contributions to Mineralogy and Petrology 148, 443-470.
243. Li, Z.X., Evans, D.A.D., Zhang, S., 2004. A 90° spin on Rodinia: possible causal links between the Neoproterozoic supercontinent, superplume, true polar wander and low-latitude glaciations. Earth and Planetary Science Letters 220, 409-421.
244. Li, Z.X., Li, X.H., 2007. Formation of the 1300-km-wide intracontinental orogen and postorogenic magmatic province in Mesozoic South China: A flat-slab subduction model. Geology 35, 179-182.
245. Li, Z.X., Li, X.H., Wartho, J.A., Clark, C., Li, W.X., Zhang, C.L., Bao, C., 2010. Magmatic and metamorphic events during the early Paleozoic Wuyi-Yunkai orogeny, southeastern South China: New age constraints and pressure-temperature conditions. Geological Society of America Bulletin 122, 772-793.
246. Lin, W., Faure, M., Monié, P., Schärer, U., Zhang, L.S., Sun, Y., 2000. Tectonics of SE China, new insights from the Lushan massif (Jiangxi Province). Tectonics 19, 852-871.
247. Lin, W., Wang, Q.C., 2006. Late Mesozoic extensional tectonics in North China block: a crustal response to the lithosphere removal of North China Craton? Bulletin de la Société Géologique de France 177, 287-297.
248. Lin, W., Faure, M., Monie, P., Wang, Q.C., 2007a. Polyphase Mesozoic tectonics in the eastern part of North China Block: insights from the Eastern Liaoning Peninsula massif (NE China). In: Mesozoic Sub-continental Lithospheric Thinning Under Eastern Asia. Geological Society, London, Special Publications 280, 153-169.
249. Lin, W., Enami, M., Faure, M., Schärer, U., Arnaud, N., 2007b. Survival of eclogite xenolith in a Cretaceous granite intruding the central Dabieshan migmatite gneiss dome (eastern China) and its tectonic implications. International Journal of Earth Sciences 96, 707-724.
250. Lin, W., Faure, M., Monié, P., Schärer, U., Panis, D., 2008a. Mesozoic Extensional Tectonics in Eastern Asia: The South Liaodong Peninsula Metamorphic Core Complex (NE China). The Journal of Geology 116, 134-154.
251. Lin, W., Wang, Q.C., Chen, K., 2008b. Phanerozoic tectonics of south China block: New insights from the polyphase deformation in the Yunkai massif. Tectonics 27, TC6004, doi:10.1029/2007TC002207.
252. Lin, W., Shi, Y.H., Wang, Q.C., 2009. Exhumation tectonics of the HP-UHP orogenic belt in Eastern China: New structural-petrological insights from the Tongcheng massif, Eastern Dabieshan. Lithos 109, 285-303.
253. Lin, W., Monié, P., Faure, M., Schärer, U., Shi, Y.H., Le Breton, N., Wang, Q.C., 2011. Cooling paths of the NE China crust during the Mesozoic extensional tectonics: example from the south-Liaodong peninsula metamorphic core complex. Journal of Asian Earth Sciences 42, 1048-1065.
254. Lin, W., Faure, M., Chen, Y., Ji, W.B., Wang, F., Wu, L., Charles, N., Wang, Q.C., 2013a. Late Mesozoic compressional to extensional tectonics in the Yiwulüshan massif, NE China and its bearing on the evolution of the Yinshan-Yanshan orogenic belt. Part I: Structural analyses and geochronological constraints. Gondwana Research 23, 54-77.
255. Lin, W., Charles, N., Chen, Y., Chen, K., Faure, M., Wu, L., Wang, F., Li, Q.L., Wang, J., Wang, Q.C., 2013b. Late Mesozoic compressional to extensional tectonics in the Yiwulüshan massif, NE China and their bearing on the Yinshan-Yanshan orogenic belt. Part II: Anisotropy of magnetic susceptibility and gravity modelling. Gondwana Research 23, 78-94.

256. Ling, M.X., Wang, F.Y., Ding, X., Hu, Y.H., Zhou, J.B., Zartman, R.E., Yang, X.Y., Sun, W.D., 2009. Cretaceous ridge subduction along the Lower Yangtze river belt, eastern China. Economic Geology 104, 303-321.
257. Liou, J.G., Ernst, W.G., Zhang, R.Y., Tsujimori, T., Jahn, B.M., 2009. Ultrahigh-pressure minerals and metamorphic terranes–The view from China. Journal of Asian Earth Sciences 35, 199-231.
258. Liu, D.Y., Jian, P., Kröner, A., Xu, S.T., 2006. Dating of prograde metamorphic events deciphered from episodic zircon growth in rocks of the Dabie-Sulu UHP complex, China. Earth and Planetary Science Letters 250, 650-666.
259. Liu, J.B., Ye, K., Sun, M., 2006. Exhumation P-T path of UHP eclogites in the Hong'an area, western Dabie Mountains, China. Lithos 89, 154-173.
260. Liu, J.L., Davis, G.A., Lin, Z.Y., Wu, F.Y., 2005. The Liaonan metamorphic core complex, Southeastern Liaoning Province, North China: A likely contributor to Cretaceous rotation of Eastern Liaoning, Korea and contiguous areas. Tectonophysics 407, 65-80.
261. Liu, J.L., Shen, L., Ji, M., Guan, H.M., Zhang, Z.C., Zhao, Z.D., 2013. The Liaonan/Wanfu metamorphic core complexes in the Liaodong Peninsula: Two stages of exhumation and constraints on the destruction of the North China Craton. Tectonics 32, 1121-1141.
262. Liu, S.F., Steel, R., Zhang G.W., 2005. Mesozoic sedimentary basin development and tectonic implication, northern Yangtze Block, eastern China: record of continent-continent collision. Journal of Asian Earth Sciences 25, 9-27.
263. Liu, X., Li, S.Z., Suo, Y.H., Liu, X.C., Dai, L.M., Santosh, M., 2011. Structural anatomy of the exhumation of high-pressure rocks: constraints from the Tongbai Collisional Orogen and surrounding units. Geological Journal 46, 156-172.
264. Liu, X.C., Wei, C.J., Li, S.Z., Dong, S.W., Liu, J.M., 2004. Thermobaric structure of a traverse across western Dabieshan: implications for collision tectonics between the Sino-Korean and Yangtze cratons. Journal of Metamorphic Geology 22, 361-379.
265. Liu, X.C., Jahn, B.-M., Dong, S.W., Lou, Y.X., Cui, J.J., 2008. High-pressure metamorphic rocks from Tongbaishan, central China: U-Pb and $^{40}Ar/^{39}Ar$ age constraints on the provenance of protoliths and timing of metamorphism. Lithos 105, 301-318.
266. Liu, X.C., Jahn, B.M., Cui, J.J., Li, S.Z., Wu, Y.B., Li, X.H., 2010. Triassic retrograded eclogites and Cretaceous gneissic granites in the Tongbai Complex, central China: Implications for the architecture of the HP/UHP Tongbai-Dabie-Sulu collision zone. Lithos 119, 211-237.
267. Liu, X.C., Wu, Y.B., Gao, S., Wang, J., Peng, M., Gong, H.J., Liu, Y.S., Yuan, H.L., 2011a. Zircon U-Pb and Hf evidence for coupled subduction of oceanic and continental crust during the Carboniferous in the Huwan shear zone, western Dabie orogen, central China. Journal of Metamorphic Geology 29, 233-249.
268. Liu, X.C., Jahn, B.M., Hu, J., Li, S.Z., Liu, X., Song, B., 2011b. Metamorphic patterns and SHRIMP zircon ages of medium-to-high grade rocks from the Tongbai orogen, central China: implications for multiple accretion/collision processes prior to terminal continental collision. Journal of Metamorphic Geology 29, 979-1002.
269. Liu, X.C., Jahn, B.M., Li, S.Z., Liu, Y.S., 2013. U-Pb zircon age and geochemical constraints on tectonic evolution of the Paleozoic accretionary orogenic system in the Tongbai orogen, central China. Tectonophysics 599, 67-88.
270. Liu, X.M., Gao, S., Diwu, C.R., Ling, W.L., 2008. Precambrian growth of Yangtze craton as revealed by detrital zircon studies. American Journal of Science 308, 421-468.
271. Liu, Y.C., Li, S.G., Xu, S.T, Jahn, B.M., Zheng, Y.F., Zhang, Z.Q., Jiang, L.L., Chen, G.B., Wu, W.P., 2005. Geochemistry and geochronology of eclogites from the northern Dabie Mountains, central China. Journal of Asian Earth Sciences 25, 431-443.

272. Liu, Y.C., Li, S.G., Gu, X.F., Xu, S.T, Chen, G.B., 2007a. Ultrahigh-pressure eclogite transformed from mafic granulite in the Dabie orogen, east-central China. Journal of Metamorphic Geology 25, 975-989.
273. Liu, Y.C., Li, S.G., Xu, S.T, 2007b. Zircon SHRIMP U-Pb dating for gneisses in northern Dabie high T/P metamorphic zone, central China: Implications for decoupling within subducted continental crust. Lithos 96, 170-185.
274. Liu, Y.C., Gu, X.F., Rolfo, F., Chen, Z.Y., 2011a. Ultrahigh-pressure metamorphism and multistage exhumation of eclogite of the Luotian dome, North Dabie Complex Zone (central China): Evidence from mineral inclusions and decompression textures. Journal of Asian Earth Sciences 42, 607-617.
275. Liu, Y.C., Gu, X.F., Li, S.G., Hou, Z.H., Sonh, B., 2011b. Multistage metamorphic events in granulitized eclogites from the North Dabie complex zone, central China: Evidence from zircon U-Pb age, trace element and mineral inclusion. Lithos 122, 107-121.
276. Lovera, O.M., Grove, M., Harrison, T.M., 2002. Systematic analysis of K-feldspar $^{40}Ar/^{39}Ar$ step heating results II: Relevance of laboratory argon diffusion properties to nature. Geochimica et Cosmochimica Acta 66, 1237-1255.
277. Lovera, O.M., Grove, M., Harrison, T.M., Mahon, K.I., 1997. Systematic analysis of K-feldspar $^{40}Ar/^{39}Ar$ step heating results: I. Significance of activation energy determinations. Geochimica et Cosmochimica Acta 61, 3171-3192.
278. Ludwig, K.R., 2003. User's manual for Isoplot 3.00: A geochronological toolkit for Microsoft Excel. Berkeley Geochronology Center Special Publication No. 4, 1-75.
279. Malaspina, N., Hermann, J., Scambelluri, M., Compagnoniet, R., 2006. Multistage metasomatism in ultrahigh-pressure mafic rocks from the north Dabie complex (China). Lithos 90, 19-42.
280. Maruyama, S., Isozaki, Y., Kimura, G., Terabayashi, M., 1997. Paleogeographic maps of the Japanese Islands: Plate tectonic synthesis from 750 Ma to present. Island Arc 6, 121-142.
281. Mattauer, M., Matte, P., Maluski, H., Xu, Z.Q, Zhang, Q.W., Wang, Y.M., 1991. La limite Chine du Nord-Chine du Sud au Paléozoïque et au Trias: Nouvelles données structurales et radiométriques dans le massif du Dabieshan (chaîne des Qinling). Comptes Rendus de l'Académie des Sciences-Series II 312, 1227-1233.
282. Mattauer, M., Matte, Ph., Malavieille, J., Tapponnier, P., Maluski, H., Xu, Z.Q., Lu, Y.L, Tang, Y.Q, 1985. Tectonics of Qinling belt: build-up and evolution of eastern Asia. Nature 317, 496-500.
283. Mazukabzov, A.M., Donskaya, T.V., Gladkochub, D.P., Sklyarov, E.V., Ponomarchuk, V.A., Sal'nikova, E.B., 2006. Structure and age of the metamorphic core complex of the Burgutui ridge (South-western Transbaikalia region). Doklady Earth Sciences 407, 179-183.
284. McDougall, I., Harrison, T.M., 1999. Geochronology and Thermochronology by the $^{40}Ar/^{39}Ar$ Method. Oxford: Oxford University Press, 1-269.
285. Meng, Q.R, Hu, J.M., Jin, J.Q., Zhang, Y., Xu, D.F., 2003. Tectonics of the late Mesozoic wide extension basin system in the China-Mongolia border region. Basin Research 15, 397-415.
286. Meng, Q.R., 2003. What drove late Mesozoic extension of the northern China-Mongolia tract? Tectonophysics 369, 155-174.
287. Meng, Q.R., Wang, E., Hu, J.M., 2005. Mesozoic sedimentary evolution of the northwest Sichuan basin: Implication for continued clockwise rotation of the South China block. Geological Society of America Bulletin 117, 396-410.
288. Menzies, M., Xu, Y.G., Zhang, H.F., Fan, W.M., 2007. Integration of geology, geophysics and geochemistry: A key to understanding the North China Craton. Lithos 96, 1-21.
289. Okay, A.I., 1993. Petrology of a diamond and coesite-bearing metamorphic terrain: Dabie Shan, China. European Journal of Mineralogy 5, 659-675.

290. Okay, A.I., Sengör, A.M.C., Satir, M., 1993. Tectonics of an ultrahigh-pressure metamorphic terrane: The Dabie Shan/Tongbai Shan orogen, China. Tectonics 12, 1320-1334.
291. Peng, S.B., Kusky, T.M., Jiang, X.F., Wang, L., Wang, J.P., Deng, H., 2012. Geology, geochemistry, and geochronology of the Miaowan ophiolite, Yangtze craton: Implications for South China's amalgamation history with the Rodinian supercontinent. Gondwana Research 21, 577-597.
292. Pommier, A., Cocherie A., Legendre, O., 2002. EPMA dating user's manual: Age calculation from electron probe microanalyser measurements of U-Th-Pb. BRGM, 9 p.
293. Qiu, Y.M., Gao, S., McNaughton, N.J., Groves, D.I., Ling, W.L., 2000. First evidence of > 3.2 Ga continental crust in the Yangtze craton of south China and its implications for Archean crustal evolution and Phanerozoic tectonics. Geology 28, 11-14.
294. Ratschbacher, L., Franz, L., Enkelmann, E., Jonckheere, R., Pörschke, A., Hacker, B.R., Dong, S., Zhang, Y., 2006. The Sino-Korean-Yangtze suture, the Huwan detachment, and the Paleozoic-Tertiary exhumation of (ultra)high-pressure rocks along the Tongbai-Xinxian-Dabie Mountains. In: Hacker, B.R., McClelland, W.C., Liou, J.G., eds., Ultrahigh pressure metamorphism: Deep continental subduction. Geological Society of America Special Paper 403, 45-75.
295. Ratschbacher, L., Hacker, B.R., Calvert, A., Webb, L.E., Grimmer, J.C., McWilliams, M.O., Ireland, T., Dong, S., Hu, J., 2003. Tectonics of the Qinling (central China): tectonostratigraphy, geochronology, and deformation history. Tectonophysics 366, 1-53.
296. Ratschbacher, L., Hacker, B.R., Webb, L.E., McWilliams, M., Ireland, T., Dong, S., Clavert, A., Chateigner, D., Wenk, H.R., 2000. Exhumation of the ultrahigh-pressure continental crust in east central China: Cretaceous and Cenozoic unroofing and the Tan-Lu fault. Journal of Geophysical Research 105, 13303-13338.
297. Ren, J.Y., Tamaki, K., Li, S.T., Zhang, J.X., 2002. Late Mesozoic and Cenozoic rifting and its dynamic setting in Eastern China and adjacent areas. Tectonophysics 344, 175-205.
298. Richardson, N.J., Densmore, A.L., Seward, D., Wipf, M., Yong, L., 2010. Did incision of the Three Gorges begin in the Eocene? Geology 38, 551-554.
299. Roger, F., Jolivet, M., Malavieille, J., 2008. Tectonic evolution of the Triassic fold belts of Tibet. Comptes Rendus Geoscience 340, 180-189.
300. Roger, F., Jolivet, M., Malavieille, J., 2010. The tectonic evolution of the Songpan-Garzê (North Tibet) and adjacent areas from Proterozoic to Present: A synthesis. Journal of Asian Earth Sciences 39, 254-269.
301. Rowley, D.B., Xue, F., Tucker, R.D., Peng, Z.X., Baker, J., Davis, A., 1997. Ages of ultrahigh pressure metamorphism and protolith orthogneisses from eastern Dabie Shan: U/Pb zircon geochronology. Earth and Planetary Science Letters 151, 191-203.
302. Schärer, U., Labrousse, L., 2003. Dating the exhumation of UHP rocks and associated crustal melting in the Norwegian Caledonides. Contributions to Mineralogy and Petrology 144, 758-770
303. Shen, C.B., Mei, L.F., Peng, L., Chen, Y.Z., Yang, Z., Hong, G.F., 2012. LA-ICPMS U-Pb zircon age constraints on the provenance of Cretaceous sediments in the Yichang area of the Jianghan Basin, central China. Cretaceous Research 34, 172-183.
304. Shi, W., Zhang, Y.Q., Dong, S.W., Hu, J.M., Wiesinger, M., Ratschbacher, L., Jonckheere, R., Li, J.H., Tian, M., Chen, H., Wu, G.L., Ma, L.C., Li, H.L., 2012. Intra-continental Dabashan orocline, southwestern Qinling, Central China. Journal of Asian Earth Sciences 46, 20-38.
305. Shi, Y.H., Lin, W., Ji, W.B., Wang, Q.C., 2014. The architecture of the HP-UHP Dabie massif: New insights from geothermobarometry of eclogites, and implication for the continental exhumation processes. Journal of Asian Earth Sciences 86, 38-58.
306. Shi, Y.H., Wang, Q.C., 2006. Changes in the peak P-T conditions across the upper contact of the UHP terrane, Dabie Shan, China: gradational or abrupt? Journal of Metamorphic Geology 24,

803-822.
307. Shu, L.S., Charvet, J., 1996. Kinematics and geochronology of the Proterozoic Dongxiang-Shexian ductile hear zone: with HP metamorphism and ophiolitic melange (Jiangnan Region, China). Tectonophysics 267, 291-302.
308. Shu, L.S., Faure, M., Wang, B., Zhou, X.M., Song, B., 2008. Late Paleozoic-Early Mesozoic geological features of South China: Response to the Indosinian collision events in Southeastern Asia. Comptes Rendus Geoscience 340, 151-165.
309. Shu, L.S., Zhou, X.M., Deng, P., Wang, B., Jiang, S.Y., Yu, J.H., Zhao, X.X., 2009. Mesozoic tectonic evolution of the Southeast China Block: New insights from basin analysis, Journal of Asian Earth Science 34, 376-391.
310. Sklyarov, E.V., Mazukabzov, A.M., Donskaya, T.V., Doronina, N.A., Shafeev, A.A., 1994. Metamorphic core complexes of the Zagan Range (Transbaikalia). Doklady Earth Sciences 339, 83-86.
311. Sun, M., Chen, N.S., Zhao, G.C., Wild, S.A., Ye, K., Guo, J.H., Chen, Y., Yuan, C., 2008. U-Pb zircon and Sm-Nd isotopic study of the Huangtuling granulite, Dabie-Sulu belt, China: implication for the Paleoproterozoic tectonic history of the Yangtze Craton. American Journal of Science 308, 469-483.
312. Sun, W.D., Williams, I.S., Li, S.G., 2002. Carboniferous and Triassic eclogites in the western Dabie Mountains, east-central China: evidence for protracted convergence of the North and South China Blocks. Journal of Metamorphic Geology 20, 873-886.
313. Sun, W.D., Ding, X., Hu, Y.H., Li, X.H., 2007. The golden transformation of the Cretaceous plate subduction in the west Pacific. Earth and Planetary Science Letters 262, 533-542.
314. Suo, S.T., Zhong, Z.Q., Zhou, H.W., You, Z.D., Zhang, H.F., Zhang, L., 2005. Tectonic evolution of the Dabie-Sulu UHP and HP metamorphic belts, east-central China: Structural record in UHP rocks. International Geology Review 47, 1207-1221.
315. Talbot, J.Y., Martelet, G., Courrioux, G., Chen, Y., Faure, M., 2004. Emplacement in an extensional setting of the Mont Lozère-Borne granitic complex (SE France) inferred from comprehensive AMS, structural and gravity studies. Journal of Structural Geology 26, 11-28.
316. Tarling, D.H., Hrouda, F., 1993. The magnetic anisotropy of rocks. Chapman and Hall, 217pp.
317. Tong, L.X., Jahn, B.M., Zheng, Y.F., 2011. Diverse P-T paths of the northern Dabie complex in central China and its reworking in the early Cretaceous. Journal of Asian Earth Sciences 42, 633-640.
318. Tong, W.X., Tobisch, O.T., 1996. Deformation of granitoid plutons in the Dongshan area, Southeast China: constrains on the physical conditions and timing of movement along the Changle-Nanao shear zone. Tectonophysics 267, 303-316.
319. Tsai, C.H., Liou, J.G., 2000. Eclogite-facies relics and inferred ultrahigh-pressure metamorphism in the North Dabie Complex, central-eastern China. American Mineralogist 85, 1-8.
320. Turrillot, P., Faure, M., Martelet, G., Chen, Y., Augier, R., 2011. Pluton-dyke relationships in a Variscan granitic complex from AMS and gravity modelling. Inception of the extensional tectonics in the South Armorican Domain (France). Journal of Structural Geology 33, 1681-1698.
321. Wang, D.Z., Shu, L.S., Faure, M., Sheng, W.Z., 2001. Mesozoic magmatism and granitic dome in the Wugongshan massif, Jingxi province and their genetiocl relationship to the tectonic events in southeast China. Tectonophysics 339, 259-277.
322. Wang, E, Meng, Q.R., Burchfiel, B.C., Zhang, G.W., 2003. Mesozoic large-scale lateral extrusion, rotation, and uplift of the Tongbai-Dabie shan belt in east China. Geology 31, 307-310.

323. Wang, F.Y., Ling, M.X., Ding, X., Hu, Y.H., Zhou, J.B., Yang, X.Y., Liang, H.Y., Fan, W.M., Sun, W.D., 2011. Mesozoic large magmatic events and mineralization in SE China: oblique subduction of the Pacific plate. International Geology Review 53, 704-726.
324. Wang, H., Wu, Y.B., Gao, S., Zhang, H.F., Liu, X.C., Gong, H.J., Peng, M., Wang, J., Yuan, H.L., 2011. Silurian granulite-facies metamorphism, and coeval magmatism and crustal growth in the Tongbai orogen, central China. Lithos 125, 249-271.
325. Wang, J.H., Sun, M., Deng, S.X., 2002. Geochronological constraints on the timing of migmatitization in the Dabie Shan, east-central China. European Journal of Mineralogy 14, 513-524.
326. Wang, Q., Zhao, Z.H., Bao, Z.W., Xu, J.F., Liu, W., Li, C.F., Bai, Z.H., Xiong, X.L., 2004. Geochemistry and petrogenesis of the Tongshankou and Yinzu adakitic intrusive rocks and the associated porphyry copper-molybdenum mineralization in southeast Hubei, east China. Resource Geology 54, 137-152.
327. Wang, Q., Wyman, D.A., Xu, J.F., Zhao, Z.H., Jian, P., Xiong, X.L., Bao, Z.W., Li, C.F., Bai, Z.H., 2006. Petrogenesis of Cretaceous adakitic and shoshonitic igneous rocks in the Luzong area, Anhui Province (eastern China): implications for geodynamics and Cu-Au mineralization. Lithos 89, 424-446.
328. Wang, Q., Wyman, D.A., Xu, J.F., Zhao, Z.H., Jian, P., Zi, F., 2007a. Partial melting of thickened or delaminated lower crust in the middle of eastern China: implications for Cu-Au mineralization. Journal of Geology 115, 149-161.
329. Wang, Q., Wyman, D.A., Xu, J.F, Jian. P., Zhao, Z.H., Li, C.F., Xu, W., Ma, J.L., He, B., 2007b. Early Cretaceous adakitic granites in the northern Dabie complex, central China: Implications for partial melting and delamination of thickened lower crust. Geochimica et Cosmochimica Acta 71, 2609-2636.
330. Wang, Q.C., Liu X.H., Maruyama, S., Cong, B.L., 1995. Top boundary of the Dabie UHPM rocks, central China. Journal of Southeast Asian Geology 11, 295-300.
331. Wang, Q.C., Shi, Y.H., Lin, W., Guo, J.H., 2008. Exhumation of the Dabie UHP terrane, China. International Geology Review 50, 15-31.
332. Wang, S.J., Li, S.G., An, S.C., Hou, Z.H., 2012. A granulite record of multistage metamorphism and REE behavior in the Dabie orogen: Constraints from zircon and rock-forming minerals. Lithos 136-139,109-125.
333. Wang, S.J., Li, S.G., Chen, L.J., He, Y.S., An, S.C., Shen, J., 2013. Geochronology and geochemistry of leucosomes in the North Dabie Terrane, East China: implication for post-UHPM crustal melting during exhumation. Contributions to Mineralogy and Petrology 165, 1009-1029.
334. Wang, T., Zheng, Y.D., Zhang, J.J., Zeng, L.S., Donskaya, T., Guo, L., Li J.B., 2011. Pattern and kinematic polarity of late Mesozoic extension in continental NE Asia: Perspectives from metamorphic core complexes, Tectonics 30, TC6007, doi:10.1029/2011TC002896.
335. Wang, T., Guo, L., Zheng, Y.D., Donskaya, T.V., Gladkochub, D., Zeng, L.S., Li, J.B., Wang, Y., Mazukabzov, A., 2012. Timing and processes of late Mesozoic mid-lower-crustal extension in continental NE Asia and implications for the tectonic setting of the destruction of the North China Craton: Mainly constrained by zircon U-Pb ages from metamorphic core complexes. Lithos 154, 315-345.
336. Wang, X.D., Neubauer, F., Genser, J., Yang, W.R., 1998. The Dabie UHP unit, central China: A Cretaceous extensional allochthon superposed on a Triassic orogen. Terra Nova 10, 260-267.
337. Wang, X.L., Zhou, J.C., Griffin, W.L., Wang, R.C., Qiu, J.S., O'Reilly, S.Y., Xu, X.S., Liu, X.M., Zhang, G.L., 2007. Detrital zircon geochronology of Precambrian base- ment sequences in the Jiangnan orogen: dating the assembly of the Yangtze Cathaysia blocks. Precambrian Researcher 159, 117-131.
338. Wang, Y., Zhou, L.Y., Li, J.Y., 2011. Intracontinental superimposed tectonics-A case study in

the Western Hills of Beijing, eastern China. Geological Society of America Bulletin 123, 1033-1055.

339. Wang, Y.J., Zhang, Y.H., Fan, W.M., Peng, T.P., 2005a. Structural signatures and $^{40}Ar/^{39}Ar$ geochronology of the Indosinian Xuefengshan tectonic belt, South China Block. Journal of Structural Geology 27, 985-998.
340. Wang, Y.J., Fan, W.M., Peng, T.P., Zhang, H.F., Guo, F., 2005b. Nature of the Mesozoic lithospheric mantle and tectonic decoupling beneath the Dabie Orogen, Central China: Evidence from $^{40}Ar/^{39}Ar$ geochronology, elemental and Sr-Nd-Pb isotopic compositions of early Cretaceous mafic igneous rocks. Chemical Geology 220, 165-189.
341. Wang, Y.J., Fan, W.M., Cawood, P.A., Ji, S.C., Peng,T.P., Chen, X.Y., 2007. Indosinian high-strain deformation for the Yunkaidashan tectonic belt, south China: Kinematics and $^{40}Ar/^{39}Ar$ geochronological constraints. Tectonics 26, TC6008, doi:10.1029/2007TC002099.
342. Wang, Y.J., Zhang, F.F., Fan, W.M., Zhang, G.W., Chen, S.Y., Cawood, P.A., Zhang, A.M., 2010. Tectonic setting of the South China Block in the early Paleozoic: Resolving intracontinental and ocean closure models from detrital zircon U-Pb geochronology. Tectonics 29, TC6020, doi:10.1029/2010TC002750
343. Wang, Y.S., Xiang, B.W., Zhu, G., Jiang, D.Z., 2011. Structural and geochronological evidence for Early Cretaceous orogen-parallel extension of the ductile lithosphere in the northern Dabie orogenic belt, East China. Journal of Structural Geology 33, 362-380.
344. Wang, Z.H., Lu, H.F., 1997. Evidence and dynamics for the change of the strike-slip direction of the Changle-Nan'ao ductile shear zone, Southeastern China. Journal of Asian Earth Sciences 15, 507-515.
345. Wawrzenitz, N., Romer, R.L., Oberhänsli, R., Dong, S., 2006. Dating of subduction and differential exhumation of UHP rocks from the Central Dabie Complex (E-China): Constraints from microfabrics, Rb-Sr and U-Pb isotope systems. Lithos 89, 174-201.
346. Webb, L.E., Graham, S.A., Johnson, C.L., Badarch, G., Hendrix, M.S., 1999a. Occurrence, age, and implications of the Yagan-Onch Hayrhan metamorphic core complex, southern Mongolia. Geology 27, 143-146
347. Webb, L.E., Hacker, B.R., Ratschbacher, L., McWilliams, M.O., Dong, S., 1999b. Thermochronologic constraints on deformation and cooling history of high-and ultrahigh-pressure rocks in the Qinling-Dabie orogen, eastern China. Tectonics 18, 621-638.
348. Webb, L.E., Ratschbacher, L., Hacker, B.R., Dong, S., 2001. Kinematics of exhumation of high- and ultrahigh-pressure rocks in the Hong'an and Tongbai Shan of the Qinling-Dabie collisional orogen, eastern China. In: Hendrix, M.S., Davis, G.A., eds., Paleozoic and Mesozoic Tectonic Evolution of Central Asia: From continental assembly to intracontinental deformation. Geological Society of America Memoir 194, 231-245.
349. Wei, W., Chen, Y., Faure, M., Shi, Y.H., Martele, G., Hou, Q.L., Lin, W., Le Breton, N., Wang, Q.C. 2014a. A multidisciplinary study on the emplacement mechanism of the Qingyang-Jiuhua Massif in Southeast China and its tectonic bearings. Part I: structural geology, AMS and paleomagnetism. Journal of Asian Earth Sciences 86, 76-93.
350. Wei, W., Martele, G., Le Breton, N., Shi, Y.H., Faure, M., Chen, Y., Hou, Q.L., Lin, W., Wang, Q.C. 2014b. A multidisciplinary study on the emplacement mechanism of the Qingyang-Jiuhua Massif in Southeast China and its tectonic bearings. Part II: Amphibole geobarometry and gravity modeling. Journal of Asian Earth Sciences 86, 94-105.
351. Wu, F.Y., Lin, J.Q., Wilde, S.A., Zhang, X.O., Yang, J.H., 2005. Nature and significance of the Early Cretaceous giant igneous event in eastern China. Earth and Planetary Sciences Letters 233, 103-119.
352. Wu, F.Y., Ji, W.Q., Sun, D.H., Yang, Y.H., Li, X.H., 2012. Zircon U-Pb geochronology and Hf isotopic compositions of the Mesozoic granites in southern Anhui Province, China. Lithos 150, 6-25.

353. Wu, Y.B., Zheng, Y.F., Zhang, S.B., Zhao, Z.F., Wu, F.Y., Liu, X.M., 2007. Zircon U-Pb ages and Hf isotope compositions of migmatite from the north Dabie terrane in China: Constraints on partial melting. Journal of Metamorphic Geology 25, 991-1009.
354. Wu, Y.B., Zheng, Y.F., Gao, S., Jiao, W.F., Liu, Y.S., 2008. Zircon U-Pb age and trace element evidence for Paleoproterozoic granulite-facies metamorphism and Archean crustal rocks in the Dabie Orogen. Lithos 101, 308-322.
355. Wu, Y.B., Hanchar, J.M., Gao, S., Sylvester, P.J., Tubrett, M., Qiu, H.N., Wijbrans, J.R., Brouwer, F.M., Yang, S.H., Yang, Q.J., Liu, Y.S., Yuan, H.L., 2009. Age and nature of eclogites in the Huwan shear zone, and the multi-stage evolution of the Qinling-Dabie-Sulu orogen, central China. Earth and Planetary Science Letters 277, 345-354.
356. Wu, Y.B., Zheng, Y.F., 2013. Tectonic evolution of a composite collision orogen: An overview on the Qinling-Tongbai-Hong'an-Dabie-Sulu orogenic belt in central China. Gondwana Research 23, 1402-1428.
357. Xiang, H., Zhang, L., Zhong, Z.Q., Santosh, M., Zhou, H.W., Zhang, H.F., Zheng, J.P., Zheng, S., 2012. Ultrahigh-temperature metamorphism and anticlockwise P-T-t path of Paleozoic granulites from north Qinling-Tongbai orogen, Central China. Gondwana Ressearch 21, 559-576.
358. Xiao, Y.L., Hoefs, J., Van Den Kerkhof, A.M., Li, S.G., 2001. Geochemical constraints of the eclogite and granulite facies metamorphism as recognized in the Raobazhai complex from north Dabie Shan, China. Journal of Metamorphic Geology 19, 3-19.
359. Xie, Z., Zheng, Y.F., Jahn, B.M., Ballevre, M., Chen, J.F., Gautier, P., Gao, T.S., Gong, B., Zhou, J.B., 2004. Sm-Nd and Rb-Sr dating of pyroxene-garnetite from north Dabie in east-central China: Problem of isotope disequilibrium due to retrograde metamorphism. Chemical Geology 206, 137-158.
360. Xie, Z., Zheng, Y.F., Zhao, Z.F., Wu, Y.B., Wang, Z.R., Chen, J.F., Liu, X.M., Wu, F.Y., 2006. Mineral isotope evidence for the contemporaneous process of Mesozoic granite emplacement and gneiss metamorphism in the Dabie orogen. Chemical Geology 231, 214-235.
361. Xie, Z., Chen, J.F., Cui, Y.R., 2010. Episodic growth of zircon in UHP orthogneisses from the north Dabie terrane of east-central China: Implications for crustal architecture of a collisional orogen. Journal of Metamorphic Geology 28, 979-995.
362. Xu, H.J., Ma, C.Q., Ye, K., 2007. Early cretaceous granitoids and their implications for the collapse of the Dabie orogen, eastern China: SHRIMP zircon U-Pb dating and geochemistry. Chemical Geology 240, 238-259.
363. Xu, H.J., Ma, C.Q., Zhang, J.F., Ye, K., 2012. Early Cretaceous low-Mg adakitic granites from the Dabie orogen, eastern China: Petrogenesis and implications for destruction of the over-thickened lower continental crust. Gondwana Research 23, 190-207.
364. Xu, J.F., Shinjo, R., Defant, M.J., Wang, Q., Rapp, R.P., 2002. Origin of Mesozoic adakitic intrusive rocks in the Ningzhen area of east China: Partial melting of delaminated lower continental crust? Geology 30, 1111-1114.
365. Xu, J.W., Zhu, G., Tong, W.X., Cui, K.R., Liu, Q., 1987. Formation and evolution of the Tancheng-Lujiang wrench fault system: a major shear system to the northwest Pacific Ocean. Tectonophysics 134, 273-310.
366. Xu, S.T., Wu, W.P., Lu, Y.Q., Wang, D.H., 2012. Tectonic setting of the low-grade metamorphic rocks of the Dabie Orogen, central eastern China. Journal of Structural Geology 37, 134-149.
367. Xu, X.B., Zhang, Y.Q., Shu, L.S., Jia, D., 2011. La-ICP-MS U-Pb and $^{40}Ar/^{39}Ar$ geochronology of the sheared metamorphic rocks in the Wuyishan: Constraints on the timing of Early Paleozoic and Early Mesozoic tectono-thermal events in SE China. Tectonophysics 501, 71-86.
368. Xu, Y.G., 2001. Thermo-tectonic destruction of the Archean lithospheric keel beneath the Sino-Korean craton in China: evidence, timing and mechanism. Physics and Chemistry of the Earth 26, 747-757.

369. Xu, Y.G., 2007. Diachronous lithospheric thinning of the North China Craton and formation of the Daxin'anling-Taihangshan gravity lineament. Lithos 96, 281-298.
370. Xue, F., Rowley, D.B., Tucker, R.D., Peng, Z.X., 1997. U-Pb zircon ages of granitiod rocks in the north Dabie complex, eastern Dabie Shan, China. Journal of Geology 105, 744-753.
371. Yan, D.P., Zhou, M.F., Song, H.L., Wang, X.W., Malpas, J., 2003. Origin and tectonic significance of a Mesozoic multi-layer over-thrust system within the Yangtze Block (South China). Tectonophysics 361, 239-254.
372. Yan, D.P., Zhou, M.F., Song, H.L., Wang, G.H., Sun, M., 2006. Mesozoic extensional structures of the Fangshan tectonic dome and their subsequent reworking during collisional accretion of the North China block. Journal of the Geological Society 163, 127-142.
373. Yan, D.P., Zhang, B., Zhou, M.F., Wei, G., Song, H.L., Liu, S.F., 2009. Constraints on the depth, geometry and kinematics of blind detachment faults provided by fault-propagation folds: An example from the Mesozoic fold belt of South China. Journal of Structural Geology 31, 150-162.
374. Yan, D.P., Zhou, M.F., Zhao, D.G., Li, J.W., Wang, G.H., Wang, C.L., Qi, L., 2010. Origin, ascent and oblique emplacement of magmas in a thickened crust: An example from the Cretaceous Fangshan adakitic pluton, Beijing. Lithos 123, 102-120.
375. Yan, D.P., Zhou, M.F., Li, S.B., Wei, G.Q., 2011. Structural and geochronological constraints on the Mesozoic-Cenozoic tectonic evolution of the Longmen Shan thrust belt, eastern Tibetan Plateau. Tetonics 30, TC6005, doi:10.1029/2011TC002867.
376. Yang, J.H., Wu, F.Y., Wilde, S.A., Belousova, E., Griffin, W.L., 2008. Mesozoic decratonization of the North China block. Geology 36, 467-470.
377. Yuan, X.C., Klemperer, S.L., Teng, W.B., Liu, L.X., Chetwin, E., 2003. Crustal structure and exhumation of the Dabie Shan ultrahigh-pressure orogen, eastern China, from seismic reflection profiling. Geology 31, 435-438.
378. Zhai, M.G., Cong, B.L., Zhang, Q., Wang, Q.C., 1994. The northern Dabieshan terrain: A possible Andean-type arc. International Geological Review 36, 867-883.
379. Zhai, M.G., Cong, B.L., Zhao, Z.Y., Wang, Q.C., Wang, G., Jiang, L.L., 1995. Petrological-tectonic units in the coesite-bearing metamorphic terrain of the Dabie Mountains, central China and their geotectonic implications. Journal of Southeast Asian Earth Sciences 11, 1-13.
380. Zhai, M.G., Fan, Q.C., Zhang, H.F., Sui, J.L., Shao, J.A., 2007. Lower crustal processes leading to Mesozoic lithospheric thinning beneath eastern North China: Underplating, replacement and delamination. Lithos 96, 36-54.
381. Zhai, X.M., Day, H.W., Hacker, B.R., You, Z.D., 1998. Paleozoic metamorphism in the Qinling orogen, Tongbai Mountains, central China. Geology 26, 371-374.
382. Zhang, B.L., Zhu, G., Jiang, D.Z., Li, C.C., Chen, Y., 2012. Evolution of the Yiwulushan metamorphic core complex from distributed to localized deformation and its tectonic implications. Tectonics, 31: TC4018. doi: 10.1029/2012TC003104.
383. Zhang, H.F., 2005. Transformation of lithospheric mantle through peridotite-melt reaction: A case of Sino-Korean craton. Earth and Planetary Science Letters 237, 768-780.
384. Zhang, J.J., Zheng, Y.D., 1999. Multistage extension and age dating of the Xiaoqinling meatmorpic core complex, central China. Acta Geological Sinica 73, 139-147.
385. Zhang, J.Y., Ma, C.Q., Li, J.W., She, Z.B., Zhang, C., 2013. Geochronology and geochemistry of the Early Cretaceous Jigongshan and Qijianfeng batholiths in the Tongbai orogen, central China: implications for lower crustal delamination. International Journal of Earth Sciences 102, 1045-1067.
386. Zhang, R.Y., Liou. J.G., Tsai, C.H., 1996. Petrogenesis of a high-temperature metamorphic terrane: A new tectonic interpretation for the north Dabieshan, central China. Journal of Metamorphic Geology 14, 319-333.

387. Zhang, R.Y., Liou, J.G., Ernst, W.G., 2009. The Dabie-Sulu continental collision zone: A comprehensive review. Gondwana Research 16, 1-26.
388. Zhang, S.B., Zheng, Y.F., Wu, Y.B., Zhao, Z.F., Gao, S., Wu, F.Y., 2006a. Zircon isotope evidence for ≥ 3.5 Ga continental crust in the Yangtze craton of China. Precambrian Research 146, 16-34.
389. Zhang, S.B., Zheng, Y.F., Wu, Y.B., Zhao, Z.F., Gao, S., Wu, F.Y., 2006b. Zircon U-Pb age and Hf-O isotope evidence for Paleoproterozoic metamorphic event in South China. Precambrian Research 151, 265-288.
390. Zhang, S.B., Zheng, Y.F., Wu, Y.B., Zhao, Z.F., Gao, S., Wu, F.Y., 2006c. Zircon U-Pb age and Hf isotope evidence for 3.8 Ga crustal remnant and episodic reworking of Archean crust in South China. Earth and Planetary Science Letters 252, 56-71.
391. Zhang, S.B., Zheng, Y.F., Zhao, Z.F., Wu, Y.B., Yuan, H.L., Wu, F.Y., 2008. Neoproterozoic anatexis of Archean Lithosphere: Geochemical evidence from felsic to mafic intrusions at Xiaofeng in the Yangtze George, South China. Precambrian Research 163, 210-238.
392. Zhang, S.B., Zheng, Y.F., Zhao, Z.F., Wu, Y.B., Yuan, H.L., Wu, F.Y., 2009. Origin of TTG-like rocks from anatexis of ancient lower crust: Geochemical evidence from Neoproterozoic granitoids in South China. Lithos 113, 347-368.
393. Zhang, Z.J, Bai, Z.M., Mooney, W., Wang, C.Y., Chen, X.B., Wang, E., Teng, J.W., Okaya, N., 2009. Crustal structure across the Three Gorges area of the Yangtze platform, central China, from seismic refraction/wide-angle reflection data: Tectonophysics, 475, 423-437.
394. Zhang, Z.J., Yang, L.Q., Teng, J.W., Badal, J., 2011. An overview of the earth crust under China. Earth-Science Reviews 104, 143-166.
395. Zhao, Z.F., Zheng, Y.F., Wei, C.S., Wu, Y.B., 2004. Zircon isotope evidence for recycling of subducted continental crust in post-collisional granitoids from the Dabie terrane in China. Geophysical Research Letters 31, L22602. doi:10.1029/2004GL021061.
396. Zhao, Z.F., Zheng, Y.F., Wei, C.S., Wu, Y.B., Chen, F.K., Jahn, B.M., 2005. Zircon U-Pb age, element and C-O isotope geochemistry of post-collisional mafic-ultramafic rocks from the Dabie orogen in east-central China. Lithos 83, 1-28.
397. Zhao, Z.F., Zheng, Y.F.,Wei, C.S.,Wu, Y.B., 2007. Post-collisional granitoids from the Dabie orogen in China: zircon U-Pb age, element and O isotope evidence for recycling of subducted continental crust. Lithos 93, 248-272.
398. Zhao, Z.F., Zheng, Y.F., Wei, C.S., Chen, F.K., Liu, X.M., Wu, F.Y., 2008. Zircon U-Pb ages, Hf and O isotopes constrain the crustal architecture of the ultrahigh-pressure Dabie orogen in China. Chemical Geology 253, 222-242.
399. Zhao, Z.F., Zheng, Y.F., Wei, C.S., Wu, F.Y., 2011. Origin of postcollisional magmatic rocks in the Dabie orogen: implications for crust-mantle interaction and crustal architecture. Lithos 126, 99-114.
400. Zheng, Y.F., Fu, B., Li, Y.L., Wei, C.S., Zhou, J.B., 2001. Oxygen isotope composition of granulites from Dabieshan in eastern China and its implications for geodynamics of Yangtze plate subduction. Physics and Chemistry of the Earth 26, 673-684.
401. Zheng, Y.F., Wu, Y.B., Chen, F.K., Gong, B., Li, L., Zhao, Z.F., 2004. Zircon U-Pb and oxygen isotope evidence for a large-scale ^{18}O depletion event in igneous rocks during the Neoproterozoic. Geochimica et Cosmochimica Acta 68, 4145-4165.
402. Zheng, Y.F., Zhou, J.B., Wu, Y.B., Xie, Z., 2005. Low-grade metamorphic rocks in the Dabie-Sulu orogenic belt: A passive-margin accretionary wedge deformed during continent subduction. International Geology Review 47, 851-871.
403. Zhou, X.M., Li, W.X., 2000. Origin of Late Mesozoic igneous rocks in Southeastern China: implications for lithosphere subduction and underplating of mafic magmas. Tectonophysics 326, 269-287.

404. Zhou, X.M., Sun, T., Shen, W.Z., Shu, L.S., Niu, Y.L. 2006. Petrogenesis of Mesozoic granitoids and volcanic rocks in South China: A response to tectonic evolution. Episodes 29, 26-33.
405. Zhu, G., Xie, C.L., Chen, W., Xiang, B.W., Hu, Z.Q., 2010. Evolution of the Hongzhen metamorphic core complex: Evidence for Early Cretaceous extension in the eastern Yangtze craton, eastern China. Geological Society of America Bulletin 122, 506-516.
406. Zhu, G., Jiang, D.Z., Zhang, B.L., Chen, Y., 2012. Destruction of the eastern North China Craton in a backarc setting: Evidence from crustal deformation kinematics. Gondwana Research 22, 86-103
407. Zhu, R.X., Yang, J.H., Wu, F.Y., 2012. Timing of destruction of the North China Craton. Lithos 149, 51-60.
408. Zorin, Y.A., 1999. Geodynamics of the western part of the Mongolia-Okhotsk collisional belt, Trans-Baikal region (Russia) and Mongolia. Tectonophysics 306, 33-56.

About the author

作者简介

冀文斌, 男, 1986 年 12 月 23 日生于陕西洛南.

2004-2008 年, 西北大学地质学系, 学士学位, 专业地质学.

2008-2014 年, 中国科学院地质与地球物理研究所, 博士学位, 专业构造地质学.

2013-2014 年, 法国奥尔良大学地球科学研究所(Université d'Orléans, Institut des Sciences de la Terre d'Orléans), 联合培养.

攻读博士学位期间发表的论文

1. **Ji**, **W.B.**, Lin, W., Faure, M., Chu, Y., Wu, L., Wang, F., Wang, J., Wang, Q.C., 2014. Origin and tectonic significance of the Huangling massif within the Yangtze craton, South China. Journal of Asian Earth Sciences 86, 59-75.

2. **冀文斌**, 林伟, 石永红, 王清晨, 褚杨, 2011. 大别山早白垩世变质核杂岩的结构与演化. 地质科学, 46(1): 161-180.

3. 林伟, **冀文斌**, 石永红, 褚杨, 李秋立, 陈泽超, 刘飞, 王清晨. 2013. 高压-超高压变质岩石的多期构造折返: 以桐柏-红安-大别造山带为例. 科学通报, 58(23): 2259-2265.

4. Lin, W., Chu, Y., **Ji**, **W.B.**, Zhang, Z.P., Shi, Y.H., Wang, Z.Y., Li, Z., Wang, Q.C., 2013. Geochronological and geochemical constraints for a Middle Paleozoic continental arc in northern margin of the Tarim Block: implications for the Paleozoic tectonic evolution of the South Chinese Tianshan. Lithosphere 5, 355-381.

5. Shi, Y.H., Lin, W., **Ji**, **W.B.**, Wang, Q.C., 2014. The architecture of the HP-UHP Dabie massif: new insights from geothermobarometry of eclogites, and implication for the continental exhumation processes. Journal of Asian Earth Sciences 86, 38-58.

6. Lin, W., Faure, M., Chen, Y., **Ji**, **W.B.**, Wang, F., Wu, L., Charles, N., Wang, J., Wang, Q.C., 2013. Late Mesozoic compressional to extensional tectonics in the Yiwulüshan massif, NE China and its bearing on the evolution of the Yinshan-Yanshan orogenic belt. Part I: Structural analyses and geochronological constraints. Gondwana Research 23, 54-77.

7. 林伟, 王军, 刘飞, **冀文斌**, 褚杨, 王清晨. 2013.华北克拉通及邻区晚中生

代伸展构造及其动力学背景的讨论. 岩石学报, 29(5): 1791-1810.

8. 徐旭峰, 石永红, 林伟, **冀文斌**. 2013.中大别腹地榴辉岩锆石 U-Pb 年龄及其类型归属. 岩石学报, 29(5): 1559-1572.

9. Chu, Y., Lin, W., Faure, M., Wang, Q.C., **Ji**, **W.B.**, 2012. Phanerozoic tectonothermal events of the Xuefengshan Belt, central South China: Implications from U-Pb age and Lu-Hf determinations of granites. Lithos 150, 243-255.

10. Chu, Y., Faure, M., Lin, W., Wang, Q.C., **Ji**, **W.B.**, 2012. Tectonics of the Middle Triassic intracontinental Xuefengshan Belt, South China: new insights from structural and chronological constraints on the basal décollement zone. International Journal of Earth Sciences 101, 2125-2150.

11. Choulet, F., Cluzel, D., Faure, M., Lin, W., Wang, B., Chen, Y., Wu, F.Y., **Ji**, **W.B.**, 2012. New constraints on the pre-Permian continental crust growth of Central Asia (West Junggar, China) by U-Pb and Hf isotopic data from detrital zircon. Terra Nova 24, 189-198.

表 3-1 桐柏杂岩锆石 U-Pb 年代学数据

Table 3-1 Zircon U-Pb data of the Tongbaishan complex

Sample #spot	U ppm	Th ppm	Th/U	f_{206} (%)	$^{207}Pb/^{206}Pb$	±σ (%)	$^{207}Pb/^{235}U$	±σ (%)	$^{206}Pb/^{238}U$	±σ (%)	$t_{207/206}$ (Ma)	±σ (Ma)	$t_{207/235}$ (Ma)	±σ (Ma)	$t_{206/238}$ (Ma)	±σ (Ma)
HO37, 混合岩淡色体																
HO37#1	440	69	0.16	0.10	0.04844	2.70	0.14076	3.10	0.02108	1.52	120.7	62.4	133.7	3.9	134.5	2.0
HO37#2	290	35	0.12	0.09	0.04883	2.43	0.14185	2.95	0.02107	1.68	139.5	56.1	134.7	3.7	134.4	2.2
HO37#3	396	53	0.13	0.07	0.05004	2.04	0.14747	2.60	0.02137	1.60	196.8	46.7	139.7	3.4	136.3	2.2
HO37#4	380	49	0.13	0.14	0.04791	2.49	0.13729	2.91	0.02078	1.51	94.7	57.9	130.6	3.6	132.6	2.0
HO37#5	692	70	0.10	0.00	0.04818	1.59	0.13936	2.19	0.02098	1.50	108.1	37.1	132.5	2.7	133.8	2.0
HO37#6	530	60	0.11	0.03	0.04859	3.04	0.14165	3.39	0.02114	1.51	128.2	69.9	134.5	4.3	134.9	2.0
HO37#7	269	34	0.13	0.00	0.04878	2.59	0.13771	3.01	0.02047	1.52	137.4	59.8	131.0	3.7	130.6	2.0
HO37#8	309	42	0.14	0.19	0.04928	3.03	0.13970	3.48	0.02056	1.71	161.1	69.4	132.8	4.3	131.2	2.2
HO37#9	161	17	0.11	0.00	0.04909	3.25	0.14382	3.60	0.02125	1.55	152.2	74.4	136.4	4.6	135.5	2.1
HO37#10	183	24	0.13	0.00	0.04930	3.62	0.14219	3.93	0.02092	1.54	162.3	82.4	135.0	5.0	133.4	2.0
HO37#11	272	37	0.14	0.17	0.04842	3.12	0.13897	3.49	0.02082	1.55	119.9	72.0	132.1	4.3	132.8	2.0
HO37#12	235	30	0.13	0.21	0.04839	3.80	0.13837	4.14	0.02074	1.64	118.5	87.2	131.6	5.1	132.3	2.1
HO37#13	347	48	0.14	0.13	0.04729	3.13	0.13683	3.49	0.02098	1.53	64.1	73.0	130.2	4.3	133.9	2.0
HO37#14	399	53	0.13	0.07	0.05013	2.03	0.14346	2.53	0.02076	1.50	200.8	46.6	136.1	3.2	132.4	2.0
HO37#15	198	27	0.13	0.22	0.04746	4.32	0.13560	4.60	0.02072	1.58	72.5	99.6	129.1	5.6	132.2	2.1
HO37#16	292	39	0.13	0.00	0.04951	2.40	0.13923	2.84	0.02039	1.50	172.2	55.2	132.4	3.5	130.1	1.9
HO37#17	225	28	0.13	0.37	0.04786	4.04	0.13796	4.33	0.02091	1.54	92.4	93.1	131.2	5.3	133.4	2.0
HO37#18	289	32	0.11	0.15	0.04892	2.82	0.13885	3.21	0.02059	1.52	143.9	64.9	132.0	4.0	131.4	2.0
HO37#19	593	55	0.09	0.10	0.04702	2.36	0.13604	2.80	0.02099	1.50	50.1	55.4	129.5	3.4	133.9	2.0
HO37#20	338	38	0.11	0.21	0.04946	2.73	0.13784	3.12	0.02021	1.52	169.5	62.5	131.1	3.9	129.0	1.9
HO37#21	110	9	0.08	0.00	0.05192	5.29	0.14611	5.52	0.02041	1.57	281.9	116.8	138.5	7.2	130.2	2.0
HO37#22	367	34	0.09	0.00	0.04851	2.26	0.13814	2.73	0.02065	1.53	124.3	52.4	131.4	3.4	131.8	2.0
HO37#23	145	16	0.11	0.62	0.05003	5.67	0.14611	5.87	0.02118	1.52	196.3	126.6	138.5	7.6	135.1	2.0
HO41, 混合岩淡色体																

HO41#1	1317	67	0.05	0.05	0.04966	1.74	0.14324	2.30	0.02092	1.50	179.1	40.2	135.9	2.9	133.5	2.0
HO41#2	1421	50	0.04	0.00	0.05005	1.71	0.14184	2.28	0.02056	1.51	197.2	39.2	134.7	2.9	131.2	2.0
HO41#3	596	102	0.17	0.09	0.16946	0.80	6.75282	2.00	0.28902	1.83	2552.3	13.3	2079.6	17.8	1636.6	26.5
HO41#4	135	60	0.45	0.00	0.04644	5.49	0.13419	5.74	0.02095	1.67	20.7	126.7	127.9	6.9	133.7	2.2
HO41#5	99	21	0.21	0.00	0.05323	5.41	0.24245	5.67	0.03303	1.71	338.6	118.1	220.4	11.3	209.5	3.5
HO41#6	921	46	0.05	0.08	0.05076	3.26	0.14474	3.59	0.02068	1.51	229.8	73.6	137.3	4.6	132.0	2.0
HO41#7	383	333	0.87	0.05	0.06502	1.34	0.94207	2.02	0.10509	1.51	774.9	27.9	674.0	10.0	644.2	9.3
HO41#8	667	47	0.07	0.00	0.04804	2.43	0.13850	2.87	0.02091	1.52	101.2	56.5	131.7	3.6	133.4	2.0
HO41#9	231	99	0.43	0.21	0.05647	3.39	0.18468	3.72	0.02372	1.52	470.8	73.4	172.1	5.9	151.1	2.3
HO41#10	37	34	0.90	0.00	0.05767	8.75	0.20028	8.93	0.02519	1.78	517.3	181.4	185.4	15.2	160.4	2.8
HO41#11	93	61	0.66	0.35	0.04928	9.86	0.17348	10.01	0.02553	1.69	161.0	215.7	162.4	15.1	162.5	2.7
HO41#12	734	43	0.06	0.00	0.04864	1.81	0.13978	2.36	0.02084	1.52	130.7	41.9	132.9	2.9	133.0	2.0
HO41#13	84	245	2.91	0.00	0.06249	2.42	0.83849	2.84	0.09731	1.50	691.0	50.7	618.3	13.3	598.6	8.6
HO41#14	502	26	0.05	0.09	0.04968	2.36	0.14358	2.80	0.02096	1.50	180.0	54.2	136.2	3.6	133.7	2.0
HO41#15	64	73	1.13	0.85	0.05995	4.08	0.62929	4.35	0.07613	1.52	601.7	85.9	495.7	17.2	473.0	6.9
HO41#16	500	26	0.05	0.09	0.04828	2.13	0.14043	2.60	0.02110	1.51	112.8	49.4	133.4	3.3	134.6	2.0
HO41#17	1308	55	0.04	0.02	0.04859	1.17	0.14281	1.91	0.02132	1.51	128.1	27.3	135.5	2.4	136.0	2.0
HO41#18	1109	42	0.04	0.00	0.04818	1.92	0.14071	2.49	0.02118	1.59	107.9	44.8	133.7	3.1	135.1	2.1
HO41#19	808	35	0.04	0.00	0.04903	1.47	0.14670	2.11	0.02170	1.51	149.3	34.2	139.0	2.7	138.4	2.1
HO41#20	79	44	0.56	0.00	0.09337	3.01	0.72004	6.76	0.05593	6.05	1495.5	56.0	550.7	29.1	350.8	20.7
HO41#21	986	42	0.04	0.04	0.04890	1.42	0.14128	2.07	0.02095	1.51	143.2	33.1	134.2	2.6	133.7	2.0
HO41#22	38	31	0.82	0.22	0.06299	3.08	0.95381	3.44	0.10983	1.51	707.8	64.3	680.1	17.2	671.7	9.7
HO41#23	139	24	0.17	0.22	0.05442	3.75	0.23643	4.04	0.03151	1.51	388.6	82.0	215.5	7.9	200.0	3.0
HO41#24	209	8	0.04	0.00	0.04912	2.65	0.17133	3.07	0.02529	1.56	153.8	60.9	160.6	4.6	161.0	2.5
HO41#25	1622	51	0.03	0.00	0.04851	1.21	0.14315	1.93	0.02140	1.50	124.2	28.2	135.8	2.5	136.5	2.0
HO41#26	92	84	0.92	0.30	0.04762	4.38	0.13697	4.69	0.02086	1.65	80.3	100.9	130.3	5.7	133.1	2.2
HO41#27	887	29	0.03	0.03	0.04897	1.51	0.14068	2.13	0.02084	1.51	146.4	35.0	133.7	2.7	132.9	2.0
HO41#28	1085	31	0.03	0.03	0.04898	1.27	0.14327	1.97	0.02121	1.51	146.9	29.5	135.9	2.5	135.3	2.0

f_{206} is the proportion of common ^{206}Pb in total measured ^{206}Pb.

表 3-2 桐柏杂岩榍石 U-Pb 年代学数据

Table 3-2 Titanite U-Pb data of the Tongbaishan complex

Sample[a]	Weight	Concentrations[b]		^{206}Pb	Radiogenic Pb (atomic %)[d]			Atomic ratios[d]			Apparent ages (Ma)[e]		
Titanite fractions	(mg)	U (ppm)	Pb_{rad} (ppm)	^{204}Pb measured[c]	^{206}Pb	^{207}Pb	^{208}Pb	$\frac{^{206}Pb}{^{238}U}$	$\frac{^{207}Pb}{^{235}U}$	$\frac{^{207}Pb}{^{206}Pb}$	$t_{206/238}$	$t_{207/235}$	$t_{207/206}$
(1) 5 very large euhedral, transparent	0.4507	68.5	1.95	38.14	57.4	2.8	39.8	0.019	0.1275	0.04860	122	122	128
(2) 8 small to medium-size grains, not abr.	0.2687	72.3	1.87	37.78	60.7	2.9	36.4	0.0182	0.1211	0.04831	116	116	115
(3) 4 large euhedral grains, not abr.	0.2044	61.7	2.01	35.46	49.8	2.4	47.8	0.0188	0.1276	0.04916	120	122	155
(4) 6 medium-size to large grains, not abr.	0.3271	106	2.41	32.06	65.9	3.1	31	0.0174	0.1146	0.04769	111	110	84.1
(5) 20 small euhedral, transparent grains, abr.	0.12	385	10.4	42.4	59.8	2.9	37.3	0.0186	0.1247	0.04852	119	119	125
(6) 10 medium-size euhedral grains, abr.	0.283	77.3	2.12	41	60.4	3.5	36.1	0.0192	0.1518	0.05732	123	143	504
(7) 4 very large euhedral grains, abr.	0.349	30.9	0.853	37.4	58.5	2.8	38.7	0.0188	0.1225	0.04737	120	117	67.8
(8) 4 large euhedral grains, abr.	0.1256	61.4	1.83	35.64	55.8	4.9	39.3	0.0193	0.2333	0.08765	123	213	1374

a All grains analyzed were individually selected after habit and quality. Most grains were yellow-brown, euhedral and transparent. Mechanical abrasion was perfomed according to Krogh (1982) with pyrite for 1/2h at 0.5 atm over-pressure. abr. = abraded; not abr. = not abraded. Very large grains: > 0.20 mm; large grains: 0.15-0.20 mm; medium-size grains: 0.10-0.15 mm; small grains: < 0.1 mm. Grain description necessarily applies to characteristics prior to abrasion.

b Corrected for (1) mass-discrimination, (2) isotopic tracer contribution, (3) Pb blank [30 pg for fractions < 0.3 mg, 150 pg for fractions > 0.3 mg, due to diffrence in chemical procedure], (4) 1 pg of U blank for alll fractions, and (5) initial Pb, as deduced from the Stacy and Kramer (1975) model for Pb isotope evolution of average continental crust.

c Corrected for mass-discrimination and isotopic tracer contribution.

d Ratios corrected for mass-discrimination, isotopic tracer contribution, Pb and U blank, and initial common Pb.

e Decay constants used were determined by Jaffey et al. (1971), recommended by IGC (Steiger and Jäger, 1977).

表 3-3 桐柏-大别造山带构造岩 Ar-Ar 年代学数据

Table 3-3 Ar-Ar data of tectonites from the Tongbai-Dabie orogen

Temperature (°C)	$^{40}Ar/^{39}Ar$	$^{37}Ar/^{39}Ar$	$^{36}Ar/^{39}Ar$	$^{40}Ar_r/^{39}Ar_k$	$^{40}Ar_r$ (%)	$^{39}Ar_k$ (%)	Age ± 2σ Ma
QD88, Biotite, J = 0.0033190							
850	17.12732	2.03465	0.00436	16.02954	93.43	7.06	93.73 ± 1.87
890	17.55740	1.03210	0.00346	16.63127	94.64	15.26	97.16 ± 1.37
910	17.28963	1.35561	0.00247	16.68706	96.40	18.59	97.48 ± 1.39
930	17.09302	1.24485	0.00239	16.50325	96.45	13.72	96.43 ± 1.09
970	17.09465	1.42535	0.00255	16.47275	96.24	11.57	96.26 ± .86
1010	17.16790	2.25453	0.00240	16.66867	96.91	11.40	97.37 ± 1.18
1050	16.90514	2.20662	0.00196	16.53108	97.60	10.54	96.59 ± 1.12
1090	16.58769	3.74276	0.00265	16.15460	97.08	6.67	94.45 ± 1.61
1150	16.53644	6.75916	0.00351	16.12884	96.97	4.17	94.30 ± 1.22
1300	19.60514	14.82216	0.00987	18.09599	91.14	1.02	105.47 ± 2.27
JS109, K-feldspar, J = 0.004878							
750	27.32911	0.00434	0.05448	11.23096	41.10	0.57	96.45 ± 2.70
770	15.90064	0.00945	0.01285	12.10528	76.13	1.60	103.75 ± .80
790	14.57728	0.00959	0.00698	12.51568	85.86	1.05	107.16 ± .70
820	14.80696	0.00478	0.00527	13.25121	89.49	1.41	113.27 ± .71
850	14.86725	0.00590	0.00395	13.70111	92.16	1.88	116.99 ± .67
870	15.05601	0.00789	0.00408	13.85175	92.00	1.70	118.24 ± .68
900	15.56376	0.00344	0.00492	14.10916	90.65	1.85	120.36 ± .61
930	15.79678	0.00293	0.00560	14.14330	89.53	1.80	120.64 ± .68
960	15.58706	0.00473	0.00531	14.01771	89.93	1.69	119.61 ± .66
1000	15.96939	0.00658	0.00598	14.20226	88.93	2.69	121.13 ± .60
1030	16.18195	0.00406	0.00636	14.30310	88.39	3.01	121.96 ± .60
1060	16.11185	0.00381	0.00560	14.45585	89.72	5.51	123.22 ± .57
1090	15.65644	0.00310	0.00373	14.55386	92.96	7.67	124.03 ± .54
1120	15.57977	0.00107	0.00336	14.58726	93.63	6.80	124.30 ± .54
1150	15.58318	0.00048	0.00341	14.57588	93.54	6.43	124.21 ± .57
1180	15.65254	0.00170	0.00321	14.70522	93.95	7.21	125.27 ± .53
1220	15.73328	0.00156	0.00319	14.79081	94.01	13.45	125.98 ± .57
1250	15.73537	0.00182	0.00305	14.83379	94.27	14.09	126.33 ± .60
1280	15.87590	0.00199	0.00301	14.98572	94.39	10.50	127.58 ± 1.93
1310	15.81088	0.00022	0.00313	14.88651	94.15	5.20	126.76 ± .58
1340	15.87854	0.00038	0.00319	14.93648	94.07	2.76	127.18 ± 1.89
1400	15.89830	0.00423	0.00348	14.87021	93.53	1.13	126.63 ± .73
DS49, Hornblende, J = 0.004800							
820	178.16328	0.74732	0.56871	10.17739	5.71	0.61	86.25 ±28.43
900	59.83617	2.93355	0.14804	16.36581	27.28	3.94	136.75 ± 5.85
1000	23.25658	3.24219	0.02685	15.62264	66.99	9.68	130.76 ± 1.71
1030	18.58435	3.26131	0.01078	15.70068	84.25	14.09	131.39 ± .89
1060	16.55704	3.29705	0.00560	15.20702	91.59	13.41	127.40 ± .63
1090	15.59463	3.20449	0.00316	14.95547	95.64	13.57	125.36 ± .62
1120	16.45332	3.33774	0.00556	15.11774	91.62	5.56	126.68 ± .68
1180	15.45898	3.23841	0.00393	14.59468	94.15	38.90	122.44 ± .60
1240	10.24472	0.54089	0.01570	5.65353	55.16	0.25	48.42 ± 6.43

QD124, Biotite, J = 0.0033440							
750	19.11405	3.03117	0.00317	18.46692	96.36	6.09	108.36 ± 1.75
800	19.27485	2.19618	0.00364	18.40732	95.32	10.42	108.02 ± 1.29
840	19.12253	1.66138	0.00327	18.31255	95.63	12.45	107.48 ± 1.01
880	18.94198	1.62326	0.00229	18.41941	97.11	14.84	108.09 ± .92
910	18.69991	1.57124	0.00178	18.32408	97.86	12.78	107.54 ± 1.11
950	18.65558	2.30802	0.00157	18.41236	98.50	11.53	108.05 ± 1.07
990	18.42932	2.18877	0.00153	18.18464	98.49	10.02	106.75 ± 1.12
1030	18.48622	2.67502	0.00134	18.34442	99.01	8.50	107.66 ± 1.13
1070	19.33506	3.01692	0.00144	19.19690	99.03	7.33	112.51 ± 2.14
1110	18.48435	4.89041	0.00172	18.44047	99.35	6.05	108.21 ± 1.88
JS100, Biotite, J = 0.004811							
750	28.50808	0.02090	0.04855	14.16235	49.68	2.13	119.19 ± 2.24
800	17.66454	0.00108	0.00968	14.80271	83.80	12.70	124.40 ± .69
820	19.46766	0.00233	0.01368	15.42552	79.24	8.80	129.45 ± .88
860	22.01036	0.00473	0.02105	15.78963	71.74	8.32	132.40 ± 1.05
900	18.19077	0.00395	0.00898	15.53762	85.41	6.30	130.36 ± .87
940	24.96170	0.01145	0.03153	15.64478	62.67	4.79	131.23 ± 1.45
980	24.99525	0.02230	0.03037	16.02375	64.11	5.50	134.29 ± 1.40
1020	18.11257	0.02104	0.00866	15.55584	85.88	12.48	130.51 ± .67
1040	16.46955	0.00279	0.00357	15.41449	93.59	13.73	129.36 ± .65
1060	16.34974	0.00368	0.00270	15.55133	95.12	12.14	130.47 ± .68
1080	16.39056	0.00443	0.00277	15.57371	95.02	7.19	130.65 ± .62
1120	16.75114	0.03306	0.00321	15.80586	94.35	3.88	132.53 ± .73
1160	16.29683	0.06927	0.00297	15.42415	94.64	1.57	129.44 ± 1.49
1260	20.92282	0.12848	0.01801	15.61232	74.61	0.46	130.97 ± 2.32
1300	57.59468	0.02939	0.09128	30.63150	53.18	0.03	248.59 ±29.16
JS349, Biotite, J = 0.004822							
750	102.33630	0.03047	0.29693	14.59540	14.26	0.85	122.99 ±70.17
800	40.05387	0.00706	0.08489	14.96999	37.37	5.32	126.04 ± 3.95
840	36.09043	0.00236	0.07126	15.03328	41.65	5.27	126.55 ± 2.96
880	25.53959	0.01029	0.03516	15.14958	59.32	5.21	127.50 ± 1.58
920	22.31365	0.00100	0.02383	15.27247	68.44	4.92	128.50 ± 1.35
960	23.42623	0.02434	0.02853	14.99616	64.01	7.09	126.25 ± 1.38
1000	19.73321	0.01132	0.01629	14.91932	75.60	14.61	125.63 ± .91
1020	17.45449	0.00827	0.00898	14.80246	84.81	12.11	124.67 ± .75
1040	16.48120	0.01131	0.00579	14.77110	89.62	10.35	124.42 ± .59
1060	16.32028	0.01075	0.00503	14.83480	90.90	8.78	124.94 ± .66
1080	16.28694	0.01958	0.00423	15.03766	92.33	8.12	126.59 ± .62
1100	15.87392	0.00246	0.00296	15.00012	94.50	7.56	126.28 ± .57
1120	15.86470	0.00503	0.00261	15.09334	95.14	5.43	127.04 ± .68
1150	17.29865	0.02123	0.00266	16.51505	95.47	2.44	138.56 ± .93
1250	34.09367	0.04374	0.00739	31.91399	93.60	1.67	258.84 ± 1.30
1300	57.44824	0.03332	0.01697	52.43788	91.28	0.27	407.64 ±19.67
JS349, Hornblende, J = 0.004848							
880	364.21948	3.26111	1.21790	4.60587	1.26	0.26	39.93 ±77.21
960	83.77334	4.68072	0.20608	23.34367	27.75	0.72	193.87 ±47.48
1040	18.95399	3.07878	0.01422	15.03651	79.12	10.79	127.24 ± 1.32

1040	18.63748	3.04580	0.01411	14.74845	78.93	10.91	124.88 ± 3.97
1070	15.41335	3.05483	0.00475	14.28952	92.47	39.96	121.12 ± .74
1090	15.30023	2.96173	0.00267	14.78432	96.38	12.49	125.18 ± .60
1120	16.65833	3.14146	0.00716	14.83200	88.80	1.94	125.57 ± .85
1170	15.36643	3.02222	0.00303	14.74940	95.74	17.28	124.89 ± .60
1190	15.96800	3.09543	0.00505	14.75956	92.19	5.13	124.97 ± .82
1250	19.24159	3.38351	0.02225	12.97259	67.23	0.52	110.29 ± 2.83
DS39, Biotite, J = 0.004768							
750	67.24378	0.00757	0.17596	14.16564	22.68	15.25	126.92 ± 7.46
800	25.79516	0.00520	0.04266	14.38080	51.13	13.19	110.28 ± 1.91
830	20.31861	0.00276	0.02311	14.81697	66.40	13.49	112.73 ± 1.21
860	21.73407	0.00673	0.02825	15.12086	61.59	13.39	111.88 ± 1.30
900	35.60980	0.01007	0.08010	15.20117	33.53	11.94	100.13 ± 4.42
940	29.41948	0.01554	0.06309	14.96703	36.64	10.78	90.62 ± 2.65
980	20.50483	0.00927	0.03139	14.72063	54.77	11.23	94.33 ± 1.37
1010	20.43442	0.00421	0.02612	14.83137	62.22	12.71	106.43 ± 1.23
1040	22.00892	0.00570	0.02916	14.92354	60.85	13.39	111.94 ± 1.35
1080	33.71764	0.05062	0.06845	15.00427	40.02	13.49	112.76 ± 3.14
1180	413.59992	4.17601	1.11794	15.10873	20.21	83.89	608.44 ±88.13
DS45, Biotite, J = 0.004791							
750	24.77854	0.00479	0.04648	11.04383	44.57	5.81	93.23 ± 2.02
800	16.26453	0.00275	0.01449	11.98372	73.68	23.51	100.95 ± .78
830	19.12269	0.00298	0.02273	12.40471	64.87	10.30	104.40 ± 1.09
870	24.99047	0.01287	0.04540	11.57463	46.32	7.97	97.60 ± 1.93
910	19.75772	0.00527	0.03236	10.19643	51.61	8.19	86.25 ± 1.41
950	19.16933	0.01147	0.03131	9.91711	51.73	12.09	83.94 ± 1.38
990	18.38058	0.00455	0.02549	10.84874	59.02	14.87	91.63 ± 1.18
1030	18.27260	0.00325	0.02079	12.12933	66.38	10.32	102.14 ± 1.04
1070	16.66727	0.00930	0.01309	12.79973	76.79	5.76	107.63 ± .89
1110	18.15503	0.09474	0.01491	13.75674	75.77	1.02	115.42 ± 1.61
1210	41.33229	0.50116	0.09868	12.22024	29.55	0.16	102.89 ±23.86

表 4-1 大云山-幕阜山岩体 AMS 数据

Table 4-1 AMS data of the Dayunshan-Mufushan batholith

采点	坐标		n	K_m	P_J	T	K_1				K_3			
	纬度(°N)	经度(°E)		(10^{-6}SI)			Dec(°)	Inc(°)	α_{95max}	α_{95min}	Dec(°)	Inc(°)	α_{95max}	α_{95min}
DM1	29.271	113.403	5	57.2	1.090	0.434	277.8	50.8	64.4	9.2	97.3	39.2	11.5	9.3
DM2	29.279	113.428	7	50.3	1.140	0.378	254.8	0.1	6.1	5.5	345.1	70.0	16.7	4.6
DM3	29.295	113.444	8	84.7	1.055	0.073	171.6	22.8	20.2	7.1	68.6	28.1	34.2	7.1
DM4	29.289	113.460	5	64.5	1.097	0.732	97.4	36.5	23.8	10.9	324.4	42.7	12.2	6.0
DM5	29.341	113.562	6	6390	1.102	-0.129	104.8	19.6	15.8	6.1	210.8	37.7	30.9	6.4
DM6	29.314	113.496	6	68.5	1.067	0.567	130.3	32.4	19.4	6.9	353.7	48.9	9.7	6.4
DM7	29.295	113.507	8	64.2	1.089	-0.626	167.2	56.2	3.2	1.5	289.9	19.9	25.6	3.2
DM8	29.277	113.511	7	81.8	1.048	0.447	36.6	27.2	12.3	2.9	299.0	14.5	8.0	3.6
DM9	29.284	113.484	9	50.2	1.119	0.679	178.6	58.9	13.4	12.5	337.3	29.4	13.1	8.1
DM10	29.314	113.519	7	54.6	1.041	0.257	67.2	26.7	20.0	4.7	306.4	45.6	13.5	3.7
DM11	29.256	113.385	9	99	1.155	0.518	287.4	14.5	20.6	6.0	35.9	50.8	13.0	3.2
DM12	29.245	113.381	6	280	1.177	0.401	279.9	1.8	16.5	3.8	11.6	43.9	8.2	2.6
DM13	29.266	113.455	7	71.3	1.037	0.119	83.3	48.7	16.0	9.2	246.1	40.0	27.2	10.5
DM14	29.248	113.435	6	48.7	1.075	0.350	225.2	52.2	8.7	7.6	336.3	15.6	8.1	2.2
DM15	29.222	113.410	7	58.8	1.019	-0.205	77.6	52.5	13.1	10.0	324.1	17.1	10.2	5.2
DM16	29.210	113.450	9	63.8	1.097	0.329	91.0	3.5	6.6	4.3	357.4	46.2	17.2	4.3
DM17	29.230	113.465	7	79.6	1.086	0.100	48.4	53.5	12.6	3.1	211.5	35.3	30.7	5.3
DM18	29.191	113.473	7	54.7	1.070	0.301	110.6	17.4	9.8	4.0	308.1	71.8	8.7	7.3
DM19	29.220	113.512	6	63.5	1.048	0.417	102.6	2.1	22.0	6.2	10.6	45.0	11.6	4.4
DM20	29.181	113.508	6	37.9	1.031	0.022	89.6	41.1	28.3	11.6	185.9	7.2	27.8	5.5
DM21	29.194	113.539	6	39.1	1.117	0.502	64.8	31.9	30.8	7.4	334.2	1.0	16.9	7.1
DM22	29.258	113.505	6	55.6	1.087	0.815	81.0	57.5	20.4	6.7	280.8	30.9	10.7	5.7
DM23	29.238	113.522	7	74.5	1.043	0.183	184.9	34.3	23.2	14.3	80.5	20.1	33.6	22.7

DM24	29.220	113.530	7	76.7	1.050	0.343	205.5	72.4	24.1	7.1	325.0	8.9	17.5	9.2
DM25	29.209	113.567	7	129	1.079	0.134	117.1	70.5	30.5	19.2	284.6	19.0	58.8	21.4
DM26	29.236	113.554	8	103	1.039	0.059	149.2	57.5	25.2	7.1	264.8	15.4	19.6	12.6
DM27	29.225	113.609	8	66.6	1.071	0.377	114.1	46.1	20.0	7.0	303.2	43.5	14.3	7.4
DM28	29.244	113.652	8	273	1.064	0.291	183.1	0.5	31.6	10.5	273.7	48.9	20.8	8.5
DM29	29.310	113.550	7	55.7	1.055	-0.150	79.6	31.1	10.7	5.5	339.4	16.4	16.9	7.2
DM30	29.309	113.571	6	52.4	1.045	0.405	21.6	32.5	53.6	21.1	247.2	47.7	44.4	20.5
DM31	29.270	113.628	8	131	1.144	0.121	87.1	53.9	34.2	12.1	301.4	31.1	35.8	11.7
DM32	29.269	113.767	9	125	1.044	0.192	226.7	55.8	69.8	23.0	330.7	9.3	34.0	26.6
DM33	29.275	113.718	8	209	1.043	0.211	49.4	21.1	15.0	10.2	241.3	68.4	17.0	12.6
DM34	29.294	113.681	7	157	1.045	0.380	38.6	14.3	55.8	10.4	297.3	37.3	18.5	9.9
DM35	29.328	113.669	6	8470	1.187	0.126	45.0	20.0	7.6	5.9	309.3	15.5	7.9	4.5
DM36	29.238	113.711	7	228	1.077	0.197	179.5	10.8	33.0	7.8	276.2	31.3	16.3	7.6
DM37	29.209	113.702	9	127	1.100	0.556	117.1	41.7	14.2	3.6	277.2	46.6	9.0	3.0
DM38	29.216	113.669	9	127	1.038	0.424	172.9	37.4	33.5	19.6	288.6	29.6	32.1	19.9
DM39	29.216	113.678	6	135	1.082	-0.334	154.5	43.7	29.2	14.8	51.9	12.9	28.4	13.0
DM40	29.210	113.630	6	72.3	1.093	0.000	254.6	2.7	51.9	19.3	12.9	84.3	38.5	28.7
DM41	29.193	113.627	6	79	1.047	0.256	156.2	65.5	34.5	15.5	261.8	7.0	15.7	9.1
DM42	29.165	113.630	7	46.6	1.099	0.765	129.4	18.2	39.8	4.5	16.7	49.6	4.5	2.0
DM43	29.142	113.607	7	49.7	1.065	0.120	189.9	15.8	25.9	11.2	339.3	71.9	24.4	10.4
DM44	29.113	113.637	6	62.8	1.107	0.659	30.0	50.9	12.7	5.1	212.2	39.0	19.5	1.2
DM45	29.172	113.718	7	82.4	1.128	-0.062	133.5	13.3	7.6	4.9	24.1	54.5	14.0	3.6
DM46	29.121	113.490	7	65.5	1.066	0.547	304.6	13.1	14.9	3.4	79.5	71.8	11.8	3.5
DM48	29.114	113.498	6	53.5	1.084	0.268	305.2	28.6	43.9	12.8	40.2	9.1	14.9	6.6
DM49	29.089	113.642	6	32.7	1.084	0.132	307.4	2.9	9.5	4.9	43.9	65.9	11.9	7.4
DM50	29.104	113.670	8	55.4	1.072	0.386	286.6	12.7	6.3	5.7	47.5	66.3	10.2	4.9
DM51	29.161	113.777	8	41.4	1.137	0.524	350.0	33.5	34.5	24.5	193.3	54.3	34.6	3.6

DM52	29.129	113.784	7	706	1.138	0.184	97.8	5.3	63.5	9.9	190.5	27.4	26.8	10.8
DM53	29.196	113.779	7	37.6	1.026	-0.180	124.8	63.1	11.7	6.7	229.0	7.1	23.9	11.6
DM54	29.106	113.754	8	167	1.086	0.502	197.1	23.3	37.0	13.9	322.3	53.3	28.8	19.4
DM55	29.097	113.742	6	93.3	1.040	0.352	82.6	16.7	29.9	9.3	336.7	42.4	9.9	6.6
DM56	29.074	113.701	6	74.5	1.074	0.477	110.7	13.8	7.8	4.6	3.6	50.2	6.5	3.5
DM57	29.059	113.678	5	57	1.099	0.251	115.8	6.9	22.9	7.2	13.6	60.1	13.0	7.8
DM58	29.047	113.660	7	17900	1.414	0.574	273.1	10.0	4.5	2.5	29.2	68.1	3.3	2.6
DM59	29.030	113.672	7	9860	1.499	0.703	260.0	41.1	23.1	1.2	42.6	42.3	3.1	1.2
DM60	29.011	113.715	6	2280	1.187	0.241	238.9	30.6	22.1	4.5	94.0	54.1	8.3	2.2
DM61	29.046	113.720	8	81.3	1.078	0.540	98.3	0.5	7.7	5.3	7.8	42.4	9.8	5.2
DM62	28.992	113.717	6	2120	1.290	0.764	250.4	52.0	43.3	10.4	61.4	37.7	10.4	5.1
DM63	28.978	113.723	7	219	1.122	0.563	188.6	0.1	23.8	6.0	98.4	63.6	11.3	4.3
DM64	29.232	113.817	7	23.9	1.031	0.357	262.1	9.3	21.7	9.4	132.3	75.6	13.5	11.6
DM65	29.211	113.843	7	53	1.056	0.345	99.9	19.5	16.9	4.5	224.0	57.8	8.5	3.9
DM66	29.187	113.835	9	62.3	1.068	0.539	128.2	19.5	12.5	2.4	249.4	55.6	5.8	2.8
DM67	29.175	113.829	8	48.4	1.042	0.415	308.1	5.4	11.6	4.4	204.4	68.1	10.5	5.1
DM68	29.181	113.909	9	62.7	1.040	0.602	341.9	2.5	10.4	3.0	235.4	81.3	5.3	3.3
DM69	29.157	113.899	7	75.1	1.077	-0.032	287.4	6.4	66.0	39.7	47.1	77.3	57.2	52.4
DM70	29.114	113.871	6	52.3	1.074	0.338	122.8	26.7	5.9	3.7	350.7	53.1	12.2	3.5
DM71	29.097	113.859	9	52.9	1.053	-0.472	116.6	46.6	6.0	3.6	6.2	17.8	21.0	3.7
DM72	29.082	113.855	7	50.4	1.044	0.137	123.9	16.5	29.4	22.1	4.4	59.1	58.4	24.1
DM73	29.145	113.890	8	82.3	1.090	0.510	152.6	26.2	11.2	5.5	267.9	41.0	14.0	5.2
DM74	29.153	113.983	10	573	1.061	0.209	166.0	37.3	16.1	3.3	262.9	8.9	13.0	3.1
DM75	29.118	113.983	7	1170	1.151	0.484	189.2	23.8	15.9	4.8	90.7	18.6	8.5	4.8
DM76	29.133	114.079	8	18700	1.156	0.578	181.4	8.1	13.8	9.4	91.1	2.5	9.5	2.9
DM77	29.126	113.946	8	195	1.104	0.494	141.8	35.2	7.6	4.1	263.1	36.4	21.3	4.2
DM78	29.106	113.932	5	57.3	1.062	0.191	134.6	7.5	21.2	1.9	277.6	80.7	9.2	2.6

DM79	29.072	113.910	8	30.6	1.025	0.285	176.9	12.7	36.8	8.4	321.2	74.4	12.2	9.0
DM80	29.050	113.895	7	89.1	1.061	-0.360	305.5	3.3	12.6	7.2	38.2	39.4	72.6	8.0
DM81	29.023	113.885	5	74.1	1.044	-0.143	354.4	32.9	19.1	2.5	175.4	57.1	28.6	3.6
DM82	29.001	113.887	7	67.4	1.021	-0.272	214.0	53.2	14.4	6.7	311.9	5.9	12.9	5.8
DM83	28.987	113.888	7	44.1	1.099	0.175	147.9	5.8	19.4	3.9	244.3	47.6	16.9	4.2
DM84	28.957	113.889	9	52.7	1.066	0.612	180.7	14.1	12.7	7.6	65.5	59.5	13.9	2.8
DM85	28.902	113.898	9	76	1.070	0.509	111.8	4.0	30.1	5.8	17.4	47.8	13.9	6.2
DM86	28.903	113.916	8	128	1.070	0.381	104.5	8.6	12.3	6.5	6.8	41.3	6.9	6.4
DM87	28.919	113.931	7	55	1.022	0.184	261.4	45.9	41.0	17.1	31.2	31.8	27.4	15.3
DM88	28.949	113.933	7	113	1.077	0.011	170.6	29.4	25.7	5.8	42.5	47.7	22.8	4.7
DM89	28.985	113.936	7	52.3	1.058	0.059	123.3	29.4	7.2	5.7	4.4	40.6	10.1	5.2
DM90	28.935	113.950	7	62.7	1.053	0.214	191.6	3.3	12.6	10.2	289.0	65.8	24.7	10.2
DM91	28.988	114.057	6	387	1.058	0.059	69.7	53.6	20.9	6.5	282.7	31.8	11.4	10.2
DM92	28.972	113.987	6	417	1.114	0.779	153.5	54.2	68.7	2.0	339.1	35.7	6.4	1.6
DM93	28.972	113.987	8	915	1.061	0.593	105.7	2.2	51.2	9.3	208.4	80.2	20.1	3.9
DM94	28.984	113.999	6	1440	1.147	0.841	175.2	42.8	51.7	6.4	325.3	43.1	8.3	5.8
DM95	29.035	113.983	6	47	1.030	0.409	293.3	8.7	29.8	9.9	155.6	78.3	20.5	10.3
DM96	29.051	114.028	6	41.5	1.051	-0.031	128.1	9.0	11.1	1.5	252.6	74.3	15.9	6.4
DM97	29.091	113.993	6	114	1.009	-0.101	307.0	30.6	40.3	5.8	202.6	22.8	22.8	16.3
DM98	29.102	114.051	8	20800	1.282	0.459	111.9	83.3	10.8	2.0	250.1	5.0	5.3	2.0
DM99	29.079	114.050	6	256	1.041	0.133	155.8	12.1	20.5	5.2	58.5	30.8	61.1	9.1
DM100	29.031	114.086	7	547	1.145	0.770	199.9	1.6	24.3	5.8	290.0	2.2	7.0	2.5
DM101	28.925	113.853	8	65.3	1.048	-0.514	128.0	3.1	11.8	6.7	34.2	51.1	70.5	9.0
DM102	28.886	113.832	8	312	1.123	0.471	159.4	58.7	12.7	4.7	270.0	12.1	12.2	4.7
DM103	28.888	113.821	7	44.2	1.061	-0.440	179.7	13.1	11.3	6.3	272.3	11.3	22.1	8.1
DM104	28.874	113.798	8	46.1	1.088	0.494	110.8	42.9	40.2	23.6	327.0	41.0	25.4	17.8
DM105	28.898	113.784	7	493	1.122	0.241	207.8	4.6	15.6	13.2	312.3	72.2	17.8	13.9

DM106	28.925	113.773	8	70.1	1.068	0.458	238.1	8.1	24.4	6.0	128.2	67.4	7.5	6.0
DM107	28.973	113.815	7	56.2	1.060	0.345	257.6	7.1	8.9	3.5	353.0	37.3	6.1	4.4
DM108	28.953	113.795	7	43.4	1.103	0.758	250.9	37.1	18.9	6.9	63.5	52.7	15.9	8.1
DM109	28.972	113.772	7	942	1.163	0.822	257.3	52.4	39.5	7.0	89.6	36.9	7.5	4.1
DM110	28.999	113.781	7	53.3	1.048	-0.261	155.4	25.0	11.4	2.8	61.5	8.2	21.9	5.3
DM111	29.027	113.829	7	58.2	1.048	0.165	176.1	16.1	14.1	6.6	334.2	72.8	16.1	7.1
DM112	29.044	113.847	8	43.1	1.054	0.793	176.7	9.3	14.3	5.9	342.0	80.4	6.3	4.8
DM113	28.866	113.623	7	281	1.255	0.552	220.2	18.9	17.9	3.8	70.8	68.3	5.0	2.0
DM114	28.890	113.662	7	164	1.084	0.593	261.4	4.1	35.9	3.8	58.9	85.6	11.8	4.0
DM115	28.906	113.669	7	1590	1.142	0.728	286.0	26.7	29.9	11.2	85.3	61.7	11.6	5.4
DM116	28.869	113.736	6	53.3	1.085	0.541	216.9	21.2	19.7	8.2	100.6	48.7	11.2	6.6
DM117	28.851	113.730	5	228	1.234	0.837	234.0	19.0	6.5	3.0	36.1	70.2	7.4	3.1
DM118	28.897	113.690	6	32.8	1.072	0.585	356.2	11.7	18.7	5.4	105.2	57.6	18.1	8.5
DM119	29.025	113.743	6	68.6	1.082	0.750	231.8	24.4	41.2	5.2	7.1	57.4	12.8	1.8
DM120	29.043	113.753	7	183	1.117	0.530	142.4	35.3	19.5	9.9	3.4	46.8	18.7	11.0
DM121	29.101	113.782	8	105	1.112	0.268	179.2	4.6	24.7	9.0	282.3	70.3	35.2	18.2
DM122	29.219	113.951	7	12700	1.250	-0.253	173.7	21.5	7.1	1.8	342.9	68.1	7.0	2.1

K_m平均磁化率; P_J磁化率各向异性度; T磁化率椭球体形状因子; Dec: 偏角, Inc: 倾角; α_{95max}和α_{95min}: Jelinek's statistic confidence at 95% level (Jelinek, 1981)

表 4-2 大云山-幕阜山岩基锆石 U-Pb 年代学数据

Table 4-2 Zircon U-Pb data of Dayunshan-Mufushan batholith

Sample#spot	U ppm	Th ppm	Th/U	f_{206}%	$^{207}Pb/^{206}Pb$	±σ (%)	$^{207}Pb/^{235}U$	±σ (%)	$^{206}Pb/^{238}U$	±σ (%)	$t_{207/206}$ (Ma)	±σ (Ma)	$t_{207/235}$ (Ma)	±σ (Ma)	$t_{206/238}$ (Ma)	±σ (Ma)
DM35																
DM35#1	874	289	0.33	0.07	0.04920	1.53	0.16198	2.16	0.0239	1.53	157.5	35.4	152.4	3.1	152.1	2.3
DM35#2	917	392	0.43	0.10	0.04835	0.91	0.15749	1.77	0.0236	1.51	116.6	21.4	148.5	2.4	150.5	2.2
DM35#3	1121	585	0.52	0.04	0.04869	1.11	0.15880	1.88	0.0237	1.51	132.7	26.0	149.7	2.6	150.7	2.3
DM35#4	1288	751	0.58	0.06	0.04894	0.77	0.15827	1.69	0.0235	1.50	144.9	17.9	149.2	2.3	149.5	2.2
DM35#5	1195	583	0.49	0.03	0.04890	0.80	0.16061	1.88	0.0238	1.70	143.3	18.6	151.2	2.6	151.7	2.5
DM35#6	1448	793	0.55	0.07	0.04919	0.74	0.16219	1.67	0.0239	1.50	156.9	17.1	152.6	2.4	152.3	2.3
DM35#7	942	419	0.45	0.02	0.04920	1.42	0.15977	2.07	0.0236	1.50	157.4	32.8	150.5	2.9	150.1	2.2
DM35#8	709	256	0.36	0.00	0.04934	1.05	0.16005	1.83	0.0235	1.51	164.0	24.3	150.7	2.6	149.9	2.2
DM35#9	517	334	0.65	0.03	0.04912	1.20	0.16261	1.92	0.0240	1.50	153.3	28.0	153.0	2.7	153.0	2.3
DM35#10	1292	725	0.56	0.04	0.04894	0.76	0.16118	1.68	0.0239	1.50	144.8	17.8	151.7	2.4	152.2	2.3
DM35#11	836	334	0.40	0.07	0.04990	1.07	0.16293	1.85	0.0237	1.50	190.4	24.8	153.3	2.6	150.9	2.2
DM35#12	2406	497	0.21	0.08	0.07332	3.24	0.43199	7.53	0.0427	6.80	1022.7	64.2	364.6	23.3	269.7	18.0
DM35#13	917	510	0.56	0.03	0.04905	0.95	0.16085	1.79	0.0238	1.51	150.3	22.2	151.4	2.5	151.5	2.3
DM35#14	882	394	0.45	0.17	0.04823	0.94	0.15866	1.77	0.0239	1.50	110.4	22.1	149.5	2.5	152.0	2.3
DM35#15	893	420	0.47	0.06	0.04941	1.34	0.16213	2.02	0.0238	1.51	167.2	30.9	152.6	2.9	151.6	2.3
DM35#16	1227	694	0.57	0.07	0.04900	1.02	0.15839	1.82	0.0234	1.51	148.0	23.7	149.3	2.5	149.4	2.2
DM35#17	887	287	0.32	0.22	0.06762	0.57	1.07765	1.61	0.1156	1.50	856.9	11.7	742.5	8.5	705.1	10.0
DM35#18	1075	584	0.54	0.15	0.04912	0.84	0.16247	1.74	0.0240	1.53	153.8	19.6	152.9	2.5	152.8	2.3
QD69																
QD69#1	1839	345	0.19	0.05	0.04833	1.10	0.15737	1.86	0.0236	1.50	115.3	25.8	148.4	2.6	150.5	2.2
QD69#2	3341	422	0.13	0.00	0.04927	1.00	0.16283	1.87	0.0240	1.58	160.5	23.3	153.2	2.7	152.7	2.4
QD69#3	2516	271	0.11	0.00	0.04917	0.93	0.16042	1.76	0.0237	1.50	155.8	21.5	151.1	2.5	150.8	2.2
QD69#4	755	27	0.04	0.00	0.04925	1.74	0.16162	2.31	0.0238	1.52	159.8	40.2	152.1	3.3	151.6	2.3
QD69#5	7007	979	0.14	0.00	0.04951	0.54	0.17165	1.60	0.0251	1.50	172.0	12.7	160.8	2.4	160.1	2.4

QD69#6	4952	771	0.16	0.34	0.05192	0.63	0.16161	1.91	0.0238	1.50	158.3	27.3	152.1	2.7	151.7	2.3
QD69#7	4816	700	0.15	0.01	0.04913	0.66	0.16316	1.64	0.0241	1.51	154.2	15.4	153.5	2.3	153.4	2.3
QD69#8	3176	612	0.19	0.06	0.04931	0.92	0.16086	1.80	0.0239	1.50	140.2	23.2	151.5	2.5	152.2	2.3
QD69#9	2483	405	0.16	0.01	0.04890	0.94	0.16172	1.77	0.0240	1.50	142.8	21.9	152.2	2.5	152.8	2.3
QD69#10	126	85	0.68	0.08	0.06625	1.49	1.26671	2.11	0.1387	1.50	814.3	30.7	830.9	12.1	837.1	11.8
QD69#11	521	397	0.76	0.15	0.04892	2.07	0.15846	2.56	0.0235	1.50	144.0	47.8	149.4	3.6	149.7	2.2
QD69#12	1466	106	0.07	0.00	0.04819	1.24	0.15587	1.95	0.0235	1.51	108.6	29.0	147.1	2.7	149.5	2.2
QD69#13	3703	727	0.20	0.07	0.04933	0.77	0.15923	1.74	0.0237	1.50	136.3	20.4	150.0	2.4	150.9	2.2
QD69#14	5370	652	0.12	0.23	0.05007	0.62	0.16664	1.69	0.0251	1.50	110.0	18.5	156.5	2.5	159.6	2.4
QD69#15	2129	217	0.10	0.12	0.05000	1.28	0.15816	2.05	0.0234	1.50	151.2	32.3	149.1	2.8	149.0	2.2
QD69#16	2873	246	0.09	0.01	0.04964	0.86	0.16333	1.77	0.0239	1.54	178.3	20.0	153.6	2.5	152.0	2.3
QD69#17	2996	340	0.11	0.04	0.04865	0.86	0.15894	1.73	0.0237	1.50	131.1	20.1	149.8	2.4	151.0	2.2
QD69#18	427	250	0.59	0.14	0.04910	2.28	0.16414	2.74	0.0242	1.53	152.8	52.5	154.3	3.9	154.4	2.3
QD69#19	1295	1783	1.38	0.06	0.04896	1.30	0.15940	1.99	0.0236	1.50	145.7	30.2	150.2	2.8	150.5	2.2
DYS14																
DYS14#1	303	185	0.61	0.31	0.05049	2.63	0.17024	3.05	0.0245	1.55	217.8	59.8	159.6	4.5	155.7	2.4
DYS14#2	381	298	0.78	0.15	0.05049	2.63	0.16478	3.04	0.0237	1.53	217.4	59.7	154.9	4.4	150.8	2.3
DYS14#3	439	226	0.52	0.26	0.04888	2.23	0.15967	2.70	0.0237	1.52	142.2	51.5	150.4	3.8	150.9	2.3
DYS14#4	330	258	0.78	0.29	0.04961	2.56	0.15909	3.02	0.0233	1.59	176.6	58.7	149.9	4.2	148.2	2.3
DYS14#5	457	216	0.47	0.02	0.05133	2.14	0.16518	2.63	0.0233	1.53	255.7	48.4	155.2	3.8	148.7	2.2
DYS14#6	378	372	0.98	0.40	0.05221	2.35	0.16049	3.83	0.0237	1.58	150.7	79.8	151.1	5.4	151.2	2.4
DYS14#7	517	168	0.32	0.15	0.04917	2.08	0.15539	2.58	0.0229	1.52	156.1	47.9	146.7	3.5	146.1	2.2
DYS14#8	532	301	0.57	0.11	0.04765	2.04	0.15615	2.53	0.0238	1.50	81.9	47.6	147.3	3.5	151.4	2.2
DYS14#9	627	281	0.45	0.13	0.05012	1.85	0.16374	2.39	0.0237	1.52	200.7	42.4	154.0	3.4	151.0	2.3
DYS14#10	942	529	0.56	0.06	0.04966	1.49	0.16027	2.13	0.0234	1.51	179.0	34.5	150.9	3.0	149.2	2.2
DYS14#11	414	277	0.67	0.38	0.04849	3.49	0.15388	3.83	0.0230	1.59	123.3	80.1	145.3	5.2	146.7	2.3
DYS14#12	326	162	0.50	0.12	0.04861	2.98	0.15723	3.34	0.0235	1.52	129.2	68.6	148.3	4.6	149.5	2.3
DYS14#13	294	258	0.88	0.11	0.04958	2.71	0.15983	3.10	0.0234	1.51	175.5	62.0	150.6	4.3	149.0	2.2

DYS14#14	694	117	0.17	0.14	0.04887	2.86	0.15945	3.23	0.0237	1.51	141.8	65.8	150.2	4.5	150.8	2.3
DYS14#15	948	74	0.08	0.01	0.06672	0.56	1.24630	1.61	0.1355	1.51	829.0	11.6	821.7	9.1	819.1	11.6
DYS14#16	699	620	0.89	0.34	0.05136	2.07	0.15739	3.04	0.0235	1.50	131.3	61.0	148.4	4.2	149.5	2.2
DYS14#17	261	166	0.64	0.72	0.04998	2.85	0.14985	4.20	0.0231	1.55	48.2	90.8	141.8	5.6	147.4	2.3
DYS14#18	676	370	0.55	0.17	0.05082	1.77	0.16449	2.33	0.0235	1.52	232.5	40.3	154.6	3.4	149.6	2.3
DYS14#19	629	381	0.61	0.47	0.05207	1.85	0.15384	3.19	0.0231	1.54	116.1	64.7	145.3	4.3	147.1	2.2
DYS14#20	726	561	0.77	0.00	0.04949	1.76	0.15499	2.32	0.0227	1.51	171.0	40.6	146.3	3.2	144.8	2.2
DYS14#21	674	504	0.75	0.23	0.04937	2.45	0.15346	3.24	0.0234	1.60	76.8	65.6	145.0	4.4	149.2	2.4
QD49																
QD49#1	5166	109	0.02	0.03	0.04867	0.60	0.14105	1.62	0.0210	1.50	132.1	14.1	134.0	2.0	134.1	2.0
QD49#2	2432	358	0.15	0.04	0.04854	0.86	0.13996	1.75	0.0209	1.53	125.5	20.2	133.0	2.2	133.4	2.0
QD49#3	3685	438	0.12	0.04	0.04878	0.54	0.14215	1.60	0.0211	1.50	137.3	12.6	135.0	2.0	134.8	2.0
QD49#4	88	81	0.92	0.72	0.04895	4.00	0.13724	4.29	0.0203	1.56	145.7	91.2	130.6	5.3	129.8	2.0
QD49#5	831	697	0.84	0.07	0.04870	1.14	0.14644	1.90	0.0218	1.52	133.5	26.5	138.8	2.5	139.1	2.1
QD49#6	162	154	0.95	0.15	0.04868	3.00	0.13679	3.37	0.0204	1.53	132.3	69.0	130.2	4.1	130.1	2.0
QD49#7	157	164	1.04	0.13	0.05268	2.73	0.14519	3.13	0.0200	1.54	315.0	60.9	137.7	4.0	127.6	1.9
QD49#8	2981	675	0.23	0.02	0.04850	0.60	0.14360	1.64	0.0215	1.53	123.8	14.0	136.2	2.1	137.0	2.1
QD49#9	938	325	0.35	0.00	0.04805	1.45	0.13668	2.13	0.0206	1.56	101.9	33.8	130.1	2.6	131.6	2.0
QD49#10	525	334	0.64	0.01	0.06737	0.44	1.27868	1.56	0.1377	1.50	849.3	9.1	836.3	8.9	831.4	11.7
QD49#11	161	92	0.57	0.16	0.05232	2.47	0.19698	2.96	0.0273	1.64	299.6	55.4	182.6	5.0	173.6	2.8
QD49#12	367	278	0.76	0.16	0.04916	2.34	0.14373	2.82	0.0212	1.56	155.7	53.9	136.4	3.6	135.3	2.1
QD49#13	618	416	0.67	0.01	0.06706	0.40	1.29991	1.56	0.1406	1.51	839.8	8.3	845.7	9.0	847.9	12.0
QD49#14	706	748	1.06	0.13	0.04862	1.37	0.13346	2.03	0.0199	1.50	129.6	31.9	127.2	2.4	127.1	1.9
QD49#15	427	188	0.44	0.02	0.06386	0.62	0.80096	1.63	0.0910	1.51	736.9	13.0	597.4	7.4	561.3	8.1
QD49#16	252	222	0.88	0.36	0.04779	2.99	0.13409	3.38	0.0203	1.58	89.0	69.4	127.8	4.1	129.9	2.0
QD49#17	1186	442	0.37	0.03	0.06102	0.48	0.49973	1.86	0.0594	1.80	639.8	10.3	411.5	6.3	372.0	6.5
QD49#18	413	119	0.29	0.08	0.04853	1.49	0.13458	2.12	0.0201	1.51	125.3	34.6	128.2	2.6	128.4	1.9
QD49#19	1272	375	0.29	0.04	0.04815	0.82	0.13839	1.71	0.0208	1.51	106.6	19.2	131.6	2.1	133.0	2.0

QD49#20	632	148	0.23	0.08	0.04861	1.20	0.13654	1.93	0.0204	1.51	129.0	27.9	130.0	2.4	130.0	1.9
QD49#21	975	525	0.54	0.01	0.08200	0.27	2.35906	1.53	0.2087	1.50	1245.5	5.4	1230.3	10.9	1221.6	16.7
QD62																
DQ62#1	3724	483	0.13	0.06	0.04816	1.30	0.13365	1.99	0.0201	1.50	107.4	30.4	127.4	2.4	128.4	1.9
DQ62#2	1266	474	0.37	0.02	0.06662	0.79	1.09491	1.71	0.1195	1.51	820.2	16.6	750.9	9.1	727.8	10.4
DQ62#3	537	50	0.09	0.18	0.04847	2.27	0.13033	2.77	0.0195	1.58	122.4	52.7	124.4	3.2	124.5	2.0
DQ62#4	9826	1410	0.14	0.04	0.04876	0.52	0.14160	1.93	0.0212	1.85	121.6	12.6	134.5	2.4	135.2	2.5
DQ62#5	1170	245	0.21	0.04	0.04907	1.52	0.13080	2.16	0.0193	1.53	151.2	35.3	124.8	2.5	123.4	1.9
DQ62#6	3033	397	0.13	0.32	0.05369	1.24	0.15528	2.50	0.0220	1.98	247.2	34.6	146.6	3.4	140.4	2.8
DQ62#7	1719	321	0.19	0.32	0.05862	1.30	0.22448	2.22	0.0290	1.53	456.4	35.1	205.6	4.1	184.4	2.8
DQ62#8	2839	425	0.15	0.33	0.05102	1.48	0.13321	2.37	0.0199	1.55	121.3	41.8	127.0	2.8	127.3	2.0
DQ62#9	1708	363	0.21	0.07	0.04891	1.27	0.13338	1.97	0.0198	1.51	143.4	29.5	127.1	2.4	126.3	1.9
DQ62#10	2516	533	0.21	0.16	0.05020	1.13	0.12682	2.01	0.0188	1.52	143.4	30.6	121.2	2.3	120.1	1.8
DQ62#11	1260	526	0.42	0.00	0.04989	1.43	0.14053	2.07	0.0204	1.51	190.0	32.8	133.5	2.6	130.4	1.9
DQ62#12	602	96	0.16	0.08	0.04828	2.54	0.13963	3.02	0.0210	1.63	113.2	58.8	132.7	3.8	133.8	2.2
DQ62#13	2099	541	0.26	0.01	0.04849	1.12	0.14456	1.87	0.0216	1.50	123.4	26.2	137.1	2.4	137.9	2.0
DQ62#14	2693	376	0.14	0.08	0.04849	1.04	0.12438	1.83	0.0186	1.51	123.3	24.3	119.0	2.1	118.8	1.8
DQ62#15	1634	186	0.11	0.12	0.04806	1.31	0.13385	1.99	0.0202	1.50	102.3	30.7	127.5	2.4	128.9	1.9
DQ62#16	2636	509	0.19	0.06	0.04832	1.01	0.13191	1.87	0.0198	1.57	114.8	23.7	125.8	2.2	126.4	2.0
DQ62#17	1802	321	0.18	0.02	0.04868	1.21	0.13246	1.94	0.0197	1.52	132.6	28.2	126.3	2.3	126.0	1.9
DQ62#18	1967	244	0.12	0.06	0.04832	1.16	0.13716	1.90	0.0206	1.50	115.1	27.1	130.5	2.3	131.4	2.0
DQ62#19	1619	291	0.18	0.04	0.04884	1.31	0.13025	2.00	0.0193	1.51	140.3	30.6	124.3	2.3	123.5	1.8
DQ62#20	1702	130	0.08	0.01	0.04961	1.99	0.12839	2.55	0.0188	1.59	176.6	45.8	122.7	3.0	119.9	1.9
DQ62#21	2239	227	0.10	0.01	0.04944	1.08	0.13796	1.87	0.0202	1.53	168.8	25.1	131.2	2.3	129.2	2.0
DQ62#22	3402	420	0.12	0.02	0.04968	0.89	0.13739	1.75	0.0201	1.50	180.0	20.5	130.7	2.1	128.0	1.9
DQ62#23	851	106	0.12	0.06	0.05185	1.81	0.13970	2.39	0.0195	1.56	278.8	41.0	132.8	3.0	124.8	1.9
DM80																

DM80#1	810	113	0.14	0.02	0.06594	0.44	1.13078	1.57	0.1244	1.51	804.4	9.1	768.1	8.5	755.7	10.8
DM80#2	405	70	0.17	0.03	0.06589	0.51	1.23105	1.61	0.1355	1.53	802.7	10.7	814.8	9.1	819.2	11.7
DM80#3	68	43	0.63	0.07	0.06772	1.36	1.31618	2.06	0.1410	1.55	860.0	27.9	852.8	11.9	850.1	12.3
DM80#4	690	535	0.78	0.04	0.06670	0.43	1.20012	1.56	0.1305	1.50	828.5	9.0	800.6	8.7	790.7	11.2
DM80#5	260	255	0.98	0.06	0.05588	1.26	0.51429	1.96	0.0668	1.50	447.6	27.8	421.3	6.8	416.5	6.1
DM80#6	1452	262	0.18	0.04	0.05923	1.41	0.37095	5.43	0.0454	5.24	575.7	30.4	320.4	15.0	286.3	14.7
DM80#7	1633	595	0.36	0.06	0.04853	1.03	0.14468	1.84	0.0216	1.52	125.4	24.1	137.2	2.4	137.9	2.1
DM80#8	2488	784	0.32	0.02	0.04879	0.73	0.15014	1.68	0.0223	1.52	137.8	17.0	142.0	2.2	142.3	2.1
DM80#9	10911	941	0.09	0.02	0.04865	0.27	0.16159	1.54	0.0241	1.51	131.1	6.3	152.1	2.2	153.4	2.3
DM80#10	1329	584	0.44	0.05	0.06371	0.45	0.76740	1.57	0.0874	1.50	731.9	9.6	578.3	6.9	539.9	7.8
DM80#11	7413	115	0.02	0.01	0.05362	0.33	0.19986	1.54	0.0270	1.51	355.1	7.4	185.0	2.6	172.0	2.6
DM80#12	6842	244	0.04	0.03	0.04888	0.36	0.15588	1.55	0.0231	1.51	142.2	8.5	147.1	2.1	147.4	2.2

f_{206} is the proportion of common ^{206}Pb in total measured ^{206}Pb.

表 4-3 大云山-幕阜山独居石 U-Th-Pb 定年数据

Table 4-3 Monazite U-Th-Pb data of Dayunshan-Mufushan area

Sample&grain	Age Ma	Error Ma	U ppm	Error %	Th ppm	Error %	Pb ppm	Error %	Th* ppm	Error %	U/Pb	Error %	Th/Pb	Error %	Corr	Th/U
QD69, 片麻状黑云母二长花岗岩																
QD69-Mz1	138	54	2160	9.26	81500	2.00	541	36.94	88428	2.57	3.989	38.08	150.520	36.99	0.969	37.73
QD69-Mz1	157	65	1770	11.30	68310	2.00	517	38.72	73995	2.71	3.427	40.33	132.245	38.77	0.959	38.59
QD69-Mz1	147	62	1830	10.93	71730	2.00	506	39.54	77603	2.68	3.618	41.03	141.824	39.59	0.963	39.20
QD69-Mz1	164	67	1550	12.90	66390	2.00	519	38.51	71371	2.76	2.984	40.61	127.818	38.56	0.947	42.83
QD69-Mz1	143	56	2020	9.90	79860	2.00	549	36.40	86342	2.59	3.676	37.72	145.338	36.45	0.963	39.53
QD69-Mz1	155	54	2290	8.73	82000	2.00	616	32.49	89354	2.55	3.720	33.65	133.217	32.55	0.964	35.81
QD69-Mz1	134	59	1670	11.98	76060	2.00	486	41.13	81415	2.66	3.434	42.84	156.406	41.18	0.959	45.54
QD69-Mz1	146	69	1340	14.93	64610	2.00	448	44.63	68911	2.81	2.990	47.06	144.175	44.67	0.947	48.22
QD69-Mz1	161	63	1730	11.56	71260	2.00	549	36.42	76818	2.69	3.151	38.22	129.781	36.48	0.952	41.19
QD69-Mz1	137	64	1620	12.35	69430	2.00	455	44.00	74626	2.72	3.564	45.69	152.730	44.04	0.962	42.86
QD69-Mz1	159	53	2410	8.30	83610	2.00	645	30.99	91352	2.53	3.735	32.08	129.566	31.06	0.964	34.69
QD69-Mz1	155	52	2640	7.58	85030	2.00	647	30.93	93509	2.51	4.083	31.84	131.501	31.00	0.969	32.21
QD69-Mz1	140	51	2560	7.81	87290	2.00	596	33.58	95503	2.50	4.299	34.48	146.581	33.64	0.972	34.10
QD69-Mz1	149	52	2530	7.91	85450	2.00	621	32.19	93572	2.51	4.073	33.15	137.551	32.26	0.969	33.77
QD69-Mz1	112	62	1790	11.17	71130	2.00	383	52.21	76861	2.68	4.673	53.39	185.675	52.25	0.977	39.74
QD69-Mz1	151	68	1600	12.50	64830	2.00	469	42.69	69967	2.77	3.415	44.48	138.376	42.74	0.959	40.52
QD69-Mz1	153	71	1710	11.70	62160	2.00	460	43.43	67651	2.79	3.714	44.98	134.989	43.48	0.965	36.35
QD69-Mz1	177	71	1410	14.18	63540	2.00	537	37.26	68076	2.81	2.627	39.87	118.383	37.32	0.933	45.06
QD69-Mz1	155	63	1660	12.05	70540	2.00	523	38.21	75871	2.71	3.172	40.07	134.775	38.26	0.952	42.49
QD69-Mz1	184	82	1140	17.54	55100	2.00	483	41.43	58769	2.97	2.362	45.00	114.152	41.48	0.920	48.33
QD69-Mz1	139	51	2190	9.13	88510	2.00	589	33.96	95535	2.52	3.718	35.17	150.285	34.02	0.964	40.42
QD69-Mz1	180	63	1760	11.36	71730	2.00	621	32.18	77393	2.69	2.832	34.13	115.423	32.24	0.941	40.76
QD69-Mz1	156	53	2300	8.70	83740	2.00	631	31.69	91127	2.54	3.644	32.86	132.678	31.75	0.962	36.41
QD69-Mz1	157	59	1720	11.63	76030	2.00	570	35.08	81555	2.65	3.017	36.95	133.344	35.13	0.948	44.20

QD69-Mz1	136	58	1750	11.43	76610	2.00	497	40.23	82222	2.64	3.520	41.82	154.113	40.28	0.961	43.78
QD69-Mz1	169	51	2210	9.05	88280	2.00	718	27.84	95385	2.53	3.076	29.27	122.888	27.91	0.949	39.95
QD69-Mz1	131	55	1970	10.15	80190	2.00	505	39.62	86506	2.60	3.903	40.90	158.866	39.67	0.967	40.71
QD69-Mz1	145	59	1750	11.43	75310	2.00	520	38.45	80926	2.65	3.364	40.11	144.777	38.50	0.957	43.03
QD69-Mz1	149	63	1600	12.50	70800	2.00	502	39.81	75936	2.71	3.185	41.73	140.927	39.86	0.953	44.25
QD69-Mz1	170	66	1650	12.12	68210	2.00	556	35.97	73515	2.73	2.968	37.96	122.680	36.03	0.946	41.34
QD69-Mz1	117	65	1440	13.89	68000	2.00	377	53.11	72612	2.76	3.824	54.89	180.563	53.14	0.967	47.22
QD69-Mz1	149	66	1580	12.66	68070	2.00	484	41.29	73142	2.74	3.262	43.19	140.526	41.34	0.955	43.08
QD69-Mz1	145	67	1490	13.42	66160	2.00	458	43.66	70942	2.77	3.253	45.68	144.421	43.70	0.955	44.40
QD69-Mz1	186	68	1540	12.99	66780	2.00	595	33.62	71737	2.76	2.589	36.04	112.255	33.68	0.931	43.36
QD69-Mz1	162	64	1800	11.11	69970	2.00	546	36.60	75754	2.70	3.294	38.25	128.056	36.66	0.955	38.87
QD69-Mz1	151	62	1770	11.30	72490	2.00	525	38.10	78173	2.68	3.371	39.74	138.077	38.15	0.957	40.95
QD69-Mz1	126	58	1910	10.47	75830	2.00	458	43.70	81951	2.63	4.173	44.94	165.686	43.75	0.971	39.70
QD69-Mz1	160	57	2060	9.71	78550	2.00	605	33.05	85168	2.60	3.405	34.45	129.821	33.11	0.958	38.13
QD69-Mz1	126	56	2030	9.85	78560	2.00	478	41.87	85066	2.60	4.250	43.01	164.464	41.92	0.972	38.70
QD69-Mz1	144	59	1870	10.70	74840	2.00	516	38.74	80841	2.65	3.622	40.19	144.955	38.79	0.963	40.02
QD69-Mz2	137	41	3940	5.08	107340	2.00	729	27.44	119976	2.32	5.406	27.91	147.276	27.51	0.981	27.24
QD69-Mz2	139	46	3030	6.60	96470	2.00	657	30.43	106190	2.42	4.610	31.13	146.760	30.49	0.975	31.84
QD69-Mz2	130	44	3730	5.36	99210	2.00	643	31.08	111167	2.36	5.797	31.54	154.174	31.14	0.983	26.60
QD69-Mz2	155	51	3160	6.33	85270	2.00	658	30.38	95418	2.46	4.799	31.03	129.510	30.44	0.977	26.98
QD69-Mz2	139	47	5980	3.34	83140	2.00	631	31.69	102322	2.25	9.476	31.87	131.741	31.75	0.993	13.90
QD69-Mz2	159	46	3040	6.58	96550	2.00	753	26.55	106316	2.42	4.036	27.35	128.169	26.63	0.968	31.76
QD69-Mz3	139	46	3700	5.41	93830	2.00	654	30.59	105699	2.38	5.658	31.06	143.494	30.65	0.983	25.36
QD69-Mz3	156	39	7720	2.59	101100	2.00	874	22.89	125895	2.12	8.835	23.03	115.697	22.97	0.990	13.10
QD69-Mz3	148	44	5220	3.83	93460	2.00	724	27.61	110215	2.28	7.206	27.87	129.018	27.68	0.988	17.90
QD69-Mz3	151	41	6560	3.05	96760	2.00	790	25.31	117821	2.19	8.302	25.49	122.451	25.39	0.990	14.75
QD69-Mz3	154	57	1890	10.58	78040	2.00	577	34.64	84109	2.62	3.273	36.22	135.157	34.70	0.955	41.29
QD69-Mz3	158	54	3520	5.68	78860	2.00	633	31.58	90167	2.46	5.558	32.09	124.528	31.65	0.982	22.40
QD69-Mz3	157	45	5260	3.80	91980	2.00	762	26.25	108876	2.28	6.903	26.52	120.706	26.32	0.987	17.49

QD69-Mz3	168	64	1680	11.90	70560	2.00	566	35.32	75960	2.70	2.967	37.28	124.621	35.38	0.946	42.00
QD69-Mz3	143	37	12430	2.00	93780	2.00	850	23.52	133665	2.00	14.619	23.61	110.291	23.61	0.993	7.54
QD69-Mz3	137	37	12430	2.00	91890	2.00	801	24.96	131757	2.00	15.510	25.04	114.662	25.04	0.994	7.39
QD69-Mz3	147	36	16030	2.00	83310	2.00	876	22.82	134759	2.00	18.292	22.91	95.066	22.91	0.992	5.20
QD69-Mz3	150	46	7400	2.70	81110	2.00	700	28.57	104867	2.16	10.570	28.70	115.860	28.64	0.993	10.96
QD69-Mz3	157	59	1870	10.70	76310	2.00	575	34.76	82316	2.63	3.250	36.37	132.622	34.82	0.954	40.81
QD69-Mz3	140	63	1990	10.05	68880	2.00	467	42.79	75264	2.68	4.258	43.96	147.377	42.84	0.972	34.61
QD69-Mz3	159	66	1700	11.76	67980	2.00	519	38.51	73441	2.73	3.273	40.26	130.887	38.56	0.955	39.99
QD69-Mz3	149	63	1870	10.70	70310	2.00	506	39.49	76313	2.68	3.692	40.91	138.824	39.54	0.964	37.60
QD69-Mz3	157	53	2170	9.22	84190	2.00	638	31.33	91160	2.55	3.399	32.66	131.888	31.39	0.957	38.80
QD69-Mz3	169	47	2840	7.04	94700	2.00	782	25.57	103830	2.44	3.631	26.53	121.089	25.65	0.961	33.35
QD69-Mz3	145	47	3570	5.60	92970	2.00	673	29.70	104427	2.40	5.302	30.23	138.069	29.77	0.980	26.04
QD69-Mz4	137	39	3850	5.19	113660	2.00	765	26.14	126008	2.31	5.032	26.65	148.558	26.22	0.978	29.52
QD69-Mz4	149	41	3420	5.85	108080	2.00	790	25.31	119059	2.35	4.328	25.98	136.770	25.39	0.971	31.60
QD69-Mz4	160	48	2630	7.60	94440	2.00	735	27.23	102890	2.46	3.581	28.27	128.571	27.30	0.961	35.91
QD69-Mz4	153	54	2020	9.90	84080	2.00	617	32.43	90566	2.57	3.276	33.91	136.345	32.49	0.955	41.62
QD69-Mz4	113	52	2320	8.62	85020	2.00	464	43.13	92448	2.53	5.004	43.99	183.367	43.18	0.980	36.65
QD69-Mz4	134	53	2360	8.47	84010	2.00	547	36.59	91578	2.54	4.318	37.56	153.704	36.65	0.973	35.60
QD69-Mz4	137	53	2240	8.93	83090	2.00	548	36.50	90274	2.55	4.088	37.57	151.631	36.55	0.970	37.09
QD69-Mz4	156	55	2000	10.00	81140	2.00	607	32.96	87563	2.59	3.296	34.44	133.702	33.02	0.955	40.57
QD69-Mz4	144	54	2170	9.22	82810	2.00	576	34.73	89773	2.56	3.768	35.93	143.800	34.79	0.965	38.16
QD69-Mz4	144	53	2150	9.30	84520	2.00	585	34.17	91419	2.55	3.674	35.42	144.413	34.23	0.963	39.31
QD69-Mz4	136	46	3710	5.39	92210	2.00	630	31.74	104108	2.39	5.888	32.20	146.346	31.80	0.984	24.85
QD69-Mz4	143	42	3930	5.09	103930	2.00	742	26.94	116540	2.33	5.293	27.41	139.975	27.01	0.980	26.45
QD69-Mz4	147	40	3900	5.13	111120	2.00	810	24.68	123638	2.32	4.812	25.21	137.110	24.76	0.976	28.49
QD69-Mz4	161	43	3180	6.29	103530	2.00	814	24.57	113747	2.39	3.906	25.36	127.164	24.65	0.966	32.56
QD69-Mz4	118	48	2670	7.49	91990	2.00	528	37.88	100542	2.47	5.057	38.61	174.219	37.93	0.980	34.45
QD69-Mz4	167	53	2190	9.13	84400	2.00	681	29.35	91440	2.55	3.214	30.74	123.871	29.42	0.953	38.54
QD69-Mz4	139	55	2160	9.26	80850	2.00	544	36.79	87779	2.57	3.974	37.94	148.741	36.85	0.968	37.43

QD69-Mz4	141	53	2120	9.43	84890	2.00	576	34.73	91692	2.55	3.682	35.99	147.420	34.79	0.963	40.04
QD69-Mz4	166	51	2170	9.22	88250	2.00	702	28.49	95224	2.53	3.091	29.95	125.725	28.56	0.949	40.67
QD69-Mz4	167	52	2330	8.58	85780	2.00	691	28.93	93269	2.53	3.370	30.17	124.063	28.99	0.956	36.82
QD69-Mz4	129	52	2290	8.73	84080	2.00	525	38.12	91420	2.54	4.365	39.11	160.264	38.17	0.973	36.72
QD69-Mz5	174	59	2300	8.70	75640	2.00	642	31.16	83037	2.60	3.584	32.35	117.857	31.23	0.961	32.89
QD69-Mz5	164	55	2890	6.92	79230	2.00	644	31.05	88517	2.52	4.486	31.81	122.995	31.11	0.974	27.42
QD69-Mz5	147	56	4890	4.09	70700	2.00	563	35.55	86395	2.38	8.693	35.79	125.678	35.61	0.992	14.46
QD69-Mz5	158	53	4760	4.20	75920	2.00	640	31.27	91210	2.37	7.442	31.55	118.699	31.33	0.989	15.95
QD69-Mz5	141	50	4550	4.40	80870	2.00	599	33.41	95468	2.37	7.601	33.70	135.093	33.47	0.990	17.77
QD69-Mz5	147	52	3490	5.73	81280	2.00	604	33.11	92482	2.45	5.778	33.60	134.560	33.17	0.984	23.29
QD69-Mz5	171	53	2320	8.62	85570	2.00	708	28.24	93029	2.53	3.276	29.53	120.842	28.31	0.954	36.88
QD69-Mz5	143	57	2230	8.97	77720	2.00	540	37.07	84875	2.59	4.133	38.14	144.054	37.12	0.971	34.85
QD69-Mz5	149	56	2140	9.35	78540	2.00	565	35.37	85410	2.59	3.785	36.58	138.901	35.43	0.965	36.70
QD69-Mz5	134	47	3910	5.12	89860	2.00	609	32.86	102397	2.38	6.424	33.26	147.641	32.92	0.986	22.98
QD69-Mz6	139	49	3040	6.58	89160	2.00	610	32.81	98911	2.45	4.987	33.46	146.265	32.87	0.979	29.33
QD69-Mz6	141	41	9290	2.15	89090	2.00	745	26.85	118895	2.04	12.470	26.93	119.589	26.92	0.994	9.59
QD69-Mz6	159	47	3210	6.23	92760	2.00	730	27.38	103072	2.42	4.395	28.08	126.999	27.46	0.972	28.90
QD69-Mz6	143	56	2910	6.87	76190	2.00	543	36.85	85527	2.53	5.362	37.49	140.391	36.91	0.982	26.18
QD69-Mz6	154	43	10240	2.00	80100	2.00	772	25.90	112983	2.00	13.261	25.98	103.731	25.98	0.994	7.82
QD69-Mz6	133	43	9810	2.04	80570	2.00	662	30.23	112024	2.01	14.828	30.30	121.783	30.30	0.996	8.21
QD69-Mz6	161	53	2150	9.30	84340	2.00	654	30.59	91248	2.55	3.289	31.98	129.007	30.66	0.955	39.23
QD69-Mz6	141	50	2250	8.89	90420	2.00	612	32.67	97638	2.51	3.676	33.86	147.714	32.73	0.963	40.19
QD69-Mz6	158	51	2120	9.43	88150	2.00	669	29.92	94960	2.53	3.171	31.37	131.853	29.98	0.952	41.58
QD69-Mz6	143	59	1810	11.05	75880	2.00	518	38.58	81688	2.64	3.492	40.13	146.380	38.63	0.960	41.92
QD69-Mz6	154	59	1590	12.58	77340	2.00	565	35.42	82446	2.66	2.816	37.59	136.969	35.48	0.941	48.64
QD69-Mz6	153	60	1450	13.79	75460	2.00	544	36.77	80116	2.69	2.666	39.27	138.725	36.82	0.935	52.04
QD69-Mz6	170	61	1350	14.81	74640	2.00	596	33.55	78980	2.70	2.265	36.68	125.223	33.61	0.913	55.29
QD69-Mz6	133	61	1370	14.60	73880	2.00	464	43.08	78273	2.71	2.951	45.49	159.137	43.13	0.946	53.93
QD69-Mz6	129	59	1400	14.29	76080	2.00	464	43.13	80568	2.68	3.019	45.43	164.053	43.17	0.948	54.34

QD69-Mz6	135	58	1700	11.76	77610	2.00	498	40.13	83062	2.64	3.411	41.81	155.707	40.18	0.958	45.65
QD69-Mz6	159	54	1880	10.64	84140	2.00	637	31.38	90179	2.58	2.949	33.13	131.998	31.44	0.945	44.76
QD69-Mz6	145	57	1900	10.53	78810	2.00	548	36.48	84907	2.61	3.466	37.97	143.768	36.54	0.959	41.48
QD69-Mz6	134	54	2180	9.17	81810	2.00	530	37.75	88800	2.56	4.114	38.85	154.402	37.80	0.970	37.53
QD69-Mz6	157	57	1890	10.58	79530	2.00	597	33.51	85601	2.61	3.167	35.14	133.245	33.57	0.952	42.08
QD69-Mz6	153	54	1980	10.10	83190	2.00	611	32.72	89548	2.58	3.240	34.25	136.113	32.78	0.954	42.02
QD69-Mz6	155	55	2130	9.39	80500	2.00	602	33.21	87341	2.58	3.537	34.51	133.677	33.27	0.961	37.79
QD69-Mz7	121	49	3080	6.49	88750	2.00	529	37.78	98617	2.45	5.818	38.33	167.640	37.83	0.984	28.81
QD69-Mz7	156	51	2310	8.66	88470	2.00	664	30.11	95889	2.52	3.478	31.33	133.197	30.18	0.959	38.30
QD69-Mz7	136	52	2150	9.30	86280	2.00	565	35.40	93175	2.54	3.805	36.60	152.698	35.45	0.966	40.13
QD69-Mz7	161	57	1880	10.64	79460	2.00	613	32.63	85500	2.61	3.068	34.32	129.655	32.70	0.949	42.27
QD69-Mz7	145	58	1960	10.20	77060	2.00	536	37.34	83350	2.62	3.659	38.71	143.858	37.39	0.963	39.32
QD69-Mz7	158	56	2000	10.00	79490	2.00	604	33.13	85914	2.60	3.313	34.60	131.658	33.19	0.956	39.75
QD69-Mz7	147	59	1670	11.98	76740	2.00	536	37.32	82100	2.65	3.116	39.19	143.180	37.37	0.951	45.95
QD69-Mz7	127	60	1720	11.63	74510	2.00	453	44.12	80023	2.66	3.795	45.63	164.387	44.17	0.966	43.32
QD69-Mz7	140	82	1320	15.15	53600	2.00	360	55.57	57835	2.96	3.668	57.60	148.939	55.61	0.964	40.61
QD69-Mz7	157	92	1140	17.54	47910	2.00	361	55.47	51572	3.10	3.162	58.17	132.868	55.50	0.953	42.03
QD69-Mz7	146	82	1220	16.39	54210	2.00	378	52.90	58126	2.97	3.227	55.38	143.384	52.94	0.955	44.43
QD69-Mz7	167	60	1890	10.58	74300	2.00	597	33.49	80375	2.65	3.165	35.12	124.405	33.55	0.952	39.31
QD69-Mz7	114	54	2330	8.58	81250	2.00	451	44.39	88711	2.55	5.171	45.21	180.318	44.43	0.981	34.87
QD69-Mz7	160	49	2860	6.99	90260	2.00	707	28.30	99448	2.46	4.047	29.15	127.711	28.37	0.968	31.56
QD69-Mz7	139	54	2380	8.40	81940	2.00	552	36.25	89574	2.55	4.314	37.21	148.513	36.30	0.973	34.43
QD69-Mz7	168	53	2220	9.01	85770	2.00	693	28.87	92906	2.54	3.204	30.24	123.797	28.94	0.952	38.64
QD69-Mz7	147	61	1780	11.24	72480	2.00	512	39.05	78193	2.67	3.475	40.63	141.511	39.10	0.960	40.72
QD69-Mz7	157	68	1520	13.16	66020	2.00	495	40.40	70902	2.77	3.070	42.49	133.348	40.45	0.950	43.43
QD69-Mz7	174	90	1140	17.54	49100	2.00	408	49.08	52766	3.08	2.797	52.12	120.481	49.12	0.941	43.07
QD69-Mz7	140	101	1060	18.87	43320	2.00	290	68.89	46720	3.23	3.651	71.43	149.219	68.92	0.964	40.87
QD69-Mz7	154	57	2000	10.00	78120	2.00	578	34.59	84542	2.61	3.459	36.01	135.115	34.65	0.959	39.06
QD69-Mz7	143	48	2560	7.81	91800	2.00	634	31.53	100014	2.48	4.035	32.48	144.703	31.59	0.969	35.86

DM26, 矽线石云母片岩

DM26-Mz1	146	77	7280	2.75	38200	2.00	398	50.26	61564	2.28	18.293	50.33	95.988	50.30	0.998	5.25
DM26-Mz1	114	79	5200	3.85	42640	2.00	301	66.43	59290	2.52	17.271	66.54	141.626	66.46	0.998	8.20
DM26-Mz1	158	90	2700	7.41	43990	2.00	369	54.23	52663	2.89	7.321	54.73	119.276	54.27	0.990	16.29
DM26-Mz1	126	74	3210	6.23	53410	2.00	356	56.14	63697	2.68	9.011	56.49	149.931	56.18	0.993	16.64
DM26-Mz1	122	71	5620	3.56	48160	2.00	358	55.80	66165	2.42	15.680	55.91	134.365	55.84	0.997	8.57
DM26-Mz1	162	74	7970	2.51	38160	2.00	459	43.59	63769	2.20	17.371	43.66	83.172	43.64	0.997	4.79
DM26-Mz1	138	74	8460	2.36	36670	2.00	389	51.35	63805	2.15	21.721	51.40	94.151	51.39	0.998	4.33
DM26-Mz1	105	69	9260	2.16	37680	2.00	314	63.66	67311	2.07	29.475	63.70	119.937	63.69	0.999	4.07
DM26-Mz1	134	72	8380	2.39	38130	2.00	385	51.93	65001	2.16	21.757	51.98	98.996	51.96	0.998	4.55
DM26-Mz1	147	78	4910	4.07	45230	2.00	399	50.09	60990	2.54	12.296	50.25	113.270	50.13	0.996	9.21
DM26-Mz1	152	68	5870	3.41	50630	2.00	469	42.63	69478	2.38	12.511	42.76	107.909	42.67	0.996	8.63
DM26-Mz1	126	47	14780	2.00	54700	2.00	571	35.01	102067	2.00	25.873	35.07	95.756	35.07	0.997	3.70
DM26-Mz1	126	60	8870	2.25	50070	2.00	440	45.44	78497	2.09	20.153	45.50	113.759	45.48	0.998	5.64
DM26-Mz1	111	71	8530	2.34	38080	2.00	321	62.24	65386	2.14	26.544	62.28	118.498	62.27	0.999	4.46
DM26-Mz1	125	69	9290	2.15	37740	2.00	375	53.34	67510	2.07	24.776	53.38	100.649	53.38	0.998	4.06
DM26-Mz2	124	77	6820	2.93	39070	2.00	336	59.55	60923	2.33	20.306	59.62	116.328	59.58	0.998	5.73
DM26-Mz2	143	78	7150	2.80	37060	2.00	381	52.53	60002	2.30	18.779	52.60	97.336	52.57	0.998	5.18
DM26-Mz2	150	78	7300	2.74	36660	2.00	398	50.20	60095	2.29	18.322	50.27	92.009	50.24	0.998	5.02
DM26-Mz2	126	75	7780	2.57	37620	2.00	349	57.29	62552	2.23	22.285	57.35	107.760	57.32	0.998	4.84
DM26-Mz2	94	78	8060	2.48	33570	2.00	248	80.63	59341	2.21	32.495	80.67	135.343	80.66	0.999	4.17
DM26-Mz2	146	80	7080	2.82	36400	2.00	382	52.29	59122	2.32	18.512	52.37	95.176	52.33	0.998	5.14
DM26-Mz2	139	76	7980	2.51	36690	2.00	384	52.04	62288	2.21	20.764	52.10	95.466	52.08	0.998	4.60
DM26-Mz2	115	78	7070	2.83	37570	2.00	307	65.12	60209	2.31	23.022	65.19	122.337	65.16	0.999	5.31
DM26-Mz2	136	77	7490	2.67	37370	2.00	371	53.92	61391	2.26	20.193	53.99	100.751	53.96	0.998	4.99
DM26-Mz3	118	75	7120	2.81	39730	2.00	326	61.29	62534	2.30	21.818	61.35	121.748	61.32	0.998	5.58
DM26-Mz3	147	79	5030	3.98	43870	2.00	392	51.08	60014	2.53	12.846	51.23	112.043	51.12	0.996	8.72
DM26-Mz3	79	65	7630	2.62	46900	2.00	251	79.73	71269	2.21	30.418	79.78	186.976	79.76	0.999	6.15

DM26-Mz4	139	52	11570	2.00	54860	2.00	565	35.42	91972	2.00	20.489	35.47	97.151	35.47	0.997	4.74
DM26-Mz4	144	62	8180	2.44	50410	2.00	490	40.81	76659	2.15	16.690	40.88	102.856	40.86	0.997	6.16
DM26-Mz4	122	68	6700	2.99	48080	2.00	376	53.22	69545	2.30	17.828	53.30	127.934	53.25	0.998	7.18
DM26-Mz4	90	69	7740	2.58	42200	2.00	266	75.18	66939	2.22	29.096	75.23	158.635	75.21	0.999	5.45
DM26-Mz4	133	68	9200	2.17	39450	2.00	406	49.20	68948	2.07	22.633	49.25	97.053	49.24	0.998	4.29
DM26-Mz4	137	65	7770	2.57	47690	2.00	443	45.19	72611	2.20	17.558	45.27	107.764	45.24	0.997	6.14
DM26-Mz4	138	61	8600	2.33	50370	2.00	477	41.95	77954	2.12	18.037	42.01	105.644	41.99	0.997	5.86
DM26-Mz4	138	58	9830	2.03	50560	2.00	504	39.69	82091	2.01	19.510	39.75	100.347	39.74	0.997	5.14
DM26-Mz5	167	73	7900	2.53	39680	2.00	482	41.50	65073	2.21	16.393	41.58	82.339	41.55	0.997	5.02
DM26-Mz5	141	72	8690	2.30	37950	2.00	412	48.55	65830	2.13	21.094	48.60	92.121	48.59	0.998	4.37
DM26-Mz5	134	73	7580	2.64	40070	2.00	384	52.15	64377	2.24	19.764	52.21	104.476	52.19	0.998	5.29
DM26-Mz5	133	73	7320	2.73	40820	2.00	380	52.65	64291	2.27	19.271	52.72	107.463	52.69	0.998	5.58
DM26-Mz5	118	74	8090	2.47	37670	2.00	333	60.14	63581	2.19	24.327	60.19	113.276	60.17	0.999	4.66
DM26-Mz5	125	76	8210	2.44	35450	2.00	342	58.49	61759	2.19	24.012	58.54	103.680	58.53	0.999	4.32
DM26-Mz5	122	73	6660	3.00	43360	2.00	349	57.30	64697	2.33	19.081	57.38	124.227	57.34	0.998	6.51
DM26-Mz5	131	71	6890	2.90	43880	2.00	382	52.34	65968	2.30	18.030	52.42	114.828	52.38	0.998	6.37
DM26-Mz5	134	73	7720	2.59	39230	2.00	380	52.65	63985	2.23	20.323	52.71	103.272	52.69	0.998	5.08
DM26-Mz5	130	72	8610	2.32	37380	2.00	374	53.41	64981	2.14	22.991	53.46	99.814	53.44	0.998	4.34
DM26-Mz5	125	67	9040	2.21	41600	2.00	389	51.37	70567	2.09	23.218	51.42	106.845	51.41	0.998	4.60
DM26-Mz5	140	71	8260	2.42	40320	2.00	416	48.13	66818	2.17	19.878	48.19	97.031	48.17	0.998	4.88
DM26-Mz5	133	68	9020	2.22	39940	2.00	406	49.26	68861	2.09	22.216	49.31	98.372	49.30	0.998	4.43
DM26-Mz5	132	69	9100	2.20	38710	2.00	398	50.29	67886	2.09	22.881	50.34	97.331	50.33	0.998	4.25
DM26-Mz5	135	69	9120	2.19	39430	2.00	412	48.58	68677	2.08	22.151	48.63	95.767	48.62	0.998	4.32
DM26-Mz5	117	73	8500	2.35	36620	2.00	331	60.33	63843	2.15	25.642	60.38	110.472	60.37	0.999	4.31
DM26-Mz5	120	72	7310	2.74	41860	2.00	346	57.76	65276	2.26	21.113	57.83	120.902	57.80	0.998	5.73
DM26-Mz5	135	73	8500	2.35	37240	2.00	387	51.66	64499	2.15	21.954	51.71	96.184	51.70	0.998	4.38
DM26-Mz5	105	70	8230	2.43	39930	2.00	308	64.87	66265	2.17	26.693	64.91	129.509	64.90	0.999	4.85
DM26-Mz5	116	70	7690	2.60	41910	2.00	343	58.34	66537	2.22	22.431	58.40	122.247	58.37	0.998	5.45
DM26-Mz5	128	71	7590	2.64	42090	2.00	377	53.09	66417	2.23	20.146	53.15	111.721	53.12	0.998	5.55

DM26-Mz5	144	76	6720	2.98	40820	2.00	398	50.25	62384	2.34	16.885	50.34	102.569	50.29	0.997	6.07
DM26-Mz5	158	72	7520	2.66	41930	2.00	463	43.17	66086	2.24	16.230	43.25	90.497	43.21	0.997	5.58
DM26-Mz5	132	72	7680	2.60	40640	2.00	383	52.19	65264	2.23	20.040	52.25	106.045	52.23	0.998	5.29
DM26-Mz6	142	67	11920	2.00	32330	2.00	442	45.21	70574	2.00	26.943	45.25	73.077	45.25	0.998	2.71
DM26-Mz6	162	67	12230	2.00	31520	2.00	509	39.26	70818	2.00	24.006	39.31	61.869	39.31	0.997	2.58
DM26-Mz6	139	80	9220	2.17	28760	2.00	360	55.60	58336	2.09	25.631	55.64	79.951	55.63	0.999	3.12
DM26-Mz6	138	76	7850	2.55	36490	2.00	378	52.98	61669	2.22	20.794	53.04	96.659	53.02	0.998	4.65
DM26-Mz6	109	76	7130	2.81	38200	2.00	295	67.68	61022	2.30	24.130	67.74	129.278	67.71	0.999	5.36
DM26-Mz6	160	71	11080	2.00	30730	2.00	470	42.56	66326	2.00	23.580	42.61	65.398	42.61	0.998	2.77
DM26-Mz6	182	65	12620	2.00	32450	2.00	589	33.96	73060	2.00	21.426	34.01	55.093	34.01	0.997	2.57
DM26-Mz6	118	70	10900	2.00	31680	2.00	349	57.37	66592	2.00	31.269	57.41	90.881	57.41	0.999	2.91
DM26-Mz6	160	74	9490	2.11	33050	2.00	449	44.53	63537	2.05	21.129	44.58	73.584	44.57	0.998	3.48
DM26-Mz7	141	74	8110	2.47	37390	2.00	398	50.31	63409	2.19	20.401	50.37	94.055	50.35	0.998	4.61
DM26-Mz7	137	81	7570	2.64	33550	2.00	351	56.93	57829	2.27	21.549	56.99	95.506	56.97	0.998	4.43
DM26-Mz7	147	75	8580	2.33	35170	2.00	408	48.98	62708	2.15	21.012	49.03	86.128	49.02	0.998	4.10
DM26-Mz7	126	83	6220	3.22	36560	2.00	316	63.26	56494	2.43	19.673	63.34	115.634	63.29	0.998	5.88
DM26-Mz7	168	76	7540	2.65	38090	2.00	464	43.09	62328	2.25	16.245	43.17	82.065	43.14	0.997	5.05
DM26-Mz7	116	71	8950	2.23	37650	2.00	341	58.57	66312	2.10	26.211	58.62	110.263	58.61	0.999	4.21
DM26-Mz7	136	74	8510	2.35	36210	2.00	383	52.17	63502	2.15	22.197	52.22	94.449	52.21	0.998	4.25
DM26-Mz7	113	89	6640	3.01	30860	2.00	261	76.62	52119	2.41	25.436	76.67	118.218	76.64	0.999	4.65
DM26-Mz7	156	77	8370	2.39	34810	2.00	427	46.88	61692	2.17	19.618	46.94	81.591	46.92	0.998	4.16
DM26-Mz7	135	75	6750	2.96	40910	2.00	374	53.46	62556	2.33	18.041	53.54	109.343	53.49	0.998	6.06
DM26-Mz7	119	85	4910	4.07	39150	2.00	290	68.90	54877	2.59	16.915	69.02	134.873	68.93	0.998	7.97
DM26-Mz7	120	77	8020	2.49	35230	2.00	323	61.93	60920	2.21	24.834	61.98	109.088	61.96	0.999	4.39
DM26-Mz7	131	79	5700	3.51	41050	2.00	345	58.00	59324	2.46	16.529	58.10	119.035	58.03	0.998	7.20
DM26-Mz7	145	75	7780	2.57	38280	2.00	405	49.35	63246	2.23	19.197	49.42	94.454	49.39	0.998	4.92
DM26-Mz7	114	75	8410	2.38	35490	2.00	314	63.70	62417	2.16	26.787	63.75	113.039	63.73	0.999	4.22
DM26-Mz7	122	79	7940	2.52	33380	2.00	319	62.78	58818	2.22	24.923	62.83	104.778	62.81	0.999	4.20
DM26-Mz7	156	80	6390	3.13	38630	2.00	409	48.87	59153	2.39	15.614	48.97	94.390	48.91	0.997	6.05

DM26-Mz7	142	89	5270	3.80	35690	2.00	331	60.48	52598	2.58	15.937	60.60	107.931	60.52	0.997	6.77
DM26-Mz8	133	73	8560	2.34	36910	2.00	379	52.77	64356	2.14	22.585	52.82	97.383	52.81	0.998	4.31
DM26-Mz8	126	71	9460	2.11	35800	2.00	370	54.05	66117	2.05	25.565	54.09	96.748	54.09	0.999	3.78
DM26-Mz8	128	76	6330	3.16	41580	2.00	350	57.10	61868	2.38	18.072	57.19	118.708	57.13	0.998	6.57
DM26-Mz8	99	71	8460	2.36	38120	2.00	284	70.33	65178	2.15	29.749	70.37	134.048	70.36	0.999	4.51
DM26-Mz8	158	72	8710	2.30	37340	2.00	459	43.58	65319	2.13	18.979	43.64	81.363	43.63	0.998	4.29
DM26-Mz8	146	75	7700	2.60	38250	2.00	409	48.90	62963	2.23	18.828	48.97	93.530	48.95	0.998	4.97
DM26-Mz9	128	123	5860	3.41	19010	2.00	215	93.19	37793	2.70	27.305	93.25	88.577	93.21	0.999	3.24
DM26-Mz9	148	76	6660	3.00	41070	2.00	409	48.88	62447	2.34	16.277	48.97	100.372	48.92	0.997	6.17
DM26-Mz9	168	80	6530	3.06	38150	2.00	441	45.34	59141	2.38	14.803	45.44	86.485	45.38	0.997	5.84
DM26-Mz9	163	73	6620	3.02	43970	2.00	472	42.33	65243	2.33	14.012	42.44	93.067	42.38	0.996	6.64
DM26-Mz9	172	69	6740	2.97	47360	2.00	527	37.96	69032	2.30	12.792	38.07	89.884	38.01	0.996	7.03
DM26-Mz9	124	103	3540	5.65	33990	2.00	250	79.98	45333	2.91	14.157	80.18	135.932	80.01	0.997	9.60
DM26-Mz9	149	109	4420	4.52	28870	2.00	285	70.08	43059	2.83	15.488	70.23	101.161	70.11	0.998	6.53
DM26-Mz9	173	75	7770	2.57	38120	2.00	483	41.37	63106	2.23	16.072	41.45	78.848	41.42	0.997	4.91
DM26-Mz9	172	78	7120	2.81	38120	2.00	465	43.05	61014	2.30	15.324	43.14	82.045	43.09	0.997	5.35
DM26-Mz9	104	94	5400	3.70	32160	2.00	228	87.60	49438	2.60	23.651	87.68	140.858	87.62	0.999	5.96
DM26-Mz9	123	120	2820	7.09	29660	2.00	211	94.73	38695	3.19	13.357	95.00	140.486	94.75	0.997	10.52
DM26-Mz9	158	82	6210	3.22	37620	2.00	403	49.57	57568	2.42	15.392	49.68	93.243	49.61	0.997	6.06
DM26-Mz9	161	76	7130	2.81	39780	2.00	448	44.59	62689	2.29	15.898	44.68	88.696	44.64	0.997	5.58
DM26-Mz9	125	104	6780	2.95	23240	2.00	250	80.10	44967	2.46	27.153	80.15	93.072	80.12	0.999	3.43
DM26-Mz10	112	91	4600	4.35	36730	2.00	256	78.25	51457	2.67	17.998	78.37	143.707	78.28	0.998	7.98
DM26-Mz10	142	76	6100	3.28	42520	2.00	392	50.99	62092	2.40	15.552	51.09	108.403	51.03	0.997	6.97
DM26-Mz10	139	71	7440	2.69	42930	2.00	413	48.45	66796	2.25	18.024	48.53	103.999	48.49	0.998	5.77
DM26-Mz10	120	77	7020	2.85	38430	2.00	325	61.52	60918	2.31	21.594	61.59	118.214	61.55	0.998	5.47
DM26-Mz10	116	72	7730	2.59	40550	2.00	336	59.59	65304	2.22	23.031	59.65	120.818	59.62	0.998	5.25
DM26-Mz10	163	75	7240	2.76	40210	2.00	459	43.56	63475	2.28	15.769	43.65	87.577	43.61	0.997	5.55
DM26-Mz10	101	73	5800	3.45	45380	2.00	288	69.55	63934	2.42	20.170	69.64	157.813	69.58	0.998	7.82
DM26-Mz10	163	70	5610	3.57	50600	2.00	498	40.18	68628	2.41	11.271	40.34	101.662	40.23	0.995	9.02

DM26-Mz10	136	70	5930	3.37	48590	2.00	409	48.95	67608	2.39	14.512	49.06	118.913	48.99	0.997	8.19
DM26-Mz10	142	75	6560	3.05	42000	2.00	398	50.27	63048	2.35	16.488	50.36	105.561	50.31	0.997	6.40
DM26-Mz11	115	86	5680	3.52	36400	2.00	278	71.94	54588	2.51	20.430	72.02	130.923	71.96	0.998	6.41
DM26-Mz11	118	83	6440	3.11	35650	2.00	295	67.88	56276	2.41	21.856	67.95	120.989	67.91	0.999	5.54
DM26-Mz11	142	88	6540	3.06	32610	2.00	338	59.11	53594	2.41	19.328	59.19	96.375	59.14	0.998	4.99
DM26-Mz11	152	87	4620	4.33	39160	2.00	366	54.72	53994	2.64	12.640	54.89	107.136	54.75	0.996	8.48
DM26-Mz11	156	59	4880	4.10	65560	2.00	562	35.58	81233	2.40	8.683	35.82	116.647	35.64	0.992	13.43
DM26-Mz11	110	96	5660	3.53	30140	2.00	235	84.94	48258	2.58	24.037	85.01	128.001	84.96	0.999	5.33
DM26-Mz11	113	79	7600	2.63	34920	2.00	297	67.45	59253	2.26	25.631	67.50	117.766	67.48	0.999	4.59
DM26-Mz11	138	84	6850	2.92	34130	2.00	343	58.24	56102	2.36	19.947	58.31	99.388	58.28	0.998	4.98
DM26-Mz11	136	109	4130	4.84	29460	2.00	257	77.68	42705	2.88	16.040	77.83	114.415	77.70	0.998	7.13
DM26-Mz11	123	84	4010	4.99	43020	2.00	305	65.56	55868	2.69	13.146	65.75	141.028	65.59	0.997	10.73
DM26-Mz11	149	63	5220	3.83	58440	2.00	496	40.31	75196	2.41	10.521	40.49	117.792	40.36	0.994	11.20
DYS22, 含石榴石的云母片岩																
DYS22-Mz1	137	90	6110	3.27	32750	2.00	318	62.93	52346	2.48	19.226	63.02	103.051	62.96	0.998	5.36
DYS22-Mz1	137	83	6020	3.32	37110	2.00	343	58.28	56418	2.45	17.541	58.37	108.132	58.31	0.998	6.16
DYS22-Mz2	103	101	3820	5.24	33800	2.00	211	94.74	46022	2.86	18.096	94.89	160.118	94.77	0.998	8.85
DYS22-Mz2	172	93	5310	3.77	33870	2.00	389	51.37	50945	2.59	13.638	51.51	86.994	51.41	0.997	6.38
DYS22-Mz2	169	90	4780	4.18	37360	2.00	396	50.47	52727	2.64	12.063	50.64	94.279	50.51	0.996	7.82
DYS22-Mz2	128	86	5730	3.49	36060	2.00	310	64.60	54426	2.50	18.508	64.69	116.473	64.63	0.998	6.29
DYS22-Mz3	119	82	5900	3.39	38020	2.00	300	66.63	56918	2.46	19.655	66.71	126.657	66.66	0.998	6.44
DYS22-Mz3	126	83	4660	4.29	41420	2.00	315	63.56	56354	2.61	14.810	63.71	131.641	63.60	0.997	8.89
DYS22-Mz3	168	84	6220	3.22	36670	2.00	423	47.29	56665	2.43	14.707	47.40	86.707	47.33	0.997	5.90
DYS22-Mz4	120	100	4910	4.07	30800	2.00	247	80.89	46528	2.70	19.859	80.99	124.574	80.92	0.998	6.27
DYS22-Mz4	122	105	4010	4.99	31770	2.00	242	82.68	44617	2.86	16.578	82.83	131.343	82.71	0.998	7.92
DYS22-Mz5	154	82	2990	6.69	48560	2.00	399	50.17	58162	2.77	7.500	50.61	121.806	50.21	0.990	16.24
DYS22-Mz5	142	104	3660	5.46	33550	2.00	285	70.16	45293	2.90	12.839	70.37	117.692	70.19	0.997	9.17
DYS22-Mz5	140	99	4300	4.65	33480	2.00	295	67.85	47275	2.77	14.588	68.01	113.586	67.88	0.997	7.79

DYS22-Mz5	105	97	3320	6.02	37250	2.00	224	89.43	47874	2.89	14.846	89.64	166.568	89.45	0.997	11.22
DYS22-Mz5	131	89	4910	4.07	37060	2.00	308	65.03	52801	2.62	15.964	65.15	120.495	65.06	0.998	7.55
DYS22-Mz6	86	81	6590	3.03	36160	2.00	217	92.21	57217	2.38	30.382	92.26	166.711	92.23	0.999	5.49
DYS22-Mz6	130	85	6030	3.32	35720	2.00	318	62.97	55050	2.46	18.986	63.06	112.467	63.00	0.998	5.92
DYS22-Mz6	132	85	5660	3.53	36740	2.00	321	62.38	54886	2.51	17.654	62.48	114.593	62.41	0.998	6.49
DYS22-Mz6	159	100	4490	4.45	32640	2.00	332	60.23	47064	2.75	13.521	60.39	98.287	60.26	0.997	7.27
DYS22-Mz6	134	79	6970	2.87	36950	2.00	353	56.65	59300	2.33	19.742	56.72	104.656	56.68	0.998	5.30
DYS22-Mz6	158	88	5130	3.90	37140	2.00	377	53.09	53619	2.58	13.617	53.23	98.585	53.13	0.997	7.24
DYS22-Mz6	138	108	2370	8.44	35890	2.00	267	75.00	43492	3.13	8.887	75.47	134.585	75.03	0.993	15.14
DYS22-Mz6	129	92	4810	4.16	35280	2.00	291	68.70	50699	2.66	16.522	68.82	121.185	68.73	0.998	7.33
DYS22-Mz6	124	81	6610	3.03	36340	2.00	316	63.32	57520	2.38	20.926	63.39	115.048	63.35	0.998	5.50
DYS22-Mz7	90	71	9140	2.19	36200	2.00	260	76.92	65414	2.08	35.152	76.95	139.225	76.95	0.999	3.96
DYS22-Mz7	120	104	4950	4.04	28830	2.00	237	84.48	44686	2.72	20.910	84.58	121.784	84.51	0.999	5.82
DYS22-Mz8	126	84	6020	3.32	36530	2.00	311	64.26	55822	2.46	19.344	64.35	117.379	64.30	0.998	6.07
DYS22-Mz8	171	88	5520	3.62	36300	2.00	409	48.86	54048	2.53	13.484	48.99	88.673	48.90	0.996	6.58
DYS22-Mz8	135	91	4990	4.01	35550	2.00	309	64.62	51552	2.62	16.123	64.74	114.863	64.65	0.998	7.12
DYS22-Mz8	107	90	4440	4.50	37260	2.00	243	82.19	51469	2.69	18.247	82.32	153.125	82.22	0.998	8.39
DYS22-Mz8	104	86	5480	3.65	36750	2.00	251	79.72	54284	2.53	21.845	79.81	146.494	79.75	0.999	6.71
DYS22-Mz8	123	91	5510	3.63	33840	2.00	280	71.49	51493	2.56	19.697	71.59	120.969	71.52	0.998	6.14
DYS22-Mz8	120	84	5800	3.45	36830	2.00	294	68.08	55409	2.49	19.745	68.17	125.378	68.11	0.998	6.35
DYS22-Mz8	150	92	4860	4.12	35800	2.00	342	58.40	51402	2.64	14.191	58.54	104.532	58.43	0.997	7.37
DYS22-Mz8	140	93	3970	5.04	37710	2.00	314	63.64	50446	2.77	12.632	63.84	119.991	63.67	0.996	9.50
DYS22-Mz9	121	90	4820	4.15	36540	2.00	278	71.99	51980	2.64	17.348	72.10	131.517	72.01	0.998	7.58
DYS22-Mz9	159	92	4920	4.07	35460	2.00	361	55.33	51265	2.64	13.612	55.48	98.106	55.37	0.997	7.21
DYS22-Mz9	87	85	5820	3.44	36120	2.00	210	95.32	54718	2.49	27.739	95.39	172.155	95.35	0.999	6.21
DYS22-Mz9	121	85	5140	3.89	38280	2.00	294	67.98	54746	2.57	17.471	68.09	130.118	68.01	0.998	7.45
DYS22-Mz10	133	83	6350	3.15	36370	2.00	334	59.92	56730	2.41	19.025	60.01	108.970	59.96	0.998	5.73
DYS22-Mz10	108	89	5280	3.79	35210	2.00	250	79.91	52109	2.58	21.096	80.00	140.681	79.93	0.999	6.67
DYS22-Mz10	106	106	3450	5.80	32860	2.00	206	96.99	43900	2.95	16.731	97.17	159.360	97.01	0.998	9.52

DYS22-Mz10	100	89	4840	4.13	36650	2.00	230	86.90	52131	2.63	21.031	87.00	159.250	86.93	0.999	7.57
DYS22-Mz10	132	86	5290	3.78	37670	2.00	320	62.50	54630	2.55	16.531	62.61	117.715	62.53	0.998	7.12
DYS22-Mz10	124	103	3660	5.46	33690	2.00	249	80.24	45417	2.89	14.684	80.43	135.166	80.27	0.997	9.20
DYS22-Mz10	134	91	5530	3.62	33740	2.00	305	65.48	51472	2.56	18.104	65.58	110.457	65.51	0.998	6.10
DYS22-Mz10	155	85	5990	3.34	36520	2.00	383	52.19	55757	2.46	15.631	52.30	95.298	52.23	0.997	6.10
DYS22-Mz11	125	82	6500	3.08	36070	2.00	315	63.50	56899	2.39	20.637	63.57	114.520	63.53	0.998	5.55
DYS22-Mz11	144	87	5640	3.55	36090	2.00	347	57.59	54189	2.52	16.240	57.70	103.918	57.62	0.998	6.40
DYS22-Mz11	110	109	3540	5.65	31430	2.00	209	95.71	42762	2.97	16.940	95.88	150.406	95.73	0.998	8.88
DYS22-Mz11	145	83	4130	4.84	43650	2.00	366	54.57	56904	2.66	11.269	54.79	119.103	54.61	0.995	10.57
DYS22-Mz11	115	89	3190	6.27	42510	2.00	268	74.57	52725	2.83	11.894	74.84	158.504	74.60	0.996	13.33
DYS22-Mz11	126	88	5810	3.44	34340	2.00	296	67.66	52959	2.51	19.655	67.75	116.171	67.69	0.998	5.91
DYS22-Mz12	152	112	3270	6.12	31580	2.00	284	70.49	42079	3.03	11.526	70.76	111.310	70.52	0.996	9.66
DYS22-Mz12	134	125	2910	6.87	28070	2.00	222	89.94	37401	3.22	13.087	90.21	126.238	89.97	0.997	9.65
DYS22-Mz12	108	80	6250	3.20	38410	2.00	278	71.84	58412	2.41	22.449	71.91	137.964	71.87	0.999	6.15
DYS22-Mz12	149	80	5640	3.55	40690	2.00	389	51.37	58795	2.48	14.485	51.49	104.502	51.40	0.997	7.21
DYS22-Mz12	138	82	5250	3.81	40460	2.00	352	56.81	57300	2.53	14.912	56.93	114.918	56.84	0.997	7.71
DYS22-Mz13	144	87	6240	3.21	34220	2.00	348	57.54	54244	2.44	17.951	57.63	98.445	57.57	0.998	5.48
DYS22-Mz13	118	97	4510	4.43	33520	2.00	251	79.56	47965	2.73	17.941	79.68	133.341	79.58	0.998	7.43
DYS22-Mz13	127	97	4100	4.88	35300	2.00	273	73.35	48440	2.78	15.037	73.51	129.466	73.38	0.997	8.61
DYS22-Mz13	133	82	6030	3.32	37690	2.00	336	59.55	57024	2.45	17.953	59.64	112.216	59.58	0.998	6.25
DYS22-Mz13	115	94	5010	3.99	33550	2.00	252	79.33	49592	2.64	19.872	79.43	133.073	79.35	0.998	6.70
DYS22-Mz13	138	105	3820	5.24	32540	2.00	274	72.99	44793	2.89	13.942	73.18	118.762	73.02	0.997	8.52
DYS22-Mz13	104	93	4550	4.40	35560	2.00	230	86.86	50118	2.70	19.761	86.97	154.439	86.88	0.998	7.82
DYS22-Mz13	102	86	6220	3.22	34140	2.00	245	81.53	54039	2.45	25.357	81.60	139.178	81.56	0.999	5.49
DYS22-Mz14	148	108	4470	4.47	29190	2.00	285	70.08	43538	2.82	15.663	70.22	102.282	70.11	0.998	6.53
DYS22-Mz14	137	103	4170	4.80	32260	2.00	278	72.03	45634	2.82	15.019	72.19	116.188	72.06	0.997	7.74
DYS22-Mz14	136	72	4380	4.57	51810	2.00	398	50.20	65857	2.55	10.995	50.41	130.056	50.24	0.995	11.83
DYS22-Mz14	142	87	5360	3.73	36900	2.00	342	58.49	54098	2.55	15.676	58.61	107.921	58.53	0.997	6.88
DYS22-Mz14	159	84	3380	5.92	45470	2.00	398	50.21	56328	2.76	8.485	50.55	114.144	50.25	0.992	13.45

DYS22-Mz14	152	93	2740	7.30	42270	2.00	344	58.11	51067	2.91	7.961	58.57	122.816	58.14	0.992	15.43
DYS22-Mz15	126	95	3530	5.67	37810	2.00	276	72.55	49123	2.84	12.805	72.77	137.158	72.58	0.997	10.71
DYS22-Mz15	107	85	5920	3.38	35790	2.00	260	76.92	54736	2.48	22.768	76.99	137.648	76.95	0.999	6.05
DYS22-Mz15	112	76	6530	3.06	40880	2.00	307	65.24	61785	2.36	21.300	65.31	133.346	65.27	0.998	6.26
DYS22-Mz16	160	77	6760	2.96	40000	2.00	438	45.65	61718	2.34	15.430	45.75	91.302	45.69	0.997	5.92
DYS22-Mz16	118	85	5270	3.80	38350	2.00	288	69.41	55229	2.55	18.290	69.52	133.097	69.44	0.998	7.28
DYS22-Mz16	158	89	4890	4.09	37420	2.00	372	53.71	53128	2.62	13.133	53.87	100.497	53.75	0.996	7.65
DYS22-Mz16	160	86	5240	3.82	38080	2.00	390	51.30	54914	2.56	13.440	51.44	97.671	51.34	0.996	7.27
DYS22-Mz17	131	87	4460	4.48	39750	2.00	314	63.78	54048	2.66	14.223	63.94	126.761	63.81	0.997	8.91
DYS22-Mz17	128	89	4570	4.38	38180	2.00	301	66.43	52828	2.66	15.179	66.57	126.813	66.46	0.997	8.35
DYS22-Mz17	132	84	4950	4.04	39840	2.00	326	61.41	55710	2.58	15.200	61.55	122.337	61.45	0.997	8.05
DYS22-Mz17	104	74	6110	3.27	43610	2.00	291	68.77	63159	2.39	21.010	68.85	149.959	68.80	0.998	7.14

All errors are 2σ. Corr: correlation between the U/Pb and Th/Pb errors.

表 5-1 黄陵背斜核部岩石钾长石 Ar-Ar 分析数据

Table 5-1 Ar-Ar analytical data of K-feldspars from the Huangling massif

Temperature (℃)	$^{40}Ar/^{39}Ar$	$^{37}Ar/^{39}Ar$	$^{36}Ar/^{39}Ar$	$^{40}Ar_r/^{39}Ar_k$	$^{40}Ar_r$ (%)	$^{39}Ar_k$ (%)	Age ± 2σ Ma
JH446, Gneiss, Kfs, Weight=12.3mg, J=0.005598, Total fusion age=759.6±3.3 GPS:31°19.982', 111°05.738'							
600	768.67	0.4641	2.1664	128.579	16.72	0.01	980.47 ± 519.29
600	1523.39	1.1305	4.1970	283.584	18.60	0.00	1719.16 ± 1218.25
650	357.47	0.1683	0.9389	80.044	22.39	0.01	669.52 ± 209.56
650	162.44	0.0618	0.4442	31.186	19.20	0.03	290.98 ± 31.40
700	503.56	0.0106	1.5083	57.862	11.49	0.09	507.41 ± 85.21
700	272.59	0.0014	0.7965	37.216	13.65	0.17	342.22 ± 47.90
750	109.03	0.0047	0.2833	25.321	23.22	0.48	239.71 ± 17.97
750	127.71	0.0038	0.3432	26.303	20.60	0.53	248.40 ± 21.56
800	60.837	0.0039	0.1117	27.824	45.73	0.94	261.76 ± 7.29
800	56.042	0.0037	0.0907	29.234	52.16	0.91	274.08 ± 5.87
850	52.844	0.0049	0.0585	35.547	67.27	1.48	328.17 ± 4.09
850	52.770	0.0024	0.0490	38.292	72.56	1.12	351.20 ± 3.83
875	55.918	0.0038	0.0401	44.083	78.83	1.00	398.84 ± 3.40
875	56.490	0.0035	0.0354	46.041	81.50	0.94	414.68 ± 3.58
900	61.936	0.0063	0.0295	53.217	85.92	0.97	471.53 ± 3.68
925	65.297	0.0052	0.0239	58.238	89.19	1.37	510.27 ± 3.36
950	68.145	0.0060	0.0195	62.389	91.55	1.87	541.69 ± 3.19
975	73.387	0.0055	0.0141	69.228	94.33	2.60	592.28 ± 3.38
1000	79.840	0.0061	0.0120	76.290	95.55	2.68	643.08 ± 3.51
1025	84.203	0.0044	0.0076	81.943	97.32	5.37	682.75 ± 3.63
1050	90.313	0.0033	0.0069	88.275	97.74	8.29	726.16 ± 4.11
1075	91.238	0.0033	0.0064	89.361	97.94	7.39	733.50 ± 3.79
1100	95.529	0.0030	0.0056	93.865	98.26	6.50	763.64 ± 3.94
1100	98.871	0.0031	0.0054	97.286	98.40	5.74	786.20 ± 4.00
1100	102.62	0.0027	0.0044	101.33	98.75	4.07	812.52 ± 4.04
1100	105.84	0.0021	0.0032	104.88	99.10	4.36	835.33 ± 4.20
1100	109.08	0.0012	0.0023	108.41	99.39	3.57	857.67 ± 4.32
1100	112.91	0.0010	0.0025	112.18	99.36	4.94	881.26 ± 4.33
1100	116.02	0.0006	0.0033	115.05	99.16	6.30	899.00 ± 4.39
1200	115.29	0.0011	0.0019	114.72	99.51	3.20	897.01 ± 4.44
1225	111.03	0.0012	0.0019	110.47	99.49	5.62	870.61 ± 4.28
1250	108.98	0.0007	0.0020	108.40	99.47	7.28	857.63 ± 4.17
1300	109.13	0.0006	0.0020	108.55	99.47	8.23	858.54 ± 5.41
1350	109.01	0.0012	0.0030	108.11	99.17	0.95	855.76 ± 4.75
1400	114.00	0.0048	0.0068	112.00	98.25	0.23	880.16 ± 7.46
1500	111.38	0.0005	0.0073	109.21	98.05	0.73	862.73 ± 5.46
JH71, Migmatite, Kfs, Weight=14.6mg, J=0.005717, Total fusion age=693.9±3.0Ma GPS:31°12.906', 111°16.829'							
600	587.80	0.5444	1.8277	47.786	8.13	0.00	436.76 ± 163.72
600	134.25	0.4680	0.3947	17.667	13.15	0.01	174.00 ± 40.06
650	111.13	0.1092	0.3269	14.546	13.09	0.02	144.45 ± 33.44
650	97.84	0.0451	0.2804	14.973	15.30	0.05	148.52 ± 32.28
700	277.26	0.0076	0.8592	23.367	8.43	0.12	226.74 ± 55.92
700	179.64	0.0177	0.5357	21.345	11.88	0.17	208.21 ± 35.21
750	75.271	0.0069	0.1972	16.998	22.58	0.47	167.70 ± 13.25
750	50.819	0.0059	0.1052	19.725	38.81	0.55	193.22 ± 7.22

800	40.757	0.0042	0.0496	26.093	64.02	1.02	251.44 ± 3.61
800	47.777	0.0060	0.0443	34.682	72.59	0.75	327.10 ± 3.64
850	57.516	0.0142	0.0440	44.523	77.41	0.96	410.07 ± 3.65
850	67.090	0.0181	0.0459	53.521	79.77	0.72	482.74 ± 4.03
875	72.315	0.0167	0.0428	59.658	82.50	0.68	530.68 ± 5.18
900	72.476	0.0161	0.0217	66.075	91.17	0.93	579.48 ± 3.84
925	73.113	0.0113	0.0153	68.587	93.81	1.52	598.23 ± 3.51
950	73.372	0.0095	0.0088	70.764	96.44	1.87	614.33 ± 3.38
975	75.568	0.0082	0.0079	73.247	96.93	2.65	632.51 ± 3.37
1000	77.136	0.0044	0.0058	75.409	97.76	4.02	648.20 ± 3.51
1025	78.652	0.0066	0.0039	77.502	98.54	6.99	663.25 ± 3.48
1050	81.314	0.0045	0.0027	80.509	99.01	10.33	684.67 ± 3.55
1075	84.073	0.0028	0.0023	83.390	99.19	8.37	704.95 ± 3.68
1100	84.930	0.0025	0.0019	84.367	99.34	6.45	711.78 ± 3.73
1100	86.684	0.0017	0.0011	86.372	99.64	6.80	725.71 ± 3.67
1100	88.732	0.0013	0.0013	88.352	99.57	5.43	739.36 ± 3.79
1100	89.998	0.0010	0.0017	89.501	99.45	6.88	747.23 ± 3.79
1100	90.829	0.0007	0.0021	90.204	99.31	5.10	752.03 ± 3.82
1100	89.342	0.0009	0.0015	88.896	99.50	9.42	743.09 ± 3.73
1100	90.075	0.0006	0.0025	89.322	99.16	8.49	746.01 ± 3.77
1150	89.940	0.0073	0.0009	89.678	99.71	0.40	748.44 ± 5.46
1200	90.277	0.0024	0.0005	90.127	99.83	1.54	751.51 ± 4.20
1225	89.995	0.0008	0.0008	89.745	99.72	2.32	748.90 ± 3.99
1250	90.024	0.0009	0.0011	89.691	99.63	2.97	748.53 ± 3.89
1275	91.409	0.0021	0.0034	90.398	98.89	1.45	753.36 ± 4.45
1300	93.721	0.0069	0.0066	91.758	97.90	0.36	762.60 ± 4.96
1350	91.364	0.0311	0.0110	88.115	96.44	0.09	737.73 ± 23.13
1400	88.350	0.0148	0.0091	85.672	96.97	0.09	720.86 ± 17.36

JH147, Granodiorite, Kfs, Weight=15.1mg, J=0.005695, Total fusion age=567.9±2.3Ma
GPS:30°51.400', 111°08.917'

600	461.75	0.6943	1.2474	93.257	20.18	0.00	770.32 ± 295.10
600	554.33	1.0998	1.4793	117.393	21.16	0.00	925.78 ± 604.47
650	96.69	0.0778	0.2434	24.784	25.63	0.04	238.76 ± 35.30
650	117.33	0.0434	0.3030	27.791	23.68	0.05	265.69 ± 26.15
700	244.30	0.0258	0.7078	35.143	14.38	0.18	329.90 ± 43.28
700	118.29	0.0239	0.3046	28.274	23.90	0.28	269.98 ± 19.42
750	56.791	0.0436	0.1061	25.450	44.81	0.76	244.76 ± 7.03
750	46.785	0.0139	0.0599	29.075	62.15	0.90	277.07 ± 4.26
800	46.183	0.0220	0.0286	37.729	81.69	1.66	351.96 ± 3.09
800	52.011	0.0129	0.0317	42.658	82.02	1.33	393.27 ± 3.01
850	57.718	0.0205	0.0268	49.798	86.28	1.72	451.48 ± 3.11
850	64.802	0.0140	0.0292	56.164	86.67	1.12	501.85 ± 3.52
875	70.111	0.0156	0.0341	60.039	85.63	0.82	531.83 ± 3.82
875	72.133	0.0132	0.0332	62.323	86.40	0.68	549.27 ± 3.95
900	70.752	0.0135	0.0276	62.590	88.46	0.56	551.30 ± 5.01
925	74.189	0.0176	0.0385	62.810	84.66	0.72	552.97 ± 4.04
950	72.025	0.0152	0.0358	61.457	85.33	0.87	542.68 ± 3.84
975	69.663	0.0178	0.0289	61.117	87.73	1.04	540.08 ± 3.67
1000	67.460	0.0160	0.0241	60.340	89.44	1.46	534.14 ± 3.44
1025	65.818	0.0134	0.0173	60.700	92.22	2.69	536.90 ± 3.06
1050	67.629	0.0121	0.0108	64.445	95.29	4.88	565.33 ± 3.09
1075	66.573	0.0147	0.0101	63.592	95.52	3.55	558.89 ± 3.12
1100	65.527	0.0134	0.0075	63.309	96.61	3.83	556.76 ± 3.02
1100	66.360	0.0115	0.0062	64.531	97.24	4.84	565.98 ± 3.12
1100	67.118	0.0095	0.0050	65.637	97.79	4.57	574.29 ± 3.05

1100	67.725	0.0080	0.0053	66.157	97.68	5.60	578.18 ± 3.11
1100	67.692	0.0066	0.0044	66.399	98.09	4.36	580.00 ± 3.19
1100	69.194	0.0055	0.0039	68.037	98.33	6.16	592.19 ± 3.16
1100	70.568	0.0045	0.0037	69.473	98.45	8.63	602.82 ± 3.24
1150	70.073	0.0070	0.0033	69.107	98.62	0.64	600.12 ± 3.81
1200	67.938	0.0075	0.0036	66.876	98.43	3.14	583.55 ± 3.18
1225	69.179	0.0042	0.0032	68.226	98.62	6.11	593.60 ± 3.19
1250	70.142	0.0021	0.0028	69.303	98.80	12.01	601.57 ± 3.11
1275	70.434	0.0021	0.0030	69.548	98.74	10.99	603.37 ± 4.14
1300	71.713	0.0029	0.0039	70.549	98.38	2.89	610.74 ± 3.27
1350	71.131	0.0041	0.0050	69.642	97.91	0.49	604.07 ± 3.90
1400	66.496	0.0157	0.0084	64.009	96.26	0.18	562.05 ± 12.59
1500	71.522	0.0042	0.0104	68.445	95.70	0.23	595.22 ± 6.01

Journal of Asian Earth Sciences 86 (2014) 59–75

Contents lists available at SciVerse ScienceDirect

Journal of Asian Earth Sciences

journal homepage: www.elsevier.com/locate/jseaes

Origin and tectonic significance of the Huangling massif within the Yangtze craton, South China

Wenbin Ji [a,b], Wei Lin [a,*], Michel Faure [c], Yang Chu [a], Lin Wu [a,b], Fei Wang [a], Jun Wang [a,b], Qingchen Wang [a]

[a] State Key Laboratory of Lithospheric Evolution, Institute of Geology and Geophysics, Chinese Academy of Sciences, Beijing 100029, China
[b] University of the Chinese Academy of Sciences, Beijing 100049, China
[c] Institut des Sciences de la Terre d'Orléans, Université d'Orléans-CNRS, 1A rue de la Férollerie, 45071 Orléans, France

ARTICLE INFO

Article history:
Available online 3 July 2013

Keywords:
Huangling massif
Structural analysis
Cooling and uplifting history
Late Mesozoic tectonics
South China

ABSTRACT

As the oldest exposed basement and the typical sedimentary cover of the Yangtze craton, the Huangling massif is a suitable place to decipher the tectonics of South China block. Structural analysis shows that the Huangling massif has an elliptic domal shape with N–S striking long axis, an asymmetric antiform with a steep western flank and a gentle eastern flank. There, three litho-tectonic units are recognized, from inner to outer parts: (1) Archean–Paleoproterozoic metamorphic rocks intruded by Neoproterozoic granitoids; (2) Neoproterozoic to Jurassic sedimentary envelope around the dome core; (3) Cretaceous terrigeneous alluvial–fluvial deposits, unconformably overlying the dome flanks. Coeval with the uplifting of the massif, the pre-Cretaceous strata on the western and eastern flanks of the Huangling massif were involved in a series of folds with nearly N–S axes and layer-parallel slip structures with top-to-the-W and top-to-the-E motion, respectively. The subsequent brittle normal faulting controlled the deposition of the graben or half-graben basins on both flanks. Cooling history reveals that the Huangling massif underwent uplifting between 160 Ma and 110 Ma with an average cooling rate of 2–3 °C/Ma. Moreover, the Huangling area was not significantly affected by the Early Paleozoic and Triassic orogenies of South China. Comparable with the contemporaneous extensional structures, such as metamorphic core complexs, syntectonic plutons bounded by ductile normal faults, and rift-related basins in eastern China, it is proposed that the Huangling massif, might be an extensional structure controlled by a weak crustal extension. In this case, it will represent the western front of the Late Mesozoic lithospheric thinning in entire eastern China. However the compressional model cannot be ruled out.

1. Introduction

The tectonic evolution of the South China block (SCB, Fig. 1) is a significant issue for understanding the geological framework of the Eurasian continent. Although controversies existed during the last decades, it is now generally accepted that the amalgamation of the Yangtze block and the Cathaysia block along the Jiangnan or Sibao orogen created the SCB during the early stage of the Neoproterozoic, corresponding to the assembly of Rodinia supercontinent (Huang, 1978; Zhang et al., 1984; Shui, 1988; Hsü et al., 1988, 1990; Guo et al., 1989; Chen et al., 1991; Gilder et al., 1991; Charvet et al., 1996; Shu and Charvet, 1996; Li, 1998; Chen, 1999; Li et al., 2004, 2009 and references therein). During the Phanerozoic, the SCB experienced three main tectonic events: (1) the Early Paleozoic intracontinental orogeny along the Wuyi–Baiyun–Yunkai belt, corresponding to the closure of the Neoproterozoic Nanhua rift (Lin et al., 2008; Faure et al., 2009; Charvet et al., 2010; Li et al., 2010; Y.J. Wang et al., 2010); (2) a series of Early Mesozoic orogenies around the periphery of the SCB, such as the Qinling–Dabie–Sulu orogenic belt to the north (e.g. Mattauer et al., 1985; Faure et al., 1999, 2003; Hacker et al., 2000; Ratschbacher et al., 2000, 2003; Lin et al., 2009); the Songpan–Ganzi fold belt and Longmenshan fold-thrust belt to the west (Burchfiel et al., 1995; Chen and Wilson, 1996; Roger et al., 2010; Yan et al., 2011); the Indosinian orogenic belt to the south (Carter et al., 2001; Carter and Clift, 2008; Wang et al., 2007; Lepvrier et al., 2008; Lin et al., 2008), as well as the intracontinental Xuefengshan–Jiuling belt in the center of the SCB (Wang et al., 2005; Shu et al., 2008; Chu et al., 2012a, 2012b, 2012c; Chu and Lin, 2014); (3) the Late Mesozoic tectonic–magmatic events, represented by widespread intracontinental compression and extension (Lin et al., 2000; Yan et al., 2003; Shu et al., 2009; Y.Q. Zhang et al., 2009; Zhang et al., 2012; Zhu et al., 2010; Li et al., 2011, 2013; Hu et al., 2012; Shi et al., 2012), as well as massive granitoids and volcanic rocks in the southeast (e.g. Li, 2000; Zhou and Li, 2000; Zhou et al., 2006; Li and Li, 2007).

* Corresponding author. Tel.: +86 10 82998546; fax: +86 10 62010846.
E-mail address: linwei@mail.iggcas.ac.cn (W. Lin).

1367-9120/$ - see front matter © 2013 Elsevier Ltd. All rights reserved.
http://dx.doi.org/10.1016/j.jseaes.2013.06.007

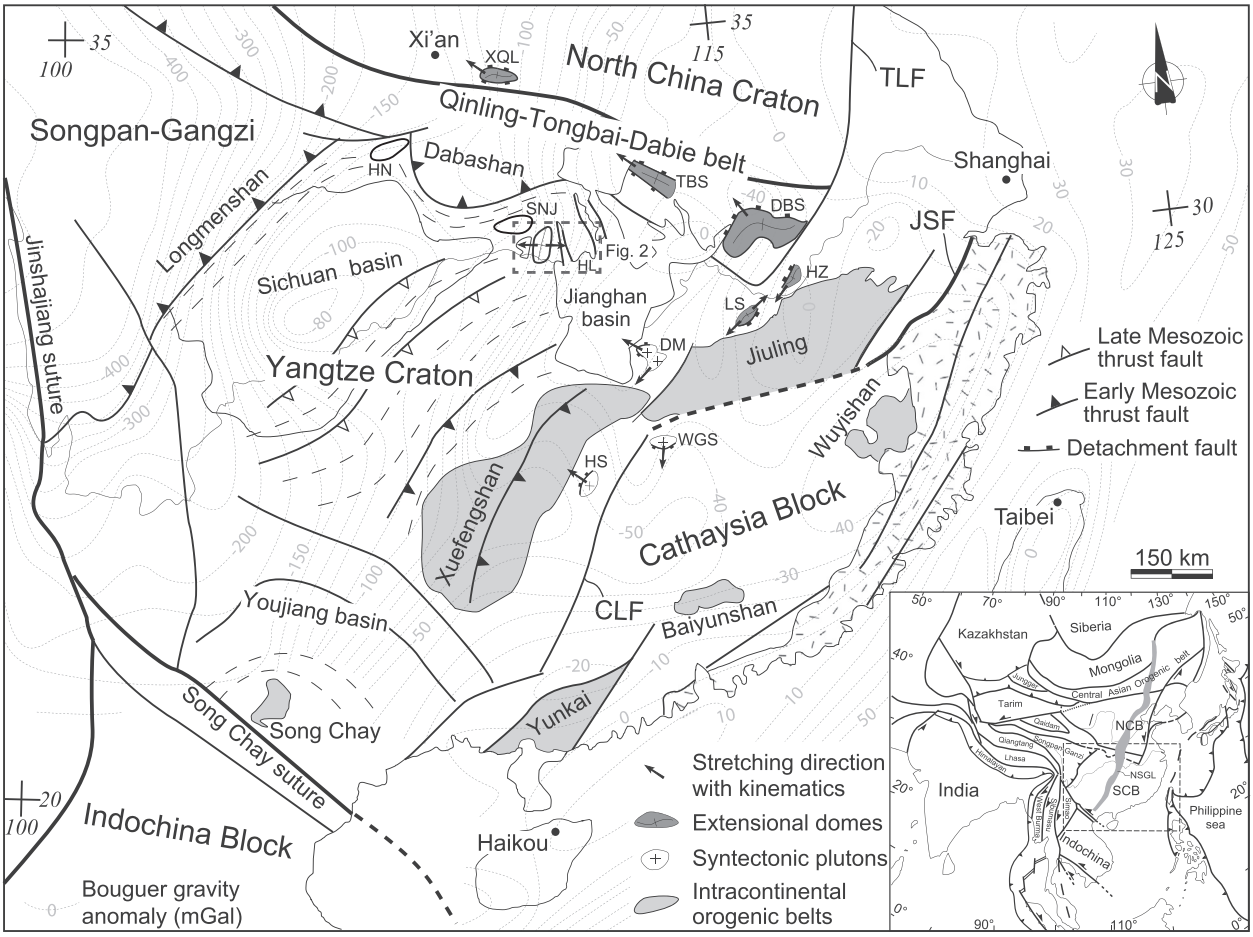

Fig. 1. Tectonic map of the South China block and the location of the Huangling massif (modified after Faure et al. (2009)). The Bouguer gravity anomaly is projected on base map. NCC, North China Craton; SCB, South China block; NSGL, N–S Gravity Lineament of China; JSF, Jiangshan–Shaoxing Fault, represents the Neoproterozoic suture between the Yangtze block and Cathaysia block; CLF, Chenzhou-Linwu fault; TLF, Tan–Lu Fault; HN, Hannan massif; SNJ, Shennongjia massif; HL, Huangling massif. Late Mesozoic extensional structures: XQL, Xiaoqinling MCC (Zhang and Zheng, 1999); TBS, Tongbaishan anticline (Our field survey); DBS, Dabieshan MCC (Ratschbacher et al., 2000; Ji et al., 2011; Y.S. Wang et al., 2011); LS, Lushan massif (Lin et al., 2000); HZ, Hongzhen MCC (Zhu et al., 2010); WGS, syntectonic granite in the Wugongshan dome (Faure et al., 1996; Wang et al., 2001); DM, Dayunshan-Mufushan syntectonic granite (Yu and Ye, 1998; our field survey); HS, Hengshan syntectonic granite (our field survey, Zhang et al., 2012).

The Jurassic–Cretaceous epoch is a complex transition period of tectonic regime in the entire eastern Eurasia from compression to extension. In eastern China, a large number of Late Mesozoic extensional structures have been documented, such as metamorphic core complexes (MCCs), metamorphic or magmatic domes and syntectonic plutons bounded by ductile normal faults, which indicate a continental-scale extension along the eastern Eurasian continental margin (e.g. Lin and Wang, 2006; T. Wang et al., 2011; Lin et al., 2013). It is also supported by numerous rift basins and giant igneous events (e.g. Ren et al., 2002; Meng et al., 2003; Wu et al., 2005; Yang et al., 2008; Li et al., 2012). However, the geodynamic mechanism of this Late Mesozoic "lithospheric thinning" or "Destruction" of the North China Craton (NCC, Fig. 1) in eastern China are still disputed (for reviews, see Menzies et al., 2007; Wu et al., 2008; Zhu et al., 2011 and references therein).

In the SCB, after the Triassic continental subduction of the SCB beneath the NCC, the Late Jurassic-Early Cretaceous magmatism and intracontinental extensional basins were notable geological features, which indicate that the SCB probably also experienced lithospheric thinning or regional extension (e.g. Gilder et al., 1996; Li, 2000; Zhou and Li, 2000; Zhou et al., 2006; Li and Li, 2007; Shu et al., 2009; Wei et al., 2014). However, the tectonics related to such an extensional setting is poorly understood, since only few extensional structures were reported within the SCB (Fig. 1), namely Tongbaishan anticline (our field survey), the Dabieshan MCC (Ratschbacher et al., 2000; Ji et al., 2011; Y.S. Wang et al., 2011), the Hongzhen MCC (Zhu et al., 2010), the Lushan dome (Lin et al., 2000), syntectonic granite in the Wugongshan dome (Faure et al., 1996; Wang et al., 2001), Dayunshan-Mufushan syntectonic granite (Yu and Ye, 1998; our field survey); Hengshan syntectonic granite (our field survey; Zhang et al., 2012). From the view of the eastern China, most of this Late Mesozoic extensional structures were superimposed upon the pre-existing orogenic belts (Central Asian orogenic belt, Yinshan–Yanshan belt, and Qinling–Dabie–Sulu orogenic belt) or along the crustal-scale faults (e.g. Tan–Lu fault), and rarely developed in inland area of stable craton (Lin and Wang, 2006; T. Wang et al., 2011; Lin et al., 2013 and references therein).

The Huangling massif (also named Huangling anticline or Huangling dome) is located at the middle Yangtze craton. As an exposed area of the oldest basement of the Yangtze craton and its typical sedimentary sequences from Neoproterozoic to Cenozoic, it provides a suitable place to understand the tectonic evolution of the SCB (Fig. 1). In spite of numerous previous studies focused on petrology, geochemistry, geochronology, sedimentology of the metamorphic basement, sedimentary cover, and granitoids (Ma et al., 1984, 1997, 2002; Feng et al., 1991; Ling et al., 1998, 2001, 2006; Gao et al., 1999, 2011; Qiu et al., 2000; Li et al., 2002, 2004, 2007, 2008; Condon et al., 2005; Liu et al., 2008; Gao and Zhang, 2009; Zhang et al., 2006a,b,c, 2008; S.B. Zhang et al.,

2009; Meng and Li, 2003; Zhao et al., 2010; Chen et al., 2013), as well as the crustal structure (Z.J. Zhang et al., 2009), the structural geology and tectonic framework of the Huangling massif are rarely documented (Zhang, 1986; Jiang et al., 2002; Ge et al., 2010; J. Wang et al., 2010). The following questions deserve attention: when and how the Huangling massif formed? Was the entire uplifting process controlled by a single event or multiphase events? How the Huangling massif recorded the different tectonic events recognized in the SCB, especially the Late Mesozoic transition of tectonic regimes in eastern China?

In this work, we present new structural and thermochronological data on the Huangling massif in order to reveal its geometry, kinematics and tectono-thermal evolution. The results provide not only new insights to decipher the complex tectonic evolution of the SCB, but also an enlightenment to understand the Late Mesozoic tectonics of eastern China.

2. Geological overview of the Huangling massif

As an antiformal structure that crops out near the north margin of the SCB, the Huangling massif is located to the northwest of Yichang city (Fig. 2). Unlike the NCC, where the Archean to Paleoproterozoic rocks are well exposed, Precambrian rocks of the SCB are dominated by Neoproterozoic ages and exposed sporadically below the thick cap of the Phanerozoic sedimentary cover. Until now, the oldest rocks in the SCB are exposed in the Huangling massif with ages of 3.2–3.3 Ga (Jiao et al., 2009; Gao et al., 2011). The core of the massif referred to as the Archean–Paleoproterozoic Kongling complex, mainly consists of orthogneiss, amphibolite, serpentinite, metapelite, quartzite, marble, as well as rare granulite (BGMRHB, 1990; Ma et al., 1997; Gao et al., 1999). Available geochronological data yield zircon protolith ages of 2.90–2.98 Ga for most of metamorphic igneous rocks, detrital populations of 2.7–3.3 Ga for the metasedimentary rocks, as well as two significant metamorphic events at ca. 2.70–2.75 Ga and ca. 1.9–2.1 Ga (Ling et al., 1998, 2001; Qiu et al., 2000; Zhao et al., 2006; Zhang et al., 2006a,b; Gao et al., 2011; Chen et al., 2013). More recently, the ultramafic–mafic rocks (ca. 1100–985 Ma) exposed in the southwestern part of the Huangling massif were considered as a Grenvillian ophiolite (Peng et al., 2012).

The Kongling complex was intruded by the large Neoproterozoic Huangling granitic pluton (Fig. 2). The Huangling granitoids occupy almost two thirds of the dome core. They are subdivided into four magmatic suites in terms of lithology, such as trondhjemite–granodiorite, quartz diorite–tonalite, monzogranite–quartz monzodiorite, as well as mafic–felsic dikes (Ma et al., 2002). Available geochronological data yield a wide range of 794–837 Ma for the emplacement age of Huangling granitoids (Ma et al., 1984, 2002; Feng et al., 1991; Li et al., 2002, 2004; Ling et al., 2006; Gao and Zhang, 2009; Zhang et al., 2008; S.B. Zhang et al., 2009).

In the Huangling massif, both the Kongling complex and the Huangling granitoids were unconformably overlain by Neoproterozoic strata. As a stable sedimentary platform, Neoproterozoic–Jurassic sedimentary series on the domal flanks are roughly continuous, except several slight discontinuities caused by the Early Paleozoic and Early Mesozoic tectonic events (Fig. 3). Some stratotype sections were established in the study area (BGMRHB, 1990). The Neoproterozoic strata, from bottom upward, are mainly composed of sandstone (Liantuo Formation), tillite (Nantuo Formation), and carbonate rocks (Doushantuo and Dengying Formations). The Cambrian to Early Triassic sedimentary series mainly consists of littoral to neritic facies carbonate and siliciclastic rocks. The most significant lithologies, as synthesized in Fig. 3, include Cambrian carbonate rocks; Ordovician limestone and minor shale; Lower-Middle Silurian shale, mudstone and minor limestone; Middle-Upper Devonian sandstone and siltstone;

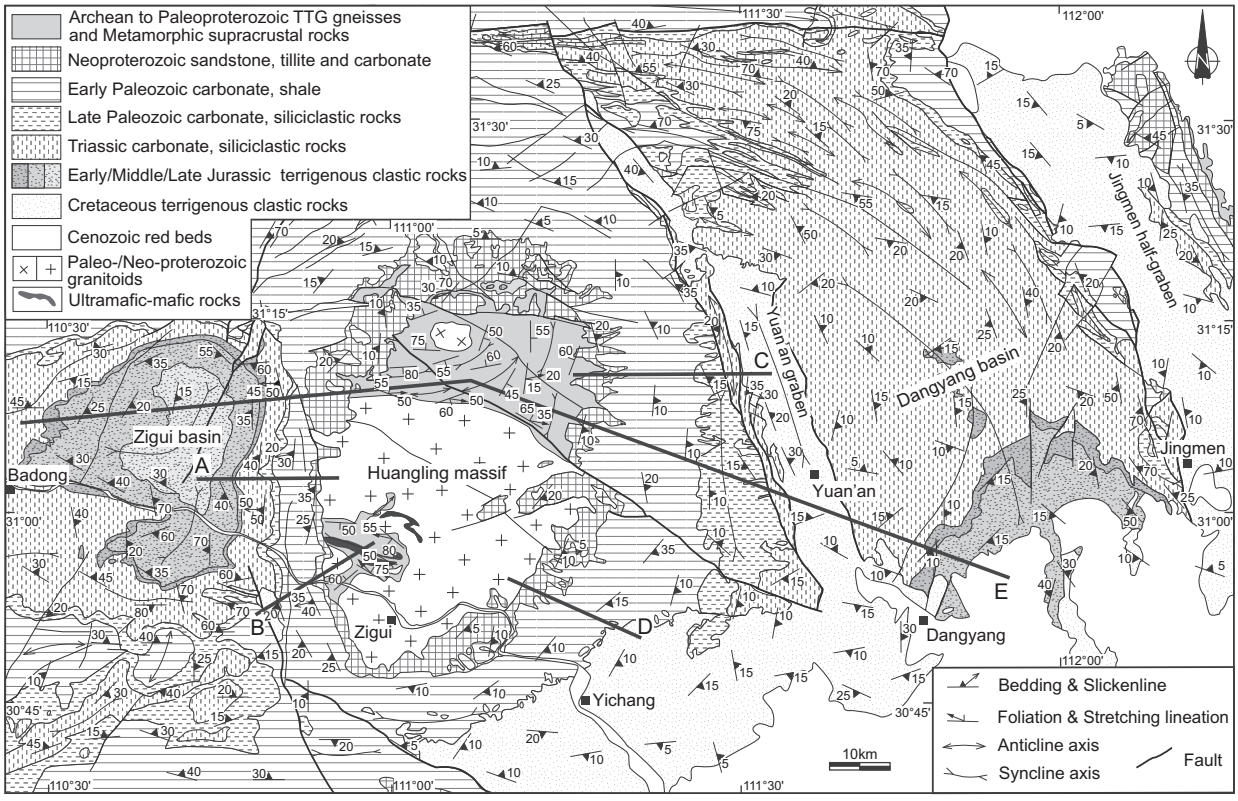

Fig. 2. Geological and structural map of the Huangling massif.

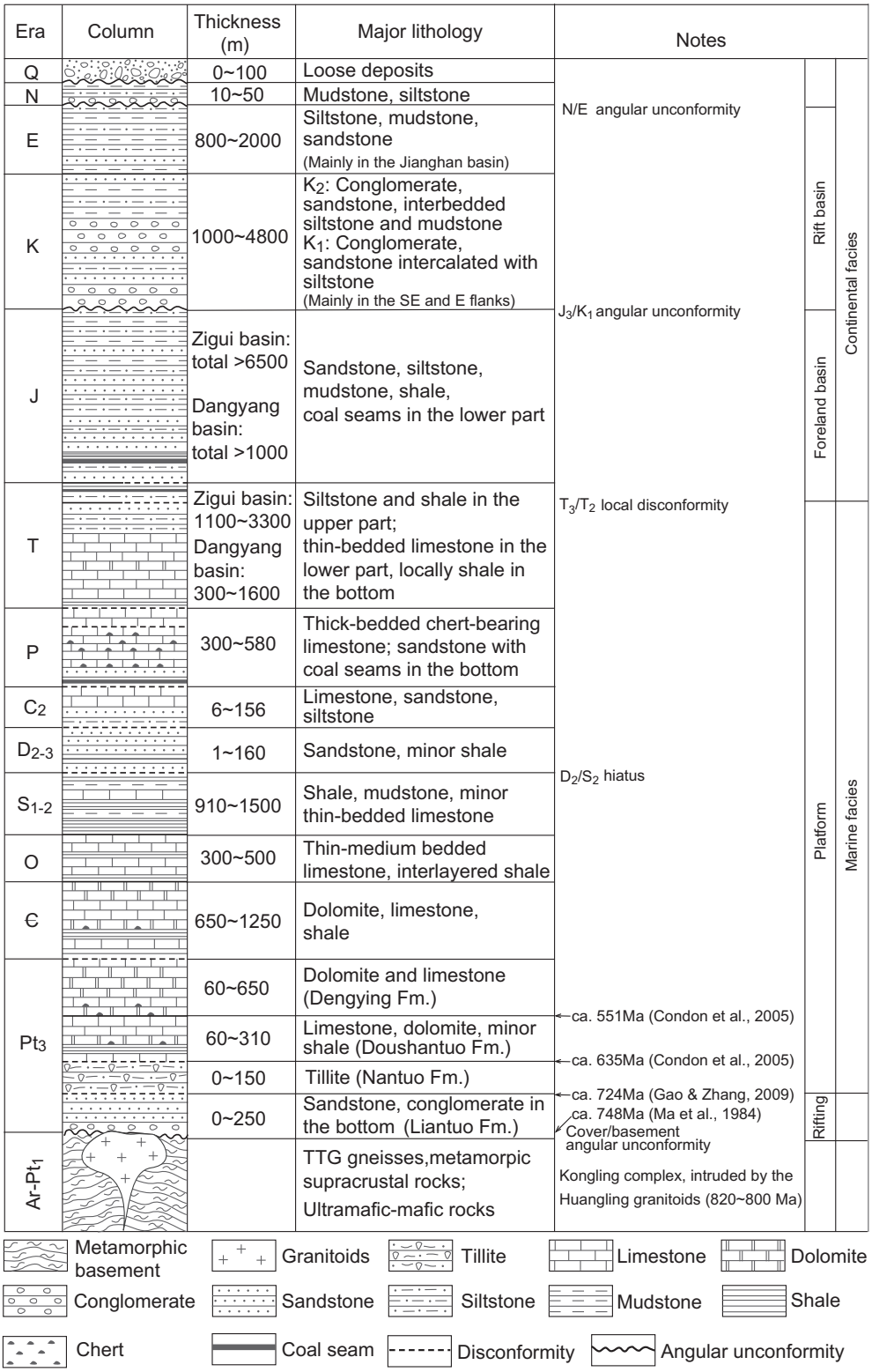

Fig. 3. Stratigraphic column of the Huangling area (BGMRHB, 1990). The boundary ages of the Neoproterozoic Liantuo, Nantuo and Duoshantuo Formations were dated by zircon U–Pb of volcanic ash or tuff beds (Ma et al., 1984; Condon et al., 2005; Gao and Zhang, 2009).

Middle Carboniferous sandstone, siltstone and limestone; Permian chert-bearing limestone, and sandstone with coal seams in the bottom; Lower Triassic limestone, locally with shale in the bottom. A few hiatuses existed during the Middle Silurian to Middle Devonian as well as the Carboniferous periods. The Middle Triassic strata are dominated by paralic facies limestone, siltstone and shale. A local discontinuity between the Middle and Lower Triassic represents a significant transition of the sedimentary environment and facies from marine to continental (Meng and Li, 2003; Li et al., 2008; Zhao et al., 2010). The Upper Triassic and Jurassic deposits are fluvial–lacustrine sandstone, siltstone, mudstone and coal seams. It is worthy to be mentioned that the Zigui and Dangyang intracontinental basins that crop out on the western and eastern flanks of the Huangling massif, respectively, were considered to

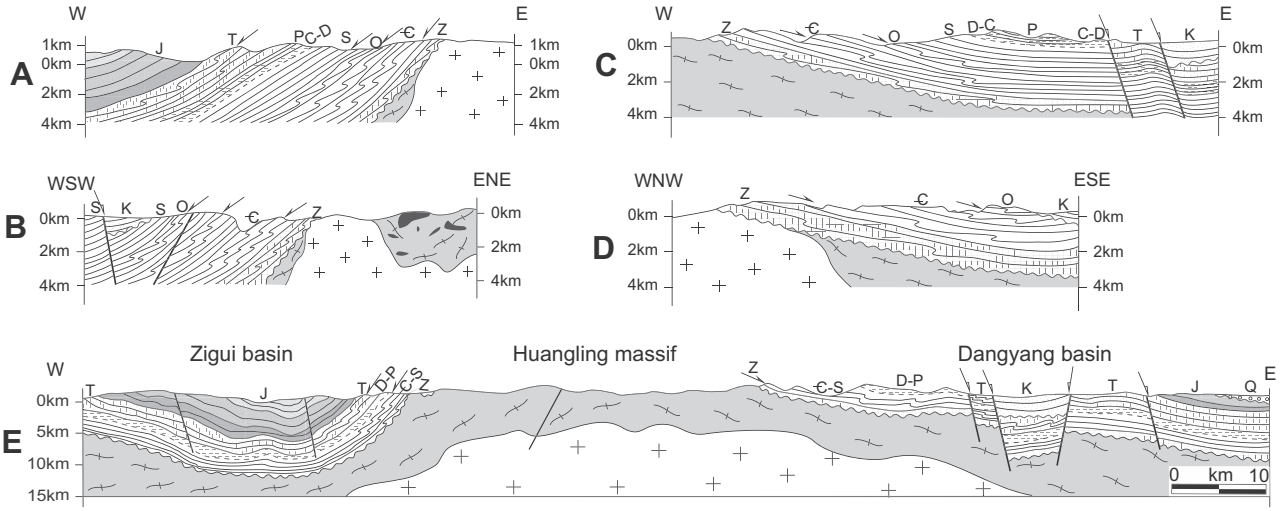

Fig. 4. Cross-sections across the Huangling massif (locations in Fig. 2). (A–D) Cross-sections of the western and eastern sides of the massif in different locations. (E) General cross-section traversing the Zigui basin, Huangling massif and Dangyang basin.

be belong to a single basin system developed in the northern Yangtze craton during the Late Triassic to Middle Jurassic (Liu et al., 2005). The Lower and Upper Cretaceous formations consist of alluvial–fluvial conglomerate, sandstone, siltstone and mudstone that unconformably overlie the older series on two flanks of the Dangyang basin, and the southwestern flank of the Huangling massif (Figs. 2 and 4).

As already stated, the SCB experienced complex geological history. Previous workers interpreted the Huangling massif was developed in a variety of tectonic settings. (1) With emphasis on the Huangling massif as an inherited paleo-uplift from Neoproterozoic to Jurassic, Zhang (1986) considered that the Triassic and Cretaceous events triggered its uplift. (2) On the basis of the regional discontinuities, Jiang et al. (2002) suggested that the Huangling massif underwent several stages of uplift and subsidence throughout the Neoproterozoic to Triassic times. (3) From the view of the tectonic evolution of the Jianghan basin (Fig. 1), Dai (1996) and Xu et al. (2004) interpreted that the Huangling massif originated from the westward escape, due to the Early Mesozoic collision of the NCC–SCB in a scissor-like fashion. (4) Ge et al. (2010) argued that the Huangling massif experienced a pre-Cretaceous compression, and a Late Cretaceous to Paleogene extensional uplifting as a metamorphic core complex. (5) According to their understanding of the regional tectonics of the Qinling–Dabie orogenic belt, Wang et al. (2003) proposed that the Mesozoic northward indentation of the SCB into the NCC to the west, coeval with a clockwise rotation of the Sichuan basin, resulted in eastward extrusion. The Hannan (HN), Shennongjia (SNJ), and Huangling (HL) massifs (Fig. 1) were regarded as indenters formed during this process. The Mesozoic tectono-sedimentary development of the northwest Sichuan basin is also thought to have pertained during the SCB clockwise rotation (Meng et al., 2005). Alternatively, several authors suggested that these three basement uplifts (HN, SNJ, and HL) as backstops played a significant role in formation of the Dabashan orocline (Fig. 1), which was controlled by a SW-directed thrusting during the Middle-Late Jurassic to Early Cretaceous (Hu et al., 2012; Shi et al., 2012; Li et al., 2013).

3. Structural analysis of the Huangling massif

3.1. Bulk architecture and litho-tectonic units

Field survey shows that the bulk architecture of the Huangling massif is an asymmetric elliptic dome with a 15°NE striking long axis, with long and short axes lengths of about 73 km and 36 km, respectively. The Zigui basin to the west is a syncline, and the Dangyang basin is a synclinorium located to the east (Fig. 2). The Yuan'an graben and Jingmen half-graben superimpose on the two flanks of the Dangyang basin. The Huangling massif, together with these basins on its two flanks, constitutes a nearly N–S trending horst and graben system (Figs. 2 and 4).

Based on the lithology and geometry, the Huangling massif could be divided into three litho-tectonic units (Figs. 2 and 4): (1) the migmatite, orthogneiss and metasupracrustal rocks of the Kongling complex, intruded by the Huangling granitoids; (2) the Neoproterozoic–Jurassic sedimentary cover, annularly surrounding the dome core; (3) the Cretaceous red-colored terrigeneous alluvial–fluvial deposits that occupy the graben or half-graben basins on the each flank of the dome. The stereographic plots of the structural elements in different units demonstrate their geometric relations (Fig. 5).

In the northern domain of the Huangling massif, migmatite and gneiss constitute the main part of the basement. These rocks are strongly foliated even mylonitized with a well developed variably oriented foliation, and a consistent NEE–SWW striking mineral and stretching lineation (Fig. 5D). It is worthy to note that the foliation in the northern domain is folded with the axes around E–W to NE–SW, and has no relation with the late deformation stages that are recorded in the sedimentary cover. On the southwestern part of the Huangling massif, to the north of the Zigui city, the exposed basement rocks consist of intensively foliated gneiss, amphibolite and serpentinite (Fig. 2). Even if the Huangling granitoids changed the geometry of this metamorphic basement, the systematic measurement of planar and linear structures shows a large SSW-verging syncline with steeply dipping foliation and WNW–ESE trending stretching lineation (Fig. 5B). All these deformed basement rocks were intruded by the undeformed Huangling granitoids, which indicate that this early ductile deformation occurred before ca. 820 Ma.

The sedimentary cover around the Huangling massif dips to the periphery of the dome. On the western side of the massif, the Neoproterozoic–Jurassic strata dip to the west with moderate plunges (20–60°, maximum around 40°, Figs. 4A, B and 5A); while on the eastern side, the Neoproterozoic–Triassic strata dip gently to the E or SEE with dip angles about 10–20° (Figs. 4C, D and 5E). Similar to the eastern side of the massif, the attitudes of the Neoproterozoic–Silurian strata in northern and southern sides are flat-lying, generally less than 15°, dipping to the north and to the south, respectively (Fig. 5C and F). The two depressions superimposed along the flanks of the Dangyang basin are mainly filled by Lower to Upper Cretaceous deposits. These beds are flat lying in the

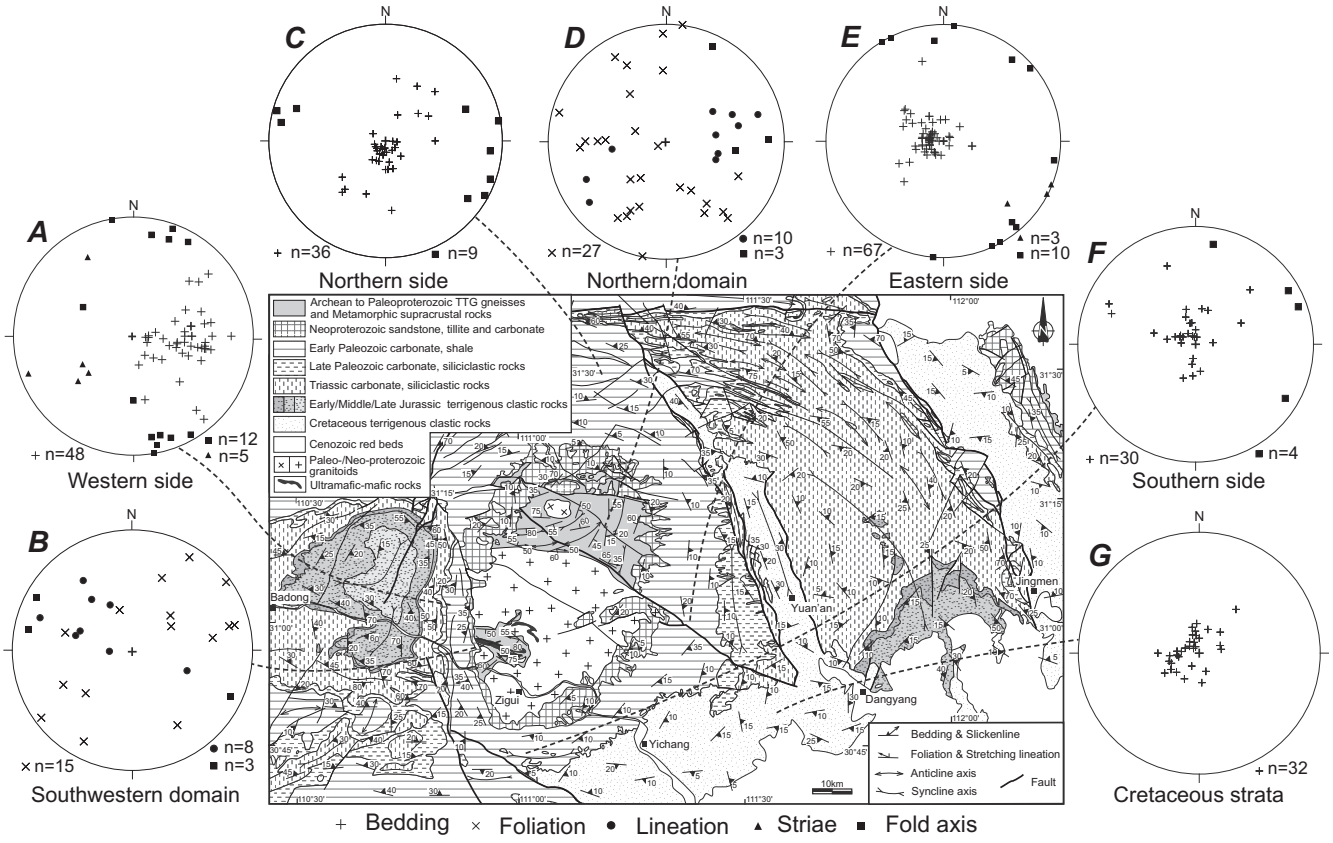

Fig. 5. Structural planar and linear elements (bedding, fold axis, striae, foliation and lineation) of the Huangling massif. All diagrams are equal area projection, lower hemisphere.

depression center and slightly tilted near the normal fault boundary (Fig. 5G). The Lower Cretaceous strata near the Yichang city dip gently to the southeast as a monocline (Fig. 5G).

3.2. Deformation styles related to the uplifting of the Huangling massif

According to our survey, the ductile deformation is limited to the Kongling complex (Fig. 2). Conversely to the previous work, there is neither detachment fault nor basal décollement layer between the metamorphic basement and the sedimentary cover, or the metamorphic rocks and the granitic intrusion (Jiang et al., 2002). Most of the deformation in the sedimentary cover is represented by folds observed in the different strata under shallow tectonic levels depending on the lithology (Fig. 4). The subsequent brittle normal faulting controlled the opening of the Cretaceous grabens and half-grabens on the dome flanks (Fig. 4B, C, and E).

3.2.1. Deformation during the doming

3.2.1.1. Deformation on the western side of the Huangling massif. Along the main road west from Zigui city, Neoproterozoic strata are represented by sandstone, limestone and dolomite (Fig. 3). Moderate to thin bedded limestone is deformed by N–S trending, and west-verging meter-scale recumbent folds (Fig. 6A). More to the west, Cambrian limestone is strongly folded with a west-verging collapse style (Fig. 6B). Several meter-scale folds overturned to the west with the same deformation style are also observed in the Ordovician moderate-bedded limestone (Fig. 6C). In the Triassic thin-bedded limestone, meter-scale décollement-related folds and transverse bedding stylolites indicate a subvertical shortening (Fig. 6D). Calcite tension veins showing normal displacement can be observed in these folded strata. Overall, the Neoproterozoic, Cambrian, Ordovician and Triassic strata are deformed by N–S trending, west-verging folds (Figs. 4A, B and 5A). These structures are related to the westward normal motion of the sedimentary cover along the western flank of the dome.

3.2.1.2. Deformation on the eastern side of the Huangling massif. As mentioned in the bulk architecture Section 3.1, on the eastern side of the dome, the strata dip gently eastward, and seem to be less deformed than the western side (Fig. 5E). In fact, similar structures are observed in the eastern side of the massif, but the deformation is relatively weaker than on another side (Fig. 4C and D). In the Cambrian thick-bedded limestone, meter-scale décollement-related east-verging folds are observed (Fig. 7A). Asymmetric strain fringes at the extremities of pelitic nodules in the Silurian shale show a top-to-the-E shearing (Fig. 7B). More to the east, meter-scale recumbent folds, overturned to the east with nearly N–S axes, were developed in the Triassic thin-bedded limestone (Fig. 7C). Moreover, the east-dipping bedding planes bear SEE-directed (i.e. down-dip) striations formed by eastward slip on the layers (Fig. 5E). Tension gashes and offset markers also indicate this normal displacement.

To summarize, a series of recumbent folds developed on the western and eastern sides of the dome. These structures can be interpreted as gravity-driven collapse folds due to the folding of the tilted beds once they have reached the critical dip. Along the two sides of the dome, the fold axes strike dominantly N–S with flat-lying axial planes, which indicate a vertical shortening accommodated to the uplifting of the massif. Therefore, these recumbent folds in the sedimentary cover are overturned to the west on the western side of the massif, and to the east on the eastern side, respectively. At the scale of the whole massif, we argue that they

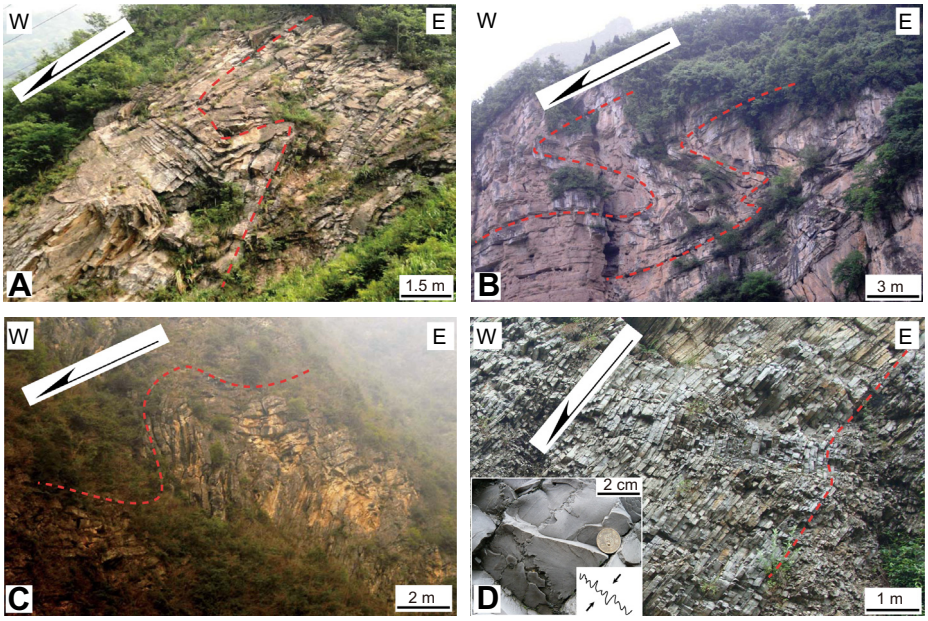

Fig. 6. Field photographs showing the deformation on the western side of the Huanling massif. (A) Meter-scale recumbent fold overturned to the west in the Neoproterozoic limestone (30°52.934′, 110°52.689′); (B) Decameter-scale recumbent fold overturned to the west in the Cambrian limestone (30°53.035′, 110°50.406′); (C) Meter-scale recumbent fold overturned to the west in the Ordovician Moderate-bedded limestone (31°08.888′, 110°50.600′); (D) Meter-scale décollement-related west-verging fold in the Triassic thin-bedded limestone (31°06.905′, 110°48.044′). It is noted that the transverse bedding stylolites indicate a bedding-parallel shortening.

are nearly coeval and result from the same deformation mechanism. Such deformation features are widely developed in the Mesozoic extensional domes in eastern China, representing gravitational décollement and layer-parallel slip coeval with the doming (Faure et al., 1996, 1998, 2003; Lin et al., 2000, 2013).

The Upper Jurassic siltstone and mudstone of the Zigui basin were involved in west limb of the dome. But the Lower Cretaceous coarse clastic deposits, totally about 2-km thick conglomerate on the southeast flank, overlie the deformed pre-Cretaceous strata with an angular unconformity (Fig 4). Therefore, the age of this deformation took place between the Late Jurassic and Early Cretaceous.

3.2.2. Brittle normal faulting superposed on the Huangling massif

To the east of the Huangling massif, the NNW–SSE trending Yuan'an graben and Jingmen half-graben are bounded by several normal faults (Figs. 2 and 4E). These high-angle boundary faults, about 60–80°, mainly cut the Cambrian–Triassic rocks and controlled the deposition of the Cretaceous alluvial–fluvial clastic rocks, forming an overall fining-upward sequence. Tension gashes, Riedel fractures, offset markers, slickenlines and steps indicate predominantly normal displacement. Moreover, on the southwestern flank of the Huangling massif, an Early Cretaceous small half-graben unconformably covers the Paleozoic strata (Figs. 2 and 4B).

4. Geochronological constraints

4.1. Previous geochronological data

In the Huangling massif, several previous studies provided different time constraints. Abundant geochronological data, including U–Pb, Rb–Sr and Ar–Ar, were concentrated on the Huangling granitoids (Fig. 8A). Zircon yields U–Pb ages of 794–837 Ma with a statistic peak around 810 Ma (Fig. 8A, Ma et al., 1984; Feng et al., 1991; Li et al., 2002, 2004; Ling et al., 2006; Zhang et al., 2008; S.B. Zhang et al., 2009; Gao and Zhang, 2009). An average whole rock-mineral Rb–Sr isochron age at 805 ± 5 Ma of diorite-quartz diorite–tonalite complex probably represents the cooling age (Feng et al., 1991). $^{40}Ar/^{39}Ar$ dating of amphibole and biotite gave a relatively wide span of 770–900 Ma (Hu et al., 1989; Li et al., 2002, 2007). It is worthy to note that the Rb–Sr and $^{40}Ar/^{39}Ar$ systems were not reset by Phanerozoic tectonic events.

Recently, in order to assess the uplifting time of the Huangling massif, an array of apatite and zircon fission-track (AFT, ZFT) and (U–Th)/He (AHe, ZHe) lower-temperature thermochronological data from the Huangling granitoids and Kongling complex were realized by several researchers (Fig. 8B, Hu et al., 2006, 2012; Shen et al., 2009; Richardson et al., 2010; Xu et al., 2010; Li and Shan, 2011). The AFT ages range from 87 to 137 Ma with a peak around 120 Ma. Three ZFT ages scatter at 158 ± 50 Ma, 178 ± 34 Ma and 195 ± 14 Ma with large error bars, which makes us difficult to take them into consideration. The AHe ages display a wide range from 39 Ma to 102 Ma, but mainly concentrate on 40–45 Ma; ZHe ages distribute at a dispersive range of 121–309 Ma. Besides of these, Liu et al. (2009) presented nine AFT ages of 81–148 Ma from the Cambrian, Silurian, Jurassic and Cretaceous clastic rocks on the eastern flank of the Huangling massif.

4.2. $^{40}Ar/^{39}Ar$ analyses and MDD modeling

Due to the lack of geochronological record during the 800–200 Ma period, we are unable to precisely depict the cooling and uplifting history of the Huangling massif in this long interval. In order to reveal more details of the tectono-thermal evolution history of the Huangling massif since Neoproterozoic, especially considering the core of the dome, three K-feldspar samples from the Kongling complex and Huangling granitoids had been analyzed by the $^{40}Ar/^{39}Ar$ incremental heating method (McDougall and Harrison, 1999) and modeled by the multi-domain diffusion (MDD) theory (Lovera et al., 1997, 2002).

Sample JH446 is a banded gneiss with clear alternating dark biotite-rich and light-colored quartzo-feldspathic bands in the field. This sample, belonging to the Kongling complex, was collected from the northernmost part of the dome core (Fig. 8A). It is composed of 25% quartz, 45% plagioclase, 15% K-feldspar and

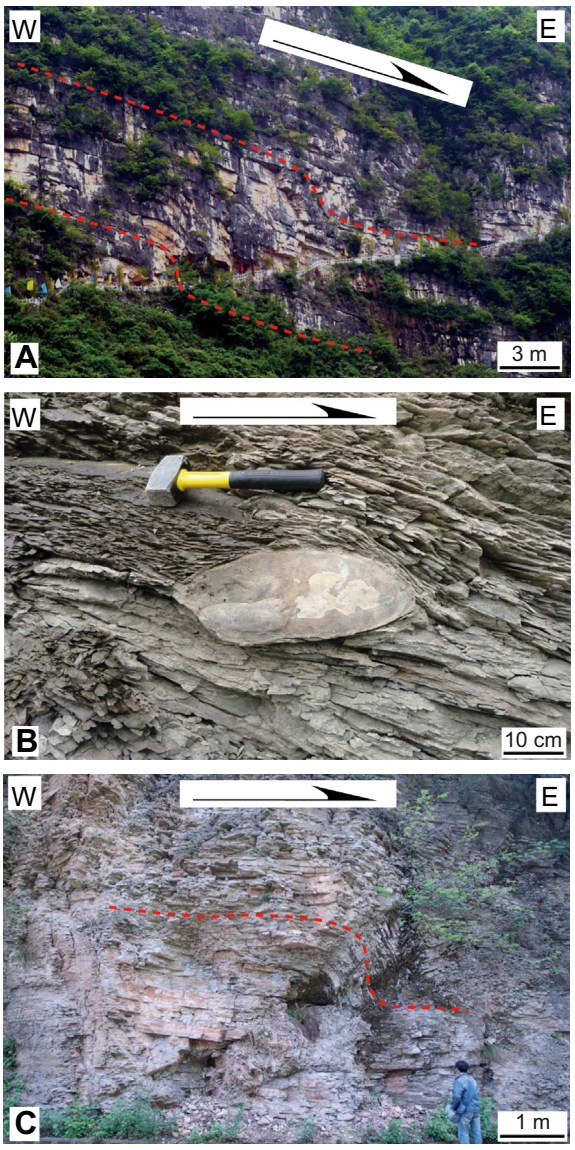

Fig. 7. Field photographs showing the deformation on the eastern side of the Huanling massif. (A) Meter-scale décollement-related east-verging fold in the Cambrian limestone (30°53.877′, 111°20.598′); (B) A pelitic nodule with strain fringes in the Silurian shale showing top-to-the-E shearing (31°10.310′, 111°25.803′); (C) Meter-scale recumbent fold overturned to the east in the Triassic thin-bedded limestone (31°11.065′, 111°30.741′).

15% biotite. Undulatory extinction is common in quartz ribbons. Biotite is euhedral to subhedral and shows yellow to brown pleochroism.

Sample JH71 is a foliated migmatite from the Kongling complex in the northern domain of the massif (Fig. 8A). The quartzo-feldspathic leucosomes are strongly folded, indicating partial melting during deformation. In thin section, JH71 was comprises about 25% quartz, 40% K-feldspar, 20% plagioclase, 10% biotite and 5% hornblende. Quartz occurs as globular recrystallized subgrains with undulatory extinction. Microcline is the dominant K-feldspar. Much of the Plagioclase crystals were altered to sericite. Subhedral biotite and hornblende grains are locally replaced by chlorite.

Sample JH147 is an undeformed granodiorite from the southeastern part of the Huangling granitoids (Fig. 8A, near Liantuo village). On outcrop, the rock is leucocratic, medium- to coarse-grained, with K-feldspar as minor phenocrysts. It contains about 30% quartz, 53% plagioclase, 10% K-feldspar, 5% biotite and 2% hornblende. Accessory minerals include magnetite, zircon and apatite. This granodiorite suite was dated at 819 ± 7 Ma by SHRIMP Zircon U–Pb method (Ma et al., 1984).

K-feldspars were obtained by the usual mineral separation techniques and finally handpicked under a binocular to remove all visible impurities. Aliquots of K-feldspar were wrapped separately in aluminum foil to form wafers and stacked in quartz vial. The samples were irradiated at the B4 position in the 49-2 Reactor (China Institute of Atomic Energy, Beijing) for 36 h. The $^{40}Ar/^{39}Ar$ analyses were performed in the Institute of Geology and Geophysics, Chinese Academy of Sciences. Detailed analytical procedures followed Wang et al. (2006). Samples were heated stepwise with a double vacuum resistance furnace. The released gas was purified with Zr–Al getters. The isotopic composition was measured using a MM-5400 mass spectrometer. After corrections for mass discrimination, system blanks, radiometric interference, $^{40}Ar/^{39}Ar$ ages were calculated according to $^{40}Ar^{*}/^{39}Ar_{K}$ ratios and J value obtained by analyses of the monitors, as well as the decay constant. The correction factors herein are: $[^{36}Ar/^{37}Ar]_{Ca} = 0.000261$, $[^{39}Ar/^{37}Ar]_{Ca} = 0.000724$ and $[^{40}Ar/^{39}Ar]_{K} = 0.000880$. The data were processed using ArArCALC software (Koppers, 2002), and the apparent ages are reported at 2σ uncertainties. The $^{40}Ar/^{39}Ar$ analytical data are listed in Table 1. After appropriate adjustment of the various model parameters, e.g. active energy, relative domain size, a modeled age spectrum and cooling history can be obtained by MDD modeling.

The age spectra and modeling results are shown in Fig. 9. The abnormally old ages of the first steps are possibly due to the excess Ar present in the margin of the mineral. Subsequent increasing age pattern of K-feldspar may record its cooling history. Apparent ages of the three samples range from 239.7 to 899.0 Ma (JH446, total fusion ages = 759.6 ± 3.3 Ma), 167.7 to 762.6 Ma (JH71, total fusion ages = 693.9 ± 3.0 Ma) and 244.8 to 610.7 Ma (JH147, total fusion ages = 567.9 ± 2.3 Ma), respectively. The modeled age spectra closely match the experimental results show that the qualities of the K-feldspar MDD modeling results are high (Fig. 9). Considering the closure temperature of K-feldspar, the cooling history between 350 °C and 150 °C is reliable. The K-feldspar MDD modeling result from JH446 gneiss shows a slow cooling before 450 Ma, then an obvious cooling event around 400 Ma (Fig. 9). Except for the asynchronous cooling in early stage, JH71 migmatite and JH147 granodiorite reveal a long-term thermal stability period during Paleozoic, and a final cooling event since Late Triassic (Fig. 9).

5. Discussion

5.1. Cooling and uplifting history of the Huangling massif

The Huangling massif witnessed the tectonic evolution of SCB. In fact, the stratigraphic column recorded several tectonic events that occurred in the Neoproterozoic, Early Paleozoic, Early Mesozoic and Late Mesozoic times (Fig. 3). The combination of the stratigraphic relationships and the thermochronological data allows us to construct a synthetic temperature–time curve, and to unravel the tectono-thermal history of the Huangling massif since the Neoproterozoic (Fig. 10A).

The Kongling complex was intruded by the Huangling granitoids, and then unconformably overlain by the terrigeneous fluvial conglomerate at the base of the Neoproterozoic Liantuo Formation (Fig. 3). Available geochronological data reveal that the Huangling granitoids emplaced around 820–800 Ma, and then experienced a cooling from the closure temperature of Zircon U–Pb system to mineral Rb–Sr and K–Ar system before 770 Ma (Fig. 10A). The U–Pb ages of the youngest zircons from the Neoproterozoic Liantuo Formation indicate that its deposition time is no later than

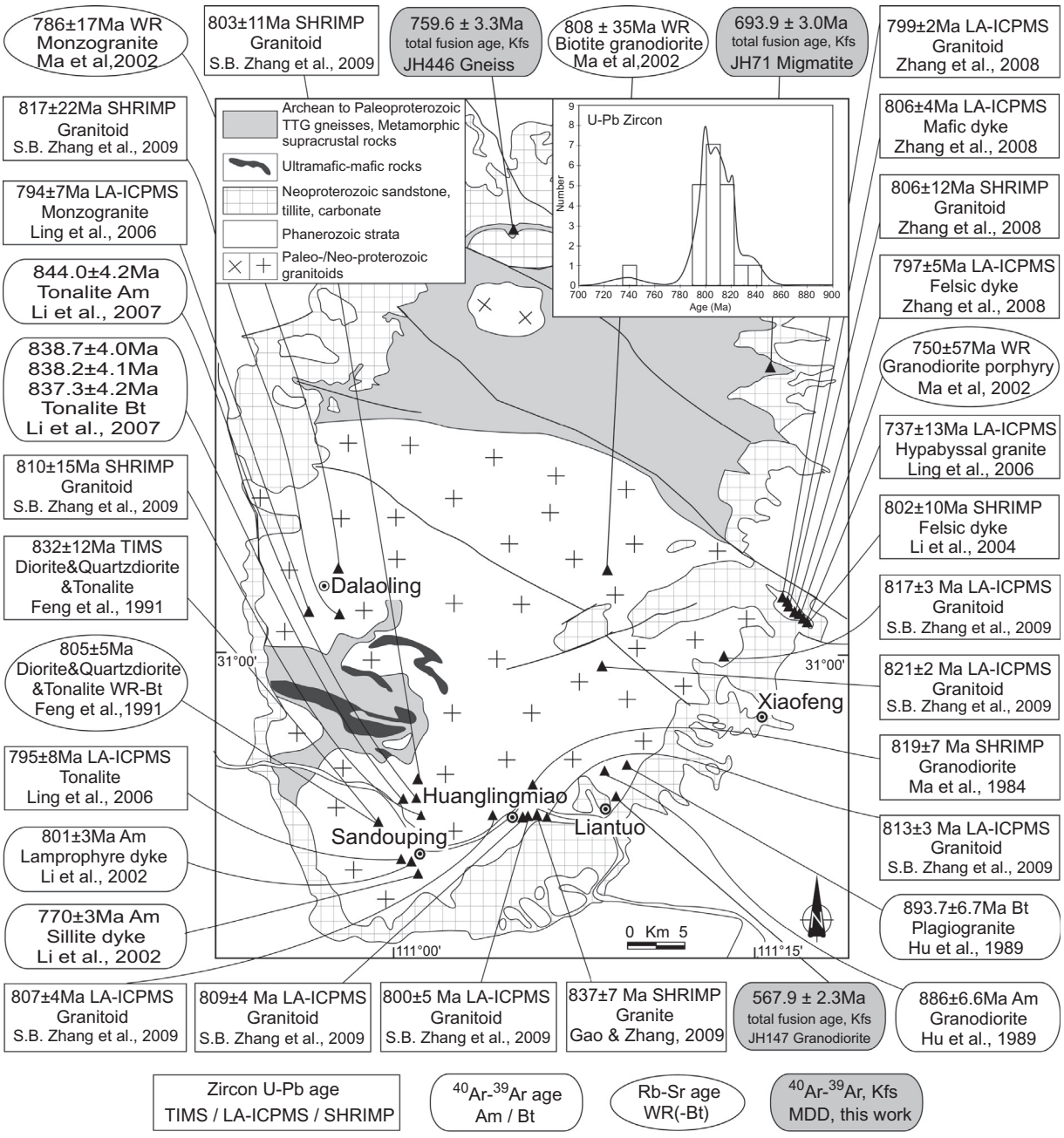

Fig. 8A. Compilation of the U–Pb, Rb–Sr and Ar–Ar ages from the Huangling granitoids. Inset statistical chart shows the results of the zircon U–Pb ages. Am, amphibole; Bt, biotote; Kfs, K-feldspar; WR(-Bt), Whole rock(-biotote).

750 Ma (Zhang et al., 2006c; Liu et al., 2008), which agree with the age of 748 ± 12 Ma from the interlayer tuff in the lower part of the Liantuo Formation (Ma et al., 1984). Our K-feldspar MDD modeling results also show differential cooling processes during the Neoproterozoic (Fig. 9). The above evidence indicates that the Huangling massif was once exposed to the surface before 750 Ma. An approximately 20 °C/Ma cooling rate can be inferred from the cooling curve (Fig. 10A).

The MDD modeling result from the gneiss (JH446) presents a distinct cooling event around 400 Ma (Fig. 9). It appears that the Huangling massif locally suffered a weak thermal disturbance during Silurian to Devonian. From the view of whole SCB, the obvious hiatus between the Middle Silurian and Middle Devonian in the Huangling area may correspond to the Early Paleozoic intracontinental orogeny of SCB. However, this event was well documented to the southeastern areas of the Jiangshan–Shaoxing fault, mainly along the Wuyi–Yunkai belt (Lin et al., 2008; Faure et al., 2009; Charvet et al., 2010; Li et al., 2010; Y.J. Wang et al., 2010). Moving to the NW, the deformation intensity is decreasing, and even absent. The Huangling massif is far away from the deformation domain of the Early Paleozoic orogeny.

The local discontinuity between the Middle and Late Triassic in the Huangling area was considered as a response to the so-called "Indosinian orogeny" of SCB (Meng and Li, 2003; Li et al., 2008; Zhao et al., 2010). As mentioned in Section 1, this Early Mesozoic orogeny was widely developed around or inside the SCB, such as the Qinling–Dabie belt to the north of the Huangling massif (e.g. Faure et al., 1999, 2003) and the Xuefengshan–Jiuling belt in the central SCB (Chu et al., 2012a; Chu and Lin, 2013). Our other two MDD samples from the migmatite (JH71) and granodiorite

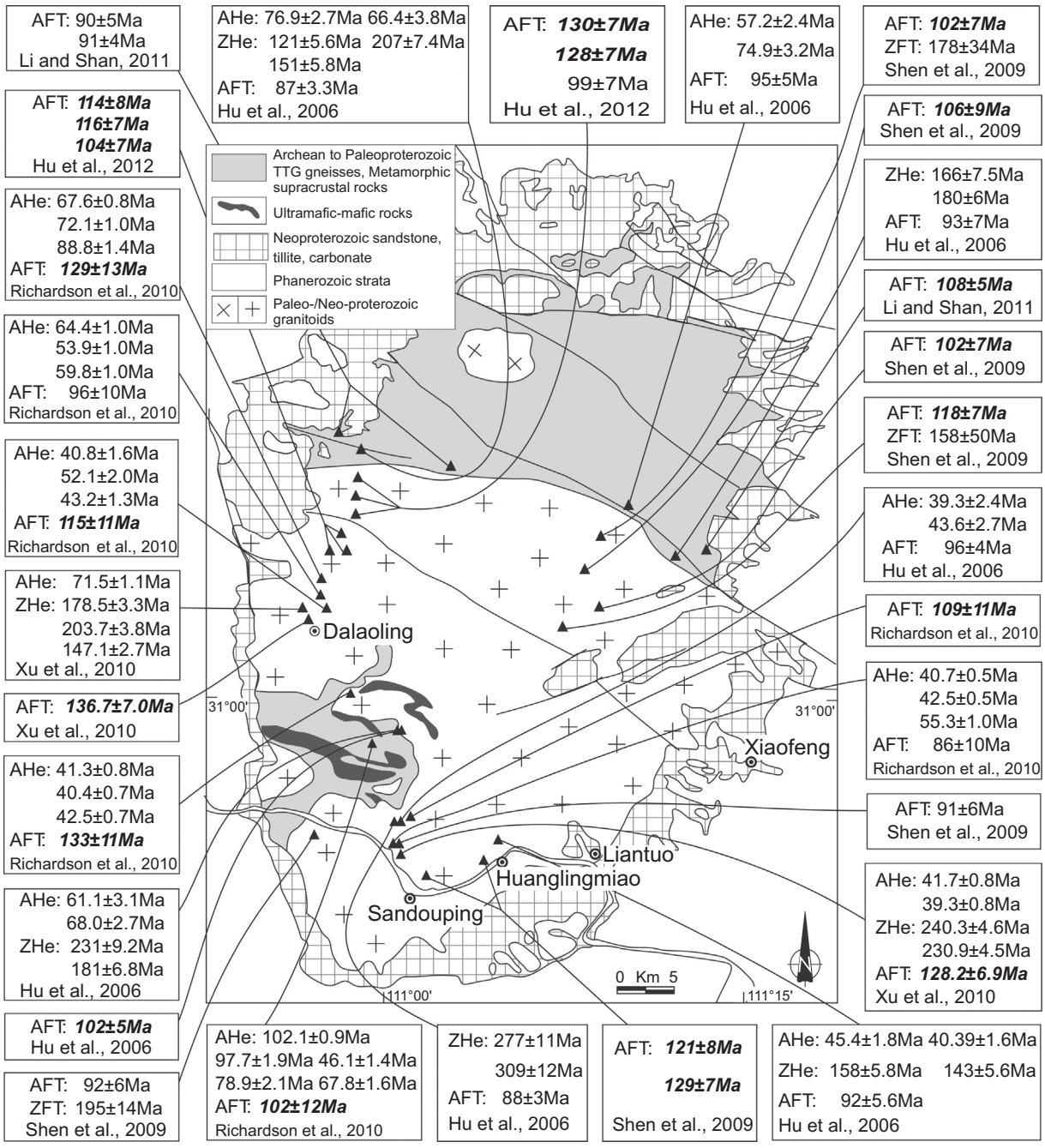

Fig. 8B. Compilation of the apatite and zircon fission-track and (U–Th)/He ages from the Huangling massif. AHe, apatite (U–Th)/He; AFT, apatite-fission track; ZHe, zircon (U–Th)/He; ZFT, zircon-fission track.

(JH147) recorded this tectonic event, showing a prolonged cooling since Late Triassic, with undistinguished Late Mesozoic process (Figs. 9 and 10B). However, it seems that this widespread tectonic event weakly influenced the Huangling massif. The Huangling massif is located in a stable triangle area between the Qinling–Dabie belt and Xuefengshan–Jiuling belt, where the Triassic deformation was rather weaker than two other domains. Indeed, as a stable sedimentary platform, there is no significant angular unconformity in the Huangling area from ca. 750 Ma until the Late Jurassic (Fig. 3). According to lithology and paleontology, the Upper Triassic and Jurassic series in Zigui and Dangyang basins are completely comparable (BGMRHB, 1990). Thus, accompanied by the Triassic regression, effect of the Indosinian orogeny is expressed as a locally slight vertical uplift of the crust in the Huangling area, but which did not built the antiformal shape of the massif (Fig. 10A).

The detailed cooling history since 200 Ma of the Huangling massif is constrained by FT and (U–Th)/He data (Shen et al., 2009; Xu et al., 2010; Li and Shan, 2011; Hu et al., 2012; Fig. 10B). AFT thermal modeling results from the dome core indicate that the Huangling massif recorded a stable stage before 160 Ma and an obvious cooling process between 160 and 110 Ma with a rate of 2–3 °C/Ma. A similar thermal modeling result has been shown in the work of Richardson et al. (2010), the increasing cooling after 40 Ma was been considered as the onset of incision in the Three Gorges. Moreover, three AFT modeling for the sedimentary rocks on the eastern flank of the Huangling massif revealed a cooling rate of 1.9–2.7 °C/Ma during 165–100 Ma (Liu et al., 2009; Fig. 10B). Instead, Hu et al. (2006) suggested that the significant cooling event occurred during 100 and 40 Ma with a cooling rate of 2.5 °C/Ma, but the GOF (goodness of fit) between the measured

Table 1
$^{40}Ar/^{39}Ar$ analytical data on K-feldspars from the core of the Huangling massif.

Termperature (°C)	$^{40}Ar/^{39}Ar$	$^{37}Ar/^{39}Ar$	$^{36}Ar/^{39}Ar$	$^{40}Ar^{*}/^{39}Ar_{K}$	$^{40}Ar^{*}$ (%)	$^{39}Ar_{K}$ (%)	Age ± 2σ (Ma)
JH446, Gneiss, Kfs, weight = 12.3 mg, J = 0.005598, total fusion age = 759.6 ± 3.3 Ma, GPS: 31°19.982′, 111°05.738′							
600	768.67	0.4641	2.1664	128.579	16.72	0.01	980.47 ± 519.29
600	1523.39	1.1305	4.1970	283.584	18.60	0.00	1719.16 ± 1218.25
650	357.47	0.1683	0.9389	80.044	22.39	0.01	669.52 ± 209.56
650	162.44	0.0618	0.4442	31.186	19.20	0.03	290.98 ± 31.40
700	503.56	0.0106	1.5083	57.862	11.49	0.09	507.41 ± 85.21
700	272.59	0.0014	0.7965	37.216	13.65	0.17	342.22 ± 47.90
750	109.03	0.0047	0.2833	25.321	23.22	0.48	239.71 ± 17.97
750	127.71	0.0038	0.3432	26.303	20.60	0.53	248.40 ± 21.56
800	60.837	0.0039	0.1117	27.824	45.73	0.94	261.76 ± 7.29
800	56.042	0.0037	0.0907	29.234	52.16	0.91	274.08 ± 5.87
850	52.844	0.0049	0.0585	35.547	67.27	1.48	328.17 ± 4.09
850	52.770	0.0024	0.0490	38.292	72.56	1.12	351.20 ± 3.83
875	55.918	0.0038	0.0401	44.083	78.83	1.00	398.84 ± 3.40
875	56.490	0.0035	0.0354	46.041	81.50	0.94	414.68 ± 3.58
900	61.936	0.0063	0.0295	53.217	85.92	0.97	471.53 ± 3.68
925	65.297	0.0052	0.0239	58.238	89.19	1.37	510.27 ± 3.36
950	68.145	0.0060	0.0195	62.389	91.55	1.87	541.69 ± 3.19
975	73.387	0.0055	0.0141	69.228	94.33	2.60	592.28 ± 3.38
1000	79.840	0.0061	0.0120	76.290	95.55	2.68	643.08 ± 3.51
1025	84.203	0.0044	0.0076	81.943	97.32	5.37	682.75 ± 3.63
1050	90.313	0.0033	0.0069	88.275	97.74	8.29	726.16 ± 4.11
1075	91.238	0.0033	0.0064	89.361	97.94	7.39	733.50 ± 3.79
1100	95.529	0.0030	0.0056	93.865	98.26	6.50	763.64 ± 3.94
1100	98.871	0.0031	0.0054	97.286	98.40	5.74	786.20 ± 4.00
1100	102.62	0.0027	0.0044	101.33	98.75	4.07	812.52 ± 4.04
1100	105.84	0.0021	0.0032	104.88	99.10	4.36	835.33 ± 4.20
1100	109.08	0.0012	0.0023	108.41	99.39	3.57	857.67 ± 4.32
1100	112.91	0.0010	0.0025	112.18	99.36	4.94	881.26 ± 4.33
1100	116.02	0.0006	0.0033	115.05	99.16	6.30	899.00 ± 4.39
1200	115.29	0.0011	0.0019	114.72	99.51	3.20	897.01 ± 4.44
1225	111.03	0.0012	0.0019	110.47	99.49	5.62	870.61 ± 4.28
1250	108.98	0.0007	0.0020	108.40	99.47	7.28	857.63 ± 4.17
1300	109.13	0.0006	0.0020	108.55	99.47	8.23	858.54 ± 5.41
1350	109.01	0.0012	0.0030	108.11	99.17	0.95	855.76 ± 4.75
1400	114.00	0.0048	0.0068	112.00	98.25	0.23	880.16 ± 7.46
1500	111.38	0.0005	0.0073	109.21	98.05	0.73	862.73 ± 5.46
JH71, Migmatite, Kfs, weight = 14.6 mg, J = 0.005717, total fusion age = 693.9 ± 3.0 Ma, GPS: 31°12.906′, 111°16.829′							
600	587.80	0.5444	1.8277	47.786	8.13	0.00	436.76 ± 163.72
600	134.25	0.4680	0.3947	17.667	13.15	0.01	174.00 ± 40.06
650	111.13	0.1092	0.3269	14.546	13.09	0.02	144.45 ± 33.44
650	97.84	0.0451	0.2804	14.973	15.30	0.05	148.52 ± 32.28
700	277.26	0.0076	0.8592	23.367	8.43	0.12	226.74 ± 55.92
700	179.64	0.0177	0.5357	21.345	11.88	0.17	208.21 ± 35.21
750	75.271	0.0069	0.1972	16.998	22.58	0.47	167.70 ± 13.25
750	50.819	0.0059	0.1052	19.725	38.81	0.55	193.22 ± 7.22
800	40.757	0.0042	0.0496	26.093	64.02	1.02	251.44 ± 3.61
800	47.777	0.0060	0.0443	34.682	72.59	0.75	327.10 ± 3.64
850	57.516	0.0142	0.0440	44.523	77.41	0.96	410.07 ± 3.65
850	67.090	0.0181	0.0459	53.521	79.77	0.72	482.74 ± 4.03
875	72.315	0.0167	0.0428	59.658	82.50	0.68	530.68 ± 5.18
900	72.476	0.0161	0.0217	66.075	91.17	0.93	579.48 ± 3.84
925	73.113	0.0113	0.0153	68.587	93.81	1.52	598.23 ± 3.51
950	73.372	0.0095	0.0088	70.764	96.44	1.87	614.33 ± 3.38
975	75.568	0.0082	0.0079	73.247	96.93	2.65	632.51 ± 3.37
1000	77.136	0.0044	0.0058	75.409	97.76	4.02	648.20 ± 3.51
1025	78.652	0.0066	0.0039	77.502	98.54	6.99	663.25 ± 3.48
1050	81.314	0.0045	0.0027	80.509	99.01	10.33	684.67 ± 3.55
1075	84.073	0.0028	0.0023	83.390	99.19	8.37	704.95 ± 3.68
1100	84.930	0.0025	0.0019	84.367	99.34	6.45	711.78 ± 3.73
1100	86.684	0.0017	0.0011	86.372	99.64	6.80	725.71 ± 3.67
1100	88.732	0.0013	0.0013	88.352	99.57	5.43	739.36 ± 3.79
1100	89.998	0.0010	0.0017	89.501	99.45	6.88	747.23 ± 3.79
1100	90.829	0.0007	0.0021	90.204	99.31	5.10	752.03 ± 3.82
1100	89.342	0.0009	0.0015	88.896	99.50	9.42	743.09 ± 3.73
1100	90.075	0.0006	0.0025	89.322	99.16	8.49	746.01 ± 3.77
1150	89.940	0.0073	0.0009	89.678	99.71	0.40	748.44 ± 5.46
1200	90.277	0.0024	0.0005	90.127	99.83	1.54	751.51 ± 4.20
1225	89.995	0.0008	0.0008	89.745	99.72	2.32	748.90 ± 3.99
1250	90.024	0.0009	0.0011	89.691	99.63	2.97	748.53 ± 3.89
1275	91.409	0.0021	0.0034	90.398	98.89	1.45	753.36 ± 4.45
1300	93.721	0.0069	0.0066	91.758	97.90	0.36	762.60 ± 4.96
1350	91.364	0.0311	0.0110	88.115	96.44	0.09	737.73 ± 23.13
1400	88.350	0.0148	0.0091	85.672	96.97	0.09	720.86 ± 17.36

(*continued on next page*)

Table 1 (*continued*)

Termperature (°C)	$^{40}Ar/^{39}Ar$	$^{37}Ar/^{39}Ar$	$^{36}Ar/^{39}Ar$	$^{40}Ar^*/^{39}Ar_K$	$^{40}Ar^*$ (%)	$^{39}Ar_K$ (%)	Age ± 2σ (Ma)
JH147, Granodiorite, Kfs, weight = 15.1 mg, J = 0.005695, total fusion age = 567.9 ± 2.3 Ma, GPS: 30°51.400′, 111°08.917′							
600	461.75	0.6943	1.2474	93.257	20.18	0.00	770.32 ± 295.10
600	554.33	1.0998	1.4793	117.393	21.16	0.00	925.78 ± 604.47
650	96.69	0.0778	0.2434	24.784	25.63	0.04	238.76 ± 35.30
650	117.33	0.0434	0.3030	27.791	23.68	0.05	265.69 ± 26.15
700	244.30	0.0258	0.7078	35.143	14.38	0.18	329.90 ± 43.28
700	118.29	0.0239	0.3046	28.274	23.90	0.28	269.98 ± 19.42
750	56.791	0.0436	0.1061	25.450	44.81	0.76	244.76 ± 7.03
750	46.785	0.0139	0.0599	29.075	62.15	0.90	277.07 ± 4.26
800	46.183	0.0220	0.0286	37.729	81.69	1.66	351.96 ± 3.09
800	52.011	0.0129	0.0317	42.658	82.02	1.33	393.27 ± 3.01
850	57.718	0.0205	0.0268	49.798	86.28	1.72	451.48 ± 3.11
850	64.802	0.0140	0.0292	56.164	86.67	1.12	501.85 ± 3.52
875	70.111	0.0156	0.0341	60.039	85.63	0.82	531.83 ± 3.82
875	72.133	0.0132	0.0332	62.323	86.40	0.68	549.27 ± 3.95
900	70.752	0.0135	0.0276	62.590	88.46	0.56	551.30 ± 5.01
925	74.189	0.0176	0.0385	62.810	84.66	0.72	552.97 ± 4.04
950	72.025	0.0152	0.0358	61.457	85.33	0.87	542.68 ± 3.84
975	69.663	0.0178	0.0289	61.117	87.73	1.04	540.08 ± 3.67
1000	67.460	0.0160	0.0241	60.340	89.44	1.46	534.14 ± 3.44
1025	65.818	0.0134	0.0173	60.700	92.22	2.69	536.90 ± 3.06
1050	67.629	0.0121	0.0108	64.445	95.29	4.88	565.33 ± 3.09
1075	66.573	0.0147	0.0101	63.592	95.52	3.55	558.89 ± 3.12
1100	65.527	0.0134	0.0075	63.309	96.61	3.83	556.76 ± 3.02
1100	66.360	0.0115	0.0062	64.531	97.24	4.84	565.98 ± 3.12
1100	67.118	0.0095	0.0050	65.637	97.79	4.57	574.29 ± 3.05
1100	67.725	0.0080	0.0053	66.157	97.68	5.60	578.18 ± 3.11
1100	67.692	0.0066	0.0044	66.399	98.09	4.36	580.00 ± 3.19
1100	69.194	0.0055	0.0039	68.037	98.33	6.16	592.19 ± 3.16
1100	70.568	0.0045	0.0037	69.473	98.45	8.63	602.82 ± 3.24
1150	70.073	0.0070	0.0033	69.107	98.62	0.64	600.12 ± 3.81
1200	67.938	0.0075	0.0036	66.876	98.43	3.14	583.55 ± 3.18
1225	69.179	0.0042	0.0032	68.226	98.62	6.11	593.60 ± 3.19
1250	70.142	0.0021	0.0028	69.303	98.80	12.01	601.57 ± 3.11
1275	70.434	0.0021	0.0030	69.548	98.74	10.99	603.37 ± 4.14
1300	71.713	0.0029	0.0039	70.549	98.38	2.89	610.74 ± 3.27
1350	71.131	0.0041	0.0050	69.642	97.91	0.49	604.07 ± 3.90
1400	66.496	0.0157	0.0084	64.009	96.26	0.18	562.05 ± 12.59
1500	71.522	0.0042	0.0104	68.445	95.70	0.23	595.22 ± 6.01

and modeled fission-track length distributions and ages are below 0.5. On the assumption that the geothermal gradient is a constant of 25 °C/km, the unroofing depth of the massif during the interval of 160–110 Ma was approximately 5 km (Fig. 10B).

Recent sedimentary evidence also supports that the Huangling massif experienced considerable uplifting during the Late Jurassic to Early Cretaceous. Before the Late Jurassic, the Zigui and Dangyang basins probably connected with each other based on paleogeography (Liu et al., 2005). Paleocurrents analysis of the Zigui basin indicates that the Huangling massif began to provide detrital material since Late Jurassic (Qu et al., 2009). To the southeast of Huangling massif, the results of detrital zircon U–Pb ages from the Cretaceous sediments reveal that the denudation of the Kongling complex and its overlying strata was active during the deposition of the Lower Cretaceous, and the Huangling granite was exposed at the surface during the Late Cretaceous (Shen et al., 2012). The uplifting of the Huangling massif led to the atrophy of the Zigui basin on its western flank, while the onset of rifting in the Dangyang basin on its eastern flank. It was also resulted in the prominent angular unconformity between Late Jurassic and Early Cretaceous.

5.2. When did the Huangling massif come into being?

On the western and eastern sides of the dome, the deformation due to gravitational décollement and layer-parallel slipping occurred in response to its uplifting (Figs. 4, 6 and 7). But the northern and southern sides of the dome are not involved into such a deformation (Fig. 2). The uplifting time of the Huangling massif is still controversial: Early Mesozoic (Dai, 1996; Xu et al., 2004), unprecisely determined between the Late Triassic to Early Cretaceous (Wang et al., 2003), or sometime between 165 Ma and 98 Ma as indicated by AFT data (Liu et al., 2009; Shen et al., 2009; Xu et al., 2010; Li and Shan, 2011; Hu et al., 2012). On the basis of regional tectonics, Ge et al. (2010) considered that this antiform shaped at ca. 24.6 Ma, corresponding to the regional angular unconformity in the end of the Paleogene. Our field work indicates that these "gravity-driven collapse folds" with east–west polarity are observed in all the strata of pre-Cretaceous age, since the Cretaceous graben and half-graben basins superimposed unconformably on these folded strata (Figs. 2 and 4). As discussed above, the Huangling area was not significantly involved into any tectonic events between the Sinian (Neoproterozoic) and Jurassic. Cooling history also reveals that the Huangling massif experienced an important uplift process around 160–110 Ma (Fig. 10). These geochronological and sedimentary constraints are in good agreement with our structural observations, which argue that the main deformation in the Huangling massif developed from the Late Jurassic to Early Cretaceous.

5.3. Compressional or extensional setting model

The origin of the Huangling massif was variously interpreted by previous workers either in terms of compression or extension. According to investigations on the tectonic evolution of the Jianghan basin, a westward escape of the Huangling massif related to the Early Mesozoic opposite-directed thrusting of the Qinling–Dabie belt and the Jiuling belt has been suggested (Fig. 11A; Dai,

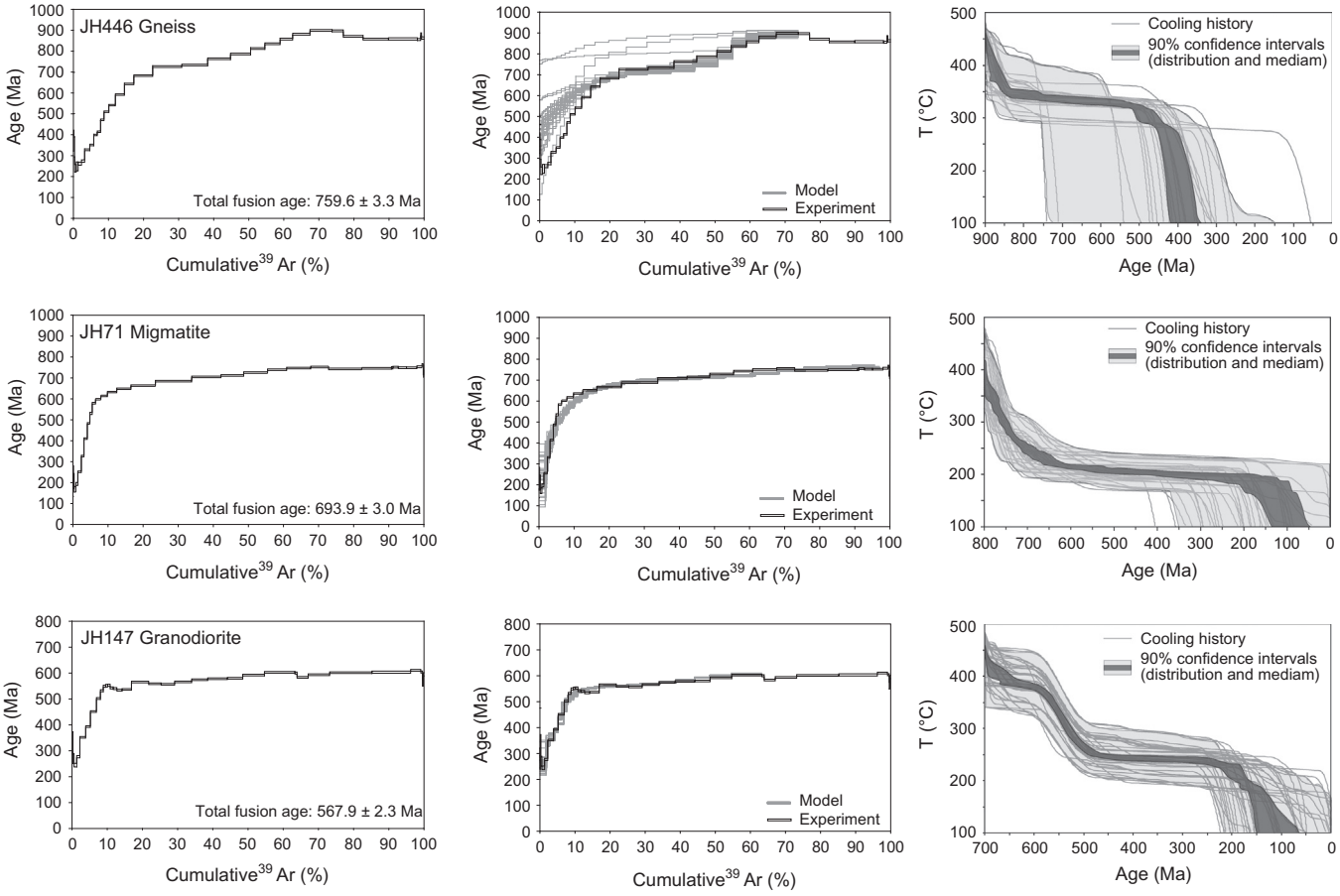

Fig. 9. ^{40}Ar–^{39}Ar age spectra and the multi-domain diffusion (MDD) modeling results of K-feldspar from different rock types in the core of Huangling massif.

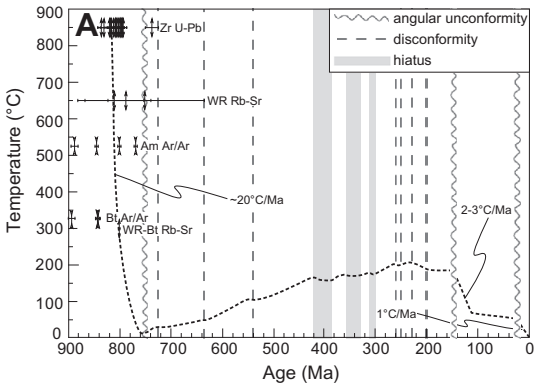

Fig. 10A. A synthetic curve showing the tectono-thermal history of the Huangling massif with emphasis on the dome core. Zr U–Pb, WR Rb–Sr, Am Ar–Ar, Bt Ar–Ar, WR-Bt Rb–Sr ages (Fig. 8A) are plotted at their closure temperatures of 850 °C, 650 °C, 525 °C, 325 °C and 300 °C, respectively.

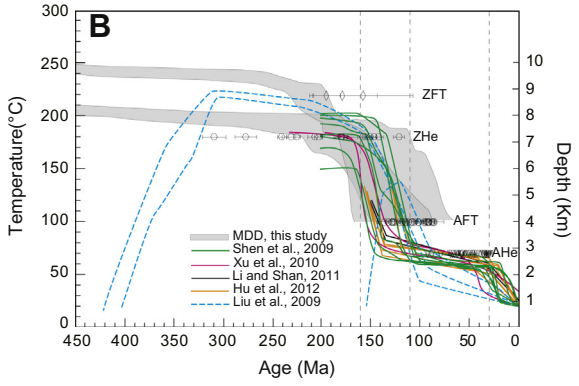

Fig. 10B. Cooling history of the Huangling massif from K-feldspar MDD modeling (this study) and AFT modeling (Liu et al., 2009; Shen et al., 2009; Xu et al., 2010; Li and Shan, 2011; Hu et al., 2012). It indicates a thermal history with four major phases: a prolonged slow cooling until 160 Ma, a obvious enhanced cooling with a rate of 2–3 °C/Ma during 160–110 Ma, a slow cooling during 110–30 Ma interval with a rate of 0.2–0.3 °C/Ma, and a final increased cooling since 30 Ma with a rate about 1 °C/Ma. AHe, AFT, ZHe and ZFT ages (Fig. 8B) are plotted at their closure temperatures of 70 °C, 100 °C, 180 °C and 220 °C, respectively.

1996; Xu et al., 2004). This model might well explain the geometry of the Huangling massif, which is an asymmetric antiform with its eastern side more gently dipping than its western side. In fact, far from the northern and southern sides of the Huangling massif, we observed a nearly N–S directed trust deformation, which is probably the response to the Triassic compression in the Qinling–Dabie belt to the north and the Xuefengshan–Jiuling intracontinental belt to the south, respectively (Fig. 1, see also Chu and Lin, 2014). However, there is a time discrepancy between the Triassic deformation and the Late Jurassic-Early Cretaceous tectonics in the Huangling massif. Moreover, it is noteworthy that the hinge of Huangling massif is nearly N–S trending, which is sub-parallel to the shortening direction of the Triassic deformation, the W-directed thrust faults and folds are not well developed around the Huangling massif. Cooling history shows that uplifting of the Huangling massif occurred between 160 Ma and 110 Ma, which is longtime

after the Triassic events. Nevertheless, asymmetry of the Huangling massif can be interpreted as a kind of ramp anticline developed on top of a blind thrust as depicted in Fig 11A. If this is the case, the westward thrusting would have taken place in the Late Jurassic to Early Cretaceous.

Another model was recently put forward, namely the Late Mesozoic eastward extrusion due to its northward indentation and coeval clockwise rotation of the SCB (Fig. 11B; Wang et al., 2003; Meng et al., 2005). The Huangling massif was considered as one of the syntaxes related to the Dabashan orocline (Fig. 1; Hu et al., 2012; Shi et al., 2012; Li et al., 2013). This model is well compatible with the age of the deformation related to uplifting of the massif. However, a problem arises as the eastward extrusion would lead to an opposite geometry of the Huangling massif with its western flank more gently dipping than the eastern one (Fig. 11B). Thus, this model is not compatible with our field observations (Fig. 4E).

Late Mesozoic extensional tectonics was widely spread on the eastern margin of Eurasian continent, which is indicated by a number of extensional domes, and syntectonic plutons bounded by ductile normal faults (e.g. Lin and Wang, 2006; T. Wang et al., 2011; Lin et al., 2013). The temporal–spatial framework of the extensional tectonics brings a reasonable assumption that the Huangling area might have experienced the same geodynamic setting. Therefore, an extensional uplifting model is proposed here: the regional extension that occurred on the eastern margin of Eurasian continent is responsible for the origin of the Huangling massif. To some extent, this extension exhumed and tilted the Huangling massif (Fig. 11C). Accompanying this uplifting, a series of oppositely directed gravity-driven collapse folds developed on the western and eastern sides of the dome. From this view, the drag-folds in the sedimentary cover, and the formation of graben or half graben basins around the Huangling massif belong to the same extensional tectonics with a slight diachronism. However, it is worth to note that low-angle ductile normal faults or detachments are lacking between the basement and sedimentary cover. Also, syntectonic plutons coeval with extension as observed in more southeasterly part of the SCB (Fig. 1, e.g. Wugongshan, Dayunshan-Mufushan, Hengshan), are absent in the Huangling area.

In the present state of knowledge, we cannot completely rule out the compressional tectonic model. Taking into account the geometry and the deformation styles of the Huangling massif presented in the previous sections, it appears that the extensional tectonic model is also plausible. In this case, the Huangling massif represents the westernmost case of the Late Mesozoic extensional tectonics in the SCB, as recognized elsewhere in many parts of the

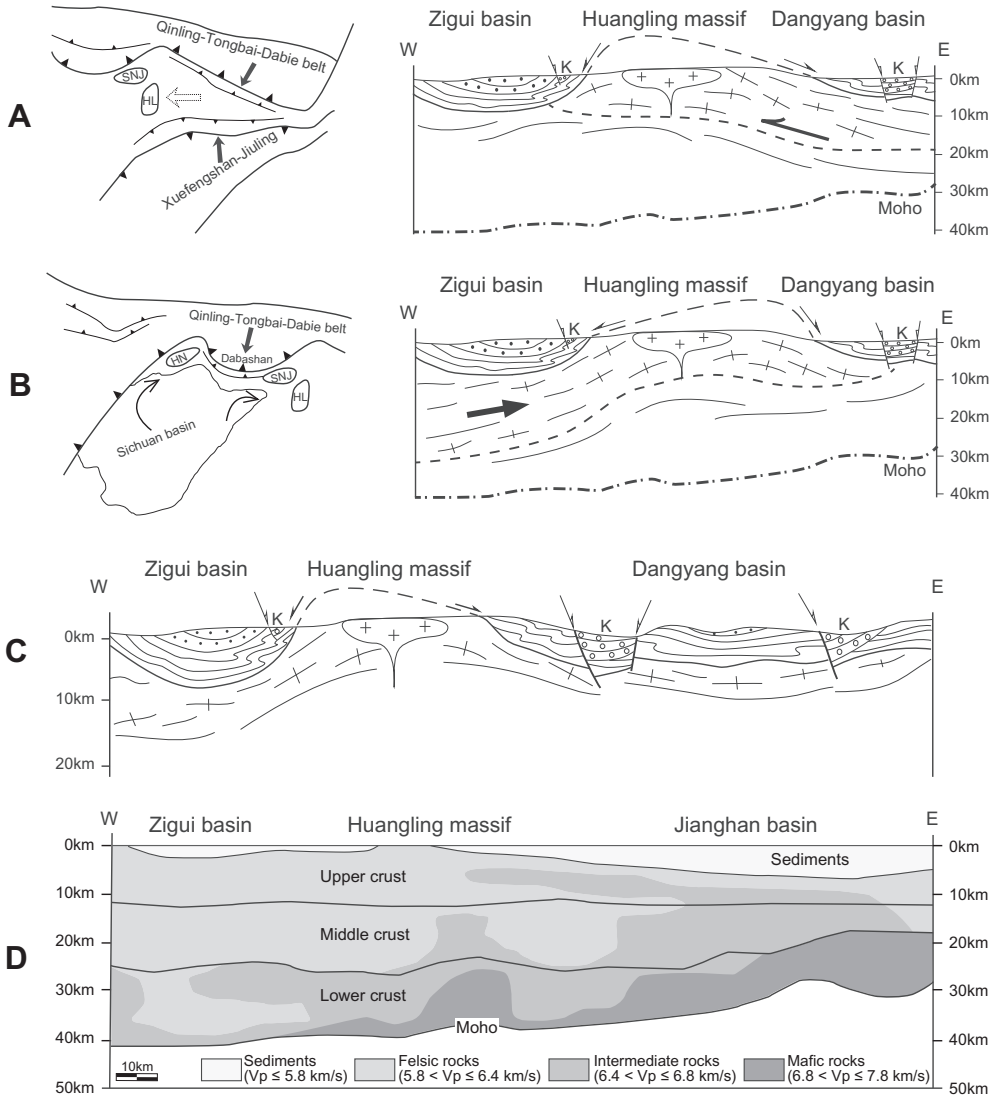

Fig. 11. Three possible tectonic models for origin of the Huangling massif. (A) Westward thrusting; (B) Eastward extrusion; (C) Extensional uplifting; (D) The profile of *P*-wave crustal velocity structure from wide angle reflection across the Huangling massif (modified after Z.J. Zhang et al. (2009)).

eastern Eurasian continent. Scope of destruction of the NCC is roughly bounded by the N–S Gravity Lineament, which was formed by diachronous lithospheric thinning since Early Cretaceous (Xu, 2007; Zhu et al., 2011). Coincidentally, the Huangling massif that recorded a weak extension of the crust also lies in this N–S Gravity Lineament (Fig. 1). Thus it could be considered as an extensional structure developed in inland area of the stable Yangtze craton, which probably represents the western front of the Late Mesozoic lithospheric thinning of the SCB. This is also comparable with the deep crustal structure indicated by the *P*-wave crustal velocity from a wide angle reflection profile (Z.J. Zhang et al., 2009). The crustal thickness decreases from 42 km to 30 km across the Zigui basin, Huangling massif and Jianghan basin (Fig. 11D).

6. Conclusions

Available structural, sedimentary and geochronological data allow us to draw a general picture of the Huangling massif that appears as an N–S striking antiform. The Huangling massif recorded an inherited paleo-relief in the Yangtze craton around 750 Ma. The Early Paleozoic and Early Mesozoic orogenies of South China had no significant imprint on the architecture of the Huangling massif. The Neoproterozoic–Triassic strata on the western and eastern sides of the Huangling massif were involved in a series of oppositely directed gravitational décollements and layer-parallel slip surfaces that accommodated the uplifting. The subsequently brittle normal faulting controlled the deposition of the rift basin on its eastern flank. The involvement of the Late Jurassic strata and the unconformable superposition of the Early Cretaceous conglomerate indicate that the uplifting of the Huangling massif occurred between the Late Jurassic and Early Cretaceous, which is in agreement with a cooling process between 160 Ma and 110 Ma revealed by thermochronology. Perhaps because of its location in stable crust of the SCB, the deformation is rather weak and developed in response to its uplift. The extensional or compressional setting of the Huangling massif is not settled yet. If compressional, the anticline may develop on top of a speculated blind thrust. If extensional, this structure probably represents the western front of the Late Mesozoic lithospheric thinning in South China.

Acknowledgements

Field and laboratory expenses have been funded by the Chinese National 973 Project (No. 2009CB825008), National Natural Science Foundation of China (No. 41225009), Innovative Project of the Chinese Academy of Sciences (No. KZCX1-YW-15-1), and the Major National Science and Technology Project (No. 2011ZX05008-001). Jacques Charvet and Liangshu Shu are gratefully appreciated for their critical and constructive reviews.

References

BGMRHB, 1990. Bureau of Geology and Mineral Resources of Hubei Province, Regional Geology of Hubei Province. Geological Publishing House, Beijing, pp. 1–705 (in Chinese with English abstract).

Burchfiel, B.C., Chen, Z., Liu, Y., Royden, L.H., 1995. Tectonics of the Longmen Shan and adjacent regions. International Geology Review 37, 661–735.

Carter, A., Clift, P., 2008. Was the Indosinian orogeny a Triassic mountain building or a thermotectonic reactivation event? Comptes Rendus Géoscience 340, 83–93.

Carter, A., Roques, D., Bristow, C., Kinny, P., 2001. Understanding Mesozoic accretion in Southeast Asia: significance of Triassic thermotectonism (Indosinian orogeny) in Vietnam. Geology 29, 211–214.

Charvet, J., Shu, L.S., Shi, Y.S., Guo, L.Z., Faure, M., 1996. The building of south China: collision of Yangzi and Cathaysia blocks, problems and tentative answers. Journal of Southeastern Asian Earth Science 13, 223–235.

Charvet, J., Shu, L.S., Faure, M., Choulet, F., Wang, B., Lu, H.F., Le Breton, N., 2010. Structural development of the Lower Paleozoic belt of South China: genesis of an intracontinental orogen. Journal of Asian Earth Science 39, 309–330.

Chen, A., 1999. Mirror thrusting in the South China Orogenic Belt: tectonic evidence from western Fujian, southeastern China. Tectonophysics 305, 497–519.

Chen, S.F., Wilson, C.J.L., 1996. Emplacement of the Longmen Shan Thrust-Nappe Belt along the eastern margin of the Tibetan Plateau. Journal of Structural Geology 18, 413–440.

Chen, J.F., Foland, K.A., Xing, F.M., Xu, X., Zhou, T.X., 1991. Magmatism along the southeast margin of the Yangtze Block. Precambrian collision of the Yangtze and Cathaysia Blokcs of China. Geology 19, 815–818.

Chen, K., Gao, S., Wu, Y.B., Guo, J.L., Hu, Z.C., Liu, Y.S., Zong, K.Q., Liang, Z.W., Geng, X.L., 2013. 2.6–2.7 Ga crustal growth in Yangtze craton, South China. Precambrian Research 224, 472–490.

Chu, Y., Lin, W., 2014. Phanerozoic polyorogenic deformation in southern Jiuling massif, northern South China block: constraints from structural analysis and geochronogy. Journal of Asian Earth Sciences 86, 117–130.

Chu, Y., Faure, M., Lin, W., Wang, Q.C., 2012a. Early Mesozoic Tectonics of the South China block: insights from the Xuefengshan intracontinental orogen. Journal of Asian Earth Sciences 61, 199–220.

Chu, Y., Faure, M., Lin, W., Wang, Q.C., Ji, W.B., 2012b. Tectonics of the Middle Triassic intracontinental Xuefengshan Belt, South China: new insights from structural and chronological constraints on the basal décollement zone. International Journal of Earth Sciences 101, 2125–2150.

Chu, Y., Lin, W., Faure, M., Wang, Q.C., Ji, W.B., 2012c. Phanerozoic tectonothermal events of the Xuefengshan Belt, central South China: implications from U/Pb age and Lu/Hf determinations of granites. Lithos 150, 243–255.

Condon, D., Zhu, M., Bowring, S., Wang, W., Yang, A., Jin, Y., 2005. U–Pb ages from the Neoproterozoic Doushantuo Formation, China. Science 308, 95–98.

Dai, S.W., 1996. Discussion on the regional structural features of Jianghan basin since Indosinian movement. Journal of Geomechanics 2, 80–84 (in Chinese with English abstract).

Faure, M., Sun, Y., Shu, L., Monié, P., Charvet, J., 1996. Extensional tectonics within a subduction-type orogen. The case study of the Wugongshan dome (Jiangxi Province, SE China). Tectonophysics 263, 77–108.

Faure, M., Lin, W., Sun, Y., 1998. Doming in the southern foreland of the Dabieshan (Yangtse block, China). Terra Nova 10, 307–311.

Faure, M., Lin, W., Shu, L., Sun, Y., Schärer, U., 1999. Tectonics of the Dabieshan (eastern China) and possible exhumation mechanism of ultrahigh-pressure rocks. Terra Nova 11, 251–258.

Faure, M., Lin, W., Schärer, U., Shu, L., Sun, Y., Arnaud, N., 2003. Continental subduction and exhumation of UHP rocks. Structural and geochronological insights from the Dabieshan (East China). Lithos 70, 213–241.

Faure, M., Shu, L., Wang, B., Charvet, J., Choulet, F., Monie, P., 2009. Intracontinental subduction: a possible mechanism for the Early Palaeozoic Orogen of SE China. Terra Nova 21, 360–368.

Feng, D.Y., Li, Z.C., Zhang, Z.C., 1991. Emplace age and isotope characteristics of massives in the south of Huangling granitoids. Hubei Geology 5, 1–12 (in Chinese with English abstract).

Gao, W., Zhang, C.H., 2009. Zircon SHRIMP U–Pb ages of the Huangling granite and the tuff beds from Liantuo Formation in the Three Gorges area of Yangtze River, China and its geological significance. Geological Bulletin of China 28, 45–50 (in Chinese with English abstract).

Gao, S., Ling, W.L., Qiu, Y.M., Zhou, L., Hartmann, G., Simon, K., 1999. Contrasting geochemical and Sm–Nd isotopic compositions of Archean metasediments from the Kongling high-grade terrain of the Yangtze craton: evidence for cratonic evolution and redistribution of REE during crustal anatexis. Geochimica et Cosmochimica Acta 63 (13–14), 2071–2088.

Gao, S., Yang, J., Zhou, L., Li, M., Hu, Z.C., Guo, J.L., Yuan, H.L., Gong, H.J., Xiao, G.Q., Wei, J.Q., 2011. Age and growth of the Archean Kongling terrain, South China, with emphasis on 3.3 Ga granitoid gneisses. American Journal of science 311, 153–182.

Ge, X.H., Wang, M.P., Liu, J.L., 2010. Redefining the Sichuan Movement and the age and background of Qingzang plateau's first uplift: the implication of Huangling anticline and its enlightenment. Earth Science Frontiers 17, 206–217 (in Chinese with English abstract).

Gilder, S., Keller, G.R., Luo, M., 1991. Timing and spatial distribution of rifting in China. Tectonophysics 197, 225–243.

Gilder, S.A., Gill, J., Coe, R.S., Zhao, X.X., Liu, Z.W., Wang, G.X., Yuan, K.R., Liu, W.L., Kuang, G.D., Wu, H.R., 1996. Isotopic and paleomagnetic constraints on the Mesozoic tectonic evolution of south China. Journal of Geophysical Research 101, 16137–16154.

Guo, L.Z., Shi, Y.S., Lu, H.F., Ma, R.S., Dong, H., 1989. The pre-Devonian tectonic patterns and evolution of South China. Journal of Southeast Asian Earth Sciences 3, 87–93.

Hacker, B.R., Ratschbacher, L., Webb, L.E., McWilliams, M., Ireland, T., Dong, S., Calvert, A., Wenk, H.R., 2000. Exhumation of ultrahigh-pressure continental crust in east-central China: Late Triassic-Early Jurassic tectonic unroofing. Journal of Geophysical Research 105, 13339–13364.

Hsü, K.J., Sun, S., Li, J.L., Chen, H.H., Peng, H.P., Şengör, A.M.C., 1988. Mesozoic overthrust tectonics in South China. Geology 16, 418–421.

Hsü, K.J., Li, J.L., Chen, H.H., Wang, Q.C., Sun, S., Şengör, A.M.C., 1990. Tectonics of South China: key to understanding West pacific geology. Tectonophysics 183, 9–39.

Hu, S.L., Liu, H.Y., Wang, S.S., Hu, W.H., Sang, H.Q., Qiu, J., 1989. On the age of Sinian lower boundary inferred from the new $^{40}Ar/^{39}Ar$ data. Scientia Geologica Sinica 1, 16–25 (in Chinese with English abstract).

Hu, S.B., Raza, A., Min, K., Kohn, B.P., Reiners, P.W., Ketcham, R.A., Wang, J.Y., Gleadow, A.J.W., 2006. Late Mesozoic and Cenozoic thermotectonic evolution along a transect from the north China craton through the Qinling orogen into

the Yangtze craton, central China. Tectonics 25, TC6009. http://dx.doi.org/10.1029/2006TC001985.
Hu, J.M., Chen, H., Qu, H.J., Wu, G.L., Yang, J.X., Zhang, Z.Y., 2012. Mesozoic deformations of the Dabashan in the southern Qinling orogen, central China. Journal of Asian Earth Sciences 47, 171–184.
Huang, T.K., 1978. An outline of the tectonic characteristics of China. Ecologae Geologicae Helvetiae 71, 611–635.
Ji, W.B., Lin, W., Shi, Y.H., Wang, Q.C., Chu, Y., 2011. Structure and evolution of the Early Cretaceous Dabieshan metamorphic core complex. Chinese Journal of Geology 46, 161–180 (in Chinese with English abstract).
Jiang, L.S., Chen, T.L., Zhou, Z.Y., 2002. Several principal geological problems in Huangling. Hubei Geology and Mineral Resources 16, 8–13 (in Chinese with English abstract).
Jiao, W.F., Wu, Y.B., Yang, S.H., Peng, M., Wang, J., 2009. The oldest basement rock in the Yangtze Craton revealed by zircon U–Pb age and Hf isotope composition. Science in China (Series D) 52, 1393–1399.
Koppers, A.A.P., 2002. ArArCALC—software for $^{40}Ar/^{39}Ar$ age calculations. Computers & Geosciences 28, 605–619.
Lepvrier, C., Van Vuong, N., Maluski, H., Truong Thi, P., Van Vu, T., 2008. Indosinian tectonics in Vietnam. Comptes Rendus Geoscience 340, 94–111.
Li, Z.X., 1998. Tectonic history of the major East Asian lithospheric blocks since the mid-Proterozoic—a synthesis. American Geophysical Union, Geodynamics Series 27, 221–243.
Li, X.H., 2000. Cretaceous magmatism and lithospheric extension in Southeast China. Journal of Asian Earth Sciences 18, 293–305.
Li, Z.X., Li, X.H., 2007. Formation of the 1300-km-wide intracontinental orogen and postorogenic magmatic province in Mesozoic South China: a flat-slab subduction model. Geology 35, 179–182.
Li, X.M., Shan, Y.H., 2011. Diverse exhumation of the Mesozoic tectonic belt within the Yangtze Plate, China, determined by apatite fission-track thermochronology. Geosciences Journal 15, 349–357.
Li, Z.C., Wang, G.H., Zhang, Z.C., 2002. Isotopic age spectrum of the Huangling granitic batholith, western Hubei. Geology and Mineral Resources of South China 3, 19–28 (in Chinese with English abstract).
Li, Z.X., Evans, D.A.D., Zhang, S., 2004. A 90° spin on Rodinia: possible causal links between the Neoproterozoic supercontinent, superplume, true polar wander and low-latitude glaciations. Earth and Planetary Science Letters 220, 409–421.
Li, Y.L., Zhou, H.W., Li, X.H., Luo, Q.H., 2007. $^{40}Ar–^{39}Ar$ plateau ages of biotite and amphibole from tonalite of Huangling granitoids and their cooling curve. Acta Petrologica Sinica 23, 1067–1074 (in Chinese with English abstract).
Li, X.B., Wang, C.S., Liu, A., 2008. Sedimentary response to the Indosinian movement—a case study of the Mid-Upper Triassic in the Zigui basin, Hubei. Geology in China 35, 984–991 (in Chinese with English abstract).
Li, X.H., Li, W.X., Li, Z.X., Lo, C.H., Wang, J., Ye, M.F., Yang, Y.H., 2009. Amalgamation between the Yangtze and Cathaysia Blocks in South China: constraints from SHRIMP U–Pb zircon ages, geochemistry and Nd–Hf isotopes of the Shuangxiwu volcanic rocks. Precambrian Research 174, 117–128.
Li, Z.X., Li, X.H., Wartho, J.A., Clark, C., Li, W.X., Zhang, C.L., Bao, C., 2010. Magmatic and metamorphic events during the early Paleozoic Wuyi–Yunkai orogeny, southeastern South China: new age constraints and pressure-temperature conditions. Geological Society of America Bulletin 122, 772–793.
Li, S.Z., Santosh, M., Zhao, G.C., Zhang, G.W., Jin, C., 2011. Intracontinental deformation in a frontier of super-convergence: a perspective on the tectonic milieu of the South China Block. Journal of Asian Earth Sciences 49, 313–329.
Li, S.Z., Zhao, G.C., Dai, L.M., Liu, X., Zhou, L.H., Santosh, M., Suo, Y.H., 2012. Mesozoic basins in eastern China and their bearing on the deconstruction of the North China Craton. Journal of Asian Earth Sciences 47, 64–79.
Li, J.H., Zhang, Y.Q., Dong, S.W., Shi, W., 2013. Structural and geochronological constraints on the Mesozoic tectonic evolution of the North Dabashan zone, South Qinling, central China. Journal of Asian Earth Sciences 64, 99–114.
Lin, W., Wang, Q.C., 2006. Late Mesozoic extensional tectonics in North China block: a crustal response to the lithosphere removal of North China Craton? Bulletin de la Société Géologique de France 177, 287–297.
Lin, W., Faure, M., Monié, P., Schärer, U., Zhang, L.S., Sun, Y., 2000. Tectonics of SE China, new insights from the Lushan massif (Jiangxi Province). Tectonics 19, 852–871.
Lin, W., Wang, Q.C., Chen, K., 2008. Phanerozoic tectonics of south China block: new insights from the polyphase deformation in the Yunkai massif. Tectonics 27, TC6004. http://dx.doi.org/10.1029/2007TC002207.
Lin, W., Shi, Y.H., Wang, Q.C., 2009. Exhumation tectonics of the HP–UHP orogenic belt in Eastern China: new structural–petrological insights from the Tongcheng massif, Eastern Dabieshan. Lithos 109, 285–303.
Lin, W., Faure, M., Chen, Y., Ji, W.B., Wang, F., Wu, L., Charles, N., Wang, Q.C., 2013. Late Mesozoic compressional to extensional tectonics in the Yiwulüshan massif, NE China and its bearing on the evolution of the Yinshan–Yanshan orogenic belt Part I: structural analyses and geochronological constraints. Gondwana Research 23, 54–77.
Ling, W.L., Gao, S., Zhang, H.F., Zhou, L., Zhao, Z.B., 1998. An Sm–Nd isotopic dating study of the Archean Kongling Complex in the Huangling area of the Yangtze Craton. Chinese Science Bulletin 43, 1187–1191.
Ling, W.L., Gao, S., Zhang, B.R., Zhou, L., Xu, Q.D., 2001. The recognizing of ca. 1.95 Ga tectono-thermal event in Kongling nucleus and its significance for the evolution of Yangtze Block. South China. Chinese Science Bulletin 46, 326–329.
Ling, W.L., Gao, S., Cheng, J.P., Jiang, L.S., Yuan, H.L., Hu, Z.C., 2006. Neoproterozoic magmatic events within the Yangtze continental interior and along its northern margin and their tectonic implication: constraint from the ELA-ICPMS U–Pb geochronology of zircons from the Huangling and Hannan complexes. Acta Petrologica Sinica 22, 387–396 (in Chinese with English abstract).
Liu, S.F., Steel, R., Zhang, G.W., 2005. Mesozoic sedimentary basin development and tectonic implication, northern Yangtze Block, eastern China: record of continent–continent collision. Journal of Asian Earth Sciences 25, 9–27.
Liu, X.M., Gao, S., Diwu, C.R., Ling, W.L., 2008. Precambrian growth of Yangtze craton as revealed by detrital zircon studies. American Journal of Science 308, 421–468.
Liu, H.J., Xu, C.H., Zhou, Z.Y., Donelick, R.A., 2009. Detrital apatite fission track thermochronological constraints on the formation of the Huangling uplift (165–100 Ma). Progress in Natural Science 19, 1326–1332 (in Chinese).
Lovera, O.M., Grove, M., Harrison, T.M., Mahon, K.I., 1997. Systematic analysis of K-feldspar $^{40}Ar/^{39}Ar$ step heating results: I. Significance of activation energy determinations. Geochimica et Cosmochimica Acta 61, 3171–3192.
Lovera, O.M., Grove, M., Harrison, T.M., 2002. Systematic analysis of K-feldspar $^{40}Ar/^{39}Ar$ step heating results II: Relevance of laboratory argon diffusion properties to nature. Geochimica et Cosmochimica Acta 66, 1237–1255.
Ma, G.G., Li, H.Q., Zhang, Z.C., 1984. An investigation of the age limits of the Sinian System in South China. Bulletin of Yichang Institute of Geology and Mineral Resources 8, 1–29 (in Chinese with English abstract).
Ma, D.Q., Li, Z.C., Xiao, Z.F., 1997. The constitute, geochronology and geologic evolution of the Kongling complex, western Hubei. Acta Geoscientia Sinica 18, 233–241 (in Chinese with English abstract).
Ma, D.Q., Du, S.H., Xiao, Z.F., 2002. The origin of Huangling granite batholiths. Acta Petrologica et Mineralogica 21, 151–161 (in Chinese with English abstract).
Mattauer, M., Matte, Ph., Malavieille, J., Tapponnier, P., Maluski, H., Xu, Z.Q., Lu, Y.L., Tang, Y.Q., 1985. Tectonics of Qinling belt: build-up and evolution of eastern Asia. Nature 317, 496–500.
McDougall, I., Harrison, T.M., 1999. Geochronology and Thermochronology by the $^{40}Ar/^{39}Ar$ Method. Oxford University Press, Oxford, pp. 1–269.
Meng, F.S., Li, X.B., 2003. Meticulous correlation of Upper Triassic Series on the eastern and western limbs of the Huangling dome, western Hubei. Geology and Mineral Resources of South China 4, 60–65 (in Chinese with English abstract).
Meng, Q.R., Hu, J.M., Jin, J.Q., Zhang, Y., Xu, D.F., 2003. Tectonics of the Late Mesozoic wide extension basin system in the China-Mongolia border region. Basin Research 15, 397–415.
Meng, Q.R., Wang, E., Hu, J.M., 2005. Mesozoic sedimentary evolution of the northwest Sichuan basin: implication for continued clockwise rotation of the South China block. Geological Society of America Bulletin 117, 396–410.
Menzies, M., Xu, Y.G., Zhang, H.F., Fan, W.M., 2007. Integration of geology, geophysics and geochemistry: a key to understanding the North China Craton. Lithos 96, 1–21.
Peng, S.B., Kusky, T.M., Jiang, X.F., Wang, L., Wang, J.P., Deng, H., 2012. Geology, geochemistry, and geochronology of the Miaowan ophiolite, Yangtze craton: implications for South China's amalgamation history with the Rodinian supercontinent. Gondwana Research 21, 577–597.
Qiu, Y.M., Gao, S., McNaughton, N.J., Groves, D.I., Ling, W., 2000. First evidence of >3.2 Ga continental crust in the Yangtze craton of south China and its implications for Archean crustal evolution and Phanerozoic tectonics. Geology 28, 11–14.
Qu, H.J., Hu, J.M., Cui, J.J., Wu, G.L., Tian, M., Shi, W., Zhao, S.L., 2009. Jurassic sedimentary filling process of Zigui basin on the eastern section of Daba mountain tectonic belt and its structural evolution. Acta Geologica Sinica 83, 1254–1268 (in Chinese with English abstract).
Ratschbacher, L., Hacker, B.R., Webb, L.E., McWilliams, M., Ireland, T., Dong, S., Clavert, A., Chateigner, D., Wenk, H.R., 2000. Exhumation of the ultrahigh-pressure continental crust in east central China: cretaceous and Cenozoic unroofing and the Tan–Lu fault. Journal of Geophysical Research 105, 13303–13338.
Ratschbacher, L., Hacker, B.R., Calvert, A., Webb, L.E., Grimmer, J.C., McWilliams, M.O., Ireland, T., Dong, S., Hu, J., 2003. Tectonics of the Qinling (central China): tectonostratigraphy, geochronology, and deformation history. Tectonophysics 366, 1–53.
Ren, J., Tamaki, K., Li, S., Zhang, J., 2002. Late Mesozoic and Cenozoic rifting and its dynamic setting in Eastern China and adjacent areas. Tectonophysics 344, 175–205.
Richardson, N.J., Densmore, A.L., Seward, D., Wipf, M., Yong, L., 2010. Did incision of the Three Gorges begin in the Eocene? Geology 38, 551–554.
Roger, F., Jolivet, M., Malavieille, J., 2010. The tectonic evolution of the Songpan–Garzê (North Tibet) and adjacent areas from Proterozoic to present: a synthesis. Journal of Asian Earth Sciences 39, 254–269.
Shen, C.B., Mei, L.F., Liu, Z.Q., Xu, S.H., 2009. Apatite and zircon fission track data, evidences for the Mesozoic–Cenozoic uplift of Huangling dome, central China. Journal of Mineralogy and Petrology 29, 54–60 (in Chinese with English abstract).
Shen, C.B., Mei, L.F., Peng, L., Chen, Y.Z., Yang, Z., Hong, G.F., 2012. LA-ICPMS U–Pb zircon age constraints on the provenance of Cretaceous sediments in the Yichang area of the Jianghan Basin, central China. Cretaceous Research 34, 172–183.
Shi, W., Zhang, Y., Dong, S., Hu, J., Wiesinger, M., Ratschbacher, L., Jonckheere, J., Li, J., Tian, M., Chen, H., Wu, G., Ma, L., Li, H., 2012. Intra-continental Dabashan orocline, southwestern Qinling, Central China. Journal of Asian Earth Sciences 46, 20–38.

Shu, L.S., Charvet, J., 1996. Kinematics and geochronology of the Proterozoic Dongxiang–Shexian ductile hear zone: with HP metamorphism and ophiolitic melange (Jiangnan Region, China). Tectonophysics 267, 291–302.

Shu, L.S., Faure, M., Wang, B., Zhou, X.M., Song, B., 2008. Late Paleozoic-Early Mesozoic geological features of South China: response to the Indosinian collision events in Southeastern Asia. Comptes Rendus Geoscience 340, 151–165.

Shu, L.S., Zhou, X.M., Deng, P., Wang, B., Jiang, S.Y., Yu, J.H., Zhao, X.X., 2009. Mesozoic tectonic evolution of the Southeast China Block: new insights from basin analysis. Journal of Asian Earth Science 34, 376–391.

Shui, T., 1988. Tectonic framework of the continental basement of southeast China. Scientia Sinica (Series B) 31, 885–896.

Wang, D.Z., Shu, L.S., Faure, M., Sheng, W.Z., 2001. Mesozoic magmatism and granitic dome in the Wugongshan massif, Jingxi province and their genetiocl relationship to the tectonic events in southeast China. Tectonophysics 339, 259–277.

Wang, E., Meng, Q.R., Burchfiel, B.C., Zhang, G.W., 2003. Mesozoic large-scale lateral extrusion, rotation, and uplift of the Tongbai–Dabie shan belt in east China. Geology 31, 307–310.

Wang, Y.J., Zhang, Y.H., Fan, W.M., Peng, T.P., 2005. Structural signatures and $^{40}Ar/^{39}Ar$ geochronology of the Indosinian Xuefengshan tectonic belt, South China Block. Journal of Structural Geology 27, 985–998.

Wang, F., He, H.Y., Zhu, R.X., Sang, H.Q., Wang, Y.L., Yang, L.K., 2006. Intercalibration of international and domestic $^{40}Ar–^{39}Ar$ dating standards. Science in China (Series D) 49, 461–470.

Wang, Y.J., Fan, W.M., Cawood, P.A., Ji, S.C., Peng, T.P., Chen, X.Y., 2007. Indosinian high-strain deformation for the Yunkaidashan tectonic belt, south China: kinematics and $^{40}Ar/^{39}Ar$ geochronological constraints. Tectonics 26, TC6008. http://dx.doi.org/10.1029/2007TC002099.

Wang, Y.J., Zhang, F.F., Fan, W.M., Zhang, G.W., Chen, S.Y., Cawood, P.A., Zhang, A.M., 2010. Tectonic setting of the South China Block in the early Paleozoic: resolving intracontinental and ocean closure models from detrital zircon U–Pb geochronology. Tectonics 29, TC6020. http://dx.doi.org/10.1029/2010TC002750.

Wang, J., Chu, Y., Lin, W., Wang, Q.C., 2010. Structural geometry and the origin of the Huangling anticline. Chinese Journal of Geology 45, 615–625 (in Chinese with English abstract).

Wang, T., Zheng, Y.D., Zhang, J.J., Zeng, L.S., Donskaya, T., Guo, L. and Li J.B., 2011a. Pattern and kinematic polarity of Late Mesozoic extension in continental NE Asia: perspectives from metamorphic core complexes, Tectonics, 30, TC6007, doi:10.1029/2011TC002896.

Wang, Y.S., Xiang, B.W., Zhu, G., Jiang, D.Z., 2011. Structural and geochronological evidence for Early Cretaceous orogen-parallel extension of the ductile lithosphere in the northern Dabie orogenic belt, East China. Journal of Structural Geology 33, 362–380.

Wei, W., Chen, Y., Faure, M., Shi, Y.H., Martelet, G., Hou Q.L., Lin, W., Le Breton, N., Wang, Q.C., 2014. A multidisciplinary study on the emplacement mechanism of the Qingyang-Jiuhua Massif in Southeast China and its tectonic bearings. Part I: structural geology, AMS and paleomagnetism. Journal of Asian Earth Sciences 86, 76–93.

Wu, F.Y., Lin, J.Q., Wilde, S.A., Zhang, X.O., Yang, J.H., 2005. Nature and significance of the Early Cretaceous giant igneous event in eastern China. Earth and Planetary Sciences Letters 233, 103–119.

Wu, F.Y., Xu, Y.G., Gao, S., Zheng, J.P., 2008. Controversial on studies of the lithospheric thinning and craton destruction of North China. Acta Petrologica Sinica 24, 1145–1174 (in Chinese with English abstract).

Xu, Y.G., 2007. Diachronous lithospheric thinning of the North China Craton and formation of the Daxin'anling–Taihangshan gravity lineament. Lithos 96, 281–298.

Xu, Z.Y., Lin, G., Liu, C.Y., Wang, Y.J., Guo, F., 2004. A discussion on amalgamation course between the South China and North China blocks: evidences from deformational characters in the Jianghan superimposed basin. Chinese Journal of Geology 39, 284–295 (in Chinese with English abstract).

Xu, C.H., Zhou, Z.Y., Chang, Y., Guillot, F., 2010. Genesis of Daba arcuate structural belt related to adjacent basement upheavals: constraints from Fission-track and (U–Th)/He thermochronology. Science China – Earth Sciences 53, 1634–1646.

Yan, D.P., Zhou, M.F., Song, H.L., Wang, X.W., Malpas, J., 2003. Origin and tectonic significance of a Mesozoic multi-layer over-thrust system within the Yangtze Block (South China). Tectonophysics 361, 239–254.

Yan, D.P., Zhou, M.F., Li, S.B., Wei, G.Q., 2011. Structural and geochronological constraints on the Mesozoic–Cenozoic tectonic evolution of the Longmen Shan thrust belt, eastern Tibetan Plateau. Tetonics 30, TC6005. http://dx.doi.org/10.1029/2011TC002867.

Yang, J.H., Wu, F.Y., Wilde, S.A., Belousova, E., Griffin, W.L., 2008. Mesozoic decratonization of the North China block. Geology 36, 467–470.

Yu, A.N., Ye, B.L., 1998. The affirmation of Dayunshan metamorphic core complex structure and its origin. Hunan Geology 17, 81–84 (in Chinese with English abstract).

Zhang, H.D., 1986. Preliminary analysis of the formation and tectonic evolution of Huangling anticline. Journal of Jianghan Petroleum Institute 10, 29–40 (in Chinese).

Zhang, J.J., Zheng, Y.D., 1999. Multistage extension and age dating of the Xiaoqinling Meatmorpic core complex, central China. Acta Geological Sinica 73, 139–147.

Zhang, Zh.M., Liou, J.G., Coleman, R.G., 1984. An outline of the plate tectonics of China. Geological Society of America Bulletin 95, 295–312.

Zhang, S.B., Zheng, Y.F., Wu, Y.B., Zhao, Z.F., Gao, S., Wu, F.Y., 2006a. Zircon isotope evidence for $\geqslant$3.5 Ga continental crust in the Yangtze craton of China. Precambrian Research 146, 16–34.

Zhang, S.B., Zheng, Y.F., Wu, Y.B., Zhao, Z.F., Gao, S., Wu, F.Y., 2006b. Zircon U–Pb age and Hf–O isotope evidence for Paleoproterozoic metamorphic event in South China. Precambrian Research 151, 265–288.

Zhang, S.B., Zheng, Y.F., Wu, Y.B., Zhao, Z.F., Gao, S., Wu, F.Y., 2006c. Zircon U–Pb age and Hf isotope evidence for 3.8 Ga crustal remnant and episodic reworking of Archean crust in South China. Earth and Planetary Science Letters 252, 56–71.

Zhang, S.B., Zheng, Y.F., Zhao, Z.F., Wu, Y.B., Yuan, H.L., Wu, F.Y., 2008. Neoproterozoic anatexis of Archean Lithosphere: geochemical evidence from felsic to mafic intrusive at Xiaofeng in the Yangtze George, South China. Precambrian Research 163, 210–238.

Zhang, S.B., Zheng, Y.F., Zhao, Z.F., Wu, Y.B., Yuan, H.L., Wu, F.Y., 2009. Origin of TTG-like rocks from anatexis of ancient lower crust: geochemical evidence from Neoproterozoic granitoids in South China. Lithos 113, 347–368.

Zhang, Y.Q., Xu, X.B., Jia, D., Shu, L.S., 2009. Deformation record of the change from Indosinian collision-related tectonic system to Yanshanian subduction-related tectonic system in South China during the Early Mesozoic. Earth Science Frontiers 16, 234–247 (in Chinese with English abstract).

Zhang, Z.J., Bai, Z.M., Mooney, W., Wang, C.Y., Chen, X.B., Wang, E., Teng, J.W., Okaya, N., 2009. Crustal structure across the Three Gorges area of the Yangtze platform, central China, from seismic refraction/wide-angle reflection data. Tectonophysics 475, 423–437.

Zhang, Y.Q., Dong, S.W., Li, J.H., Cun, J.J., Shi, W., Su, J.B., Li, Y., 2012. The new progress in the study of Mesozoic tectonics of south China. Acta Geoscientica Sinica 33, 257–279 (in Chinese with English abstract).

Zhao, F.Q., Zhao, W.P., Zuo, Y.C., Li, Z.H., 2006. Zircon U–Pb ages of the migmatites from Kongling complex. Geological Survey and Research 29, 81–85 (in Chinese with English abstract).

Zhao, X.M., Tong, J.N., Yao, H.Z., Tian, Y., 2010. Sedimentary response to the Indosinian movement in Three Gorges area. Journal of Palaeogeography 12, 177–184 (in Chinese with English abstract).

Zhou, X.M., Li, W.X., 2000. Origin of Late Mesozoic igneous rocks in Southeastern China: implications for lithosphere subduction and underplating of mafic magmas. Tectonophysics 326, 269–287.

Zhou, X.M., Sun, T., Shen, W.Z., Shu, L.S., Niu, Y.L., 2006. Petrogenesis of Mesozoic granitoids and volcanic rocks in South China: a response to tectonic evolution. Episodes 29, 26–33.

Zhu, G., Xie, C.L., Chen, W., Xiang, B.W., Hu, Z.Q., 2010. Evolution of the Hongzhen metamorphic core complex: evidence for Early Cretaceous extension in the eastern Yangtze craton, eastern China. Geological Society of America Bulletin 122, 506–516.

Zhu, R.X., Chen, L., Wu, F.Y., Liu, J.L., 2011. Timing, scale and mechanism of the destruction of the North China craton. Science China – Earth Sciences 54, 789–797.

La tectonique extensive à la fin du Mésozoïque en Chine du Sud

Les structures extensives d'âge Mésozoïque tardif (Crétacé) sont très répandues en Eurasie orientale, depuis la Transbaïkalie en Russie jusqu'à l'intérieur de la Chine du Sud. Elles constituent la plus grande province de distension crustale dans le monde. Cette thèse a sélectionné des structures développées dans trois endroits différents du bloc de Chine du sud en utilisant les méthodes de la géologie structurale, de l'anisotropie de la susceptibilité magnétique et de la géochronologie (U-Pb sur zircon et titanite, U-Th-Pb sur monazite et Ar-Ar sur micas et amphiboles). L'expression des structures extensives diffère selon les endroits étudiés: (1) la ceinture orogénique de HP/UHP Tongbai-Dabie, le long de la bordure nord du bloc de Chine du sud a été remaniée par au Crétacé par la formation d'un antiforme ou d'un dôme métamorphique extensif. Contemporaine de la migmatisation et du magmatisme syn-tectonique, le régime extensif a commencé à environ 145 Ma et s'est approché de son point culminant vers 130 Ma. Ce qui a été interprété comme le résultat de la suppression de la racine orogénique. Localement, un nouvel épisode de distension vers 110-90 Ma a également été enregistré; (2) le batholite de Dayunshan-Mufushan intrudif dans l'orogène Neoproterozoic Jiangnan se compose de deux phases d'intrusions granitiques d'âge Jurassique (ca. 150 Ma) et Crétacé inférieur (ca. 132 Ma). Le pluton le plus récent s'est mis en place dans un contexte d'extension NW-SE correspondant au processus amincissement crustal du Crétacé inférieur, avec une faille de détachement développée le long de sa bordure ouest; (3) l'anticlinal de Huangling dans le craton du Yangtze est un pli asymétrique d'axe N-S formé entre le Jurassique et le Crétacé inférieur. Sur les deux flancs, la couverture sédimentaire a participé à une série de plis d'effondrement de vergence opposée et de glissements banc-sur-banc des couches. Les exemples étudiés ci-dessus représentent une série de structures d'extension d'âge Crétacé développées dans différents niveaux structuraux: exhumation de croûte inférieure et moyennede accommodée parun fort étirement, mise en place syn-tectonique de plutons granitiques avec étirement limité, déformation de la couverture sédimentaire sous une faible extension. Ils indiquent que la Chine du Sud a également participé au régime extensif bien connu en Chine du Nord. Ces résultats apportent des données nouvelles de première main permettant de discuter le cadre tectonique et géodynamiques spatio-temporel du régime extensif du Crétacé sur la marge orientale de l'Eurasie.

Late Mesozoic extensional tectonics in South China

Late Mesozoic extensional structures are widespread in eastern Eurasia (from Transbaikalia region in Russia to inland South China). They constitute the largest crustal extensional province in the world. This thesis selected extensional structures developed in three different tectonic settings in the South China block. Detailed studies including structural geology, anisotropy of magnetic susceptibility and geochronology (zircon and titanite U-Pb, monazite U-Th-Pb, and mica Ar-Ar) were conducted. The expression of these extensional structures is not the same for each area: (1) the Tongbai-Dabie HP/UHP orogenic belt along the northern edge of the South China block was reworked by Cretaceous extensional antiform or metamorphic core complex. Coeval with migmatization and syn-tectonic magmatism, the extensional regime started at ca. 145 Ma, and approached its climax at ca. 130 Ma that was signaled by removal of the orogenic root. Locally, a late (110-90 Ma) extensional event was also recorded; (2) the Dayunshan-Mufushan batholith intruding the Neoproterozoic Jiangnan orogen is composed of two phases of granitic intrusions with Late Jurassic (ca. 150 Ma) and Early Cretaceous (ca. 132 Ma) ages, respectively. The late pluton emplaced under a NW-SE extensional setting corresponding to the Early Cretaceous crustal thinning process, with a detachment fault developed along its western margin; (3) the Huangling anticline within the Yangtze craton is a nearly N-S striking asymmetric dome formed between the Late Jurassic and Early Cretaceous. The sedimentary cover on the two flanks was involved in a series of oppositely-directed collapse folding and layer-parallel slipping. These examples of Cretaceous extensional structures in different tectonic levels (exhumation of middle-lower crust by strong stretching, syn-tectonic emplacement of granitic pluton with limited stretching, deformation of sedimentary cover under a weak extension) indicates that South China also was involved into the regional extensional regime coeval with the destruction of the North China craton. These results provide first-hand new structural evidence for further discussing the temporal-spatial framework and geodynamic setting of the Cretaceous extensional tectonics on the eastern margin of Eurasia.

UNIVERSITE D'ORLEANS

Institut des Sciences de la Terre d'Orléans, 45067 Orléans, France

Institut des Géologie et Géophysique (CAS), 100029 Pékin, Chine

INSTITUTE OF GEOLOGY AND GEOPHYSICS, CAS